



**Jorge Augusto  
Oliveira Carneiro**

**Modificação superficial de nanocontentores de  
inibidores de corrosão para melhoria da  
compatibilidade com revestimentos protetores**

**Surface modification of nanocontainers of corrosion  
inhibitors for improved compatibility with protective  
polymer coatings**





**Jorge Augusto  
Oliveira Carneiro**

**Modificação superficial de nanocontentores de  
inibidores de corrosão para melhoria da  
compatibilidade com revestimentos protetores**

**Surface modification of nanocontainers of corrosion  
inhibitors for improved compatibility with protective  
polymer coatings**

Tese apresentada à Universidade de Aveiro para cumprimento dos requisitos necessários à obtenção do grau de Doutor em (Ciência e Engenharia de Materiais), realizada sob a orientação científica do Doutor João André da Costa Tedim, Professor Auxiliar do Departamento de Engenharia de Materiais e Cerâmica da Universidade de Aveiro e do Professor Doutor Mário Guerreiro Silva Ferreira, Professor Catedrático do Departamento de Engenharia de Materiais e Cerâmica da Universidade de Aveiro



Dedicado aos meus pais, irmão, irmã e à Catarina.



## **o júri**

presidente

Prof. Doutor José Carlos Esteves Duarte Pedro  
professor Catedrático da Universidade de Aveiro

Prof. Doutor Fernando Manuel Bico Marques  
professor Catedrático da Universidade de Aveiro

Prof. Doutora Verónica Cortés de Zea Bermudez  
professora Catedrática da Universidade de Trás-os-Montes e Alto Douro

Prof. Doutora Maria de Fátima Grilo da Costa Montemor  
professora Catedrática da Universidade de Lisboa

Doutor Vladimír špacek  
Head of Department da Synpo, República Checa

Prof. Doutor João André da Costa Tedim  
professor auxiliar da Universidade de Aveiro



## agradecimentos

Os meus agradecimentos vão para os meus orientadores Doutor João Tedim e Professor Doutor Mário Ferreira, pela orientação, pela compreensão e apoio incondicional, em todos os momentos. De igual modo agradeço ao Doutor Mikhail Zheludkevich pela orientação dada no início desta tese. Aos três agradeço a confiança depositada em mim para a realização desta tese.

Agradeço ao pessoal técnico do departamento de Cerâmica: Célia, Marta, Maria João, Artur, Bruno, Luísa, Dra. Alexandra. Às técnicas do departamento de Química: Celeste e Margarete. Aos técnicos das oficinas do departamento de Física: Ivo e Mário.

Agradeço o apoio financeiro dos projetos TATA STEEL (2.15.400.22 – Corus) e MSCA-RISE project SMARCOAT (REF: 645662). Também agradeço à Synpo akciová společnost pelas condições despendidas para a realização deste trabalho.

Agradeço às Professoras Paula Seabra e Florinda Costa pela enorme disponibilidade concedida e apoio dado para a finalização desta tese.

Quero agradecer o apoio especial dos colegas do grupo SECOP: Alena, Maksim, Tiago, Cristina, Isabel, Stanley, Aleksey, Silvar, Alexandre, Andrei, Daniel, Marco, Manon, Eddy, Andreia e Diogo. Devo um especial agradecimento ao Dr. Kiryl Yasakau pela ajuda indispensável no desenvolvimento desta tese, nas áreas de revestimentos sol-gel e técnicas eletroquímicas.

Agradeço de forma especial à Ana Caetano e Susana Pereira pelo apoio e amizade dispensados ao longo dos anos.

Finalmente agradeço de forma sentida aos meus pais, irmãos e à Catarina. À Catarina agradeço todo o amor e apoio disponibilizado, a ti devo o enorme crescimento emocional que me permitiu concluir esta tese. Aos meus pais agradeço a oportunidade que me deram de prosseguir os meus estudos, muitas vezes com sacrifícios pessoais consideráveis. À minha irmã Diana pelo apoio e boa disposição, fazendo-me um irmão mais velho muito orgulhoso. Ao meu irmão Rui devo-lhe toda a minha carreira académica. Nenhum texto é suficiente para agradecer o seu enorme sacrifício pessoal que me permitiu terminar os meus estudos. Ele mostrou o verdadeiro significado de ser um irmão! É deles este trabalho, espero ter estado a sua altura.



## palavras-chave

Nanocontentores, modificação da superfície, hidróxidos duplos lamelares, nanocápsulas de sílica, corrosão, compatibilidade, revestimentos, propriedades barreira, espectroscopia de impedância eletroquímica.

## resumo

A aplicação de revestimentos orgânicos é uma das medidas preventivas mais utilizadas na proteção contra corrosão em ligas metálicas. Tipicamente, revestimentos anti-corrosão combinam proteção passiva e ativa, sendo a primeira baseada no efeito barreira do revestimento contra o ingresso de espécies ativas e a segunda devido à presença de inibidores de corrosão dispersos diretamente na matriz do revestimento. Não obstante, a adição direta de inibidores de corrosão a formulações de revestimentos leva normalmente a ocorrência de efeitos negativos, assim prejudicando a desempenho global do revestimento. De forma a contornar esta limitação, micro e nanocontentores, estruturas hospedeiras para o armazenamento e libertação controlada de inibidores de corrosão, têm sido propostos. Se esta libertação for desencadeada por condições adversas que resultam na iniciação de corrosão o efeito de autorreparação tem lugar, o que pode trazer grandes benefícios em aplicações de elevada desempenho. O trabalho apresentado nesta tese tem como objetivo a modificação superficial de nanocontentores a fim de melhorar o papel da inibição e das propriedades barreira de revestimentos, assim como a melhoria da dispersibilidade e compatibilidade dentro do revestimento. Este último é geralmente um tópico que não é abordado na literatura científica e que ao mesmo tempo necessita de um certo nível de interação dos produtores de formulações para revestimentos de forma a corresponder às propriedades desejadas numa formulação comercial. Dois nanocontentores, com comprovada atividade como reservatórios de inibidores de corrosão, foram selecionados: hidróxidos duplos lamelares e nanocápsulas de sílica. A modificação superficial de hidróxidos duplos lamelares intercalados com 2-mercaptobenzotiazol com poliestireno sulfonato/hidrocloreto de polialilamina pela técnica de automontagem camada-a-camada permitiu a incorporação de um segundo inibidor de corrosão, nitrato de cério, ao mesmo tempo melhorando as propriedades barreira do revestimento de sol-gel híbrido. Além de que, o perfil de libertação do 2-mercaptobenzotiazol também foi alterado com a modificação da superfície. Este trabalho à escala laboratorial foi estendido para uma colaboração industrial com um produtor de aço. Neste caso, a modificação de hidróxidos duplos lamelares intercalados com gluconato com alginato levou a melhorias nas propriedades barreira de um revestimento de base poliamida.



**resumo  
(continuação)**

No caso de nanocápsulas de sílica diversos grupos funcionais foram ligados a estes nano-materiais a base de sílica, permitindo uma análise detalhada do efeito que a química de superfície tem na dispersibilidade e compatibilidade com revestimentos. Testes foram realizados em sistemas com uma complexidade crescente, desde solventes, até formulações de sol-gel híbrido e revestimentos comerciais de base aquosa e solvente. As propriedades barreira dos revestimentos foram, na sua maioria, avaliadas por espectroscopia de impedância eletroquímica, frequentemente complementada com diferentes técnicas eletroquímicas, espectroscópicas e de caracterização de superfície, e em alguns casos com testes padrão realizados em ambiente industrial.

Os resultados provaram a importância que a modificação da superfície tem na dispersão dos nano-contentores e na compatibilidade entre nano-contentores e revestimentos.

Os resultados obtidos demonstram que a modificação da superfície destes nanocontentores pode permitir ajustar a sua interação com a matriz do revestimento, abrindo perspectivas para a industrialização destas tecnologias de liberação controlada na área dos revestimentos de proteção.



**keywords**

Nanocontainers, surface modification, layered double hydroxides, silica nanocapsules, corrosion, compatibility, coatings, barrier properties, electrochemical impedance spectroscopy.

**abstract**

The application of organic coatings is one of the most widely used preventive measures to protect metal alloys against corrosion. Typically, anti-corrosion coatings combine passive and active protection, the former being based upon barrier effect of the matrix against ingress of active species and the latter due to the presence of corrosion inhibitors directly dispersed in the coating matrix. Nevertheless, the direct addition of corrosion inhibitors to coating formulations often leads to detrimental effects, thus impairing the overall coating performance. To circumvent this limitation, micro and nanocontainers as hosting structures for storage and controlled release of corrosion inhibitors, have been proposed. If this release is triggered by adverse conditions that result in corrosion initiation self-healing takes place, which can bring great benefit to high-performance applications.

The work presented in this thesis aims at modifying the nanocontainers surface in order to enhance the role of inhibition and barrier properties of the coatings as well as improving their dispersibility and compatibility within the coating. This latter part of the study had not been in general addressed in the scientific literature and requires interaction with the coating producer in order to match the desired properties for a commercial formulation.

Two nanocontainers to store the corrosion inhibitors were selected: layered double hydroxides (LDH) and silica nanocapsules (Si<sub>2</sub>NC). The surface modification of LDH loaded with 2-mercaptobenzothiazole (2-MBT) with poly(styrene sulfonate)/poly(allylamine hydrochloride) by the layer-by-layer self-assembly technique allowed the incorporation of a second corrosion inhibitor, cerium nitrate, but at the same time improve the coating barrier properties of the hybrid sol-gel coatings. Moreover, the release profile of 2-MBT was also changed with this surface modification. This lab-scale work was extended to an industrial collaboration with a steel producer. In this case, the modification of gluconate loaded LDH with alginate lead to improvement in coating barrier properties of a polyamide-based coating.



**Abstract  
(continuation)**

In the case of Si<sub>3</sub>N<sub>4</sub> NC several functional groups were grafted onto these silica-based nanomaterials, allowing a thorough analysis of the effect the surface chemistry on the dispersibility and compatibility with coatings. Tests were carried out in systems with increasing complexity from solvents, to hybrid sol-gel formulations and water- and solvent-based coating formulations industrially available.

The coating barrier properties were mainly assessed by electrochemical impedance spectroscopy, often complemented with other electrochemical methods. Spectroscopic and surface-characterization techniques, and in some cases standard tests carried out under an industrial environment were also used. The results prove the importance that the surface modification has on the nanocontainer dispersibility and in the nanocontainer/coating compatibility.

These results obtained show that surface modification of these nanocontainers can tune the interaction with coating matrix, opening prospects for the industrialization of these controlled-release technologies in the area of protective coatings.



# Contents

<b>CONTENTS .....</b>	<b>1</b>
<b>LIST OF ABBREVIATIONS AND SYMBOLS.....</b>	<b>5</b>
<b>LIST OF FIGURES.....</b>	<b>9</b>
<b>LIST OF TABLES .....</b>	<b>21</b>
<b><u>1 INTRODUCTION.....</u></b>	<b><u>25</u></b>
<b><u>2 STATE OF THE ART .....</u></b>	<b><u>31</u></b>
<b>2.1 CORROSION .....</b>	<b>33</b>
2.1.1 UNIFORM CORROSION.....	34
2.1.2 INTERGRANULAR CORROSION .....	35
2.1.3 GALVANIC CORROSION.....	37
2.1.4 PITTING CORROSION .....	38
2.1.5 CREVICE CORROSION.....	41
2.1.6 CORROSION COSTS .....	42
<b>2.2 ACTIVE METAL ALLOYS.....</b>	<b>46</b>
2.2.1 ALUMINUM ALLOY 2024-T3.....	46
2.2.2 STEEL.....	52
<b>2.3 CORROSION PROTECTION .....</b>	<b>60</b>
2.3.1 SUBSTRATE SURFACE PRETREATMENT.....	60
2.3.2 CORROSION INHIBITORS .....	66
2.3.3 PROTECTIVE COATINGS .....	71
<b>2.4 MULTI-LEVEL PROTECTION .....</b>	<b>78</b>
2.4.1 LAYERED DOUBLE HYDROXIDES (LDH) .....	79
2.4.2 SILICA NANOCAPSULES (SI_NC).....	81
2.4.3 OTHER RELEVANT HOSTING SYSTEMS.....	84
<b>2.5 NANOCONTAINERS SURFACE MODIFICATION .....</b>	<b>87</b>
2.5.1 COMPATIBILITY WITH COATINGS .....	88
2.5.2 SURFACE MODIFICATION .....	91
<b><u>3 PRINCIPLES OF EXPERIMENTAL TECHNIQUES.....</u></b>	<b><u>101</u></b>
<b>3.1 SPECTROSCOPIC CHARACTERIZATION.....</b>	<b>103</b>

3.1.1	FOURIER TRANSFORM INFRARED (FTIR) .....	103
3.1.2	X-RAY DIFFRACTION .....	106
3.1.3	X-RAY PHOTOELECTRON SPECTROSCOPY .....	107
<b>3.2</b>	<b>IMAGING .....</b>	<b>109</b>
3.2.1	SCANNING ELECTRON MICROSCOPY .....	109
3.2.2	ATOMIC FORCE MICROSCOPY .....	111
<b>3.3</b>	<b>THERMAL ANALYSIS .....</b>	<b>113</b>
3.3.1	THERMOGRAVIMETRIC ANALYSIS .....	113
3.3.2	DIFFERENTIAL SCANNING CALORIMETRY .....	114
<b>3.4</b>	<b>MECHANICAL CHARACTERIZATION .....</b>	<b>115</b>
<b>3.5</b>	<b>ELECTROCHEMICAL TESTS .....</b>	<b>116</b>
3.5.1	POTENTIODYNAMIC POLARIZATION .....	116
3.5.2	ELECTROCHEMICAL IMPEDANCE SPECTROSCOPY .....	118
3.5.3	SCANNING VIBRATING ELECTRODE TECHNIQUE .....	127
<b>4</b>	<b><u>EXPERIMENTAL PROCEDURE .....</u></b>	<b><u>131</u></b>
<b>4.1</b>	<b>METAL SUBSTRATE PRETREATMENT.....</b>	<b>134</b>
4.1.1	AA2024-T3 .....	134
4.1.2	STEEL.....	135
<b>4.2</b>	<b>PREPARATION OF NANOCONTAINERS .....</b>	<b>136</b>
4.2.1	SYNTHESIS OF LAYERED DOUBLE HYDROXIDES (LDHs) .....	136
4.2.2	SURFACE MODIFICATION OF LDH WITH ALGINATE .....	137
4.2.3	SURFACE MODIFICATION OF LDH WITH POLYELECTROLYTES .....	138
4.2.4	SYNTHESIS OF SILICA NANOCAPSULES (SI_NC).....	139
4.2.5	SURFACE MODIFICATION OF SI_NC WITH SILOXANE DERIVATIVES .....	139
<b>4.3</b>	<b>PREPARATION OF PROTECTIVE COATINGS .....</b>	<b>141</b>
4.3.1	SOL-GEL BASED FORMULATIONS.....	141
4.3.2	WATER-BORNE FORMULATION.....	142
4.3.3	SOLVENT-BASED FORMULATIONS .....	143
<b>4.4</b>	<b>EQUIPMENT AND METHODOLOGY .....</b>	<b>144</b>
4.4.1	FOURIER TRANSFORM INFRARED SPECTROSCOPY .....	144
4.4.2	X-RAY DIFFRACTION .....	144
4.4.3	ZETA POTENTIAL .....	144
4.4.4	SEM/EDS .....	144
4.4.5	UV-VIS SPECTROPHOTOMETRY .....	145
4.4.6	X-RAY PHOTOELECTRON SPECTROSCOPY .....	146

4.4.7	ATOMIC FORCE MICROSCOPY .....	146
4.4.8	ELECTROCHEMICAL IMPEDANCE SPECTROSCOPY .....	146
4.4.9	DC POLARIZATION .....	147
4.4.10	CONTACT ANGLES/SURFACE ENERGY .....	148
4.4.11	THERMOGRAVIMETRIC ANALYSIS .....	148
4.4.12	DIFFERENTIAL SCANNING CALORIMETRY .....	148
4.4.13	SCANNING VIBRATING ELECTRODE TECHNIQUE .....	148

## **5 LAYERED DOUBLE HYDROXIDES HYBRID NANORESERVOIRS – LBL MODIFIED LDH NANOCONTAINERS..... 151**

<b>5.1</b>	<b>LAYERED DOUBLE HYDROXIDES AS A RESERVOIR FOR CORROSION INHIBITOR 2-MERCAPTOBENZOTHAZOLE.....</b>	<b>153</b>
<b>5.2</b>	<b>LDH MODIFIED TO PROVIDE DUAL RELEASE.....</b>	<b>157</b>
5.2.1	STRUCTURAL CHARACTERIZATION .....	158
5.2.2	INHIBITOR RELEASE STUDIES .....	165
<b>5.3</b>	<b>ELECTROCHEMICAL STUDIES .....</b>	<b>167</b>
5.3.1	AA2024 SURFACE CHARACTERIZATION.....	167
5.3.2	CERIUM (III) NITRATE AND 2-MBT AS A CORROSION INHIBITOR FOR AA2024.....	172
5.3.3	LDH MODIFIED TO PROVIDE DUAL RELEASE.....	174
5.3.4	LDH MODIFIED TO PROVIDE DUAL RELEASE IN SOLVENT-BASED HYBRID SOL- GEL....	178
<b>5.4</b>	<b>PARTIAL CONCLUSIONS.....</b>	<b>183</b>

## **6 GLUCONATE-CONTAINING LDHS ..... 185**

<b>6.1</b>	<b>LDHS CONTAINING GLUCONATE.....</b>	<b>187</b>
<b>6.2</b>	<b>LDH MODIFICATION WITH POLYELECTROLYTES .....</b>	<b>190</b>
6.2.1	STRUCTURAL CHARACTERIZATION .....	190
6.2.2	INHIBITOR RELEASE STUDIES .....	194
6.2.3	STABILITY OF THE NANOCONTAINER .....	196
<b>6.3</b>	<b>GALVANNEALED STEEL AND COLD ROLLED STEEL SUBSTRATES.....</b>	<b>198</b>
6.3.1	MORPHOLOGICAL AND CHEMICAL PROPERTIES .....	198
6.3.2	ELECTROCHEMICAL CHARACTERIZATION IN NaCl SOLUTION.....	201
<b>6.4</b>	<b>GLUCONATE AS A CORROSION INHIBITOR FOR GS .....</b>	<b>204</b>
6.4.1	GLUCONATE DIRECTLY ADDED IN NaCl SOLUTION .....	204
6.4.2	LDH-GLUC IN NaCl SOLUTION.....	209
6.4.3	LDH-GLUC_ALG IN NaCl SOLUTION.....	214

Contents	2018
<b>6.5 GLUCONATE AS CORROSION INHIBITOR FOR CRS</b> .....	<b>219</b>
6.5.1 GLUCONATE DIRECTLY IN NaCl SOLUTION .....	219
6.5.2 LDH-GLUC AND LHD-GLUC_ALG IN NaCl SOLUTION .....	223
<b>6.6 COATED GS AND CRS SUBSTRATES</b> .....	<b>230</b>
6.6.1 MODIFIED COATINGS ON GS SUBSTRATES .....	230
6.6.2 MODIFIED COATINGS ON CRS SUBSTRATES .....	237
<b>6.7 PARTIAL CONCLUSIONS</b> .....	<b>243</b>
<b><u>7 SILICA NANOCAPSULES</u></b> .....	<b><u>245</u></b>
<b>7.1 SYNTHESIS AND CHARACTERIZATION OF MODIFIED SI_NC</b> .....	<b>247</b>
7.1.1 SI_NC MODIFICATION WITH (3-AMINOPROPYL)TRIETHOXSILANE .....	249
7.1.2 SI_NC SURFACE MODIFICATION .....	252
<b>7.2 STABILITY OF SILICA NANOCONTAINERS IN DIFFERENT MEDIA</b> .....	<b>254</b>
<b>7.3 COATING PERFORMANCE</b> .....	<b>257</b>
7.3.1 ADDITION OF MODIFIED DRIED SI_NC TO MODEL SOL-GEL BASED COATINGS .....	257
7.3.2 ADDITION OF MODIFIED SI_NC TO COMMERCIAL COATINGS .....	275
<b>7.4 PARTIAL CONCLUSIONS</b> .....	<b>293</b>
<b><u>8 CONCLUSIONS</u></b> .....	<b><u>297</u></b>
<b>8.1 HOLISTIC OVERVIEW OF THE WORK CARRIED OUT</b> .....	<b>299</b>
<b>8.2 FINAL CONCLUSIONS</b> .....	<b>302</b>
<b>8.3 FUTURE PERSPECTIVES</b> .....	<b>305</b>
<b><u>9 REFERENCES</u></b> .....	<b><u>307</u></b>

## List of abbreviations and symbols

### General symbols and abbreviation

CRS	Cold rolled steel
CPE	Constant phase element
E	Electrode potential
$E^0$	Equilibrium potential
$E_{\text{corr}}$	Corrosion potential
$E_{\text{eq}}$	Equilibrium potential
$E_{\text{oa}}, E_{\text{oc}}$	Equilibrium potential of the anodic and cathodic reactions
$E_{\text{pit}}$	Pitting potential
f	Frequency
I	Current
$I_0$	Exchange current
$I_{\text{corr}}$	Corrosion current density
IGC	Intergranular corrosion
GDP	Gross domestic product
GS	Galvannealed steel
LbL	Layer-by-layer
LDH	Layered double hydroxides
N	Number of electrons involved in electrochemical process
nm	Nanometer
$R_{\text{coat}}$	Coating resistance
RE	Reference electrode
$R_{\text{ox}}$	Oxide resistance
$R_{\text{pol}}$	Polarization resistance
$R_{\text{ct}}$	Resistance of charge transfer
$R_{\text{sol}}$	Solution resistance
Si_NC	Silica nanocapsules
SCE	Saturated calomel electrode
Mt	Million tones
V	Voltage
W, $Z_w$	Warburg impedance

wt. %	Weight percentage
$Y_0$	Admittance
$Z, Z_0, Z(\omega)$	Impedance
$Z_r, Z_i$	Real and imaginary part of impedance
$\alpha$	Fraction of polarization
$\text{Å}$	Angstrom
$\beta_a, \beta_c$	Cathodic and anodic Tafel constant
$\Delta G_f^*, \Delta G_b^*$	Activation energy of forward and backward reaction
$\Delta V$	Potential difference
$\varepsilon$	Dielectric permittivity
$\varepsilon_0$	Dielectric permittivity of vacuum
$\varepsilon_w$	Dielectric permittivity of water
$\mu\text{m}$	Micrometer
$\sigma$	Warburg coefficient
$\varphi$	Phase shift
$\omega$	Angular frequency

#### Experimental techniques

AFM	Atomic Force Microscopy
DC-polarization	Direct current polarization
DSC	Differential scanning calorimeter
DTA	Differential thermal analysis
EIS	Electrochemical impedance spectroscopy
EDS	Energy Dispersive Spectroscopy
FTIR	Fourier Transformed Infrared Spectroscopy
SEM	Scanning Electron Microscopy
SVET	Scanning Vibrating Electrode Technique
TGA	Thermogravimetric analysis
UV-Vis	Ultra violet-visible spectrophotometer
XRD	X-ray diffraction
XPS	X-ray Photoelectron Spectroscopy

## Inhibitors and reagents

Alg	Alginate
APS	(3-aminopropyl)triethoxysilane
CTAB	Cetyltrimethylammonium bromide
GPTMS	3-glycidoxypropyltrimethoxysilane
HDTMS	Hexadecyltrimethoxysilane
2-MBT	2-mercaptobenzothiazole
MPTMS	(3-Mercaptopropyl) trimethoxysilane
MTEOS	Methyltriethoxysilane
NaGluc	Sodium gluconate
PAH	Poly(allylamine hydrochloride)
2-prop	2-propanol
PSS	Poly(sodium styrene sulfonate)
PTMS	Phenyl trimethoxysilane
TEOS	Tetraethyl orthosilicate
TMOS	Trimethoxy(octadecyl)silane
TPOZ	Tetra-n-propoxyzirconium
TPOT	Titanium (IV) propoxide



## List of Figures

Figure 1: Types of corrosion in metals. Adapted from reference [7].	34
Figure 2: Corrosion process in iron.	35
Figure 3: Scheme of intergranular corrosion in austenitic stainless steel. Adapted from reference [11].	36
Figure 4: Scanning electron micrographs and electron backscattered diffraction maps of AA2024-T3 aluminum alloy after immersion in 0.5 M NaCl solution for 18 h, (a) 80 x BSE, (b) 800 x SE 70° tilting (corrected). Adapted from the work of C. Luo and colleagues.[13]	36
Figure 5: Galvanic series in sea water. The blue boxes indicate the active behavior for listed active/passive alloys. Adapted from reference [15].	37
Figure 6: Scheme of galvanic corrosion between Zn and Fe.	38
Figure 7: Most common types or shapes of pits.[24, 25]	39
Figure 8: Schematic representation of pit corrosion mechanism of AA2024 in chloride solution. Reprinted with permission from Yasakau, K.A., et al., Mechanism of Corrosion Inhibition of AA2024 by Rare-Earth Compounds. The Journal of Physical Chemistry B, 2006. 110(11): p. 5515-5528). Copyright (2017) American Chemical Society.[27]	40
Figure 9: Scheme of crevice corrosion mechanism.[25]	41
Figure 10: The distribution of aluminum by product type in North America in 2014 (a) and by end-use market in Europe in 2007 (b) and in North America in 2014 (c).[44]	48
Figure 11: Schematic representation of Fe-Zn phase layer formation, over time, in a galvanizing bath. Adapted from the references [69, 71]	58
Figure 12: Schematics of the different types of galvanized coatings.[73]	59
Figure 13: Schematic representation of changes occurring in an aluminum alloy surface: a) before and b) after alkaline etching; c) before and d) after acid cleaning.[82]	63
Figure 14: Schematic representation of alumina pore formation by electrochemical anodization: (a) formation of the anodic oxide on aluminum; (b) local field distribution correlated to the surface	

morphological fluctuations; (c) initiation of the pore growth due to the field-enhanced dissolution; (d) pore growth in steady-state conditions; (e) represents the current transient recorded during anodization of Al; (f) and (g) show the influence of the volume expansion and the local acidity on the alumina pore growth, respectively. Reproduced from [87] with the authorization of RSC. ....	64
Figure 15: Class I hybrid material (no covalent bonds are formed between inorganic and organic phases) (a). Figure (b) class II hybrid materials; (1) hybrid network with added functionality (Y) linked by inorganic bonds; (2) hybrid network linked by inorganic and organic bonds; (2) organic-inorganic network made of nano-building blocks linked through organic Bonds. Reproduced from the work of K. Yasakau [89]. ....	65
Figure 16: Various steps in the sol-gel process to control the final morphology of the product. Reproduced from reference [135] with the authorization of Springer International Publishing AG. ....	73
Figure 17: Scheme of a typical coating system used in metals.[150] .....	74
Figure 18: Classification of important film-forming agents. Adapted from reference [77]......	75
Figure 19: Factors affecting the final coating result in a spray application process. Adapted from reference [77] .....	76
Figure 20: Scheme of the controllable release of inhibitor from the nanocontainers and the “smart self-healing” process.[156] Reprinted with permission from Zheludkevich, M.L., et al., Anticorrosion Coatings with Self-Healing Effect Based on Nanocontainers Impregnated with Corrosion Inhibitor. Chemistry of Materials, 2007. 19(3): p. 402-411. Copyright 2016 American Chemical Society. ....	78
Figure 21: Schematic view of the LDHs action in corrosion protection.[96] Reprinted with permission from (Tedin, J., et al. (2010). "Enhancement of Active Corrosion Protection via Combination of Inhibitor-Loaded Nanocontainers." ACS Applied Materials & Interfaces 2(5): 1528-1535.). Copyright (2016) American Chemical Society. ....	81
Figure 22: TEM pictures of Si_NC with different magnifications; inset: electron diffractogram.[160] Reproduced by permission of The Royal Society of Chemistry (RSC) on behalf of the Centre National de la Recherche Scientifique (CNRS) and the RSC.....	82
Figure 23: Schematic illustration of the fabrication of 2-mercaptobenzothiazole-loaded halloysite/polyelectrolyte nanocontainers.[192] Reprinted with permission from Shchukin, D. G.,	

et al. (2008). "Active Anticorrosion Coatings with Halloysite Nanocontainers." The Journal of Physical Chemistry C 112(4): 958-964. Copyright 2016 American Chemical Society.....	84
Figure 24: Scheme summarizing the application of 2-MBT loaded PU capsules in sol-gel coatings for corrosion protection. Reproduced from [199] with the authorization of Elsevier.....	85
Figure 25: Schematics represents a stable suspension and the process leading to sedimentation. Based on the reference [211].....	89
Figure 26: Potential energy curve for the approach of two nanoparticles. Reproduced from reference [210] with the authorization of Springer Nature. ....	90
Figure 27: A) Schematic illustration of the procedure for benzotriazole loading for SiO <sub>2</sub> nanoparticle containers, B) halloysite nanotubes and C) polyelectrolyte capsules. Reproduced from the reference [195] with the authorization of John Wiley and Sons.....	94
Figure 28: Chemical modification of the silica surface in an aqueous system. Adapted from.[234] .....	97
Figure 29: Optical layout of a typical FTIR spectrophotometer. Reproduced from reference [248] with the authorization of Elsevier. ....	104
Figure 30: Diagram of an optical column of SEM and types of electron guns and objective lenses used in SEM system. Reproduced from reference [260] with the authorization of Elsevier. ...	110
Figure 31: Sketch illustrating the principle of atomic force microscopy. Reproduced from reference [264] with the authorization of Elsevier. ....	111
Figure 32: Example of a potentiodynamic polarization curve and classic Tafel analysis.....	117
Figure 33: Schematic representation of the instrumentation used for EIS measurements. Adapted from the references [89, 279] .....	119
Figure 34: Sinusoidal current response in a linear system, based on [280]. ....	120
Figure 35: Origin of the Lissajous figure in a) and the Argand diagram in b) showing relationships among complex impedance, magnitude, and phase angle. Adapted from [89, 277, 280].....	121
Figure 36: Nyquist Plot with an Impedance Vector. Adapted from [280] .....	123

Figure 37: Bode plot graphs and corresponding equivalent circuits at different coating-metal degradation stages. Intact coating a) and b), porous coating (c and d) and porous coating with the start of corrosion activity (e and f). Adapted from the reference [89]. .....	126
Figure 38: Experimental setup used for SVET. a) Vibrating electrode, b) electrochemical cell and c) interaction schematics between the different modules present in the SVET system (used from the aSet program manual). Adapted from the work of A.C. Bastos.[287] .....	129
Figure 39: Dip coater and scheme of the procedure used to coat samples with sol-gel formulations. ....	141
Figure 40: FTIR spectra of 2-MBT, LDH-NO <sub>3</sub> , and LDH-MBT.....	154
Figure 41: XRD patterns of LDH-NO <sub>3</sub> and after intercalation of 2-MBT, LDH-MBT. Adapted from [94]. ....	155
Figure 42: FTIR patterns of LDH-MBT powders throughout the LbL process.....	158
Figure 43: XRD patterns of LDH powders before (LDH-NO <sub>3</sub> ) and after intercalation with MBT <sup>-</sup> (LDH-MBT). The inset shows the range of (110) diffraction reflections. XRD patterns of LDH-MBT powders throughout the modification process. Diffraction peaks associated with cerium oxide phase are represented by red dots.[94] Reproduced by permission of The Royal Society of Chemistry (RSC) on behalf of the Centre National de la Recherche Scientifique (CNRS) and the RSC. ....	159
Figure 44: Top: XRD patterns of (1) the powder obtained as a result of calcination of LDH-MBT sample after the second modification step and (2) nano-powder of CeO <sub>2</sub> . Bottom: diffraction peaks of CeO <sub>2</sub> in the XRD patterns of the mechanical mixture of LDH-MBT + nano- CeO <sub>2</sub> (open symbols) and the LDH-MBT sample after the second modification step (solid symbols). [94] Reproduced by permission of The Royal Society of Chemistry (RSC) on behalf of the Centre National de la Recherche Scientifique (CNRS) and the RSC. ....	160
Figure 45: XPS survey spectrum of LDH-MBT + nano-CeO <sub>2</sub> . [94] Reproduced by permission of The Royal Society of Chemistry (RSC) on behalf of the Centre National de la Recherche Scientifique (CNRS) and the RSC. ....	161
Figure 46: XPS spectra of the Ce(3d <sub>5/2,3/2</sub> ) core level region with deconvolution assigned to Ce states for determination of the Ce <sup>4+</sup> /Ce <sup>3+</sup> ratio. [94] Reproduced by permission of The Royal Society of Chemistry (RSC) on behalf of the Centre National de la Recherche Scientifique (CNRS) and the RSC.....	162

Figure 47: SEM and EDS mapping of LDHs: (a) SEM image, (b) Zn mapping, (c) S mapping and (d) Ce mapping. Overlapping of SEM image, O mapping and Ce mapping of LDH\_P(-)\_Ce sample (e). EDS analysis throughout the modification process (f). [94] Reproduced by permission of The Royal Society of Chemistry (RSC) on behalf of the Centre National de la Recherche Scientifique (CNRS) and the RSC. .... 163

Figure 48: 2-MBT release profiles for LDH-MBT and LDH\_Mod under different conditions ( $\lambda=320$  nm). [94] Reproduced by permission of The Royal Society of Chemistry (RSC) on behalf of the Centre National de la Recherche Scientifique (CNRS) and the RSC. .... 165

Figure 49: SEM micrographs of the AA2024 surface after pre-treated with: (a) acetone, (b) industrial treatment I and (c) industrial treatment II. .... 168

Figure 50: EDS analysis of AA2024 pretreated samples with acetone, industrial treatment I and industrial treatment II. .... 169

Figure 51: AFM images for AA2024 pretreated with acetone, industrial treatment I and industrial treatment II. .... 170

Figure 52: Bode representation and phase angle of EIS spectra acquired for AA2024 bare substrates after 90 minutes, 1 day and 2 days in 50 mM NaCl solution. .... 171

Figure 53: DC polarization curves for AA2024 samples immersed in 50 mM NaCl solution with 1 mM  $\text{Ce}(\text{NO}_3)_3$ , a saturated solution of 2-MBT (2 mM solution) and a mixture of both (5 mM  $\text{Ce}(\text{NO}_3)_3$ /2 mM 2-MBT) after 1 hour of immersion. [94] Reproduced by permission of The Royal Society of Chemistry (RSC) on behalf of the Centre National de la Recherche Scientifique (CNRS) and the RSC. .... 173

Figure 54: Bode representation of EIS spectra acquired for AA2024 bare substrates after 4 hours of immersion in 50 mM NaCl solution with LDH loaded with  $\text{NO}_3$  and 2-MBT, with LbL modification and LbL modification with cerium-based compounds incorporated (Table 2). (a) impedance magnitude and (b) phase angle. [94] Reproduced by permission of The Royal Society of Chemistry (RSC) on behalf of the Centre National de la Recherche Scientifique (CNRS) and the RSC. .... 176

Figure 55: Equivalent circuits used to fit EIS data (Figure 54), summarized in Table 15. .... 177

Figure 56: Bode representation of EIS spectra for AA2024 coated with sol-gel, and sol-gel loaded with LDH-MBT and LDH-Mod after (a) 4 hours and (b) 5 days of immersion in a 0.5 M NaCl

solution. (c) EDS analysis after immersion tests of the coated AA2024 sample in regions with agglomeration of LDHs, as observed in (d). .....	179
Figure 57: Evolution over time of the $R_{coat}$ for AA2024 panels coated with a hybrid solvent-based sol-gel (Sg_Ti) without nanocontainers and loaded with 0.5 wt.% of LDH-MBT and LDH-Mod immersed in 0.5 M NaCl solution. Equivalent circuits used to fit EIS data (Figure 56), summarized in Table 16.....	181
Figure 58: Photographs of AA2024 coated with a hybrid solvent-based sol-gel (Sg_Ti) without nanocontainers and loaded with 0.5 wt.% of LDH-MBT and LDH-Mod, added to the formulation as a water-based slurry. Photographs obtained after 4 hours, 1 day, 5 days and 10 days immersion in a 0.5 M NaCl solution. ....	182
Figure 59: FTIR spectra of NaGluc, LDH-NO <sub>3</sub> , and LDH-Gluc. ....	188
Figure 60: XRD patterns of LDH-NO <sub>3</sub> and after intercalation of NaGluc, LDH-Gluc. ....	189
Figure 61: FTIR spectra for LDH-NO <sub>3</sub> (a) and LDH-Gluc surface modification with alginate. ....	191
Figure 62: FTIR spectra for LDH-Gluc surface modification with PSS.....	192
Figure 63: XRD patterns of LDH-Gluc and of LDH-Gluc after modification with alginate (LDH-Gluc_Alg) and PSS (LDH-Gluc_PSS).....	192
Figure 64: SEM micrographs of LDH-NO <sub>3</sub> (a), LDH-Gluc (b), LDH-Gluc_PSS (c) and LDH-Gluc_Alg (d). ....	193
Figure 65: Gluconate release profiles for LDH-Gluc under different NaCl concentrations. ....	195
Figure 66: LDH-NO <sub>3</sub> , LDH-Gluc and LDH-Gluc_Alg suspension stability in water over time. ....	197
Figure 67: SEM pictures of GS (a) and CRS (b) after industrial cleaning. Magnification:a1 and b1 x600; a2 and b2 x1.50k; a3 and b3 x6.00k.....	199
Figure 68: EDS analysis of GS and CRS cleaned samples. ....	200
Figure 69: AFM topographic images for GS (a) and CRS (b) for different areas: 50x50 $\mu\text{m}$ (1), 30x30 $\mu\text{m}$ (2) and 5x5 $\mu\text{m}$ (3). ....	200

- Figure 70: Bode representation of EIS spectra acquired for GS substrates after 90 minutes, 1 day and 3 days immersion in 50 mM NaCl solution (a). The surface of GS test samples after 90 minutes (b), 1 day (c) and 3 days (d). Equivalent circuit used in the interpretation of the data presented in Bode representations (e). ..... 201
- Figure 71: Bode representation and phase angle of EIS spectra acquired for CRS substrates after 90 minutes, 1 day and 3 days immersion in 50 mM NaCl solution (a). CRS test samples after 90 minutes (b), 1 day (c) and 3 days. Equivalent circuit used in the interpretation of the data presented in Bode representations (e)..... 202
- Figure 72: DC polarization of GS samples immersed in 50 mM NaCl solution without NaGluc and with 0.5, 1, 2 and 5 mM NaGluc after 1 hour of immersion. The inset shows OCP evolution before measurement. .... 204
- Figure 73: Bode representation of EIS spectra after 15 min and 3 days of immersion in 50 mM NaCl solution without NaGluc, with 2 mM NaGluc and 5 mM NaGluc. .... 206
- Figure 74: Photographs of samples measured in Figure 73. GS samples immersed in 50 mM NaCl, 2 mM NaGluc in 50 mM NaCl and 5 mM NaGluc in 50 mM NaCl after 15 minutes and 3 days. .... 207
- Figure 75: Evolution of  $R_{ct}$  (a) and  $CPE_{dl}$  (b) fitting parameters of GS immersed in 50 mM NaCl (reference), 50 mM NaCl with 2 mM NaGluc and 50 mM NaCl with 5 mM NaGluc; equivalent circuit scheme (c) used for fitting of EIS data presented in Figure 73. .... 208
- Figure 76: EIS spectra of galvanized steel samples in 50 mM NaCl, 50 mM NaCl containing LDH-NO<sub>3</sub> and 50 mM NaCl containing LDH-Gluc containers after a) 90 min and b) 2 day of immersion..... 210
- Figure 77: Photographs of the plates before immersion and after 2 days of immersion in 50 mM NaCl solution. .... 211
- Figure 78: SEM microphotographs of the plates without immersion (a) and after 2 days of immersion in 50 mM NaCl solution without gluconate (b), in a NaGluc solution (c) and LDH-Gluc (d). .... 212
- Figure 79: Evolution of  $R_{ct}$  (a) and  $CPE_{dl}$  (b) fitting parameters of GS immersed in 50 mM NaCl (reference), 50 mM NaCl with LDH-NO<sub>3</sub> and 50 mM NaCl with LDH-Gluc; equivalent circuit scheme (c) used for fitting of EIS data presented in Figure 76. .... 213

Figure 80: EIS Spectra of GS samples in 50 mM NaCl, 50 mM NaCl containing LDH-Gluc and 50 mM NaCl containing LDH-Gluc_Alg containers after a) 15 minutes and c) 1 day of immersion. .....	215
Figure 81: GS photographs during the EIS tests after 15 min, 1 day and 1 week immersion in a 50 mM NaCl solution, with 50 mM NaCl plus LDH-Gluc and 50 mM NaCl plus LDH-Gluc_Alg. .....	216
Figure 82: Evolution of $R_{ct}$ (a) and $CPE_{dl}$ (b) fitting parameters of GS immersed in 50 mM NaCl (reference), 50 mM NaCl with LDH-Gluc and 50 mM NaCl with LDH-Gluc_Alg; equivalent circuit scheme (c) used for fitting of EIS data presented in Figure 80.....	217
Figure 83: Bode representation of EIS spectra after 15 min and 3 days of immersion in 5 mM (a and b) and 50 mM NaCl (c and d) solution without NaGluc and with 2 mM or 5 mM NaGluc. .....	220
Figure 84: Photographs of bare CRS in a 50 mM NaCl solution, and 50 mM NaCl plus 2 mM NaGluc and 50 mM NaCl plus 5 mM NaGluc after 15 minutes, 1 day and 3 days of immersion. .....	221
Figure 85: Evolution of $R_{ct}$ (a) and $CPE_{dl}$ (b) fitting parameters of CRS immersed in 5 mM NaCl (reference), 5 mM NaCl with 2 mM NaGluc and 5 mM NaCl with 5 mM NaGluc; evolution of $R_{ct}$ (c) and $CPE_{dl}$ (d) fitting parameters of CRS immersed in 50 mM NaCl (reference), 50 mM NaCl with 2 mM NaGluc and 50 mM NaCl with 5 mM NaGluc equivalent circuit scheme (e) used for fitting of EIS data presented in Figure 83.....	222
Figure 86: EIS spectra of CRS samples in 5 mM NaCl and 5 mM NaCl containing $NaNO_3$ , LDH- $NO_3$ , NaGluc, LDH-Gluc and LDH-Gluc_Alg after 4 hours (a and b) and 2 days (c and d) of immersion.....	224
Figure 87: Photographs of bare CRS in a 5 mM NaCl solution, and 5 mM NaCl plus: 0.1 wt.% of $NaNO_3$ , 0.1 wt.% of NaGluc, 0.5 wt.% of NO LDH- $NO_3$ , 0.5 wt.% of LDH-Gluc and 0.5 wt.% of LDH-Gluc_Alg. Photographs taken after 15 minutes, 4 hours and 2 days of immersion. ...	226
Figure 88: Evolution of $R_{ct}$ (a) and $CPE_{dl}$ (b) fitting parameters of CRS immersed in 5 mM NaCl (reference), 5 mM NaCl with $NaNO_3$ , LDH- $NO_3$ , NaGluc, LDH-Gluc, and LDH-Gluc_Alg; (c) equivalent circuits used for fitting of EIS data presented in Figure 86. ....	228
Figure 89: SEM images of coating applied on GS substrates: without additives (a), with NaGluc (2 wt.%) (b), with LDH-Gluc (5 wt.%) (c) and with LDH-Gluc_Alg (5 wt.%) (d).....	231

Figure 90: EIS spectra for coatings with NaGluc, LDH-Gluc with and without modification applied on GS substrates and after 1 hour and 28 days of immersion in a 0.5 M NaCl solution. ....	232
Figure 91: Evolution of $R_{coat}$ (a) and $R_{ct}$ (b) fitting parameters of GS samples coated with TATA formulation, and TATA formulation loaded with 2 wt.% of NaGluc and $NaNO_3$ and 5 wt.% of LDH- $NO_3$ LDH-Gluc, LDH-Gluc_PSS, and LDH-Gluc_Alg. The samples were tested under immersion in a 0.5 M NaCl; (c) and (d) equivalent circuits used for fitting of EIS data presented in Figure 90. ....	234
Figure 92: Photographs of coatings with NaGluc, LDH- $NO_3$ , LDH-Gluc and LDH-Gluc modified with alginate applied on GS substrates after 1 day, 1 week and 4 weeks of immersion in a 0.5 M NaCl solution. ....	235
Figure 93: SVET analysis of coated GS, coating loaded with gluconate and LDH with and without modification immersed in a 50 mM NaCl solution. The current color scale bar indicates ionic current densities between -5 to 5 $\mu A cm^{-2}$ .....	237
Figure 94: EIS spectra for coatings loaded with LDH-Gluc and modified LDH-Gluc after 1 day (a and b) and 14 days (c and d) of immersion in 0.5 M NaCl. ....	238
Figure 95: Evolution of $R_{coat}$ (a) and $R_{ct}$ (b) fitting parameters of CRS samples coated with TATA formulation, and TATA formulation loaded with NaGluc, LDH-Gluc and LDH-Gluc_Alg. The samples were tested under immersion in a 5 mM NaCl; (c) and (d) equivalent circuits used for fitting of EIS data presented in Table 27.....	241
Figure 96: Photographs of coated samples with gluconate, LDH-Gluc with and without modification. ....	242
Figure 97: FTIR spectra for Si_NC and Si_NC modified with APS. ....	250
Figure 98: TG analysis of Si_NC calcine, Si_NC and Si_NC modified with APS. ....	251
Figure 99: FTIR spectra for Si_NC modified silane derivatives APS, GPTMS, TMOS, and HDTMS.....	252
Figure 100: SEM micrographs of Si_NC (a), Si_NC_APS (b), Si_NC_GPTMS (c), Si_NC_TMOS (d) and Si_NC_HDTMS. The samples were dispersed in water and ethanol (Si_NC_TMOS and Si_NC_HDTMS) prior to deposition. ....	253

- Figure 101: 0.5 wt.% (50 mg of nanocontainers in 10 ml of water) of Si\_NC and modified Si\_NC with APS, GPTMS, TMOS and HDTMS added to water to assess its stability as a function of time: 5, 10 and 60 minutes. The particles were added as dry powders, dispersed for 5 min in ultrasounds immediately before the test..... 254
- Figure 102: Photographs of different vials with water-based dispersions prepared with 0.5 wt.% (50 mg of nanocontainers in 10 ml of water) of Si\_NC\_APS under different pH conditions (pH 3, 6.5 and 10), immediately after dispersion and after 10 minutes. The particles were added as dry powders, dispersed for 5 min in ultrasounds immediately before the test. .... 255
- Figure 103: 0.5 wt.% (50 mg of nanocontainers in 10 ml of 2-propanol) of Si\_NC and modified Si\_NC with APS, GPTMS, TMOS and HDTMS added to 2-propanol to assess its stability over time: 5, 10 and 60 minutes. The particles were added as dry powders, dispersed during 5 min in ultrasounds and manually immediately before the test. .... 256
- Figure 104: Bode representation of EIS spectra for AA2024 panels coated with water-based sol-gel and solvent-based sol-gel after 90 min of immersion in a 0.5 M NaCl solution..... 258
- Figure 105: EIS spectra for AA2024 panels coated with water-based sol-gel loaded with Si\_NC, Si\_NC\_APS, Si\_NC\_GPTMS and Si\_NC\_TMOS after 15 min (a and b for 1 wt.%; e and f for 10 wt.%) and 4 hours (c and d for 1 wt.%; g and h for 10 wt.%) immersion in a 0.5 M NaCl solution. .... 261
- Figure 106: Equivalent circuits used to fit EIS data (Figure 105). The fitting parameters are summarized in Table 31. .... 263
- Figure 107: Evolution over time of the  $R_{coat}$  for AA2024 panels coated with a water-based sol-gel loaded with Si\_NC, Si\_NC\_GPTMS and Si\_NC\_TMOS immersed in 0.5 M NaCl solution.. 265
- Figure 108: Photographs of AA2024 coated with a water-based sol-gel and water-based sol-gel loaded with 1 wt.% and 10 wt.% of Si\_NC, Si\_NC\_APS, Si\_NC\_GPTMS and Si\_NC\_TMOS after 15 min and 4 hours, 1 day immersion in a 0.5 M NaCl solution. .... 266
- Figure 109: EIS spectra for AA2024 panels coated with hybrid solvent-based sol-gel loaded 1 wt.% of Si\_NC, Si\_NC\_APS, Si\_NC\_GPTMS and Si\_NC\_TMOS after 4 hours (a and b) and 5 days (c and d) immersion in a 0.5 M NaCl solution..... 267
- Figure 110: Photographs of AA2024 coated with a 2-propanol-based sol-gel and 2-propanol-based sol-gel loaded with 1% of Si\_NC, Si\_NC\_APS, Si\_NC\_GPTMS and Si\_NC\_TMOS after 4 hours, 1 day and 5 days immersion in a 0.5 M NaCl solution. .... 269

Figure 111: Equivalent circuits used to fit EIS data (Figure 109 (1 wt.%) and Figure 112 (10 wt.%)), summarized in Table 32 and Table 33 (see below).....	270
Figure 112: EIS spectra for AA2024 panels coated with a hybrid solvent-based sol-gel loaded 10 wt.% of Si_NC, Si_NC_APS, Si_NC_GPTMS and Si_NC_TMOS after 90 minutes (a and b) and 5 days (c and d) immersion in a 0.5 M NaCl solution.....	271
Figure 113: Evolution overtime of the $R_{coat}$ for AA2024 panels coated with a hybrid solvent-based sol-gel loaded with Si_NC, Si_NC_APS, Si_NC_GPTMS and Si_NC_TMOS in different proportions (1 and 10%) immersed in 0.5 M NaCl solution. ....	273
Figure 114: Photographs of AA2024 coated with a 2-propanol-based sol-gel and 2-propanol-based sol-gel loaded with 10% of Si_NC, Si_NC_APS, Si_NC_GPTMS and Si_NC_TMOS after 4 hours, 1 day and 5 days immersion in a 0.5 M NaCl solution. ....	274
Figure 115: Photographs of AQ CC 080 coatings loaded with 1 wt.% of Si_NC, Si_NC_APS and Si_NC_HD applied on carbon steel, added to the formulation as a dry powder and as a toluene-based slurry. ....	277
Figure 116: EIS spectra for AA2024 panels coated with a water borne polymeric formulation (AQ CC 080) loaded 1 wt.% of Si_NC, Si_NC_APS and Si_NC_HDTMS, added to the formulation as a dry powder and as a toluene-based slurry, after 4 hours (a and b) and 7 days (c and d) immersion in a 0.05 M NaCl solution. ....	280
Figure 117: a) EIS values at 1 kHz for AA2024 panels coated with a waterborne polymeric formulation (AQ CC 080) loaded 1 wt.% of Si_NC, Si_NC_APS and Si_NC_HDTMS, added to the formulation as a dry powder and as a toluene-based slurry, until 7 days immersion in a 0.05 M NaCl solution. In b) are presented the values of $R_{coat}$ obtained from the same samples during the same time period. ....	281
Figure 118: Photographs of AA2024 coated with a water born polymeric formulation (AQ CC 080) loaded 1 wt.% of Si_NC, Si_NC_APS, and Si_NC_HDTMS, added to the formulation as a dry powder and as a toluene-based slurry, after 4 hours, 1 days, 7 days and 60 days immersion in a 0.05 M NaCl solution. ....	283
Figure 119: Chemical reaction to form polyurethane and polyurea groups.....	284
Figure 120: Photographs of AQ CC 100 coatings loaded with 1 wt.% of Si_NC, Si_NC_APS and Si_NC_HDTMS applied on carbon steel, added to the formulation as a dry powder and as a toluene-based slurry. ....	285

Figure 121: EIS spectra for AA2024 panels coated with a solvent based polymeric formulation (AQ CC 100) loaded with 1 wt.% of Si_NC, Si_NC_APS and Si_NC_HDTMS, added to the formulation as a dry powder and as a toluene-based slurry, after 4 hours (a and b) and 60 days (c and d) immersion in a 0.5 M NaCl solution. ....	288
Figure 122: Equivalent circuits used to fit EIS data (Figure 121), summarized in Table 38....	289
Figure 123: Evolution over time of the $R_{coat}$ for AA2024 panels coated with a solvent-based polymeric formulation (AQ CC 100) loaded with 1 wt.% of Si_NC, Si_NC_APS, Si_NC_GPTMS and Si_NC_HDTMS immersed in 0.5 M NaCl solution. ....	291
Figure 124: Photographs of AA2024 coated with a solvent based polymeric formulation (AQ CC 100) loaded 1 wt.% of Si_NC, Si_NC_APS and Si_NC_HDTMS, added to the formulation as a dry powder and as a toluene-based slurry, after 4 hours, 7 days, 21 days and 60 days immersion in a 0.5 M NaCl solution. ....	292

## List of Tables

Table 1: Corrosion costs by sector and region in 2013. Adapted from reference [39] .....	43
Table 2: Wrought aluminum alloys, primary alloying element, and properties.[41, 46, 47] .....	49
Table 3: Aluminum alloys temper designations.[45] .....	50
Table 4: Examples of classification parameters used in steel.[57].....	53
Table 5: Four-digit index classification of alloy steels and primary alloying element and properties based on the SAE/AISI carbon steel naming conventions.[57-59] .....	53
Table 6: Steel products export values worldwide in 2014.[55].....	54
Table 7: Stainless steel series and main characteristics.[65].....	56
Table 8: Release properties of polyelectrolytes capsules. Reproduced from reference [222].....	95
Table 9: Functional groups and their characteristic absorption wavenumber. ....	105
Table 10: Electrical impedance of most common elements.[281, 283] .....	127
Table 11: List of reagents used in the frame of the present work. ....	133
Table 12: Zeta potential values of LDH particles throughout the modification process. [94] Reproduced by permission of The Royal Society of Chemistry (RSC) on behalf of the Centre National de la Recherche Scientifique (CNRS) and the RSC. ....	164
Table 13: Water contact angles for AA2024 samples pretreated with acetone, industrial treatment I and industrial treatment II.....	171
Table 14: LDH-based systems prepared and used in electrochemical impedance measurements. IE values of LDH-based systems in dispersed in 50 mM NaCl in bare AA2024. ....	175
Table 15: Results obtained from the fitting of EIS spectra depicted in Figure 54. ....	177
Table 16: Results obtained from the fitting of EIS spectra for AA2024 panels coated with a hybrid solvent-based sol-gel (Sg_Ti) without nanocontainers and loaded with 0.5 wt.% of LDH-MBT and LDH-Mod after 4 hours and 5 days immersion in a 0.5 M NaCl solution, depicted in Figure 56.....	180

Table 17: Main FTIR peaks observed in the LDH-NO <sub>3</sub> , LDH-Gluc and NaGluc spectra.....	187
Table 18: Zeta potential values of LDH-Gluc and LDH-Gluc modified with PSS and alginate in distilled water.....	194
Table 19: Determination of the corrosion rates by Tafel extrapolation from the polarization curves and inhibition efficiency for GS panels after 1 hour immersion in a 50 mM NaCl without and with 0.5 mM, 1 mM, 2 mM and 5 mM NaGluc.....	205
Table 20: Results obtained from the fitting of EIS spectra after 3 days of immersion in 50 mM NaCl solution, depicted in Figure 73.....	209
Table 21: Results obtained from the fitting of EIS spectra depicted in Figure 76.....	214
Table 22: Results obtained from the fitting of EIS spectra depicted in Figure 80.....	218
Table 23: Results obtained from the fitting of EIS spectra depicted in Figure 83.....	223
Table 24: Results obtained from the fitting of EIS spectra depicted in Figure 86.....	227
Table 25: Inhibition efficiency for CRS immersed in 5 mM NaCl loaded with: 0.1 wt.% of NaNO <sub>3</sub> , 0.5 wt.% of LDH-NO <sub>3</sub> , 0.1 wt.% of NaGluc, 0.5 wt.% of LDH-Gluc and 0.5 wt.% of LDH-Gluc_Alg.....	229
Table 26: Results obtained from the fitting of EIS spectra depicted in Figure 90.....	233
Table 27: Results obtained from the fitting of EIS spectra depicted in Figure 94.....	240
Table 28: Samples' identification, modification agents, and main functional groups present at the nanocontainer surface after modification.....	247
Table 29: Weight loss percentages obtained from TGA thermograms of Si_NC and SI_NC_APS samples.....	251
Table 30: Si_NC modified and hybrid sol-gel coatings used.....	257
Table 31: Results obtained from the fitting of EIS spectra depicted in Figure 105. *The value of R <sub>ct</sub> is very high due to the few points available, at low frequencies, to properly fit the results.	264
Table 32: Results obtained from the fitting of EIS spectra depicted in Figure 109. For systems loaded with 1 wt.% of nanocontainers.....	268

Table 33: Results obtained from the fitting of EIS spectra for AA2024 panels coated with a hybrid solvent-based sol-gel loaded 10 wt.% of Si_NC, Si_NC_APS, Si_NC_GPTMS and Si_NC_TMOS after 90 minutes and 5 days immersion in a 0.5 M NaCl solution, depicted in Figure 112. ....	272
Table 34: $T_g$ of the cooling step for AQ CC 080 formulation with 1 wt.% of Si_NC, Si_NC_APS, and Si_NC_HDTMS, added to the formulation as a dry powder and as a toluene-based slurry. ....	278
Table 35: Microhardness according to Martens for AQ CC 080 formulation with 1 wt.% of Si_NC, Si_NC_APS, and Si_NC_HDTMS, added to the formulation as a dry powder and as a toluene-based slurry. ....	279
Table 36: $T_g$ of the cooling step for AQ CC 100 formulation with 1 wt.% of Si_NC, Si_NC_APS, and Si_NC_HDTMS, added to the formulation as a dry powder and as a toluene-based slurry. ....	286
Table 37: Microhardness according to Martens test for AQ CC 100 formulation with 1 wt.% of Si_NC, Si_NC_APS, and Si_NC_HDTMS, added to the formulation as a dry powder and as a toluene-based slurry. ....	287
Table 38: Results obtained from the fitting of EIS spectra for AA2024 panels coated with a solvent based polymeric formulation (AQ CC 100) loaded 1 wt.% of Si_NC, Si_NC_APS, Si_NC_GPTMS and Si_NC_HDTMS after 4 hours and 60 days immersion in a 0.5 M NaCl solution, depicted in Figure 121. *The value of R is very high due to the few points available, at low frequencies, to properly fit the results. ....	290



# 1

## Introduction

*“One example of the principle is this: If you’ve made up your mind to test a theory, or you want to explain some idea, you should always decide to publish it whichever way it comes out. If we only publish results of a certain kind, we can make the argument look good. We must publish both kinds of result. For example - let’s take advertising again - suppose some particular cigarette has some particular property, like low nicotine. It’s published widely by the company that this means it is good for you, they don’t say, for instance, that the stars are a different proportion, or that something else is the matter with the cigarette. In other words, publication probability depends upon the answer. That should not be done.”*

Richard P. Feynman, in “Some remarks on science, pseudoscience, and learning how to not fool yourself. Caltech’s 1974 commencement address”.



Decay and destruction are an inherent part of existence and something that none can escape. The world around us is in a constant process of degradation and rebirth, which inspires the Humanity to pursue solutions to prevent degradation and to extend the functional life of equipment and structures, in the same way, it seeks the same for himself. The reasons for preventing the degradation of structures, probably, are not related to philosophic concerns but rather with the other great stimulus in Human history, the economic gain.

Corrosion protection is a major issue nowadays, in particular in highly industrialized countries where the costs associated with corrosion are estimated to be 3-5% of the GDP.[1] A substantial portion of the costs is related to infrastructures, utilities and transportation, for replacement of parts and maintenance operations, among others. In the last decades, issues such as these lead corrosion prevention to become a major topic in scientific research, particularly since the introduction of more restrictive environmental legislation over the years. Chromate-based coatings, namely conversion coatings and organic coatings loaded with chromate-based pigments such as strontium chromate, were particularly affected by these legislations due to the carcinogenic effect of Cr(VI)-derived species.[2]

The research and development of new materials aiming at the improvement of corrosion protection has increased in complementary areas such as materials design, development of new inhibitors and coating improvement. Great effort has been invested in the development of new corrosion inhibitors as effective as chromates, this being the main problem when replacing the well-established and highly efficient chromate-based coatings. An additional challenge is tuning the delivery of the corrosion inhibitor to be efficient while preserving the coating integrity. A common approach is the encapsulation of corrosion inhibitors in nanocontainers, enabling the protection of both the coating and the corrosion inhibitor properties. Nevertheless, some issues arise, namely coating/nanocontainer compatibility, inhibitor release profile and nanocontainer dispersibility. The surface modification of nanocontainers emerges as a possible answer to this problem.[3]

The goal of the present work is to improve compatibility between well-established nanocontainers, already being used as hosts for corrosion inhibitors, and selected coatings among the currently commercially available protective systems (paint formulations). The compatibility of nanocontainers were investigated for different systems, with increasing level of complexity, from solvent dispersions (aqueous and organic) that are the basis of

the selected formulations to simplified model films (without corrosion pigments, particle fillers, and stabilizers, etc.) and finally industrial coating formulations. The ultimate aim is the incorporation of nanocontainers without causing negative effects on the coating. In this thesis different coating systems were employed, namely sol-gel-based coating developed in our group and organic-based coating (water- and solvent-based) commercially available or developed by industrial partners. Some of these coatings are developed for and currently being used in the aeronautical and automotive industries.

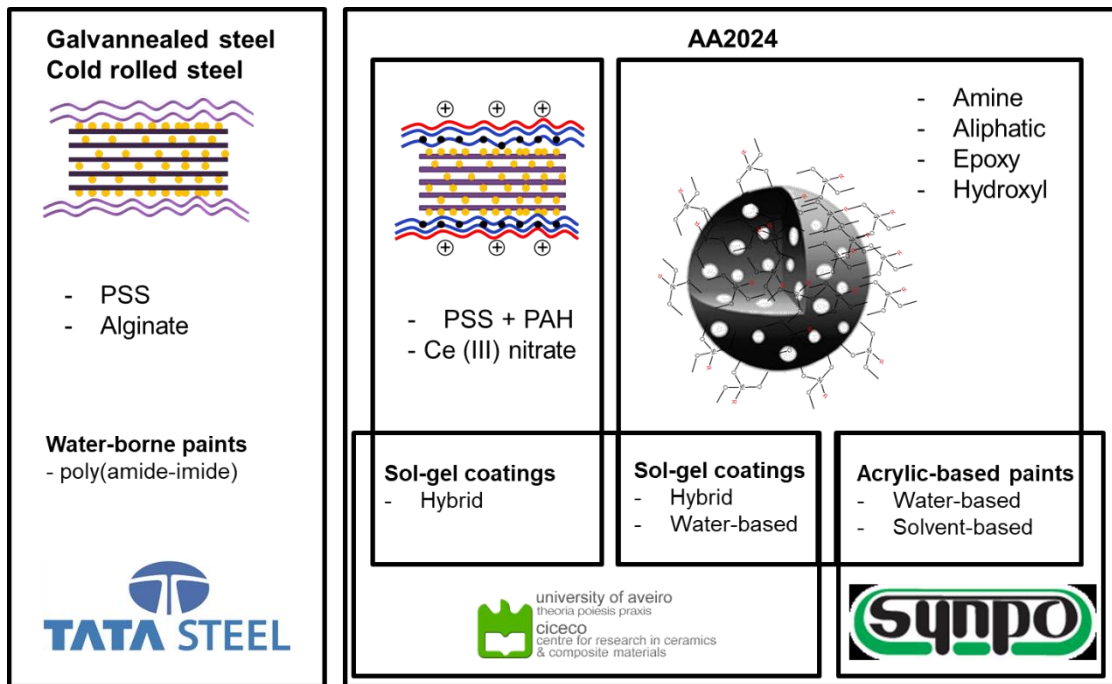
The specific objectives associated with this thesis are:

- 1) Selection of a set of different nanocontainers to be modified, representative of the most promising materials currently used as reservoirs for corrosion inhibitors.
- 2) Modification of different reservoirs, by grafting distinct functional groups onto its structure.
- 3) Physicochemical characterization of the synthesized materials.
- 4) Assessment of the stability of modified reservoirs in different solutions.
- 5) Release tests to ascertain the effect of grafting on nanocontainers release capabilities.
- 6) Incorporation of nanocontainers in selected model systems and analysis of the coating properties.
- 7) Evaluation of coating barrier properties relative to undoped coatings and coatings with unmodified nanocontainers.
- 8) Compatibility and stability tests with industrial products, close to end user applications.
- 9) Evaluation of the suitability of electrochemical impedance spectroscopy (EIS) as a tool for monitoring the quality of coating barrier properties and comparison with standard techniques used in industry.

A simplified scheme of the approach followed is presented in Scheme 1. The work is divided according to the type of nanocontainers, modification, inhibitors and coating formulations used. Part of this work was carried out in the frame of a bilateral project funded by TATA STEEL, whereas another part was performed in collaboration with coating producer SYNPO akciová společnost in the frame of MSCA-RISE project SMARCOAT (REF: 645662). The thesis is divided into the following chapters:

- Chapter 1: (current) short introduction to the problem and main objectives.

- Chapter 2: description of the state of the art.
- Chapter 3: description of the principles of the main experimental techniques employed.
- Chapter 4: description of the experimental procedure used.
- Chapter 5: LDH modified for double release.
- Chapter 6: LDH-Gluc modified with alginate for improve compatibility with industrial coating formulation.
- Chapter 7: modified silica nanocontainers for improved compatibility with increasingly complex coatings.
- Chapter 8: conclusions obtained in the frame of this thesis.
- Chapter 9: list of references used.



Scheme 1: Overview of the approach followed in the frame of this thesis.



# 2

## State of the art

*“For time will rust the brightest blade,  
And years will break the strongest bow;  
Was never wight so starkly made,  
But time and years would overthrow.”*

Walter Scott, in “Old Mortality”



## 2.1 Corrosion

The impact of corrosion in modern day life is unquestionable, accounting for a considerable amount of resources that must be allocated to its management and prevention. To better tackle the problem of corrosion is necessary to understand its mechanisms. In this section corrosion will be defined and the most relevant forms of corrosion affecting metal alloys will be listed and described in detail.

As it happens with all complex issues, corrosion may be defined in different terms. The American Society for Testing and Materials' corrosion glossary describes corrosion as "the chemical or electrochemical reaction between a material, usually a metal, and its environment that produces a deterioration of the material and its properties".[4] In more detail, IUPAC defines corrosion as, "an irreversible interfacial reaction of a material (metal, ceramic and polymer) with its environment which results in its consumption or dissolution into the material of a component of the environment. Often, but not necessarily, corrosion results in effects detrimental to the usage of the material considered. Exclusively physical or mechanical processes such as melting and evaporation, abrasion or mechanical fracture are not included in the term corrosion".[5]

Corrosion can be separated into three main groups: wet corrosion, corrosion in other fluids (such as fused salts and molten metals) and dry corrosion.[6] In wet corrosion the corrosion environment is water-based with dissolved species, creating an electrolyte. The corrosion processes associated with this type of corrosion is commonly electrochemical. Dry corrosion, also designated chemical corrosion, occurs when the corrosive environment is a dry gas, from which high-temperature corrosion is the best-known example.[6]

In this work only wet corrosion will be considered, thus the best approach to classify corrosion is by its morphology and mechanism. When classified according to its mechanism, as presented in Figure 1, the following types of corrosion can be listed: uniform/general corrosion, intergranular corrosion, galvanic corrosion, crevice corrosion, pitting, stress corrosion, cracking, and exfoliation. This classification appears to be more comprehensive, addressing a considerable number of corrosion processes characteristics of different metals.

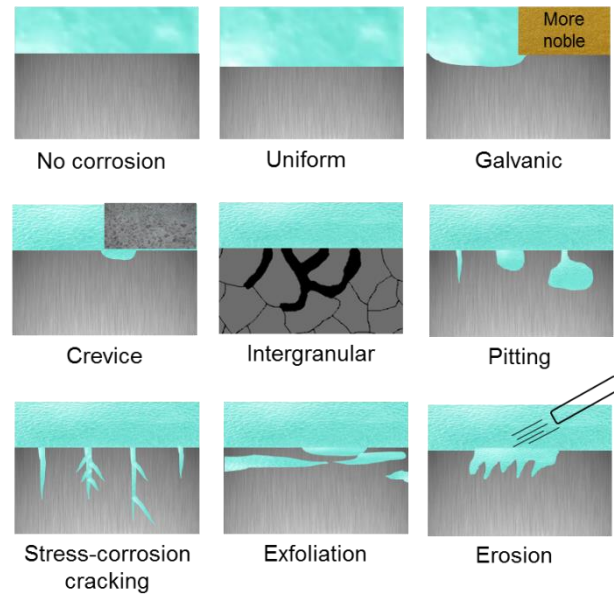


Figure 1: Types of corrosion in metals. Adapted from reference [7].

In the following sections, different corrosion mechanisms which can occur under experimental conditions addressed in this thesis will be described. Stress corrosion, cracking, exfoliation and erosion will be omitted.

### 2.1.1 Uniform corrosion

Being the most common type of corrosion by waste production, uniform corrosion is characterized by a fairly extended area of the metal surface undergoing aggressive oxidation, leading to its thinning over time, which can be also called general corrosion. Despite the large extension of this corrosion, the danger associated with it is relatively small since the corrosion rate can be easily detected and its evolution predicted, rendering catastrophic failures rare. Classic examples of uniform corrosion are the rusting of steel, the green patina on copper, tarnishing silver and white deposits on zinc. This form of corrosion has different effects depending on the metal: loss of metal, as in the case of steel, with rust forming an uneven film on the surface that can be peeled out or dissolved. On the other hand, the copper patina and silver tarnishing result in fairly uniform and adherent coatings, which ultimately protect the metal.[8]

Figure 2 depicts the corrosion mechanisms of iron-rich substrates, with metal dissolution in the anodic site (equation 1), the formation of hydroxide ions in the cathodic sites (equation 2) and rust formation due to iron oxide precipitation (equations 3 and 4).

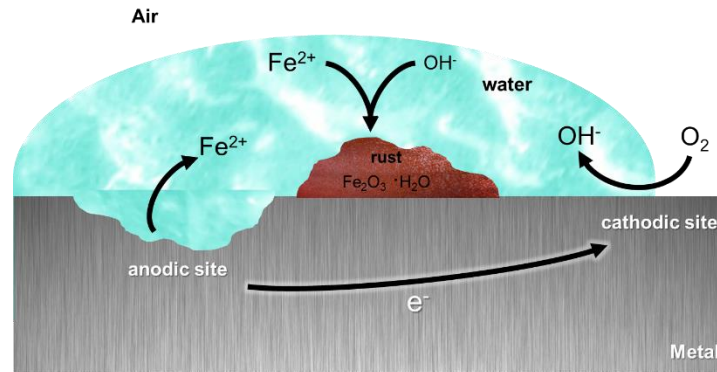
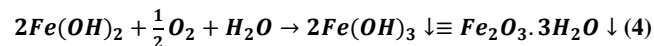
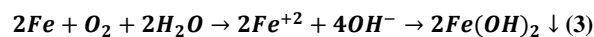
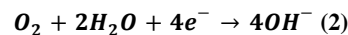
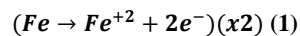


Figure 2: Corrosion process in iron.

The protection against uniform corrosion is relatively simple. The main approaches used cathodic protection, application of coatings and paints or establishing a tolerance mark for the amount of weight loss allowed for a specific structure.[4]



### 2.1.2 Intergranular corrosion

Intergranular corrosion (IGC) usually occurs in alloys, occurring in the grain boundaries as a result of the manufacturing process that creates significant differences in term of properties between the areas around the grains and those inside the grains. These can be a result of regions depleted of alloying elements, second phase precipitates or regions with segregated alloying or impurity elements.[9] The corrosion typically occurs when a difference in potential exists between the grain boundary and the grain interior, the material at the boundaries being more susceptible to corrosion (working as an anode). This type of corrosion is particularly troublesome in aluminum alloys rich in copper and austenitic stainless steels containing carbon. Figure 3 depicts IGC in austenitic stainless steel, with chromium depleted regions working as the anode and the grain areas as the cathode.[8, 10]

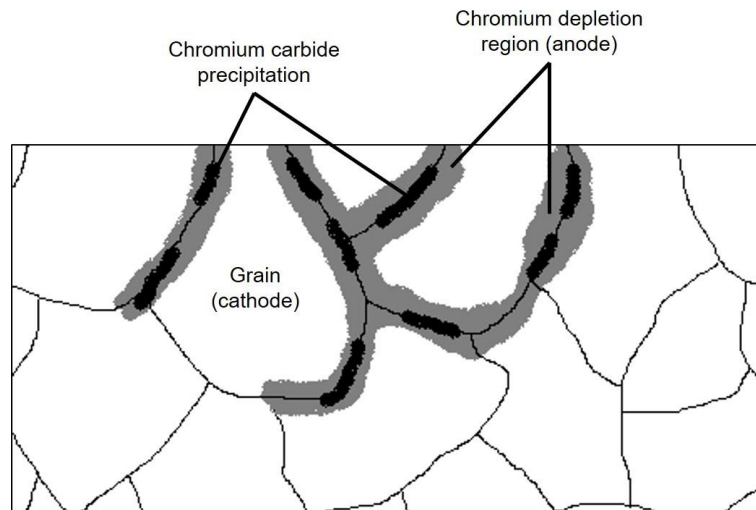


**Figure 3: Scheme of intergranular corrosion in austenitic stainless steel. Adapted from reference [11].**

The effect of IGC in aluminum alloys is more common for high strength alloys, in particular, 2XXX and 7XXX series, subjected to heat treatments, such as quenching and aging after a solution annealing.[9, 12] In Figure 4, the consequences of IGC in AA2024-T3 are displayed, with the appearance of deep trenches (grain boundary) running on the surface, creating what seems to be isolated areas (grain). The IGC in AA2024-T3 usually is a result of a slow quench leading to the formation of large copper-rich precipitates ( $\text{CuAl}_3$  and  $\text{CuMgAl}_3$ ).[12]

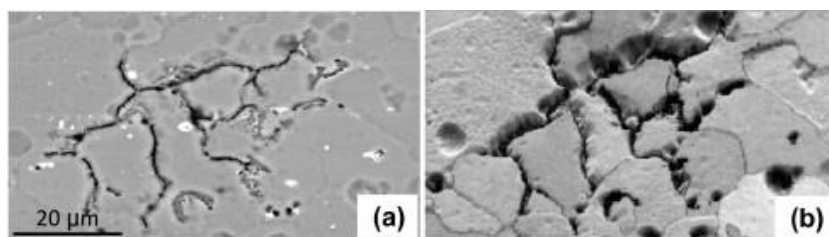


**Figure 4: Scanning electron micrographs and electron backscattered diffraction maps of AA2024-T3 aluminum alloy after immersion in 0.5 M NaCl solution for 18 h, (a) 80 x BSE, (b) 800 x SE 70° tilting (corrected). Adapted from the work of C. Luo and colleagues.[13]**

The IGC can occur without being detected on the metal surface leading to a decrease in mechanical strength and, eventually, structural failure when a load is applied or to the destruction of the material due to the falling out of individual grains. The depth reached by IGC is limited when compared with other forms of corrosion, like pitting corrosion, due to limits in the transport of oxygen and corrosion species in such narrow areas. Nonetheless, when the depth limits are reached, IGC starts to spread throughout the metal surface.[8, 12]

### 2.1.3 Galvanic corrosion

Galvanic corrosion can be defined as the degradation of a metal due to an electrical interaction with a more noble metal or nonmetallic conductors, the one with a more negative potential corroding preferentially, in a corrosive environment.[14] For the galvanic corrosion to occur the two metals must come in contact with an electrolyte to establish the connection between the metals thus forming a closed circuit. A crucial factor is a difference in potential between the metals, with large values favoring greater corrosion extent. The difference in potential leads to electrons to flow in the circuit, with oxidation processes (corrosion) and consequent metal dissolution occurring at the anode, and reduction processes (electrolyte reduction) taking place at the cathode.

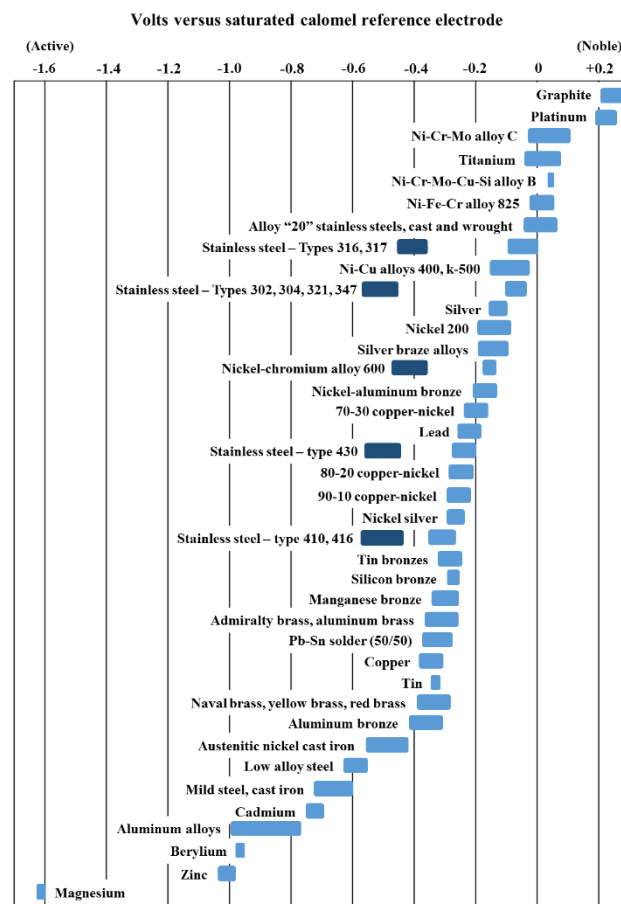


Figure 5: Galvanic series in sea water. The blue boxes indicate the active behavior for listed active/passive alloys. Adapted from reference [15].

Several factors can interfere in the extent of galvanic corrosion: the difference in metal potential (higher difference in potentials usually leads to higher corrosion extent),[14] oxygen concentration in the solution (corrosion is more extensive for higher oxygen

concentration),[16] temperature,[17] electrolyte conductivity and cathode/anode surface area ratio.[18] The galvanic series of different metals in seawater with respect to the saturated calomel reference electrode is presented in Figure 5. The figure indicates the metals and metal alloys more prone to galvanic corrosion. The materials with higher nobility (higher values of electrode potential) will be less susceptible to galvanic corrosion. Graphite and platinum are two examples. On the other hand, materials with higher activity (more negative values of potential) will be more susceptible to galvanic corrosion like zinc and magnesium.

A classic example of galvanic corrosion between two metals is shown in Figure 6, between Fe and Zn. This couple will be analyzed in more detail from its corrosion protection mechanism in section 2.3.3.1. The less noble metal, in this case Zn, will act as the anode, with the Zn starting to dissolve into the medium as  $Zn^{2+}$ . Fe, because is more noble, will act as the cathodic electrode, receiving the electrons from the Zn and will remain intact with  $O_2$  and/or  $H_2O$  reduction occurring on its surface.[14, 15, 19]

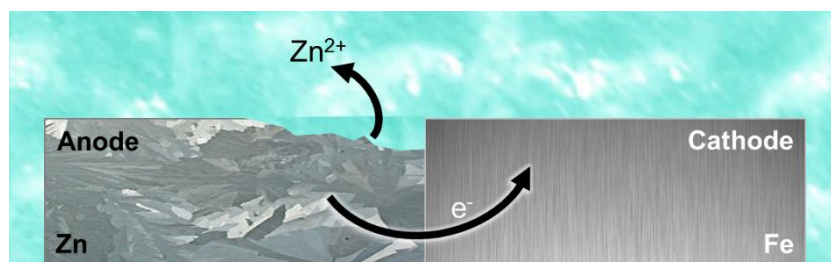


Figure 6: Scheme of galvanic corrosion between Zn and Fe.

#### 2.1.4 Pitting corrosion

Pitting corrosion is a form of localized corrosion, characterized by the presence of small spots on a metal surface with high corrosion rate. Pitting corrosion, according to the review work of M.G. Alvarez and J.R. Galvele,[20] can be divided into three types: electrochemical depassivation,[20] chemical depassivation,[21] and etch pitting.[22] Chemical depassivation and etch pitting are relatively rare and marginal forms of pitting corrosion.

Possible causes for the initiation of pitting corrosion are: a) the disruption of the passive film due to mechanical damage, leading to a corrosion process based on the exposed metal surface functioning as an anode and the passive layer surrounding it as a cathode[23]; b) inhomogeneity on the metal surface, that promote the loss of the passive film and

consequently the loss of the protective oxide layer;[23] c) adsorption of aggressive ions, which tend to penetrate through defects on protective coatings or through defects in the metal natural oxide layer leading to the depassivation of that small area.[24]

As observed for other mechanisms, the pitting corrosion rate tends to be boosted by temperature, pH, and bacteria but also by the presence of chlorides and sulfates in a medium with neutral pH.[24] Nevertheless, after a significantly rapid development at early stages, pitting corrosion tends to grow until a limited depth upon which the supply of oxygen is no longer efficiently provided by mass transport, impairing pit growth.[12] The pit that results from the corrosion process does not have a standard shape, depth or size and can be open or covered in a thin layer of corrosion products.[24] The overall shape and size of the pit are usually dependent on the type of rate-controlling reactions taking place during the pit growth and the anodic sites potential values.[25] Some of the most common types of pits shapes are shown in Figure 7.

In aluminum alloys pitting corrosion can be particularly destructive, often serving as the starting point for other forms of corrosion, potentially affecting the properties of the metal structure.[26] What provides AA2024 its remarkable mechanical properties is also its downfall in pitting corrosion: the presence of intermetallic precipitates. The AA2024 surface is covered with a passive oxide layer that becomes thinner and defective over the intermetallics due to the presence of different elements.[27] Pitting corrosion evolves differently according to different intermetallics, as in the case of  $Al_2CuMg$  (S-phase) and  $Al_6(Cu, Fe, Mn)$  intermetallics. For  $Al_2CuMg$  (S-phase) dissolution occurs, leaving a pit and for  $Al_6(Cu, Fe, Mn)$  the attack takes place in the bulk surrounding the intermetallic leaving inclusion nearly intact resulting in the formation of a trench.[26]

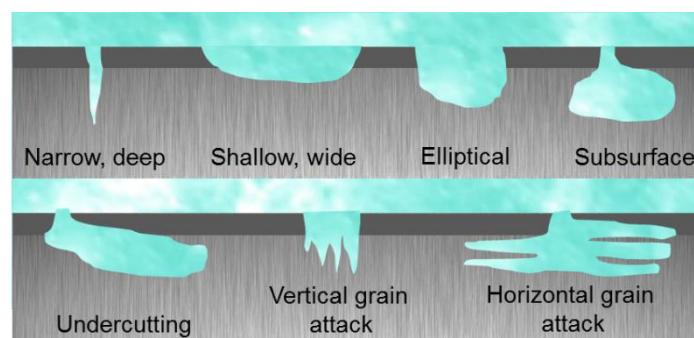


**Figure 7: Most common types or shapes of pits.[24, 25]**

The pitting corrosion occurring in Al<sub>2</sub>CuMg (S-phase) intermetallics of AA2024, presented in Figure 8, has been described in detail by Yasakau and colleagues.[27] The passive oxide layer at the intermetallics, due to its fragility, is attacked by aggressive species exposing the Al<sub>2</sub>CuMg (S-phase) surface to the water and initiating the chemical reaction with the active Al and Mg. These reactions result in the chemical dealloying of the S phase precipitates forming copper-rich areas and local non-uniformity of the intermetallics composition. With the evolution of the corrosion process leading to the increased deposit/concentration of copper at their surface and local pH increase, S phase intermetallics dissolution changes from chemical to electrochemical, considerably accelerating the corrosion process. The process continues with further dealloying of the intermetallics leaving the remaining Cu-rich S phase precipitate with a porous like form.[27, 28]

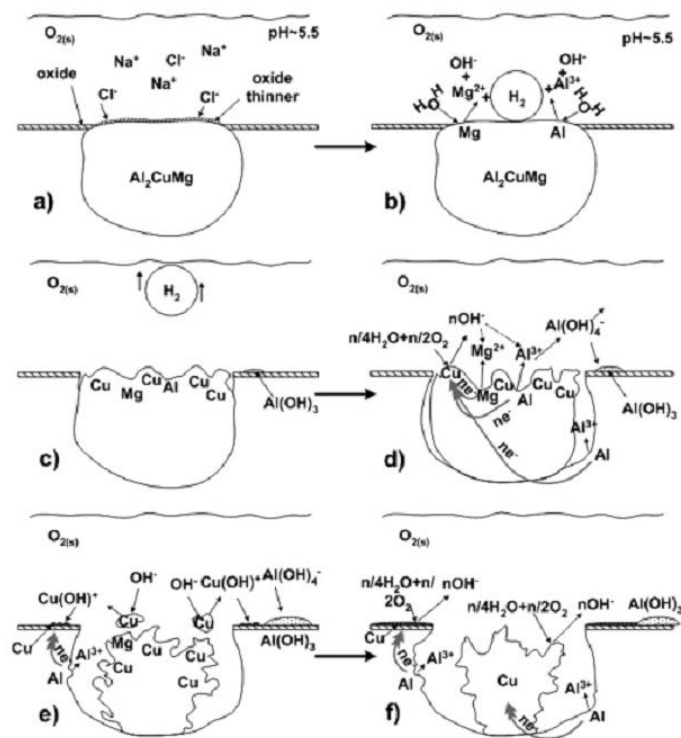


Figure 8: Schematic representation of pit corrosion mechanism of AA2024 in chloride solution. Reprinted with permission from Yasakau, K.A., et al., Mechanism of Corrosion Inhibition of AA2024 by Rare-Earth Compounds. The Journal of Physical Chemistry B, 2006. 110(11): p. 5515-5528). Copyright (2017) American Chemical Society.[27]

Pitting corrosion can be mitigated by changes in the alloy composition, alloy structure and decreasing the environment aggressiveness (chlorides concentration and temperature). More often, these changes are impossible to implement or out of human

control, so to decrease the threat of pitting corrosion one can resort to other alternatives: application of conversion films, introducing cathodic or anodic protection and making use of corrosion inhibitors.[29]

### 2.1.5 Crevice corrosion

Crevice corrosion, as in the case of pitting corrosion, is a type of localized corrosion. Contrasting with pitting corrosion, usually, a result of the alloys chemical composition, crevice corrosion tends to result from structural design flaws (*e.g.*, overlapping fuselage skins on aircraft), biofouling or debris. Crevice corrosion occurs when water and debris are accumulated in small crevices, confined regions of metallic components, usually found in bolt gasket, rivets, overlapping fuselage skins on aircraft, flanges on pipes and multiple layers in integrated circuit interconnected surface deposits.[30] The crevice design should be such that prevents the washing of the aggressive species that have accumulated inside it, usually a result of a narrow entrance point, ranging from 50  $\mu\text{m}$  to 200  $\mu\text{m}$ .[25, 29, 30]

The accumulation of aggressive species on the crevice leads to the formation of concentration cells (in particular oxygen) and areas of dissolution.[10] The oxygen-depleted areas inside the crevice will work as anodes, where the metal dissolution takes place, while the adjacent areas around the crevice entrance, rich in oxygen will function as cathodes, as illustrated in Figure 9.[29]

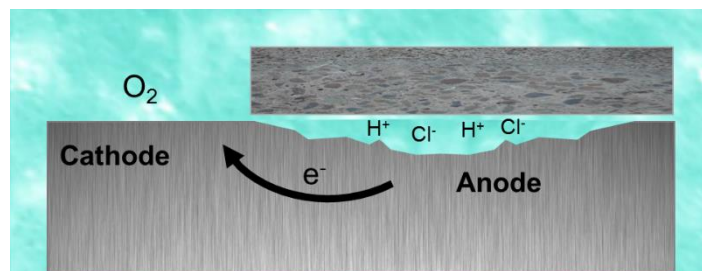


Figure 9: Scheme of crevice corrosion mechanism.[25]

Crevice corrosion in aluminum alloys is particularly relevant in the aerospace industry since a big part of the airplane structure is made of aluminum alloys. The difficulty of detection is one of the most challenging aspects of it, often leading to structural catastrophic failure of the structural components, in particular in older equipment. The corrosion can take place in unsealed or with damaged seal joints, on the riveted structure and

on the fuselage in contact with wet insulation blankets.[31, 32] During an airplane service life, moisture, maintenance and cleaning procedures, pollutant and chloride ions can be drawn into crevices attacking the oxide layer and starting the crevice corrosion processes.[31]

The corrosion protection against crevice corrosion uses similar approaches to pitting corrosion. The most common approach to avoid crevice corrosion is careful structural design, preventing the existence of crevices. Material selection is another important way to prevent crevice corrosion, by selecting a material with a more stable oxide layer and rich in specific alloying elements such as Cr, Mo, and N in stainless steel.[30, 32] Both approaches are strongly limited by the material application, which in most cases prevents material replacement or structural modifications. In these cases protection is achieved by the addition of inhibitors or through potential control. The addition of corrosion inhibitors follows an identical approach to protection against pitting corrosion. Nevertheless, for crevice corrosion, the effect is limited due to higher transport lengths for inhibitors to arrive in the active areas and low inhibitor concentration.[30]

### **2.1.6 Corrosion costs**

Costs associated with corrosion are considerable, with estimated costs around 3-5 % GDP in industrialized countries. This estimative accounts for direct costs, such as materials, equipment, and services (repair, maintenance, and replacement). Nevertheless, most of the reports overlook environmental damage, waste of resources, loss of production and personal injury as a result of corrosion.[33] The corrosion costs can be estimated using different methodologies, the most used are Uhlig method, Hoar method, and the In/Out method. The Uhlig method uses corrosion costs based on corrosion prevention methods, the calculation based on the direct corrosion costs from the production aspect.[34, 35] The Hoar method makes use of the cumulative costs of direct losses from corrosion for each industrial sector and the countermeasures associated with their mitigation.[35, 36] The In/Out method uses an input-output matrix summarizing the monetary transitions for each industry.[7, 35, 37]

One of the most relevant reports on corrosion costs was produced by the Federal Highway Administration (FHWA) in 2002.[38] The cost, calculated only for the USA, was estimated at \$276 billion per year, 3.1 % GDP.[38] A more recent work (2016) published by NACE international gives one of the most recent estimate on the cost of corrosion, in this

case a global perspective.[39] The authors compiled information from the available reports from different regions and by sector of application. The results for the year 2013 are displayed in Table 1. The fact that the costs of corrosion have different weights depending on the country, is not a surprise, with more industrialized countries presenting higher costs in sectors like industry and services compared with agriculture. In less industrialized regions the corrosion costs in agriculture tend to have a higher impact and in the case of India even presents values close to the ones obtained for industry and services.

The overall percentage of the GDP associated with corrosion costs tend to be similar between different regions, from 1 % for Japan to 5 % register in the Arab world. These values must have into account not only the level of industrialization but also climatic features from each region. Averaging the values worldwide gives corrosion costs around 3.4 % of the GDP. This value does not fall far from the one reported in 2002 by FHWA, around 3.1 % only for the USA.

The results show the relevance of corrosion from an economic point of view. The costs, direct or indirect, associated with corrosion have a significant impact on companies and countries budget, making it mitigation a paramount issue which can impact at different levels: economic, safety and environmental.

Due to the scope of metals used in this thesis and the industrial partners involved, a closer look into the costs of corrosion for the automotive and aeronautic industries will be shown. It is not easy to find a general report in open literature which compiles the costs from a worldwide perspective. Even when analyzing country by country is difficult to find update values resulting from the application of uniform methodologies. Nevertheless, case studies will be presented and some level of extrapolation can be done to obtain a wider view of the corrosion impact in both industries.

**Table 1: Corrosion costs by sector and region in 2013. Adapted from reference [39].**

<b>Economic regions</b>	<b>Agriculture (USD billion)</b>	<b>Industry (USD billion)</b>	<b>Services (USD billion)</b>	<b>Total (USD billion)</b>	<b>% GDP</b>
<b>USA</b>	2.0	303.2	146.0	451.3	2.7 %
<b>India</b>	17.7	20.3	32.3	70.3	4.2 %
<b>European region</b>	3.5	401	297	701.5	3.8 %
<b>Arab world</b>	13.3	34.2	92.6	140.1	5.0 %
<b>China</b>	56.2	192.5	146.2	394.9	4.2 %
<b>Russia</b>	5.4	37.2	41.9	84.5	4.0 %
<b>Japan</b>	0.6	45.9	5.1	51.6	1.0 %
<b>Four Asian Tigers plus Macau</b>	1.5	29.9	27.3	58.6	2.5 %
<b>Rest of the World</b>	52.4	382.5	117.6	552.5	3.4 %
<b>Total</b>	<b>152.7</b>	<b>1446.7</b>	<b>906.0</b>	<b>2505.4</b>	<b>3.4 %</b>

### *Automotive industry*

The impact of corrosion costs in two of the main automotive producers will be presented, USA and Japan. Unfortunately, the available results are from 1997 (Japan) and 1999 (USA). In the case of the USA is possible to see the evolution in corrosion associated costs since the 1970s, with a steady decrease due to improvements in all levels of product development and production.

#### Japan

The corrosion costs associated with vehicle production was divided into the car body and the car parts. The corrosion costs for the body materials was calculated around 171 USD per car per year, to which is added 54 USD per car associated with vehicle parts. Overall, the 225 USD per car per year accounts for 1.8 % of the total price. Maintenance costs were also calculated around 42 USD per car per year.[35]

#### USA

The direct costs of corrosion in the automotive industry in the USA was estimated at 23.4 billion USD per year. The value was divided into three main components: manufacturing costs related with corrosion engineering and the use of corrosion resistant materials (2.56 billion USD per year), corrosion-related repairs and maintenance (6.45 billion USD per year) and vehicle depreciation due to corrosion (14.46 billion USD per year).[38] Extrapolating these values for individual units the value is 192 USD per car per year.[39] The values associated with corrosion are significant. However, improvements have been made to reduce the impact of corrosion in this industry. Comparing studies from 1975 and 1999 is possible to observe a significant improvement in the cost associated with corrosion per car. In 1975 the manufacturing cost associated with corrosion was 344 USD per vehicle per year which compares with the 192 USD per vehicle per year in 1999.[39] The cost reduction was possible due to a change in the top manufactures philosophy involving improvements in various areas: design, materials, and processing.[39]

### *Aeronautic industry*

The corrosion-related costs in the USA aircraft industry were estimated in 2.2 billion USD per year, value divided into design and manufacturing (0.2 billion USD), corrosion maintenance (1.7 billion USD) and downtime (0.3 billion USD).[38, 40]

## 2.2 Active metal alloys

The overview of some of the main forms of corrosion is not complete without knowledge of the metal substrate where it can take place. Some of the types of corrosion addressed previously are intrinsically related with specific metal alloy compositions, namely pit corrosion in aluminum alloys or uniform corrosion in carbon steel. Therefore, it is important to make an overview of the history, characteristics, and applications of some of the most studied metallic substrates.

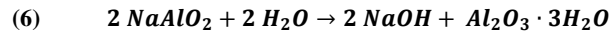
### 2.2.1 Aluminum alloy 2024-T3

#### 2.2.1.1 Aluminum production

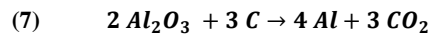
Aluminum, as an element, has been known to man only for the last two centuries and as a workable metal in the last 100 years. Since its production has been made economically viable, its applications were extended to almost all facets of our lives. The widespread use of aluminum and its alloys is due to their properties, endowing them a remarkable versatility.

Aluminum was identified for the first time by Sir Humphry Davy in 1808 but only in 1854 was the first commercial process of production developed, by Henri Sainte-Claire Deville. Nonetheless, its production would be too expensive during the next 40 years until Charles Martin Hall in the United States and Paul L.T. Héroult in France, almost simultaneously, developed the electrolyte method in 1886.[41, 42]

Aluminum is obtained from alumina that is recovered from bauxite ore. Alumina usually is recovered using the Bayer process, developed in 1888 by Karl Josef Bayer. The reaction takes place between strong sodium hydroxide solutions and crushed bauxite at 240 °C, at which most of the alumina is dissolved, as described in Equation (5). The next stage, described in Equation (6), requires cooling the alumina and adding  $\text{Al}_2\text{O}_3 \cdot 3\text{H}_2\text{O}$  crystals, which work as nucleation seeds, promoting the precipitation of alumina particles. The final process before obtaining alumina is the calcination of  $\text{Al}_2\text{O}_3 \cdot 3\text{H}_2\text{O}$  in a two-step process, the first between 300-600 °C (removing the water of crystallization and producing the more chemical active  $\gamma$ -form) and the second at 1200 °C (converting partly or fully into  $\alpha$ -alumina form).[42]

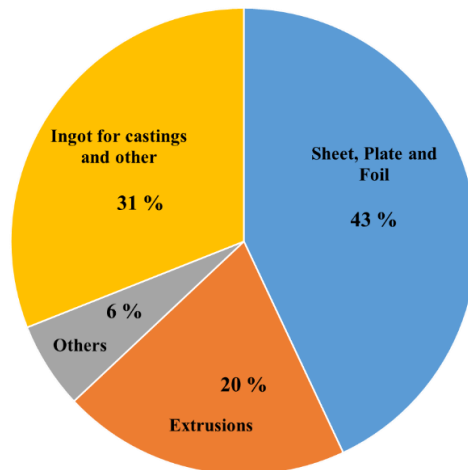


The production of aluminum from alumina usually is done according to the Hall–Héroult process, consisting of an electrolytic reduction under high temperature. The modern version of this process takes place at 950 °C in a carbon or graphite coated steel container, designated by “reduction pot”. The reaction preceded by dissolving alumina in molten cryolite ( $Na_3AlF_6$ ), along with  $AlF_3$  and  $CaF_3$  as additives, in a proportion of 80–90% cryolite to 2–8% alumina. The reasoning behind dissolving alumina in cryolite is to make it more workable and affordable since alumina has a high melting point, around 2040 °C. The electrolytic reduction is initiated by inducing a current (5.25 V) between an anode (positively charged), carbon obtained from petroleum coke, and a cathode (negatively charged), the reduction pot internal coating of carbon and graphite. The anode and cathode are 4–5 cm apart. The reaction that takes place is described, in its simplest form, in Equation (7).[42]

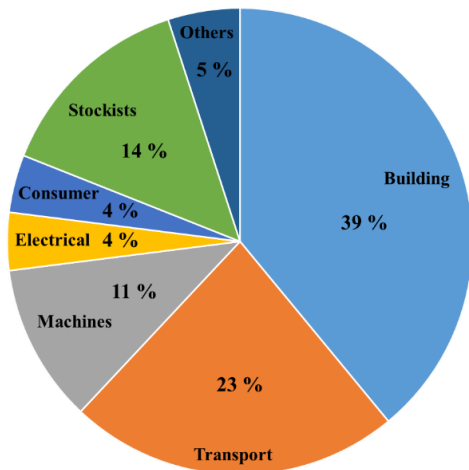


Aluminum and its alloys have potential applications in a wide variety of fields. Figure 10 shows the distribution of aluminum mill products by product type in North America (a) and application in Europe (b) and North America (c). The main types of products are ingot, sheet, plate, and foil primarily used in machinery, equipment, and transportation. The use of aluminum has steadily increased since its entry into the market, reaching values around 57,890 thousand metric tons of aluminum in 2015, compared with 24,657 thousand metric tons produced in 2000.[43] This sizeable growth is justified by the considerable advantages provided by aluminum, either as a pure metal or in the form of alloys, such as: high strength-to-weight ratio, resilient, ductile at low temperatures, corrosion resistant, non-toxic, heat conducting, reflective, electrically conducting, non-magnetic, attractive appearance, wide range of finishes, easy to fabricate, recyclable and cost-effective.

a



b



c

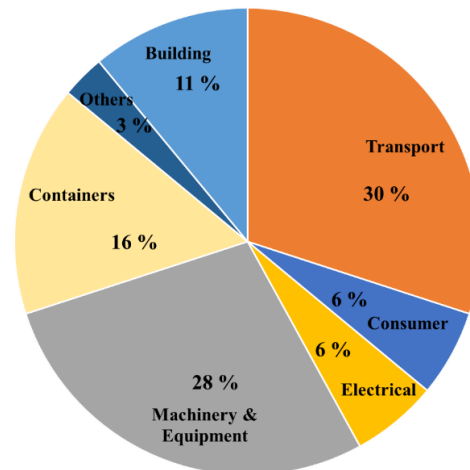


Figure 10: The distribution of aluminum by product type in North America in 2014 (a) and by end-use market in Europe in 2007 (b) and in North America in 2014 (c).[44]

### 2.2.1.2 Aluminum alloys

Aluminum alloys are, usually, divided into two major types: cast and wrought. Among these two main categories, there are subdivisions, based on the main alloying element. For wrought aluminum alloys the classification is done into series from 1XXX to 8XXX, as summarized in Table 2. For cast aluminum alloys the series designation is slightly different, 1XX.X to 9XX.X with the designation 6XX.X not being used. The serial number of wrought and cast aluminum do not necessarily coincide in the main alloying element.[41] The digit after the series identification number also provides specific information concerning the alloy composition. Taking AA2024-T3 as an example: the first digit (2), as seen above, identifies the series and consequently the major alloying elements (Cu and Mg for AA2024). The second digit (0) concerns some modifications to the alloy or limits to the level of impurities. The third and fourth digits

(24) identify the specific alloy or in the case of the 1XXX series the minimum Al percentage.[45]

Table 2 summarizes the wrought aluminum series along with their main alloying element and properties. The variety of properties and diversity of elements able to alloy with aluminum are considerable, making it one of the most versatile metals. Among other applications aluminum alloys are used as structural elements in the construction of aircraft (2XXX, 6XXX, 7XXX and 8XXX), in a variety of parts for the automotive industry (5XXX, 6XXX and 7XXX), electrical conductors (1XXX), storage tanks (3XXX) and heat exchangers (3XXX and 8XXX), among others. The alloying element along with its percentage is key in the resulting metal properties.

**Table 2: Wrought aluminum alloys, primary alloying element, and properties.[41, 46, 47]**

Series	Major alloying elements	Properties
1XXX	Al $\geq$ 99%	Low strength; excellent thermal/electrical conduction; excellent corrosion resistance
2XXX	Al-Cu-(Mg)	High strength; relatively low corrosion resistance; good elevated temperature resistance
3XXX	Al-Mn	Medium strength; good corrosion resistance
4XXX	Al-Si	High castability; high machinability; low ductility
5XXX	Al-Mg	Medium strength; good formability; excellent marine corrosion resistance
6XXX	Al-Mg-Si	Medium-high strength; good corrosion resistance
7XXX	Al-Zn-(Mg)-(Cu)	Very high strength; prone to stress corrosion; poor corrosion resistance
8XXX	Al-Other	Very high strength; low density

Besides the alloy series, based on the major alloying elements after aluminum, the type of temper also takes place in the alloy designation. Using AA2024-T3 as an example is possible to identify the major alloying elements as Cu and Mg and the tempering process used, in the case of T3. The designation T3 accounts for an aged-hardened alloy (T) that was solution-treated, cold-worked and then naturally aged (3). The complete designations for tempers used in aluminum alloys are presented in Table 3. Each type of temper endows the metal with specific mechanical properties.[41, 45]

Among the great variety of aluminum applications, the aeronautical field stands as one of the most demanding concerning the metal's mechanical properties and overall performance, due to its very rigorous safety concerns. Aluminum and its alloys account for 80 % of the modern aircraft structure,[45] being replaced, in some components, by composite materials, in the most recent models where the aluminum accounts for only 20 %. Two examples of these changes in material usage can be found in the airplane models A350 from Airbus and the 787 from Boeing. Nevertheless, the demand for

aluminum alloys remains high, being by far the most commonly used aluminum alloys in the aircraft industry the 2XXX (Cu and Mg), the 6XXX (Si and Mg) and the 7XXX (Zn, Mg, and Cu). In common they have the characteristic of being precipitation-hardenable alloys. Their microstructure is carefully controlled by heat-treatment aiming at achieving the formation of fine and coherent precipitates whose morphology and distribution will control the mechanical properties of the material.[45, 48]

**Table 3: Aluminum alloys temper designations.[45]**

<b>Designation</b>	<b>Properties</b>
<b>S</b>	<b>As fabricated (e.g. forged, cast)</b>
<b>O</b>	<b>Annealed (only wrought)</b>
	<b>Cold-worked (strain hardened)</b>
<b>H</b>	H1x: cold-worked only (x refers to the amount of cold working and strengthening) H2x: cold-worked and partial annealed H3x: cold-worked and stabilized at a low temperature
<b>W</b>	<b>Solution-treated</b>
	<b>Age-hardened</b>
<b>T</b>	T1: cooled from fabrication temperature and naturally aged T2: cooled from fabrication temperature, cold-worked and naturally aged T3: solution treated, cold-worked and naturally aged T4: solution treated and naturally aged T5: cooled from fabrication temperature and artificially aged T6: solution-treated and artificially aged T7: solution-treated and stabilized by over-aging T8: solution-treated, cold-worked and artificially aged T9: solution-treated, artificially aged and cold-worked T10: cooled from fabrication temperature, cold-worked and artificially aged

AA2024 applications in aircraft are vast, being used in the manufacture of aircraft skins, cowls and aircraft structures. These aircraft parts require strong and flexible materials, in agreement with the characteristics of aluminum from the 2XXX series which forms high strength precipitates when aluminum is heat treated, in an age-hardener process.[48] Its composition typically is: Cu 3.8-4.9 %, Mg 1.2-1.8 %, Mn 0.3-0.9 %, Fe 0.5 %, Si 0.5 %, Zn 0.25%, Ti 0.15 %, Cr 0.1 %, other 0.15 %, balance Al. The formation of intermetallic precipitates and their homogeneity in the aluminum matrix are vital for its mechanical properties, thus a more detailed analysis of AA2024 microstructure is presented.

### 2.2.1.3 AA2024 microstructure

The microstructural analysis of AA2024 is not a straightforward task, exempt from controversy. Studies have been performed almost since the first sheet of AA2024 was produced, with the interpretation drawn from the results not necessarily agreeing with the intermetallics' full composition. The high concentration of alloying elements,

compared to other aluminum alloys and impurities, accounts for the complexity in microstructures found on AA2024.[49]

Intermetallic particles tend to be divided into three main groups based on their size: first coarse constituents and impurity particles ( $> 0.5 \mu\text{m}$ ), second dispersoids ( $100\text{--}500 \mu\text{m}$ ) and third hardening precipitates ( $< 200 \text{nm}$ ). Most of the dispersoids are composed by  $\text{Al}_{20}\text{Mn}_3\text{Cu}_2$  and, along with impurities, they tend to form during the ingot casting, remaining fairly insoluble throughout the subsequent treatments. Hardening precipitates are usually subdivided into two categories based on the clusters formed by the aggregation of Cu, Mg, and Al. These aggregates are designated Guinier-Preston when formed by Al-Cu, and Guinier-Preston-Bagaratsky when composed by Al-Cu-Mg.[49]

Studies performed by Buchheit and colleagues points toward S-phase  $\text{Al}_2\text{CuMg}$  particles accounting for 60 % of the intermetallic particles found in the AA2024-T3 structure.[50] The remaining particle compositions include  $\text{Al}_7\text{CuFe}_2$ ,  $\text{Al}_6\text{Mn}$ ,  $\text{Cu}_6\text{Mn}$ ,  $\text{Al}_6\text{Cu}$ , and  $\text{Al}_6\text{Fe}$ . [51] The importance of S-phase intermetallic particles cannot be underrated. Not only it accounts for a considerable percentage of the intermetallic particles in the AA2024 structure, but also is prone to corrosion initiation, namely pitting corrosion, leading to dissolution and dealloying phenomena.[28, 50]

Corrosion in AA2024 has been already addressed in the section dealing with the main forms of corrosion, where it was often used as an example for specific types of corrosion. The corrosion in AA2024 relates closely with their intermetallic composition and distribution, these sites being associated with the initiation of localized corrosion due weaknesses in the oxide layer, prompted by the presence of intermetallic particles. The formation of galvanic coupling between the intermetallic precipitates and the aluminum matrix also promotes the occurrence of localized corrosion.[52]

The main forms of localized corrosion affecting AA2024 are pitting corrosion, intergranular corrosion, stress corrosion cracking and exfoliation.[28] In most cases, galvanic corrosion is associated with one of these forms of corrosion. Pitting and intergranular corrosion in aluminum have been described in detail previously.

### 2.2.2 Steel

Steel is an iron alloy where the major alloying element is carbon, with percentages varying from 0.2 % until 1.7 % for most commercial steel products. It is the carbon percentage that defines what is considered steel and, more relevantly, its properties. If the carbon percentage is too low, it is deemed wrought iron (0.02 % to 0.08 %), having enough carbon to harden the metal without losing malleability. If the carbon percentage is between 3 % and 4.5 %, the metal will be designated cast iron, because the molten iron is poured into a mold (a cast), resulting in a very hard material which cannot be worked afterward due to being brittle and nonmalleable.[53, 54] Steel lies between these two extremes, with its intermediate carbon content allowing for a good compromise of strength and flexibility. The discovery of iron ushered in an unprecedented era in human history, the start of the Iron Age, bringing the Bronze Age to an end, around 1200 B.C. The origins of wrought iron lie in those forges where the iron ore was worked. Contamination with small amounts of carbon led to a new material, harder but still malleable, the very first wrought iron. This fueled the replacement of most of the bronze tools and weapons since wrought iron was more resistant, durable and in the particular case of weapons, was able to keep the edge. The advent of the cast iron is associated with the appearance of better quality forges and dates back to the Middle Ages. This innovation allowed for the melting of iron and, consequently, of a higher amount of carbon being incorporated into the metal, leading to the creation of very hard materials. The excessive hardness and brittleness of these materials rendered them unworkable. The optimization of furnaces, with the appearance of blast furnaces, which introduced oxygen directly into the molten iron, led to the decrease of the carbon percentage in molten pig iron (high values of carbon), as carbon was removed in the form of carbon dioxide. This strategy was designated “Bessemer process”. Improvements were made in the manufactory process, namely the introduction of coke, a more pure form of carbon, and the addition of limestone, to remove phosphates contaminants. These changes, together with improvements in the production design, led to the manufacture of steel in accordance with required specifications, resulting in cheaper steel with higher quality, making it the material by excellence in many areas of our lives.[53] Modern society depends heavily on steel to build its world, as easily perceived by considering the values of steel consumed worldwide, reaching 1,665 million tones (Mt) in 2014.[55] Steel applications include, among others: construction, appliances, equipment, and vehicles. Flexibility in

applications and consumption values are a statement of steel as the most successful and cost-effective material, in part due to the possibility to process steel with a huge variety of microstructures and properties.[56]

**Table 4: Examples of classification parameters used in steel.[57]**

Classification parameter	Examples
<b>Composition</b>	<b>such as:</b> carbon, low alloy, or stainless steel
<b>Manufacture methods</b>	<b>such as:</b> open hearth, basic oxygen process, or electric furnace methods
<b>Finishing method</b>	<b>such as:</b> hot rolling or cold rolling
<b>Product form</b>	<b>such as:</b> bar plate, sheet, strip, tubing, or structural shape
<b>Deoxidation practice</b>	<b>such as:</b> killed, semi-killed, capped, or rimmed steel
<b>Microstructure</b>	<b>such as:</b> ferritic, pearlitic, or martensitic
<b>Required strength level</b>	<b>such as:</b> as specified in various industry standards
<b>Heat treatment</b>	<b>such as:</b> annealing, quenching and tempering, and thermomechanical processing
<b>Quality descriptors</b>	<b>such as:</b> forging quality and commercial quality

The classification of types of steel can be done using a considerable array of parameters, as exemplified in Table 4.[57] This table shows in detail the possible ways to classify steel, but can be summed up into three major categories: composition (alloying elements percentages and microstructure), methodologies of production (finishing method, product form, deoxidation and heat treatment), quality control (required strength and quality descriptors).

**Table 5: Four-digit index classification of alloy steels and primary alloying element and properties based on the SAE/AISI carbon steel naming conventions.[57-59]**

Series	Major alloying elements	Examples
<b>1XXX</b>	C	<b>10XX</b> - Plain carbon steel, Mn 1.00 % max <b>11XX</b> - Resulfurized free cutting <b>12XX</b> - Resulfurized. Rephosphorized free cutting <b>13XX</b> - Mn 1.75 % <b>15XX</b> - Plain carbon steel, Mn 1.00-1.65 %
<b>2XXX</b>	Ni	<b>23XX</b> - Ni 3.50 % <b>25XX</b> - Ni 5.00 %
<b>3XXX</b>	Ni and Cr	<b>31XX</b> - Ni 1.25 %, Cr 0.65-0.80 % <b>32XX</b> - Ni 1.75 %, Cr 1.07 % <b>33XX</b> - Ni 3.50 %, Cr 1.50-1.57 % <b>34XX</b> - Ni 3.00 %, Cr 0.77 %
<b>4XXX</b>	Mo	<b>40XX</b> - Mo 0.20-0.25 % <b>41XX</b> - Cr 0.50-0.95 %, Mo 0.12-0.30 % <b>42XX</b> - Ni 1.82 %, Cr 0.50-0.80 %, Mo 0.25 % <b>43XX</b> - Ni 1.82 %, Cr 0.50-0.80 %, Mo 0.25 % <b>44XX</b> - Mo 0.40-0.52 % <b>46XX</b> - Ni 0.85-1.82 %, Mo 0.20-0.25 % <b>47XX</b> - Ni 1.05 %, Cr 0.45 %, Mo 0.20-0.35 % <b>48XX</b> - Ni 3.50 %, Mo 0.25 %
<b>5XXX</b>	Cr	<b>50XX</b> - Cr 0.27-0.65 % <b>51XX</b> - Cr 0.80-1.05 % <b>51XXX</b> - Cr 1.02 %, C 1.00 % min <b>52XXX</b> - Cr 1.45 %, C 1.00 % min <b>50XXX</b> - Cr 0.50 %, C 1.00 % min
<b>6XXX</b>	Cr and V	<b>61XX</b> - Cr 0.60-0.95 %, V 0.10-0.15 %
<b>7XXX</b>	W	<b>72XX</b> - W 1.75 %, Cr 0.75 %
<b>8XXX</b>	Ni, Cr and Mo	<b>81XX</b> - Ni 0.30 %, Cr 0.40 %, Mo 0.12 % <b>86XX</b> - Ni 0.55 %, Cr 0.50 %, Mo 0.20 % <b>87XX</b> - Ni 0.55 %, Cr 0.50 %, Mo 0.25 % <b>88XX</b> - Ni 0.55 %, Cr 0.50 %, Mo 0.35 % <b>92XX</b> - Si 1.40-2.00 %, Mn 0.65-0.85 % <b>94XX</b> - Ni 0.45 %, Cr 0.40 %, Mo 0.12 %
<b>9XXX</b>	Si and Mn	<b>97XX</b> - Ni 0.55 %, Cr 0.20 %, Mo 0.20 % <b>98XX</b> - Ni 1.00 %, Cr 0.80 %, Mo 0.25 % <b>93XX</b> - Ni 3.25 %, Cr 1.20 %, Mo 0.12 %

An accepted form of steel classification was developed by the Society of Automotive Engineers (SAE) and the American Iron and Steel Institute (AISI) which

follows a similar format as aluminum alloys, as listed in Table 5. It makes use of four-digit numbers, sometimes five, to classify the steel alloy according to the main alloying elements. The series runs from 1XXX to 9XXX where the first digit indicates a general category of the steel, associated with the main alloying elements. The second digit indicates the present elements that can affect the steel properties. The last two digits give the amount of carbon present in the alloy, in percentage.[60]

The variety of steel products is in line with the huge variety of types of steel. Table 6 describes different forms of steel products form and their export values in million tons, in 2014, for the global market.[55] Ingots, bars, wire hot-rolled sheets and coils, plates, and tubes are among the most commercialized. Worthy of notice is the high volume of exports worldwide for cold-rolled steel sheets and galvanized steel, averaging 35 to 38 Mt. Due to their commercial relevance, especially in demanding areas of application (e.g. automotive), there is great economic interest in advancing corrosion protection studies, aiming at increasing the material's service life and its overall performance.

**Table 6: Steel products export values worldwide in 2014.[55]**

<b>Steel product</b>	<b>2014 exports (Mt)</b>	<b>Steel product</b>	<b>2014 exports (Mt)</b>
<b>Ingots and semi-finished material</b>	49.2	<b>Cold-rolled sheets and coils</b>	35.0
<b>Railway track material</b>	2.1	<b>Electrical sheet and strip</b>	4.0
<b>Angles, shapes, and sections</b>	23.0	<b>Tin mill products</b>	6.5
<b>Concrete reinforcing bars</b>	19.3	<b>Galvanized sheet</b>	37.7
<b>Bars and rods, hot-rolled</b>	28.5	<b>Other coated sheet</b>	16.6
<b>Wire rod</b>	28.2	<b>Steel tubes and fittings</b>	38.6
<b>Drawn wire</b>	7.9	<b>Wheels (forged and rolled) &amp; axles</b>	0.7
<b>Other bars and rods</b>	5.5	<b>Cold-rolled strip</b>	3.7
<b>Hot-rolled strip</b>	3.3	<b>Plates</b>	32.2
<b>Hot-rolled sheets and coils</b>	72.1	<b>Castings</b>	0.9

#### 2.2.2.1 Cold-rolled steel

The designation of cold-rolled steel does not directly relate with the steel composition, but rather with the conditions in which the steel was worked. To better understand the designation 'cold-rolled steel', one should compare it with hot-rolled steel. Their names denounce the nature of their manufacturing process, one being worked at high temperature and the other at room temperature. Hot-rolled steel is worked at temperatures above the steels recrystallization point, around 925 °C. This allows for the

steel to be worked more easily and in larger sizes. Cold-rolled steel starts like hot-rolled steel but it is subjected to further treatment, with the steel being cooled down to room temperature in cold reducing mills followed by annealing and/or tempers rolling. Comparing with hot-rolling steel, cold-rolled steel allows for a more controlled finish product: higher dimensions control (allowing for tighter thickness tolerances) and the possibility to apply different surface finishes. This control over the final product's specifications, together with the extra work and time put into production, makes it more expensive.

'Cold-rolled steel', as a form of steel treatment during the manufacturing process, cannot be associated with a specific type of steel, since the term can be equally used to designate types of carbon steel or types of stainless steel. Nevertheless, in this work, when the designation cold-rolled steel is used it refers to carbon steel. Carbon steel can be subject to several types of corrosion depending on the environment, an aqueous medium (general corrosion, pitting corrosion, crevice corrosion or erosion-corrosion), environmental assistant cracking (hydrogen embrittlement) and microbiologically-induced corrosion.[61]

#### 2.2.2.2 Stainless steel

The development of stainless steel took place around the beginning of the 20<sup>th</sup> century and is wrapped in some controversy, with several researchers in different countries claiming its paternity. But in most cases, the honors have been given to Harry Brearley, an English researcher trying to develop more durable steel for cannons when he discovered a low carbon high chromium steel that was corrosion resistant. Brearley saw the considerable economic prospects of stainless steel in the cutlery industry, hence the designation of 'stainless', coming from its high resistance to oxidation in the presence of acids, ascertained by Brearley by testing the steel in a vinegar solution.[62]

Stainless steel is an iron alloy, but carbon is not the main alloying element, being surpassed by chromium, which confers its superior corrosion protection properties. In fact, the carbon values are very low, usually below 0.24 %, compared with the amount of chromium, around 11.5 % or more.[62, 63] This corrosion protection is given by the formation of a protective layer on the metal surface, a process named 'passivation'. Passivation is the formation of an inactive or less reactive surface as a result of a chemical treatment. In stainless steel, it is achieved by the reaction between chromium and oxygen forming a chromium oxide layer.[64] The combination of good corrosion properties

together with their appealing aesthetic aspect renders stainless steel the material of choice for surgical instruments, cookware, hospital appliances and pharmaceutical processing facilities. Stainless steels are divided, as in the case of aluminum and other steel alloys, into series numbered from 1XX to 5XX, according to the element composition, as shown in Table 7. Contrasting with the other alloys and with the exception of the first digit, stainless steel identification does not have any direct link with the material composition. Information concerning material specifications is given by number and letters following the series number. Another form of classification, that in some aspects follows the one presented in Table 7, is based on classes connected with the alloying elements that affect their microstructure, which designates the classes. The classes are: austenitic stainless steels, ferritic stainless steels, martensitic stainless steels, duplex or austenoferritic stainless steels and precipitation-hardened (P-H) stainless steels.[59, 63, 65] The austenitic, ferrite and martensite are basic microstructures. Austenitic have a face-centered cubic structure comparing with a body-centered cubic structure of ferrite, with martensite being a result of the complex transformation of an austenitic microstructure. Austenitic forms of stainless steel account for almost 50 % of the world production of this corrosion-resistant iron alloy.[66]

**Table 7: Stainless steel series and main characteristics.[65]**

Series	Characteristics	Properties
1XX	Austenitic: general purpose stainless steel	Not heat treatable
2XX	Austenitic: Cr, Ni, and Mn steel	Not heat treatable
3XX	Austenitic: Cr and Ni steel	Heat treatable
4XX	Ferritic and martensitic Cr steel	Heat treatable
5XX	Heat resistant steel	

The corrosion resistance properties of stainless steel are known and, when compared with other iron-based alloys, the difference is substantial. As stated before, chromium plays a key role in the superior corrosion resistance of stainless steel. In fact, the amount of Cr has increased from around 12 % in most of the early alloys to around 18 %, the percentage found nowadays in most common steel grades.[66] Nevertheless, stainless steel is not impervious to corrosion and eventually falls victim to it. Corrosion, regardless of the type, is associated with loss of the permanent oxide passive layer. Localized defects tend to originate pitting and crevice corrosion, usually occurring in neutral solution or at low pH. The high corrosion rates associated with these two forms of corrosion often result in catastrophic structural failure. The localized loss of the oxide layer also can lead to the start of intergranular corrosion along the grain. Uniform

corrosion can occur in the cases where the passive film is completely lost and can occur at high or low pH.[66, 67]

### 2.2.2.3 Galvanized and galvanized steel

The susceptibility of steel to corrosion has been addressed by diverse approaches: application of protective coatings (e.g. organic coatings), the addition of corrosion inhibitors, cathodic protection, anodic protection or the application of a metallic coating (e.g. Zn or Al). Galvanized steel makes use of two of these approaches to provide protection by applying a Zn layer on top of the steel substrate. The Zn layer offers two forms of corrosion protection, namely by providing a barrier protection and as a sacrificial anode. Firstly, it works as a physical barrier, isolating the steel substrate from aggressive media being affected first. Secondly, the Zn layer will provide galvanic protection, since Zn is less noble than iron, by sacrificial protection, corroding first, thus protecting the steel substrate, even protecting areas where iron is exposed.[68, 69]

The first studies reporting the application of a Zn layer in an iron substrate dates from 1742 and were done by the French physician Paul Jacques Melouin. A century later (1837) another French chemist, Stanislas Sorel filed a patent describing the application of a zinc layer in iron through the immersion of the metal substrate in a bath of molten zinc, naming it galvanizing. In few years the method was adopted by industry and galvanized steel started to be produced in factories throughout Europe and North America.[68, 70] Since its development, galvanized steel had an important role in several areas, namely, in later decades, in automotive and building industries, which boosted research on steel galvanization.[69]

The zinc layer on galvanized steel can be applied in different ways: thermal spraying of zinc (metalizing), electroplating of zinc, sherardizing (diffusion zinc coating), mechanical plating, zinc-rich paints and hot-dip galvanizing (bath or continuous), the latter being the most common. Hot-dip galvanizing allows for the metal substrate to be enriched with some excellent properties: high strength, formability, lightweight, corrosion resistance, low cost, and recyclability.[68, 70]

The hot-dip galvanizing process can be done in a static (bath) or continuous approach. Both approaches follow the same principles: a first step consisting of cleaning and preparation of the steel surface, followed by the application of the Zn by immersion. Cleaning is normally done in three steps: degreasing the surface (alkaline treatment under temperature), surface pickling to remove iron oxides (using solutions of hydrochloric or

sulfuric acid) and fluxing to dissolve any oxide film left after pickling (a mixture of zinc chloride and ammonium chloride). After cleaning, the metal substrate is immersed in a molten zinc bath (98 % pure) at 450 °C for approximately 5 minutes and finally removed at a controlled velocity. The bath composition, temperature, time of immersion and speed of removal can be adjusted according to the specifications.[68-70]

The immersion of steel in the molten zinc bath results in the formation of a zinc layer that bonds with the metal substrate to form a multilayer system where each layer has a specific iron to zinc ratio. A scheme showing the process leading to the formation of a multi-layer Zn coating during the hot-dip process is presented in Figure 11. After the hot-dip process the Zn layer can be separated into an outer layer of 100 % zinc followed by a zeta layer (94 % Zn to 4 % Fe), a delta layer (90 % Zn to 10 % Fe) and a gamma layer (75 % Zn to 25 % Fe) closest to the steel surface.[68]

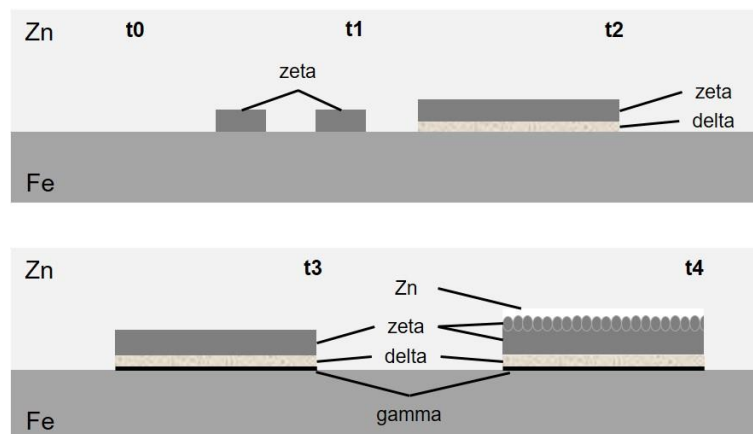


**Figure 11: Schematic representation of Fe-Zn phase layer formation, over time, in a galvanizing bath. Adapted from the references [69, 71]**

The manufacture of galvanized steel is identical to galvanized steel concerning the application of the zinc layer enabling both to be produced in the same production line. The difference between them occurs after the application of the zinc layer since in galvanized steel there is no further treatment whereas for galvanized the substrate passes through an annealing process at 500 °C, which leads to the formation of Zn-Fe intermetallic phases.[69, 72] The annealing process gives galvanized steel better corrosion resistance, improved paintability, and better weldability than galvanized steel.[68]

The formation of galvanized coatings was found to be based on a three morphological steps process that takes place during the annealing and is classified as type

0, 1 and 2.[73] A schematic of their structure is shown in Figure 12. The type 0 occurs in the first few seconds of the immersion (1 to 5 seconds) and is characterized by the formation of an uneven layer of a zeta and delta Fe-Zn alloy (1-2  $\mu\text{m}$ ), the rest of the layer (8  $\mu\text{m}$ ) being almost pure zinc. Type 1 is characterized by a fully Fe-Zn alloyed layer, a mixture of zeta and delta phases with some remaining zinc on the surface. Type 2 no longer has unalloyed zinc and is characterized by a gamma layer near the metal surface (1-3  $\mu\text{m}$ ). A thick and compact layer of Fe-Zn alloy composed of delta phase makes the bulk of the zinc layer. On the surface, it is possible to identify some remaining forms of the Fe-Zn zeta phase.[69, 73]

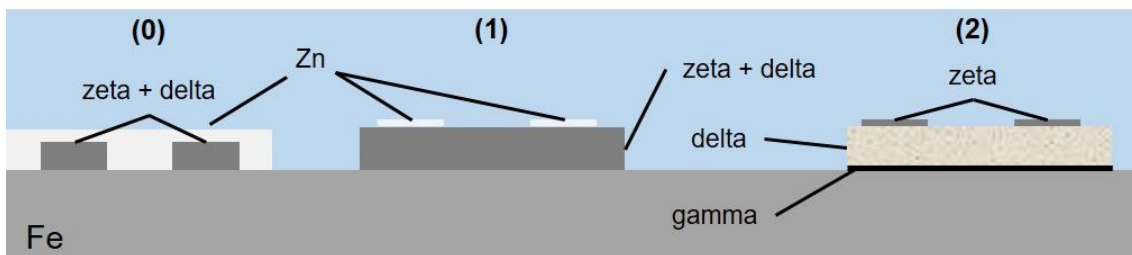


Figure 12: Schematics of the different types of galvanized coatings.[73]

The corrosion performance of galvanized steel is more complex than its galvanized counterpart due to the presence of a higher amount of Fe, around 10 %, making the zinc layer less galvanically active. This decrease in galvanic activity accounts for smaller rates of Zn consumption. Nevertheless, in terms of corrosion performance, both have similar performances. An important note has to be made concerning some aesthetic problems raised by the high content of iron, which results in the appearance of an orange hue when the galvanized surface gets wet, as a result of the formation of iron oxide. This is not an indication of corrosion taking place on the steel substrate but rather stems from the oxidation of the iron present on the galvanized layer. In most cases, galvanized steel structures require the application of a coating to prevent the appearance of stains.[72]

## 2.3 Corrosion protection

The most common approach to prevent corrosion is the application of a protective coating. The coating provides a physical barrier against the environment, avoiding substrate degradation. Nevertheless, paints and primers will only work as barrier layers without active corrosion protection, meaning that when coating disruption occurs due to damage or coating degradation, barrier properties are lost and the coating no longer provides protection to the metal substrates. One way to compensate the loss of barrier properties is through the addition of active species (corrosion inhibitors) that will inhibit the corrosion process, decreasing corrosion rate and propagation, and allowing time for repairing or replacing the damaged section before the structure reaches catastrophic failure.[74, 75]

The direct addition of corrosion inhibitors to coating formulations, in some cases, leads to the decrease of barrier properties and the deactivation of the active properties of the inhibitor, due to chemical interaction with the coating. The alternative is the incorporation of corrosion inhibitors in capsules, avoiding the negative interaction between coating and inhibitor, while also conferring a controlled release profile to the inhibitor loaded nanocontainers, preventing uncontrolled leaching of the inhibitor into the medium.[76]

### 2.3.1 Substrate surface pretreatment

Surface preparation plays an important role in corrosion protection. Without proper cleaning or surface preparation, problems with coating adhesion can occur, leading to the decrease in coating protection efficiency.

Contaminants can result from the metal manufacturing process. Lubricants and protective oils are the most common, with the first used during metal processing and the second as a temporary protective layer against corrosion, mainly for steel. The pretreatment also plays a key role in providing extra adhesion by giving roughness to the metal substrate. Pretreatments can be divided into physical methods, chemical methods or a combination of both. Chemical methods can also include the application of conversion coatings and anodization. The anodization permits the formation of an anodic film on the metal surface with controlled thickness. An example of conversion films is

the application of chromate-based coatings, after a first cleaning step, that will increase adhesion of subsequent layers.[77, 78] Often metal surfaces are subjected to a combination of treatments, where degreasing or surface cleaning constitute an obligatory step. Further treatments tend to relate more to the type of metal and the final requirements of the structure.

#### 2.3.1.1 Surface cleaning

Surface cleaning is inevitable if one wants good adhesion between the coating and the metal substrate. Most metals have residues or protective grease applied during the manufacturing process. The transport and storage also account for the presence of dust and contaminants, making cleaning an obligatory first step.[79]

Most common approaches used in industry to clean and degrease substrates are solvent based approaches (vapor-degreasing and using a soaked cloth) and alkaline degreasing agents. Vapor-degreasing is widely used to clean metals, bringing the metal in contact with trichloroethylene, perchloroethylene or hydrocarbons. The condensation of vapors on the metal surface will dissolve contaminants, which drip off along with the solvent. An alternative is the use of a soaked cloth, normally in acetone, to wipe the metal surface. This approach is more time consuming and therefore more expensive.

The use of alkaline degreasing agents as an alternative to solvent-based approaches avoids the pernicious environmental and health consequences of the latter. The metal is sprayed or immersed in alkaline solutions, a step that could involve temperature, then rinsed with water and thoroughly dried. Ultrasonic degreasing is also used regularly for cleaning metals, mostly for small parts, by combining ultrasounds with different solvents, including water, acetone, alcohols, and hydrocarbons.[80]

#### 2.3.1.2 Mechanical pretreatment

Mechanical pretreatment uses a physical action to clean the surface, the most common methods being brushing, sanding, and blasting. In addition to removing contaminants, rust and old paint, these treatments change the surface roughness increasing coating adhesion since these methods lead inevitably to the removal of some material from the substrate. Brushing and sanding require a mechanical movement, done in dry or wet media, applied by manual or electrical means. The desired roughness is a result of choosing the appropriate abrasive and brush design, along with exerting the right amount of pressure. Blasting follows the same principle of brushing and sanding but tends

to be more efficient since uses the projection of a hard material, by pressurized air, to erode the surface. Materials more commonly used are sharp quartz sand, corundum ( $\text{Al}_2\text{O}_3$ ), glass beads or steel shot. Comparing with the two previous methods, blasting increases significantly the roughness of the metal surface, requiring some level of optimization to avoid excessive roughness. Excessive roughness could lead to an improper coating application, likely to result in a deficient coverage of the surface and weakening of coating barrier properties.[77, 81]

### 2.3.1.3 Chemical and electrochemical pretreatments

#### 2.3.1.1.1 Etching

The application of chemical etching is another common approach for cleaning metal surfaces, preceding the application of an electrochemical pretreatment such as electrodeposition or anodization. The first goal is improving adhesion while minimizing the negative impact on corrosion protection. Chemical pretreatment includes alkaline and acid etching, acid pickling and anodization processes. The etching and pickling processes differ mainly in the intensity of the attack, with pickling only removing the surface oxides and part of the underlying surface, while etching besides the removal of the oxide layer also removes intermetallic particles present on the metal surface.

One example of chemical etching is the surface pretreatment employed for several aluminum alloys, namely AA2024, comprising a solvent cleaning (degreasing) followed by alkaline etching and acid cleaning. This procedure can be used with different levels of intensity, but the end result will roughly be the one depicted in Figure 13. The alkaline etching removes part of the natural oxide layer alongside with some aluminum and intermetallics present on the surface, leaving behind some corrosion products (oxides). The acid etching (desmutting) will then remove corrosion products left from the alkaline etching together with exposed intermetallics resulting in surfaces with increased roughness and lower amount of intermetallics.[82-84]

Two examples of acid etching, commercially used in the pretreatment of AA2024, are the Forest Products Laboratory etch (FPL etch) and P2 etch. FPL etching procedure was developed in the 1950's and further improved in 1975 being them designated optimized FPL etching. The procedure starts with the surface degreasing followed by an alkaline cleaning, neither of which change the surface nature. Etching is done by immersing metallic surfaces in a solution of water, sulfuric acid and sodium dichromate

under elevated temperature (between 65-70 °C). The optimization of the process led to the dissolution of very small amounts of AA2024 prior to the treatment. P2 etch shares the degreasing and alkaline cleaning steps with optimized FPL etching, with the etching solution consisting of water, sulfuric acid, and ferric sulfate. The P2 etched procedure was developed in 1976 aiming at the development of a chromate-free pretreatment procedure with equal efficiency to the FLP etching method.[85]

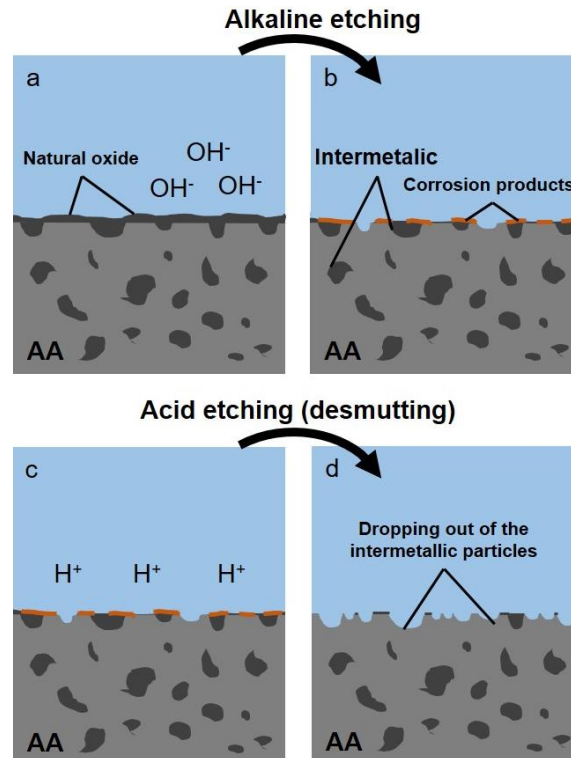


**Figure 13: Schematic representation of changes occurring in an aluminum alloy surface: a) before and b) after alkaline etching; c) before and d) after acid cleaning.[82]**

#### 2.3.1.1.2 Anodization

The application of an anodization methodology in aluminum was done at an industrial scale, in order to enhance aluminum corrosion protection in seaplane components, in 1923. The process is based on the application of an electrolytic treatment, making use of different electrolytes with an applied current, alternating or direct. The treatment allows the formation of an anodic oxide film on the metal surface, with its specific composition and thickness being controlled by the conditions used during the process. There are several commercial anodization processes such as chromic acid anodizing (CAA), sulfuric acid anodizing (SAA), phosphoric acid anodizing (PAA) and boric-sulfuric acid anodizing (BSAA).[86]

CAA was one of the most used pretreatments, in part due to the corrosion resistant oxide layer it produces. The process starts with the cleaning of the surface, following a similar approach as the etching, with a degreasing and alkaline cleaning processes. That is followed by a deoxidizing step, having an effect similar to a P2 etching solution. The anodization process takes place in a solution consisting of water and chromic acid gently stirred at temperatures between 33 and 37 °C. The voltage is applied step by step from initial voltages of 5-10 V, with increments of 5-10 V, until 4062 V and a current density of 1 A/m<sup>2</sup>. The anodization creates a porous coating on the metal surface, which in most of the application is sealed using water at temperatures around 85 °C. In the specific case of CAA, the sealing solution consists of a diluted chromic acid solution in water.[85]

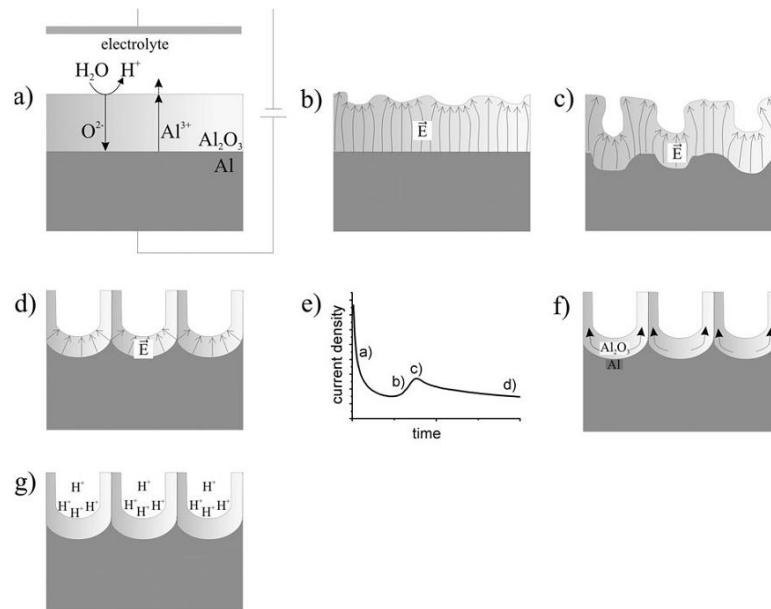


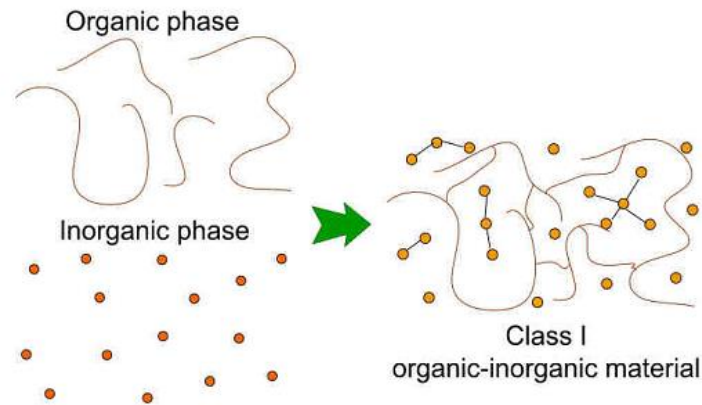
**Figure 14: Schematic representation of alumina pore formation by electrochemical anodization: (a) formation of the anodic oxide on aluminum; (b) local field distribution correlated to the surface morphological fluctuations; (c) initiation of the pore growth due to the field-enhanced dissolution; (d) pore growth in steady-state conditions; (e) represents the current transient recorded during anodization of Al; (f) and (g) show the influence of the volume expansion and the local acidity on the alumina pore growth, respectively. Reproduced from [87] with the authorization of RSC.**

In general, the process of anodization can be described as shown in Figure 14. The process starts with the formation of a compact and uniform anodic oxide layer, Figure 14 a). The electrochemical field in the oxide layer is affected by the surface morphology which leads to the focusing of the electrochemical field starting the dissolution of the oxide layer and the growth of the porous layer (Figure 14 b) and c)). This growth continues until the porous phase becomes steady and uniformly distributed (Figure 14 d).[87]

### 2.3.1.1.3 Sol-gel

Sol-gel technology has experienced a considerable increase in interest during the last decades, fueled by its versatility and properties.[88] A more detailed view of sol-gel technology and application possibilities is presented in section 2.3.3.2, with the role of sol-gel in the pretreatment of metal substrates being assessed in this section. The application of a sol-gel layer can improve the metal corrosion resistance, the aesthetic appeal (used as a top coat) and coating adhesion (used as a primer). Sol-gels have been used, for several years now, by Boeing as an adhesive bonding of aluminum alloys, steel, titanium, and composites.[85]

a



b

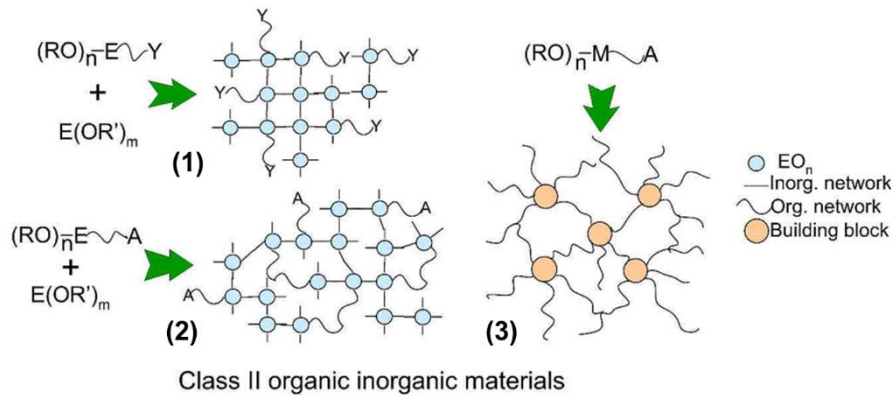


**Figure 15:** Class I hybrid material (no covalent bonds are formed between inorganic and organic phases) (a). **Figure (b)** class II hybrid materials; (1) hybrid network with added functionality (Y) linked by inorganic bonds; (2) hybrid network linked by inorganic and organic bonds; (2) organic-inorganic network made of nano-building blocks linked through organic Bonds. Reproduced from the work of K. Yasakau [89].

The sol-gel layer consists of a 3-D network of silicon and metal alkoxide precursors. The list of precursors is extensive and largely depends on the specific requirements of the product. Most commonly used are tetraethyl orthosilicate (TEOS), tetra-n-propoxyzirconium (TPOZ), titanium (IV) propoxide (TPOT) and

methyltriethoxysilane (MTEOS). These will be the backbone of the 3-D structure promoting cross-linking connections. In order to enhance addition to both the metal and the organic coating being applied other organometallic precursors can be used such as 3-glycidoxypropyltrimethoxysilane (GPTMS), where the epoxy moiety improves adhesion to the organic coatings while (3-mercaptopropyl) trimethoxysilane (MPTMS) improves adhesion to some metals. The sol-gel layer is achieved by hydrolysis of the precursors (sol component), promoted by the addition of acidic water, followed by condensation reactions (gel component).

The initial sol-gel materials (oxide powders, bulk composites, glasses, mixed ceramics and inorganic coatings) were inorganic. The main issue with inorganic sol-gel, particularly for protective coatings, is the appearance of cracks upon curing. Crack-free coatings were only possible for coatings thickness up to 100 nm. Thus, the need to improve the coating properties by adding an organic component to the inorganic sol-gel increasing in this way the elasticity of the coating.[89].

Sol-gel composed by organic and inorganic components are designated by hybrid sol-gel and can be classified into two major classes according to Judeinstein et al.[90], as presented in Figure 15. Class I is the result of mixing physically organic and inorganic phases, with Van der Waals, ionic and hydrogen bonding interactions as the forces arising from the interaction of both phases. There are no covalent bonds between the two phases (Figure 15a). The hybrid materials Class II is characterized by the existence of chemical bonds formed between inorganic and organic components, through the presence of functional groups or organically modified silanes (Figure 15b).[89]

### **2.3.2 Corrosion inhibitors**

Coatings provide a physical barrier against aggressive species and by isolating the metal from the environment prevent corrosion. In specific cases, the coating will last for the entire service life of the materials. Nevertheless, organic coatings still allow the ingress of water, oxygen, and electrolytes. Moreover, coating wear, thermal stress, UV exposure and mechanical defects lead to the complete loss of barrier properties. Even if the defect or damage area is relatively small compared to the whole coating surface area, the consequences can be unpredictable. So, a strategy to solve the loss of barrier properties is the addition of pigments with active anti-corrosion properties.

Information concerning corrosion inhibitors is abundant in literature, whether based on their nature (organic or inorganic), inhibition mechanism (anodic, cathodic or a combination of both) or the type of metal that it protects. In the present project only corrosion inhibitors used in the corrosion protection of AA2024, mild steel, galvanized and galvanized steel will be highlighted.

#### 2.3.2.1 Corrosion inhibitors for AA2024

AA2024 has a high strength to weight ratio, making it widely used in the aerospace industry. Due to its high profile applications, the development of good corrosion inhibitors to prevent material failure is important. Chromate-based conversion coatings and coatings loaded with Cr (VI) as corrosion inhibitor have been used with excellent results in the prevention of corrosion in AA2024. Nevertheless, its environmental and carcinogenic issues led to the development of restrictive legislation and ultimately their prohibition.[2] AA2024 has been extensively used in literature as a model substrate in the development and study of anti-corrosion systems, focusing on the development of new corrosion inhibitors,[27, 91, 92] new coatings[76, 93] or new systems to deliver corrosion inhibitor on demand improving both inhibitor and coating performance.[94-97]

Even with all their advantages, AA2024 is susceptible to corrosion due to the presence of intermetallic particles which confer superior strength to the alloy but may also form galvanic couples in contact with moisture, promoting localized corrosion.[98] The Al<sub>2</sub>CuMg are the main intermetallic inclusions in AA2024 and exhibit a Volta potential higher than the matrix, recall section 2.1.3.[91] Several corrosion inhibitors have been developed, with good results, to mitigate these corrosion problems in AA2024: triazole and thiazole derivatives,[91] rare-earth elements,[27, 92, 99] 8-hydroxyquinoline,[100] sodium molybdate[101] and vanadates.[102] Among the available corrosion inhibitors, cerium salts and thiazole-based compounds were selected to be incorporated in the nanocapsules in this thesis, due to their inhibition efficiency.[27, 91, 103]

Well-known corrosion inhibitors for copper, triazole and thiazole derivatives, have been also tested for AA2024, due to its high Cu content, with good results.[91] The mechanism of protection is based on the formation of a protective film on the AA2024 surface which impairs the corrosion process. Rare-earth elements also show good inhibition properties, as shown in the work of Yasakau and colleagues[27] with cerium(III) and lanthanum(III) salts. In this case, the inhibition mechanism is based on

the formation of hydroxide deposits in the S-phase locations, areas rich in  $Al_2CuMg$ , hindering both anodic and cathodic processes. The formation of hydroxides occurs due to an increase in the pH in such locations as a result of the electrochemical processes. Cerium (III) has a higher inhibition efficiency than lanthanum (III), probably associated with the lower solubility of the corresponding hydroxide form.

#### 2.3.2.2 Corrosion inhibitors for galvanized and galvanized steel

Galvanized steel is widely used in a variety of applications, from automotive, construction to structural parts and water distribution systems. The versatility shown by galvanized steel is partly due to its good corrosion resistance in both atmospheric and aqueous environments, including marine environments. The protection provided by galvanized steel results from the Zn layer on its surface that also provides cathodic protection.

The good corrosion protection shown by galvanized steel on its own is remarkable, but as it is the result of the effect of the Zn layer, as described above, this protection will only last as long as the zinc layer itself lasts. With prolonged exposure to corrosion this protective layer will wear off and the structural properties of the material will be affected. Another setback is the production of corrosion products, zinc oxide, as a result, the Zn layer degradation. One way to avoid it is the application of corrosion inhibitors, aiming at the prevention or at least a significant decrease of the Zn layer's rate of dissolution. In literature a variety of corrosion inhibitors can be found for application on galvanized steel: sodium nitrite, molybdate-based compounds,[104-106] diethanolamine[107] and rare-earth elements.[108-112]

Similarly to AA2024, two approaches can be found in the form of corrosion protection in galvanized steel: first based on the formation of a conversion film (passive layer) on the metal surface and a second that focus on the passivation of the corrosion cathodic sites after the beginning of the corrosion process. The molybdate-based approach works by establishing a protective layer on the metal surface, as shown in the work of Liu and colleagues[104] where a combination of molybdate–phytic acid was used to form a passive layer on the zinc surface. The results show corrosion protection by both elements when added singularly, but an improved effect was detected when applied together.[104]

The use of milled cerium and silica particles as anticorrosion pigments to impair corrosion in galvanized steel was studied by Deflorian and colleagues.[112] It was verified that the conjugation of the two milled particles, when added to an aggressive

medium (NaCl solution), led to the decrease in corrosion degradation in galvanized steel samples. The use of Ce (III) has been extensively reported in the passivation of cathodic sites in particular for AA2024 (see 2.3.2.1), but from Ce (IV) the same level of protection is not expected. Nevertheless, the authors verified a double protection effect, leading to the passivation of cathodic sites, in galvanized steel, which resulted in lower current densities. The effect was attributed to the  $\text{SiO}_3^{2-}$  anion, the product of the reaction between  $\text{SiO}_2$  and  $\text{OH}^-$ , reaction with the metal ions at the anodic sites that lead to the formation of a passive film. The cerium appeared to be working in a similar way by forming insoluble oxides on the metal cathodic sites. The authors found it more difficult to interpret the role of Ce (IV) particles, proposing two theories: first the release of soluble cerium species from the cerium oxides and second due to the potential of the cerium oxide particles to act as a complex agent, reacting with zinc ions, thus leading to the formation of the passive layer.[112]

#### 2.3.2.3 Corrosion inhibitors for cold rolled steel

The corrosion protection of mild steel cannot be diminished due to the extension in which this metal is used. The literature presents a significant number of studies on the corrosion protection of mild steel using corrosion inhibitors. These inhibitors can be constituted by a variety of molecules: organic or inorganic, synthetic or natural. Another clear separation that can be observed in these studies is the medium in which the corrosion takes place, acidic or neutral in the presence of chlorides. The vast majority focuses on corrosion protection in acidic media, namely HCl and  $\text{H}_2\text{SO}_4$ , due to the application of cold rolled steel in the production of pipelines and oil drilling, where acidic conditions are predominant and equipment security is paramount.

In acidic conditions, the best performing inhibitors have been organic compounds containing electronegative functional groups and  $\pi$ -electrons in conjugated double and triple bonds, which work by supplying electrons through  $\pi$ -orbitals. Some functional groups containing nitrogen, oxygen, sulfur or aromatic rings in their molecular structure (inhibition efficiency increases like  $\text{O} < \text{N} < \text{S} < \text{P}$ ) also exert an inhibitory effect by the interaction of their free lone pair of electrons with the metal surface.[113] The combination of both factors leads to an increase in the inhibition effect.[114, 115] Some organic compounds being used as corrosion inhibitors in acidic conditions include: acetylenic alcohols, aromatic aldehydes, alkenylphenones, amines, amides, nitrogen-containing heterocycles (e.g. imidazoline-based), nitriles, iminium salts, triazoles,

pyridine and its derivatives or salts, quinoline derivatives, thiourea derivatives, thiosemicarbazide, thiocyanates, quaternary salts and condensation products of carbonyls and amines.[116]

The application of plant extracts as corrosion inhibitors for mild steel in acidic conditions registered a remarkable increase in interest during the last years. Their inhibition mechanism works mainly by adsorption of the natural extracts on the metal surface and its efficiency depends on the surface conditions, medium conditions and inhibitor concentration. So far plant extracts show promising indications of acting as functional corrosion inhibitors for mild steel in acidic conditions,[117-119] as observed in the variety of compounds summarized in the review done by Chigondo and Chigondo.[115]

For neutral conditions, the available corrosion inhibitors, and the research being done on it is considerably lower when compared with acidic media. In part, this is due to the higher demand of inhibitors for acidic media, but also due to difficulties in finding good corrosion inhibitors for neutral conditions. Some of the corrosion inhibitors studied so far are 5-phenyltetrazole,[120] sodium laurate,[121] fatty amine associated with phosphonocarboxylic acid salts, hydroxyethane diphosphonic acid (HEDP), hydroxyphosphonoacetic acid (HPA), Kraft lignin (KL), soda lignin [113] and sodium gluconate.[122, 123]

The main form of inhibition mechanism taking place in neutral NaCl conditions is by adsorption of corrosion inhibitors on the metal surface, similar to the case of acidic media. Taking Kraft lignin and soda lignin as an example, it has been verified that they successfully inhibit corrosion on mild steel at pH around 6 and 8 for temperatures around 25 °C. The authors notice that soda lignin possess a higher inhibition efficiency than Kraft lignin, and both follow a Langmuir adsorption isotherm. The formation of the ferric-lignin bond was verified by FTIR.[113]

The corrosion protection of steel in concrete is another significant field of research, where corrosion inhibitors are employed in an attempt to mitigate the consequences of corrosion. Concrete is characterized by its high alkalinity, normally presenting pHs between 12.5 and 13.8, depending on the type of cement used.[124] The steel inside the concrete is primarily protected by a very thin passive film of oxide, with corrosion starting when this barrier is breached. Two main mechanisms are responsible for the depassivation of this film, chloride ions (from sea salt or deicing salt) and carbonation (from the air and acid rain).[124] The corrosion inhibition in this field has

been done by three main types of compounds amines and alkanolamines (AMA), monofluorophosphate (MFP) and calcium nitrites.[125] The inhibitors are added to the concrete mainly in two ways: directly to fresh concrete or to the hardened concrete surface with the inhibitor migrating into the inside of the concrete. Two other methodologies are reported: the addition of inhibitors to repair mortars and their application as a surface treatment on the reinforcement bars before concreting.[125]

AMA inhibitors are reported to work as chelating agents that form a layer on the steel surface. Examples of AMA-based corrosion inhibitors are ethanolamine and dimethylethanolamine. The nature of their inhibition is not consensual, with some authors claiming they work as retarding cathodic activity and others defending they act as a mixed type of inhibitor, covering both anionic and cathodic sites.[125, 126] MFP inhibition effect is thought to work through the formation of phosphates and so the anodic formation of a passive layer of  $\text{Fe}_3\text{O}_4$ ,  $\gamma\text{Fe}_2\text{O}_3$ , and  $\text{FePO}_4\cdot\text{H}_2\text{O}$ . Similar to AMA the inhibition mechanism is not clear.[125, 127] The inhibition mechanism of calcium nitrite is anodic. Nitrites compete with chloride ions for the ferrous ions at the anode to form a film of ferric oxide ( $\text{Fe}_2\text{O}_3$ ).[125, 128]

The way sodium gluconate operates in the suppression of corrosion is also based on the adsorption onto the metal surface preventing its dissolution and thus mitigating corrosion. Its efficiency was assessed for cooling water systems, with the gluconate adsorption on the metal surface following a Langmuir isotherm, confirming that the main inhibition process occurs via adsorption.[123]

### **2.3.3 Protective coatings**

Coatings have been used throughout history to provide protection and enhance aesthetic appeal. Protective coatings are a vital part of our daily lives, and it is almost impossible for someone standing in a room, street or any form of transportation and not be in the presence of some form of protective coating. Organic based-coatings are the most widely applied form of coating materials and may be used as a liquid, paste or powder.[77] The amount and sort of coatings, either commercially available or under development, is huge and exceeds the scope of this dissertation. A more concise approach is required, focusing on the most common coatings used in corrosion protection, particularly the ones studied in the frame of this thesis. In the next sections, the coatings are classified according to the nature of their components: metallic, organic and inorganic.

### 2.3.3.1 Metallic coatings

The addition of a metallic coating layer intends to change the metal surface properties, creating materials with the same load-bearing capability but improved durability and corrosion resistance.[1] Methodologies used to deposit metallic coatings include electroplating, electroless plating, spraying, hot dipping, chemical vapor deposition and ion vapor deposition. Some of the most relevant metals used are cadmium, chromium, nickel, aluminum, zinc, copper, gold, and silver.

A good example of a protective metallic coating which has been presented in detail in section 2.2.2.3, is the Zn layer applied on steel surface thus increasing the metal corrosion resistance. Even with this level of protection, GS is still subject to corrosion, and in some cases, the galvanic and barrier protection provided by Zn is not sufficient, often due to the aggressive medium or to improper GS manufacturing.[129, 130]

### 2.3.3.2 Sol-gel based coatings

The first studies from where sol-gel science will eventually emerge dates from the nineteenth century in the form of work developed by Ebelman and Graham. Ebelman was the first to prepare an alkoxide by reaction between  $\text{SiCl}_4$  and an alcohol in air, observing the gelation of the compound. Also, experiments were conducted with TEOS under acidic conditions to obtain “glass-like” structures that could be shaped into fibers or lenses. The preparation of monoliths through this approach appealed considerably to researchers since it could be achieved at low temperatures contrasting with the glass manufacturing that requires high temperature to manipulate the material into the desired form. Nevertheless, the long periods of time needed to prepare the monoliths without cracking them, almost a year, constituted a serious drawback for potential industrial interest.[131, 132]

The interest in sol-gel methods was renewed in the 20's and 30's of the twentieth century with researchers like Geffcken preparing oxide films using alkoxides, and Blodgett, developing antireflection coatings.[132, 133] Since then, the interest and the application range for sol-gel methods have grown considerably and now covers areas such as protective coatings, adsorption, chromatography, biotechnology, and energy conservation, among others.[134]

The sol-gel method comprises the transformation of a material from a “sol” (a colloidal suspension of solid particles, in a liquid), with fluid-like properties, into a “gel”, with solid-like properties. In the sol-gel process a liquid solution, called “sol”, is

converted into a “gel” through hydrolysis followed by condensation polymerization. Thermal treatments after gelation lead to the formation of an inorganic or hybrid ceramic oxide coating, depending on the precursors used.[78]

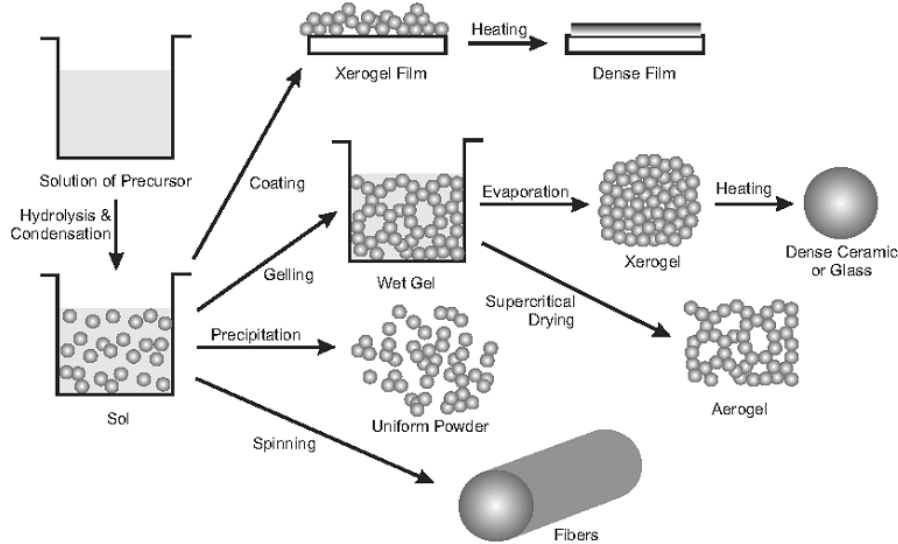
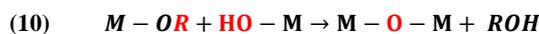


**Figure 16:** Various steps in the sol-gel process to control the final morphology of the product. Reproduced from reference [135] with the authorization of Springer International Publishing AG.

Figure 16 depicts some possible morphologies obtained by the sol-gel method, together with the steps to achieve them. Starting from the same solution but using different procedures it is possible to obtain dense films (coatings), dense ceramics, aerogel, fibers and uniform powder. Dense films can be used as protective coatings against corrosion in different metals.[135]

The versatility given by the sol-gel process in terms of chemistry and morphology is considerable. It is possible to use alkoxide precursors with different elements (silane, zirconia, titanium) and with different functional groups (amine, epoxy, thiol, among others).[78] The reactivity of the alkoxides is different, with silicon-based alkoxides less reactive than metal alkoxides (e.g. titanium), which are very reactive toward nucleophilic reagents, such as water.[136]



The sol-gel synthesis is based on two main reactions, hydrolysis, and condensation. The generic reactions are presented in Equations (8), (9) and (10). Equation

(8) represents the hydrolysis process taking place on the alkoxy silane, originating a silanol and an alcohol group. Equation (9) shows the water condensation reaction occurring from the reaction between two silanol groups, originating a siloxane and water. Equation (10) is also a condensation, but an alcoholic based condensation, as a result of the reaction between a silanol and an alkoxy silane groups originating a siloxane and an alcohol group.[136, 137]

The development of protective coatings for metals[138] based on sol-gel technologies has seen an increase in the last two decades with viable applications of sol-gel coatings in copper,[139] magnesium alloys,[140, 141] steel[142, 143] and aluminum alloys.[144-147] Sol-gel coatings present good adhesion and barrier properties, rendering them a good alternative to conversion films. Additionally, sol-gel coatings can provide active protection when loaded with corrosion inhibitors.[76, 148] The low temperature of processing brings some advantages, the ease of application and their possible classification as “green” coating since VOC’s emissions are low and their application may be waste-free depending on the method employed.[149]

### 2.3.3.3 Organic-based coatings

Compared with the previous types of protective coatings, organic-based coatings are the most used due to their versatility, good performance, and excellent aesthetic appeal. The widespread use of organic coatings can be partly due to the petroleum industry, responsible for the production of the basic ingredients from which most synthetic resins were developed, like most of the unsaturated compounds employed in the synthesis of polymers such as vinyl and acrylics.[1]



Figure 17: Scheme of a typical coating system used in metals.[150]

Organic based coatings, for most of the applications, tend to be applied as a three-layer system: primer, intermediate and topcoats, as schematized in Figure 17. The first

layer aims at the improvement of coating/substrate adhesion and confers a certain level of flexibility to the coating. In some cases, the development of conversion coatings on the metal surface to further increase primer adhesion is required. Intermediate layer adds thickness to the coating, strong chemical resistance, improves cohesion and provides a good barrier against moisture and vapor transfer. The topcoat is the first barrier against the environment, is a resistant seal for the coating system and provides a pleasant appearance.

Organic coatings are composed of film-forming agents, pigments, and solvents. The purpose of film-forming agents is to confer coherence and uniformity to coatings by creating a dense, solid and adherent membrane. Film-forming agents can be divided according to their chemical reactions: oxygen reactive film-forming agents (epoxy esters, urethane alkyds), lacquers (polyvinyl chloride polymers, acrylics) heat-conversion film-forming agents (hot melts, powder coating) and co-reactive film-forming agents (epoxies, polyurethanes).[77]

Figure 18 depicts the main film-forming agents in organic coating technology. Natural types of film forming agents are natural resins, carbohydrates, albumen and the most relevant oils. Oils have been extremely useful throughout the history of coatings but started to be replaced in the last century by synthetic counterparts. The necessity for industrial independence in Germany at the beginning of the XX century led to a push in research to replace the existent natural film forming agents. The final result is the modern coating industry based in synthetic film-forming agents that can be divided into polyaddition, polymeric resins, polycondensation and deriving from this the crosslinker. More detailed information can be found in the work of A. Goldschmidt and H.-J. Streitberger.[77]

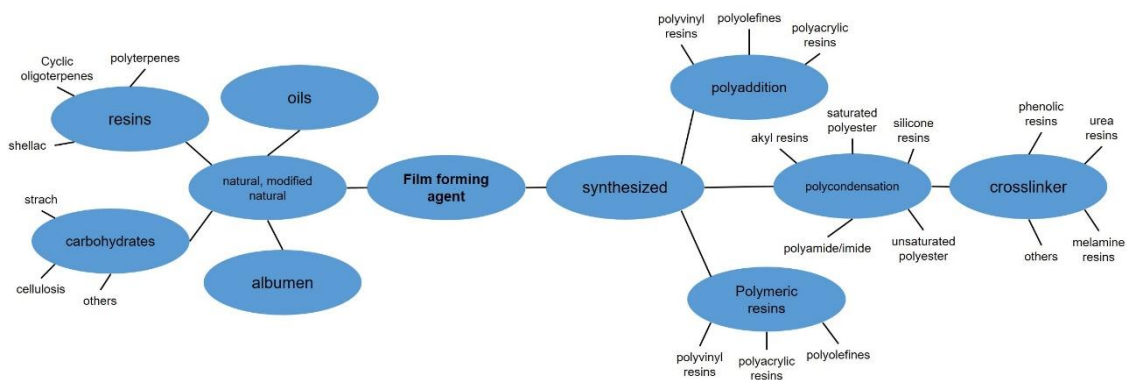


Figure 18: Classification of important film-forming agents. Adapted from reference [77].

Pigments consist of insoluble powders added to the paint medium and confer specific properties such as color, corrosion inhibition, corrosion resistance, film reinforcement and adhesion. Their nature, as its uses, varies considerably from naturally occurring materials to artificial compounds. For most of the applications, a combination of different pigments is employed, adding different functionalities to the coatings and tuning it according to the application.

The solvent influence on the coating characteristics is paramount, affecting viscosity, flow properties, drying speed, spraying, brushing and gloss. The selection of a solvent is directly related to the binder and pigments present in the paint formulation and in most of the cases, it is not just one solvent but rather a mixture of solvents that are employed, enabling the optimization of the above-cited characteristics.

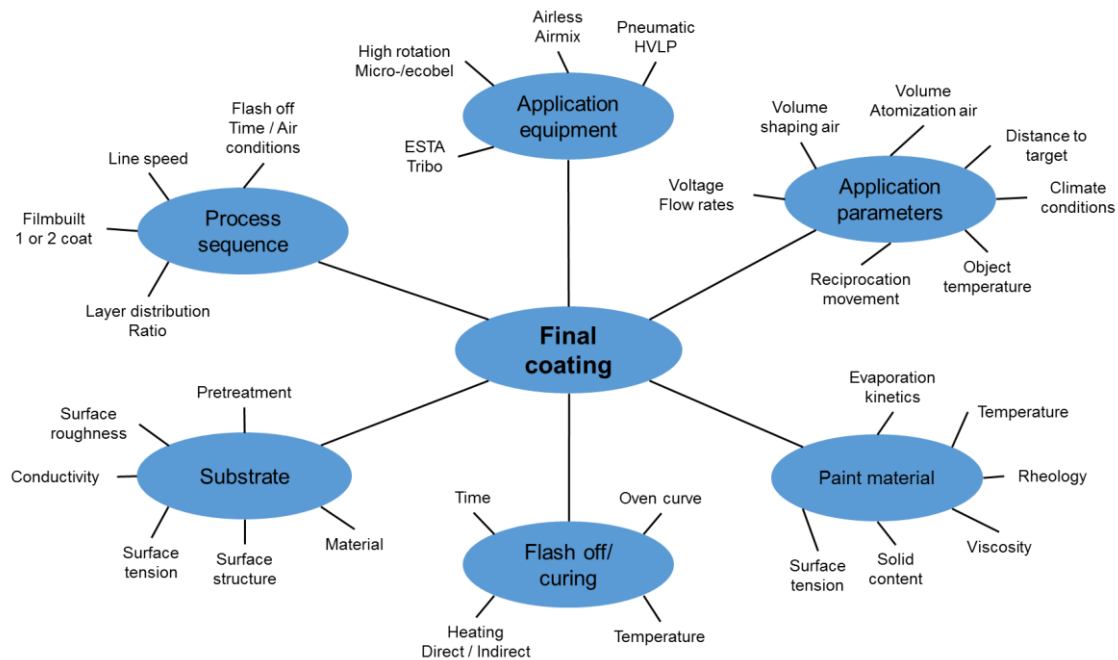


Figure 19: Factors affecting the final coating result in a spray application process. Adapted from reference [77]

The complexity of a good coating does not only depend on their components. Figure 19 attempts to illustrate the complexity of coating application, in the case of coatings applied by spray. But most of the parameters used to assess the qualities of coating applied by spray can be also relevant for other forms of application. Making the difference in the overall aesthetic appeal and performance of the coatings are various factors such as application equipment, application parameters, process sequence, paint material, substrate and curing. Parameters common to almost all the coating applications are painting material, substrate, and curing. In the paint material, one must account for

factors such as evaporation kinetics, temperature, rheology, viscosity, solid content and surface tension. Concerning the substrate, the variables can be the pretreatment, surface roughness, surface tension, surface structure and the material. Finally, the curing process includes different parameters such as time, oven curve (when necessary) and temperature.

In this section, the complexity behind coating application has been presented, showing a clear picture of the sizable amount of parameters behind the development of a coating with good properties. Therefore, the addition of any other components, such as the novel nanocontainers which are the object of study of this thesis, must undergo similar development if robust and reproducible results are to be obtained.

## 2.4 Multi-level protection

In the last decade much attention has been devoted to the development of self-healing coatings. The self-healing concept in corrosion protection is achieved mainly by two strategies: (i) mending of defects formed in the polymeric coating matrix by the addition of polymerizable agents and (ii) inhibition of corroding areas due to the presence of corrosion inhibitors.[151] The reparation of defects on coatings makes use of capsules and nanoparticles sensitive to external stimuli loaded with polymerisable species. When a damage or degradation of the coating takes place, the capsules are ruptured and release their contents, which polymerize restoring the coating original barrier properties. Several works have been reported making use of this approach.[152-155]

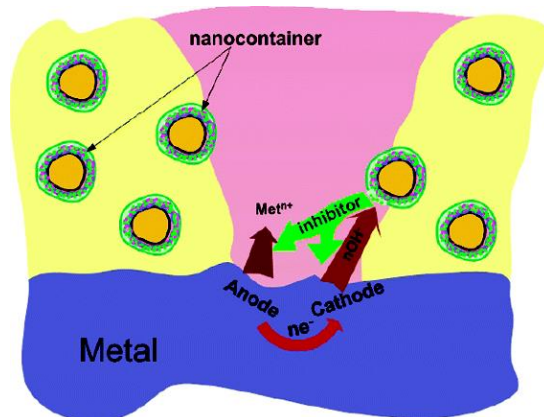


Figure 20: Scheme of the controllable release of inhibitor from the nanocontainers and the “smart self-healing” process.[156] Reprinted with permission from Zheludkevich, M.L., et al., *Anticorrosion Coatings with Self-Healing Effect Based on Nanocontainers Impregnated with Corrosion Inhibitor*. *Chemistry of Materials*, 2007. 19(3): p. 402-411. Copyright 2016 American Chemical Society.

The second approach and the one explored in this work makes use of nanocontainers capable of storing corrosion inhibitors to be added to different coatings, working as a suitable alternative to the direct addition of corrosion inhibitors. Encapsulation can confer several advantages to a functional coating such as limiting the spontaneous leaching of inhibitor from the coating into the environment, avoiding detrimental interactions between coating matrix and inhibitor and confer release mechanisms that allow the corrosion inhibitors to be released on demand (the so-called “smart” release). Figure 20 depicts an example of a “smart” coating in action, with the incorporated nanocontainers releasing the corrosion inhibitors on demand, in the area where the coating has been damaged. Several systems have been used as containers for

corrosion inhibitors: polyurethane microcapsules,[157] silica-based nanoparticles and nanocapsules,[158-161] halloysites,[100, 162, 163] and layered double hydroxides (LDHs).[152-155]

### 2.4.1 Layered double hydroxides (LDH)

LDHs are hydrotalcite materials structures based on layers composed of mixed M(II) and M(III) hydroxide, where M stands for a metal cation, intercalated by anions and water molecules in a structure that can be represented by the formula  $[M^{2+}_{1-x}M^{3+}_x(OH)_2]A^{n-}_{x/n} \cdot mH_2O$ .  $M^{2+}$  and  $M^{3+}$  are the metal ions and  $A^{n-}$  is the anion intercalated in the LDH galleries. The LDH structure usually can be constituted by  $M^{2+}$  and  $M^{3+}$  metal ions with similar ionic radius to  $Mg^{2+}$  (0.65 Å). Some of the metal cations that can be part of LDHs are  $Mg^{2+}$ ,  $Fe^{2+}$ ,  $Co^{2+}$ ,  $Cu^{2+}$ ,  $Ni^{2+}$ ,  $Cd^{2+}$ ,  $Zn^{2+}$  for  $M^{2+}$  and  $Al^{3+}$ ,  $Cr^{3+}$ ,  $Ga^{3+}$  for  $M^{3+}$ . [164] On the other hand, LDHs can allocate a variety of anions in the galleries. The following anion families were intercalated successfully into LDH structures: halides ( $F^-$ ,  $Cl^-$ ,  $Br^-$  and  $I^-$ ), non-metal oxoanions ( $BO_3^{3-}$ ,  $CO_3^{2-}$ ,  $NO_3^-$ ,  $Si_2O_5^{2-}$ ,  $HPO_4^{2-}$ ,  $SO_4^{2-}$ ,  $ClO_4^-$ ,  $AsO_4^{3-}$ ,  $SeO_4^{2-}$  and  $BrO_4^-$ ), oxometallate anions ( $VO_4^{3-}$ ,  $CrO_4^{2-}$ ,  $MnO_4^-$ ,  $V_{10}O_{28}^{6-}$ ,  $Cr_2O_7^{2-}$ ,  $Mo_7O_{24}^{6-}$ ,  $W_{10}O_{32}^{4-}$ , and  $PW_{12}O_{40}^{3-}$ ), anionic complexes of transition metals ( $Fe(CN)_6^{2-}$ ,  $Eu$  (tris-dipicolinate) $^{3-}$  and anionic metal porphyrins), organic anions  $R-A^q$  ( $A^q = -COO^-$ ,  $-PO_3^-$ ,  $-SO_3^-$ ,  $-PO_4^{2-}$  and  $-SO_4^-$ ), anionic biomolecules (amino acids, enzymes, proteins, DNA and TPA) and anionic polymers (poly(styrene sulphonate) and poly(methyl methacrylate)). [165]

LDH occurrence in Nature is possible and has been reported for mixed metal–Al hydroxide phases at the surface of phyllosilicates [166] and gibbsite and Ni-LDH in silt, sandy and loam soils. [167] Nevertheless, the most common naturally occurring form is hydrotalcite, presenting the chemical structure  $[Mg_6MA_2(OH)_{16}] (CO_3) \cdot 4H_2O$  and composed of a white hydrous mineral with a rhombohedral crystalline system, low hardness, and low density. Hydrotalcite-like structures can be found in some natural deposits like in Snarum (Norway) the deposit where it was first identified and in New South Wales and Tasmania (Australia), this two being recent discoveries. [165]

LDH can be synthesized in the laboratory, using a relatively simple and inexpensive approach. Some parameters must be accounted for in order to obtain pure LDH phases, such as controlling the pH and preventing  $CO_2$  contamination that can ultimately cause the precipitation of impurities and contamination with carbonate

anions.[165] LDH can be synthesized following two main approaches: co-precipitation in aqueous media[168] and the sol-gel route.[169] The most common approach is by co-precipitation and can be further divided into synthesis at variable and constant pH, synthesis by urea hydrolysis and induced hydrolysis. Another important synthesis parameter to ensure a pure and stable LDH phase is the treatment applied after the synthesis: microwave, ultrasound, and hydrothermal treatments.[170, 171]

The co-precipitation approach usually employs a solution made with M(II) and M(III) salts, providing metal cations that will form the LDH structure, added to a “guest” solution containing the anion that will be present in the LDH galleries and a third solution to adjust the pH. To achieve a good size distribution and prevent contaminations the pH must be kept stable and the reaction must be kept under an inert gas (usually nitrogen). The pH is stabilized by constant monitorization of the pH and addition of an alkaline solution (NaOH, KOH, and NH<sub>3</sub>). The solution with the metal anions is added in a controlled way to the guest solution under stirring and inert atmosphere (to prevent contamination by carbonates due to the dissolution of atmospheric CO<sub>2</sub>), making sure that the pH is kept stable throughout the synthesis (ensuring higher crystallinity).[165, 168] After the synthesis, the LHDs are subjected to further treatment to stabilize their structure. Among the different methods presented above the hydrothermal treatment is one of the most popular, thanks to its simplicity, consisting simply of the LDH being placed in a bath at 100 °C for several hours.[96]

LDHs have been extensively studied as nanocontainers for corrosion inhibitors in the last years, being used successfully in different coatings and substrates.[97, 100, 152-154, 168] The most interesting advantage of LDH is its ability to release the inhibitor on demand, by ion exchange, as shown in Figure 21.[97, 172] Particularly advantageous is its capacity to exchange corrosion inhibitor with chlorides, working at the same time as a “trap” for aggressive species and releasing inhibitor where it is needed.[154, 164] Several studies have presented LDH as a versatile container for corrosion protection, demonstrating good efficiency when loaded with 2-mercaptobenzothiazole (2-MBT),[154] 2-benzothiazolythio-succinic acid,[153] tungstate[152] and vanadate ions.[155]

LDHs loaded with corrosion inhibitors have been studied in coatings enhancing anti-corrosion properties of organic coatings[97, 100, 153] and sol-gel based formulations.[94] Furthermore, the use of LDHs has not been restricted to the application as “smart” reservoirs, but also as nanostructured layers directly grown on the surface of

the metallic substrates. Since the pioneering works of Buchheit and colleagues [173-175] other groups have worked on the development of LDH conversion films to render protection to the underlying substrate. These include the preparation of LDH layers with superhydrophobic properties,[176] LDHs intercalated with carbonates to decrease anion-exchange capability[177] and works by our group on the intercalation and controlled release of corrosion inhibitors.[178, 179]

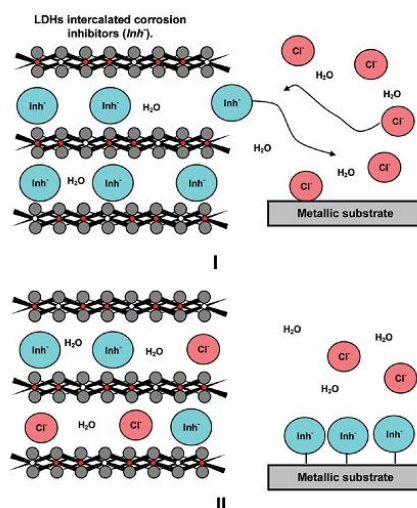


**Figure 21: Schematic view of the LDHs action in corrosion protection.[96] Reprinted with permission from (Tedim, J., et al. (2010). "Enhancement of Active Corrosion Protection via Combination of Inhibitor-Loaded Nanocontainers." ACS Applied Materials & Interfaces 2(5): 1528-1535.). Copyright (2016) American Chemical Society.**

## 2.4.2 Silica nanocapsules (Si\_NC)

The versatility of sol-gel chemistry has been illustrated in section 2.3.3.2, showing the sol-gel method to allow the preparation of fibers, aerogel, glass, dense films and particles. The work done by W. Stober[180] is a good example of sol-gel chemistry being used in the preparation of nanoparticles, in the case solid microparticles with narrow particle size and the possibility of tuning particle size by changing the synthesis parameters. Nevertheless, solid particles present severe limitations when the idea is the encapsulation of active species inside the nanoparticles. One possible solution is the development of mesoporous structures with a high surface area and able to encapsulate active species. The use of microemulsion allows for the synthesis of mesoporous frameworks, as presented in the work of S. Schacht.[181] Figure 22 depicts TEM images of SI\_NC produced by a microemulsion method. It is possible to see the hollow “channels” inside the capsule, excellent structures to host active species.[160]

The possible applications of SiO<sub>2</sub> based nanocontainers as host structures for active species have been extensively studied, namely for drug-delivery.[182, 183] Their versatility is expressed in the variety of compounds that can be incorporated, in the ability to synthesize particles with specific sizes (particle and porous size) and the feasibility of modifying the surface of nanocontainers. The growing interest in using silica nanocontainers in corrosion protection is demonstrated by the existence of several groups using silica nanocontainers for encapsulation of corrosion inhibitors in the last decades.[157-160, 184]

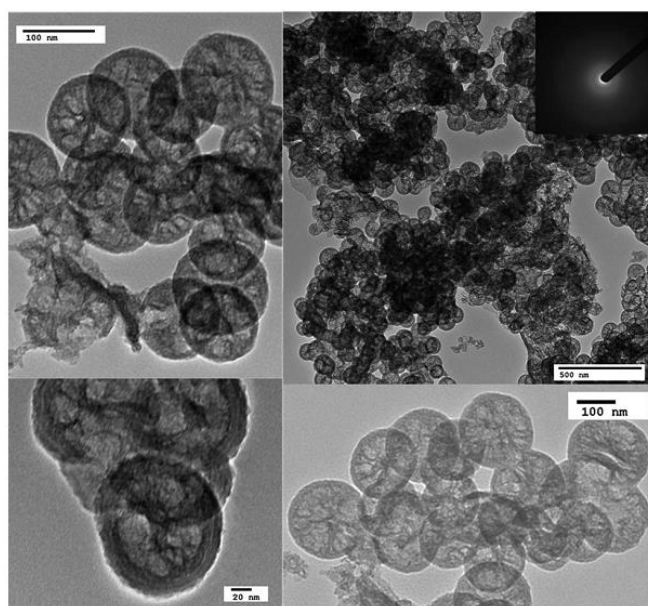


**Figure 22: TEM pictures of Si\_NC with different magnifications; inset: electron diffractogram.[160] Reproduced by permission of The Royal Society of Chemistry (RSC) on behalf of the Centre National de la Recherche Scientifique (CNRS) and the RSC.**

### *Si\_NC synthesis*

Si\_NC can be easily prepared by a micro-emulsion method. The initial studies that lead to the application of microemulsion to Si\_NC synthesis can be traced back to the development of M41S at Mobil Oil Corporation.[185, 186] The approach followed involves the preparation of a liquid crystal whose surfactant structure serves as an organic template, directing the growth of the silica structure, which is built around it.[186] The solid structure is created by hydrolysis and condensation reactions by silica precursors that take place on the template surface, thus creating a solid structure.

The great majority of groups synthesize Si\_NC following a microemulsion process (oil-in-water approach), but alternatively, it is possible to use a reverse microemulsion. Both strategies yield nanocontainers with narrow size distribution. The

selection of the approach is based on the nature of the material to be incorporated, whether it is soluble in aqueous media or in solvent-based media. Some parameters can affect the modification such as the type of precursor, surfactant, the organic phase component, the existence of active elements dissolved in the organic or in the aqueous phases and finally the precursor ratio used in the synthesis.

As examples of the variety of approaches that can be found when preparing Si<sub>3</sub>N<sub>4</sub> are the works of Schacht[181] that uses microemulsion of oil-in-water but the hydrolysis and condensation reactions are done under acidic conditions, compared with the work R. Schiller,[187] where the authors made use of a reverse microemulsion and the hydrolysis and condensation reactions were carried out under alkaline conditions. In both examples, the focus was only on the synthesis of the capsules and on their structural characterization. In their approach, Maia and colleagues,[160] used an oil-in-water microemulsion in alkaline conditions. Diethyl ether is used as the oil phase, distilled water as the aqueous phase, TEOS as the silane precursor and ammonia to adjust the reaction pH. The obtained Si<sub>3</sub>N<sub>4</sub> presented a diameter of around 200 nm with a well-defined mesoporous structure, as shown in Figure 22. Moreover, in this specific work an active species were incorporated into the capsules during the synthesis process, corrosion inhibitor 2-mercaptobenzothiazole (2-MBT), by dissolving it into the oil phase.

As presented above, Si<sub>3</sub>N<sub>4</sub> have a considerable surface area, making them excellent materials to host different compounds, with the main focus being drug delivery/release studies. The use of Si<sub>3</sub>N<sub>4</sub> in corrosion protection systems follows a similar approach to drug release, differing on the compound encapsulated. Several studies have shown the potentialities of Si<sub>3</sub>N<sub>4</sub> to work as nanocontainers for corrosion inhibitors.

The Si<sub>3</sub>N<sub>4</sub> versatility as a host structure is visible in the variety of corrosion inhibitors that were successfully incorporated: 1H-benzotriazole (BTA),[158] 2-mercaptobenzothiazole (2-MBT),[159, 160, 184] poly aspartic acid (PAA)[188] and molybdate.[189] The strategies used to incorporate corrosion inhibitors are selected accordingly with the synthesis approach and with the type of inhibitor. Some works follow a two-step approach, where firstly the capsules are prepared followed by the inhibitor encapsulation, normally by diffusion.[188-191] Alternative paths use a one-step approach, where the inhibitor is incorporated during the Si<sub>3</sub>N<sub>4</sub> synthesis. Both options have some limitations, firstly the inhibitor solubility, and in the case of one-step incorporation, the addition of corrosion inhibitors can affect the Si<sub>3</sub>N<sub>4</sub> synthesis,

decreasing its efficiency, lower percentages of viable Si<sub>3</sub>N<sub>4</sub> for batch and lower control over the particle size distribution.

Borisova and colleagues[158] firstly prepared mesoporous silica nanoparticles and later incorporated the corrosion inhibitor 1H-benzotriazole (BTA) by dispersing the nanocontainers in a concentrated solution of BTA under reduced pressure. In the work of M. Yeganeh and colleagues[191] the two-step approach is also used, but the Si<sub>3</sub>N<sub>4</sub> synthesis is done differently, using a PVC/CTAB template in which the silica structure will be formed, using TEOS. The incorporation of 2-MBT is done by dispersing Si<sub>3</sub>N<sub>4</sub> in an ethanol-based solution with a specific concentration of 2-MBT. The 2-MBT was incorporated into the Si<sub>3</sub>N<sub>4</sub> by diffusion processes and reached loading efficiencies of around 72 %.[191]

### 2.4.3 Other relevant hosting systems

#### *Halloysites*

Halloysites (HS) particles can be defined as two-layered (1:1) aluminosilicates, chemically similar to kaolin, which exhibit a range of morphologies. A predominant form is a hollow tubular structure in the submicrometer range. HS vary in size from 500-1000 nm in length and 15-100 nm in inner diameter. HS are found in Nature and their general appearance and size vary considerably according to the deposit from which they were obtained.[163, 192-194]

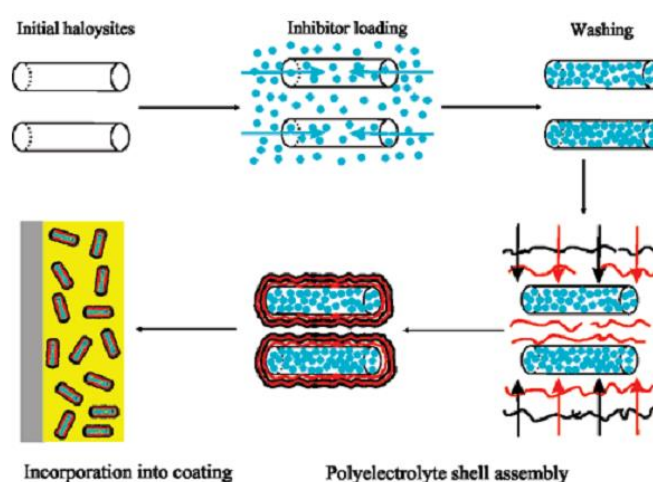


Figure 23: Schematic illustration of the fabrication of 2-mercaptobenzothiazole-loaded halloysite/polyelectrolyte nanocontainers.[192] Reprinted with permission from Shchukin, D. G., et al. (2008). "Active Anticorrosion Coatings with Halloysite Nanocontainers." *The Journal of Physical Chemistry C* 112(4): 958-964. Copyright 2016 American Chemical Society.

The application of halloysites as containers has been extensively reported in the literature[163, 194] for different corrosion inhibitors including azole-based compounds[162, 192, 195, 196] and 8-hydroxyquinoline.[100] Incorporation is attained by HS dispersion in an inhibitor solution under vacuum to ensure a higher loading content as exemplified in Figure 23. HS versatility has been shown by Snihirova and colleagues,[100] testing 8-hydroxyquinoline loaded HS in epoxy-based coatings, with the HS loaded coatings becoming effective after an initial step of corrosion activity, providing good corrosion protection.

### *Polymeric capsules*

The term polymeric capsules comprise a considerable variety of containers, differing mainly in their chemical composition.[197, 198] The preparation of polymeric nanocapsules can be done following different methodologies: pan coating, spray drying, centrifugal extrusion, and emulsion-based methods. Considering all the methods, emulsion-based synthesis has been the most extensively explored for anti-corrosion purposes.

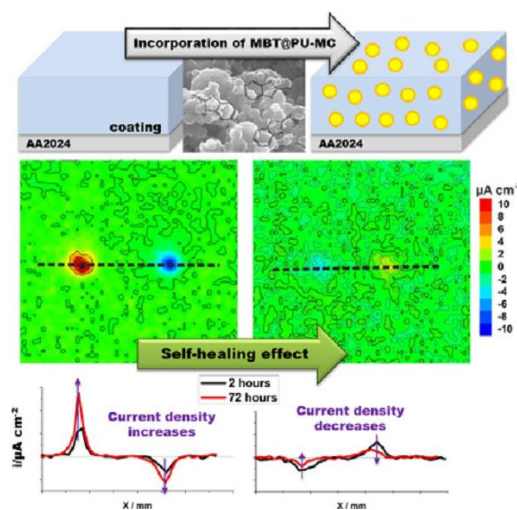


Figure 24: Scheme summarizing the application of 2-MBT loaded PU capsules in sol-gel coatings for corrosion protection. Reproduced from [199] with the authorization of Elsevier.

Emulsification polymerization presents several advantages, among them high strength and thickness of the shell walls and the ability to perform large-scale synthesis. Nevertheless, there are some disadvantages. It is difficult to encapsulate aqueous cores, active species can only be loaded once, results vary widely depending on the surfactant and polymerization mechanism often yield large size distributions. Taking all the

advantages and disadvantages into account, there is a huge potential to be explored. Some work has been published concerning the use of polymeric based capsules for encapsulation of corrosion inhibitors and their addition to protective coatings.[157, 199, 200] Work developed by Maia and colleagues[199] focuses on the preparation of polyurea (PU) microcapsules loaded with corrosion inhibitor 2-MBT, as illustrated in Figure 24. The addition of these microcapsules to sol-gel based coatings leads to better coating barrier properties and active corrosion protection when applied to AA2024 substrates, rendering it a promising system to prevent detrimental effects associated with the direct addition of the inhibitor.

## 2.5 Nanocontainers surface modification

The particle/coating interaction, as stressed above, is paramount to preserve good coating barrier properties, by improving particle dispersion and particle/coating chemical interaction. Modifying the nanocontainer surface chemistry is one approach used to improve and solve limitations arising from poor particle/coating compatibility. Particle surface modification has been a reality in the past decades for several areas, from biomedical applications,[201, 202] biotechnology,[203] and pulp industry[204] to the development of composites.[3, 205]

The approach used in each modification is based on the purpose intended for the particle. For example, in biomedicine, it could be the targeting of specific cells, while in pulp and composite industries the main objective is to prevent particle aggregation and preserve nanocontainer/composite properties. Surface modification can be achieved by chemical modification (changing surface chemistry)[206] and adsorption of polymers, polyelectrolytes, and surfactants.[94]

Compatibility is, understandably, a vital factor when developing paint formulations, being extensively studied by industry in the development of their products. The second area with an intense interest in the compatibility between the nanocontainer and the matrix is the production of composites.[205, 207] An interesting study was performed by Ma and colleagues[205] where the properties of a polypropylene (PP)/brucite (BC) composite was enhanced by surface modification with APS (siloxane derivative) of BC. For a content level of 2.9 % APS an increase of approximately 90% and 30% in tensile strength and impact strength was observed in relation with PP/BC without APS, respectively. The BC surface modification also improved its dispersibility in the matrix.

Following a similar approach, Wang and Sheng[207] used methacryloxypropyl trimethoxysilane (MPTMS) to modify the surface of attapulgite (ATP), thus forming a new kind of organophilic clay and enhancing the mechanical properties of a polypropylene (PP)/org-attapulgite nanocomposite. The grafting reaction improved the dispersion of ATP particle in the PP matrix without affecting the crystalline structure. Moreover, the mechanical properties of PP nanocomposites were improved by the addition of ATP.

### 2.5.1 Compatibility with coatings

The concept of compatibility must be understood, in the context of this work, as the sum of the physical and chemical interactions between coating and particle and the effect they produce on the coating barrier properties. As mentioned previously, the addition of a particle to a coating without affecting its properties can be an arduous task. On one hand is difficult to achieve a good particle dispersion and stability, on the other hand, chemical reactions between the particle and the coating formulation can be taking place. The literature regarding coating technology tends to focus more on issues regarding particle stability, paint shelf-life, and particle dispersibility on coatings. Nevertheless, these are intrinsically connected with the coating properties after application, such as appearance and mechanical properties.

#### *The stability in a suspension*

Two main characteristics are expected from a stable particle suspension, the lack of aggregation (flocculation) and uniform dispersion of the particles, as exemplified in Figure 25. These issues are common in paint industry with a considerable number of publications on the matter.[77, 208, 209] The two main mechanism affecting particle stabilization are electrostatic stabilization and steric stabilization. Electrostatic stabilization happens when particles with the same charge come into contact. Since they have the same charge they will repel each other. The repulsion between the charged particles, based on Coulomb forces, allows for the system to remain stable. Steric stabilization occurs when the particle-particle interaction is prevented by covering the particle with a polymeric layer. The flocculation process is then prevented by the strong interactions occurring between the polymer and the solvents. Figure 26 depicts the potential energy curve the approach of two nanoparticles, exemplifying the process leading to particle aggregation when in suspension. Where the total potential energy curve (VT) is a superposition of an attractive curve (VA) and a repulsive curve (VR). If two particles came together and are able to overcome the energy barrier (VM) this could lead to particle aggregation.[210]

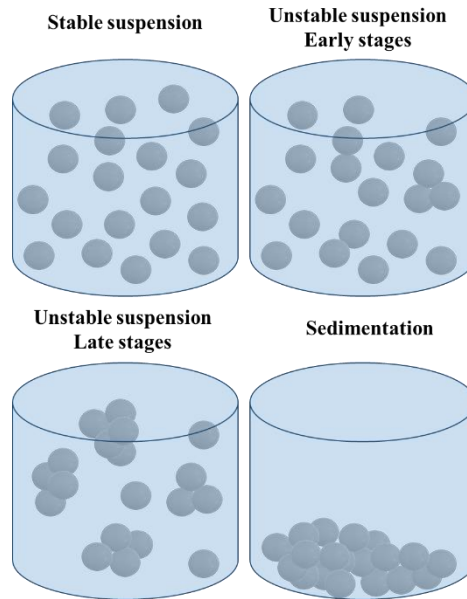


**Figure 25:** Schematics represents a stable suspension and the process leading to sedimentation. Based on the reference [211].

#### *Derjaguin-Landau-Vervey-Overbeek (DLVO)*

One theory used to explain the interactions between colloidal particles and their aggregation behavior is the Derjaguin-Landau-Vervey-Overbeek (DLVO) theory. DLVO was first developed by Boris Derjaguin, in 1939, being extended some years later in a combined work between Derjaguin and Lev Landau.[212] The final contributions were added by Evert Verwey and Jan Overbeek in their book, increasing the theory visibility.[213] The theory states that the repulsive forces on the particles surface are responsible for the creation of an energy barrier that will prevent two particles to approach each other and form agglomerates. This repulsive energy barrier can be overcome when the particle collide with sufficient energy, causing the particle to attract strongly (van der Waals forces) resulting in the irreversible agglomeration of the particles. In the cases the repulsion forces are strong between the particles, a stable colloidal system will be formed. When the repulsion forces are not strong enough, particle agglomeration starts to occur.[214]

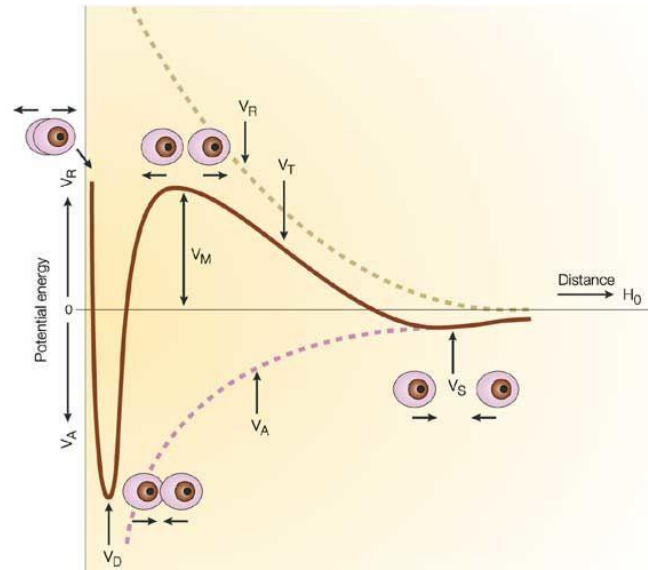


**Figure 26: Potential energy curve for the approach of two nanoparticles. Reproduced from reference [210] with the authorization of Springer Nature.**

The force between two colloidal particles ( $F(h)$ ) can be calculated using equation (11), by relating the known distance between them ( $h$ ) with the free energy of two plates ( $W(h)$ ) per unit area. The effective radius is given by the equation (12) where the  $R_+$  and  $R_-$  are the radii of the particles, for particles of identical size the  $R_{eff}$  is given by  $R/2$ . Knowing the force enables the calculation of the interaction free energy ( $U(h)$ ) of the two particles using equation (13).

$$(11) F(h) = 2\pi R_{eff}W(h)$$

$$(12) R_{eff} = \frac{R_+R_-}{R_++R_-}$$

$$(13) U(h) = \int_h^\infty F(h')dh'$$

The DLVO theory assumes that the value of free energy is similar to the contributions of the van der Waals and double layer interactions, as presented in equation (14). The van der Waals are often presented as the result of the interactions of the rotating or fluctuating dipoles of atoms and molecules. The van der Waals interaction can be described using equation (15), where  $H$  is the Hamaker constant (defines strength). The expression can be only applied when particles are close, becoming quite inaccurate at separations greater than about 10% of the particle radius.[214]

$$(14) W(h) = W_{vdw}(h) + W_{dl}(h)$$

$$(15) W_{vdw}(h) = -\frac{H}{12\pi h^2}$$

$$(16) W_{dl}(h) = -\frac{2\sigma_+\sigma_-}{\epsilon_0\epsilon_k} \exp(-kh)$$

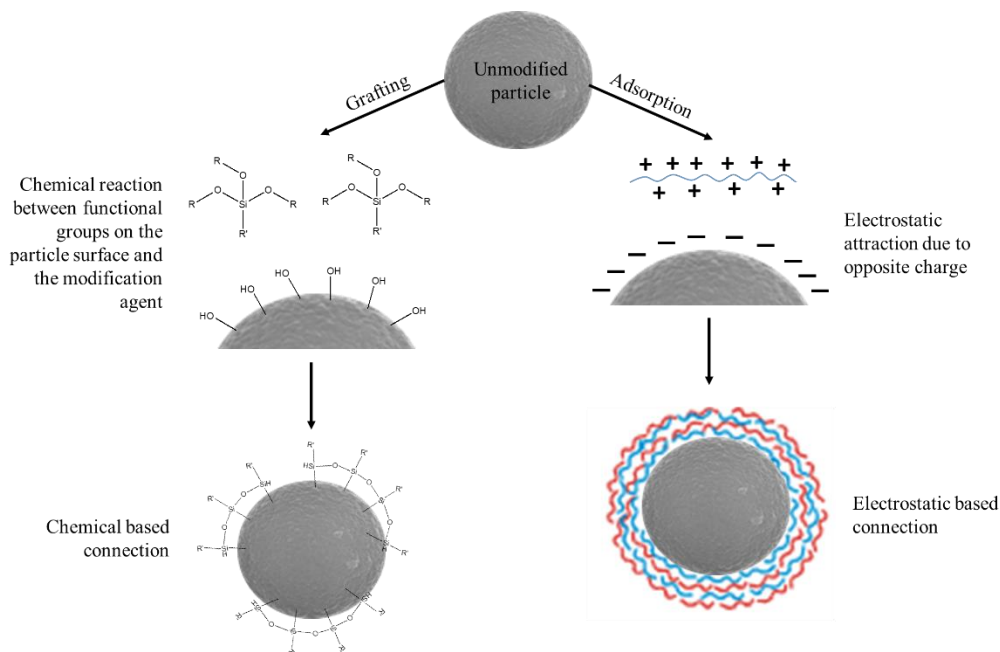
$$(17) k^{-1} = \left(\frac{k_B T \epsilon_0 \epsilon}{2q^2 N_A l}\right)^{1/2} = \frac{0.3 \text{ nm}}{\sqrt{I}}$$

$$(18) \quad I = \frac{1}{2} \sum z_i^2 c_i$$

The double layer contribution becomes increasingly relevant for lower salt levels. The  $W_{dl}(h)$  can be described by equation (16), where  $\sigma_+$   $\sigma_-$  are the surface charge densities per unit area of the two surfaces,  $\epsilon_0$  is the permittivity of vacuum,  $\epsilon$  is the dielectric constant of water and  $k$  is the inverse Debye length (equation (17)). In the inverse Debye length equation,  $q$  is the elementary charge,  $N_A$  is the Avogadro's number,  $I$  is the ionic strength,  $K_B$  is the Boltzmann constant and  $T$  the temperature. The second equality can be valid for water at room temperature, with the ionic strength of the solution given by equation (18), where  $z_i$  is the valence of the in type  $i$ ,  $c_i$  is the concentration expressed in mol/L and  $i$  runs over all types of ions in solution.[211]

## 2.5.2 Surface modification

The surface modification in the context of anti-corrosion applications addresses three key characteristics: coating/nanocontainer interaction,[215] nanocontainers dispersibility[215, 216] and release profile.[94, 217] The work developed by Sari and co-workers[216] focus on the influence of surface modification of nanoclay particles with the polyester-amide hyperbranched polymer (HBP) to be added to an epoxy-based coating. The objective was the improvement of particle dispersion as well as coating/particle interaction, being the best results observed for coatings loaded with 5 wt.% of modified particles according to the electrochemical impedance results.



**Scheme 2: Schematic representation of two possible approaches used in the surface modification of particles.**

The surface modification can be done in a variety of forms and materials, which may be divided into two main groups, modification by electrostatic interaction and modification by chemical reaction, as shown in Scheme 2. The selection of the methodology to be employed depends considerably on the material used and the intended purpose. In this section, a brief overview of some examples of modifications that used these methodologies will be presented, providing a conceptual background for the experimental path followed in the frame of this thesis.

### 2.5.2.1 Adsorption

#### LbL approach

The use of polyelectrolytes in corrosion protection has been extensively reported in the literature. The approaches vary, some of them inspired by systems developed from other fields, namely biomedical applications. The study of polyelectrolytes use in the preparation of polyelectrolyte capsules and in the surface modification of nanocontainers will be privileged in this work. The examples presented will englobe systems developed for corrosion protection, but occasionally the system that inspired them will also be mentioned in an effort to contextualize the use of polyelectrolytes, particularly the employment of the layer-by-layer (LbL) approach.

LbL is a method based on the adsorption of oppositely charged molecules, on a solid surface[195] or in the interface of an emulsion,[195, 218] in order to form a multilayer system. In some cases a combination of the previous approaches is used, the deposition of polyelectrolytes in solid capsules, by LbL method, followed by the dissolution of the solid capsules leaving only the polyelectrolyte shell.[219] Making use of the same mechanism of interaction, a monolayer system can be imagined, where a molecule with an opposite charge is deposited as a single layer on the surface of particles. This level of control allows for the formation of nanocontainers modified with polyelectrolyte shells with known chemistry and controlled thickness.

The first works concerning LbL date back some decades and made use of the Langmuir-Blodgett technique, where monolayers are formed on a water surface and then transferred onto a solid support.[220, 221] In the majority of the cases the adsorption is due to electrostatic forces among oppositely-charged polymers and surfaces, but other mechanisms include hydrogen bonding, covalent bonding, base-pair interaction, guest-host interactions, hydrophobic interactions or biological recognition.[222] Included in the

list of materials suitable for LbL are polyelectrolytes (natural or synthetic), nucleic acids, peptides, enzymes, polysaccharides, and lipids, among others.[222]

In corrosion protection the use of LbL tends to follow two distinct approaches: in the first, the LbL produces shells that will function as a container for corrosion inhibitors on its own and in the second approach the LbL is used as a surface modifier for nanocontainers. The standalone polyelectrolyte capsule for corrosion protection has been reported by M. Plawecka and colleagues.[218] In this work, nanocontainers loaded with corrosion inhibitor 2-MBT were added to a water-based coating and applied in AA5083 and galvanized steel substrate showing good results.[218] The polyelectrolyte nanocontainers used in the encapsulation of 2-MBT were developed by K. Szczepanowicz and colleagues.[223] The authors used a microemulsion approach to create a stable hydrophobic liquid core to which several layers of polyelectrolyte are applied, designing liquid core encapsulation by polyelectrolyte multilayer adsorption. A key step when following this approach is the surfactant selection since it must provide the emulsion with enough stability in such a way that the polyelectrolyte layers do not disrupt the emulsion. This requirement was satisfied by using AOT as an emulsifier and further stabilization was obtained by the formation of AOT/PDADMAC surface complexes. The positively-charged liquid cores were modified with various combinations of polyelectrolytes: PDADMAC, chitosan, PSS, and alginate.[223]

Following a similar procedure, D.G. Shchukin and H. Möhwald have prepared DADMAC/PSS polyelectrolyte capsules, shown in Figure 27c. The authors' study focuses on the ability of the nanocontainers to encapsulate and hold the corrosion inhibitor benzotriazole. The release profile was analyzed, observing a high release of the inhibitor on neutral pH water. The uncontrolled release of inhibitor renders them as unfit to be incorporated into "smart" systems since they do not hold the inhibitor long enough for it to be triggered by corrosion processes taking place.[195]

The use of polyelectrolyte nanocontainers for corrosion protection is not the most common approach in use. In fact, the main interest in the polyelectrolyte shell is not their ability to form nanocapsules, but rather their response to a stimulus. This specific response can be added to an already functional nanocontainer, making it not only a good host for corrosion inhibitors but causing the capsules to release them on demand. Different types of polyelectrolyte shells have been used to modify the surface of different nanomaterials: HS and SiO<sub>2</sub> nanoparticles. [192, 195]

The application of polyelectrolytes is presented in three different approaches in the study performed by D.G. Shchukin and H. Möhwald.[195] In this work, the concept of polyelectrolyte shells is applied to solid capsules, hollow HS, and polyelectrolyte capsules, as shown in Figure 27. The aim was the tuning of the release of corrosion inhibitor in order to improve the corrosion efficiency of coatings. In all the three approaches the authors used benzotriazole as the corrosion inhibitor and LbL assembly of poly(diallyldimethylammonium chloride)/poly(styrene sulfonate) (PDADMAC/PSS), poly(allylamine hydrochloride)/poly(styrene sulfonate) (PAH/PSS), and poly(allylamine hydrochloride)/poly(methacrylic acid) (PAH/PMA) polyelectrolyte bilayers.

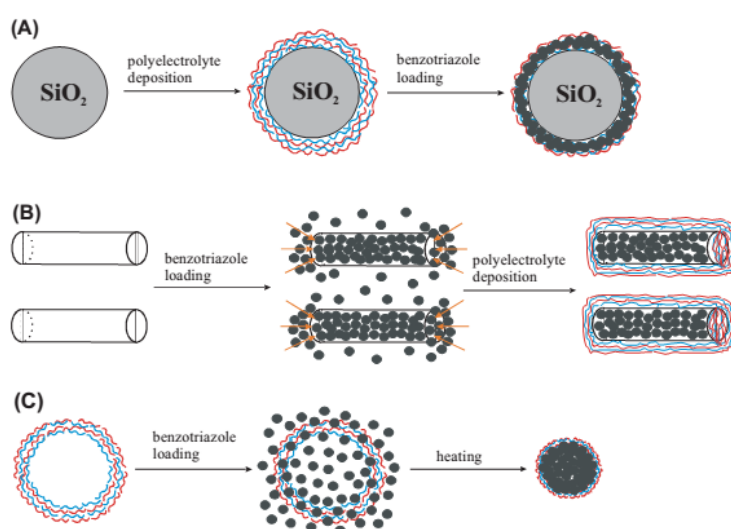


**Figure 27:** A) Schematic illustration of the procedure for benzotriazole loading for SiO<sub>2</sub> nanoparticle containers, B) halloysite nanotubes and C) polyelectrolyte capsules. Reproduced from the reference [195] with the authorization of John Wiley and Sons.

The modification of SiO<sub>2</sub> was done to add new functionalities to the nanocontainers: first and most common when speaking of polyelectrolytes is the change in the release profile and a second feature, exclusive to this system, is the use of the different polyelectrolyte layers to encapsulate the corrosion inhibitor in between them. The authors made use of different pairs of electrolytes: PAH/PSS, PAH/PMA, and PDADMAC/PSS. In the case of HS the polyelectrolyte modification function is to tune the inhibitor release and prevent uncontrolled release of the inhibitor since HS releases its content by diffusion. The HS loaded were also modified with the polyelectrolytes pairs PAH/PSS, PAH/PMA and PPDADMAC/PSS. The authors observed different release profiles according to the electrolyte used in the modification and also the type of particle. Analyzing only the systems that use nanocontainers (solid particles) they observed a fast

release of inhibitor for SiO<sub>2</sub> nanoparticles modified with PAH/PSS and PAH/PMA, together with HS modified with PAH/PMA. A more steady release of inhibitor was observed for SiO<sub>2</sub> nanoparticles modified with PDADMAC/PSS and HS modified with PDADMAC/PSS and PAH/PSS. This work is a good example of the versatility of polyelectrolyte modification applied to different systems, nanocontainers. Moreover, the impact produced by different polyelectrolytes pairs in the inhibitor release, even for the same nanocontainer, can be extremely useful when tuning the response of a protective coating.

**Table 8: Release properties of polyelectrolytes capsules. Reproduced from reference [222].**

Factor	Release characteristics
<b>Local changes of pH</b>	Capsules can be opened/closed depending on pH value at all pH range (0–14). Applicable only for capsules with weak polyelectrolytes in the shell
<b>Local changes of ionic strength</b>	An increase of the ionic strength of the solution leads to the capsule opening. Applicable for all polyelectrolyte capsules
<b>Solvent changes</b>	Non-polar solvents damage integrity of polyelectrolyte shell and open capsules
<b>Temperature</b>	Temperature increase leads to the capsule closing. Applicable for capsules with a strong polyelectrolyte in the shell
<b>Light</b>	Irradiation leads to the capsule opening. Applicable for capsules with light-sensitive elements in the shell
<b>Magnetic field</b>	Magnetic treatment opens capsules. Applicable for capsules with magnetic particles in the shell
<b>Ultrasound</b>	Ultrasonic treatment leads to irreversible capsule opening. Applicable for capsules with nanoparticles in the shell
<b>Redox treatment</b>	Oxidation/reduction of the capsule shell can lead to the capsule opening. Applicable for capsules with redox materials in the shell (conductive polymers)
<b>Enzymatic degradation</b>	Enzymatic treatment irreversibly opens capsules with biodegradable components in the shell

There is the possibility of making use of a conjugation of nanocontainers, some adding a fast response, while others assure a prolonged release of inhibitor translating into a tunable response of the coating in terms of corrosion protection. The introduction of polyelectrolyte shells can add to corrosion protection systems an aura of “smartness”, since it changes or adds specific release triggers to the capsules, making the release of their content on demand. A good list of factor and release characteristics can be found in the report of D. Grigoriev and colleagues and reproduced in Table 8.[222, 224]

### *Surface active agents*

One of the main aims when changing the surface of nanocontainers is the improvement of its dispersibility, in particular for nano-size range containers. At this scale, particle dispersion becomes a problematic issue, with the nanocontainer behavior

in the suspension being highly affected by Brownian motion. Brownian motion increases with decreasing particle size, ultimately leading to an increased interaction between nanoparticles, and as a result of van der Waals attractive forces, they tend to aggregate.[225] A theory that models the dispersion of nanoparticles in aqueous medium taking into account the van der Waals attractive forces and electrostatic interactions due to the electrical double layer is the theory by Deryagin, Landau, Verwey, and Overbeek (DLVO), presented before.[226]

A simple approach to improve particle dispersion is to create a steric repulsive force between them, which can be achieved by the surface modification of the nanocontainers with polymeric chains. Some examples of polymers used in the surface modification can be found in the literature, such as polyacrylic acid,[227] polyacrylic acid sodium salts,[228] copolymers of polyacrylic acid/maleic acid,[225] maleimide propyl trimethyl ammonium chloride[229] and polyethyleneimine.[230] These polymers were used in the surface modification of several nanoparticles, such as BaTiO<sub>3</sub>,[231] TiO<sub>2</sub>,[228] Al<sub>2</sub>O<sub>3</sub>,[227] MgO[232], Fe<sub>2</sub>O<sub>3</sub>[233] and SiO<sub>2</sub>. [229]

The surface modification of SiO<sub>2</sub> with an oppositely charged polymer was done by S.-C. Liufu and colleagues,[229] where the particles were modified with maleimide propyl trimethyl ammonium chloride (MPTMAC), for improving the SiO<sub>2</sub> stability in aqueous media.[229] The authors studied the adsorption of MPTMAC as a function of the polymer concentration, solution pH, type of salt in solution and its concentration. The conclusion went towards all the factors listed above to have some level of influence on the polymer adsorption and in the layer thickness. The quantity of material adsorbed, expressed on the average thickness layer, was found to be related with the electrolyte concentration. The maximum value was dependent on the counter ion being used. The authors concluded that at low concentrations the polyelectrolyte adsorbs in a flat conformation, and the particle aggregation was not prevented. Higher concentrations of polyelectrolyte leads to thicker adsorbed layer, causing an electrosteric stabilization of the particles dispersion due to the high particle coverage. The decrease in pH shows a tendency of the MPTMAC to form a structure with loops and tails on the SiO<sub>2</sub> surface that improved the particle stabilization in suspension.[229]

### 2.5.2.2 Chemical surface modification

The adsorption of polyelectrolytes has been shown to be a good strategy to confer new features to nanomaterials, including the improvement of stability in suspensions, release profile and compatibility with coatings. Another valid and largely used alternative is surface modification based on the grafting of new substituents in the surface. Similarly to adsorption, this strategy allows the tuning of the nanocontainers surface chemistry. However, rather than simply attaching a steric spacer on the nanocontainer surface, the grafting allows for a more controlled and irreversible chemistry, with the possibility of inserting specific functional groups, as exemplified in Figure 28.

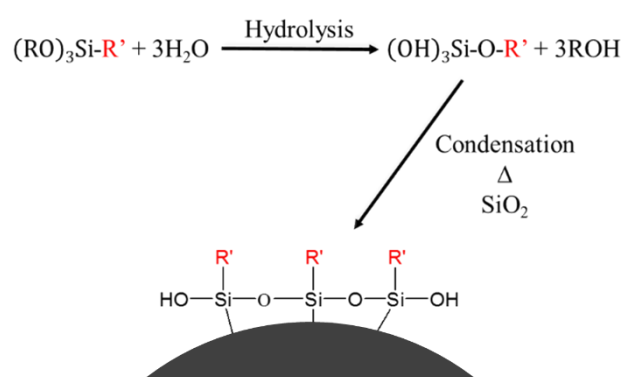


**Figure 28: Chemical modification of the silica surface in an aqueous system. Adapted from.[234]**

The surface modification of nanocontainers is extensively represented in the literature.[235-241] Their applications go from the more “simplistic” applications, such as the improvement of compatibility between nanocontainers and coating matrix applied on composites and paints,[237, 239] to the more sophisticated ones, such as those in the biomedical field.[201, 203, 242] The variety of nanoparticles in which the surface modification was performed also varies, with reported works involving  $\text{SiO}_2$  nanoparticles or silica capsules (in a wide range of sizes),[237, 241, 242] iron oxides nanoparticles[201, 203] and zinc oxide.[243]

Biomedical and bioengineering applications have made use of iron oxide nanoparticles for numerous application such as magnetic resonance imaging contrast enhancement, tissue repair, immunoassay, detoxification of biological fluids, hyperthermia, drug delivery and in cell separation. These applications require high magnetization values and small size (less than 100 nm), as well as a narrow size distribution in order to produce particles with uniform chemical and physical properties. The surface modification of these particles allows for the introduction of molecules able

to target specific areas, provided that the coatings are non-toxic and biocompatible.[201] Silica, gold or gadolinium are examples of materials used in the coating of iron oxide nanoparticles, enabling the change of the nanoparticles magnetic properties and at the same time the properties of the particles. In the case of gold, the nanoparticles magnetic properties can be tuned according to need, but the gold layer also functions as a platform for further functionalization with chemical or biological agents.

The modification with a silica layer is the one that opens more options relating to the incorporation of new functional groups and further modifications, due to the presence of the silanol groups, which can react easily with alcohols and silane coupling agents.[201, 244] The covering of nanoparticles with silica has been reported using three main approaches: the Stöber method, in which the silica coating is created via hydrolysis and condensation reactions of a sol-gel precursor, the deposition of silica using a silicic acid solution, and the microemulsion method, in which the silica coating forms in confinement provided by the micelles and reverse micelles of the microemulsion. The second approach, silicic acid solution, tends to yield a better covering of iron oxide nanoparticles than the Stöber method. The microemulsion tends to pose considerable difficulties in the removal of the surfactants required to create the microemulsion.[203]

Modification of ZnO was performed by R.Y. Hong aiming at the improvement of its dispersion properties. The authors grafted polystyrene on the nanoparticles surface and besides studying the nanoparticles dispersion, the authors, also analyzed the photocatalytic properties of the ZnO with and without the surface modification. The dispersion was improved by the grafting of polystyrene but on the other hand, the surface modification hinders the photocatalytic active of the ZnO.[243]

As referred before, the use of SiO<sub>2</sub>-based materials gives a wide range of possibilities concerning surface modification via the use of different silane coupling agents, allowing the introduction of different functional groups.[234] The surface modification of SiO<sub>2</sub>, as a solid nanoparticle or as a mesoporous nanocontainer, has been reported for silane derivatives with a variety of functional groups: aminopropyltriethoxy (APS),[234, 242] 3-mercaptopropyl trimethoxysilane (MPTS),[242, 245] 3-bromopropyltrichlorosilane,[242] nonionic poly(oxyethylene methacrylate) (POEM) and ionic poly(styrene sulfonic acid) (PSSA).[246]

One of the most common approaches in the grafting of silane derivatives uses hydrolysis and condensation reactions. The fact that similar materials are used in both nanoparticles synthesis and its modification makes the surface modification considerably

easy. P. Rostamzadeh and colleagues[206] modified SiO<sub>2</sub> nanoparticles (Aerosil 200) with an average particle size of 12 nm with APS. The particles were dispersed in ethanol to which was added a solution containing ethanol and APS together with a specific amount of water. The hydrolyzed solution was added dropwise to the nanoparticles suspension. The condensation process, leading to the APS grafting, was done at room temperature and at 80 °C. The authors observed that the silane and water concentration plays an important effect on the modification process. The reaction at room temperature yields higher grafting percentages when comparing with reactions at higher temperatures.

An alternative approach to the use of silane derivatives was done by Park and colleagues,[246] in a process that requires more steps to achieve its goal. In this case, the researchers modified SiO<sub>2</sub> nanoparticles with nonionic POEM and PSSA making use of the advanced polymerization technique “atom transfer radical polymerization” (ATRP). The aim of the modification was the incorporation of hydrophilic water-soluble polymers. Even with a more time consuming and complex methodology than the examples presented so far, Park’s work highlights the clear versatility of the nanoparticles to be surface modified, allowing the tuning of surface properties according to needs.

An example of the relevance of nanoparticle surface modification in sophisticated applications, such as biomedicine, is the work developed by Tsai and colleagues.[245] In their work, an antibody (anti-Her2/neu) was grafted into silica particles modified with MPTS, in order for the nanoparticles to target breast cancer cells. The authors linked the antibody to an NHS-PEGmaleimide and then mixed it with the functionalized Si<sub>3</sub>N<sub>4</sub>. The functionalized Si<sub>3</sub>N<sub>4</sub> proved to be selective, as their tendency to penetrate Her2/neu positive cells (cancerous cells) scored over 80 %, compared with less than 20 % of Her2/neu negative cells (non-cancerous cells).



## 3

# Principles of experimental techniques

*It was six men of Indostan,  
To learning much inclined,  
Who went to see the Elephant  
(Though all of them were blind),  
That each by observation  
Might satisfy his mind.*

*The First approach'd the Elephant,  
And happening to fall  
Against his broad and sturdy side,  
At once began to bawl:  
"God bless me!—but the Elephant  
Is very like a wall!"*

*The Second, feeling of the tusk,  
Cried: "Ho!—what have we here  
So very round and smooth and sharp?  
To me 't is mighty clear  
This wonder of an Elephant  
Is very like a spear!"*

*The Third approach'd the animal,  
And happening to take  
The squirming trunk within his hands,  
Thus boldly up and spake:  
"I see," quoth he, "the Elephant  
Is very like a snake!"*

*The Fourth reached out an eager hand,  
And felt about the knee.  
"What most this wondrous beast is like  
Is mighty plain," quoth he;  
" 'T is clear enough the Elephant  
Is very like a tree!"*

John Godfrey Saxe version of "Blind Men and the Elephant"

*The Fifth, who chanced to touch the ear,  
Said: "E'en the blindest man  
Can tell what this resembles most;  
Deny the fact who can,  
This marvel of an Elephant  
Is very like a fan!"*

*The Sixth no sooner had begun  
About the beast to grope,  
Than, seizing on the swinging tail  
That fell within his scope,  
"I see," quoth he, "the Elephant  
Is very like a rope!"*

*And so these men of Indostan  
Disputed loud and long,  
Each in his own opinion  
Exceeding stiff and strong,  
Though each was partly in the right,  
And all were in the wrong!*

**MORAL,**

*So, oft in theologic wars  
The disputants, I ween,  
Rail on in utter ignorance  
Of what each other mean;  
And prate about an Elephant  
Not one of them has seen!*



## 3.1 Spectroscopic characterization

### 3.1.1 Fourier transform infrared (FTIR)

Infrared (IR) spectroscopy is routinely used, nowadays, in virtually all fields of science. The versatility given by the technique allows samples to be analyzed in various physical states (e.g. liquid, gas or solid) and in a broad range of temperatures. Thus, the importance of IR has in different fields such as quality control, identification of specific functional groups or in-depth analysis of compounds. IR allows for a qualitative analysis, for example verifying if a chemical modification occurred, but also a quantitative analysis, for example by calculating the degree of substitution in a reaction when the proper experimental methodology is employed.[247]

The origins of IR spectroscopy dates back to the invention of the interferometer by Michelson in 1891, used to measure the wavelength of light. But until the WWII IR was regarded as a challengeable technique due to the lack of computing and instrumental technology, which limited considerably its use. In the decades immediately after WWII the field of IR spectroscopy saw increasing advances both in the field of data treatment, exemplified by the developments in instrumentation science (e.g. Fellgett advantage of interferometers, Jacquinot advantage, and Cooley–Tukey algorithm) and equipment development, of which the Helium-Neon lasers, improved IR detectors and analog-to-digital converts are good examples.[247, 248]

In the present work a Fourier transform infrared (FTIR) spectrometer was used, which is the third generation infrared spectrometer. Comparing with IR of previous generations possesses several advantages: higher signal-to-noise ratio; higher wavenumber accuracy (an error of  $\pm 0.01 \text{ cm}^{-1}$ ); shorter scan time for all frequencies ( $\sim 1 \text{ s}$ ); higher resolution ( $0.1 \sim 0.005 \text{ cm}^{-1}$ ); wider scan range ( $1000 \sim 10 \text{ cm}^{-1}$ ); and reduced interference from stray light.[248]

A general layout of what can be found in an FTIR spectrophotometer is shown in Figure 29, with the main components identified: IR source, a beam splitter, detector and reference laser. IR source usually works as a heat generator based on the resistance of the source to conduction of current and can be made of silicon carbide, ceramic or nichrome wire and a mixture of yttrium and zirconium oxides. The beam splitter, as the name indicates, splits and recombines the IR light waves. It can be made of different materials,

but usually is a result of the combination of semitransparent substrates and coatings. The substrates can be quartz, calcium fluoride ( $\text{CaF}_2$ ) and potassium bromide (KBr). The coating material changes according to the manufacturer but germanium is one of the most used.

The detectors work by transforming the light intensity into an electrical signal. The most common detectors in use are deuterated triglycine sulfate (DTGS) detectors and the mercury cadmium telluride (MCT) detectors. The reference laser serves two purposes: to function as a wavenumber standard and to determine the moving mirror position. The most common laser used is the red He-Ne laser (light at exactly  $15798.637 \text{ cm}^{-1}$ ).<sup>[248]</sup> As should be expected, the number of possibilities in an FTIR design concerning instrumental configuration is considerable. In some cases, the instruments are designed only to be used in a specific application.

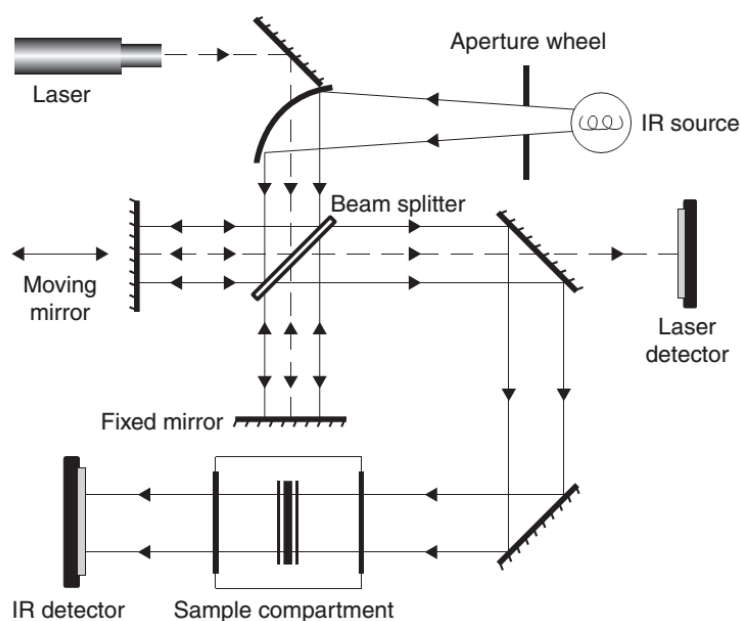


**Figure 29:** Optical layout of a typical FTIR spectrophotometer. Reproduced from reference [248] with the authorization of Elsevier.

Being a type of vibrational spectroscopy, in line with RAMAN, IR spectroscopy measures transitions between molecular vibrational energy levels as a result of the absorption of IR radiation, vibrations of the atoms within molecules.<sup>[247, 249]</sup> The IR measurement is presented as a spectrum that determines the fraction of the incident radiation (on the sample) that is absorbed in a particular energy.<sup>[249, 250]</sup>

The IR radiation is generally defined, in terms of wavenumber, as near-IR ( $14000 \text{ cm}^{-1}$  to  $4000 \text{ cm}^{-1}$ ), mid-IR ( $4000 \text{ cm}^{-1}$  to  $400 \text{ cm}^{-1}$ ) and far-IR ( $400 \text{ cm}^{-1}$  to

$10 \text{ cm}^{-1}$ ). Usually, the spectra are presented with the intensity (ordinate axis) as a function of wavelength (abscissa axis).[250, 251]

The determination of vibrations ascribed to new chemical bonds or associated with the presence of new molecular species is the main objective when employing FTIR in the frame of this thesis, namely for identification of functional groups grafted onto the surface of silica capsules or the presence of corrosion inhibitors intercalated into LDH galleries. The qualitative analysis of FTIR spectra representing the incorporation of new molecules into a material is relatively straightforward, with a direct comparison between the spectra of unmodified material, the material after modification, and the molecule. The sample characterization is done making use of table values of vibrational modes combined with knowledge of the material being used.[249] Without any information regarding the sample, it is almost impossible to do an accurate attribution of bands to the corresponding functional groups. Table 9 presents some of the most relevant functional groups and their usual IR frequency. The band position of the vibrational bonds can also be shifted according to the chemical environment.

**Table 9: Functional groups and their characteristic absorption wavenumber.**

Functional group	Structure	IR frequency ( $\text{cm}^{-1}$ )
Alkane (C-H)	$\text{R}_3\text{C-H}$ (R= H or C)	3000-2800
Alkyne (C $\equiv$ C)	$\text{RC}\equiv\text{CR}$ (R= H or C)	2260-2100
Alkene (C=C)	$\text{R}_2\text{C}=\text{CR}_2$ (R= H or C)	1600-1680
Alcohol (O-H)	RO-H	3600-3200
Nitrile (C $\equiv$ N)	$\text{RC}\equiv\text{N}$ (R= C)	2260-2200
Amines, amide (N-H)	$\text{R}_2\text{NH}$	3500-3300 1650-1560
Carboxylic acid (O-H)	RCOOH	3200-2500
Benzene ring (C=C)	$\text{C}_6\text{H}_6$	1450-1600
Aldehydes or ketones (C=O)	RCOR	1750-1705
Alcohol or ether (C-O)	C-O-R (R= H or C)	1300-1000
Carboxylic acid (C=O)	RCOOH (R= H or C)	1790-1680
Alkyne (C-H)	$\text{RC}\equiv\text{C-H}$ (R= C)	3300
Amide (C=O)	$\text{RCONR}_2$ (R= H or C)	1850-1680 1700-1730

### 3.1.2 X-ray diffraction

X-ray diffraction (XRD) is a widely used technique for the characterization of materials in different fields, with special relevance in materials science. X-rays are high-energy electromagnetic waves with wavelengths around 1 Å.[252] The XRD methodology is based on the ability of crystals to diffract X-rays in a characteristic manner permitting the study of the structure of crystalline phases.

The study of the diffraction pattern peaks allows for the understanding of several microstructural features of the sample. From the peak position is possible to obtain information concerning lattice parameters, space group, chemical composition, macro stresses, or qualitative phase analysis. The peak intensity gives information concerning crystal structure (atomic positions, temperature factor, or occupancy) as well as texture and quantitative phase analyses. The peak shape allows for information regarding sample broadening contributions (microstrains and crystallite size) to be obtained.[253]

X-rays were first discovered in 1895 by the German/Dutch physicist Wilhelm Conrad Röntgen. This discovery opened new possibilities for researchers to innovate in different fields, from medical applications to materials science. In materials science, the first studies, concerning XRD characterization of crystals, were reported by Max von Laue and W.L. Bragg and W.H. Bragg, in 1912 and 1913 respectively.[252, 254]

The typical XRD apparatus found in research facilities is composed of five main components: X-ray source, primary and secondary optics, a goniometer, sample holder and a detector. X-rays, in laboratory equipment, are produced by sealed tubes and rotating anodes following the same principle: electrons generated by heating a tungsten filament in a vacuum are accelerated through a high potential field and directed to the sample that will emit the X-rays. The X-rays are induced by two mechanisms, the deceleration of the electrons leading to the emission of X-ray and the ionization of the impinged atoms by ejecting electrons from the inner shells.[253]

The goniometer allows for a very precise movement of the sample, X-ray source, and the detector. The apparatus usually makes use of the Bragg-Brentano geometry in which the distance between the sample and the detector is constant for all  $\theta$  angles. The primary and secondary optics work under the same principle defining the size and form of the beam to achieve the highest possible signal intensity or a precise selection of a specific wavelength. The lens can be constituted by a single crystal monochromator, Göbel mirrors (optical systems coated with a succession of strongly and weakly scattering

materials arranged in a defined manner), Soller slits (composed of 20-40 thin plates of metals with high absorption, piled in parallel with a small gap and with a defined length) and pinhole collimators.

The detectors are used in order to convert the X-ray photons into a signal that can be analyzed and can be gas detectors, solid detectors, and semiconductor detectors. Gas detectors work by the recording of voltage pulses due to the ionization of a gas by the incoming X-ray photons. Solid detectors make use of the fluorescence phenomenon of specific materials that convert the X-ray photons into voltage pulses or into visible light. Semiconductor provides very good energy resolution.[253]

In the frame of this thesis, XRD was vital to assess the LDH structure and the identification of intercalated species. The presence of the molecules can be easily proven by complementary analysis with other characterization techniques, such as FTIR, but information concerning the presence of molecules inside the LDHs, in their galleries, can only be determined by XRD, by calculating the galleries height from the basal spacing.

### 3.1.3 X-ray photoelectron spectroscopy

X-ray photoelectron spectroscopy (XPS) is a highly regarded technique in the field of surface science since it allows for the measurement of elemental composition, determination of empirical formula, chemical state and the electronic state of the elements. The XPS analysis is based upon the photoelectric effect, by analyzing electrons (core) that are emitted from the sample after the absorption of an X-ray photon, in the cases when the incident photon energy is larger than the binding energy of the electron (sample). The technique allows for the study of all elements, except for H and He.[255, 256] The core electron binding energy ( $BE_x$ ) is defined as the difference between the energy of the primary photon ( $h\nu$ ) and the kinetic energy of the photoelectron ( $KE_p$ ), as presented in equation (19).[255, 257]

$$(19) \quad BE_x = h\nu - KE_p$$

An XPS apparatus usually is composed by the X-ray source (X-ray tube or synchrotron) and by a detector composed by an electrostatic lens and energy-analyzed by a spectrometer, most commonly a hemispherical electron energy analyzer. The measurements require high vacuum ( $P \sim 10^{-8}$  millibar) or ultra-high vacuum ( $P < 10^{-9}$  millibar) conditions for the samples and for the path taken by the electron between the sample and the detector. The incident photon energies in an XPS experiment typically set

between several 10 eV to well over 1000 eV, with kinetic energies of the same order.[256]

In this work, XPS was used to infer/understand whether cerium incorporated in LDHs as Ce(III) remained in the same oxidation state or if it was in higher oxidation state.

## 3.2 Imaging

### 3.2.1 Scanning electron microscopy

Electron microscopy (EM) is quite relevant in the study of micro- and nano-scale materials, allowing a glimpse of a world that otherwise will be out of our possibilities. The development of EM analysis is key in a variety of areas and has an impact in virtually all forms of modern science that leads with micro- and nano-scale structures: corrosion, nanoparticles, electronic components, among others.[258]

The first primitive form of a scanning electron microscope (SEM) appeared in 1937 as a result of efforts performed by several research groups. The development of the SEM came following the studies of De Broglie equation in 1923, showing that highly accelerated electrons possess a wavelength four to five orders of magnitude smaller than the wavelength of visible light. The studies of H. Busch on the geometrical electron optics in 1926, proving the lens properties of a magnetic coil, also contributed to launching the idea of using electron lenses, one behind the other to imitate the imaging process in the light microscope.[259] From this point onwards, the development of the modern SEM has had several contributors, with a variety of groups aiding in its development. A more broad analysis of the main early contributors can be found in the article written by C.W. Oatley.[259]

The typical SEM apparatus is presented in Figure 30, where the main components can be identified: electron gun, a condenser lens, aperture, objective lens, and detector. The electrons are generated on the top of a column in an electron gun, being probed and scanned by a system of lens until they hit the sample. An electron detector then detects the secondary electrons (SEs) and backscattered electrons (BEs).[260]

The electron gun accounts for one of the most relevant features on an SEM apparatus and can consist of a thermionic emission gun, a Schottky-emission electron gun or a field emission electron gun. Thermionic emission guns produce thermoelectrons by heating a tungsten filament or a LaB<sub>6</sub> crystal. The LaB<sub>6</sub> crystal tends to produce reduced energy spread compared with tungsten filament but requires a high vacuum. Tungsten filament, due to the energy spread, is not suitable for high-resolution SEMs. The Schottky-emission electron gun comprises a cathode made of a single crystal of W coated with ZrO, ZrO/W. It allows the production of small energy spread, one order of magnitude lower than the previous gun due to its beam current high stability it tends to be the one

selected for analytical SEMs. Field emission electron guns are made of a sharp W single crystal tip with a radius of a 100 nm. The energy spread produced by this electron gun is the smallest of all the guns presented here, translating into a more coherent and brighter signal with an improved signal-to-noise ratio. Field emission electron guns can be used in high-resolution SEMs and transmission electron microscopes.[260]

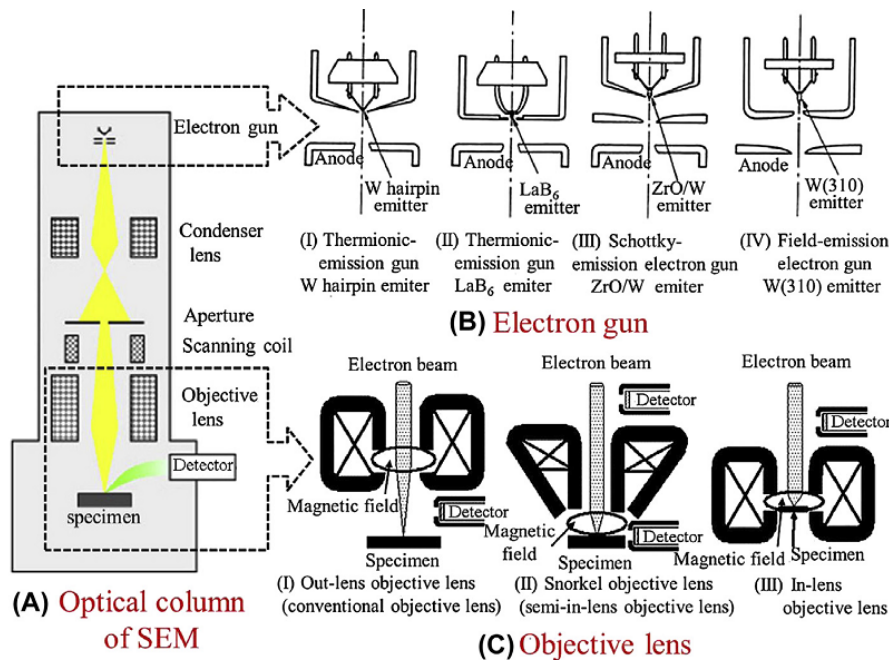


Figure 30: Diagram of an optical column of SEM and types of electron guns and objective lenses used in SEM system. Reproduced from reference [260] with the authorization of Elsevier.

The detectors can also be divided into three groups: SE detection, BSE and X-ray spectrometers. The SE is the most abundant electrons and is the base imaging mode used in the image specimen shape. BSEs are less abundant than SEs but much more energetic. Lastly, X-rays are abundant and emitted in all directions from the specimen. They can be used to do a chemical analysis of the sample, by energy dispersive X-ray analysis (EDS).[258]

In the field of corrosion protection is vital to have a closer look on the materials under study: active metals subject to corrosion processes, investigation of coatings used for their protection and the nanoadditives used to improve the coating performance. In the frame of this work, the focus should be placed on the nanocapsules characterization: morphology, structural integrity throughout modification and the dispersion in coatings. Moreover, the use of the EDS, analysis of the X-rays coming from the sample, allows for

the study of nanocapsules composition and element distribution in coatings or in modified nanocapsules, by performing EDS mapping.

### 3.2.2 Atomic force microscopy

Atomic force microscopy (AFM) is a surface characterization technique and is part of a family of scanning near-field tools, the scanning probe microscopes (SPMs). The first microscope development in the field of SPM was the scanning tunneling microscope (STM) developed in 1981 by Binnig and Rohrer.[261, 262] The SPM analysis generate a contrast map based on bringing a small probe to close proximity with a surface and doing a surface scan. AFM was developed to solve limitations on the STM, which requires the samples to be conductive, in 1986.[261]

AFM makes use of a very sharp probe to measure and map the sample surface morphology, at a submicron and nanometer scale. The versatility of the equipment allows for measurements under atmospheric conditions, within a liquid phase, and under vacuum without destroying the sample. The AFM provides very high-resolution topographic images of a surface down to atomic resolution, which can render information on chemical, mechanical (modulus, stiffness, viscoelastic, frictional), electrical and magnetic properties at the nanoscale.[263]

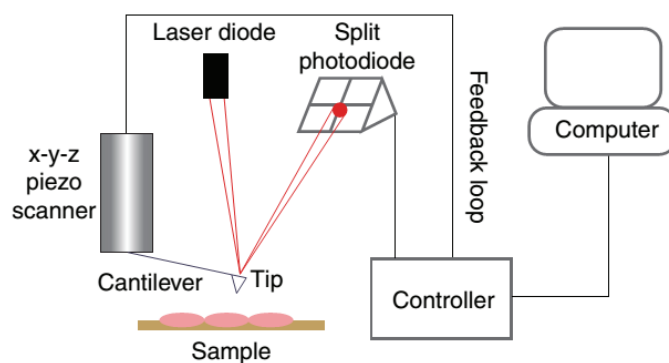


**Figure 31: Sketch illustrating the principle of atomic force microscopy. Reproduced from reference [264] with the authorization of Elsevier.**

Figure 31 depicts a representation of an AFM apparatus. The sample is probed by a very sharp tip (probe) on the end part of a microcantilever that scans over the surface and detects a physical property that provides a contrast mechanism. The piezo scanner controlling the probe-scanner separation, provides movements in x, y, z directions, with

angstrom-level of accuracy. A laser beam is detected by a split photodiode after coming from a laser diode and reflecting on the cantilever (where the tip is located). The signal is then positioned into a feedback loop with the system controlling the piezo movements, where the tip is lowered and lifted to adjust its interaction with the sample surface. The piezo movement will then originate a topographic image of the sample.[261, 264]

## 3.3 Thermal analysis

### 3.3.1 Thermogravimetric analysis

Thermogravimetric analysis (TGA) is a thermal method of investigation for sample characterization (element, compound or mixture) by measuring the physicochemical properties as a function of increasing temperature.[265] The drawback when using TGA is the complete degradation of the sample. From the TGA thermogram is possible to extract a variety of physical and chemical information such as crystalline transition, second-order transition (glass-transition temperature ( $T_g$ )), fusion, vaporization, sublimation, absorption, adsorption, desorption, chemisorption, desolvation (dehydration), decomposition, oxidative degradation and solid-gas reactions.[265]

The history of TGA is complex with various contributions during the XX century. The beginning of the story is more or less consensual and is attributed to the works of W. Nernst and E. Riesenfeld, 1903, due to the publications of the design of a quartz beam balance equipped with an electric oven.[266] Since then, several advances have been made by different researchers and research groups, being the term “thermogravimetry” introduced by K. Honda (Japanese) and C. Duval (French). A detailed history of the development of TGA can be found in the review work on the TG history done by J. Czarnecki and J. Sestak.[267]

The TGA works by coupling a very sensitive set of balances and a programmable furnace. The atmosphere can be also controlled, using air or inert atmosphere depending on the sample and desired methodology.[268] The analysis can monitor the sample weight loss within a temperature range using a specific temperature change rate. Factors affecting the quality of the results are: the gas flow (to purge the sample chamber without affecting the balance), the type of gas (inert or reactive), the proximity of the thermocouple to the sample, for an accurately recording of the temperature, the inert nature of the sample holder, preventing reactions with the sample, and the sample initial weight, shape and size must be consistent with the equipment capabilities.[268]

When applied to nanocapsules for use in corrosion protection systems, TGA gives invaluable information regarding the loading content of the nanocapsules and degree of surface modification with organic substituents.

### 3.3.2 Differential scanning calorimetry

Differential scanning calorimetry (DSC) is a thermal characterization method like TGA, but tends to be more precise and renders a comparatively higher level of information. DSC is defined by the International Committee for Thermal Analysis (ICTA) as a technique in which the heat flux (power) to the samples is monitored against time or temperature, while the temperature of the sample is programmed. It measures the difference in the heat flux between a holder with the sample under investigation and an empty holder (control).[269]

DSC can be found in two forms, as a power-compensation DSC, and as a heat-flux DSC. In the power-compensation DSC two identical cells are used, one which is usually a sealed aluminum pan for the sample under investigation (with a mass lower than 1 g) and another that is the reference pan (sealed empty pan). In this case, the cells are completely independent, with each one having an individual heat source and an individual temperature sensor. The measurement takes place with the increase in temperature for both cells at a constant rate (e.g., 1, 2, 5, or 10 °C min<sup>-1</sup>). When differences start to be observed due to exothermic or endothermic process a second-differential-control starts to work and the differential power signal is recorded as a function of the actual sample temperature.[269, 270] The heat-flux DSC makes use of only one heater for both the sample cell and the reference cell. The enthalpy or heat capacity changes in the sample due to the exothermic and endothermic process taking place, resulting in small differences in temperature between the samples and the reference cell. The differences observed can be converted into the heat flow information through calibration experiments and programmed temperature.[269, 270]

The DSC, in polymer science, is mainly used to determine the glass-rubber transition temperature ( $T_g$ ), the melting/recrystallization temperatures, and heat ( $T_m/T_c$  and  $H_f/H_c$ ) determinations.

In the frame of this thesis, DSC was used to assess the nanocontainer influence in the curing of organic based paints. The analysis was based mainly on the value of  $T_g$ .  $T_g$  is a temperature range where the polymer changes from a glass state to a more flexible state. As the thermal energy increases, the cross-linked polymer chains start to move more freely and the modes of polymer chain movement also increase. These results in a temperature range, rather than a discrete temperature.

### 3.4 Mechanical characterization

Micro-hardness (Martens hardness)

The hardness of a material to deformation is an important characteristic expected for a coating, giving the resistance of the coating to damages. The existing test methodologies can be classified into micro- and macro-hardness. A common approach to calculate the coating hardness is to use the Martens hardness, which provides both plastic and elastic deformation of the material tested.

$$(20) \quad HM = \frac{F}{A_s}, A_s = \frac{4 \times \sin^2 \frac{\alpha}{2}}{\sin(\frac{\alpha}{2})^2} \times h^2$$

The Martens hardness, using a Vickers indenter, is obtained from the force/indentation depth curve during an increase of the test force, following the equation (20), where  $HM$  is the Martens hardness,  $F$  is the test force,  $h$  is the relevant depth of indentation,  $A_s(h)$  the surface area of the indenter penetrating beyond the zero-point of the contact and  $\alpha$  is the angle between opposite faces of vertex of the pyramid for Vickers indenter.[271]

As in the case of DSC, the determination of the coating micro-hardness was done to assess the quality of the curing after the addition of nanocontainers to the paint formulations.

## 3.5 Electrochemical tests

### 3.5.1 Potentiodynamic polarization

The potentiodynamic polarization technique is an electrochemical technique that provides information on the corrosion rate, pitting susceptibility, passivity and the cathodic behavior of an electrochemical system.[272] The electrochemical system comprises an anode, a cathode, and an ionic and electrical conduction path between the two. The method can be applied by controlling the potential or the current, potentiostatic and galvanostatic, respectively.

The common electrochemical cell comprises a reference electrode, a counter electrode and a working electrode (sample). The reference electrode can be of a different nature with the most common being the standard hydrogen electrode (SHE), the saturated calomel electrode (SCE), the silver-silver chloride electrode and the copper-copper sulfate electrode. The reference electrode allows an accurate measurement of the potential applied to the working electrode (sample). The reference electrode reaction is at equilibrium and is not influenced by changes occurring in the working electrode.[272]

The measurements take place in an electrolyte solution that will act as the ionic conduction path between the working and the counter electrodes. The electrical conduction path will occur through a potentiostat that is used to control the driving force (potential) for electrochemical reactions taking place on the working electrode. The sample polarization will occur when the potential of the sample in solution is forced away from the corrosion potential ( $E_{oc}$ ). The sample response to this perturbation, in the form of a current, is measured at different potentials and can be used to study the electrochemical behavior of the electrode.

An example of a potentiodynamic polarization scan is presented in Figure 32, showing the anodic and cathodic branches as E-log i. The anodic and cathodic branches were measured independently for a more accurate analysis. The Tafel lines allow the estimation of the corrosion current ( $I_{corr}$ ) that can be used to assess the corrosion rate if the area of the electrode is known, that cannot be measured directly.

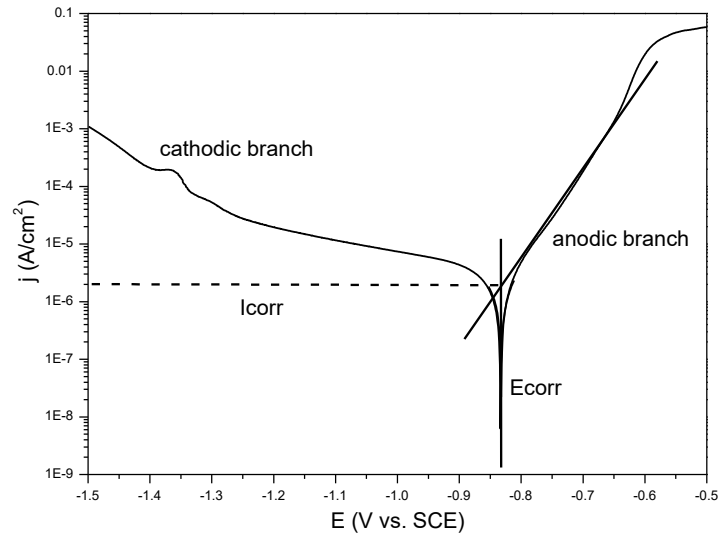


Figure 32: Example of a potentiodynamic polarization curve and classic Tafel analysis.

The  $I_{corr}$  cannot be measured directly but can be estimated from  $I$  vs  $E$  data. A possible approach makes use of Equation (21), designated by Tafel equation, that describes the behavior of one isolated reaction controlled by activation, but one must have in mind that a corrosion process has at least two different reactions, anodic and cathodic. In Equation (21),  $I$  is the current resulting from the reaction at potential  $E$ ,  $I_0$  the exchange current,  $E^0$  the equilibrium potential and  $\beta$  the Tafel constant. The combination of both anodic and cathodic equations for a corrosion system gives the Butler-Volmer equation, Equation (22). In this equation the  $I$  is the measured cell current,  $I_{corr}$  the corrosion current,  $E$  the electrode potential,  $E_{oa}$  and  $E_{oc}$  the equilibrium potential of the anodic and cathodic reactions and  $\beta_a$  and  $\beta_c$  the anodic and cathodic Tafel constants for the anodic and cathodic branches, respectively. The  $I_{corr}$  can also be extrapolated directly from the intersection of the Tafel slopes, as shown in Figure 32, from which is possible to extract the  $E_{corr}$  and the  $I_{corr}$  directly from the polarization plot.[273]

$$(21) \quad I = I_0 e^{(2.3(E-E^0)/\beta)}$$

$$(22) \quad I = I_a + I_c = I_{corr} [e^{(2.3(E-E_{oa})/\beta_a)} - e^{(-2.3(E-E_{oc})/\beta_c)}]$$

The Tafel line extrapolation method presents some limitations (due to interferences from the solution resistance and diffusion), so the plot of  $\log |j|$  versus  $E$  must have, at least, a linear one-decade length; due to the slow diffusion rate of different species a concentration gradient between the metal surface and the solution can occur, leading to variation of the potential,  $E$ . [274]

In the present work potentiodynamic polarization was used to assess the corrosion efficiency of corrosion inhibitors on different metals (AA2024, galvanized steel and cold rolled steel) in aggressive media (NaCl solutions).

### 3.5.2 Electrochemical impedance spectroscopy

The electrochemical impedance spectroscopy (EIS) is a powerful tool used in the study of electrochemical systems, namely assessing the performance of an anticorrosion system (corrosion inhibitor or protective coating) by studying the properties of the oxide layer, the evolution of the coatings barrier properties when subjected to an aggressive media and the corrosion process. It can be found applications for EIS in various fields: biological membranes, sensors, semiconductors, batteries, fuel cells, supercapacitors, membranes, electrocatalytic reactions, conductive monolayers and with relevance for the present work on corrosion, coatings, and paints.[275]

EIS has its beginnings in the 1880s in the works developed by Oliver Heaviside[276] that allowed for the understanding of integro-differential equations that were part of the solutions of electrical circuits. By introducing differentiation ( $s$ ) and integration ( $1/s$ ) became possible to transform integrodifferential equations into a system of algebraic equations. It was also Heaviside that introduced and defined the terms inductance, capacitance and impedance applied to the treatment of electrochemical systems together with the relation between Laplace and Fourier transforms through complex operators ( $S = \sigma + j\omega$ ).[275, 277] Applications in biological fields, such as vegetable cells (resistance and capacitance), blood (dielectric response), muscle fibers and skin tissues. The next step was done by the Cole brothers in 1941 with the verification that the frequency-dependent complex dielectric constant can be represented in a two-dimensional plane. An imaginary component,  $\epsilon''$  on the y-axis, and a real component,  $\epsilon'$  on the x-axis.

In the 1950s EIS started to be applied to more complex reactions, and several developments were achieved: the role of reactions intermediates in the formation of low-frequency inductive loops being studied by Epelboin and Loric; the impedance response to porous and rough electrodes done by Levie; the development of kinetic models for reaction intermediates done by Armstrong and Epelboin, in separated works. But the development of equivalent electric circuits, that has become the most used method in impedance interpretation was developed by Macdonald and Bukamp in the 1970s with

the developments in the nonlinear complex regression techniques. From this point onwards, the research has moved towards more technical applications like electrodeposition and corrosion.[277, 278]

The relevance of EIS in the frame of this thesis is considerable. It was used in a similar way as the potentiodynamic polarization, to assess the inhibition efficiency of corrosion inhibitors in different metals under aggressive conditions. But it had a broader application, being extensively used to monitor the coating barrier properties of the different systems, over time under immersion in aggressive media.

### 3.5.2.1 Instrumentation

Nowadays, most EIS measurements are based on the single-sine technique, made possible by the development of the frequency response analyzer (FRA). The measurement is performed by applying a single frequency small amplitude sine wave signal to a cell and measuring, simultaneously its response. The frequency is then changed, by sweeping of frequencies, usually, done from higher frequencies to lower ones, thus minimizing sample perturbation. The generation of the perturbation and the response analysis is done by the FRA, which is a digitally demodulated, stepped frequency impedance meter. The FRA allows the measuring of the impedance values by correlating the response from the cell with two reference signals, one in phase with the sine wave and the other with a 90° shift.[279]

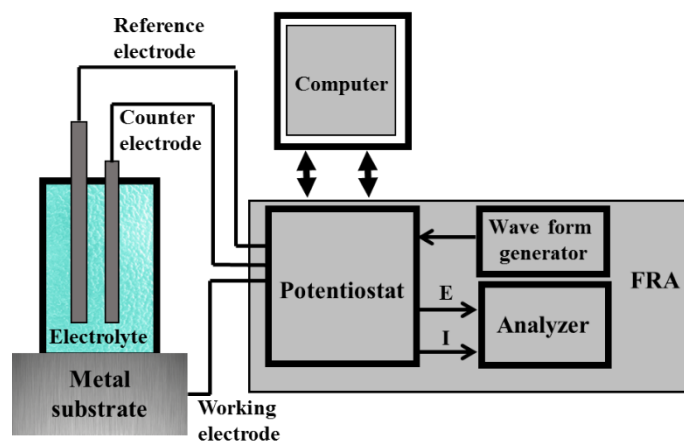


**Figure 33:** Schematic representation of the instrumentation used for EIS measurements. Adapted from the references [89, 279]

Figure 33 shows the schematics of a typical EIS apparatus, with the FRA, computer, and sample. The FRA is constituted by the waveform generator, to create the sine waves, connected to the potentiostat, to control the potential. Due to the complexity

of the measurement is necessary the use of a computer to treat the results. The EIS measurement is usually done in a three-electrode cell: reference electrode (saturated calomel electrode (SCE)), counter electrode (platinum foil) and the working electrode (the metal sample).

### 3.5.2.2 Theoretical background

The concept of electrical resistance can be described as the ability of a circuit element to resist to the flow of electrical current, described as  $R = V/I$  by Ohm's law, where  $V$  is the voltage and  $I$  the current. This is true only for the ideal resistor: it follows Ohm's Law at all current and voltage levels, its resistance value is independent of frequency, and AC current and voltage signals through a resistor are in phase with each other.[280] Unfortunately, this cannot be extrapolated for most of the cases, in real systems the process tends to be more complex. Impedance is a measure of the ability of a circuit to resist the flow of A.C. electrical current, as in the case of the resistance, but it is not limited by the simplifying properties observed for the ideal resistor.[280]

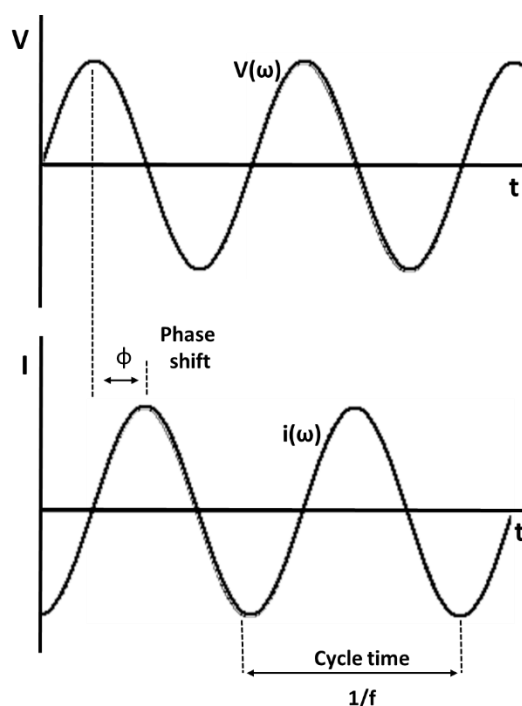


Figure 34: Sinusoidal current response in a linear system, based on [280].

EIS is measured, in most cases, by applying a small excitation signal, in the form of AC potential, to an electrochemical cell. This will result in the response coming from the cell to be a pseudo-linear one, meaning that the current response to a sinusoidal

potential will be also sinusoidal, identical in frequency but with a phase shift, as exemplified in Figure 34.[280] The excitation signal is presented in the form of Equation (23), where  $V(\omega)$  is the potential,  $V_0$  is the amplitude of the signal and  $\omega$  is the radial or angular frequency.

The frequency  $f$  (Hz) can be related with  $\omega$  (radians/second) by Equation (24). In a linear system the  $I(\omega)$ , response signal, has a phase shift ( $\phi$ ) with amplitude  $I_0$ . When using an analogous expression to the Ohm's law the impedance can be calculated according to Equation (26), where the impedance is given as a magnitude ( $Z_0$ ) and a phase shift ( $\phi$ ).

$$(23) V(\omega) = V_0 \sin(\omega t)$$

$$(24) \omega = 2\pi f$$

$$(25) I(\omega) = I_0 \sin(\omega t + \phi)$$

$$(26) Z = \frac{V(\omega)}{I(\omega)} = \frac{V_0 \sin(\omega t)}{I_0 \sin(\omega t + \phi)} = Z_0 \frac{\sin(\omega t)}{\sin(\omega t + \phi)}$$

The result of plotting an applied voltage signal (sinusoidal signal  $V(\omega)$ ) on the X-axis and the current response signal (sinusoidal response signal  $I(\omega)$ ) on the Y-axis results in the formation of an ellipse, designated Lissajous figure, shown in Figure 35a. The Euler's relationship, equation (27), allows for the impedance to be expressed as a complex function, as described in equation (28). The complex numbers allow for the representation of the impedance in an Argand diagram, Figure 35b. The Argand diagram allows the representation of complex numbers by points in the plane as coordinates in which the real and imaginary parts,  $x + jy$ , are represented by the point  $(x, y)$  or vector  $\langle x, y \rangle$ .

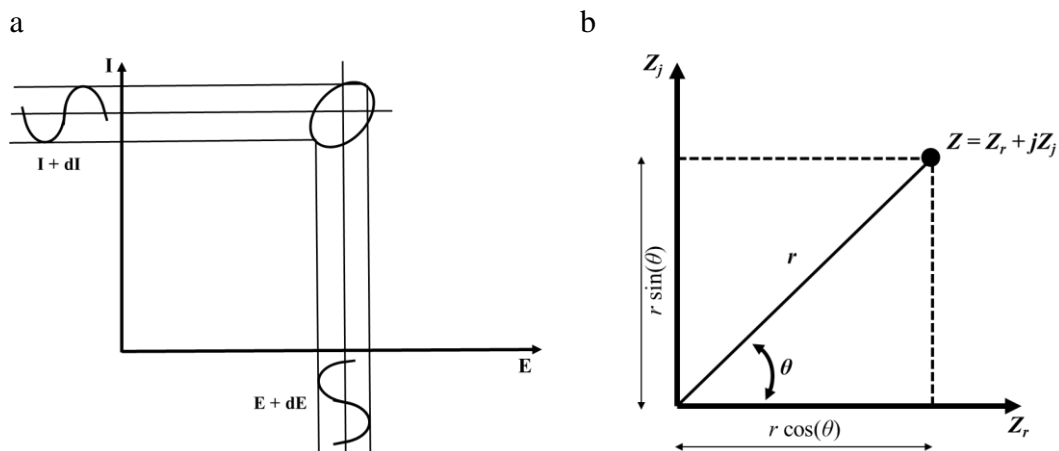


Figure 35: Origin of the Lissajous figure in a) and the Argand diagram in b) showing relationships among complex impedance, magnitude, and phase angle. Adapted from [89, 277, 280].

The impedance can be also presented as a "Nyquist Plot", composed of a real and an imaginary part, as shown in Figure 36. The real component is plotted on the X-axis and the imaginary part is plotted in the Y-axis. The impedance modulus ( $|Z|$ ), shown as a vector (equation (29)), corresponds to a single frequency at each point, with lower frequencies on the right side of the plot and higher frequencies on the left. Unfortunately, this general idea on the low and high frequencies does not allow to associate directly a data point on the plot with the frequency that was used to record that point. The angle ( $\phi$ ) between the vector and the X-axis is designated phase angle and can be described by the equation (30).

$$(27) \quad \exp(j\phi) = \cos \phi + j \sin \phi$$

$$(28) \quad Z(\omega) = \frac{V}{I} = Z_0 \exp(j\phi) = Z_0(\cos \phi + j \sin \phi)$$

$$(29) \quad |Z| = \sqrt{Z_{REAL}(\omega)^2 + Z_{IM}(\omega)^2}$$

$$(30) \quad \phi = \arctan \frac{Z_{IM}}{Z_{REAL}}$$

Another way of depicting impedance is the Bode plot, where the impedance is plotted with the X-axis showing log frequency and the Y-axis the impedance magnitude values ( $|Z|=Z_0$ ) or the phase shift. This method has some advantages over the Nyquist plot, such as the points appear equally scattered comparing with the Nyquist plot where most of the points are concentrated in the extremities of the spectrum, identifying the curves based on the frequencies limits can be difficult, Bode plots present clear and defined resistive and capacitive regions, the phase angle dependence on the frequency represents a very sensitive indicator of the small changes in the spectra, the plot of impedance magnitude and phase angle allows for a simple and fast analysis of the processes detected in the spectrum, in part due to the use of the logarithmic scale.[280, 281]

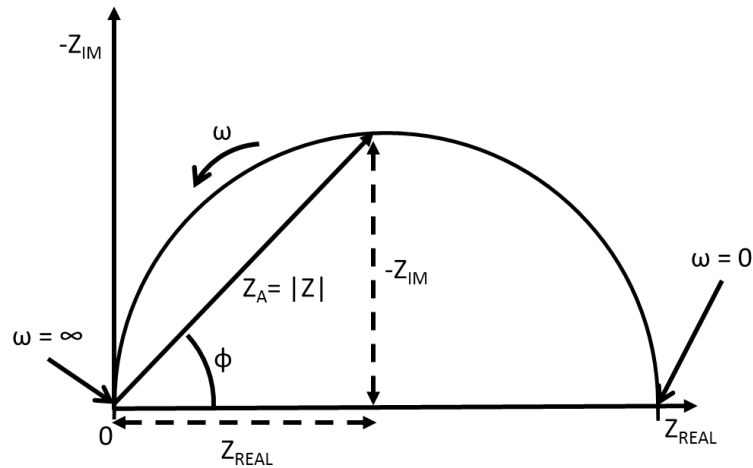


**Figure 36: Nyquist Plot with an Impedance Vector. Adapted from [280]**

The measurements done using EIS must meet some requirements to be valid. These requirements are causality, linearity, stability, and finity.[89, 281, 282]

- Causality: the response given by the system is based only on the perturbation applied to it and not have significant components from others sources.
- Linearity: the impedance is independent on the magnitude of the perturbation. This can be only achieved when the applied perturbation is small enough that the system is pseudo-linear, typically perturbation should be between 1- 10 mV. This is necessary since the current exponentially depends on the applied potential.
- Stability: the system must return to its original state after the perturbation. In the cases where corrosion is taking place, this requirement is considerably difficult to achieve since the system could be changed to another state by the end of the measurement, is advisable to perform the measurement as fast as possible to prevent it.
- Finity: the transfer function must be finite-valued at  $\omega \rightarrow 0$  and  $\omega \rightarrow \infty$  and must be a continuous and finite-valued function at all intermediate frequencies. The validity of impedance data has been checked using the Kramers-Kronig transforms. Some authors have performed it for linear systems over a wide range of frequencies but its application was also attempted on electrochemical and corrosion systems, with the equations showing the impedance real component being calculated from the imaginary component and vice versa.

### 3.5.2.3 EIS spectra interpretation

The EIS analysis is normally done using one of two approaches, the fundamental analysis or the phenomenological approach. The fundamental approach requires a physical model of the processes taking place during the measurement in terms of physico-electrochemical valid concepts. Producing a mathematical representation of the relation between the input and output of the system, accounting for all parameters of the model and fitted to the data, the information is obtained directly from the EIS data. Two major shortcomes can be found with this approach, namely the need for a full understanding of the reaction mechanism and second the excess in complexity found in most of the electrochemical reactions. Both factors make very difficult to produce accurate transfer functions. The phenomenological approach overcomes the drawbacks from the fundamental analysis making use of electric equivalent circuits to interpret the EIS data. The equivalent circuits used are designed to have similar characteristics as the measured impedance data.[283]

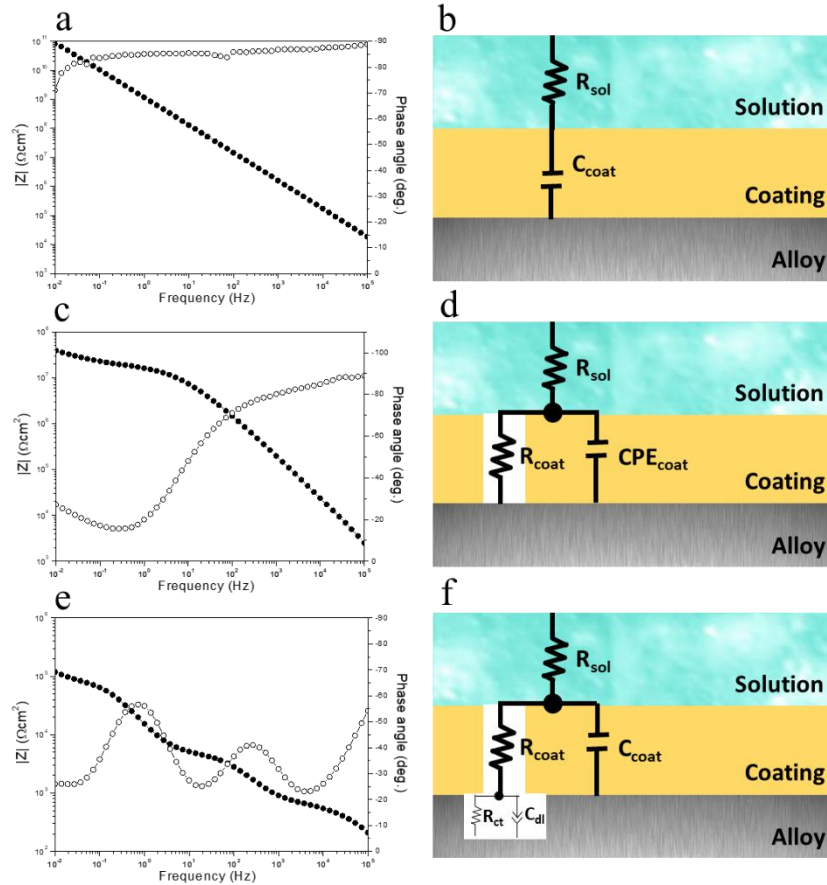
Figure 37 shows three typical stages of an EIS test of metal coated samples. In Figure 37a the early stage of the test when only the  $R_{sol}$  and  $C_{coat}$  are visible since at this stage only minor electrolyte penetration took place so far. With the increase in electrolyte penetration due to coating defects and microscope pores, the  $R_{coat}$  starts to be detected (Figure 37c). As stated the  $R_{coat}$  decreases with the uptake of electrolyte being possible to follow coating degradation. When the coating is no longer effective corrosion starts on the metal substrate, as indicated in Figure 37e, with  $C_{dl}$  and  $R_{ct}$  being detected.

Figure 37a, d, and f represent examples of Bode plots (modulus of impedance and phase angles vs.  $\log f$ ) for a coated sample in different stages of testing. The respective equivalent circuits are shown in Figure 37b, d, and f. The elements composing the circuits and used currently in equivalent circuits when fitting EIS data in corrosion science correspond to solution resistance ( $R_{sol}$ ), coating capacitance ( $C_{coat}$ ), pore resistance ( $R_{coat}$ ), the capacitance of the electric double layer ( $C_{dl}$ ) and resistance of the charge transfer process ( $R_{ct}$ ).[281, 283]

- Solution resistance ( $R_{sol}$ ) is the resistance of the solution between the reference electrode and the working electrode. The  $R_{sol}$  is determined by  $R_{sol} = d_{sol}/\gamma_{sol} A_{sol}$ , where  $d_{sol}$  is the distance between the reference electrode and the working electrode,  $\gamma_{sol}$  is the conductivity of the solution and  $A_{sol}$  is the immersed area of the sample.  $R_{sol}$  value is affected significantly by the distance between electrodes and the solution conductivity.  $R_{sol}$  increases

with the distance between electrodes and decreases with an increase in solution conductivity. The internal resistance of the electrodes and wires of the apparatus can also add to the  $R_{sol}$  values, nevertheless, its contribution is negligible.[281, 283]

- Coating capacitance ( $C_{coat}$ ) in an analogy of the coating with a capacitor represents charge separation at the coating-solution and coating-metal interfaces.  $C_{coat}$  is determined by  $C = \epsilon\epsilon_0 A/d$ , where  $\epsilon$  is the relative permeability of the coating,  $\epsilon_0$  is the permittivity of vacuum,  $A$  is the immersed area of the coating and  $d$  is the coating thickness. At early stages of the test, the value  $C$  can be associated with the water permeation into the coating, with an increase in its value due to an increase of the dielectric constant originated by the ingress of water.[281, 283]
- Pore resistance ( $R_{coat}$ ) is usually defined as the coating pore resistance as a consequence of electrolyte penetration through microscopic pores or when the water uptake by the coating is not uniform usually associated with faulty coatings. Thus, the magnitude of  $R_{coat}$  can be used to establish the state of degradation of the coating. Nevertheless, the value of  $R_{coat}$  can increase over time if corrosion products block the pores of defects, producing misleading results.[281, 283]
- The capacitance of the electric double layer ( $C_{dl}$ ) is formed in the metal/solution interface. The  $C_{dl}$  is formed when ions, from the solution, are adsorbed onto the metal surface. A charge separation arises between the charged metal and the charged ions in the solution, originating an insulating space, usually in the orders of angstroms. This charge separation by an insulator forms a capacitor. The  $C_{dl}$  in corrosion studies  $C_{dl}$  is correlated with corrosion process.[89, 281, 283, 284]
- Charge transfer resistance ( $R_{ct}$ ) is related to the “leakage” of charge through the double layer and is always a result of electrochemical reactions.  $R_{ct}$  is related to the rate of the anodic and cathodic reactions. Thus, being an excellent parameter to monitor the protective properties of a protective coating or the action of corrosion inhibitors in solution, by following the corrosion rate,  $i_{corr}$ . [281, 283]



**Figure 37: Bode plot graphs and corresponding equivalent circuits at different coating-metal degradation stages. Intact coating (a) and b), porous coating (c and d) and porous coating with the start of corrosion activity (e and f). Adapted from the reference [89].**

Table 10 lists the most common electrical impedance elements together with their impedance expressions and symbols used in the equivalent circuits:[281, 283]

- Resistor (R) is usually associated with the resistance of the solution, the oxide layer or the charge transfer resistance associated with the corrosion process.
- The capacitor (C) is usually associated with the coating, the oxide layer or the double layer.
- The Warburg element (W) is used to model the linear semi-infinite diffusion occurring when the diffusion layer has infinite thickness.
- The constant phase element (CPE or Q) represents various elements: inductance ( $n = -1$ ), resistance ( $n = 0$ ), Warburg element ( $n = 0.5$ ), capacitance ( $n = 1$ ) or non-ideal dielectric behavior ( $-1 \leq n \leq 1$ ). Normally, CPE is used when a pure capacitive response cannot be obtained from the EIS data, usually due to the complexity of the systems.

**Table 10: Electrical impedance of most common elements.[281, 283]**

Component	Impedance	Symbol
Resistor (R)	$R$	
Inductor (L)	$j\omega L$	
Capacitor (C)	$\frac{1}{j\omega C}$	
CPE (Q)	$\frac{1}{Y_0(j\omega)^n}$	
Warburg	$W = \sigma\omega^{-1/2} - j\sigma\omega^{-1/2}$ $\sigma = \frac{RT}{n^2 F^2 \sqrt{2}} \left[ \frac{1}{C_{Hg^{2+}}(D_{Hg^{2+}})^{1/2}} + \frac{1}{C_{Hg}(D_{Hg})^{1/2}} \right]$	

### 3.5.3 Scanning vibrating electrode technique

Scanning Vibrating Electrode Technique (SVET) is an electrochemical technique that allows the determination of ionic fluxes in solution. It has been used extensively to investigate localized corrosion, galvanic corrosion, coatings, inhibitors, interfaces and grain boundaries, second-phase particles, stress corrosion cracking and microbial corrosion.[285] This technique was first developed for biological applications in the 1950 and 1960 aiming at the measurement of ionic currents associated with cellular differentiation processes and tissue regeneration. Its application as a characterization technique in corrosion protection started in 1980 by H.S. Isaacs.[286, 287] In corrosion science SVET has been used to study different types of corrosion mechanisms, the effect of corrosion inhibitors and protection by coatings.

The ionic flux measurement is done at the extremes of the vibration of the probe, as shown in Figure 38 a). This technique has a very low noise level and greater sensitivity since only one electrode is used to determine the difference in potential and the vibration frequency is known, which eliminates all the remaining vibrations as noise. By calibration the potentials measured can be converted into an ionic current density map. Equation (31) is used to calculate the current density,  $i$ , making use of the potential values,  $\Delta V$  measured at the vibration extremes of the probe,  $\Delta r$ .

$$(31) \quad i = kE = -k \frac{\Delta V}{\Delta r}$$

The technique presents some limitations as the measurement is not done at the metal surface, but rather at a specific distance above it, which makes impossible to

account for the current flowing between the anode and the cathode below that height, the ascending current crosses the measuring area but when returning to the surface can occur outside that area, meaning that this current will not be measured, the SVET sensitivity for typical testing solutions (0.01 M – 0.1 M) is about  $1 \mu\text{A}\cdot\text{cm}^{-2}$ , meaning that smaller current values are not detected. The fact that the current flows in three directions and the technique only measures the component z, makes the current measured underestimated.[287]

Figure 38 shows the different components in an SVET apparatus together with interaction schematics between the different modules. In Figure 38 a) the tip of the probe in stationary and vibrational mode is presented. The vibrating probe is usually a metallic rod of platinum-iridium (80 % / 20 %) with 1.5 cm in length and 250  $\mu\text{m}$  in diameter covered with a 3  $\mu\text{m}$  layer of parylene-C, with a sharpened end. The electrode edge, around 3  $\mu\text{m}$ , is the only part where the coating was removed. To be applied in SVET it is necessary to enlarge the probe active electrical area by creating a deposit of platinum, by electrodeposition. In Figure 38 b) the electrochemical cell, with the vibrating electrode, ground, and pseudo-reference together with the sample under immersion in an electrolyte solution are presented, while in Figure 38 c) the overall scheme of the modulus used in an SVET measurement is shown. It consists of a video camera to control the electrode position and the recording of images from the sample. Electrical motors allow the positioning and movement of the microelectrode. Electronic systems are used to reduce noise during the measurements, a preamplifier and an IPA-2 amplifier that integrates two lock-in amplifiers, one for each vibration. The microelectrode is connected with a plastic arm, that is connected to two piezoelectric oscillators responsible for the vibrations x and z. All process is controlled by software. The measurements are usually done in an anti-vibration table and in a Faraday cage to prevent external interferences.[287]

In the frame of this work, SVET was used to study the inhibition efficiency of corrosion inhibitor when added to coatings, in a free form or loaded into nanocontainers. For this purpose, two defects were done on the coating surface with the help of a needle, in such a way that the metal surface became exposed at those sites. The samples were immersed in a NaCl solution and the technique was then used to measure the currents at the coating surface. By analyzing and comparing the current intensities at those points was possible to verify the way corrosion progressed and when inhibitors were presented, how corrosion was suppressed. The SVET results can corroborate the EIS results,

allowing a more complete assessment of the corrosion inhibitor efficiency and the relevance or not of having the inhibitors encapsulated.

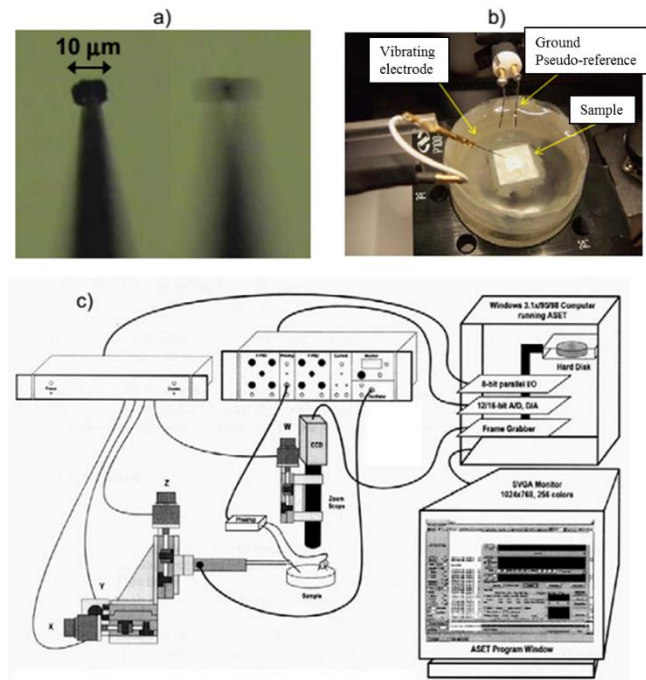


**Figure 38:** Experimental setup used for SVET. a) Vibrating electrode, b) electrochemical cell and c) interaction schematics between the different modules present in the SVET system (used from the aSEt program manual). Adapted from the work of A.C. Bastos.[287]



# 4

## Experimental procedure

*Sing, clear-voiced Muses, of Hephaestus famed for inventions. With bright-eyed Athene he taught men glorious gifts throughout the world, -- men who before used to dwell in caves in the mountains like wild beasts. But now that they have learned crafts through Hephaestus the famed worker, easily they live a peaceful life in their own houses the whole year round. Be gracious, Hephaestus, and grant me success and prosperity!*

Homer, in “The Homeric Hymns: 20-To Hephaestus”



For a better understanding of the experimental component of this thesis the present section was divided into sub-sections focusing on specific steps of the work. Firstly, the metal substrates used and their pretreatments are presented, followed by the preparation of the nanocontainers, the application of the protective coatings (loaded with the nanocontainers) on the metal substrates. The last two sections focus on the release studies done on nanocontainers loaded with corrosion inhibitors and the final sub-section lists all the experimental techniques employed in the accomplishing of this thesis work.

A list of the reagents used throughout the work is presented in Table 11.

**Table 11: List of reagents used in the frame of the present work.**

Acronym/ chemical formula	Reagent	Purity	CAS	Supplier
TEOS	tetraethylorthosilicate	98 %	78-10-4	Aldrich
TPOT	titanium (IV) propoxide	70% w/w in n-propanol	546-68-9	Aldrich
GPTMS	3-glycidoxypropyltrimethoxysilane	97 %	2530-83-8	ABCR
PTMS	phenyl trimethoxysilane	97 %	2996-92-1	ABCR
HDTMS	Hexadecyltrimethoxysilane	> 85 %	16415-12-6	Aldrich
APS	(3-aminopropyl)triethoxysilane	>= 98 %	919-30-2	ABCR
C <sub>3</sub> H <sub>8</sub> O	2-propanol	p.a.	67-63-0	Sigma-Aldrich
C <sub>3</sub> H <sub>6</sub> O	acetone	p.a.	67-64-1	Sigma-Aldrich
PSS	poly(sodium styrene sulfonate)	Mw~70000 30 wt.% in water	25704-18-1	Aldrich
PAH	poly(allylamine hydrochloride)	99 %	71550-12-4	Alfa Aesar
(C <sub>6</sub> H <sub>8</sub> O <sub>6</sub> ) <sub>n</sub>	alginate		9005-38-8	Aldrich
CTAB	cetyltrimethylammonium bromide	> 98%	57-09-0	Sigma
NH <sub>4</sub> OH	ammonia	25%	7664-41-7	Fluka
C <sub>5</sub> H <sub>8</sub> O <sub>2</sub>	acetylacetone	p.a.	123-54-6	Fluka
HNO <sub>3</sub>	Nitric acid	68-70%	7697-37-2	Alfa Aesar
2-MBT	2-mercaptobenzothiazole	97 %	149-30-4	Aldrich
Zn(NO <sub>3</sub> ) <sub>2</sub> .6H <sub>2</sub> O	zinc nitrate hexahydrate	99 %	10196-18-6	Sigma-Aldrich
Al(NO <sub>3</sub> ) <sub>3</sub> .9H <sub>2</sub> O	aluminum nitrate nonahydrate	98 %	7784-27-2	Alfa Aesar
NaNO <sub>3</sub>	sodium nitrate	p.a.	7631-99-4	Sigma-Aldrich
NaOH	Sodium hydroxide	pure	1310-73-2	Sigma-Aldrich
C <sub>6</sub> H <sub>11</sub> NaO <sub>7</sub>	Sodium gluconate	> 97 %	527-07-1	Aldrich
TMOS	Trimethoxy(octadecyl)silane	90 %	3069-42-9	Sigma-Aldrich

## 4.1 Metal substrate pretreatment

### 4.1.1 AA2024-T3

Unclad AA2024-T3 with the following composition was used: Cu 3.8-4.9 %, Mg 1.2-1.8 %, Mn 0.3-0.9 %, Fe 0.5 %, Si 0.5 %, Zn 0.25%, Ti 0.15 %, Cr 0.1 %, other 0.15 %, balance Al.

AA2024 pretreatments:

a) Acetone

The first surface treatment applied to AA2024 panels consisted of a simple surface degreasing using acetone. The degreasing was done by immersing the panels in acetone in an ultrasonic bath for 10 minutes, followed by a cleaning of the surface (wiping with a paper tissue). The samples were consequently immersed in a second acetone bath and the same ultrasonic treatment applied. Afterward, the panels were dried using compressed air.

b) Industrial treatment I (Aluminetch®)

AA2024 panels were chemically etched following a three-step industrial cleaning procedure consisting of: (i) alkaline cleaning in a Metaclean T2001 (from Turco Chemie GmbH) at 60-70 °C for 15-25 min, followed by (ii) alkaline etching in a Turco Liquid Aluminetch N2 (from Turco Chemie GmbH) at  $60 \pm 5$  °C for 30-60 s and, finally, (iii) acid etching in a Turco Liquid Smutgo NC (from Turco Chemie GmbH) at  $30 \pm 5$  °C for 5-10 min. After the chemical etching, all the metallic panels were thoroughly washed with distilled water and left to dry at room temperature.

c) Industrial treatment II (Gardacid®)

AA2024 panels were chemically etched by a two-step cleaning procedure. Firstly, the panels were immersed in a 2 wt. % solution of a commercial cleaning product (Gardacid® P 4307 from Chemetall) at room temperature for two periods of 45 seconds, with an intermediate washing step in distilled water. Then, the panels were subjected to an acid etching in a Turco Liquid Smutgo NC (Turco Chemie GmbH) at  $30 \pm 5$  °C for

5- 10 min. Afterward, the metallic panels were thoroughly washed with distilled water and left to dry at room temperature.

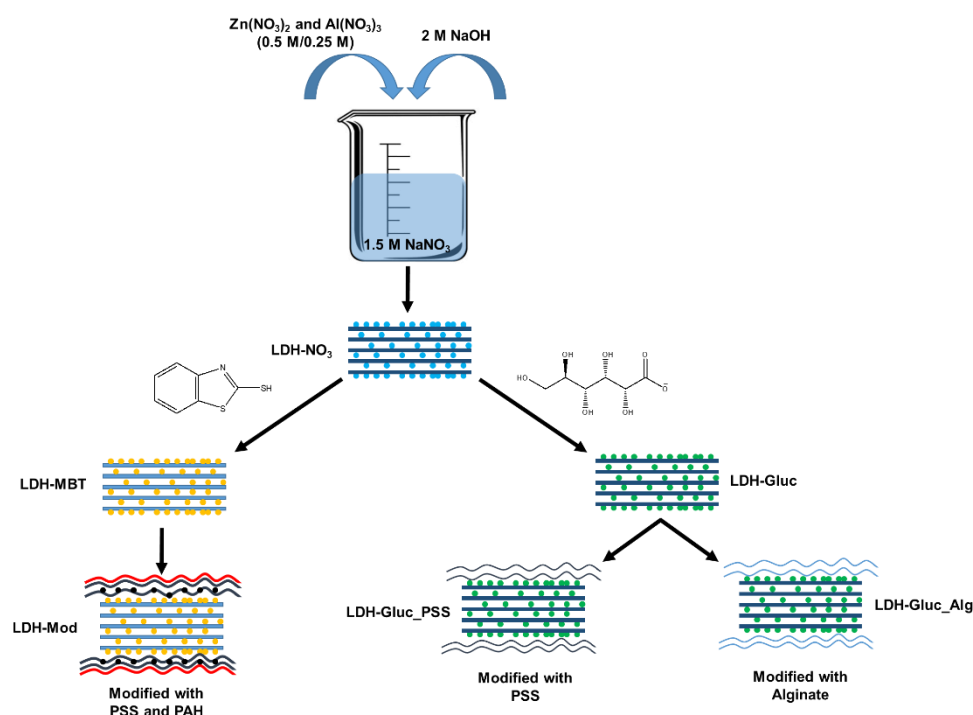
#### **4.1.2 Steel**

Two types of steels were employed, a carbon steel (cold rolled steel) and a steel with a zinc layer on its surface (galvannealed steel). Both steels were kindly provided by TATA STEEL Europe. Their detailed chemical composition was not provided. The pretreatment consisted of an alkaline cleaning step using an aqueous solution of 2 wt. % of an alkaline surfactant powder (cleaner 219 (CS 4994) supplied by TATA STEEL Europe) heated up to 58-60° C. The steel panels were immersed in the solution for 60 seconds under vigorous stirring followed by a rinsing step with deionized water. If a continuous water-film was not obtained on the metal surface the process was repeated until a flawless water film was visible on the panel surface. In the end, the samples were dried using pressurized air and stored in a desiccator.

## 4.2 Preparation of nanocontainers

### 4.2.1 Synthesis of layered double hydroxides (LDHs)

LDH synthesis was done following the co-precipitation methodology (Scheme 3) as described in the literature.[168] A solution prepared by dissolution of  $\text{Zn}(\text{NO}_3)_2 \cdot 6\text{H}_2\text{O}$  and  $\text{Al}(\text{NO}_3)_3 \cdot 9\text{H}_2\text{O}$  (0.5 M/0.25 M) was added to 1.5 M  $\text{NaNO}_3$  under vigorous stirring at room temperature. To avoid contamination with carbonate all solutions were prepared using boiled distilled water and the synthesis was carried out under a nitrogen atmosphere. The pH was kept stable ( $\text{pH} = 10 \pm 0.5$ ) and controlled by simultaneous addition of a 2 M  $\text{NaOH}$  solution. The final suspension was subjected to hydrothermal treatment at 100 °C during 4 h for crystallization of the LDH material. Then the obtained slurry was centrifuged and washed four times with boiled distilled water.



Scheme 3: Schematic representation of the approach used in the preparation of LDHs and subsequent surface modification with polyelectrolytes or alginate.

#### *Intercalation of sodium gluconate (NaGluc):*

The obtained LDHs intercalated with nitrate ( $\text{LDH-NO}_3$ ) were used in the intercalation of gluconate by ion-exchange. The ion-exchange reaction was carried out by dispersing  $\text{LDH-NO}_3$  in an aqueous solution containing 0.1 M of  $\text{NaGluc}$  ( $\text{pH} \approx 7$ ) under

a nitrogen atmosphere. The intercalation was done in a two-step process to ensure an optimal intercalation yield. A 120 ml 0.1 M of NaGluc solution was split into two portions of 60 ml. The LDH precursors were added to one of these portions and let under stirring for 24 hours. Then, the resulting material was recovered by centrifugation and washed successively 2-4 times. This procedure was repeated with the second portion of the organic anion solution. Finally, the gluconate-loaded LDH was washed two times with boiled distilled water and stored as a water-based slurry.

#### *Intercalation of 2-mercaptobenzothiazole (2-MBT):*

The intercalation of 2-MBT follows a similar methodology applied in the intercalation of gluconate. For the ion-exchange reaction, 0.1 M of 2-MBT solution (pH=9) was prepared using an equivalent amount of NaOH (0.1 M). The deprotonation of 2-MBT in basic conditions is important for its successful intercalation since the anionic form is the one involved in the exchange reaction with nitrates. The higher solubility of MBT anion also ensures higher loadings of corrosion inhibitor in the LDHs.[96] LDH-NO<sub>3</sub> was added to the inhibitor-containing solution and left under stirring for 24 hours. After centrifugation and washing steps (2 times), the procedure was repeated with the second portion of the 2-MBT solution to ensure that the maximum amount of NO<sub>3</sub><sup>-</sup> was replaced by 2-MBT. Then, the reaction products were isolated by centrifugation and washed 2-4 times with boiled distilled water to ensure that all 2-MBT in excess was removed. The washed yellowish LDH deposit was stored at room temperature in sealed containers to ensure a stable water content and avoid contamination with carbonates from the atmosphere.

#### **4.2.2 Surface modification of LDH with alginate**

The modification was done by mixing a 20 ml solution of alginate (0.5 wt. %) with 80 ml of a water-based suspension of LDHs (0.5 g/100 ml). The pH of the alginate solution had to be adjusted to values around 5 to ensure a complete dissolution of the alginate. The suspension was stirred for 15 min at room temperature. Afterward, the LDH was separated by centrifugation, followed by a three times washing process consisting of the re-dispersion of modified particles in deionized water followed by centrifugation to ensure that all alginate in excess was removed. As in the case of unmodified LDHs, modified samples were store as a water-based slurry in sealed containers.

### 4.2.3 Surface modification of LDH with polyelectrolytes

#### *Singular layer of Poly(styrene sulfonate)*

The modification method of LDH using poly(styrene sulfonate) (PSS) polyelectrolyte involves the dispersion of LDH in solutions of PSS as follows: 0.5 g of LDHs (dry content) were added to a 0.5 wt. % PSS solution in deionized water. The LDH dispersion was achieved by mechanical stirring and ultrasound treatment (10 min each). After its complete dispersion, the resulting suspension was left under magnetic stirring for 20 min. The final stage consisted in the separation of the modified LDHs by centrifugation followed by a three times washing process consisting in the re-dispersion of LDHs in deionized water followed by centrifugation to ensure that all PSS in excess was removed. The modified LDH was stored as a water-based slurry in a sealed container.

#### *Multilayer coating of PSS/Ce/PSS/PAH (LDH\_Mod)*

The modification of LDHs was carried out by the LbL method, with the addition of cerium (III) nitrate during the deposition process, using negatively-charged poly(sodium styrene sulfonate) (PSS) and positively-charged poly(allylamine hydrochloride) (PAH) polyelectrolytes. In the first step, an aqueous LDH slurry (0.5 g of dry content) was added to 0.5 wt. % of PSS solution in deionized water. Thereafter, the slurry was dispersed with magnetic stirring (10 min) and ultrasound treatment (10 min). After a complete dispersion, the suspension was left under magnetic stirring for 20 min. Finally, LDHs were recovered by centrifugation, followed by washing/centrifugation (10,000 rpm for 3 minutes) repeated three times to remove PSS in excess.

In the second step, the LDH particles were re-dispersed in a 0.1 M cerium (III) nitrate solution and left for one day under stirring at room temperature. Then, LDHs were recovered by centrifugation and washed with distilled water, a process repeated three times. In the third step, the second layer of PSS was deposited after treatment with cerium solution, following the same procedure used in the first deposition, to ensure that cerium incorporation was not reversible and to prepare the surface for the subsequent positive polyelectrolyte. Then, a layer of PAH was applied using similar conditions of concentration and time applied for PSS. The modified LDH was kept as a water-based slurry in a sealed container.

#### 4.2.4 Synthesis of silica nanocapsules (Si\_NC)

The Si\_NC were prepared via a micro-emulsion procedure (Scheme 4) described in the literature.[160] The aqueous phase is prepared by dissolving 0.25 g of the cationic surfactant cetyltrimethylammonium bromide (CTAB) in 35.0 g water, under vigorous stirring. After the complete dissolution of the surfactant, under vigorous stirring, 0.25 ml of ammonia (NH<sub>4</sub>OH) was added. The organic phase was composed of 25 ml of diethyl ether, added dropwise under vigorous stirring. Afterward, 2 ml of tetraethyl orthosilicate (TEOS) was added dropwise to the emulsion. The process was carried out at room temperature and left under stirring for 24 hours for the reaction to occur. Then, the dispersion was filtered and washed several times with distilled water. The resulting material was dried at 60 °C in a ventilated oven.

#### 4.2.5 Surface modification of Si\_NC with siloxane derivatives

##### *“Dry” approach:*

The Si\_NC obtained following the approach described in the previous section, where they were used as dry powders, as shown in Scheme 4. Before modification, the Si\_NC were milled in a mortar until a sample with fine powder was obtained. Then, the Si\_NC powder (2 g) was added to toluene (40 ml) under stirring. The suspension was placed under reflux under a nitrogen atmosphere (T=130 °C).[288] The siloxane precursors (APS, GPTMS, TMOS and HDTMS) were added in different proportions (1:1, 1:2 and 1:4 in mass) to the solution immediately after the beginning of the reflux. The reaction was maintained under these conditions for 4 hours. After modification, the suspension was filtered under vacuum and the powder dried at room temperature.

##### *“Wet” approach:*

In the wet route, the silica nanocontainers were kept in a slurry form throughout the whole process of modification including right after the synthesis, modification, and storage, as represented in Scheme 4. The aim of this approach was to investigate whether agglomeration could be prevented, ensuring a better dispersion of the containers when added to coating formulations.

The Si\_NC obtained after synthesis, as described in section 4.2.4, is a water-based slurry. Before proceeding with the modification step, it was subjected to a solvent exchange process, by dispersing the Si\_NC in toluene (50 g of slurry in 200 ml of toluene)



## 4.3 Preparation of protective coatings

### 4.3.1 Sol-gel based formulations

#### *Solvent-based hybrid sol-gel:*

The hybrid-based coating was prepared by a controllable hydrolysis of metalorganic titanium (IV) propoxide (TPOT) and 3-glycidoxypropyltrimethoxysilane (GPTMS), phenyl trimethoxysilane (PTMS) and hexadecyltrimethoxysilane (HDTMS) under acidic conditions.[145] The first sol was obtained by mixing the TPOT solution, formed by mixing the precursor (70 wt. % in 2-propanol) with 2-propanol in a 2.5:1 weight ratio, with acetylacetone in 2:1 volume ratio during 20 min. Afterward, the solution was hydrolyzed for 1 h in the presence of 0.32 M HNO<sub>3</sub> aqueous solution with molar ratio 3:1 of acidified water to TPOT. The second solution was obtained by mixing GPTMS, PTMS, and HDTMS in 1:1:0.15 volume ratio. The solution was hydrolyzed by adding 0.1 M HNO<sub>3</sub> in 4:1 molar ratio of water to GPTMS under constant mechanical stirring for 1 hour. Consequently, the two solutions were mixed and left at 22 ± 1 °C under constant stirring for 1 hour. Then, the nanocontainers were added to the formulation (0.5 wt. % with respect to the total formulation) and stirred until obtaining a uniform dispersion (~10 minutes).

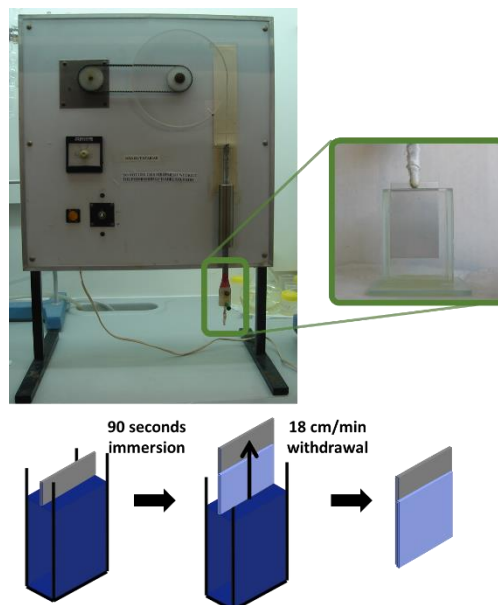


Figure 39: Dip coater and scheme of the procedure used to coat samples with sol-gel formulations.

AA2024 panels, 2.5 cm x 4 cm, were dipped into the sol-gel solution and held in the solution during 90 seconds followed by withdrawal at 18 cm/min, as shown in Figure 39. After application, the coated samples were left for 30 min at room temperature and then transferred to an oven preheated at 60 °C and held at this temperature for 10 min. The setpoint temperature of the oven was then changed to 120 °C and samples heat treated during 15 min with a temperature ramp up to 120 °C. Then, the temperature was kept at 120 °C for 80 min. Subsequently, the coated samples were removed from the oven.

*Water-based hybrid sol-gel:*

The water-based sol-gel coating was prepared by a controllable hydrolysis of metalorganic tetraethylorthosilicate (TEOS) and 3-glycidoxypropyltrimethoxysilane (GPTMS) under acidic conditions.[89] The solution was prepared by adding GPTMS to TEOS in a 1:3 volume ratio. The solution was hydrolyzed by adding 0.05 M HNO<sub>3</sub> in 11:1 molar ratio of water to GPTMS under constant mechanical stirring for 2 h. Afterward, the capsules were added to the formulation (in different weight percentages with respect to the total formulation) and stirred until obtaining a uniform dispersion (~10 minutes). The coating and curing procedure are identical to the ones used for solvent-based hybrid sol-gel coatings.

### **4.3.2 Water-borne formulation**

*TATA STEEL protective coating:*

The TATA STEEL water-based formulation (internal reference PXM10174), referred to in the frame of this work as TATA formulation, was kindly provided by TATA STEEL Europe. Its full composition was not disclosed, is a polyamide-based formulation. The LDH nanocontainers were dispersed by stirring for 10 minutes, in some cases longer periods were used, until the nanocontainers were completely dispersed. Afterward, the formulations were left to rest for 10 minutes before application by bar-coating. For the coating application was used an Elcometer 3520 baker film applicator, providing a 30 μm wet film on the substrate. The films were applied on galvanized steel and cold rolled steel substrates. After application the samples were kept for 10 min at room temperature and then cured in an oven for 10 min at 95 °C, followed by curing at 270 °C for 10 min in another furnace.

*Lacquer AQ CC 080 and hardener AQ BU 16:*

As referred in the producer (akrylmetal - SYNPO) data sheet, lacquer AQ CC 080 is a water-based polyurethane lacquer for transparent glossy topcoats. The density, weight % of solids and the content of total organic carbon for the lacquer and the hardener respectively are presented in Table 11. AQ CC 080 solvent composition, kindly provided by Synpo is: 2-(2-butoxyethoxy) ethanol (4-5 %), 2-butoxyethan-1-ol (< 0.5 %), 1-butoxypropan-2-ol (2-3 %), etan-1,2-diol (<0.5 %), 2-(dimethylamino)ethan-1-ol (1-2 %), balance water. In this work, it was used in combination with the hardener AQ BU 16, in a mixing ratio of 2.5 AQ CC 080: 1 AQ BU 16. The curing process was the following: 24 h at room temperature ( $\approx 23$  °C) followed by 30 min at 100 °C.

**Table 11. Producer specifications for AQ CC 080 and AQ BU 16.**

	Parameter	Value	Units
AQ CC 080	Density	1.0	$\text{g}\cdot\text{cm}^{-3}$
	Weight % of solids in the mixture	35	%
AQ BU 16	Density	1.030	$\text{g}\cdot\text{cm}^{-3}$
	Content of total organic carbon	0.460	$\text{kg}\cdot\text{kg}^{-1}$

**4.3.3 Solvent-based formulations***Lacquer LC CC 100 and hardener LV BU 45 N:*

As referred in the producer (SYNPO) data sheet, lacquer LV CC 100 is a two-component polyurethane acrylic top coating with high weather resistance and UV stability. The density, weight % of solids and the content of total organic carbon for the lacquer and the hardener respectively are presented in Table 12. LC CC 100 solvent composition, kindly provided by Synpo, is: n-butylacetate (50-60 %), 2-methoxy-1-methylethyl-acetate (5-30 %), xylene (5-30 %). In this work, it was used in combination with the hardener LV BU 45 N, with a mixing ratio of 3 LV CC 100: 1 LV BU 45 N. The coating curing procedure was performed as follows: 24 h at room temperature ( $\approx 23$  °C) followed by 1 hour in an oven at 100 °C.

**Table 12. Producer specifications for LC CC 100 and LV BU 45N.**

	Parameter	Value	Units
LC CC 100	Density	1.01	$\text{g}\cdot\text{cm}^{-3}$
	Weight % of solids in the mixture	50	%
LV BU 45N	Density	0.995	$\text{g}\cdot\text{cm}^{-3}$
	Content of total organic carbon	0.389	$\text{kg}\cdot\text{kg}^{-1}$

## **4.4 Equipment and methodology**

### **4.4.1 Fourier transform infrared spectroscopy**

The ATR-FTIR spectra were recorded with a Bruker IFS55 spectrometer equipped with a single horizontal Golden Gate ATR cell. 128 scans were acquired for each measurement using a  $4\text{ cm}^{-1}$  resolution for an interval between  $4000\text{ cm}^{-1}$  and  $350\text{ cm}^{-1}$ . The measurements were performed directly on the samples. In the case of nanocontainers, the characterization was always performed on dry powders.

### **4.4.2 X-ray diffraction**

X-ray diffraction (XRD) analysis was performed using a PANalytical XPert MPD PRO diffractometer (Ni-filtered  $\text{CuK}\alpha$  radiation, PIXEL 1D detector, and the exposition corresponded to about 2 s per step of  $0.02^\circ$  at room temperature). LDHs were characterized by XRD as dried powders.

### **4.4.3 Zeta potential**

The nanocontainers were dispersed in water, in small concentrations, adjusted to the equipment measurement quality. The nanocontainers were dispersed using ultrasounds, for 10 min, a few minutes afterward the samples were measured. Particle zeta potential was assessed using a Zetasizer Nano ZS, performed by the combination of laser Doppler velocimetry and phase analysis light scattering (PALS) in a Malvern's patented M3-PALS technique. Five measurements were done for each sample.

### **4.4.4 SEM/EDS**

Samples in two forms were analyzed by SEM/EDS, powder and surfaces (coated substrates or bare metal specimens). For powders, a very small amount of nanocontainers was dispersed in a liquid, usually water, and dispersed by ultrasounds. A droplet of the suspension was then put in a silicon substrate glued to an SEM support by carbon glue and dry in a ventilated oven at  $60\text{ }^\circ\text{C}$ . Afterward, a carbon layer was deposited on the samples by electrodeposition. In the case of substrates, the samples were cut (area of  $0.5\text{ cm}^2$ ) glued to the SEM support using carbon tape of carbon glue. A carbon layer was also applied by electrodeposition.

SEM/EDS analysis was performed using a Hitachi S-4100 with an electron beam energy of 25 kV. The EDS mapping was performed by a Hitachi SU-70 microscope with electron beam energy of 25 kV for EDS. SEM micrographs obtained by the SU-70 used an electron beam energy of 15 kV.

#### 4.4.5 UV-Vis spectrophotometry

The UV-Vis spectrophotometer (Scanspec UV-Vis) was used to study the release profile of 2-MBT at 320 nm wavelength and gluconate at 660 nm wavelength.

##### *Gluconate release studies from LDHs*

Gluconate release studies were performed under stirring conditions at room temperature via immersion of 200 mg of dried powders of each type of containers in a 0.5 M NaCl solution. Aliquots were taken at 2 h, 24 h, and 48 h after the start of experiments. The quantification of gluconate follows the methodology developed by Alt.[270] The detection procedure is based on the formation of a blue colored complex of copper with gluconate in alkaline medium and measuring, in a UV-Vis, the absorbance at 660 nm wavelength, using 0.5 M NaOH solution as the blank. However, the limitation associated with this methodology prevents its use for concentrations below 1 mM. Due to the precipitation of cupric ions in alkaline medium with further decreased values of complex absorbance. Thereby, detection methodology errors can be high at low gluconate concentration.

##### *2-MBT release studies from LDHs*

The release of 2-MBT from LDHs was performed under stirring at room temperature, under the following conditions: 0.05 M NaCl, pH=11, and pH=4. Three replicas were obtained for all the conditions investigated (standard deviation was lower than 3%). UV-Vis measurements were performed following the same timescale for all the samples: 0 min, 30 min, 1 h, 2 h, 3 h, and 4 h. The total amount of 2-MBT intercalated in LDHs was determined by complete dissolution of LDHs into 0.1 M HNO<sub>3</sub>, followed by UV-Vis measurement of 2-MBT in solution.

#### 4.4.6 X-ray photoelectron spectroscopy

XPS was carried out, in cooperation with Helmholtz-Zentrum Geesthacht Centre for Materials and Coastal Research GmbH Institute of Materials Research (Germany), using a Kratos DLD Ultra Spectrometer with an Al-K $\alpha$  X-ray source (monochromator) operated at 225 W. For the survey spectra a pass-energy (PE) of 160 eV was used while for the region scans PE was 40 eV. Spectra were calibrated for 284.8 eV binding energy of C1s signal. For all samples charge neutralization was necessary. With respect to deconvolution of the region files background subtraction (linear or Shirley) was performed before calculation. Smoothing was necessary for quantitative calculations on the Ce(3d) core region.

#### 4.4.7 Atomic force microscopy

The metallic panels (AA2024, galvanized steel (GS) and cold roll steel (CRS)) after pretreatment were cut ( $\sim 1 \text{ cm}^2$ ) and glued to a support. In the case of AA2024, the aim was to assess the influence that different pretreatments have on the AA2024 surface morphology. Three pretreatments were analyzed: acetone, industrial treatment I and industrial treatment II, in a procedure described in section 4.1.1. In the case of GS and CRS, the aim was to compare both metallic substrates. AFM was performed in a Veeco Nanoscope IV Multimode AFM; images were acquired in tapping mode, using silicon probes (from Nanoworld) operating at a resonance frequency of about 320 KHz and a force constant of 42 N/m. Image analysis was performed using Gwyddion 2.37 software (<http://gwyddion.net/>).

#### 4.4.8 Electrochemical impedance spectroscopy

The measurements were carried out with a Gamry potentiostat/galvanostat/ZRA interface 1000 at open circuit potential with an applied 10 mV sinusoidal perturbation in the 100 kHz to 10 mHz frequency range, taking 7 points per decade. For this purpose, a conventional three-electrode cell was used, composed of a saturated calomel reference electrode, a platinum foil as the counter electrode and the samples as the working electrodes. The impedance plots were fitted using different equivalent circuits with the Gamry Echem Analyst software version 5.1. The equivalent circuits used were based on RC circuits (instead of pure capacitances constant phase elements were used), and the goodness of fittings evaluated by the values of  $\chi^2$ .

Electrochemical impedance spectroscopy (EIS) was performed on samples prepared accordingly with the specificities of the measurement.

#### *Coated substrates*

An acrylic tube with a transversal area of 3.14 cm<sup>2</sup> was glued to a coated metallic sample. The NaCl solution, 0.05 M (for Sg\_W and AQ CC 080) or 0.5 M (for Sg\_Ti, TATA coatings and AQ CC 100), was poured into the tube. The metallic coated substrates used (AA2024, GS and CRS), work as the working electrodes, with the counter (platinum) and a reference electrode (saturated calomel electrode) placed inside the tube under immersion.

#### *Uncoated substrates*

For nanocontainers in suspension: the metal substrate (AA2024, GS, and CRS) was protected with bee wax, leaving exposed an area between 3-4 cm<sup>2</sup>. The metallic substrates, working electrodes, were then immersed vertically in a beaker with 0.05 M NaCl solution together with the counter and reference electrodes. A constant distance between the working and reference electrode was kept. This methodology was used to prevent the influence of the nanocontainers deposition on the EIS measurements. In the case of assessing the inhibitor efficiency the studies were performed on bare metallic substrates (AA 2024, GS and CRS) with 0.005 M and 0.05 M NaCl solutions containing corrosion inhibitors 2-MBT and Ce(NO<sub>3</sub>)<sub>3</sub> for AA2024, and gluconate for GS and CRS. In these cases the studies were performed using the acrylic tubes, in a similar design to the one used on coated samples.

### **4.4.9 DC polarization**

The DC polarization was used to study the efficiency of corrosion inhibitors. Metallic panels of 1.2x4 cm were covered with a protective varnish leaving an exposed area of ~1 cm<sup>2</sup>. The metallic panels were immersed in a solution of 5 mM or 50 mM NaCl together with reference and counter electrodes. Solutions containing 2-MBT and Ce(NO<sub>3</sub>)<sub>3</sub> (2 mM of 2-MBT; 5 mM of Ce(NO<sub>3</sub>)<sub>3</sub> and a mixture of both) were tested on AA2024, and solutions containing gluconate (0.5, 1, 2 and 5 mM) were tested on GS.

The DC polarization curves were obtained using a Gamry potentiostat PCI4. The potential was scanned with a sweep rate of 1 mVs<sup>-1</sup> in the range of -1.2 to -0.3 V vs. SCE.

The OCP was stabilized for 1 h prior to the beginning of measurements. A three-electrode cell, consisting of the metal sample with a known area (working electrode), Pt spring with a total surface area of 2 cm<sup>2</sup> (counter electrode) and a saturated calomel electrode (reference) combined with the Luggin capillary, was used.

#### **4.4.10 Contact angles/surface energy**

Contact angle measurements were carried out in a Contact Angle System OCA 15 at room temperature, using water in AA2024 substrates. The angles were measured 5 seconds after contact between water droplets and the sample surface was established. Five measurements were done for each sample.

#### **4.4.11 Thermogravimetric analysis**

Thermogravimetric analysis (TGA) was carried out in a TGA-50 Shimadzu system under air atmosphere, with a heating rate of 10 °C min<sup>-1</sup> from room temperature up to 800 °C.

#### **4.4.12 Differential scanning calorimetry**

The temperatures of glass transition ( $T_g$ ) and the respective variation of heat capacity ( $\Delta C_p^0$ ) of several cured coating formulations were measured in a TA instrument Q2000 differential scanning calorimeter. The samples were sealed in aluminum crucibles and measured using the following method: first step, heating from the minimum temperature ( $T_{min}$ ) °C until the maximum temperature ( $T_{max}$ ) with a heating rate of 20.00 °C·min<sup>-1</sup>; second step, cooling from  $T_{max}$  until  $T_{min}$  with a cooling rate of 20.00 °C·min<sup>-1</sup>; and final step, heating from  $T_{min}$  to  $T_{max}$  with a heating rate of 20.00 °C·min<sup>-1</sup>.  $T_{min}$  and  $T_{max}$  were chosen according to the analyzed samples. The  $T_g$  is reported in this work according to the convention, as a single temperature, corresponding to the midpoint between the tangents of the heat flow curve corresponding to the glass state and the heat flow curve corresponding to the more flexible state.

#### **4.4.13 Scanning Vibrating Electrode Technique**

The coated GS samples with ~1 cm<sup>2</sup> were glued on a support. Bee wax was used to protect the sample leaving exposed a small area, 0.3 cm<sup>2</sup>. Two defects were done on

the coating, using a needle, in such a way that the GS metal substrate became exposed. Before the start of the test, a 50 mM NaCl was added to the cell, immersing the sample. A commercial system from Applicable Electronics, controlled by the ASET program (Sciencewares), was used to perform the scanning vibrating electrode technique (SVET). Insulated Pt–Ir probes (Microprobe, Inc.) with platinum black deposited on a spherical tip of 15  $\mu\text{m}$  diameter was used as a vibrating electrode for the SVET system. The probe was placed  $200 \pm 3 \mu\text{m}$  above the surface, vibrating in the planes perpendicular (Z) and parallel (X) to the sample's surface. The amplitude of vibration was 18  $\mu\text{m}$ , vibration frequencies of the probe were 124 Hz (Z) and 325 Hz (X). Only the vertical component was used for treating experimental data and calculating total current.



# 5

## **Layered double hydroxides**

### **Hybrid nanoreservoirs – LBL modified LDH nanocontainers**

*“It is paradoxical, yet true, to say, that the more we know, the more ignorant we become in the absolute sense, for it is only through enlightenment that we become conscious of our limitations. Precisely one of the most gratifying results of intellectual evolution is the continuous opening up of new and greater prospects.”*

Nikola Tesla



The use of layered double hydroxides (LDH) as a container for corrosion inhibitors is well documented in the literature.[96, 97, 153, 154, 168] Its ability to release inhibitors on demand via an anion exchange-based mechanism, makes LDH one of the most interesting materials in the development of smart coatings for corrosion protection.[151] Nevertheless, all the work reported so far presents LDH as a host to only one corrosion inhibitor, namely negatively-charged species. When the application of a second corrosion inhibitor to enhance active corrosion protection is required, most of the reported approaches used two types of containers, each one loaded with a corrosion inhibitor.[96] In this context, the application of a nanocontainer able to allocate two different corrosion inhibitors simultaneously, sounds an interesting approach, particularly if the coating formulation must comply with low pigment volume concentrations.

Moreover, in the specific case of combining polyelectrolytes together with LDHs, the resulting reservoir can be sensitive to different triggers and trigger conditions. In this chapter, the LDHs ability to host the well-known corrosion inhibitor - 2-mercaptobenzothiazole (2-MBT) [91] - combined with a second corrosion inhibitor immobilized between polyelectrolyte shells - cerium (III) nitrate [92] - will be presented. The aim is the preparation of an anticorrosion system with superior active corrosion protection, presenting at the same time good coating/nanocontainer compatibility.

## 5.1 Layered double hydroxides as a reservoir for corrosion inhibitor 2-mercaptobenzothiazole

The incorporation of 2-mercaptobenzothiazole (2-MBT) into LDHs was carried out according to the procedure described in detail in section 4.2.1. The chemical structure of LDHs is represented by the generic formula  $[M^{2+1-x}M^{3+x}(OH)_2]^{x+} A^{z-}_{x/z} \cdot nH_2O$ , where  $M^{2+}$  and  $M^{3+}$  are the bi- and trivalent metal cations,  $A^{z-}$  is the intercalated anion and  $n$  is the molar fraction of crystal water.[289-291] The successful incorporation of 2-MBT was assessed by ATR-FTIR and XRD analysis.

The ATR-FTIR spectra for 2-MBT, LDH-NO<sub>3</sub>, and LDH-MBT are presented in Figure 40. The spectrum of 2-MBT is characterized by a series of intense bands observed at 565 and 599 cm<sup>-1</sup>, associated with the torsion of the aromatic ring, and a set of signals at 1240 cm<sup>-1</sup>, 1421 cm<sup>-1</sup> and 1493 cm<sup>-1</sup> corresponding to CN stretching and to NH bending of the CNH group. An intense band is observed at 1458 cm<sup>-1</sup> attributed to CC and NH

stretching and CH bending vibrations. In addition, bands occurring at  $669\text{ cm}^{-1}$  correspond to the CS stretching and at  $1016\text{--}1085\text{ cm}^{-1}$  are attributed to CS stretching in the SCS. At  $1285\text{ cm}^{-1}$ ,  $1319\text{ cm}^{-1}$  and  $1248\text{ cm}^{-1}$  are visible bands that can be assigned to CN stretching. A strong signal appears at  $745\text{ cm}^{-1}$  associated with the CH wagging.[292, 293].

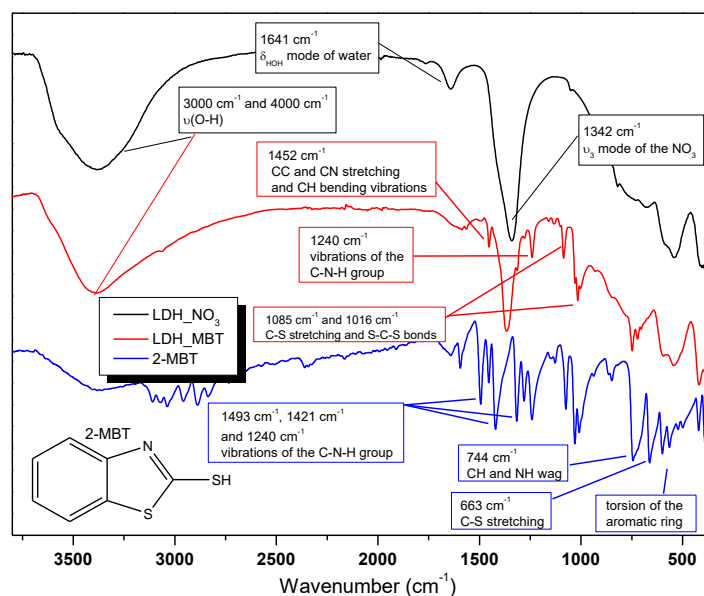


**Figure 40: FTIR spectra of 2-MBT, LDH-NO<sub>3</sub>, and LDH-MBT.**

The infrared spectrum of LDH-NO<sub>3</sub> is in agreement with the literature,[168] presenting a broad, intense band with a maximum at  $1340\text{ cm}^{-1}$  and a shoulder at  $1385\text{ cm}^{-1}$ , ascribed to the vibrational mode  $\nu_3$  of the NO<sub>3</sub><sup>-</sup> groups. The unconstrained NO<sub>3</sub><sup>-</sup> molecule has a planar trigonal arrangement of D<sub>3h</sub> symmetry that originates IR active vibrational modes: out-of-plane deformation ( $\nu_2$ ) at  $830\text{ cm}^{-1}$ , out-of-phase N-O stretching ( $\nu_3$ ) at  $1370\text{ cm}^{-1}$  and in-plane bending ( $\nu_4$ ) at  $723\text{ cm}^{-1}$ . [294] When incorporated into the LDH galleries the symmetry of the nitrate anion appears to decrease, most probably due to a C<sub>2v</sub> arrangement, which originates an out-of-phase NO stretching ( $\nu_3$ ) band at  $1340\text{--}1400\text{ cm}^{-1}$ . The symmetry reduction could be a result of local constraints on the free NO<sub>3</sub><sup>-</sup> and/or the presence of hydrogen bonds between nitrate anions and the hydroxyl layers or water molecules.[294, 295] The band at  $1342\text{ cm}^{-1}$  could be attributed to carbonate anions, but the presence of a small band at  $1049\text{ cm}^{-1}$  reveals the presence of asymmetric nitrate anions.[296, 297] The weak band at  $1643\text{ cm}^{-1}$  arises from the deformation vibration of water molecules in the interlayer domain. A broadband at

$3395\text{ cm}^{-1}$  that stems from OH stretching vibrations of the hydroxide layer and water is detected as well.[172]

The ATR-FTIR spectrum of LDH-MBT presents a combination of the LDH-NO<sub>3</sub> and 2-MBT bands. After the incorporation of 2-MBT, the resulting FTIR spectrum is characterized by the presence of two intense bands, one at  $1361\text{ cm}^{-1}$  associated with the vibrational mode  $\nu_3$  of the NO<sub>3</sub><sup>-</sup> group, and another at  $3395\text{ cm}^{-1}$  associated with the stretching of the OH groups of the hydroxide layer and water. Nevertheless, the band occurring at  $1641\text{ cm}^{-1}$ , attributed to the deformation vibration of water molecules in the interlayer domain, decreased significantly. Moreover, characteristic bands associated with the structure of 2-MBT are now visible at  $1452\text{ cm}^{-1}$  (C-N stretching and to N-H bending of the C-N-H group),  $669\text{ cm}^{-1}$  (C-S stretching),  $1016\text{-}1085\text{ cm}^{-1}$  (C-S stretching in the S-C-S group) and  $1248\text{ cm}^{-1}$  (vibrations of the C-N-H group).

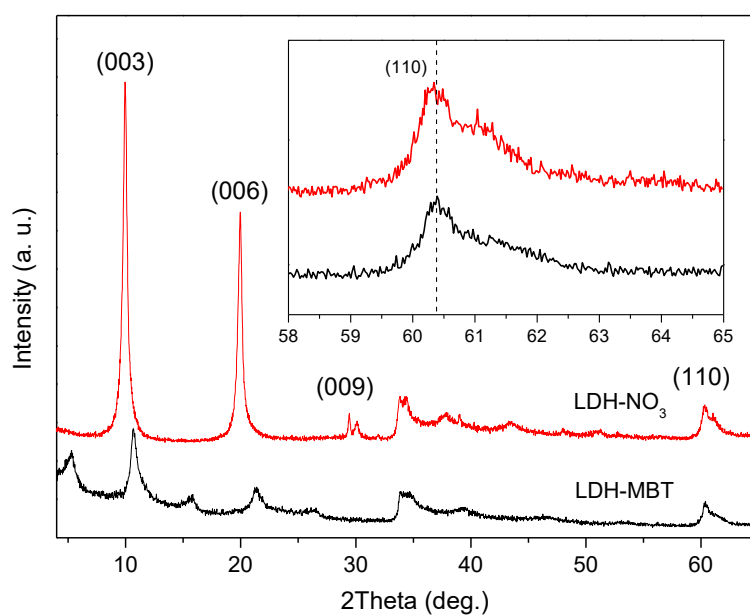


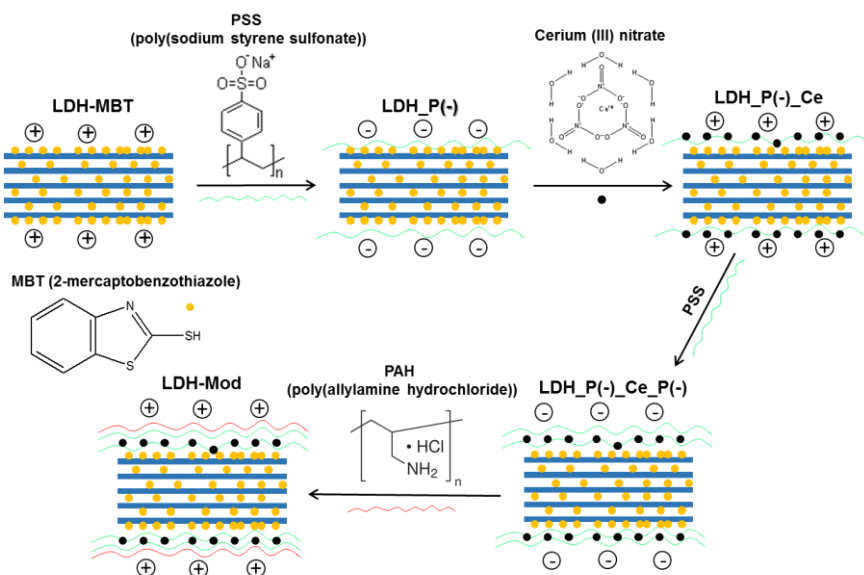
Figure 41: XRD patterns of LDH-NO<sub>3</sub> and after intercalation of 2-MBT, LDH-MBT. Adapted from [94].

The XRD diffractograms for LDH-NO<sub>3</sub> and LDH-MBT are presented in Figure 41. The LDH-MBT diffractogram shows two LDH phases with  $d$ -values of  $16.7\text{ \AA}$  and  $7.6\text{ \AA}$ , respectively. These phases correspond to LDHs intercalated with either MBT<sup>-</sup> or OH<sup>-</sup> anions.[96, 154, 168] This corresponds to galleries height of  $11.93\text{ \AA}$  for 2-MBT and  $2.83\text{ \AA}$  for OH<sup>-</sup> anions. The presence of the LDH-OH phase in the LDH-MBT sample was estimated to be around 15 %. The differences in the gallery height are a strong indication of the successful incorporation of 2-MBT since the latter is considerably larger than NO<sub>3</sub><sup>-</sup>. No shift in the position of the (110) reflection peak for both the parent LDH-

$\text{NO}_3^-$  and LDH-MBT was observed (see inset in Figure 41), indicating that the ion exchange 'NO<sub>3</sub>-to-MBT' has not affected the cation composition of the hydroxide layers.

## 5.2 LDH modified to provide dual release

In this section, the modification of LDHs to transform single type corrosion inhibiting nanocontainers into multiple-intercalated systems is described (Scheme 5). The strategy followed consists of using a system already described for its intrinsic controlled release mechanism, LDHs, which are subsequently modified with polyelectrolytes by the layer-by-layer (LbL) technique. The use of polyelectrolytes allows the intercalation of additional corrosion inhibitors between layers, which can be released due to the pH-dependent permeability of polyelectrolytes.[192, 298] The LDHs surface modification is presented in detail in section 4.2.3. The modified LDH nanocontainers (LDH-Mod) were characterized by FTIR, XRD, and SEM-EDS.



Sample	MBT within LDH	Cerium-based species between polyelectrolyte layers	LbL layers
LDH-MBT	Yes	No	No
LDH_P(-)	Yes	No	PSS
LDH_P(-)_Ce	Yes	Yes	PSS
LDH_P(-)_Ce_P(-)	Yes	Yes	PSS:PSS
LDH-Mod	Yes	Yes	PSS:PSS:PAH

Scheme 5: Approach used in the surface modification of LDH with PSS, PAH, and cerium (III) nitrate.[94] Reproduced by permission of The Royal Society of Chemistry (RSC) on behalf of the Centre National de la Recherche Scientifique (CNRS) and the RSC.

### 5.2.1 Structural characterization

The ATR-FTIR analysis was conducted throughout the LDH-MBT modification by LbL process and is presented in Figure 42. The most significant change was observed during the first modification with PSS (LDH\_P(-)), where the characteristic bands associated with the PSS became visible in the LDH-MBT spectrum. Notably, no significant changes were observed after modification with PAH and after the incorporation of  $\text{Ce}^{3+}$  (cf. spectra for LDH-Mod, LDH\_P(-)\_Ce\_P(-), LDH\_P(-) and LDH\_P(-)\_Ce), probably due to band overlapping. The FTIR spectrum for LDH\_P(-) shows a new band at  $1122\text{ cm}^{-1}$  associated with the S-O stretching of the  $-\text{SO}_3\text{H}$  group, when compared to LDH-MBT (recall Section 5.1).[299]

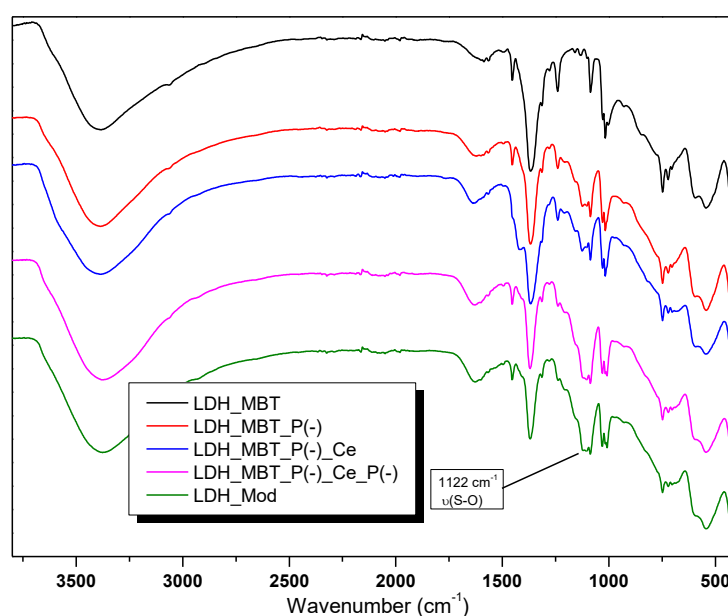
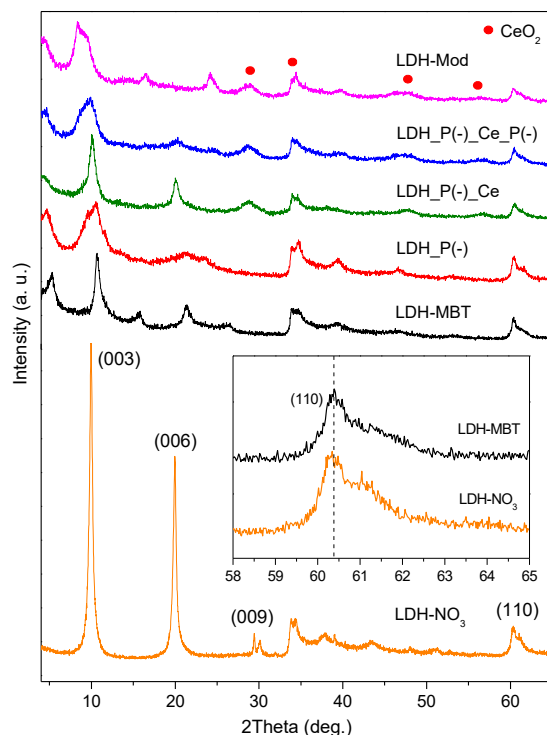


Figure 42: FTIR patterns of LDH-MBT powders throughout the LbL process.

The XRD analysis of the incorporation of 2-MBT into the LDH- $\text{NO}_3$  was presented in section 5.1. In this section, a closer analysis of the XRD patterns will be presented aiming not only at the structural characterization of LDH-MBT throughout the modification process but also to evaluate the presence of cerium and in which form it can be.



**Figure 43:** XRD patterns of LDH powders before (LDH-NO<sub>3</sub>) and after intercalation with MBT<sup>-</sup> (LDH-MBT). The inset shows the range of (110) diffraction reflections. XRD patterns of LDH-MBT powders throughout the modification process. Diffraction peaks associated with cerium oxide phase are represented by red dots.[94] Reproduced by permission of The Royal Society of Chemistry (RSC) on behalf of the Centre National de la Recherche Scientifique (CNRS) and the RSC.

The process of surface modification applied to LDH-MBT, with its different steps, led to significant changes in the LDH-MBT phases, with the *d*-values observed being different from the ones characteristic of LDH-MBT or LDH-OH. After the first modification with PSS (LDH\_P(-)) there is the appearance of a new phase, at 4.5°, with *d*~19.7 Å (Figure 43). The new phase can be the result of MBT<sup>-</sup> re-arrangements, taking place during the modification step, or due to a partial anion-exchange of MBT<sup>-</sup> and OH<sup>-</sup> with charged species available in the PSS solution. The incorporation of Ce, in the second modification step, results in the appearance of additional reflections at 28.8, 33.1, 47.5 and 56.3°, characteristic of the crystalline phase of cerium (IV) oxide.[300-302] These reflections presented symmetric broadening peaks indicative that the CeO<sub>2</sub> crystallites are nano-sized. A relevant outcome of this second modification was the appearance of a phase ascribed to LDH-NO<sub>3</sub>,[295] *d*~9.0 Å, with the relative amount of LDH-MBT, 16.7 Å, being estimated in values around 10 % compared with the initial LDH-MBT phase. The third modification step, consisting of incorporation a second layer of PSS (LDH\_P(-)\_Ce\_P(-)), produced XRD spectra similar to the ones obtained for LDH\_P(-), with a significant difference observed in the amount of LDH-MBT phase, which is smaller in

LDH\_P(-)\_Ce\_P(-), when compared with LDH\_P(-). The final modification with PAH resulted in changes of basal spacing ascribed to LDH-MBT phases (from 19.7 and 16.7 Å to 19.0 and 10.9 Å, respectively) and to the disappearance of the LDH-OH phase. Two main results can be highlighted from the XRD analysis done so far: first the loss of 90 % of the LDH-MBT phase when compared with the starting material and second the stability of the crystalline cerium (IV) oxide, that remains constant throughout the process after its incorporation (LDH\_P(-)\_Ce).

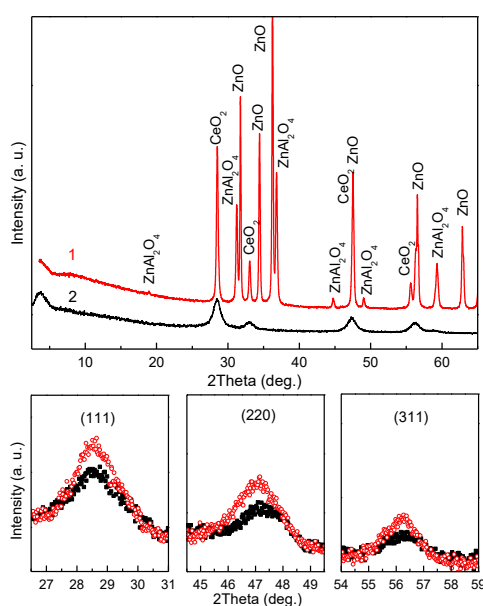


**Figure 44:** Top: XRD patterns of (1) the powder obtained as a result of calcination of LDH-MBT sample after the second modification step and (2) nano-powder of CeO<sub>2</sub>. Bottom: diffraction peaks of CeO<sub>2</sub> in the XRD patterns of the mechanical mixture of LDH-MBT + nano-CeO<sub>2</sub> (open symbols) and the LDH-MBT sample after the second modification step (solid symbols). [94] Reproduced by permission of The Royal Society of Chemistry (RSC) on behalf of the Centre National de la Recherche Scientifique (CNRS) and the RSC.

The appearance of crystalline phases of nano-sized CeO<sub>2</sub> raised the question if all the cerium present on the LDH-Mod was in the form of Ce<sup>4+</sup> or some were kept as Ce<sup>3+</sup>. To answer this question powders were calcined at 1000 °C and the relative metal cations ratio was estimated by XRD analysis. From the calcined LDH\_P(-)\_Ce spectrum (Figure 44) three crystalline phases can be identified and their respective proportions established: ZnO (48.7 wt.%), ZnAl<sub>2</sub>O<sub>4</sub> (39.5 wt.%), and CeO<sub>2</sub> (11.9 wt.%). These values enabled the determination of the following metal cation ratios: Zn/Al=1.9 and Zn/Ce=11.9. If all the cerium present on the LDH\_P(-)\_Ce was in the form of Ce<sup>4+</sup>, the latter would correspond to the weight ratio of LDH-MBT to CeO<sub>2</sub> of about 17. For comparison a sample containing LDH-MBT and CeO<sub>2</sub>, prepared according to reference [301] were mixed in the same proportion as mentioned above, milled in a mortar and analyzed by XRD (Figure

44). The results show that the reflections obtained for  $\text{CeO}_2$  in LDH\_P(-)\_Ce are regularly smaller than the respective intensities observed for the samples mechanically mixed (LDH-MBT + nano- $\text{CeO}_2$ ). When the quantitative comparison between the intensities of those reflections was performed, it was verified that approximately 15-20 % of cerium in the modified LDH-MBT is in some sort of “hidden”, non-crystalline form.[94]

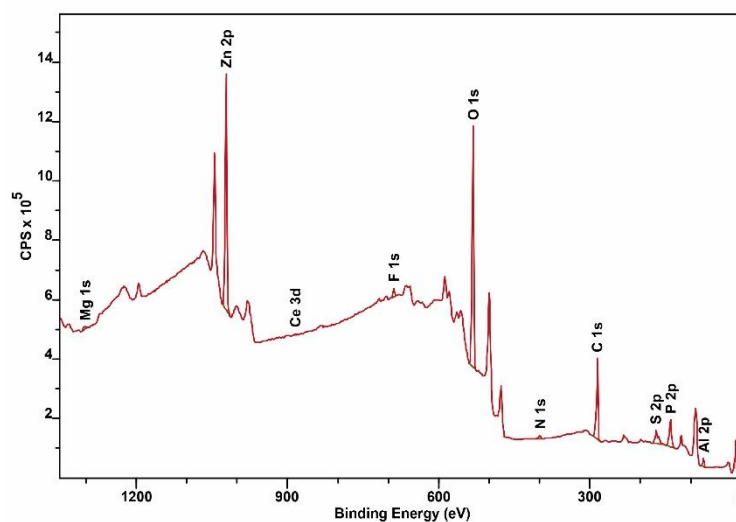
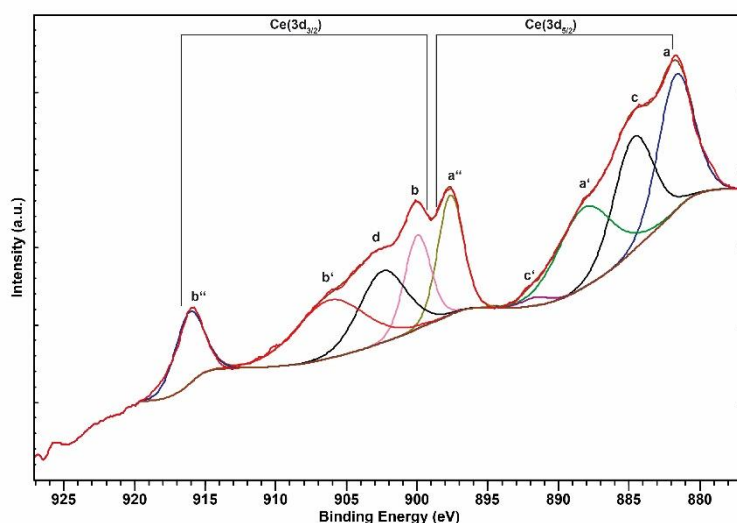


Figure 45: XPS survey spectrum of LDH-MBT + nano- $\text{CeO}_2$ . [94] Reproduced by permission of The Royal Society of Chemistry (RSC) on behalf of the Centre National de la Recherche Scientifique (CNRS) and the RSC.

The results presented above indicate the presence of cerium in an amorphous state, a form that could be relevant in anticorrosion applications. Nevertheless, nothing can be concluded concerning the oxidation degree of cerium cations only from these XRD analyses. To overcome this issue an additional XPS study was performed, enabling the identification of the oxidation degree of Ce-based species. The LDH-Mod XPS survey spectrum is presented in Figure 45. The results indicate that the polyelectrolyte coverage cannot be thicker than approximately 5 nm, which is the depth of response for the accelerate photoelectrons still to be detected.[94]

The analysis of the Ce(3d) core level region, obtained from 256 scans to increase the signal-to-noise ratio, indicates different states that can be described by three spin-orbit doublets as discussed in detail by Kotani and Ogasawarab.[303] In Figure 46 the deconvolution of the Ce(3d<sub>5/2,3/2</sub>) is presented in accordance with Sharma,[304] Katta[305] and Sudarsama.[5] Characteristic peaks ascribed to  $\text{CeO}_2$  can be found in the form of  $\text{Ce}^{4+}$ (3d<sub>5/2</sub>) binding energies at 881.7 eV (a) and its satellites at 888.2 eV (a') and

897.7 eV (a'') as well as for  $\text{Ce}^{4+}(3d_{3/2})$  at 900.0 eV (b) and its satellites at 906.2 eV (b') and 916.1 eV (b''). Peaks belonging to  $\text{Ce}^{3+}$  oxidation state can be found as well at 884.7 eV (c), 891.7 eV (d) for  $\text{Ce}^{3+}(3d_{5/2})$  and at 902.4 eV (c') belonging to  $\text{Ce}^{3+}(3d_{3/2})$ . These results confirm the presence of cerium in both oxidation states,  $\text{Ce}^{4+}$  and  $\text{Ce}^{3+}$ . Due to the way Ce is embedded into the polyelectrolyte shell covering the LDH-Mod it is not possible to establish with a great level of accuracy the ratio between  $\text{Ce}^{4+}/\text{Ce}^{3+}$ . Nevertheless, a rough estimation was obtained from the deconvolution, obtaining a ratio of 3:1. The existing Ce species are best described by the formula  $\text{Ce}_{x-a}\text{O}_{y-b}$ .



**Figure 46:** XPS spectra of the  $\text{Ce}(3d_{5/2,3/2})$  core level region with deconvolution assigned to Ce states for determination of the  $\text{Ce}^{4+}/\text{Ce}^{3+}$  ratio. [94] Reproduced by permission of The Royal Society of Chemistry (RSC) on behalf of the Centre National de la Recherche Scientifique (CNRS) and the RSC.

In Figure 47 SEM micrographs and the EDS analysis of LDH-Mod are presented. The presence of Zn and sulfur-rich areas coincide with the LDH cluster in the micrograph. The former is due to the LDH structure and the latter is due to the presence of intercalated 2-MBT and an outer shell composed by PSS. The signal associated with Ce was found to be small. Therefore, to be able to investigate the presence of cerium, the EDS analysis presented in Figure 47 was carried out immediately after its incorporation (LDH\_P(-)\_Ce), thereby avoiding the interference of subsequent polyelectrolyte layers. In this analysis is possible to detect the signal of Ce and O in areas overlapping LDH particles (Figure 47e). The EDS analysis for different LDHs, throughout all LDH-Mod synthesis steps, are presented in Figure 47f. The starting material, LDH-MBT, presents clear peaks attributed to zinc (1.03 keV and 8.62 keV), aluminum (1.5 keV), oxygen (0.52 keV) and sulfur (2.32 keV). The successful incorporation of cerium in modified

LDH particles is verified by the presence of peaks associated with cerium at 4.85 keV and 5.3 keV, for samples after the incorporation of Ce (from LDH\_P(-) onwards). These results are in agreement with the XRD and XPS data presented above. Noteworthy is the fact that the cerium-based compounds were not removed by the successive modification/washing processes.

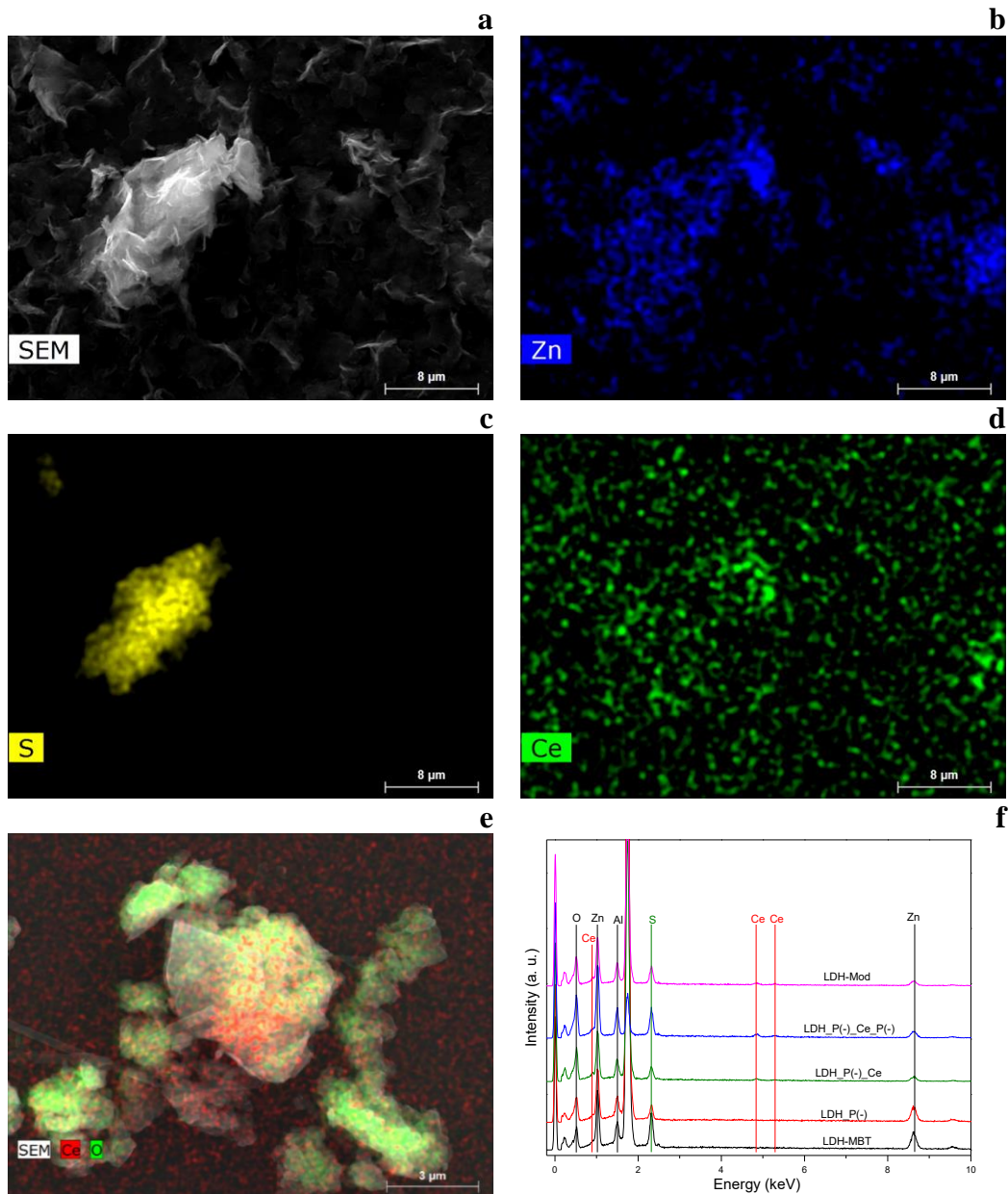


**Figure 47: SEM and EDS mapping of LDHs: (a) SEM image, (b) Zn mapping, (c) S mapping and (d) Ce mapping. Overlapping of SEM image, O mapping and Ce mapping of LDH\_P(-)\_Ce sample (e). EDS analysis throughout the modification process (f). [94] Reproduced by permission of The Royal Society of Chemistry (RSC) on behalf of the Centre National de la Recherche Scientifique (CNRS) and the RSC.**

The zeta potential of the modified LDH platelets with polyelectrolytes are presented in Table 12. The starting material, LDH-MBT, shows values of zeta potential

around +30 mV. The application of a layer of PSS, first modification (LDH\_P(-)), decreases the value to ~+10 mV due to the negative nature of the polyelectrolyte. Considering its negative nature and since PSS is a strong polyanion,[306] one would expect a negative value. Nevertheless, the presence of heterogeneities arising from uneven charge distribution on the LDH platelets[307, 308] could limit the full coverage of the LDHs surface with PSS, hence the partially positive charged measured. In addition, the incomplete coverage of LDHs by PSS may explain why part of 2-MBT was released during the LbL process, as already discussed in section 5.2.1.

**Table 12: Zeta potential values of LDH particles throughout the modification process. [94] Reproduced by permission of The Royal Society of Chemistry (RSC) on behalf of the Centre National de la Recherche Scientifique (CNRS) and the RSC.**

Sample	LDH-MBT	LDH_P(-)	LDH_P(-)_Ce	LDH_P(-)_Ce_P(-)	LDH_Mod
Zeta potential (mV)	+31.8	+9.8	+29.5	-21.3	+22.8

The incorporation of a cationic inhibitor, second modification (LDH\_P(-)\_Ce), could be affected by the yet positive value of zeta potential on the LDH surface, despite the presence of PSS. However one can admit that PSS, when adsorbed locally, retains its negative charge allowing the deposition of  $\text{Ce}^{3+}$ . This assumption is supported by the structural and compositional analysis presented in Figure 44 and Figure 47. The second modification led to the increase in the zeta potential values up to ~+30 mV, which can be attributed to the adsorption of  $\text{CeO}_2$  nanoparticles, formed during the process of deposition, by the PSS layer. The values of zeta potential found in the literature are in agreement with this assumption (~+37mV).[309] The third step (LDH\_P(-)\_Ce\_P(-)) consisted of the deposition of a second PSS layer to cover the cerium-containing species. This modification changed the zeta potential to values around -21 mV, supporting now a full coverage of the LDH platelets with PSS.

The application of positively-charged polyelectrolyte PAH in the final modification step had two main purposes. First, to reinforce the polyelectrolyte shell around the LDH, thus providing additional control over the release of  $\text{Ce}^{3+}$ , due to the additional thickness of the polyelectrolyte layer. Second, the modification with PAH allowed the final value of zeta potential to be positive, enabling a direct comparison between LDH-Mod and LDH-MBT from a colloidal standpoint. After the final modification, the LDH-Mod presented values of zeta potential around +23 mV.

## 5.2.2 Inhibitor release studies

Inhibitor release studies were performed for LDH-MBT and LDH-Mod. The loading content of MBT in the different LDHs was experimentally determined by complete dissolution of LDHs under acidic conditions and quantification of MBT in solution. The values obtained were 38 wt.% for unmodified LDH-MBT and ca. 8 wt.% for LDH-Mod. The difference in loading content must be analyzed taking into account that is done with respect to the total mass of the particles and the modified particles have an additional contribution due to the introduction of several layers of polyelectrolyte and addition of cerium (III) nitrate. However, the decrease in 2-MBT is consistent with the release of MBT during the preparation of LDH-Mod, as observed by XRD in previous sections.

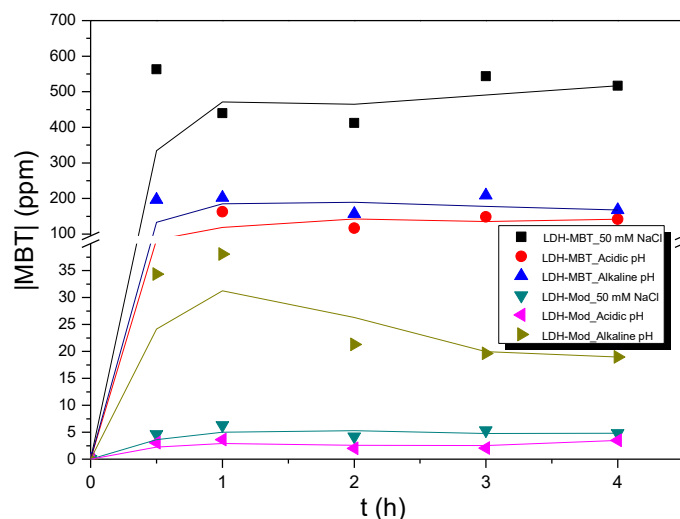


**Figure 48:** 2-MBT release profiles for LDH-MBT and LDH-Mod under different conditions ( $\lambda=320$  nm). [94] Reproduced by permission of The Royal Society of Chemistry (RSC) on behalf of the Centre National de la Recherche Scientifique (CNRS) and the RSC.

The LDHs ability to release 2-MBT was tested under different conditions, namely in the presence of NaCl and for different pH values, as presented in Figure 48. The release of 2-MBT from LDH-MBT was already discussed in previous works[168] and is consistent with the release by ion-exchange. In fact, the results obtained in this work confirm the release of higher amounts of 2-MBT in 50 mM NaCl. However, when LDH-MBT is modified with polyelectrolyte shells, the release of this organic inhibitor is affected dramatically, with LDH-Mod in 50 mM NaCl presenting 2-MBT concentration values two orders of magnitude smaller than LDH-MBT. The combination of two factors could be contributing for this result: the 2-MBT loading content of LDH-Mod is lower

than LDH-MBT and the presence of the polyelectrolyte shell that restricts the release of MBT<sup>-</sup> under neutral conditions.

The release of 2-MBT from LDH-Mod was found to be dependent on the pH, with a preferentially release under alkaline conditions. This is an important feature of the imparted modification, since the main trigger for unmodified LDH-MBT is the presence of NaCl, whereas for LDH-Mod pH is the preferential trigger. This preference for pH-based release can be explained by the pH-dependent permeability of the polyelectrolyte layers covering the LDHs, as already described in the literature.[306, 310]

## 5.3 Electrochemical studies

### 5.3.1 AA2024 surface characterization

Pretreatment of the metallic substrate prior to coating application is one of the most important steps when considering long-lasting protective measures. In particular, the removal of contaminants, together with the increase in surface roughness can lead to improvements in adhesion between the metal and the protective coating. Therefore, in this section, the effect of different surface pretreatments on the aluminum alloy 2024 was studied. One of the pretreatment consists simply of washing the substrate with acetone, whereas the other two pretreatments were developed using different industrial products (industrial treatments I and II). The latter treatments aim not only at cleaning but also to etching and removal of surface inhomogeneities that can hamper the adhesion at the interface. More details concerning the treatments are described in section 4.1.1.

Figure 49 presents the SEM micrographs of AA2024 subjected to different pretreatments. Acetone cleaning does not impart any change in terms of surface morphology, working only as a degreasing agent, with no influence on the microstructure. The Industrial treatment I and industrial treatment II, on the other hand, lead to changes on the metal surface as a result of the removal of intermetallic microparticles, with industrial treatment II being the most effective in this regard Figure 49(c).

EDS analysis shows the typical profile considering the composition of AA2024: high amount of Al followed by the two most abundant alloying elements, Cu and Mg.[49, 51] No significant difference are observed. This is expected because EDS is not a surface-sensitive technique, so part of the AA2024 matrix is being probed as well.

The surface characterization using AFM allows for a quantification of the surface roughness for the different surface pretreatments. It is observable a difference in the roughness for all samples, being the sample cleaned with acetone the one with lower roughness, followed by the industrial treatment I and finally the sample treated with the industrial treatment II. These results are in full agreement with SEM observations.

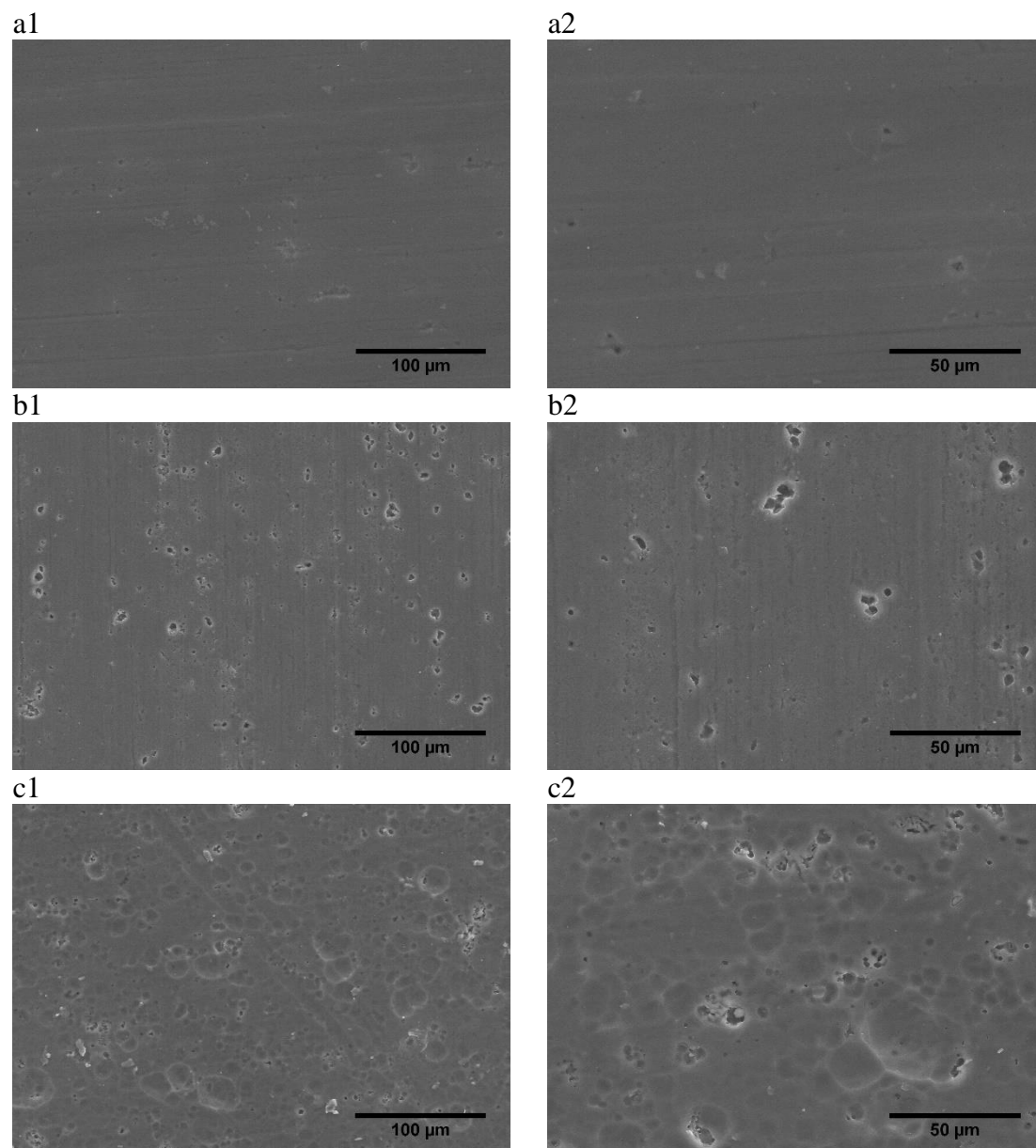


**Figure 49:** SEM micrographs of the AA2024 surface after pre-treated with: (a) acetone, (b) industrial treatment I and (c) industrial treatment II.

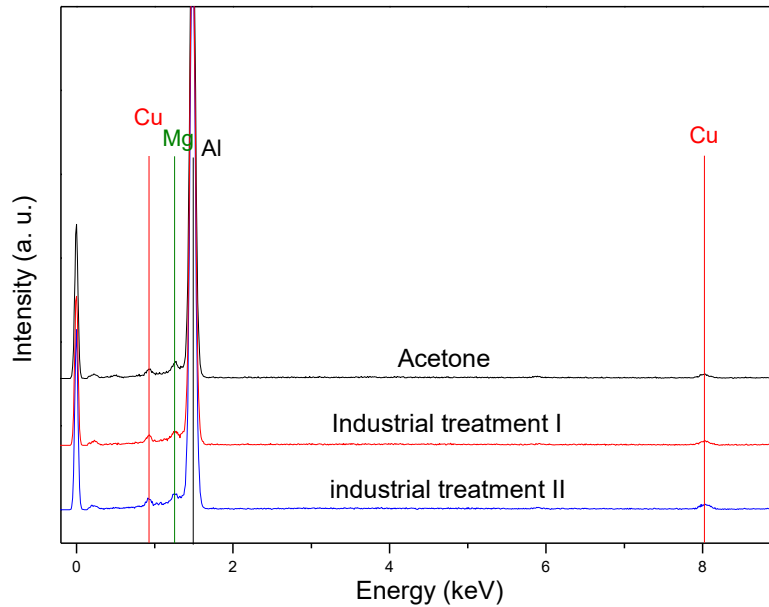


**Figure 50: EDS analysis of AA2024 pretreated samples with acetone, industrial treatment I and industrial treatment II.**

Sessile drop technique is a good technique to assess surface wettability towards coating formulations. A lower water contact angle indicates a higher surface affinity towards water-based formulations. In Table 13 the water contact angle values are indicated for different pre-treated samples. AA2024 presents water contact angles around  $98.5^\circ$  when cleaned with acetone only. The more active chemical pretreatments produce different results, with the industrial treatment I giving more hydrophobic surfaces ( $108^\circ$ ) and the industrial treatment II more hydrophilic surfaces ( $65.7^\circ$ ). The differences in wetting when comparing the aluminum alloy surfaces pre-treated with different industrial pretreatments can be explained by the increase in surface roughness combined with changes in the surface chemical composition due to the type of chemical agents present in the different commercial products. In any case, these results indicate that industrial treatment II can be a good pretreatment when applying hydrophilic coating formulations.

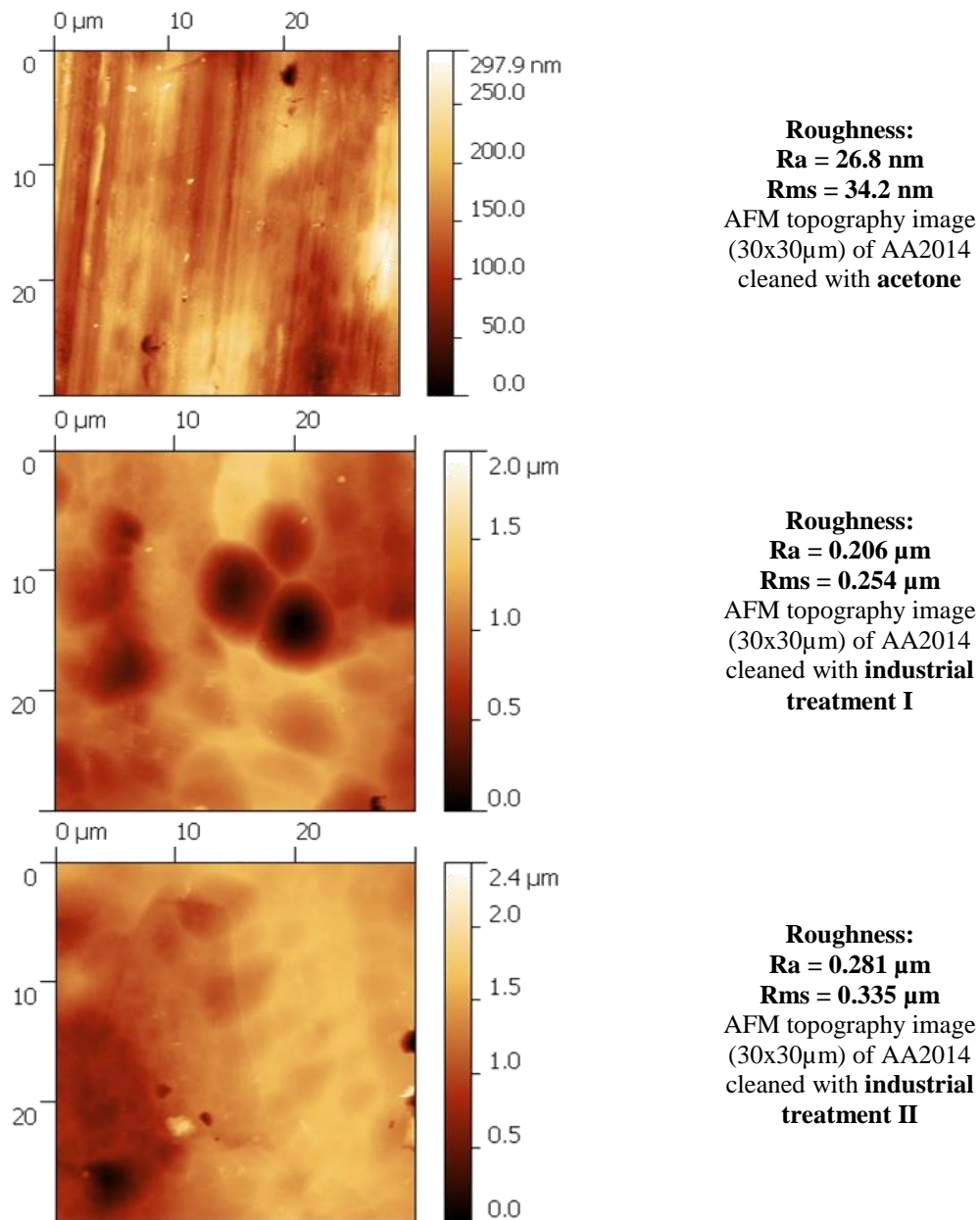


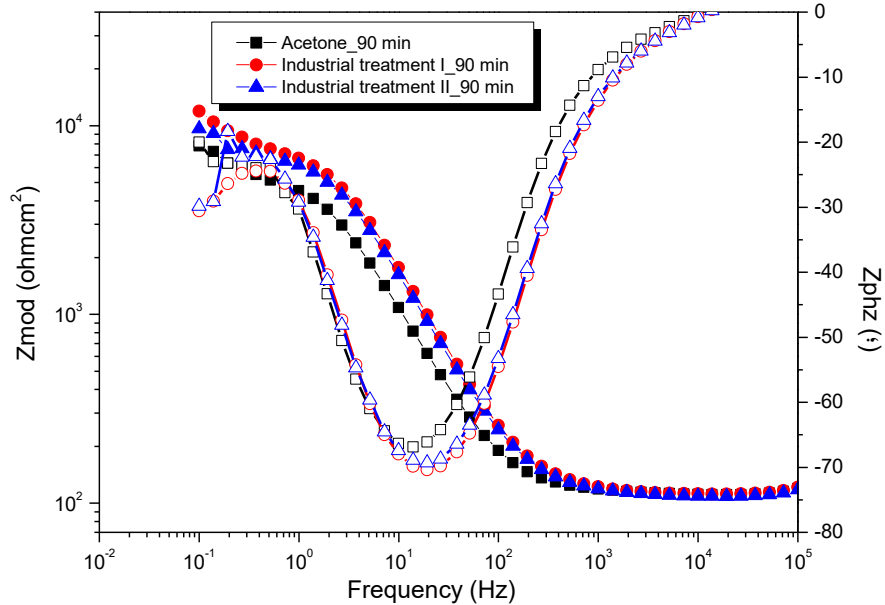
Figure 51: AFM images for AA2024 pretreated with acetone, industrial treatment I and industrial treatment II.

The electrochemical characterization of different pre-treated surfaces was carried out by EIS and the corresponding results are presented in Figure 52. After 90 minutes of immersion in 50 mM NaCl solution, all systems show one well-defined time constant, at intermediate frequencies ( $10^1$  Hz), associated with the presence of the natural oxide layer on the AA2024 surface. A second time constant occurs at low frequencies ( $10^{-2}$  Hz) and can be ascribed to corrosion processes. After 2 days of immersion, the oxide layer is severely attacked and only corrosion processes are detected at intermediate frequencies while at low frequencies mass transport controlled processes can be seen. No significant differences are visible between samples subjected to different pretreatments.

**Table 13: Water contact angles for AA2024 samples pretreated with acetone, industrial treatment I and industrial treatment II.**

Pretreatment	Water contact angle	Standard deviation
Acetone	98.5	2.6
Industrial treatment I	108.0	1.5
Industrial treatment II	65.7	3.5

a



b

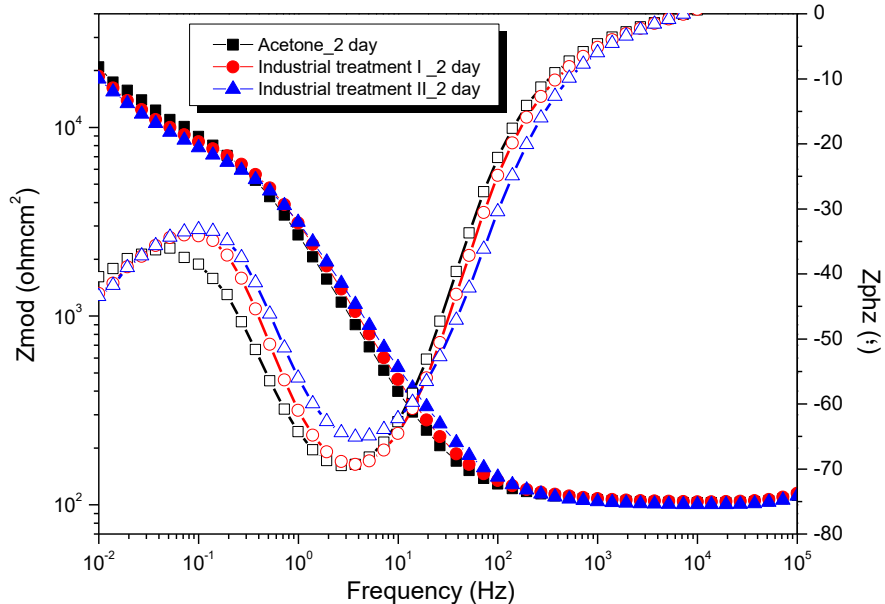


**Figure 52: Bode representation and phase angle of EIS spectra acquired for AA2024 bare substrates after 90 minutes, 1 day and 2 days in 50 mM NaCl solution.**

However, the previously showed results indicate the need for some type of pretreatment on the AA2024 surface, the water contact angle and the surface roughness being the two main parameters contributing to this conclusion. Furthermore, the removal

of intermetallic particles is important to increase the stability of the native aluminum oxide covering the surface. Taking into account all these factors, industrial treatment II was selected for substrate pretreatment prior to corrosion studies directly in solution and in coated samples as well.

### **5.3.2 Cerium (III) nitrate and 2-MBT as a corrosion inhibitor for AA2024**

The corrosion inhibiting properties of  $\text{Ce}^{3+}$  and 2-MBT towards AA2024 was investigated by DC polarization (Figure 53). The DC polarization measurements were performed for the cathodic and anodic branches separately, in a potential interval ranging -1.2 V to -0.3 V, starting each measurement next to the open circuit potential (OCP). The measurements were carried out after 1 hour of immersion, with the OCP being recorded during this period. Bare pre-treated (industrial treatment II) AA2024 plates were immersed in the following solutions: 50 mM NaCl, 50 mM NaCl with 5 mM  $\text{Ce}(\text{NO}_3)_3$ , 50 mM NaCl with 2 mM 2-MBT, and 50 mM NaCl with a mixture of 5 mM  $\text{Ce}(\text{NO}_3)_3$  and 2mM 2-MBT.

When AA2024 was immersed in a 50 mM NaCl, a plateau associated with diffusion-limited oxygen reduction appeared on the cathodic branch (potentials below -0.55 V vs. SCE). When the potential becomes more negative an increase in current is observed, associated with hydrogen reduction, which starts to become dominant. The anodic branch presents a continuous current increase up to  $1 \text{ mA cm}^{-2}$  at -0.3 V vs. SCE.

The application of  $\text{Ce}^{3+}$  based compounds as corrosion inhibitors for AA2024 has been reported in the literature,[311-315] with its main inhibition mechanism consisting of the precipitation of insoluble salts, in places where the oxygen reduction occurs. Analyzing its effect on the anodic and cathodic branches, the effectiveness of  $\text{Ce}^{3+}$  is more pronounced at low polarization levels in either direction, a result that is consistent with the formation of cerium hydroxide and oxide deposits on the S-phase intermetallics.[27] When compared with the 50 mM NaCl solution, the solution with  $\text{Ce}^{3+}$  gives lower current density in the cathodic branch down to ca. -0.8 V. The same tendency is observed in the anodic current density, with a decrease in the anodic polarization curve up to -0.4 V vs. SCE. At low polarization, the anodic current is associated with the dissolution of magnesium and aluminum from S-phase. Thus, this process is reduced due to the precipitation of Ce oxides and hydroxides (Figure 53).

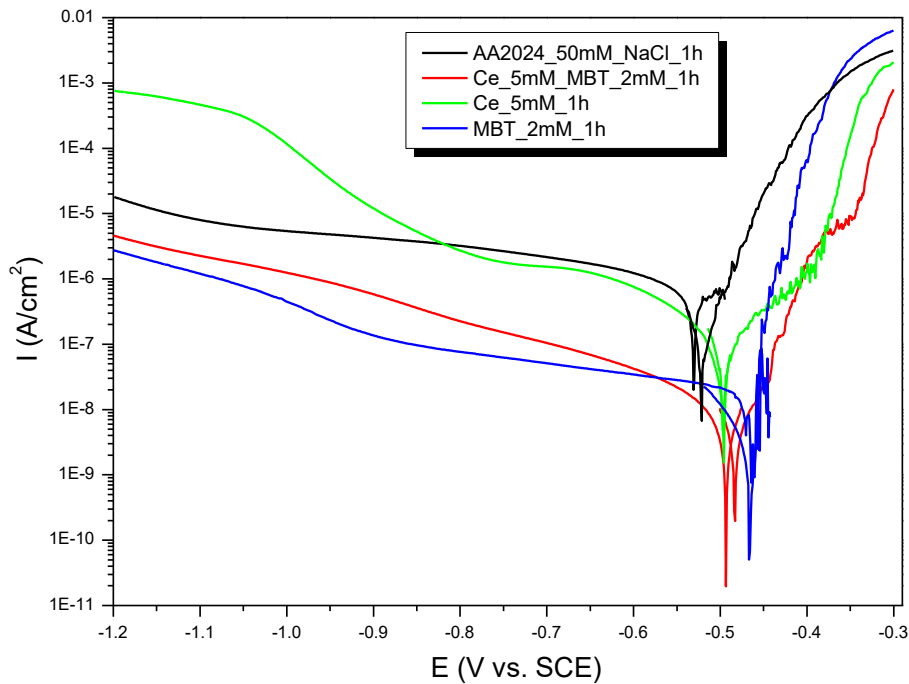


**Figure 53:** DC polarization curves for AA2024 samples immersed in 50 mM NaCl solution with 1 mM  $\text{Ce}(\text{NO}_3)_3$ , a saturated solution of 2-MBT (2 mM solution) and a mixture of both (5 mM  $\text{Ce}(\text{NO}_3)_3$ /2 mM 2-MBT) after 1 hour of immersion. [94] Reproduced by permission of The Royal Society of Chemistry (RSC) on behalf of the Centre National de la Recherche Scientifique (CNRS) and the RSC.

As indicated previously (section 2.3.2.1), 2-MBT is a highly efficient corrosion inhibitor for AA2024.[91] The way 2-MBT protects the surface is by forming a protective film on the metal surface, which decreases the rate of the anodic reaction. The high affinity of the thiol-based compounds towards Cu could offer an explanation for the hampering effect 2-MBT has in the reduction process as well. 2-MBT deposits on copper-rich intermetallics, thereby decreasing both anodic and cathodic activities occurring at these sites. In this work, for solutions containing 2-MBT, a decrease in the cathodic current density around one order of magnitude relative to the reference was observed (Figure 53). Additionally, when in presence of 2-MBT the curve ascribed to anodic polarization can be divided into different sections. At low polarization is a section associated with the dissolution of S-phase intermetallics. A second section is characterized by a current-stabilizing region followed by a third one related to intergranular corrosion, at higher polarization levels.[28]

Comparing the different systems, the presence of corrosion inhibitors originated open circuit potential values more positive (“nobler”) than the reference (no inhibitor):  $E_{oc}(\text{reference}) < E_{oc}(\text{Ce}) < E_{oc}(\text{Ce}+2\text{-MBT}) < E_{oc}(2\text{-MBT})$ . The samples immersed in solutions with 2-MBT and 2-MBT+Ce showed one order of magnitude decrease in the

cathodic current density. The current densities at  $-0.8$  V vs. SCE were  $0.1 \mu\text{A cm}^{-2}$  for 2-MBT,  $0.5 \mu\text{A cm}^{-2}$  for Ce+2-MBT, and  $10 \mu\text{A cm}^{-2}$  for Ce and reference.

For the anodic branch, the current density is also lower for systems with inhibitors (less than  $1 \mu\text{A cm}^{-2}$  at  $-0.45$  V vs. SCE) compared with reference system ( $10 \mu\text{A cm}^{-2}$  at  $-0.45$  V vs. SCE). Moreover, the most significant decrease in current density of the anodic branch was observed for  $\text{Ce}^{3+} + 2\text{-MBT}$  ( $\approx 0.05 \mu\text{A cm}^{-2}$  at  $-0.45$  V vs. SCE). This result could be the consequence of the formation of some sort of mixed protective film deposited on the aluminum matrix, due to the combination of both inhibitors, which could be providing additional stability compared with each inhibitor alone. Therefore, these results are indicative of a positive effect provided by the combination of 2-MBT + Ce, which seems to aid in the stability of the aluminum matrix, compared with 2-MBT or  $\text{Ce}^{3+}$  on their own, which is in agreement with EIS data presented in the following section.

### 5.3.3 LDH modified to provide dual release

The LDH-Mod inhibition efficiency towards AA2024 was studied by EIS. The modification process with polyelectrolyte layers lead to a significant decrease in the amount of 2-MBT and a pH-dependent release in modified LDHs, as observed in the XRD data and release studies (recall sections 5.2.1 and 5.2.2). Bode representations of EIS spectra obtained on bare AA2024 after 4 hours of immersion in 50 mM NaCl solution are depicted in Figure 54, whereas in Table 14 a description of all the LDH-containing solutions tested is presented.

The values of impedance at low frequencies indicate LDH-Mod as the best system, followed by LDH-MBT\_LbL, LDH- $\text{NO}_3$ \_LbL, LDH-MBT, LDH- $\text{NO}_3$ \_Mod, and LDH- $\text{NO}_3$  that were still better than the reference. For all the systems two-time constants were detected at intermediate ( $10^1$  Hz) and low frequencies ( $10^{-2}$ - $10^{-1}$  Hz). Nevertheless, their assignment varied depending upon the system under investigation. For LDH-Mod and LDH-MBT\_LbL, the time constant at intermediate frequencies can be assigned to the response of the native aluminum oxide, while the time constant at low frequencies is associated to corrosion processes, which can be represented by a charge-transfer resistance in parallel with double layer capacitance. The highest values of oxide resistance were observed for LDH-Mod,  $R_{\text{ox}} 2.46 \times 10^5 \Omega \text{ cm}^2$ , indicative of the protective effect rendered by these modified LDH. The corrosion progression tended to be more accentuated when in the presence of other types of LDHs, with the oxide response is no

longer detected. For these cases, the two-time constants detected were ascribed to corrosion processes at the metal/solution interface ( $10^1$  Hz) and mass-transport controlled processes ( $10^{-2}$ - $10^{-1}$  Hz).

The LDHs inhibition efficiency (IE) was calculated using the value of  $R_{ct}$  obtained by EIS, which is inversely proportional to the corrosion rate.[316, 317] In Table 14 are presented the values of inhibition efficiency based on the values of  $R_{ct}$  obtained by fitting of EIS spectra (Table 15) and applying the equation (32), where  $R_{ct0}$  is the charge transfer resistance for the bare metal and  $R_{ct}$  is the charge transfer resistance in the inhibiting medium.

$$(32) IE\% = \left[ 1 - \frac{R_{ct0}}{R_{ct}} \right] * 100$$

The presence of MBT leads to higher values of IE, 62.9 % for LDH-MBT comparing with 55.4 % for LDH- $\text{NO}_3$ . The modification with polyelectrolytes leads to a significant increase in the IE, 90.9 % for LDH- $\text{NO}_3$ \_LbL and 80.6% for LDH- $\text{NO}_3$ \_Mod. The best IE were verified for LDH-MBT\_LbL and LDH-Mod, with IE values higher than 96%.

**Table 14: LDH-based systems prepared and used in electrochemical impedance measurements. IE values of LDH-based systems in dispersed in 50 mM NaCl in bare AA2024.**

System	2-MBT within LDH	Surface modification with polyelectrolytes by LbL	Cerium-based species between polyelectrolyte layers	IE (%)
LDH- $\text{NO}_3$	No	No	No	55.4
LDH- $\text{NO}_3$ _LbL	No	Yes	No	90.9
LDH- $\text{NO}_3$ _Mod	No	Yes	Yes	80.6
LDH-MBT	Yes	No	No	62.9
LDH-MBT_LbL	Yes	Yes	No	96.5
LDH-Mod	Yes	Yes	Yes	96.0

LDH-MBT\_LbL presented slightly higher inhibition efficiency than LDH-Mod (calculated from the  $R_{ct}$ ). However, the highest oxide resistance observed for LDH- Mod has to be considered when referring the corrosion protection of AA2024. The presence of Ce-based species in LDH-Mod produced a positive effect in increasing the oxide stability of the aluminum substrate, which adds to the high  $R_{ct}$  associated with the presence of 2-MBT. Thus, the combination of both inhibitors,  $\text{Ce}^{3+}$  and 2-MBT, in LDH- Mod contributes to the highest impedance measured among the studied systems.

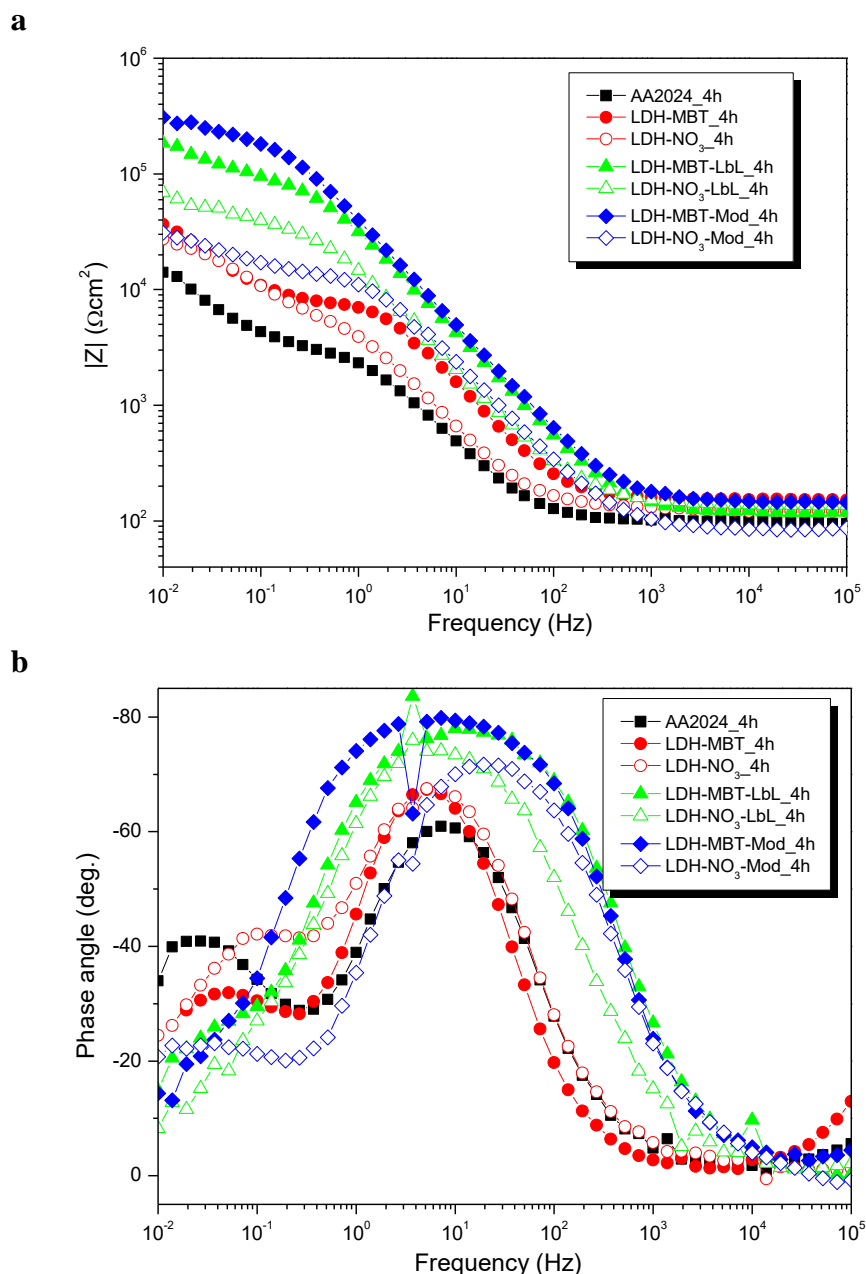


Figure 54: Bode representation of EIS spectra acquired for AA2024 bare substrates after 4 hours of immersion in 50 mM NaCl solution with LDH loaded with NO<sub>3</sub> and 2-MBT, with LbL modification and LbL modification with cerium-based compounds incorporated (Table 2). (a) impedance magnitude and (b) phase angle. [94] Reproduced by permission of The Royal Society of Chemistry (RSC) on behalf of the Centre National de la Recherche Scientifique (CNRS) and the RSC.

The EIS data were fitted using the equivalent circuits depicted in Figure 55. The first circuit (Figure 55 a) was used for systems where the corrosion activity is still low and the relaxation time constant associated with the native aluminum oxide layer is visible. However, a second time constant can be detected already at low frequencies, ascribed to the electrochemical corrosion processes.

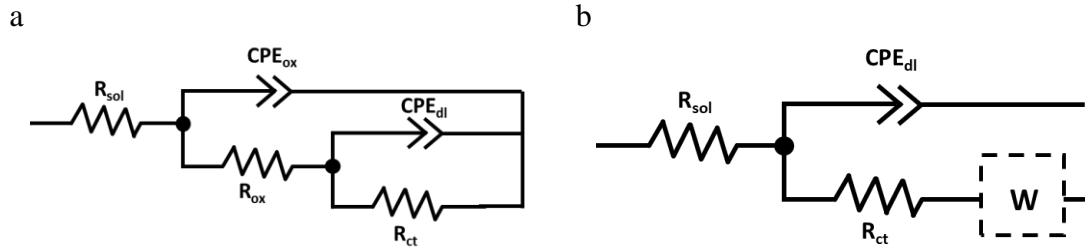


Figure 55: Equivalent circuits used to fit EIS data (Figure 54), summarized in Table 15.

Equivalent circuit b was used when corrosion processes are in more advanced stages. In these cases, the native oxide film response is no longer detected, and only activity associated with corrosion processes and, in more severe cases, mass transport-controlled processes are visible. Table 15 summarizes the main results obtained for the LDHs in solution, after 4 h of immersion in NaCl, Figure 54.

Table 15: Results obtained from the fitting of EIS spectra depicted in Figure 54.

System	$(\chi^2)$	$Y(CPE_{ox})$ $Ss^n cm^{-2}$	$R_{ox}$ $\Omega cm^2$	$Y(CPE_{dl})$ $Ss^n cm^{-2}$	$R_{ct}$ $\Omega cm^2$
Reference	$(9.95 \times 10^{-4})$	-	-	$5.58 \times 10^{-5}$ ( $n=0.879$ )	$3.44 \times 10^3$
LDH-NO <sub>3</sub>	$(1.21 \times 10^{-3})$	-	-	$3.58 \times 10^{-5}$ ( $n=0.897$ )	$7.71 \times 10^3$
LDH-NO <sub>3</sub> -LbL	$(1.91 \times 10^{-3})$	-	-	$1.47 \times 10^{-5}$ ( $n=0.882$ )	$3.81 \times 10^4$
LDH-NO <sub>3</sub> -Mod	$(8.48 \times 10^{-4})$	-	-	$8.79 \times 10^{-6}$ ( $n=0.885$ )	$1.77 \times 10^4$
LDH-MBT	$(7.76 \times 10^{-4})$	-	-	$1.11 \times 10^{-5}$ ( $n=0.944$ )	$9.28 \times 10^3$
LDH-MBT-LbL	$(8.77 \times 10^{-4})$	$5.47 \times 10^{-6}$ ( $n=0.907$ )	$1.08 \times 10^5$	$7.99 \times 10^{-5}$ ( $n=0.972$ )	$9.69 \times 10^4$
LDH-MBT-Mod	$(8.21 \times 10^{-4})$	$4.58 \times 10^{-6}$ ( $n=0.915$ )	$2.46 \times 10^5$	$1.06 \times 10^{-4}$ ( $n=0.990$ )	$8.63 \times 10^4$

The results allowed for some important points to be highlighted: first the combination of 2-MBT and cerium-based compounds indeed impart additional protection to AA2024, when compared to individual systems. Second, the application of polyelectrolyte shells produces a positive effect on the performance of LDHs, possible due to higher control over the inhibitors release and reduction of alkalization effect associated to the presence of LDHs, as discussed by Poznyak and colleagues.[168]

### 5.3.4 LDH modified to provide dual release in solvent-based hybrid sol-gel

The direct addition of corrosion inhibitors to coating formulations are often detrimental to the coating barrier properties. The addition of cerium (III) nitrate and 2-MBT directly to sol-gel based coating has already been reported in the literature, with coating loaded with corrosion inhibitors being compared with undoped coatings. The direct addition of  $\text{Ce}^{3+}$  to a hybrid sol-gel matrix was found to decrease the barrier properties of the coating.[92, 154] Similarly, the direct addition of azole-based corrosion inhibitors into coating formulations,[92, 318] leads to the loss of coating protective properties. In principle, by isolating  $\text{Ce}^{3+}$  and 2-MBT from direct contact with coating matrices one could limit the above referred negative interactions.

In the previous section, the inhibiting properties of LDH-MBT modified with polyelectrolytes and containing  $\text{Ce}^{3+}$  was found to provide the best protection towards AA2024, when added to an aggressive electrolyte solution. However, one can expect that the presence of an outer polyelectrolyte shell may also influence coating/nanocontainer interactions. In this section, the effect of different LDHs in the corrosion protection properties of a solvent-based hybrid sol-gel coating is presented.

Figure 56 presents the EIS spectra for AA2024 substrates coated with a sol-gel coating without LDHs and after addition of LDH-MBT and LDH-Mod. Only one-time constant is observed after 4h of immersion in 0.5 M NaCl (Figure 56a), ascribed to the coating response. The samples can be ranked based on the impedance magnitude at low frequency as follows:  $|Z|(\text{Sg\_Ti\_LDH-MBT}) < |Z|(\text{Sg\_Ti}) < |Z|(\text{Sg\_Ti\_LDH-Mod})$ . The difference between the coatings is related to the variation of the coating barrier properties since the coating capacitance of all the films is similar. After 5 days of immersion, the difference between the coatings becomes clear. The sol-gel coating loaded with LDH-Mod rendered the best results, with the highest impedance magnitude at low frequencies and only one time constant detected, ascribed to the coating response. The other two systems display three-time constants, ascribed to the coating response ( $10^4$  - $10^3$  Hz), oxide response ( $10^1$  Hz), and starting electrochemical activity ( $10^{-2}$  Hz). Sol-gel coatings loaded with unmodified LDH-MBT appears to have lower barrier properties than the reference system, undoped sol-gel. This could be due to the detrimental interaction between 2-MBT and the sol-gel matrix, possibly as a consequence of the release of

2-MBT at the early stages of coating preparation. Nevertheless, the oxide stability is significantly improved and the corrosion onset is delayed.[160]

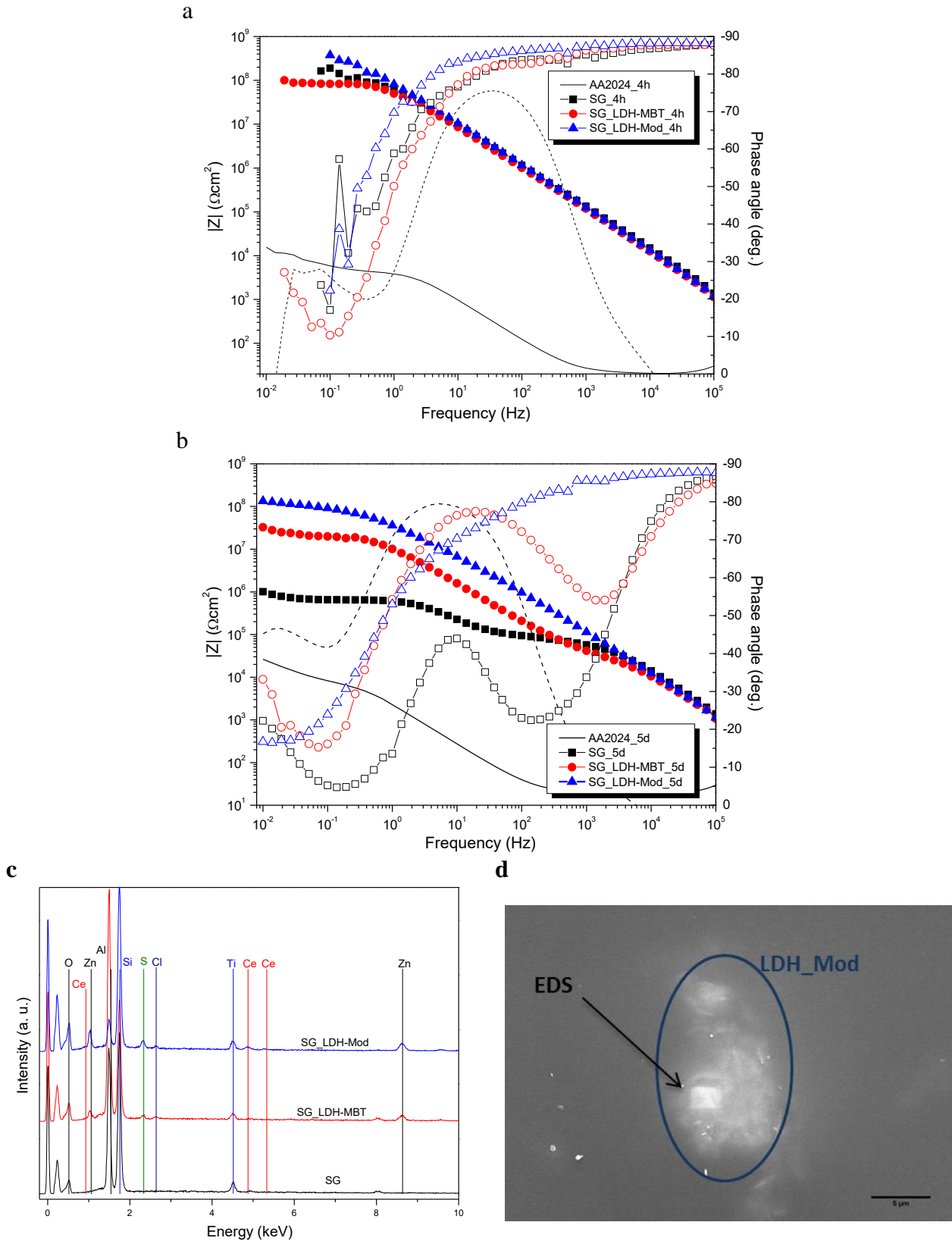


**Figure 56:** Bode representation of EIS spectra for AA2024 coated with sol-gel, and sol-gel loaded with LDH-MBT and LDH-Mod after (a) 4 hours and (b) 5 days of immersion in a 0.5 M NaCl solution. (c) EDS analysis after immersion tests of the coated AA2024 sample in regions with agglomeration of LDHs, as observed in (d).

The EDS analysis for the different systems is presented in Figure 56c. When no LDHs are present in the sol-gel coatings, only the elements belonging to the sol-gel matrix and AA2024 are detected: Ti (4.53 and 4.95 keV), Si (1.75 keV), Al (1.49 keV) and O (0.51 keV). When LDH-MBT is presented in the sol-gel coatings, in addition to the above-referred elements, peaks ascribed to the LDH-MBT are also visible: Zn (1.04 and 8.61 keV) and S (2.33 keV). LDH-Mod besides all the peaks mentioned before shows one additional signal assigned to the successfully incorporated cerium, Ce (4.87 keV). After immersion in 0.5 M NaCl solution LDHs exhibit the presence of chlorides (Cl, 2.63 keV) in the areas where LDHs are concentrated (Figure 56d), possibly as a result of ion exchange with 2-MBT. The LDHs ability to entrap chlorides has been described in a previous work and contributes significantly to the protection of substrates.[154]

In Table 16 the results from the fitting of the EIS plots presented in Figure 56 are presented. The evolution of coating pore resistance until 5 days of immersion is displayed in Figure 57. The fitting was done using the four equivalent circuits shown in Figure 57, which were employed according to the system evolution over the immersion test.[145, 199] The equivalent circuit with one-time constant, Figure 57b, was used when only the coating response was observed ( $CPE_{coat}$  and  $R_{coat}$ ). The equivalent circuit with two-time constants, Figure 57c, was used for systems displaying the response of the natural oxide layer in AA2024 ( $CPE_{ox}$  and  $R_{ox}$ ) together with the coating response. The equivalent circuit in Figure 57e was used when three-time constants were detected: coating response, the native oxide film and electrochemical activity (corrosion processes) at the metal interface. The remaining equivalent circuit in Figure 57d was used when three-time constants were observed: two-time constants belonging to the coating (similar findings have been reported in the literature [319-321]) and a third one ascribed to the AA2024 natural oxide layer.

**Table 16: Results obtained from the fitting of EIS spectra for AA2024 panels coated with a hybrid solvent-based sol-gel (Sg\_Ti) without nanocontainers and loaded with 0.5 wt.% of LDH-MBT and LDH-Mod after 4 hours and 5 days immersion in a 0.5 M NaCl solution, depicted in Figure 56.**

System	Ti me	( $\chi^2$ )	$Y(CPE_{coat})$ $Ss^n cm^{-2}$	$R_{coat}$ $\Omega cm^2$	$Y(CPE_{coat})$ $Ss^n cm^{-2}$	$R_{coat}$ $\Omega cm^2$	$Y(CPE_{ox})$ $Ss^n cm^{-2}$	$R_{ox}$ $\Omega cm^2$	$Y(CPE_{dl})$ $Ss^n cm^{-2}$	$R_{ct}$ $\Omega cm^2$
Sg_Ti	4 h	(1.02x10 <sup>-2</sup> )	2.30x10 <sup>-9</sup> (n=0.933)	1.31x10 <sup>8</sup>						
	5 d	(3.46x10 <sup>-3</sup> )	1.84x10 <sup>-9</sup> (n=0.959)	7.46x10 <sup>4</sup>			1.47x10 <sup>-7</sup> (n=0.830)	6.06x10 <sup>5</sup>	3.27x10 <sup>-5</sup> (n=1)	7.77x10 <sup>5</sup>
Sg_Ti_LDH-MBT	4 h	(5.53x10 <sup>-3</sup> )	2.30x10 <sup>-9</sup> (n=0.949)	8.48x10 <sup>7</sup>						
	5 d	(1.37x10 <sup>-3</sup> )	1.79x10 <sup>-9</sup> (n=0.979)	3.86x10 <sup>4</sup>	1.41x10 <sup>-8</sup> (n=0.873)	2.20x10 <sup>7</sup>	4.36x10 <sup>-7</sup> (n=1)	4.86x10 <sup>7</sup>		
Sg_Ti_LDH-Mod	4 h	(7.81x10 <sup>-3</sup> )	1.86x10 <sup>-9</sup> (n=0.962)	3.34x10 <sup>8</sup>						
	5 d	(3.69x10 <sup>-2</sup> )	3.80x10 <sup>-9</sup> (n=0.903)	1.00x10 <sup>8</sup>						

The results after 4 h of immersion are similar for the three systems, with only one time constant being detected, ascribed to the response of the sol-gel coating. The values of the coating pore resistance indicate some loss of coating barrier properties for Sg\_Ti\_LDH-MBT when compared with the other two systems.  $R_{coat}$  was found to be  $8.48 \times 10^7 \Omega\text{cm}^2$  for the latter system, which compares with  $1.31 \times 10^8 \Omega\text{cm}^2$  and  $3.34 \times 10^8 \Omega\text{cm}^2$ , for Sg\_Ti and Sg\_Ti\_LDH-Mod, respectively.

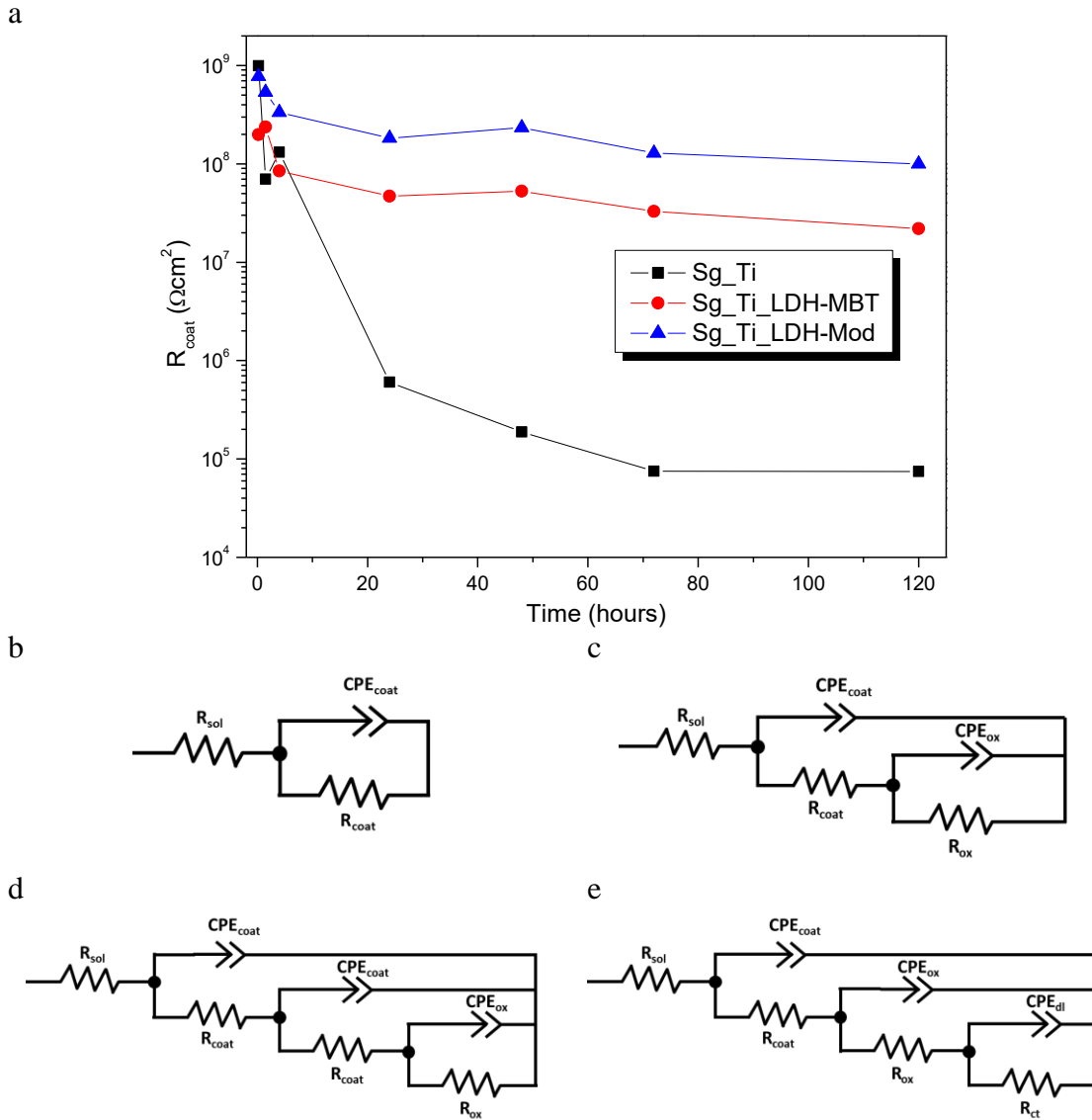
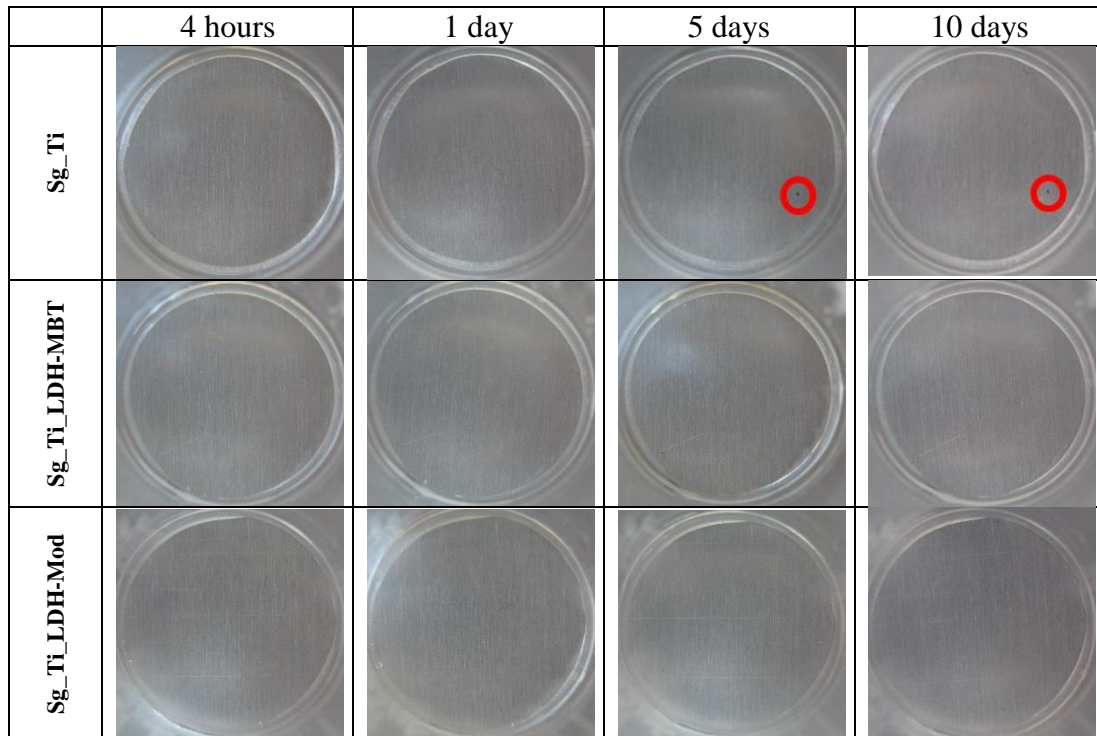


Figure 57: Evolution over time of the  $R_{coat}$  for AA2024 panels coated with a hybrid solvent-based sol-gel (Sg\_Ti) without nanocontainers and loaded with 0.5 wt.% of LDH-MBT and LDH-Mod immersed in 0.5 M NaCl solution. Equivalent circuits used to fit EIS data (Figure 56), summarized in Table 16.

After 5 days of immersion the systems give three different responses, with Sg\_Ti\_LDH-Mod only displaying one time constant (coating), Sg\_Ti three-time constants and Sg\_Ti\_LDH-MBT also three time constants. The values of  $R_{coat}$  are

indicative of the coating barrier properties, with Sg\_Ti\_LDH-Mod presenting values around  $1.00 \times 10^8 \Omega\text{cm}^2$  and the other two systems with values 1 and 4 orders of magnitude lower,  $2.20 \times 10^7 \Omega\text{cm}^2$  for Sg\_Ti\_LDH-MBT and  $7.46 \times 10^4 \Omega\text{cm}^2$  for Sg\_Ti. These results are in agreement with the photographs presented in Figure 58, where only Sg\_Ti presents signs of corrosion, in the form of one small pit after 5 days of immersion.



**Figure 58: Photographs of AA2024 coated with a hybrid solvent-based sol-gel (Sg\_Ti) without nanocontainers and loaded with 0.5 wt.% of LDH-MBT and LDH-Mod, added to the formulation as a water-based slurry. Photographs obtained after 4 hours, 1 day, 5 days and 10 days immersion in a 0.5 M NaCl solution.**

## 5.4 Partial conclusions

In this section, the possibility of using LDH as a nanocontainer for two corrosion inhibitors in order to enhance its corrosion protection properties as well as tune its release profile was described. LDHs were loaded with two corrosion inhibitors, directly with 2-MBT (in anionic form) and indirectly with cerium (III) nitrate. The first one was intercalated by ion-exchange, whereas the second one was incorporated by layer-by-layer (LbL) method, between polyelectrolyte layers adsorbed on the LDH nanoplatelets. The structural and compositional data showed that LDH behaves as a dynamic system during the LbL process, exchanging part of the anionic inhibitor previously intercalated with species available in cerium- and polyelectrolyte-containing aqueous solutions. Furthermore, cerium was incorporated in the nanocontainers, both as nano-sized crystalline  $\text{CeO}_2$  as well as in amorphous forms. The modification of LDHs with polyelectrolytes changes the main triggering conditions of release of inhibitors intercalated within layered double hydroxides, from ion exchange with aggressive species (NaCl) to pH-dependent release (spectrophotometric data). Bearing in mind that most of the corrosion sites can have significant changes in solution pH, this provides opportunities to transform LDH into active nanocontainers able to respond to the presence of chlorides and/or to local changes in pH when corrosion processes are occurring.

The addition of modified layered double hydroxides to sol-gel formulations was found to impart the highest barrier properties and active corrosion protection. These results open prospects for development of smart-coatings based on nanocontainers with dual release of active species, to enhance a specific functionality or combine different functionalities.



# 6

## Gluconate-containing LDHs

### Soneto ditado na agonia

*Já Bocage não sou!... À cova escura  
Meu estro vai parar desfeito em vento...  
Eu aos Céus ultrajei! O meu tormento  
Leve me torne sempre a terra dura;*

*Conheço agora já quão vã figura,  
Em prosa e verso fez meu louco intento:  
Musa!... Tivera algum merecimento  
Se um raio da razão seguisse pura.*

*Eu me arrependo; a língua quasi fria  
Brade em alto pregão à mocidade,  
Que atrás do som fantástico corria:*

*Outro Aretino fui... a santidade  
Manchei!... Oh! Se me creste, gente ímpia,  
Rasga meus versos, crê na eternidade!.*

**Bocage, in 'Rimas'**



The versatility of LDHs to work as containers for corrosion inhibitors has been assessed in the previous section using 2-MBT, a corrosion inhibitor already described in the literature.[168] In this section, a different corrosion inhibitor incorporated in the LDHs is presented: gluconate. The results obtained show that gluconate has inhibiting properties towards galvanized and cold rolled steel. Moreover, the functional application of LDH loaded with gluconate into commercial coatings was analyzed, giving particular attention to its surface modification with polyelectrolytes as a viable approach to decrease coating/nanocontainer detrimental interactions, to improve coating barrier properties.

## 6.1 LDHs containing gluconate

The incorporation of gluconate into LDH galleries was achieved by an ion exchange process between  $\text{NO}_3^-$  and gluconate, following the procedure described in section 4.2.1. The exchange was done with the nanocontainers in a suspension over two cycles of 24 hours, with the replacement of the sodium gluconate (NaGluc) solution between cycles. The resulting material was characterized by ATR-FTIR and XRD.

The ATR-FTIR spectra acquired for NaGluc, LDH loaded with  $\text{NO}_3^-$  (LDH- $\text{NO}_3$ ) and gluconate (LDH-Gluc) are presented in Figure 59, with the main peaks listed in Table 17. The detailed analysis of the LDH- $\text{NO}_3$  spectrum have been presented in the previous section 5.1 and are in agreement with the literature.[295]

**Table 17: Main FTIR peaks observed in the LDH- $\text{NO}_3$ , LDH-Gluc and NaGluc spectra.**

Sample	FTIR main bands			
LDH- $\text{NO}_3$	Between 4000 $\text{cm}^{-1}$ and 3000 $\text{cm}^{-1}$ $\nu(\text{OH})$	1643 $\text{cm}^{-1}$ $\delta_{\text{HOH}}$ mode of water	1342 $\text{cm}^{-1}$ $\nu_2$ mode of the $\text{NO}_3$	
LDH-Gluc	Between 4000 $\text{cm}^{-1}$ and 3000 $\text{cm}^{-1}$ $\nu(\text{OH})$	1585 $\text{cm}^{-1}$ $\nu$ asym (C=O)	1380 $\text{cm}^{-1}$ $\nu$ sym (C=O)	1085 $\text{cm}^{-1}$ C-O stretching mode
NaGluc		1612 $\text{cm}^{-1}$ $\nu$ asym (C=O)	1396 $\text{cm}^{-1}$ $\nu$ sym (C=O)	1093 $\text{cm}^{-1}$ C-O stretching mode

The successful intercalation of gluconate is verified firstly by the presence of new bands in the LDH-Gluc spectrum at 1029  $\text{cm}^{-1}$  and 1085  $\text{cm}^{-1}$  ascribed to the  $\nu(\text{C-O})$  of the primary and secondary alcohol groups, respectively.[322, 323] LDH-Gluc FTIR spectrum presents two bands with identical intensity at 1380  $\text{cm}^{-1}$  and at 1585  $\text{cm}^{-1}$ , respectively, ascribed to the symmetric,  $\nu_{\text{sym}}(\text{C=O})$ , and asymmetric,  $\nu_{\text{asym}}(\text{C=O})$ , stretching modes of the carboxylate anion.[322]

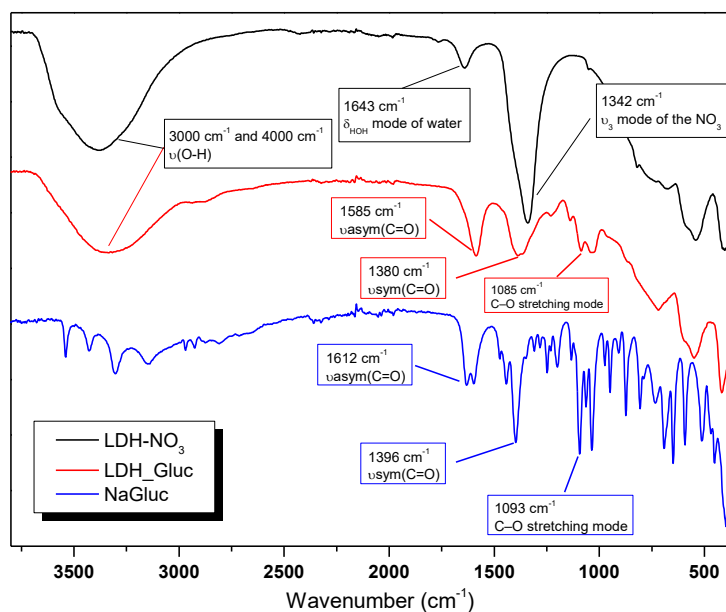


Figure 59: FTIR spectra of NaGluc, LDH-NO<sub>3</sub>, and LDH-Gluc.

The FTIR also gave some indications concerning possible interactions between gluconate in the LDH structure. The redshift observed for  $\nu_{\text{sym}}(\text{C}=\text{O})$  band, from 1396  $\text{cm}^{-1}$  to 1380  $\text{cm}^{-1}$ , and  $\nu_{\text{asym}}(\text{C}=\text{O})$  band, from 1612  $\text{cm}^{-1}$  to 1585  $\text{cm}^{-1}$ , could indicate interactions between the carbonyl group of the gluconate and the LDH structure that leads to a decrease in the C=O strength.[324]

The LDH diffractograms for LDH-NO<sub>3</sub> and LDH-Gluc are presented in Figure 60, with the main peaks set in a  $2\theta$  interval between 4° and 40°. LDH-NO<sub>3</sub> is characterized by three well-defined peaks at 9.96° (003), 19.96° (006) and 30.04° (009). The (003) peak position was used to calculate the basal spacing, with a value of 8.92 Å which is consistent with reported data for Zn-Al LDHs intercalated with NO<sub>3</sub><sup>-</sup>. [99, 154, 168] Assuming a brucite-like structure, the thickness of the cationic sheets is estimated to be 4.77 Å. By subtracting this value to the basal spacing one finds a gallery height of 4.15 Å.[325] The difference between the galleries height and the NO<sub>3</sub><sup>-</sup> diameter (3.78 Å) can be attributed to the fact that some of the NO<sub>3</sub><sup>-</sup> groups are in a planar structure in a vertical alignment, together with the presence of water that could lead to the increase of interlayer spacing.[97, 326, 327]

The LDH-Gluc diffractogram presents four major peaks in the interval between 4° and 40° set in  $2\theta$ . The peaks appear at 6.37°, 12.62°, 18.95° and 25.36°, with the first three peaks corresponding to (001) fundamental reflections (003), (006) and (009), respectively. Estimation of interlayer distance using the (003) peak position yields values around 13.9 Å, and a gallery height of approximately 9.13 Å. This increase in gallery

height, compared to LDH-NO<sub>3</sub>, is related to the larger size of the intercalated gluconate anion, leading to the expansion of the LDH gallery.[295] Altogether, FTIR and XRD results are a strong indication that the gluconate incorporation into the LDH galleries was successful. The (around 60°) reflection peak for LDH-NO<sub>3</sub> and LDH-Gluc did not suffer any changes indicating that the cation composition of the hydroxide layers was not affected by the ion exchange, as observed with LDH-MBT (section 5.1).

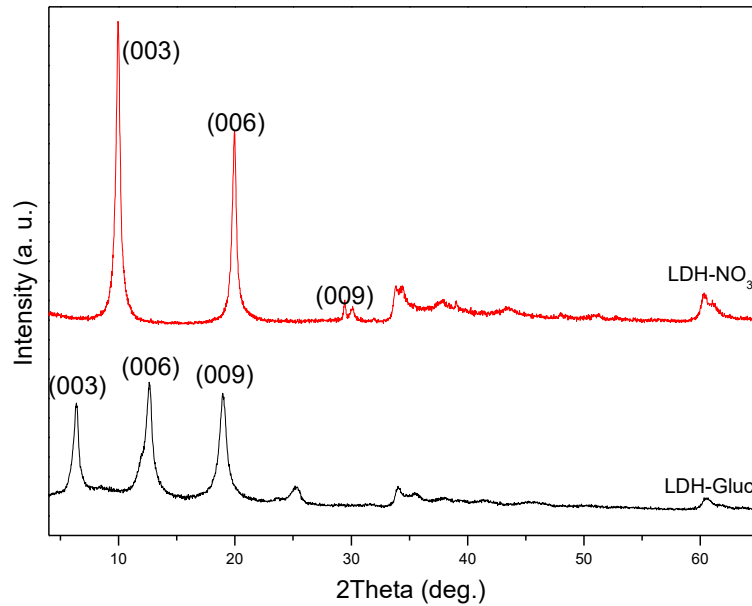


**Figure 60: XRD patterns of LDH-NO<sub>3</sub> and after intercalation of NaGluc, LDH-Gluc.**

## 6.2 LDH modification with polyelectrolytes

The main purpose behind the LDHs surface modification is to change its surface properties aiming at the improvement of compatibility between LDH and polymeric formulations. This change can also induce changes in terms of release mechanism, extent and trigger conditions. As presented in Chapter 5, the modification of LDHs with polyelectrolytes can improve compatibility/stability within a coating matrix, while making the release of the inhibitor more sensitive to pH changes.

Two negatively charged polyelectrolytes were selected to modify LDH-Gluc surface. One was selected to work as a reference, PSS, due to the extensive work available in the literature in which PSS is applied in LbL systems.[192, 195] The second, alginate, was selected based on three main characteristics: cost, ease of application (with industrial applications in mind) and environmental sustainability.

### 6.2.1 Structural characterization

The successful modification of the LDH surface was verified by conventional ATR-FTIR and supported by the determination of zeta potential. The LDH structural and morphological properties after modification were assessed by XRD and SEM, respectively.

The FTIR spectra of LDH modified with alginate are presented in Figure 61. The FTIR spectrum of sodium alginate is characterized by the presence of bands between  $3000\text{ cm}^{-1}$  and  $3600\text{ cm}^{-1}$ , associated with the stretching vibration of O-H bonds, and bands at  $1594\text{ cm}^{-1}$  ( $\nu_{\text{asym}}(\text{COO}^-)$ ) and  $1405\text{ cm}^{-1}$  ( $\nu_{\text{sym}}(\text{COO}^-)$ ) ascribed to the asymmetric and symmetric stretching vibrations of the carboxylate, respectively.[328, 329] The spectrum of LDH-NO<sub>3</sub>\_Alg (Figure 61a), in addition to the characteristic bands of LDH-NO<sub>3</sub>, exhibits also bands that can be attributed to the presence of alginate. At  $1026\text{ cm}^{-1}$  a band associated with the C-O stretching mode of the alginate molecule can be observed. A shift of the band occurring at  $1641\text{ cm}^{-1}$  to  $1622\text{ cm}^{-1}$  is also observed and could be the result of interference by the band at  $1594\text{ cm}^{-1}$ , associated with the  $\nu_{\text{asym}}(\text{COO}^-)$  of the alginate. In the case of LDH-Gluc, the modification of LDH with alginate does not produce new bands, which may be due to overlapping of gluconate and alginate main vibration modes, as observed in Figure 61b.

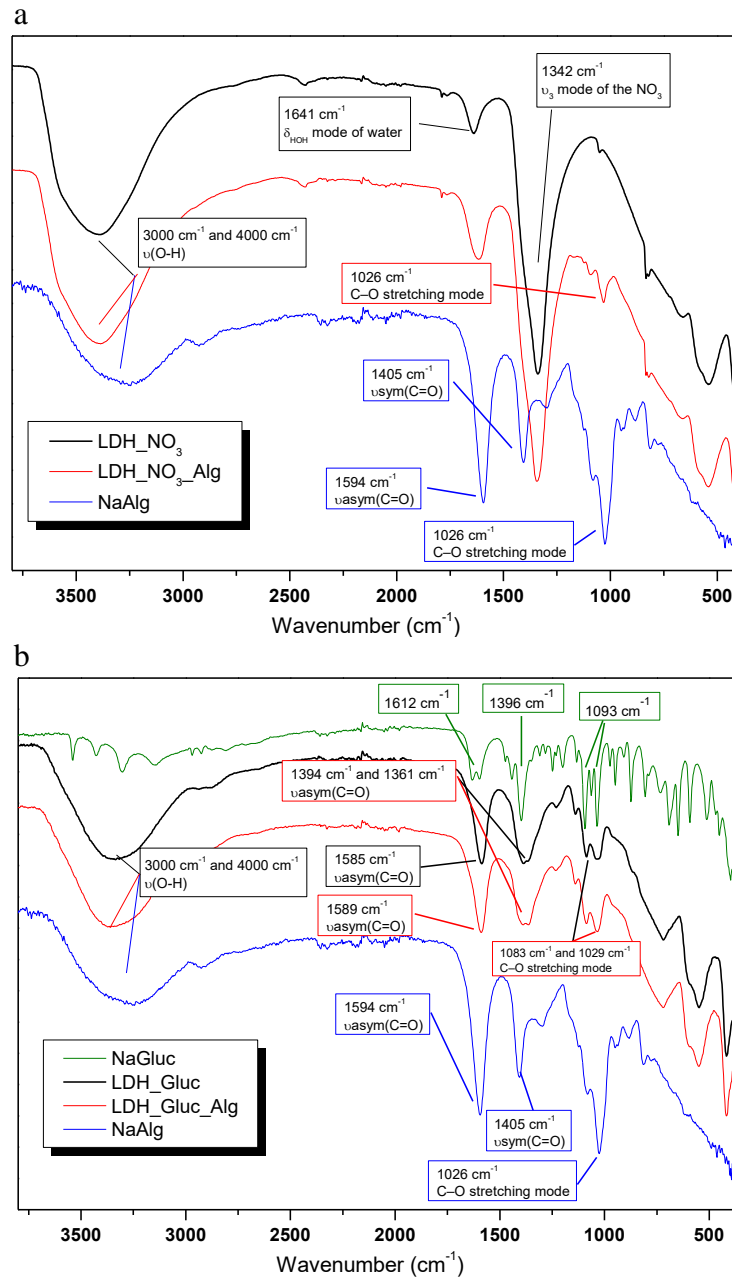


Figure 61: FTIR spectra for LDH-NO<sub>3</sub> (a) and LDH-Gluc surface modification with alginate.

In comparison with LDH-Gluc\_Alg, LDH-Gluc\_PSS provides a spectrum with new bands, confirming the successful modification of the LDH-Gluc, as shown in Figure 62. The FTIR spectrum for PSS shows characteristic bands at 1126 cm<sup>-1</sup> associated with the S-O stretching of the SO<sub>3</sub>H group, at 1035 cm<sup>-1</sup>, ascribed to the antisymmetric vibration in the SO<sub>3</sub><sup>-</sup> and at 1005 cm<sup>-1</sup>, which corresponds to the in-plane bonding vibration of the phenyl ring.[299] In the spectrum of LDH-Gluc\_PSS is possible to identify all three characteristic bands, in particular, the bands at 1035 cm<sup>-1</sup> and 1005 cm<sup>-1</sup>.

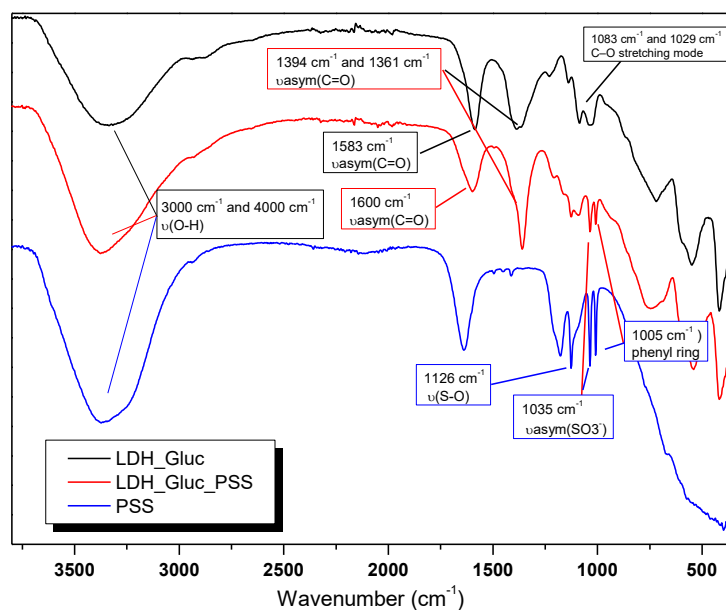


Figure 62: FTIR spectra for LDH-Gluc surface modification with PSS.

The XRD diffractograms for LDH-Gluc modified with alginate and PSS (Figure 63) show no significant changes comparing with LDH-Gluc, except for the relative intensity of the peaks. In addition, the (110) reflection peak shows no shift, which indicates the inexistence of changes in the composition of the metal hydroxide layers.

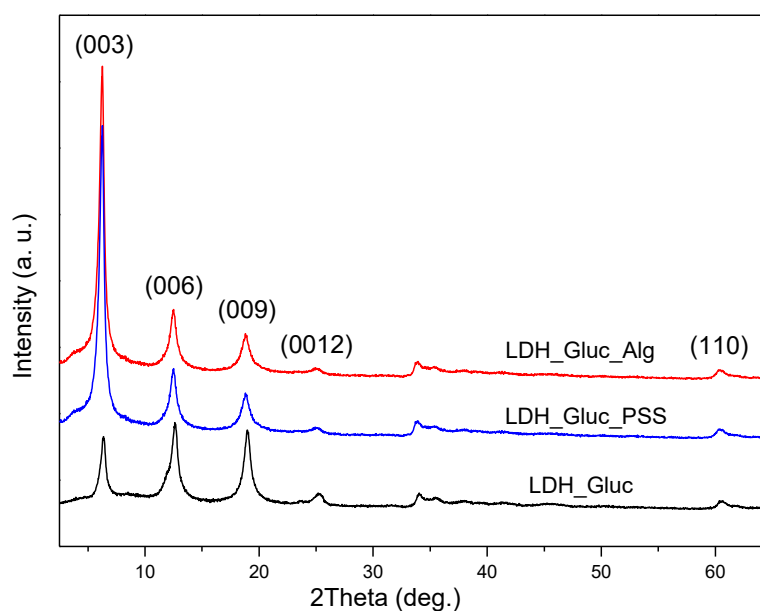
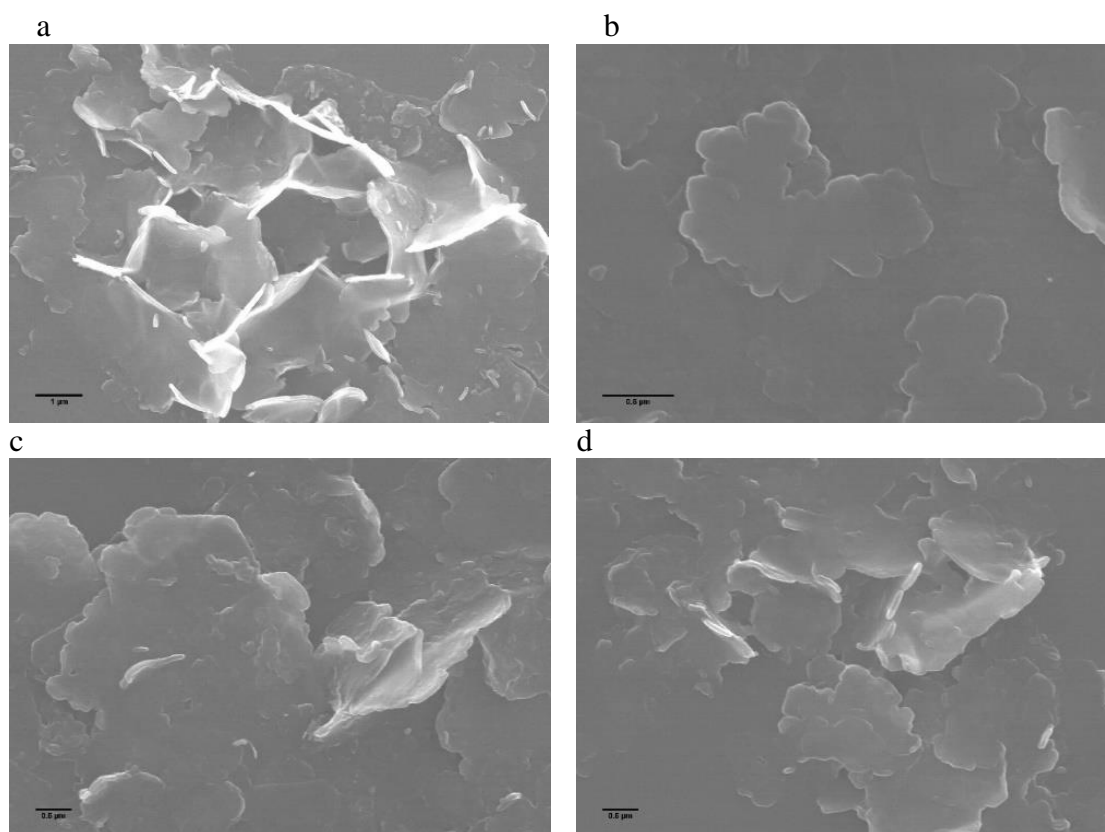


Figure 63: XRD patterns of LDH-Gluc and of LDH-Gluc after modification with alginate (LDH-Gluc\_Alg) and PSS (LDH-Gluc\_PSS).

The morphology of LDH after the modification was assessed by SEM (Figure 64). The Zn/Al LDH-NO<sub>3</sub> used in this work presents a plate-like morphology with average

size within the sub-micrometer range, and height around 50 nm (Figure 64a). The incorporation of gluconate has no impact on the overall morphology of LDH plates (Figure 64b). Similar results are observed after modification with PSS or alginate (Figure 64c for PSS and Figure 64d for alginate). The lack of significant changes in LDH morphology is regarded as positive, thereby ensuring the non-destructive character of the modification.



**Figure 64:** SEM micrographs of LDH-NO<sub>3</sub> (a), LDH-Gluc (b), LDH-Gluc\_PSS (c) and LDH-Gluc\_Alg (d).

The measurement of zeta potential can indicate the existence of changes at a surface level in the LDH. The incorporation of a negatively-charged polyelectrolyte is expected to change the electric potential of the interfacial double layer, from positive values, observed for LDH-Gluc, to negative ones, after modification. This assumption was confirmed for PSS (Table 18). The zeta potential values for LDH-Gluc changes from values around +13.9 mV to negative values around -8.3 mV for LDH-Gluc\_PSS, at neutral pH. The modification with alginate does not produce significant changes in the zeta potential values, with values around +12.3 mV, being difficult to determine the success of the modification by this method. This result could be a consequence of the insufficient charge density of the polyelectrolyte, which does not allow it to fully counter balance the LDHs surface charge, with only a small decrease from 13.9 to 12.3 mV. The

insufficient coverage of the alginate compared with PSS could be related with differences in the number of charged groups, as verified by the values of  $pK_a$  around 1 (PSS) and 3.5-4.5 (alginate).[330, 331]

**Table 18: Zeta potential values of LDH-Gluc and LDH-Gluc modified with PSS and alginate in distilled water.**

	LDH-Gluc	LDH-Gluc_PSS	LDH-Gluc_Alg
<b>Zeta potential (mV)</b>	+13.9	-8.3	+12.3

## 6.2.2 Inhibitor release studies

Loading a corrosion inhibitor into a nanocontainer is not the ultimate aim *per se*. In corrosion protection, the goal is to achieve a controlled release. The encapsulation or immobilization process must be designed in a way that the inhibitor is kept stored during coating formulation processing, storage and application, since a premature release could result in highly adverse consequences for the final coating properties. On the other hand, the ability to hold indefinitely the corrosion inhibitor will be also counterproductive, since no inhibitor will reach the corrosion sites. Hence, a compromise between the ability of the nanocontainer to hold the inhibitor must be matched with the ability to release it when necessary. The present work was developed together with TATA STEEL Europe. The selection of alginate with respect to PSS was driven by its environmental advantages and the preliminary results performed in coatings, which indicate alginate as an excellent option to modify the LDH surface.

The release profile of a corrosion inhibitor from the nanocontainer provides relevant information concerning the way it will work under different conditions. One of the major advantages of LDH is the ability to release inhibitor in a controlled way, by an ion exchange mechanism. This feature applied to LDH-Gluc allows for the release of gluconate at the same time that  $Cl^-$  are trapped into the LDH galleries, thus decreasing the aggressiveness of the medium.[154] Due to the LDH dependence on  $Cl^-$  concentration to release gluconate, it is relevant to survey the release profiles of this active species under different NaCl concentrations.[154]

In Figure 65 the release profile of LDH-Gluc and LDH-Gluc\_Alg are depicted for three NaCl concentrations: 5 mM, 50 mM, and 500 mM. From the release studies, two relevant trends for alginate-modified samples are visible: the decrease in the amount of

inhibitor released for short immersion times and a correlation between the amount released and the NaCl concentration.

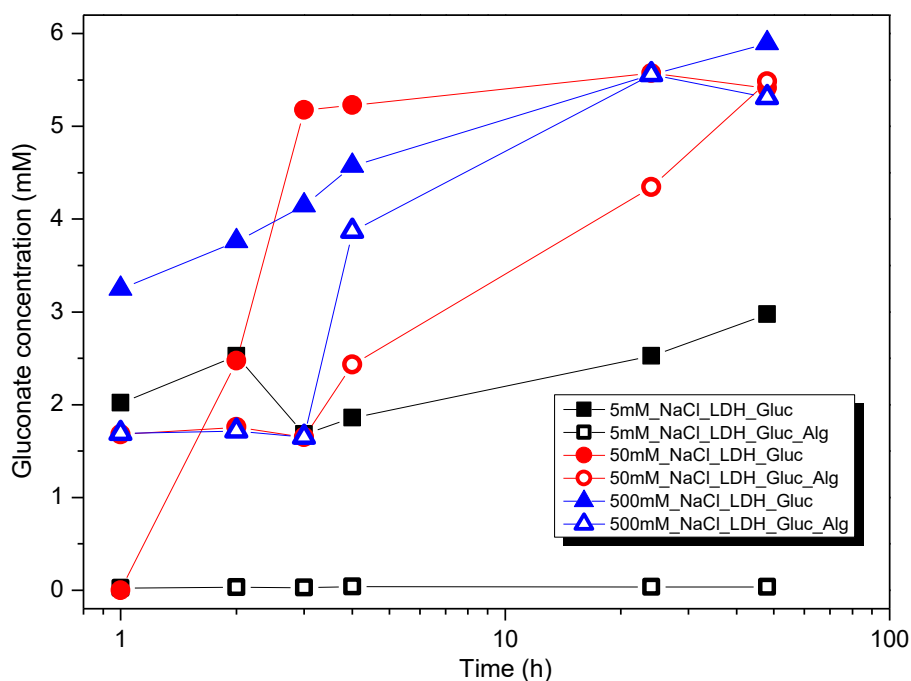


Figure 65: Gluconate release profiles for LDH-Gluc under different NaCl concentrations.

LDHs modified with alginate show a decrease in the amount of gluconate released for all the NaCl concentrations investigated, compared to unmodified nanocontainers. This difference is more relevant for low NaCl concentrations, though. For high NaCl concentrations, the differences tend to decrease as time progresses. In the case of unmodified LDH-Gluc, the increase in released gluconate follows the expected trend based on the anion-exchange mechanism, reported in previous studies. There is a direct correlation between the concentration of chlorides and the extent of the inhibitor released.[168] With the modification using alginate this trend seems to persist but the presence of alginate induces additional effects. This can be explained by the dependence on the permeability of polyelectrolytes on ionic strength.[306, 310, 332]

The maximum amount of gluconate released was obtained for higher NaCl concentrations of 50 mM and 500 mM. The presence of alginate does not impair the inhibitor release at such high NaCl concentrations, with 5-6 mM gluconate released after 48 hours of immersion, which is consistent with the literature where a relation between the polyelectrolyte response to the ionic strength is described.[332] For 5 mM NaCl the amount of gluconate release is considerably smaller, around 2.5 mM for LDH-Gluc with

a negligible amount for LDH-Gluc\_Alg. The negligible amounts of Gluc released under low NaCl concentration for the modified LDHs further emphasizes the polyelectrolyte dependence on the ionic strength to release inhibitor. It appears that in such reduced ionic strength medium the alginate shell becomes less permeable, thus preventing a premature release of inhibitor.[332]

The results above mentioned prove the adjustable nature of LDH-Gluc, with higher amounts of inhibitor being release when in presence of a more aggressive media, higher concentrations of NaCl. The modification with alginate does not change this characteristic but rather enhances it. Modified LDH releases the same amount of inhibitor but in a less pronounced way. In less aggressive media, lower NaCl concentrations, the alginate suppresses the release of inhibitor, probably due to the smaller ionic strength of the media. The fact that LDH-Gluc\_Alg is not sensitive to low ionic-strength media can be an advantage when considering its application in coatings, as a possibility to tune the extent of release for a higher concentration of NaCl, thus keeping the inhibitor stored until harsh conditions can occur.

### **6.2.3 Stability of the nanocontainer**

The surface chemistry plays an important role in the stability and dispersibility of nanocontainers when added to coating formulations. Encasing the LDH in a polyelectrolyte shell can help to prevent the direct interaction between nanocontainer and other formulation components. The corrosion protection properties of LDH-Gluc in this thesis were tested in a water-borne coating formulation provided by TATA STEEL Europe. Therefore, the stability of LDHs was assessed in water. Only studies performed in LDH-Gluc\_Alg are presented for the same reasons presented above for the release studies, namely decisions taken in the frame of the industrial project in which was developed.

In Figure 66 photographs of LDH-NO<sub>3</sub>, LDH-Gluc and LDH-Gluc\_Alg suspensions in water at different times are shown. The nanocontainers were added as a water-based slurry, 0.5 wt.%. Immediately after the formation of the suspension, no significant changes were found between them. After 1 hour, some differences started to be visible, with LDH-NO<sub>3</sub> slightly less stable than LDH-Gluc, with phase separation and occurrence of deposits being detected in the former case.

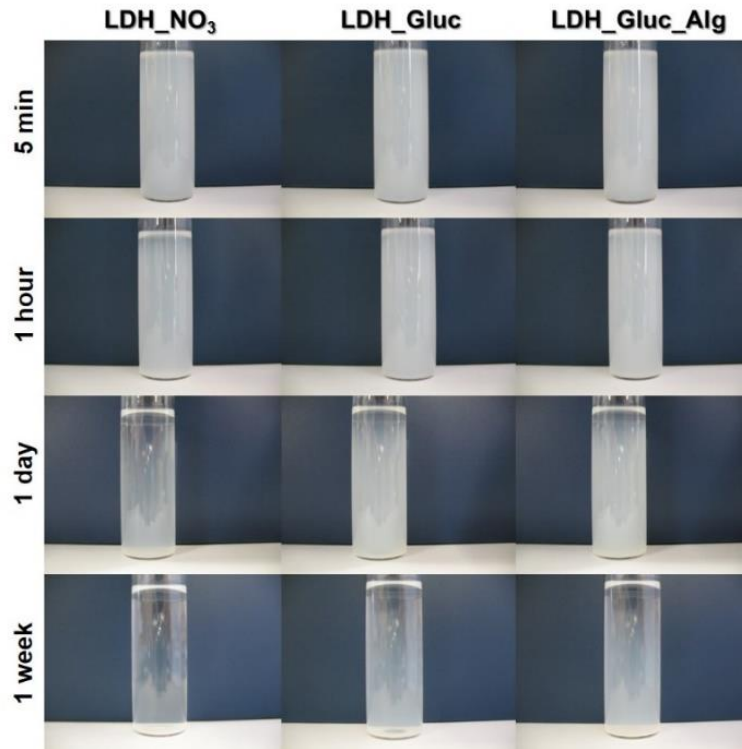


Figure 66: LDH-NO<sub>3</sub>, LDH-Gluc and LDH-Gluc\_Alg suspension stability in water over time.

After one week LDH-NO<sub>3</sub> powders appeared almost completely deposited, with LDH-Gluc and LDH-Gluc\_Alg presenting some deposits, but with a considerable amount of nanocontainers still in suspension. It is not possible to infer stability improvements from the surface modification with alginate, results that are in line with the values of zeta potential obtained for LDH-Gluc (+12.9) and LDH-Gluc\_Alg (+12.3), which showed a minor variation. Nevertheless, the modification does not affect negatively the system.

## 6.3 Galvannealed steel and cold rolled steel substrates

### 6.3.1 Morphological and chemical properties

The metals used in the frame of this thesis were subjected to surface pretreatments. The resulting surface-treated substrates were studied in which concerns their morphological, chemical and electrochemical properties. The morphology was studied by SEM and AFM, whereas the relation between surface chemistry and corrosion processes was assessed by EDS and EIS analysis, respectively.

Figure 67 depicts SEM micrographs of galvannealed steel (GS) (a) and cold rolled steel (CRS) (b) at different magnifications after pretreatment (industrial cleaning), consisting of a degreasing process that follows an industrial approach, alkaline cleaning using a 2 wt.% aqueous solution of industrial cleaner 219 (CS 4994) heated up to 58-60 °C (recall experimental section 4.1.2). Morphologically, the two substrates are significantly different, with CRS considerably smoother than GS. This was expected since CRS is processed under a cold roll system with no further treatments, which tends to create flat surfaces (Figure 67b). In the case of GS, after the preparation of the steel sheet, it was immersed in a bath of molten zinc followed by a second temperature treatment to ensure the formation of a Fe/Zn alloy. This process resulted in changes in terms of the microstructure. The surface is characterized by flat, smooth areas separated by depressions with filiform-like structures 2 μm wide and several microns long (>10 μm), with grains between them (Figure 67a).

The elemental characterization of the metal surface, obtained using EDS analysis (Figure 68), provided the expected results: Fe as the main element in CRS and Zn in GS. GS also show some traces of Fe since the technique allows for the detection of elements several microns in depth. The Fe detected is probably part of a Zn-Fe alloy that makes the delta phase, which comprises most of the Zn protective layer. The zinc layer, in their different phases, is around 14 μm thick.[333]

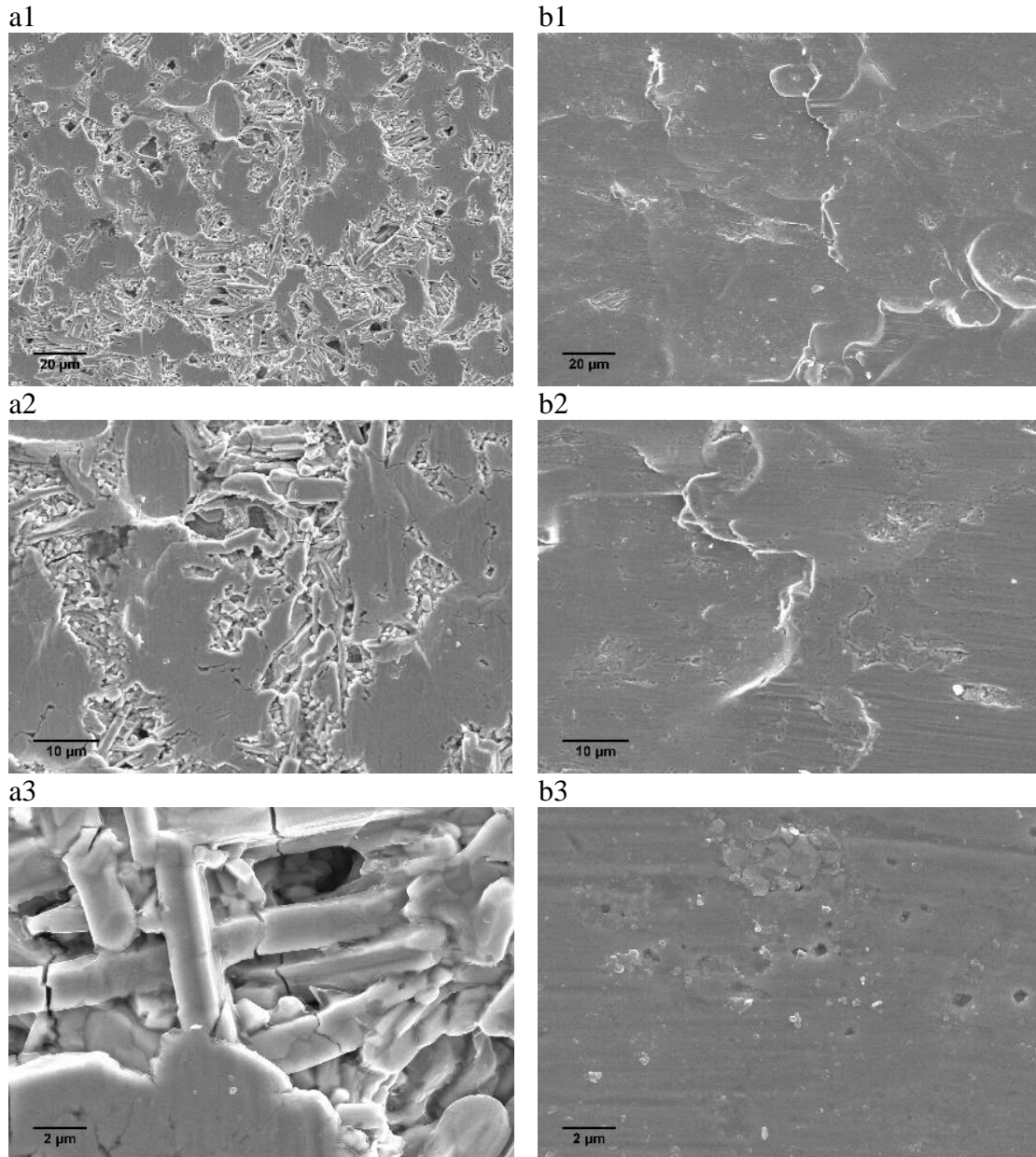


**Figure 67:** SEM pictures of GS (a) and CRS (b) after industrial cleaning. Magnification: a1 and b1 x600; a2 and b2 x1.50k; a3 and b3 x6.00k.

The surface roughness was quantified by AFM. Figure 69 depicts the AFM topographic images for GS (a) and CRS (b) for different surface areas. Firstly, the topographic images are in agreement with SEM micrographs, showing the presence of “holes” for GS comparing with the smoother CRS surface. This was confirmed by the average values of roughness obtained for different scanned areas. The decrease in the values of roughness with the scan size is a consequence of the decrease in the selected area, although the microstructure features being the same.

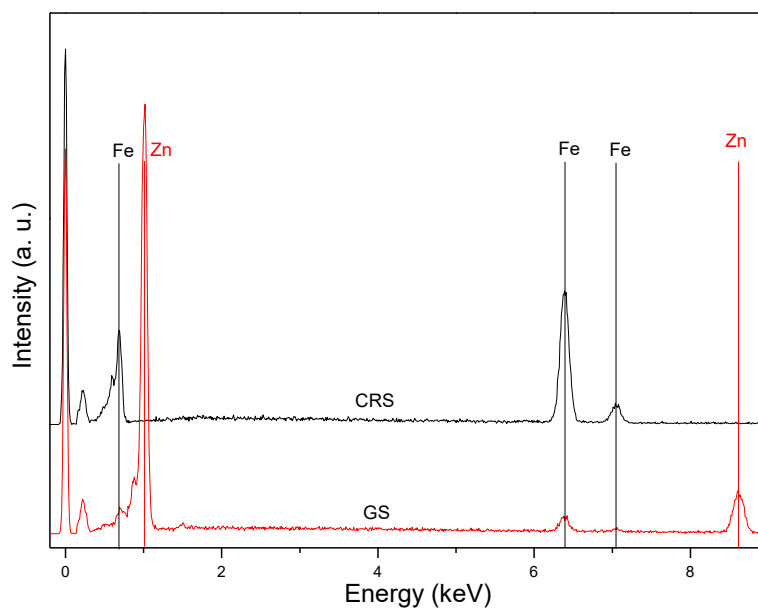


Figure 68: EDS analysis of GS and CRS cleaned samples.

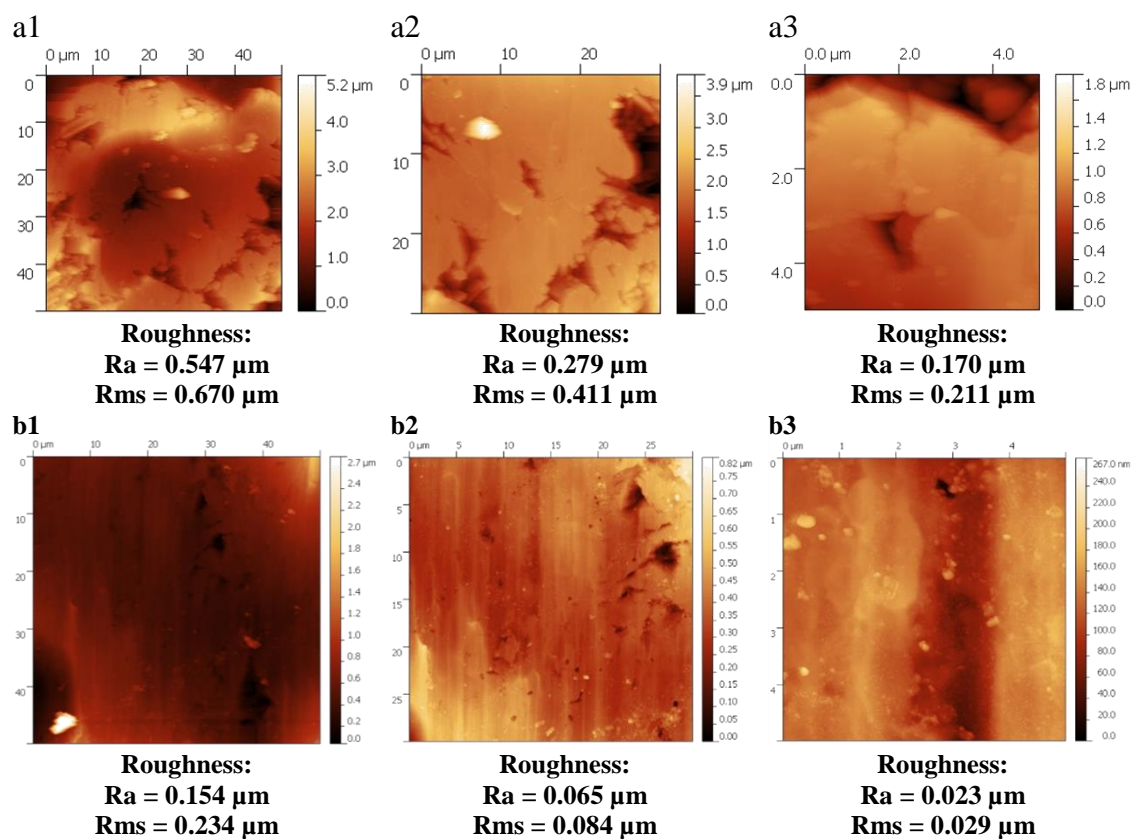


Figure 69: AFM topographic images for GS (a) and CRS (b) for different areas: 50x50 μm (1), 30x30 μm (2) and 5x5 μm (3).

### 6.3.2 Electrochemical characterization in NaCl solution

The behavior of GS and CRS substrates in NaCl solution was assessed by EIS. In Figure 70 Bode representation of EIS spectra for GS substrates immersed in 50 mM NaCl are presented, together with optical photographs of the substrates under testing. Analyzing the substrates for immersion times of 90 minutes, 1 day and 3 days, it is possible to detect the appearance of white deposits, probably zinc hydroxide/oxide corrosion products. This assumption is consistent with the evolution of EIS spectra.

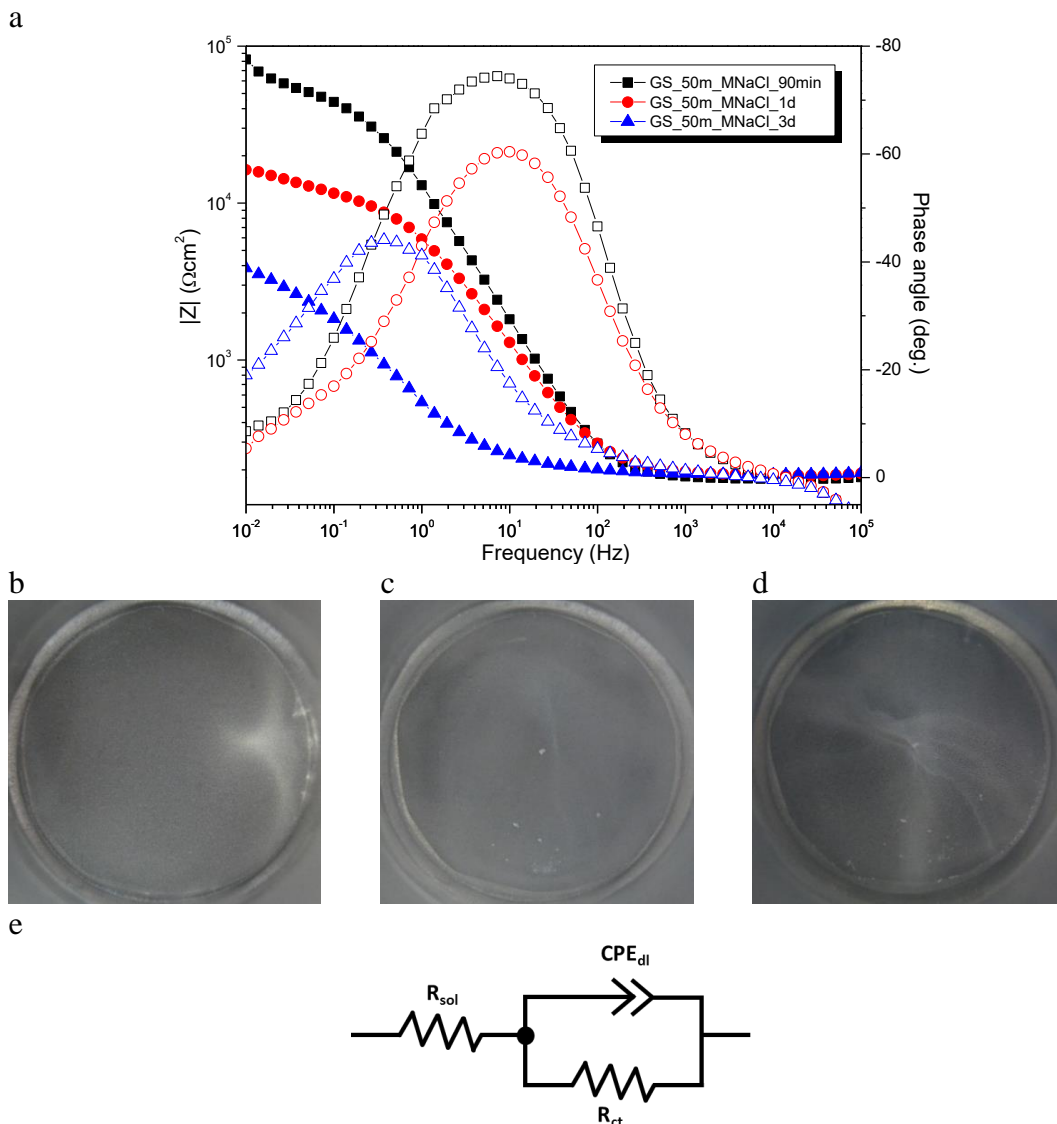
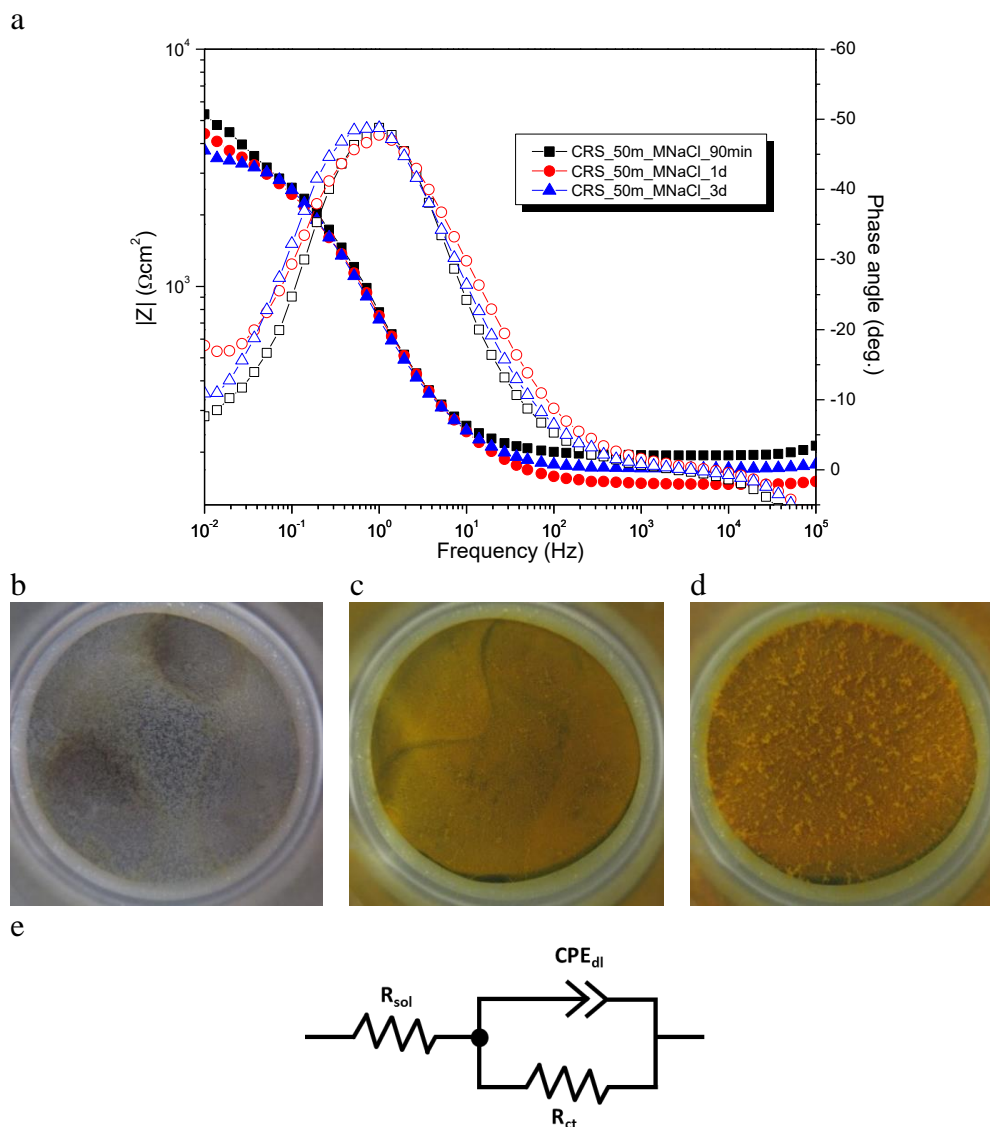


Figure 70: Bode representation of EIS spectra acquired for GS substrates after 90 minutes, 1 day and 3 days immersion in 50 mM NaCl solution (a). The surface of GS test samples after 90 minutes (b), 1 day (c) and 3 days (d). Equivalent circuit used in the interpretation of the data presented in Bode representations (e).

The overall impedance magnitude values at low frequencies decrease more than one order of magnitude after 3 days of immersion. The time constant occurring at intermediate frequencies is associated with the ongoing electrochemical processes and

may be represented by charge transfer resistance ( $R_{ct}$ ) in parallel with double layer capacitance ( $CPE_{dl}$ ), Figure 70e. In addition, a low-frequency time constant not well resolved seems to occur, which may be associated with mass transport controlled processes.



**Figure 71:** Bode representation and phase angle of EIS spectra acquired for CRS substrates after 90 minutes, 1 day and 3 days immersion in 50 mM NaCl solution (a). CRS test samples after 90 minutes (b), 1 day (c) and 3 days. Equivalent circuit used in the interpretation of the data presented in Bode representations (e).

Contrastingly, CRS does not have a Zn protective layer, resulting in the widespread corrosion on its surface. Due to the lack of protection, the EIS spectra are characterized by only one time constant at lower frequencies for the duration of the test, associated with corrosion processes, as presented in Figure 71. In this figure, EIS spectra and optical photographs are presented for CRS substrates immersed in 50 mM NaCl solution.

The EIS spectra obtained for different immersion times reveal low impedance magnitude values with respect to GS since the beginning of immersion, maintaining a similar response throughout the monitored time. Photographs support the extent of corrosion processes ongoing on the surface with significant deposition of iron oxide deposits (Figure 71 b to d).

## 6.4 Gluconate as a corrosion inhibitor for GS

### 6.4.1 Gluconate directly added in NaCl solution

The inhibition efficiency of gluconate towards GS was assessed by electrochemical techniques, namely potentiodynamic polarization (Figure 72) and EIS (Figure 73).

DC polarization measurements were carried out after 1 hour of immersion at open circuit potential for bare GS samples immersed in 50 mM NaCl and in 50 mM NaCl solutions containing 0.5, 1, 2 and 5 mM sodium gluconate (NaGluc) salt. The polarization curves show a shift in the corrosion potential as well as a decrease in the current density, most notable in the anodic branch, thereby suggesting the tendency of gluconate to inhibit the anodic half-reaction of the corrosion process. The results are consistent with information found in the literature, where the inhibiting effect of NaGluc is attributed to the adsorption of gluconate molecules on the GS surface and the displacement of  $\text{Cl}^-$  from the interface.[123]

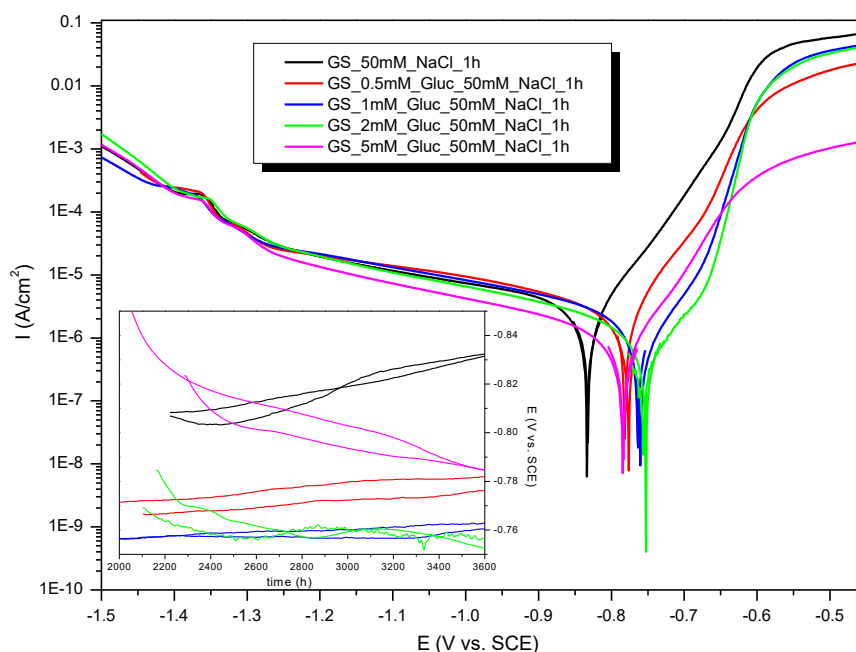


**Figure 72:** DC polarization of GS samples immersed in 50 mM NaCl solution without NaGluc and with 0.5, 1, 2 and 5 mM NaGluc after 1 hour of immersion. The inset shows OCP evolution before measurement.

The corrosion current density ( $i_{corr}$ ) shows a tendency to decrease with the increase in NaGluc concentration, exception made to 5 mM. The values of  $i_{corr}$  are presented in Table 19, with the reference sample presenting values around  $1.15 \times 10^{-6} \text{ A/cm}^2$

comparing with  $1.64 \times 10^{-7}$  and  $1.99 \times 10^{-7}$  A/cm<sup>2</sup> for 1 mM and 2 mM NaGluc, respectively. The 5 mM NaGluc solution gives slightly worse values of  $i_{corr}$  than the previous concentrations, with values of  $4.69 \times 10^{-7}$  A/cm<sup>2</sup>. For concentrations of NaGluc lower than 1 mM the inhibition effect is not observed, with 0.5 mM NaGluc showing a similar result, even slightly worse, than the control ( $3.28 \times 10^{-6}$  A/cm<sup>2</sup>).

NaGluc inhibiting efficiency (IE) was calculated from  $i_{corr}$  applying eq. (33), [334] where  $i_{corr}^o$  is the current density measured for the reference (50 mM NaCl solution) and  $i_{corr}$  the current density measured for the sample in the same medium with NaGluc.

$$(33) IE\% = \left[ 1 - \frac{i_{corr}}{i_{corr}^o} \right] * 100$$

The inhibition efficiency after 1 hour of immersion (Table 19) is 85.7 % for 1 mM NaGluc, 82.7 % for 2 mM NaGluc and 59.2 % for 5 mM NaGluc. The results point towards an optimal NaGluc concentration for corrosion protection between 1 mM and 2 mM, where an adsorption equilibrium may be achieved, enabling the protection of the metal substrates.

**Table 19: Determination of the corrosion rates by Tafel extrapolation from the polarization curves and inhibition efficiency for GS panels after 1 hour immersion in a 50 mM NaCl without and with 0.5 mM, 1 mM, 2 mM and 5 mM NaGluc.**

	$i_{corr}$ (A/cm <sup>2</sup> )	$E_{corr}$ (mV)	$\beta_A$ (V/decade)	$\beta_C$ (V/decade)	IE%
GS_50mM_NaCl_1h	$1.15 \times 10^{-6}$	-832	$58.40 \times 10^{-3}$	$53.10 \times 10^{-3}$	
GS_0.5mM_NaGluc_50mM_NaCl_1h	$3.28 \times 10^{-6}$	-782	$76.50 \times 10^{-3}$	-	-
GS_1mM_NaGluc_50mM_NaCl_1h	$1.64 \times 10^{-7}$	-761	$40.50 \times 10^{-3}$	$16.40 \times 10^{-3}$	85.7
GS_2mM_NaGluc_50mM_NaCl_1h	$1.99 \times 10^{-7}$	-756	$77.70 \times 10^{-3}$	$85.60 \times 10^{-3}$	82.7
GS_5mM_NaGluc_50mM_NaCl_1h	$4.69 \times 10^{-7}$	-784	$59.50 \times 10^{-3}$	$61.80 \times 10^{-3}$	59.2

The EIS spectra obtained after 15 minutes and 3 days for samples immersed in a 50 mM NaCl solution, with and without NaGluc, are presented in Figure 73. The EIS spectra are characterized by the presence of a time constant at intermediate and lower frequencies ascribed to the electrochemical activity of ongoing processes at the metal interface - charge and mass transfer related processes. After just 15 minutes of immersion, the values of impedance at low frequencies (10 mHz) show high corrosion protection provided by the gluconate. The ranking of the systems using these impedance magnitudes are in agreement with the results obtained from the DC analysis presented earlier:  $|Z|$  (reference) <  $|Z|$  (5 mM Gluc) <  $|Z|$  (2 mM Gluc).

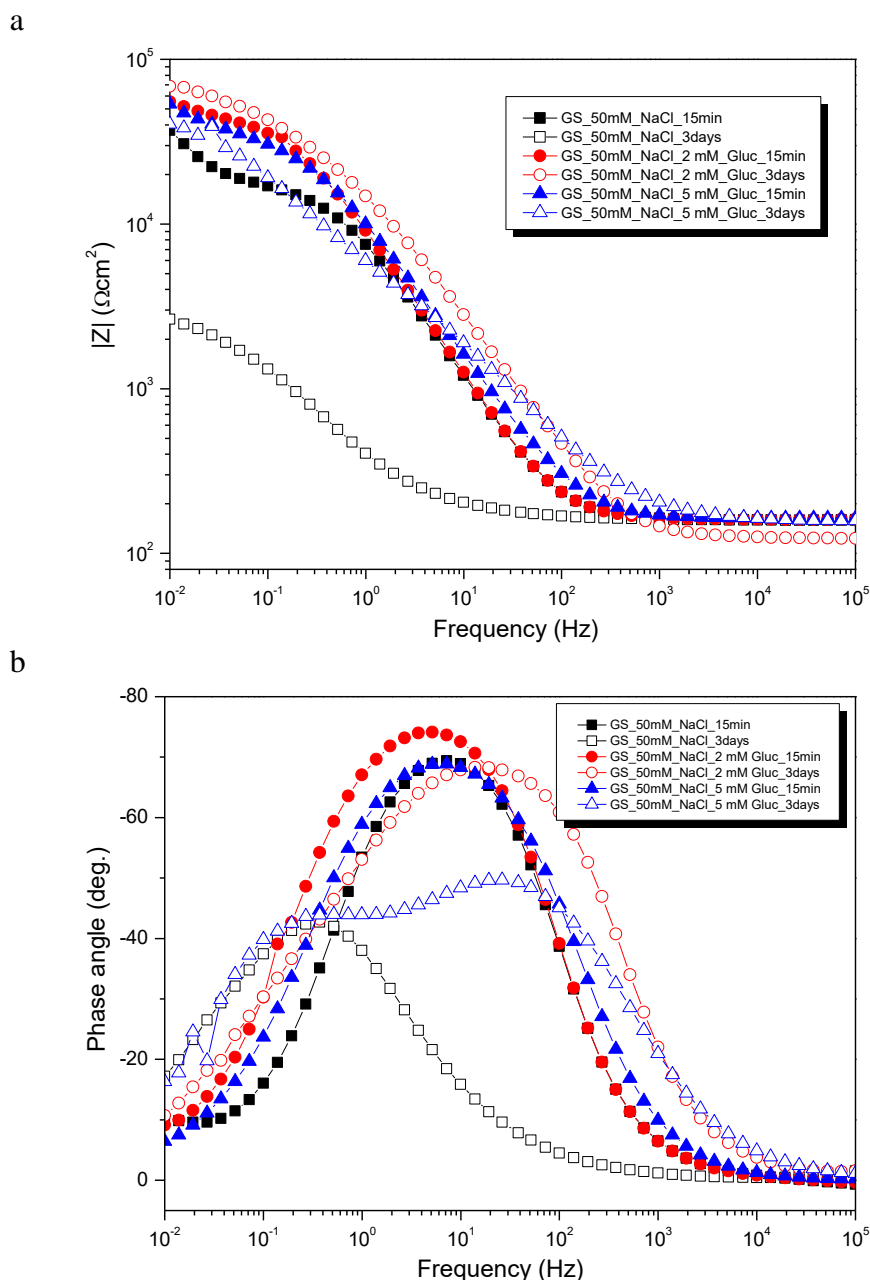
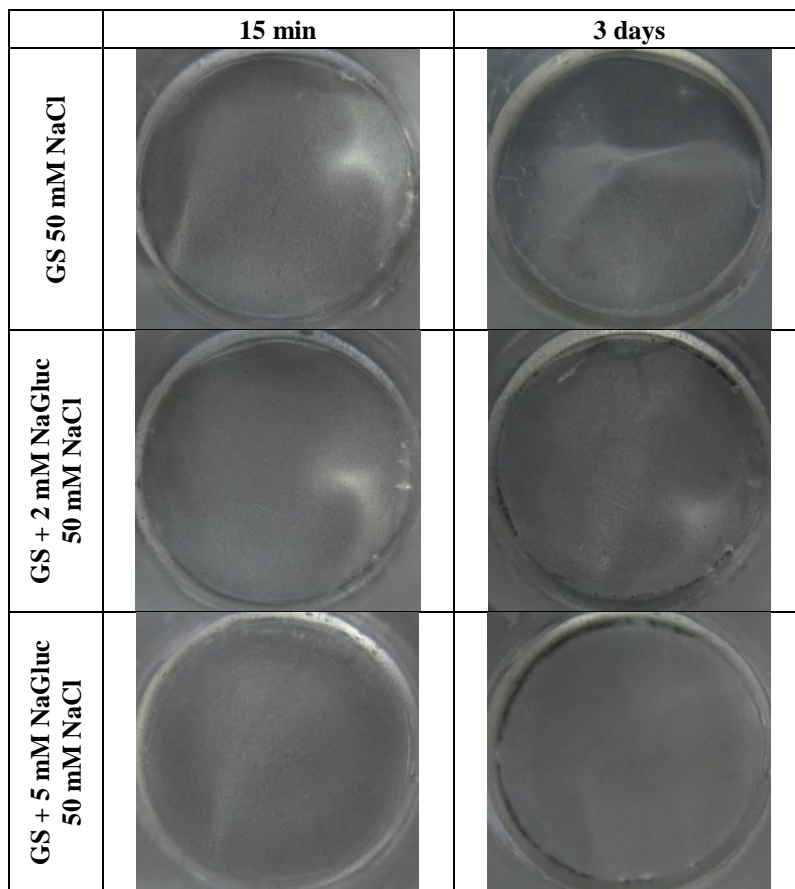


Figure 73: Bode representation of EIS spectra after 15 min and 3 days of immersion in 50 mM NaCl solution without NaGluc, with 2 mM NaGluc and 5 mM NaGluc.

After 3 days of immersion, a slight decrease in impedance values for systems with corrosion inhibitor starts to be noticed, with a second-time constant occurring at low frequencies. This time constant is more defined for 5 mM NaGluc, indicating the presence of diffusion-controlled processes taking place on the GS surface. The time constant at intermediate frequencies can be associated with corrosion processes. In the case of the reference, only one time constant is detected at low frequencies, possibly associated corrosion processes overlapped with mass transport phenomena. This, together with evidence of a significant decrease in impedance values at low frequencies, more than one

order of magnitude, are indicative of GS degradation due to corrosion processes. Visually, the degradation is not so clear. Nevertheless, it is possible to identify the presence of zinc hydroxide deposits (white precipitates) on the GS sample without NaGluc. Moreover, when analyzing the samples in SEM, the degradation of the zinc layer becomes evident, as shown in Figure 78. The results obtained from polarization curves and EIS spectra are in agreement, indicating gluconate as a good corrosion inhibitor for GS, particularly when present in concentrations around 2 mM.



**Figure 74:** Photographs of samples measured in Figure 73. GS samples immersed in 50 mM NaCl, 2 mM NaGluc in 50 mM NaCl and 5 mM NaGluc in 50 mM NaCl after 15 minutes and 3 days.

The fittings of the impedance spectra were carried out to assess the dynamics of corrosion inhibition processes taking place on GS, using the equivalent circuit presented in Figure 75c. It includes the solution resistance ( $R_s$ ), a CPE element associated with the electrochemical double layer ( $CPE_{dl}$ ) and a charge transfer resistance ( $R_{ct}$ ) associated with the corrosion process. The tendency observed (reference  $< 2$  mM NaGluc  $< 5$  mM NaGluc) confirms the qualitative analysis of the EIS spectra, as shown in Figure 75a and b. Nonetheless, for short immersion times, all samples show similar  $R_{ct}$ , with values

around  $3 \times 10^4 \Omega \text{ cm}^2$ . In the case of reference, it starts to decrease fast after 90 minutes, presenting values around  $8 \times 10^3 \Omega \text{ cm}^2$  after only 4 hours of immersion. These values decrease continuously until reaching its lowest value after 3 days, around  $3 \times 10^3 \Omega \text{ cm}^2$ .

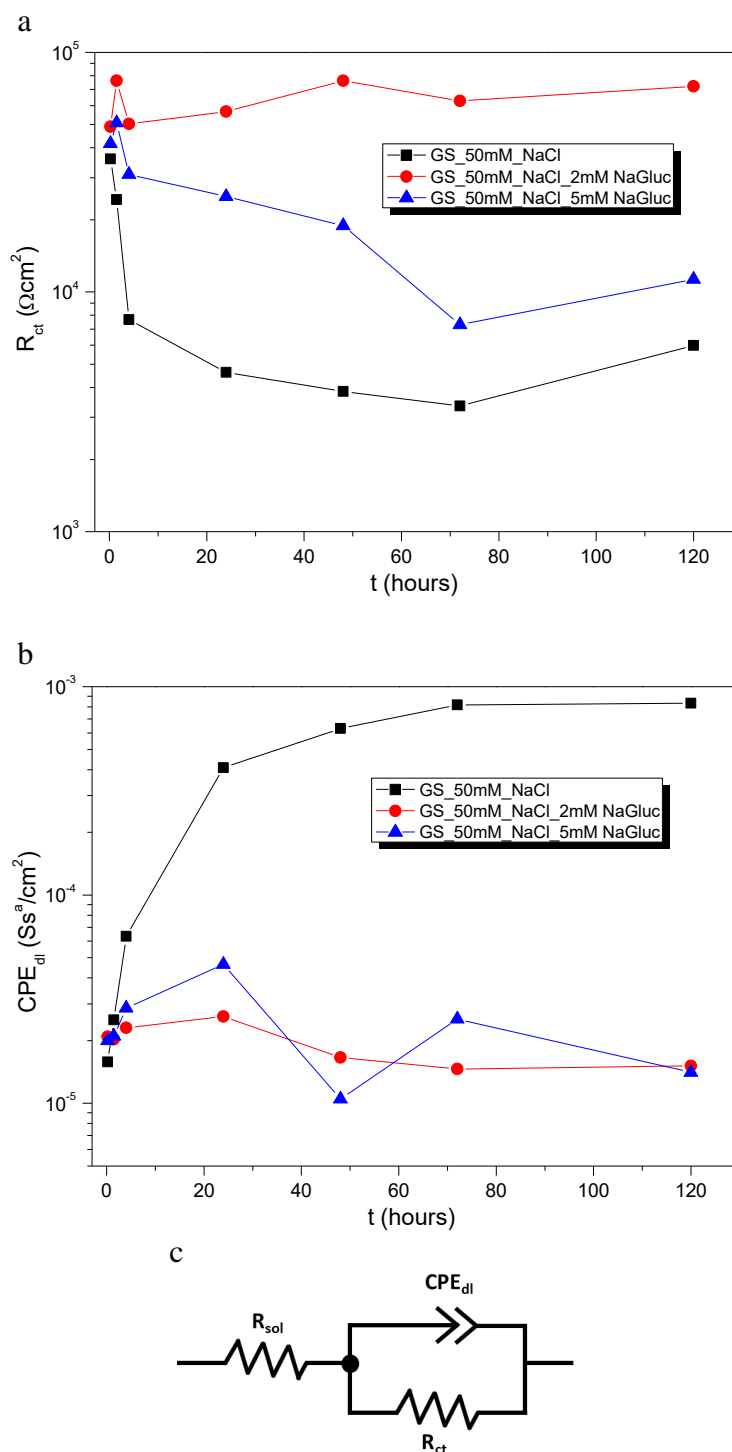


Figure 75: Evolution of  $R_{ct}$  (a) and  $CPE_{dl}$  (b) fitting parameters of GS immersed in 50 mM NaCl (reference), 50 mM NaCl with 2 mM NaGluc and 50 mM NaCl with 5 mM NaGluc; equivalent circuit scheme (c) used for fitting of EIS data presented in Figure 73.

In contrast, samples immersed in solutions with NaGluc show a slight increase in the  $R_{ct}$  values after 90 minutes. However, for 5 mM NaGluc and after 4 hours the values

of  $R_{ct}$  start to decrease steadily, and like the reference, reaches its lowest value after 3 days of immersion, with  $R_{ct}$  around  $8 \times 10^3 \Omega \text{ cm}^2$ . According to the qualitative assessment of EIS spectra, 2 mM NaGluc is the best system with constant  $R_{ct}$  values throughout the immersion test, around  $6 \times 10^4 \Omega \text{ cm}^2$ . The  $CPE_{dl}$  shows a similar behavior, with reference presenting higher values, around 1.5 orders of magnitude than samples immersed in NaGluc solutions, regardless of the concentration used.

**Table 20: Results obtained from the fitting of EIS spectra after 3 days of immersion in 50 mM NaCl solution, depicted in Figure 73.**

System	$(\chi^2)$	$Y(CPE_{dl})$ $Ss^n \text{cm}^{-2}$	$R_{ct}$ $\Omega \text{cm}^2$	IE %
GS_50mM_NaCl	$(2.37 \times 10^{-4})$	$8.18 \times 10^{-4}$ (n=0.818)	$3.34 \times 10^3$	-
GS_50mM_NaCl + 2 mM NaGluc	$(7.11 \times 10^{-3})$	$1.46 \times 10^{-5}$ (n=0.790)	$6.28 \times 10^4$	94.7
GS_50mM_NaCl + 5 mM NaGluc	$(8.84 \times 10^{-4})$	$2.54 \times 10^{-5}$ (n=0.704)	$7.31 \times 10^3$	54.4

The inhibition efficiency (IE) was calculated considering that  $R_{ct}$ , obtained by EIS, is inversely proportional to the corrosion rate.[316, 317] Using  $R_{ct}$  values obtained by fitting of EIS spectra available in Table 20 and applying the equation (34), inhibition efficiencies were obtained (Table 20):

$$(34) IE(\%) = \left(1 - \frac{R_{ct0}}{R_{ct}}\right) \times 100$$

where  $R_{ct0}$  is the charge transfer resistance in the corrosive medium and  $R_{ct}$  is the charge transfer resistance in the inhibiting medium. The IE calculated using charge transfer resistance points towards the trend of IE calculated using current density values. Both show that the NaGluc concentration of 2 mM is the best concentration to inhibit GS (IE of 94.7 % for 2 mM NaGluc vs. 54.4 % obtained for 5 mM NaGluc).

#### 6.4.2 LDH-Gluc in NaCl solution

The corrosion protection efficiency of gluconate intercalated into LDH was assessed by EIS and visual analysis of samples under testing. In Figure 76 the Bode representation of EIS spectra for GS immersed in 50 mM NaCl (reference), and 50 mM NaCl mixed with 0.5 wt.% of LDH- $\text{NO}_3$  and LDH-Gluc are presented. The results are indicative of the inhibiting effect provided by the released gluconate. After 90 minutes of immersion, a significant difference in impedance values at low frequencies (10 mHz) is already visible, with LDH-Gluc presenting values of impedance around  $4 \times 10^4 \Omega \text{ cm}^2$ , comparing with values around  $1 \times 10^4 \Omega \text{ cm}^2$  for both reference and LDH- $\text{NO}_3$ . Moreover,

one time constant is detected at intermediate frequencies for LDH-Gluc ( $10^1$  Hz) and at low frequencies for both reference and LDH- $\text{NO}_3$  ( $10^0$ – $10^{-1}$  Hz). This time constant can be ascribed to the charge transference resistance ( $R_{ct}$ ) and double layer capacitance ( $CPE_{dl}$ ) of the process associated with electrochemical activity taking place on the metal surface. In the case of systems without gluconate, the time constant can be a result of the overlapping of time constants associated with electrochemical activity and mass controlled processes.

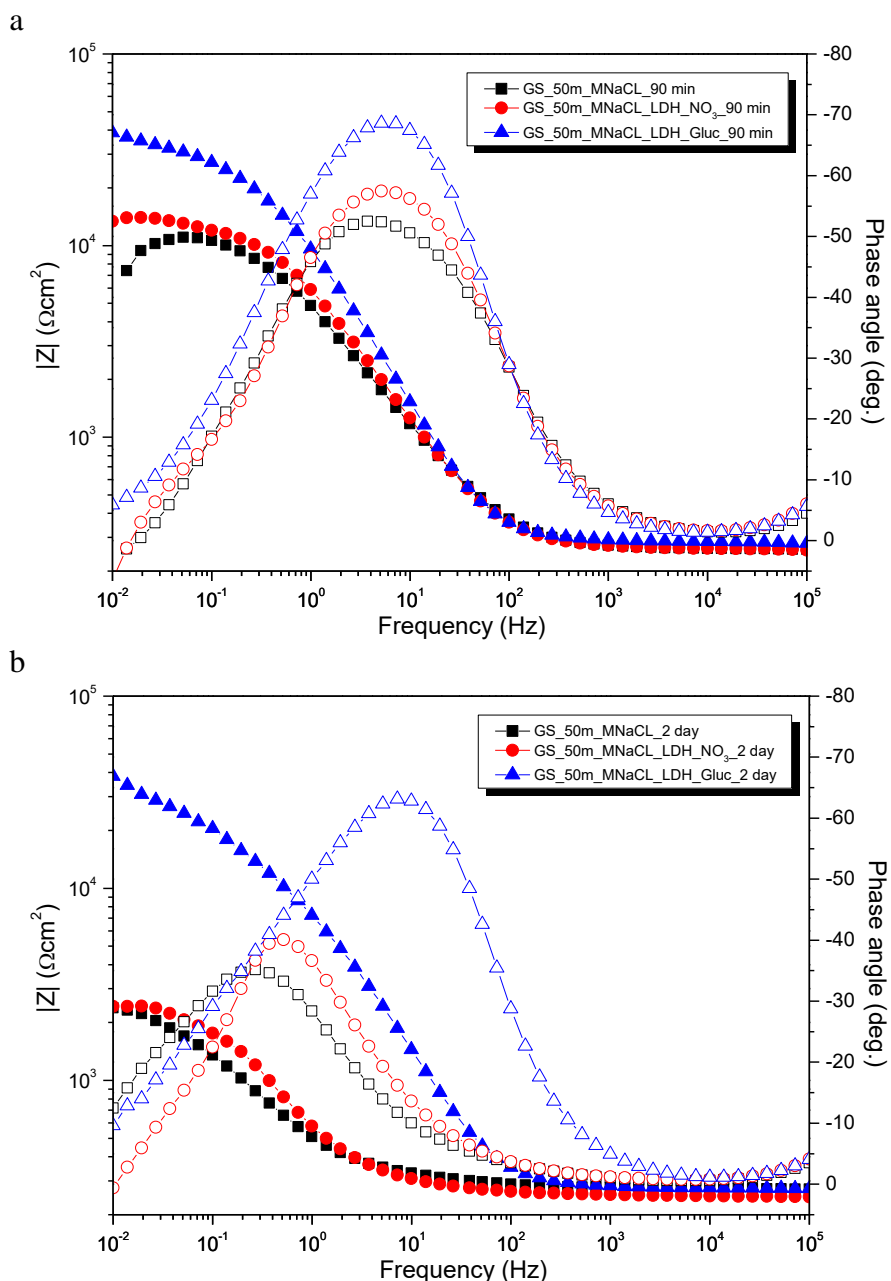


Figure 76: EIS spectra of galvanneated steel samples in 50 mM NaCl, 50 mM NaCl containing LDH- $\text{NO}_3$  and 50 mM NaCl containing LDH-Gluc containers after a) 90 min and b) 2 day of immersion.

With the evolution of immersion time, the impedance values at low frequencies decrease for the reference and LDH-NO<sub>3</sub> systems, while remaining stable for LDH-Gluc. The reference and LDH-NO<sub>3</sub> show similar EIS spectra over time, with low impedance values around  $2 \times 10^3 \Omega \text{ cm}^2$  vs.  $4 \times 10^4 \Omega \text{ cm}^2$  observed for LDH-Gluc. These results support the inhibiting action of LDH-Gluc towards GS substrates.

The EIS results were corroborated by the visual assessment of the GS panels throughout the test, shown in Figure 77. The photographs after two days of immersion show corroded GS panels in the cases of control and LDH-NO<sub>3</sub>, with the former severely attacked showing several white spots of zinc-based corrosion products. Comparatively, the panels immersed in LDH-Gluc remained clear of any signs of corrosion activity.

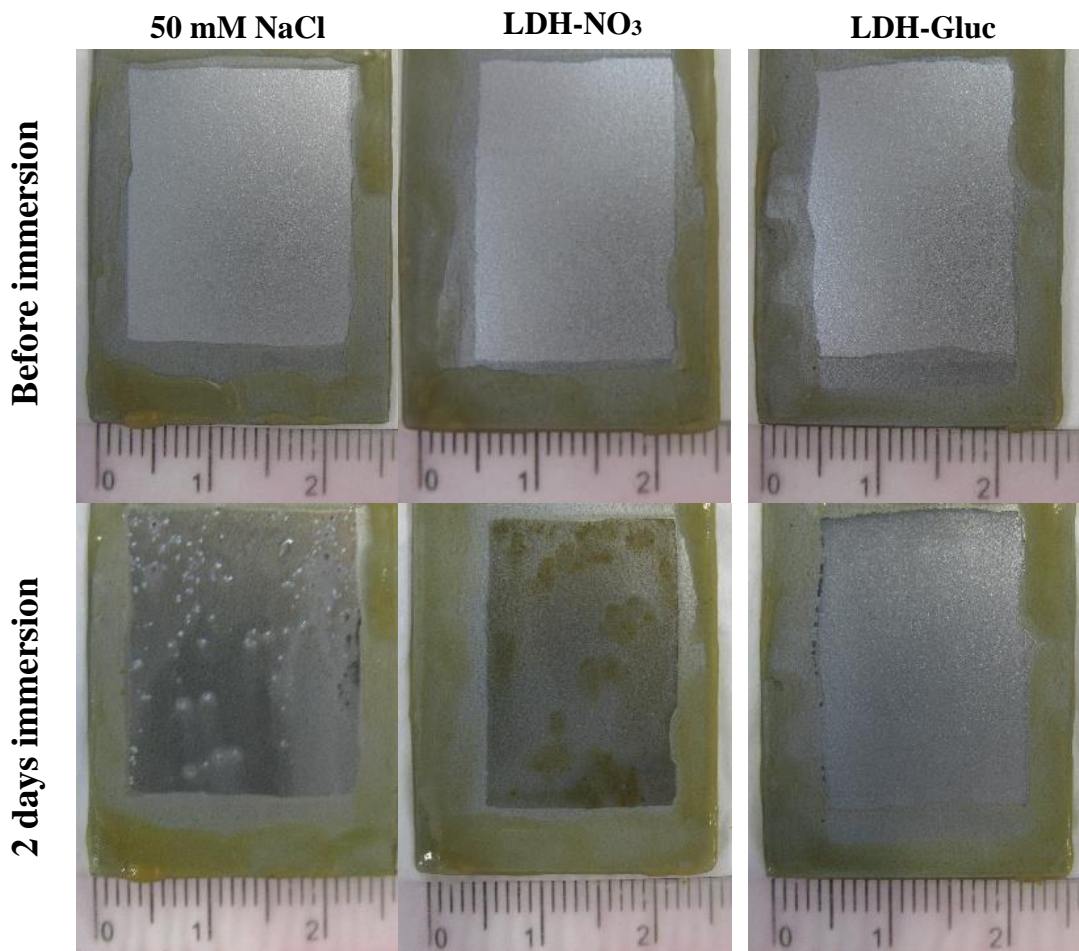
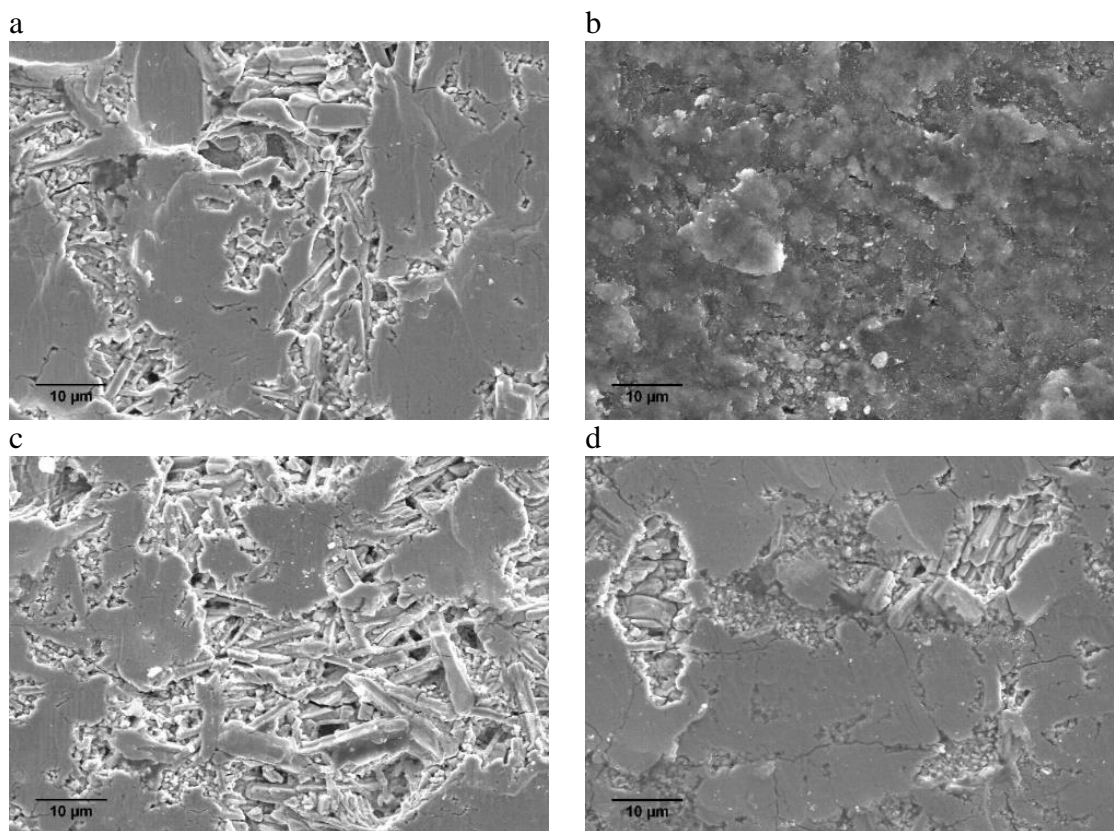


Figure 77: Photographs of the plates before immersion and after 2 days of immersion in 50 mM NaCl solution.

A more detailed surface analysis was carried out using SEM (Figure 78). The characteristic morphological structures present on the GS surface are visible without considerable differences for samples immersed in NaGluc solution and LDH-Gluc. In the cases where GS was immersed in 50 mM NaCl solutions without inhibitor, the surface

morphology changes drastically, losing the characteristic structure, with porous zinc-based corrosion products being detected.



**Figure 78:** SEM microphotographs of the plates without immersion (a) and after 2 days of immersion in 50 mM NaCl solution without gluconate (b), in a NaGluc solution (c) and LDH-Gluc (d).

The EIS results presented above provide a clear picture regarding the LDH-Gluc corrosion protection efficiency, but by fitting of the EIS data is possible to obtain quantitative results regarding that efficiency. The EIS spectra were fitted using the equivalent circuit shown in Figure 79c, to obtain the values for  $R_{ct}$  and  $CPE_{dl}$ , shown in Figure 79a and Figure 79b, respectively. The values of  $R_{ct}$  are very similar after 15 minutes of immersion ( $1 \times 10^4 \Omega \text{ cm}^2$ ). However, after only 90 minutes of immersion opposite tendencies start to unveil. LDH-Gluc starts to show an increase in  $R_{ct}$  contrasting with reference and LDH- $\text{NO}_3$ , which both reveal a decrease in this parameter. The  $R_{ct}$  increase observed for LDH-Gluc occurs up to 4 hours of immersion, after which stabilizes in values around  $4 \times 10^4 \Omega \text{ cm}^2$  for the remaining testing period. On the other hand, both reference and LDH- $\text{NO}_3$  systems exhibit a continuous decrease in  $R_{ct}$  values up to 4 hours of immersion. After 4 hours the values of  $R_{ct}$  tend to stabilize around  $2 \times 10^3 \Omega \text{ cm}^2$ .

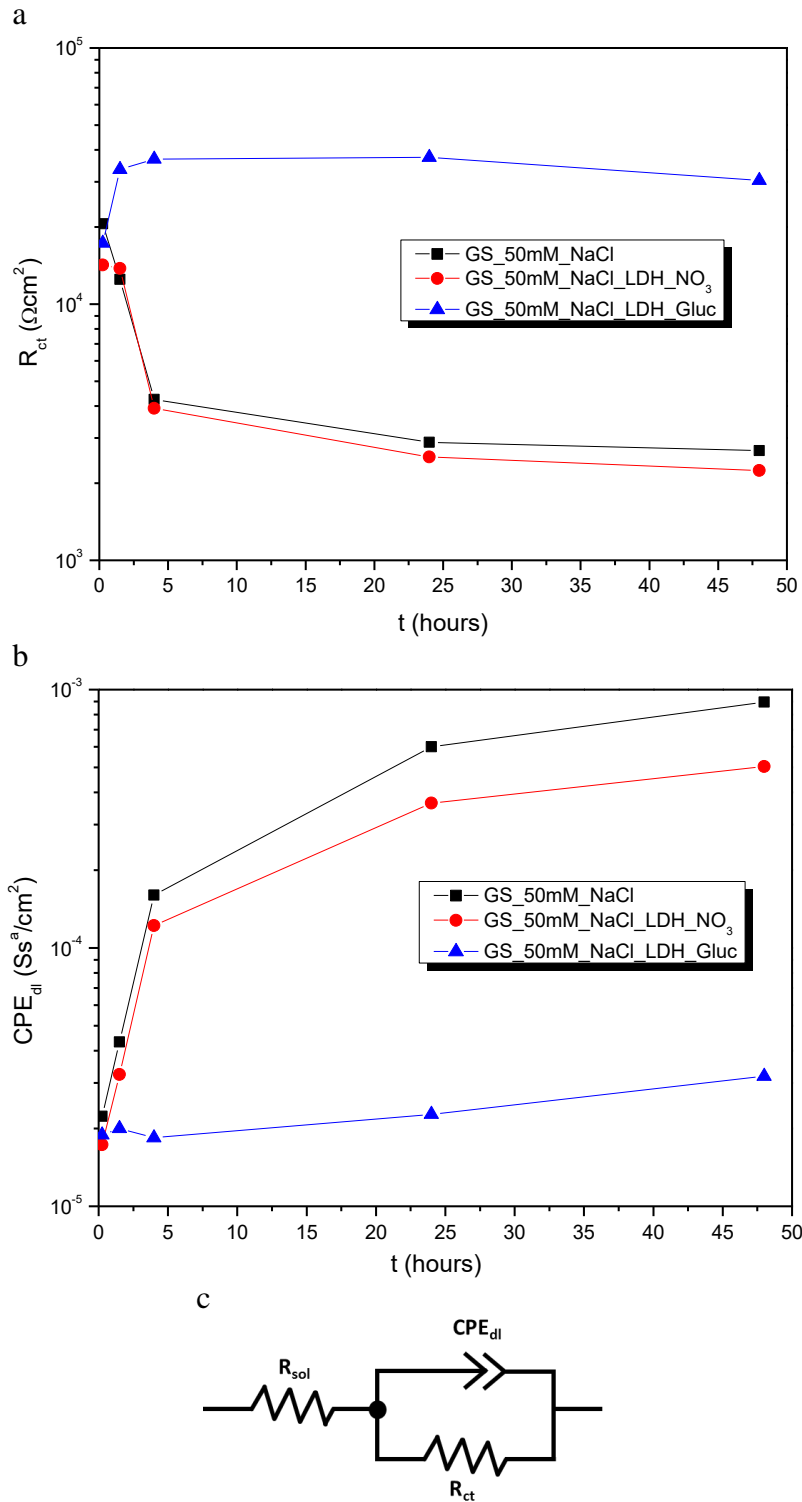


Figure 79: Evolution of  $R_{ct}$  (a) and  $CPE_{dl}$  (b) fitting parameters of GS immersed in 50 mM NaCl (reference), 50 mM NaCl with LDH-NO<sub>3</sub> and 50 mM NaCl with LDH-Gluc; equivalent circuit scheme (c) used for fitting of EIS data presented in Figure 76.

The  $CPE_{dl}$  values are in agreement with the profiles of  $R_{ct}$  for the different systems.  $CPE_{dl}$  shows an increase for both reference and LDH-NO<sub>3</sub> contrasting with the low and stable value observed for LDH-Gluc. After 2 days of immersion, this difference is roughly one order of magnitude. Together with the values of  $R_{ct}$ ,  $CPE_{dl}$  gives a good

indication of the positive effect of LDH-Gluc, strengthening the qualitative indications of EIS, SEM and visual analysis.

The IE was calculated using  $R_{ct}$  values and equation (34). In the case of LDH- $\text{NO}_3$ , the  $R_{ct}$  value is lower but very close to the reference. Hence, one can assume IE in this case as 0%. In fact, this result was expected since  $\text{NO}_3^-$  does not possess inhibiting properties towards zinc. Furthermore, these results allowed to discard LDH influence on the corrosion processes, besides the already reported removal of  $\text{Cl}^-$  from the medium.[154] The IE value for LDH-Gluc is 91.2 %. The close values of IE for LDH-Gluc and 2 mM NaGluc (94.7 %), indicate that the amount of gluconate release from the LDH is enough to produce an inhibition effect similar to the one obtained for the best gluconate concentration.

**Table 21: Results obtained from the fitting of EIS spectra depicted in Figure 76.**

System	$(\chi^2)$	$Y(\text{CPE}_{dl})$ $\text{Ss}^n \text{cm}^{-2}$	$R_{ct}$ $\Omega \text{cm}^2$	IE %
GS_50mM_NaCl	$(5.57 \times 10^{-4})$	$8.94 \times 10^{-4}$ (n=0.669)	$2.68 \times 10^3$	-
GS_50mM_NaCl + LDH- $\text{NO}_3$	$(2.19 \times 10^{-3})$	$5.04 \times 10^{-4}$ (n=0.779)	$2.24 \times 10^3$	0
GS_50mM_NaCl + LDH-Gluc	$(9.50 \times 10^{-3})$	$3.19 \times 10^{-5}$ (n=0.779)	$3.04 \times 10^4$	91.2

### 6.4.3 LDH-Gluc\_Alg in NaCl solution

When modifying the surface of nanocontainers it is important to be aware of changes in the inhibitor release properties and its impact on the corrosion protection. Consequently, when modifying LDH-Gluc with alginate, some changes in the quantity and release rate of gluconate should be expected, as observed in the release studies (recall section 6.2.2). By studying the impedance of bare GS in a suspension of nanocontainers containing alginate in 50 mM of NaCl, the inhibiting efficiency can be studied, thus assessing the effect of alginate.

Figure 80 shows EIS results obtained for GS samples immersed in 50 mM NaCl solution without LDHs (reference), with LDH-Gluc and with LDH-Gluc\_Alg, after 15 min and 1 day of immersion. The spectra show a well-defined time constant for all the samples, which can be ascribed to the electrochemical activity ongoing at the metal interface. The first results, obtained after 15 minutes of immersion, indicate a clear improvement in terms of impedance values at low frequencies for LDH-Gluc\_Alg when compared with LDH-Gluc and reference, but after 1 day the results for LDH with and without alginate are very similar. The results point towards a non-interfering modification

in terms of corrosion protection for relatively long timescales. This is somehow in agreement with the release profile of gluconate, which is similar for LDH unmodified and modified with alginate for 50 and 500 mM NaCl.

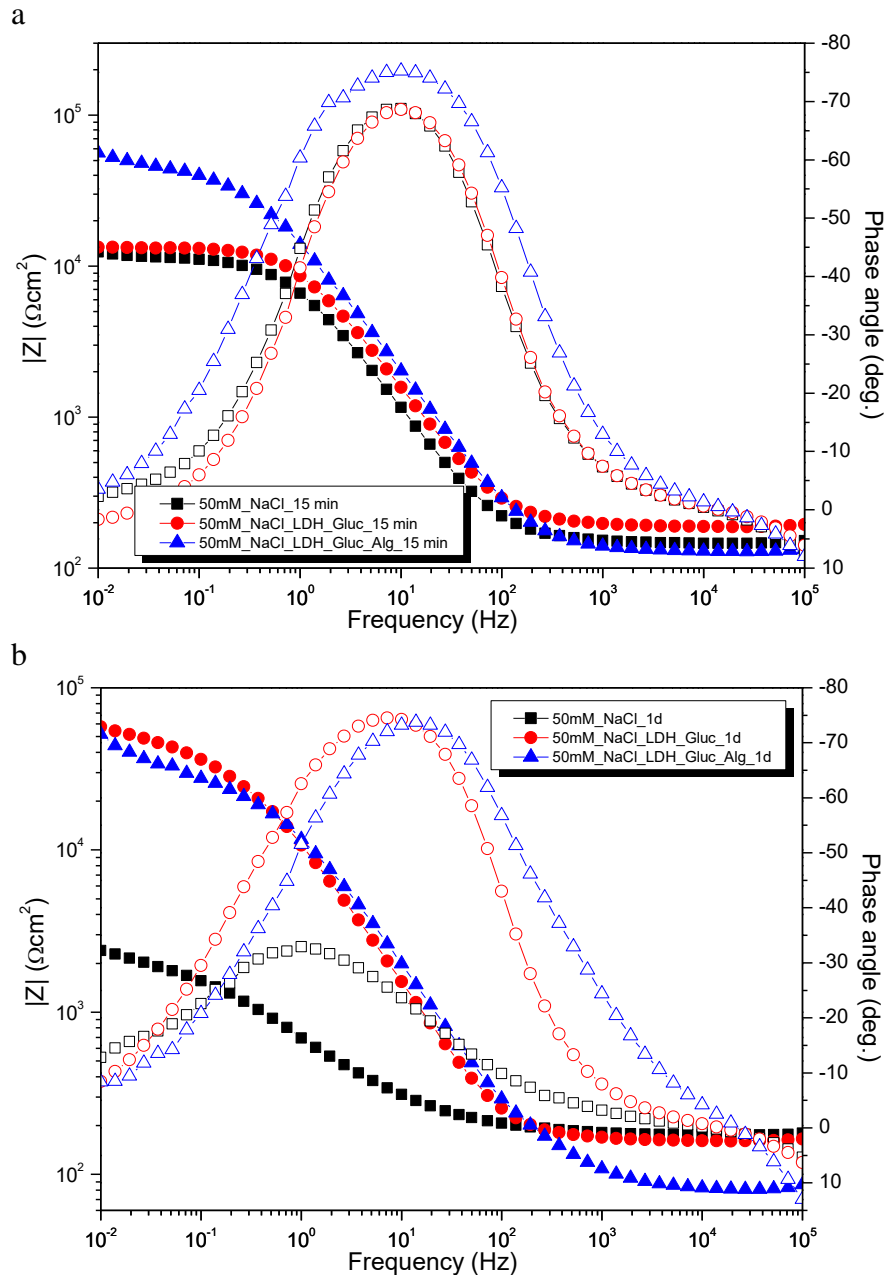


**Figure 80:** EIS Spectra of GS samples in 50 mM NaCl, 50 mM NaCl containing LDH-Gluc and 50 mM NaCl containing LDH-Gluc\_Alg containers after a) 15 minutes and c) 1 day of immersion.

A simple approach to corroborate the EIS results is the sample visual analysis presented in Figure 81. Regardless of the modification with alginate, both LDH-Gluc systems show similar results without significant signs of corrosion, even after one week of immersion. Conversely, GS panel immersed in 50 mM NaCl without LDH particles reveals clear signs of corrosion (white deposits on the surface).

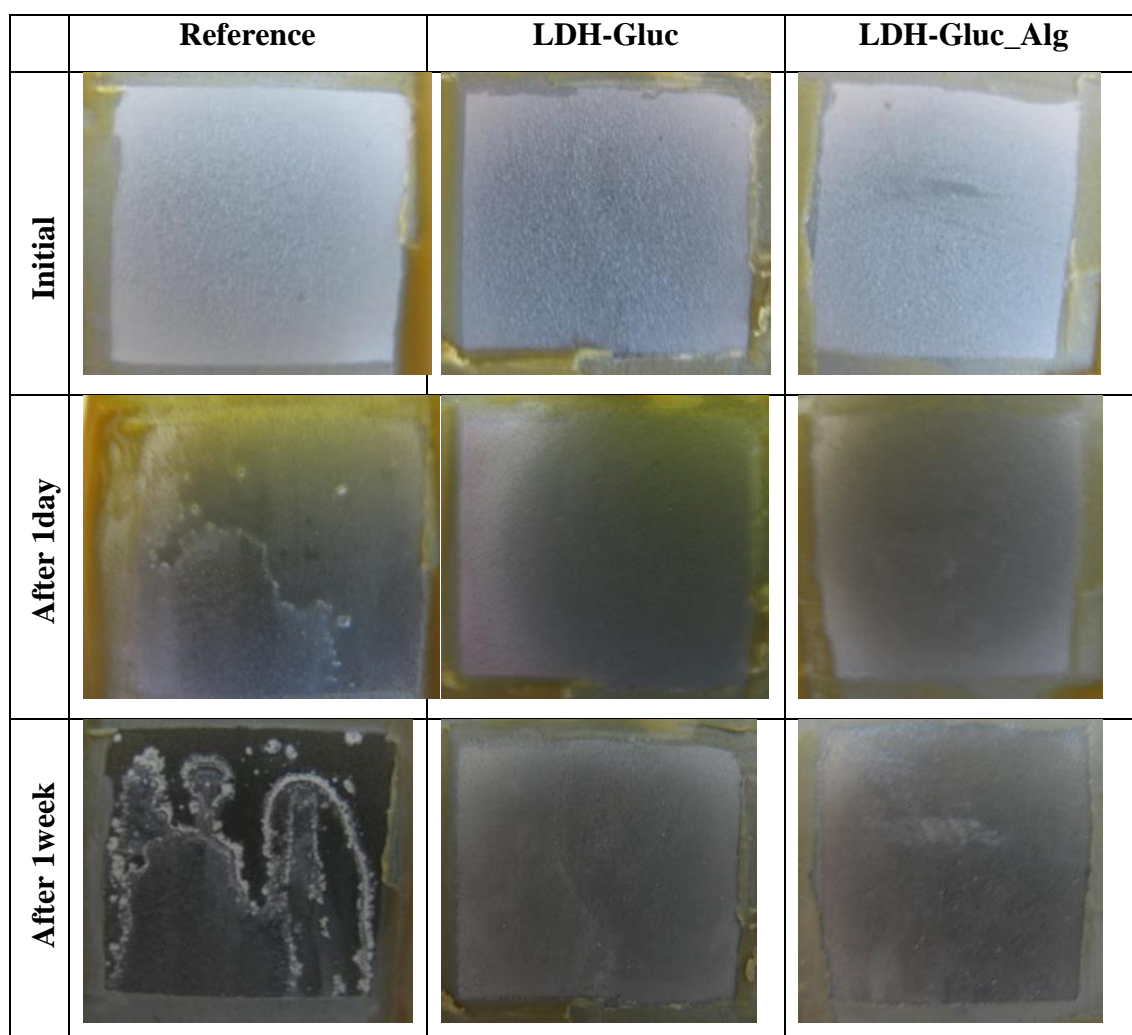


Figure 81: GS photographs during the EIS tests after 15 min, 1 day and 1 week immersion in a 50 mM NaCl solution, with 50 mM NaCl plus LDH-Gluc and 50 mM NaCl plus LDH-Gluc\_Alg.

The EIS data were fitted using the equivalent circuit shown in Figure 82c, from where the values of  $R_{ct}$  and  $CPE_{dl}$  were extracted. As in the previous analysis, these parameters are associated with electrochemical processes occurring on the GS surface. After the first 15 minutes of immersion, an improvement in the protection conferred by LDH-Gluc\_Alg is observed. The  $R_{ct}$  value for LDH-Gluc\_Alg is around  $5 \times 10^4 \Omega \text{ cm}^2$  comparing with values around  $1 \times 10^4 \Omega \text{ cm}^2$  for the remaining systems. These results are in line with the release studies performed in LDH-Gluc and LDH-Gluc\_Alg, recall section 6.2.2. The amount of gluconate released was higher in the case of LDH-Gluc\_Alg compared with LDH-Gluc. Moreover, the amount released at the initial times for LDH-Gluc\_Alg system is 2 mM, which was found earlier to be the optimal gluconate concentration to ensure a good corrosion inhibition, as shown in the DC polarization studies (6.4.3).

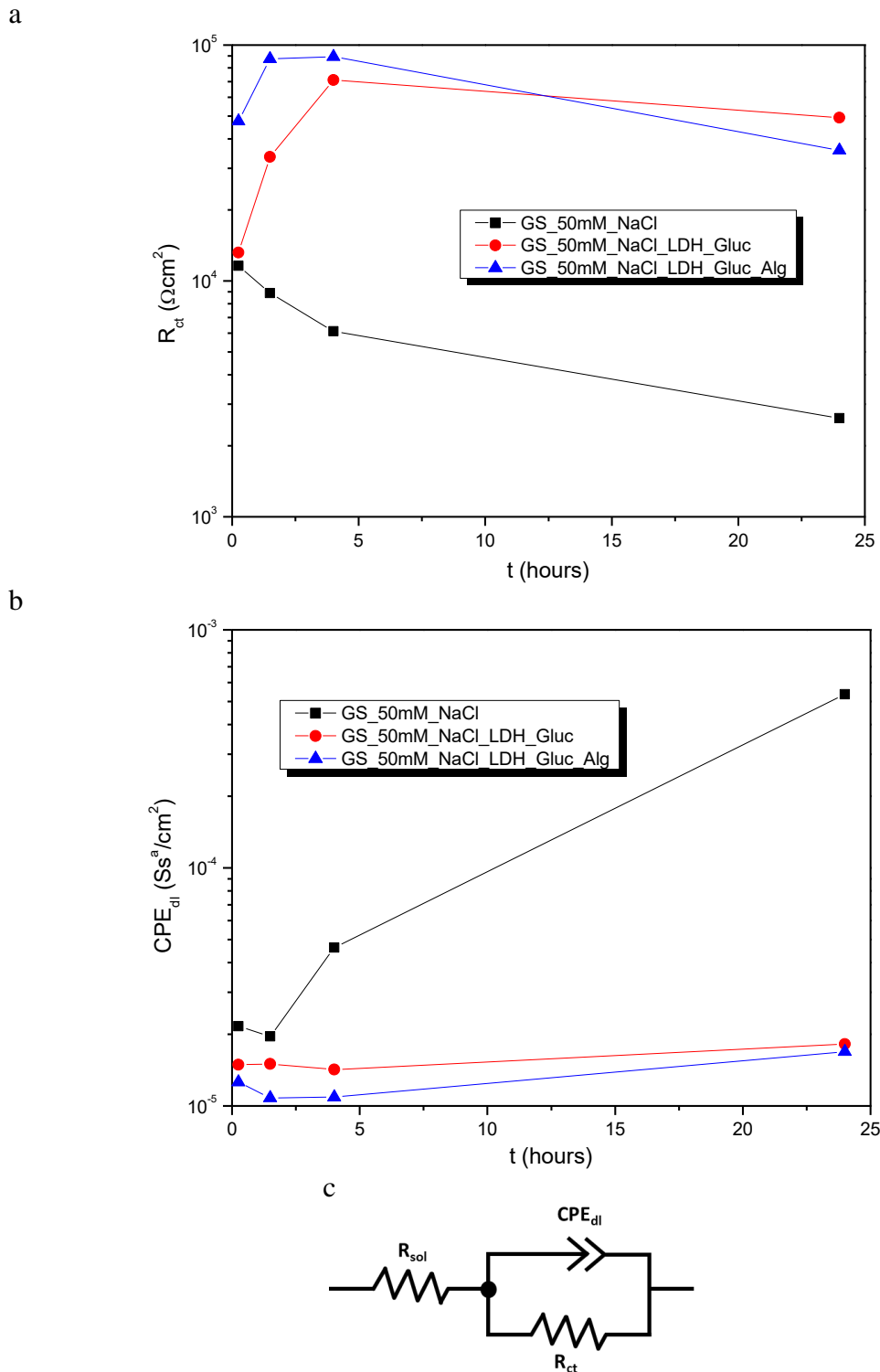


Figure 82: Evolution of  $R_{ct}$  (a) and  $CPE_{dl}$  (b) fitting parameters of GS immersed in 50 mM NaCl (reference), 50 mM NaCl with LDH-Gluc and 50 mM NaCl with LDH-Gluc\_Alg; equivalent circuit scheme (c) used for fitting of EIS data presented in Figure 80.

The reference shows a steady decrease in  $R_{ct}$ , with  $R_{ct}$  values around  $3 \times 10^3 \Omega \text{ cm}^2$  after 24 hours of immersion. In contrast, LDH-Gluc and LDH-Gluc\_Alg show an increase in the values of  $R_{ct}$  during the first 4 hours of immersion, to values around  $8 \times 10^4 \Omega \text{ cm}^2$ .

The value of  $R_{ct}$  decreases slightly after 24 hours, to values around  $5 \times 10^4 \Omega \text{ cm}^2$ . Nonetheless, these results are still one order of magnitude higher than the system without nanocontainers. The  $CPE_{dl}$  follows the opposite trend, which is in agreement with the expected results.

Equation (34) was used to calculate the IE for LDH-Gluc and LDH-Gluc\_Alg, using the  $R_{ct}$  obtained by fitting the EIS data. The IE calculated using data after 1 day of immersion for LDH-Gluc is 94.7 %, similar to the IE obtained after 2 days of immersion presented in the previous section (91.2 %). The consistency of IE obtained in different tests supports the inhibitory effect of gluconate on GS, probably due to the stable gluconate concentration in the medium combined with its relatively fast inhibition effect.

The modification with alginate yields IE percentages slightly lower, though comparable to the ones obtained for LDH-Gluc (92.7 %). Overall, these results show that LDH-Gluc\_Alg exhibits similar performance as LDH-Gluc.

**Table 22: Results obtained from the fitting of EIS spectra depicted in Figure 80.**

System	$(\chi^2)$	$Y(CPE_{dl})$ $Ss^n \text{cm}^{-2}$	$R_{ct}$ $\Omega \text{cm}^2$	IE %
GS_50mM_NaCl	$(7.11 \times 10^{-4})$	$5.36 \times 10^{-4}$ (n=0.572)	$2.62 \times 10^3$	-
GS_50mM_NaCl + LDH-Gluc	$(5.30 \times 10^{-3})$	$1.82 \times 10^{-4}$ (n=0.878)	$4.92 \times 10^4$	94.7
GS_50mM_NaCl + LDH-Gluc_Alg	$(1.14 \times 10^{-2})$	$1.69 \times 10^{-5}$ (n=0.829)	$3.58 \times 10^4$	92.7

## 6.5 Gluconate as corrosion inhibitor for CRS

### 6.5.1 Gluconate directly in NaCl solution

In this thesis, the corrosion inhibition performance of gluconate in CRS immersed in a 5 mM and 50 mM NaCl solution was assessed by EIS, as shown in Figure 83. Contrasting with the studies performed for GS, in CRS there was the need to use also a less aggressive medium, 5 mM NaCl solution, to assess the corrosion evolution. The tests are difficult to follow at higher concentrations of NaCl due to the higher vulnerability of CRS to corrosion in this medium compared to zinc-based substrates. Two concentrations of NaGluc were used, 2 mM and 5 mM, in a similar approach used for GS substrates previously. The lower NaCl concentration has some influence on the EIS spectra by reducing ionic conductivity and hence corrosion rate, with the substrates not corroding so extensively in 5 mM as in 50 mM NaCl solution for short timescales. However, the difference in electrolyte concentration becomes irrelevant after 3 days of immersion, with CRS displaying similar impedance values at lower frequencies for both electrolyte media.

In 5 mM NaCl solution, after short immersion times, the relevance of gluconate as corrosion inhibitor becomes clear, with impedance values at low frequencies ( $10^{-2}$  Hz) being 1.5 orders of magnitude higher for solutions containing 5 mM NaGluc ( $6 \times 10^4 \Omega \text{ cm}^2$ ). For 2 mM NaGluc the positive effect is still visible but in a less pronounced way than in 5 mM NaGluc solution. After 3 days of immersion, the impedance values for 5 mM NaGluc decreased and tended to get closer to the ones for 2 mM NaGluc due to a slight increase in its impedance values at low frequencies ( $1 \times 10^4 \Omega \text{ cm}^2$ ). However, both systems still display higher impedance magnitude when compared to the reference system ( $4 \times 10^3 \Omega \text{ cm}^2$ ).

The EIS results obtained for 5 mM and 50 mM NaCl are similar, with higher amounts of NaGluc providing higher protection at short immersion times. The difference between 2 mM and 5 mM of NaGluc, observed for shorter immersion times, tend to decrease over time. The presence of NaGluc yields impedance values around  $1 \times 10^4 \Omega \text{ cm}^2$  for 50 mM NaCl solutions after 15 minutes of immersion, notably the same value observed for 5 mM NaCl solutions. These results qualitatively validate gluconate as species with corrosion inhibiting properties for CRS substrates in NaCl media.

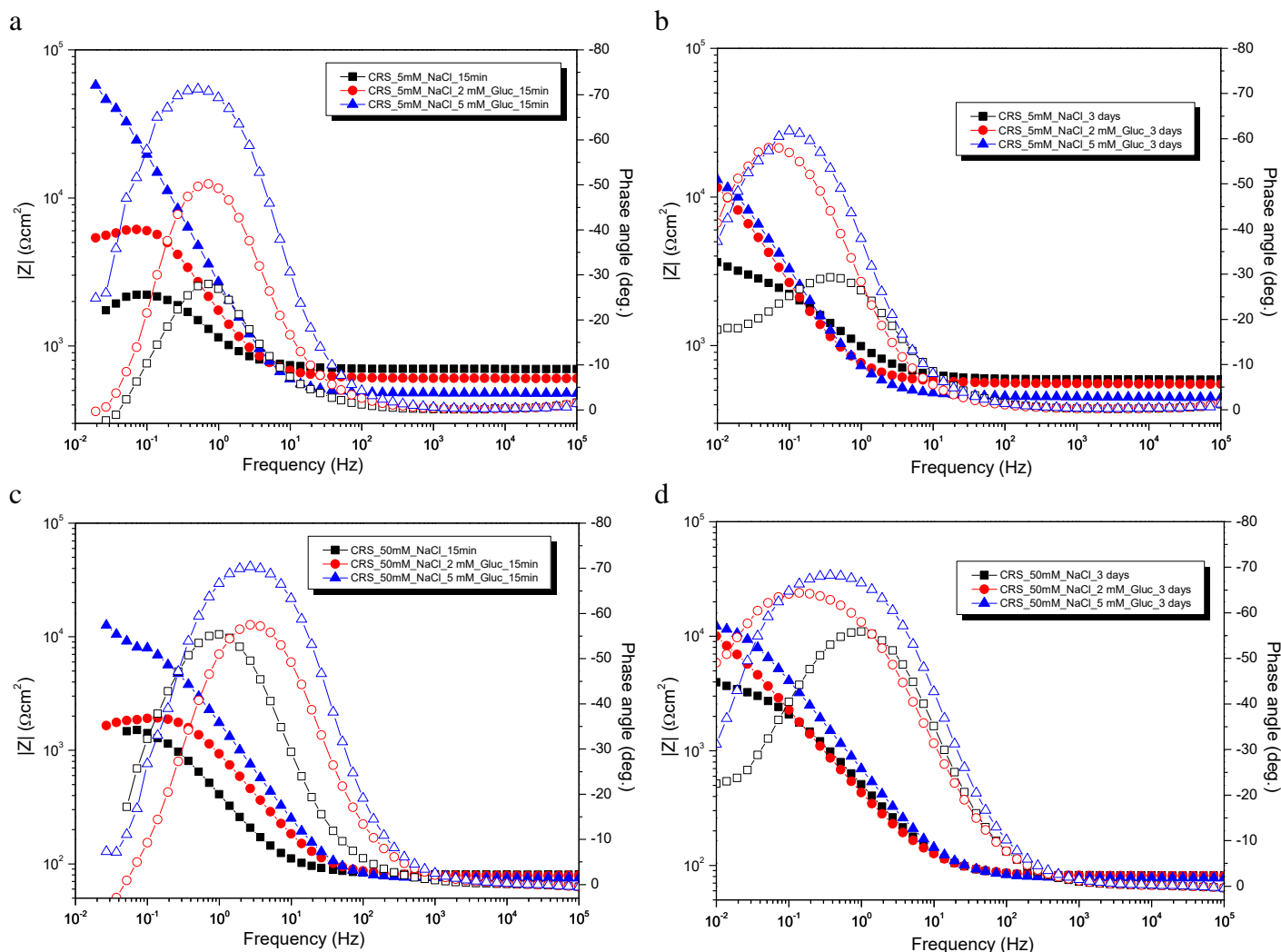


**Figure 83:** Bode representation of EIS spectra after 15 min and 3 days of immersion in 5 mM (a and b) and 50 mM NaCl (c and d) solution without NaGluc and with 2 mM or 5 mM NaGluc.

The EIS analysis was complemented by the visual assessment of the samples (Figure 84). The presence of NaGluc clearly inhibits corrosion processes on CRS. In the photographs, CRS immersed in solutions without NaGluc present a considerable amount of corrosion products after one day of immersion. Contrastingly, CRS immersed in solutions with NaGluc reveal fewer corrosion products.

Parameters from the fittings of the EIS results, that are shown in Figure 85a to d, were obtained using the equivalent circuit displayed in Figure 85e. For short immersion times in 5 mM NaCl, 5 mM NaGluc provides a higher level of protection with  $R_{ct}$  around  $5 \times 10^4 \Omega \text{ cm}^2$ , 1.5 orders of magnitude higher than reference and almost 1 order of magnitude higher than 2 mM NaGluc. With the increase in immersion time,  $R_{ct}$  for CRS immersed in 5 mM NaGluc tend to decrease, compared with the increase of  $R_{ct}$  observed for 2 mM NaGluc leading to identical values after 2 days of immersion. The  $R_{ct}$  values

for the reference remains stable throughout the test since the corrosion of CRS in solution without inhibitor starts immediately after immersion.

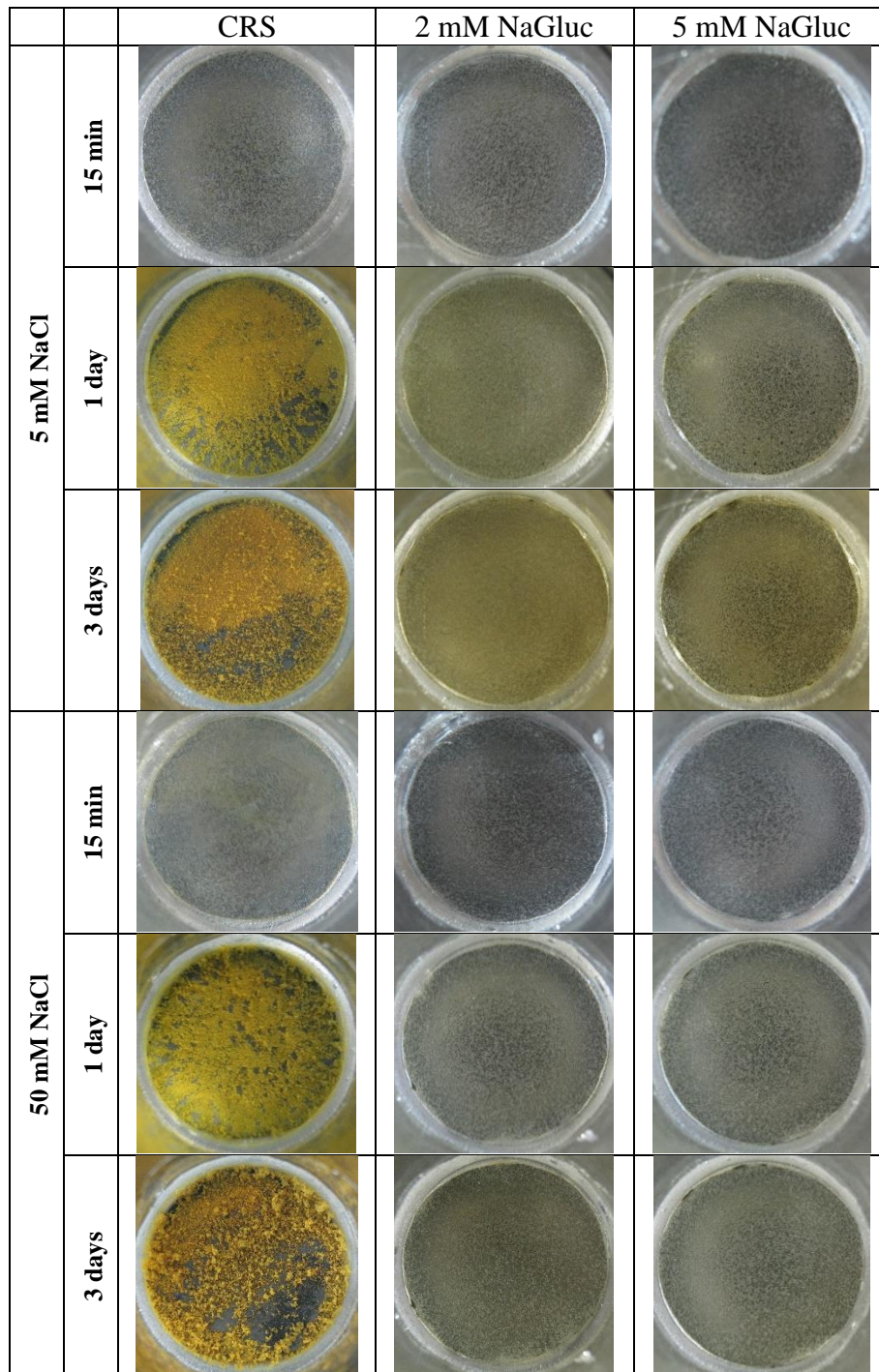


Figure 84: Photographs of bare CRS in a 50 mM NaCl solution, and 50 mM NaCl plus 2 mM NaGluc and 50 mM NaCl plus 5 mM NaGluc after 15 minutes, 1 day and 3 days of immersion.

When studying the inhibition efficiency for a more aggressive medium, 50 mM NaCl, NaGluc still proves to be a good corrosion inhibitor for CRS. The observed trend, however, is different from the tests in 5 mM NaCl as discussed earlier, with CRS in both

NaGluc-containing solutions presenting a similar trend. Both show an increase in  $R_{ct}$  values after 4 hours of immersion until a maximum value is reached after 3 days of immersion -  $1 \times 10^4 \Omega \text{ cm}^2$  for 5 mM NaGluc and  $2 \times 10^4 \Omega \text{ cm}^2$  for 2 mM NaGluc. The reference shows stable  $R_{ct}$  values since the beginning, as observed for 5 mM NaCl ( $2 \times 10^3 \Omega \text{ cm}^2$ ).

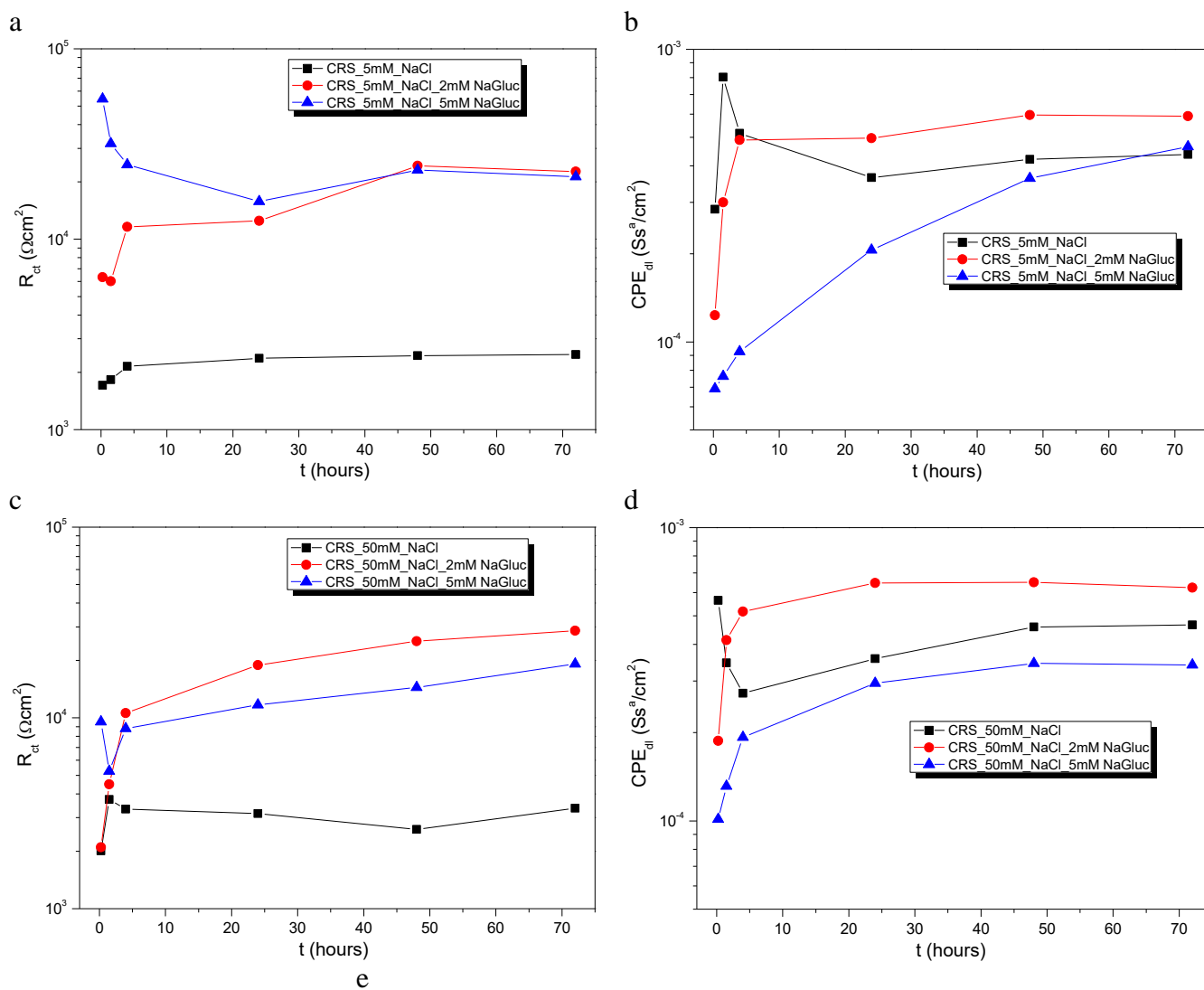


Figure 85: Evolution of  $R_{ct}$  (a) and  $CPE_{dl}$  (b) fitting parameters of CRS immersed in 5 mM NaCl (reference), 5 mM NaCl with 2 mM NaGluc and 5 mM NaCl with 5 mM NaGluc; evolution of  $R_{ct}$  (c) and  $CPE_{dl}$  (d) fitting parameters of CRS immersed in 50 mM NaCl (reference), 50 mM NaCl with 2 mM NaGluc and 50 mM NaCl with 5 mM NaGluc equivalent circuit scheme (e) used for fitting of EIS data presented in Figure 83.

The IE after 3 days of immersion, as shown in Table 23, was calculated using the values of  $R_{ct}$  obtained by fitting the EIS results and applying the equation Equation (34). Gluconate proved to be a good inhibitor for CRS, with IE values higher than 80 %. The range of NaCl concentration tested in this work seems to have no clear effect on the IE results after 3 days of immersion, although some differences can be observed in terms of IE in 50 mM NaCl, with CRS in 2mM NaGluc solution displaying higher IE when compared to 5 mM NaGluc solution.

The gluconate inhibition mechanism taking place in CRS is probably based on the adsorption of gluconate on the metal oxide layer, thus suppressing anodic reactions.[122] Results presented in the literature showed gluconate working as an efficient corrosion inhibitor in low concentrations for mild steel immersed in a NaCl solution. Similar positive results were observed when gluconate was added to ordinary steel-based cooling water systems, with gluconate being adsorbed in the active sites of ordinary steel.[123]

**Table 23: Results obtained from the fitting of EIS spectra depicted in Figure 83.**

System	$(\chi^2)$	$Y(CPE_{dl})$ $Ss^n cm^{-2}$	$R_{ct}$ $\Omega cm^2$	IE %
CRS_5mM_NaCl	$(5.22 \times 10^{-5})$	$4.38 \times 10^{-4}$ (n=0.740)	$2.48 \times 10^3$	-
CRS_5mM_NaCl_2mM NaGluc	$(1.40 \times 10^{-4})$	$5.91 \times 10^{-4}$ (n=0.811)	$2.27 \times 10^4$	89.1
CRS_5mM_NaCl_5mM NaGluc	$(3.16 \times 10^{-4})$	$4.65 \times 10^{-4}$ (n=0.832)	$2.13 \times 10^4$	88.4
CRS_50mM_NaCl	$(8.39 \times 10^{-5})$	$4.66 \times 10^{-4}$ (n=0.799)	$3.37 \times 10^3$	-
CRS_50mM_NaCl_2mM NaGluc	$(3.23 \times 10^{-4})$	$6.24 \times 10^{-4}$ (n=0.758)	$2.87 \times 10^4$	88.3
CRS_50mM_NaCl_5mM NaGluc	$(1.87 \times 10^{-3})$	$3.40 \times 10^{-4}$ (n=0.815)	$1.92 \times 10^4$	82.5

### 6.5.2 LDH-Gluc and LHD-Gluc\_Alg in NaCl solution

In the previous section, the inhibition efficiency of gluconate towards CRS was discussed. Following the same approach use for LDH-Gluc in GS, the inhibition efficiency of LDH-Gluc was assessed by immersing bare CRS in a suspension of nanocontainers in a 5 mM NaCl solution. CRS was tested in 5 mM NaCl solution without nanocontainers and 5 mM NaCl loaded with: 0.1 wt.% of  $NaNO_3$ , 0.5 wt.% of LDH- $NO_3$ , 0.1 wt.% of NaGluc, 0.5 wt.% of LDH-Gluc and 0.5 wt.% of LDH-Gluc\_Alg.

After 4 hours of immersion (Figure 86a and b) all systems with gluconate show identical spectra, meaning that there are no differences between the direct addition of the

inhibitor, the encapsulated inhibitor and the modified encapsulated inhibitor using alginate. At low frequencies (10 mHz) the systems with gluconate present impedance values 1 order of magnitude higher compared with LDH-NO<sub>3</sub> and 1.5 when compared with the reference and direct addition of NaNO<sub>3</sub>. All samples are characterized by the presence of a time constant at  $f \sim 10^0 - 10^1$  Hz, which can be ascribed to charge transference resistance ( $R_{ct}$ ) and double layer ( $CPE_{dl}$ ) associated with the electrochemical process taking place on the metal surface. In the case of NaNO<sub>3</sub>, an additional time-constant occurring at low frequencies ( $10^{-2}$  Hz) can be associated with mass transport controlled processes in the corroding substrate. At high frequencies ( $f \sim 10^3 - 10^5$  Hz) is detectable the appearance of an artifact, visible in all the measurements, that cannot be attributed to the system under study. Probably, this anomaly can be associated with electronic issues with the equipment. Nevertheless, the presence of such an artifact does not affect the overall analysis of the systems studied.

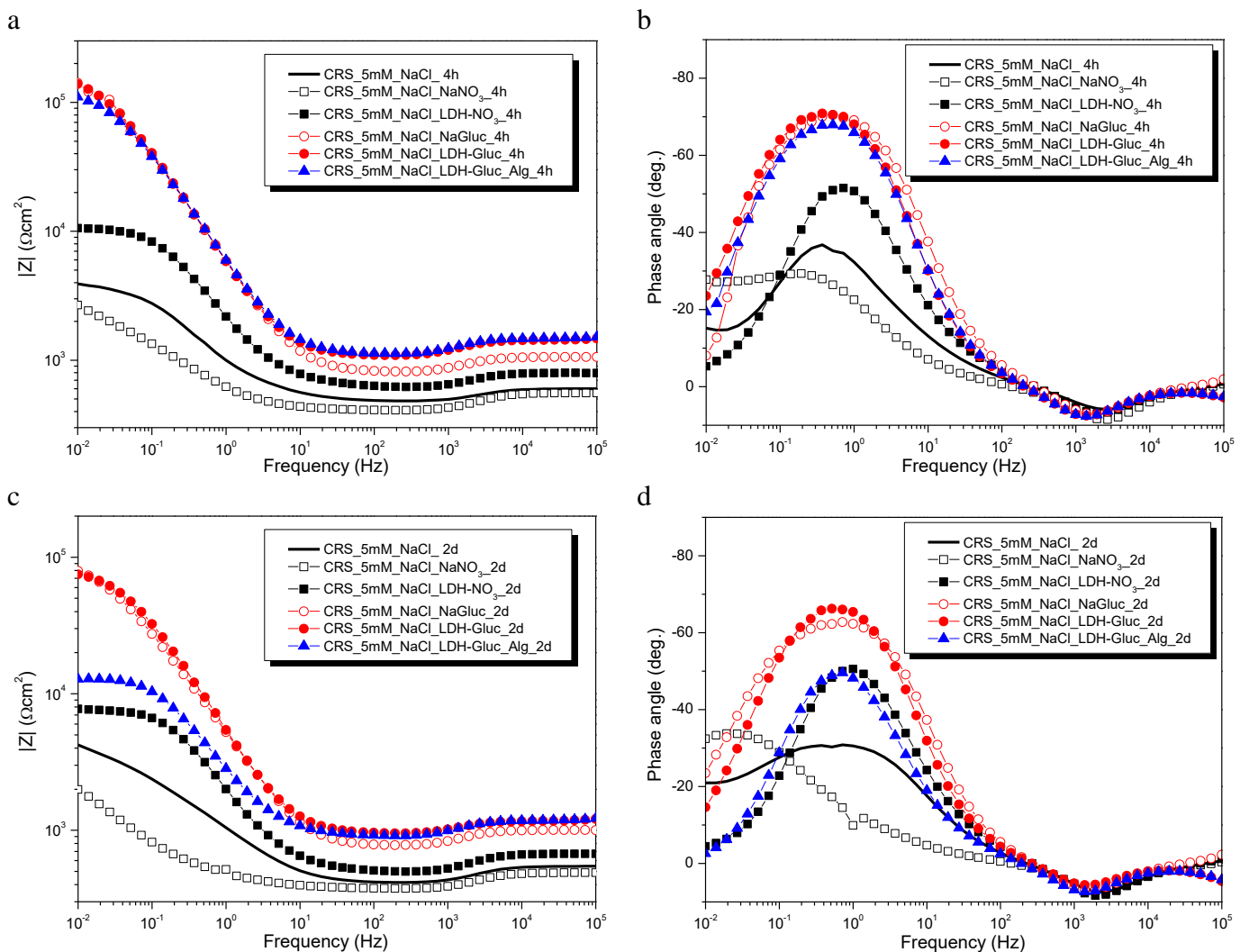


**Figure 86:** EIS spectra of CRS samples in 5 mM NaCl and 5 mM NaCl containing NaNO<sub>3</sub>, LDH-NO<sub>3</sub>, NaGluc, LDH-Gluc and LDH-Gluc\_Alg after 4 hours (a and b) and 2 days (c and d) of immersion.

After two days of immersion, the values of impedance for samples immersed in a NaGluc solution and in a suspension of LDH-Gluc decreased slightly, although still maintaining a superior performance with respect to the other systems. Nonetheless, a significant decrease in the impedance values is observed for LDH-Gluc\_Alg. This decrease may be explained by the reduced amount of gluconate released in low concentrations of NaCl due to the alginate modification, a consequence of the low ionic strength of the medium (recall release studies presented in section 6.2.2).[332] On the other hand, both reference and NaNO<sub>3</sub> show similar values of impedance at low frequencies, but a shift in the time constant is visible on the phase angle spectra, which may be explained by the severely attacked substrate.

These assumptions are confirmed by the visual assessment of the photographs taken during the immersion tests (Figure 87). The photographs reveal the presence of corrosion products on the surface of CRS in NaCl after just 4 hours of immersion, becoming completely covered with a layer of corrosion products after 2 days of immersion. For samples with LDHs in suspension, it was not possible to obtain focused images of the substrate. However, it is possible to detect the appearance of orange corrosion products in the presence of LDH-NO<sub>3</sub> after two days of immersion. This observation contrasts with results in the presence of LDH-Gluc and LDH-Gluc\_Alg. A whitish color with no formation of red rust is observed, supporting the protective action inferred from the electrochemical measurements. The protective effect of gluconate is easily seen in systems with only NaGluc. Contrastingly, the presence of only the nitrate does not show any signs of corrosion inhibition when added to the systems as NaNO<sub>3</sub>.

The parameters ( $R_{ct}$  and  $CPE_{dl}$ ) obtained from the fitting of the EIS spectra at different times are presented in Figure 88 and Table 24, show the inhibition conferred by gluconate to CRS, when directly added to a solution and when added as a host element intercalated into LDHs. The values of  $R_{ct}$  can be separated into three groups: (i) NaGluc, LDH-Gluc and LDH-Gluc\_Alg; (ii) LDH-NO<sub>3</sub>; (iii) NaNO<sub>3</sub> and reference. The values of  $R_{ct}$  of the systems where gluconate is present are around  $1 \times 10^5 \Omega \text{ cm}^2$ , compared to  $8 \times 10^3 \Omega \text{ cm}^2$  for LDH-NO<sub>3</sub> and  $3 \times 10^3 \Omega \text{ cm}^2$  for both reference and NaNO<sub>3</sub> (after 2 days of immersion). Noticeably, the presence of LDH increases in some extent the values of  $R_{ct}$ , when comparing LDH-NO<sub>3</sub>/NaNO<sub>3</sub> and LDH-Gluc/NaGluc. This increase can be ascribed to the LDH ability to entrap Cl<sup>-</sup> anions in solution leading to a decrease in the medium aggressiveness, in particular when the amount of Cl<sup>-</sup> available is reduced, 5 mM NaCl.

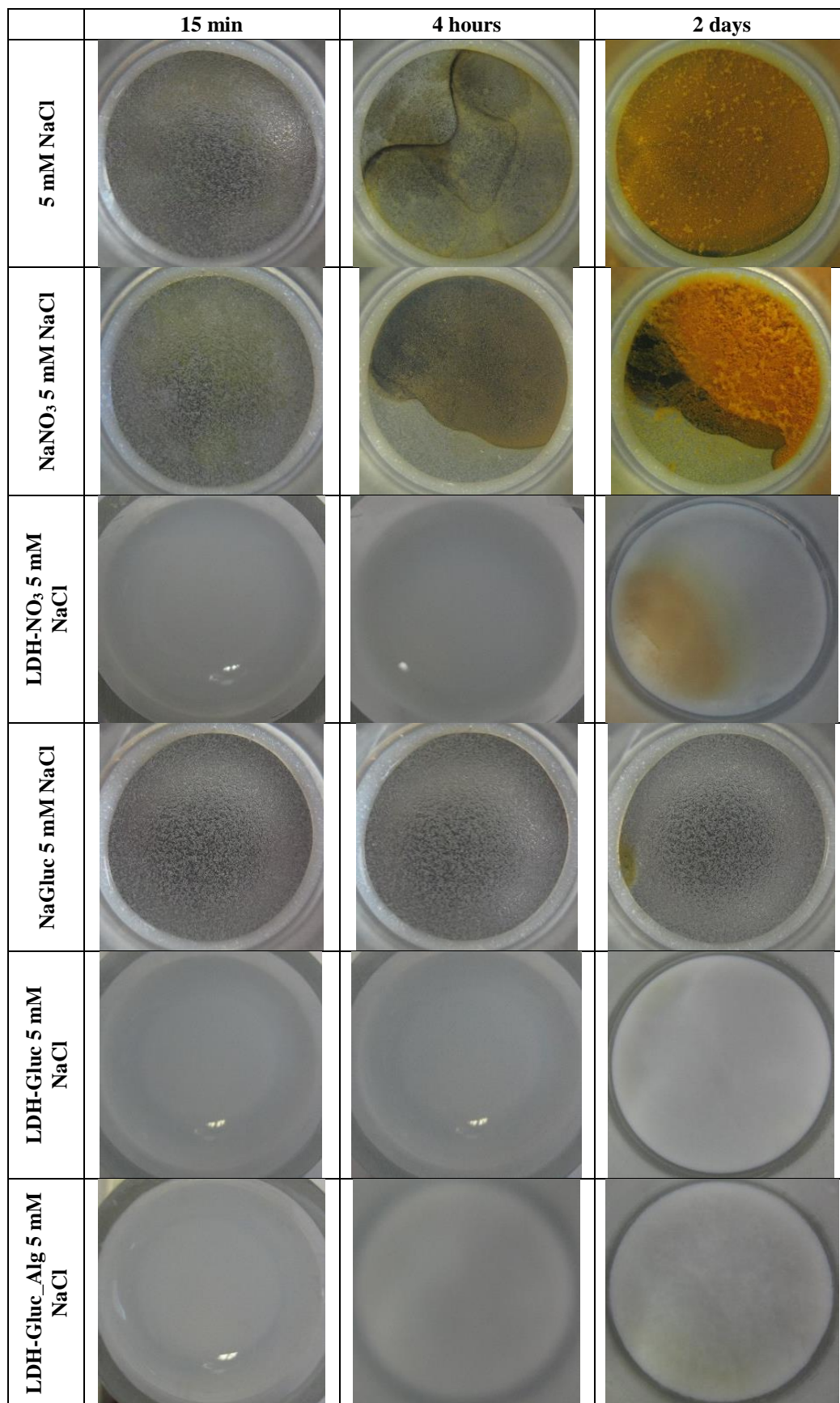


Figure 87: Photographs of bare CRS in a 5 mM NaCl solution, and 5 mM NaCl plus: 0.1 wt.% of NaNO<sub>3</sub>, 0.1 wt.% of NaGluc, 0.5 wt.% of NO LDH-NO<sub>3</sub>, 0.5 wt.% of LDH-Gluc and 0.5 wt.% of LDH-Gluc\_Alg. Photographs taken after 15 minutes, 4 hours and 2 days of immersion.

The comparison between the three systems with gluconate, NaGluc, LDH-Gluc, and LDH-Gluc\_Alg, gives for very short periods of immersion LDH-Gluc with the highest  $R_{ct}$  value (around  $4 \times 10^5 \Omega \text{ cm}^2$ ), followed by LDH-Gluc\_Alg ( $1 \times 10^5 \Omega \text{ cm}^2$ ) and finally the directly added NaGluc ( $9 \times 10^4 \Omega \text{ cm}^2$ ). After 4 hours of immersion, the  $R_{ct}$  values for these three systems are similar. After 2 days, the  $R_{ct}$  values are similar in the presence of NaGluc and LDH-Gluc, whereas for LDH-Gluc\_Alg decreased.

**Table 24: Results obtained from the fitting of EIS spectra depicted in Figure 86.**

System	Time	$(\chi^2)$	$Y(CPE_{dl})$ $Ss^n \text{ cm}^{-2}$	$R_{ct}$ $\Omega \text{ cm}^2$
CRS	4 h	$(4.26 \times 10^{-3})$	$4.04 \times 10^{-4}$ ( $n=0.831$ )	$3.47 \times 10^3$
	2 d	$(1.4 \times 10^{-2})$	$3.66 \times 10^{-4}$ ( $n=0.674$ )	$5.19 \times 10^3$
NaNO <sub>3</sub>	4 h	$(1.09 \times 10^{-2})$	$3.91 \times 10^{-4}$ ( $n=0.852$ )	$1.80 \times 10^3$
	2 d	$(1.58 \times 10^{-2})$	$1.95 \times 10^{-3}$ ( $n=0.665$ )	$2.95 \times 10^3$
LDH-NO <sub>3</sub>	4 h	$(9.70 \times 10^{-3})$	$8.50 \times 10^{-5}$ ( $n=0.970$ )	$5.80 \times 10^3$
	2 d	$(1.12 \times 10^{-2})$	$1.11 \times 10^{-4}$ ( $n=0.861$ )	$1.92 \times 10^4$
NaGluc	4 h	$(1.26 \times 10^{-2})$	$3.41 \times 10^{-5}$ ( $n=0.921$ )	$1.05 \times 10^5$
	2 d	$(8.27 \times 10^{-3})$	$4.15 \times 10^{-5}$ ( $n=0.862$ )	$9.00 \times 10^4$
LDH-Gluc	4 h	$(8.60 \times 10^{-3})$	$3.37 \times 10^{-5}$ ( $n=0.905$ )	$2.02 \times 10^5$
	2 d	$(9.54 \times 10^{-3})$	$3.24 \times 10^{-5}$ ( $n=0.906$ )	$2.09 \times 10^5$
LDH-Gluc_Alg	4 h	$(1.30 \times 10^{-2})$	$3.56 \times 10^{-5}$ ( $n=0.899$ )	$1.29 \times 10^5$
	2 d	$(1.32 \times 10^{-2})$	$3.73 \times 10^{-5}$ ( $n=0.875$ )	$6.58 \times 10^4$

The IE for LDH-Gluc was calculated using equation (34) and the  $R_{ct}$  values obtained from the fitting of the EIS data after 2 days of immersion. The relevance of gluconate is clear, with IE values around 97 % for CRS samples immersed in solutions with gluconate directly added or incorporated into the LDH (Table 25). The capsules surface modification with alginate decreases the IE for values around 82 %. In comparison, LDH without inhibitor, NO<sub>3</sub><sup>-</sup> intercalated instead of gluconate, have IE values around 69.7 % for LDH-NO<sub>3</sub> and 47.7 % for NaNO<sub>3</sub>.

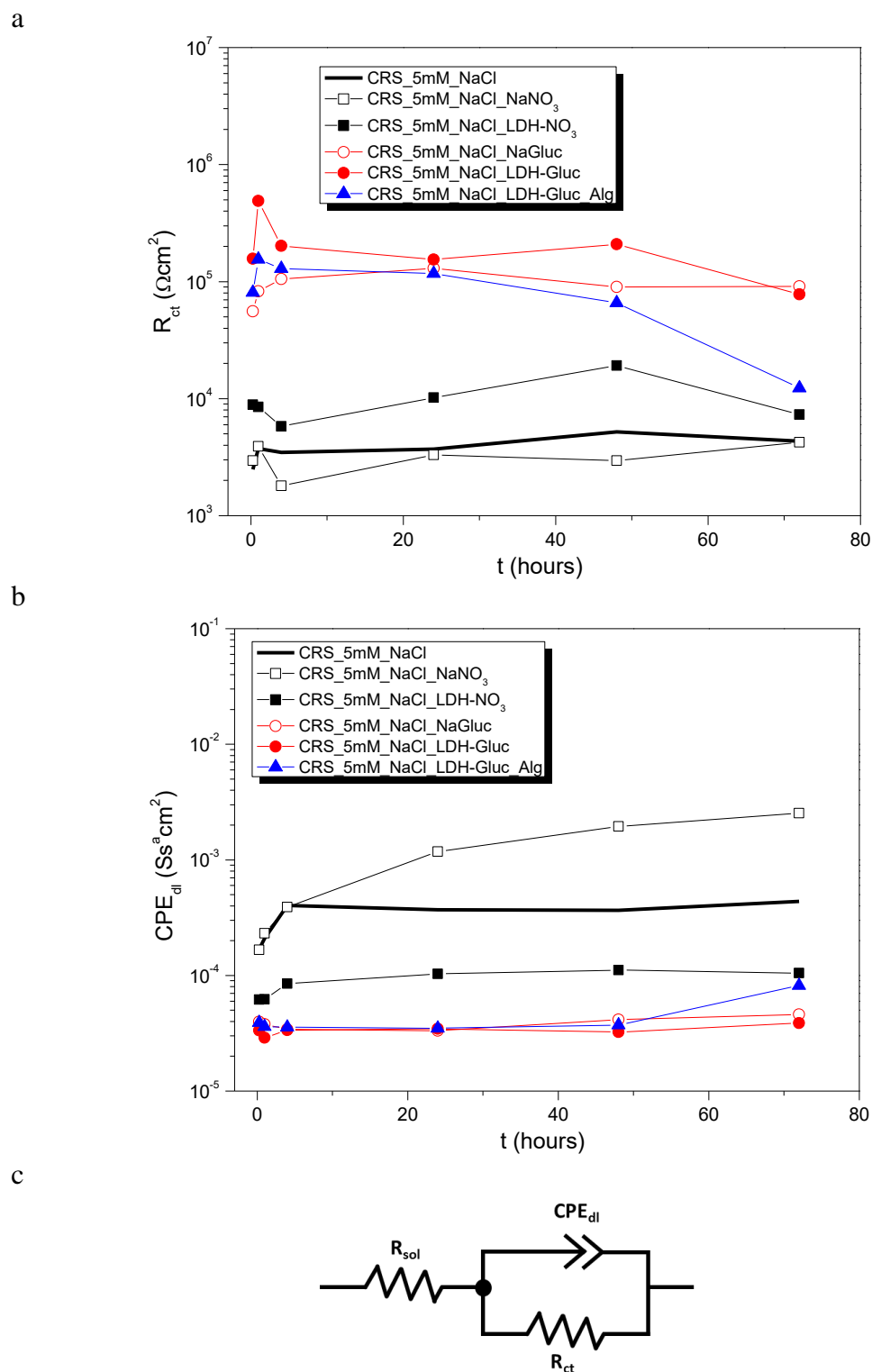


Figure 88: Evolution of  $R_{ct}$  (a) and  $CPE_{dl}$  (b) fitting parameters of CRS immersed in 5 mM NaCl (reference), 5 mM NaCl with  $NaNO_3$ , LDH- $NO_3$ , NaGluc, LDH-Gluc, and LDH-Gluc\_Alg; (c) equivalent circuits used for fitting of EIS data presented in Figure 86.

The modification with alginate decreases the inhibition efficiency of LDH-Gluc. This decrease could be related to the amount of gluconate release by the modified nanocontainers. In 5 mM NaCl the amount of gluconate release by LDH-Gluc\_Alg was

below the detection limit of the methodology used, recall (6.2.2). Nevertheless, besides the lower amount detected during the release studies in 5 mM NaCl when compared with higher concentrations, 50 and 500 mM NaCl, LDH-Gluc\_Alg display good corrosion inhibition for shorter immersion times, first 48 h. Afterward, the inhibition ability of LDH-Gluc\_Alg decreases significantly compared with LDH-Gluc and gluconate directly in solution, thus indicating the inability of the modified nanocontainers to release enough gluconate to coop with corrosion in CRS over extended periods of immersion. The full potential of LDHs loaded with gluconate will be further tested in protective coatings applied to CRS substrates. The detailed analysis of coatings loaded with “free” inhibitor, encapsulated inhibitor and encapsulated inhibitor into modified nanocontainers is presented in section 6.6.2.

**Table 25: Inhibition efficiency for CRS immersed in 5 mM NaCl loaded with: 0.1 wt.% of NaNO<sub>3</sub>, 0.5 wt.% of LDH-NO<sub>3</sub>, 0.1 wt.% of NaGluc, 0.5 wt.% of LDH-Gluc and 0.5 wt.% of LDH-Gluc\_Alg.**

System	IE %
CRS_5mM_NaCl	-
CRS_5mM_NaCl_NaNO <sub>3</sub>	47.7
CRS_5mM_NaCl_LDH-NO <sub>3</sub>	69.7
CRS_5mM_NaCl_NaGluc	97.6
CRS_5mM_NaCl_LDH-Gluc	97.1
CRS_5mM_NaCl_LDH-Gluc_Alg	82.0

## 6.6 Coated GS and CRS substrates

### 6.6.1 Modified coatings on GS substrates

In this section, besides the impact, the surface modification of LDHs produced in the coating barrier properties, the effect of the direct addition of corrosion inhibitor to coating formulations is presented as well. The potential benefits of immobilization of corrosion inhibitors have been addressed throughout this work, from examples presented in the state of the art (section 2.4) to experimental data presented in Chapter 5. These benefits include control over the release of the inhibitor and improved compatibility between the coating and the nanocontainers. The latter is explored in detail in this section by studying NaGluc interaction with TATA's coating formulation. The immobilization of gluconate in LDHs is justified only if its direct addition changes detrimentally the coating properties or the gluconate becomes less active. Thus, a comparative study between the direct addition of NaGluc and LDH-Gluc was performed. To infer on gluconate inhibition efficiency,  $\text{NaNO}_3$  and LDH- $\text{NO}_3$  were used as references.

The addition of LDHs in the form of a slurry can improve nanocontainer dispersibility since it avoids completely drying and irreversible agglomeration of particles, which can ultimately disrupt coating barrier properties. The nature of the coating formulation naturally determines the type of solvent used in the slurry.

The dispersion of the LDH slurry into TATA's formulation was achieved by mechanical stirring (in some cases being enough) or by a combination of short periods in an ultrasound bath and mechanical stirring. The LDH dispersion in the coatings after curing was surveyed qualitatively by SEM analysis (Figure 89). In these cases, LDH nanocontainers seem well dispersed, with no signs of significant agglomeration. Furthermore, the surface modification of LDH with alginate does not yield significant visual changes to the LDH dispersed in the coatings.

EIS was performed for GS panels coated with TATA's formulation, an industrial polyamide-based coating, and placed under immersion in 0.5 M NaCl solution. The resulting EIS spectra are depicted in Figure 90. After 1 day of immersion, the modification with alginate appears to improve coating barrier properties, with LDH-Gluc\_Alg presenting only one time constant, ascribed to the coating response (pore resistance in parallel with coating capacitance) and impedance values at least 1.5 orders of magnitude higher than the remaining systems at low frequencies ( $10^{-2}$  Hz). The

coatings where  $\text{NaNO}_3$  and  $\text{NaGluc}$  were added directly showed the worst results, with corrosion-related phenomena already taking place, as indicated by the presence of a second time constant at lower frequencies ( $10^{-2}$ - $10^0$  Hz), perhaps in consequence of reduced coating barrier properties. These results highlight the importance of the encapsulation/immobilization of active species to prevent detrimental interactions with the coating formulation. After 1 day of immersion, and based on the EIS results, the systems can be ranked as follows:  $\text{LDH-Gluc\_Alg} > \text{LDH-NO}_3 \approx \text{LDH-Gluc} \approx \text{reference} > \text{NaGluc} \approx \text{NaNO}_3$ .

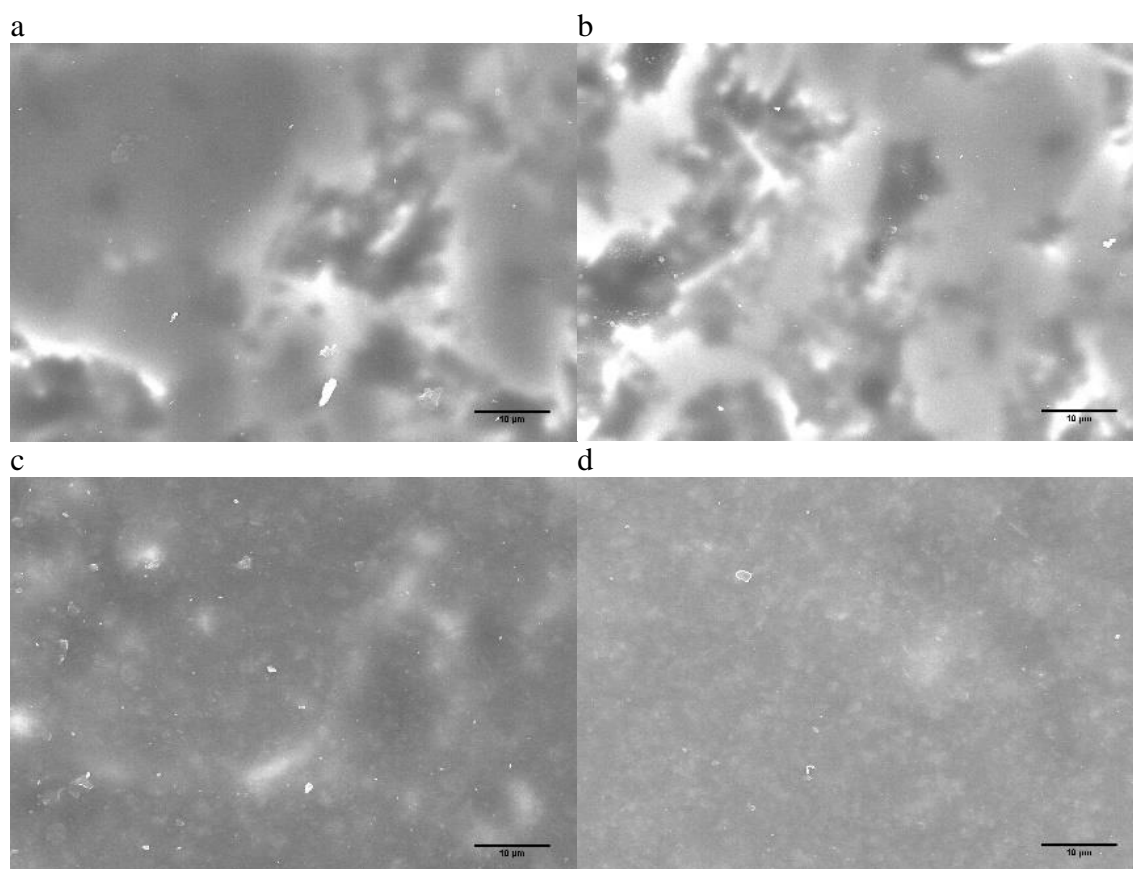


**Figure 89:** SEM images of coating applied on GS substrates: without additives (a), with  $\text{NaGluc}$  (2 wt.%) (b), with  $\text{LDH-Gluc}$  (5 wt.%) (c) and with  $\text{LDH-Gluc\_Alg}$  (5 wt.%) (d).

With the progress of immersion times up to 14 days, all the coatings lose protective properties, with impedance magnitude values decreasing and at this stage a second time constant being visible for all systems at low frequencies, associated with corrosion processes. In this case, the coatings with gluconate present the best performance ( $\text{NaGluc}$ ,  $\text{LDH-Gluc}$ , and  $\text{LDH-Gluc\_Alg}$ ). Compared with systems where  $\text{NaGluc}$  is not present these coatings show impedance values almost 2 orders of magnitude higher, at low frequencies ( $10^{-2}$  Hz). When comparing coatings loaded with  $\text{NaGluc}$ , the

improvement in coating performance in the cases where NaGluc was added in immobilized form (LDHs) is observed. Three factors could be contributing to the improved results of having NaGluc encapsulated: gluconate active properties are not affected by interaction with the coating, the coating is not significantly affected by the addition of LDH-Gluc as it is by the addition of free gluconate and the ability of LDH to entrap  $\text{Cl}^-$ . [154]

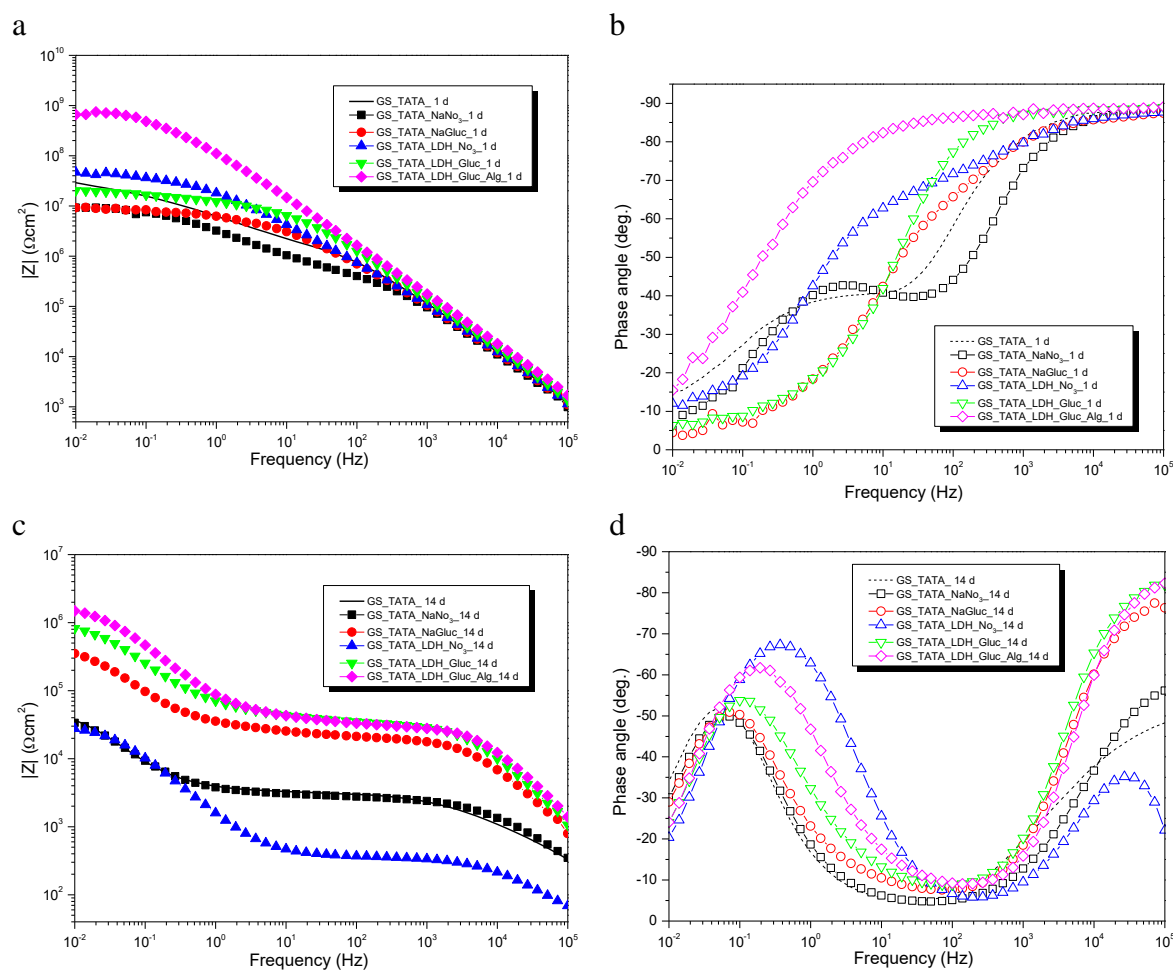


**Figure 90:** EIS spectra for coatings with NaGluc, LDH-Gluc with and without modification applied on GS substrates and after 1 hour and 28 days of immersion in a 0.5 M NaCl solution.

Noteworthy is the improvement rendered by the surface modification with alginate, already visible after 1 day of immersion and confirmed at the 14<sup>th</sup> day. Thus, after 14 days of immersion, the systems can be ranked as follows: LDH-Gluc\_Alg > LDH-Gluc > NaGluc > reference  $\approx$  NaNO<sub>3</sub>  $\approx$  LDH-NO<sub>3</sub>.

For a better understanding of the processes occurring during the immersion tests and to have a quantitative assessment of the coating barrier properties, the EIS data were fitted with the equivalent circuits presented in Figure 91c and d, with the results being

presented in Table 26, for measurements after 1 day and 14 days, and in Figure 91a and b for all the measurements until 14 days. The two equivalent circuits include the coating response ( $CPE_{coat}$  and  $R_{coat}$ ) and for the second one the presence of the corrosion process taking place at the metal surface, double layer response ( $CPE_{dl}$ ) and charge transference ( $R_{ct}$ ). The equivalent circuit in Figure 91c was used in the cases when only one-time constant was visible and was ascribed to the coating. Equivalent circuit in Figure 91d was used when the EIS spectrum indicates the presence of two-time constants, ascribed to the coating and corrosion processes.

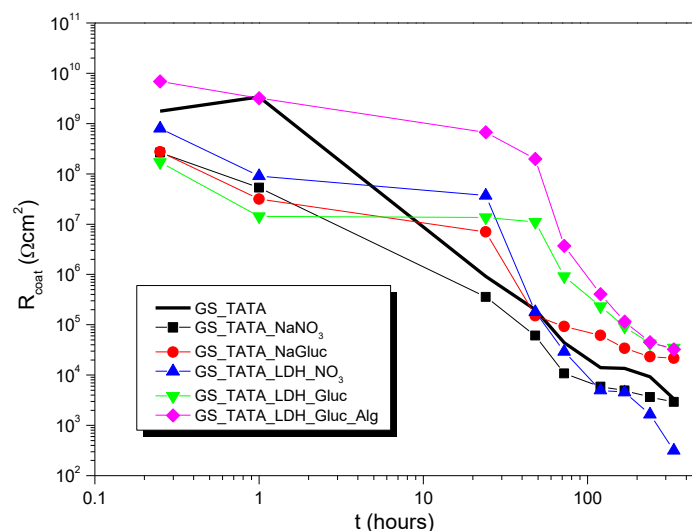
**Table 26: Results obtained from the fitting of EIS spectra depicted in Figure 90.**

System	Time	$(\chi^2)$	$Y(CPE_{coat})$ $Ss^n cm^{-2}$	$R_{coat}$ $\Omega cm^2$	$Y(CPE_{dl})$ $Ss^n cm^{-2}$	$R_{ct}$ $\Omega cm^2$
TATA	1 d	$(9.25 \times 10^{-4})$	$1.59 \times 10^{-9}$ (n=0.984)	$9.13 \times 10^5$	$5.67 \times 10^{-8}$ (n=0.984)	$3.56 \times 10^7$
	14 d	$(4.46 \times 10^{-4})$	$1.07 \times 10^{-6}$ (n=0.588)	$3.35 \times 10^3$	$1.87 \times 10^{-4}$ (n=0.827)	$5.73 \times 10^4$
NaNO <sub>3</sub>	1 d	$(1.54 \times 10^{-3})$	$1.93 \times 10^{-9}$ (n=0.976)	$3.57 \times 10^5$	$8.54 \times 10^{-8}$ (n=0.615)	$1.02 \times 10^7$
	14 d	$(1.44 \times 10^{-3})$	$2.73 \times 10^{-7}$ (n=0.685)	$2.92 \times 10^3$	$1.71 \times 10^{-4}$ (n=0.782)	$5.23 \times 10^4$
NaGluc	1 d	$(3.72 \times 10^{-2})$	$5.60 \times 10^{-9}$ (n=0.875)	$7.03 \times 10^6$		
	14 d	$(6.32 \times 10^{-3})$	$8.27 \times 10^{-9}$ (n=0.880)	$2.15 \times 10^4$	$1.47 \times 10^{-5}$ (n=0.703)	$6.71 \times 10^5$
LDH-NO <sub>3</sub>	1 d	$(4.50 \times 10^{-2})$	$6.47 \times 10^{-9}$ (n=0.859)	$3.71 \times 10^7$		
	14 d	$(9.72 \times 10^{-4})$	$7.08 \times 10^{-7}$ (n=0.783)	$3.17 \times 10^2$	$1.34 \times 10^{-4}$ (n=0.867)	$3.19 \times 10^4$
LDH-Gluc	1 d	$(3.74 \times 10^{-2})$	$2.03 \times 10^{-9}$ (n=0.944)	$1.37 \times 10^7$		
	14 d	$(6.31 \times 10^{-3})$	$3.88 \times 10^{-9}$ (n=0.916)	$3.50 \times 10^4$	$5.38 \times 10^{-6}$ (n=0.726)	$1.30 \times 10^6$
LDH-Gluc_Alg	1 d	$(1.87 \times 10^{-2})$	$1.51 \times 10^{-9}$ (n=0.949)	$6.73 \times 10^8$		
	14 d	$(5.97 \times 10^{-3})$	$2.86 \times 10^{-9}$ (n=0.922)	$3.26 \times 10^4$	$3.03 \times 10^{-6}$ (n=0.794)	$2.06 \times 10^6$

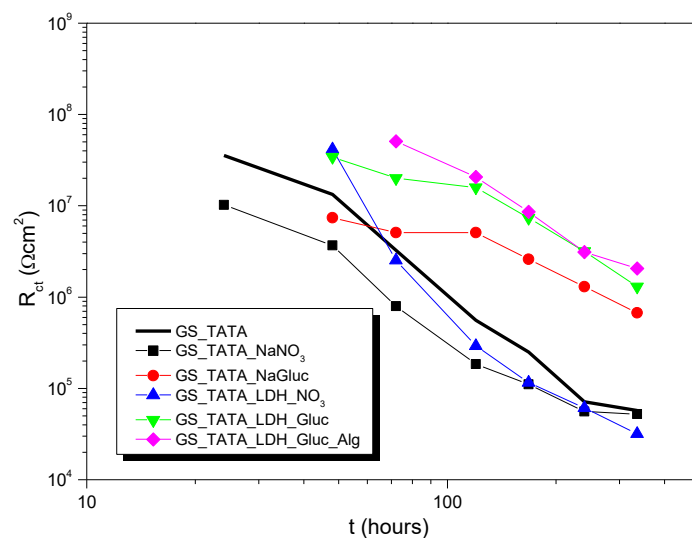
The addition of LDHs improved the coating pore resistance when compared with the coating with the direct addition of additives, NaNO<sub>3</sub> and NaGluc. After 1 day of immersion, significant differences are visible in the values of  $R_{coat}$  (Figure 91a), around  $10^7$  and  $10^8 \Omega cm^2$ , which compare with values around  $10^5$  and  $10^6 \Omega cm^2$  for the reference and coatings loaded with NO<sub>3</sub> and NaGluc. Overall, the coating with modified LDH-Gluc\_Alg provides the largest  $R_{coat}$ ,  $6.73 \times 10^8 \Omega cm^2$ . After 14 days of immersion, the coatings barrier properties decrease significantly for all the system, although values of  $R_{coat}$  are still one order of magnitude higher for the best systems (coatings loaded with gluconate added directly or encapsulated) when compared to the remaining systems. For this immersion time, the second time constant ascribed to corrosion process taking place on the metal surface ( $CPE_{dl}$  and  $R_{ct}$ ), can be used to differentiate the protective level conferred by the coating from an active corrosion protection perspective, Figure 91b. As

expected, the presence of gluconate improves the corrosion protection, yielding higher values of  $R_{ct}$ . For the systems where gluconate was absent (reference,  $\text{NaNO}_3$ , and LDH- $\text{NO}_3$ ) the values of  $R_{ct}$  were found to be around  $10^4 \Omega\text{cm}^2$ , while in the case of NaGluc directly added and in cases where gluconate was encapsulated, LDH-Gluc and LDH-Gluc\_Alg, the values were around  $10^5 \Omega\text{cm}^2$  and  $10^6 \Omega\text{cm}^2$ , respectively. Again, the best results were observed for LDH-Gluc-Alg.

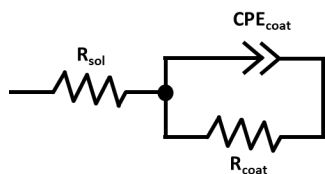
a



b



c



d

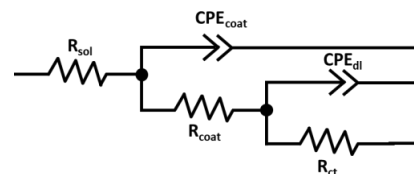


Figure 91: Evolution of  $R_{coat}$  (a) and  $R_{ct}$  (b) fitting parameters of GS samples coated with TATA formulation, and TATA formulation loaded with 2 wt.% of NaGluc and  $\text{NaNO}_3$  and 5 wt.% of LDH- $\text{NO}_3$  LDH-Gluc, LDH-Gluc\_PSS, and LDH-Gluc\_Alg. The samples were tested under immersion in a 0.5 M NaCl; (c) and (d) equivalent circuits used for fitting of EIS data presented in Figure 90.

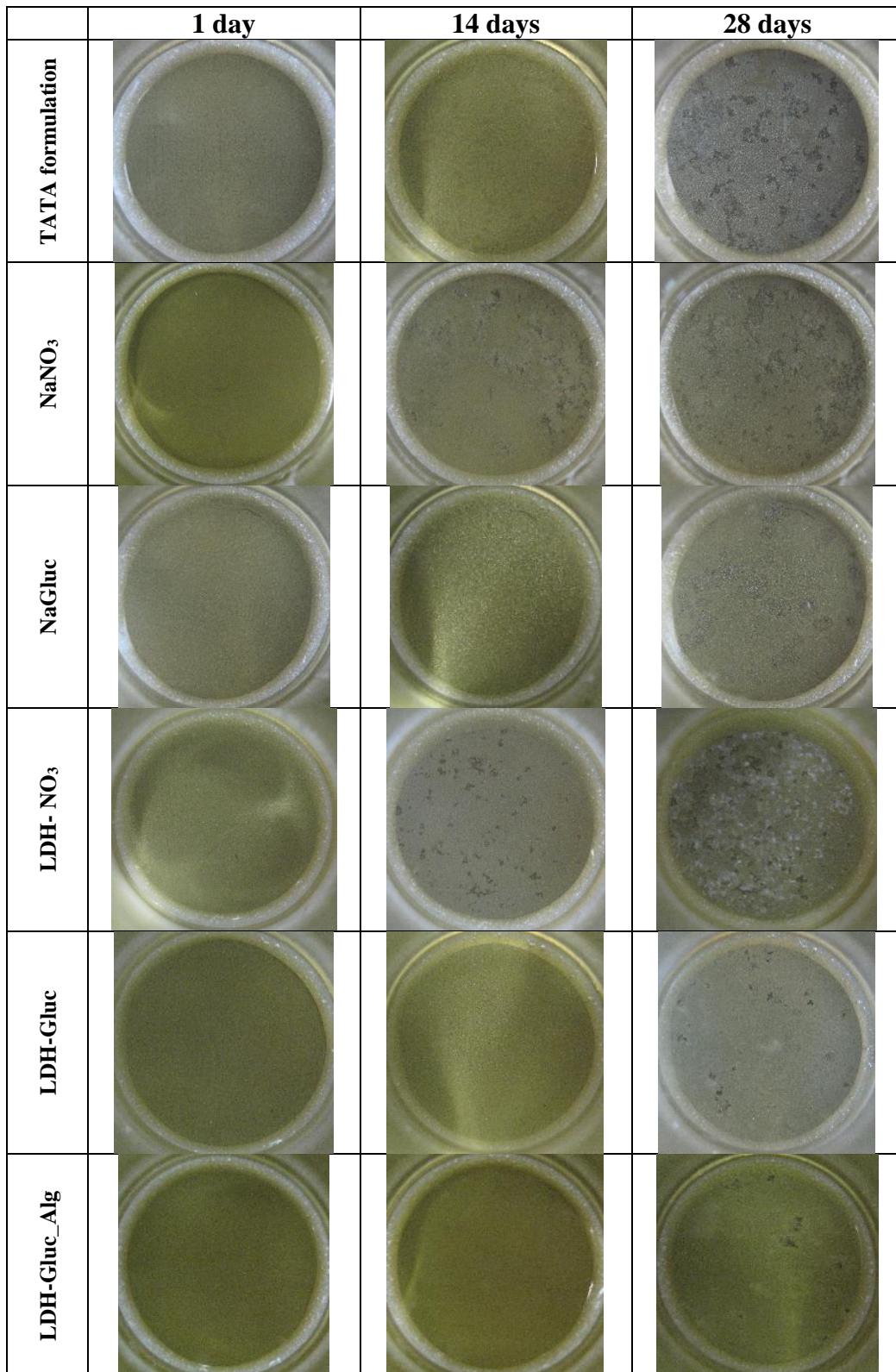


Figure 92: Photographs of coatings with NaGluc, LDH-NO<sub>3</sub>, LDH-Gluc and LDH-Gluc modified with alginate applied on GS substrates after 1 day, 1 week and 4 weeks of immersion in a 0.5 M NaCl solution.

The visual assessment of the samples, presented in Figure 92, is in agreement with the EIS findings, with coatings with Gluc-based systems showing no significant signs of corrosion after 14 days of immersion. In the case of coating loaded with  $\text{NaNO}_3$  and LDH- $\text{NO}_3$ , it is possible to detect the appearance of some defects (dark spots) on the coating and some discoloration at the metal surface. After 28 days of immersion, all the coatings indicate the existence of corrosion processes taking place at the metal surface, with different levels of degradation. In systems where gluconate is present the corrosion tended to be less extensive compared with the reference and coatings loaded with  $\text{NO}_3$ -based systems.

To further analyze the active corrosion protection provided by gluconate and separate it from the coating barrier effect, SVET - Scanning Vibrating Electrode Technique measurements were performed and the resulting current density maps are presented in Figure 93. Before starting the measurements coated samples were artificially damaged (using a sharp needle) to expose the metal substrate and thus be able to measure ionic currents in a 50 mM NaCl solution.

The coating without any anticorrosion additive shows a continuous increase in the current density close to the sites where the defects had been previously done. This is fully expected, considering that lack of active species to stop corrosion on the exposed sites. Moreover, the coating loaded with gluconate shows a similar behavior, which can be due to the fact that gluconate is not fully available in sufficient amounts to stop the progression of corrosion in these sites. This may be rationalized in terms of the strong interaction between gluconate and functional groups from the coating matrix. On the other hand, both LDH-Gluc and LDH-Gluc\_Alg show a significant reduction in terms of corrosion processes in the defect areas, inferred from the significant lower anodic and cathodic ionic current densities measured.

Surface modification of LDH-Gluc with alginate appears to improve anticorrosion properties of waterborne organic-based coatings, mostly by improving coating barrier properties. Comparing coatings loaded with LDH-Gluc vs. NaGluc, an improvement of active protection is visible in the former case.

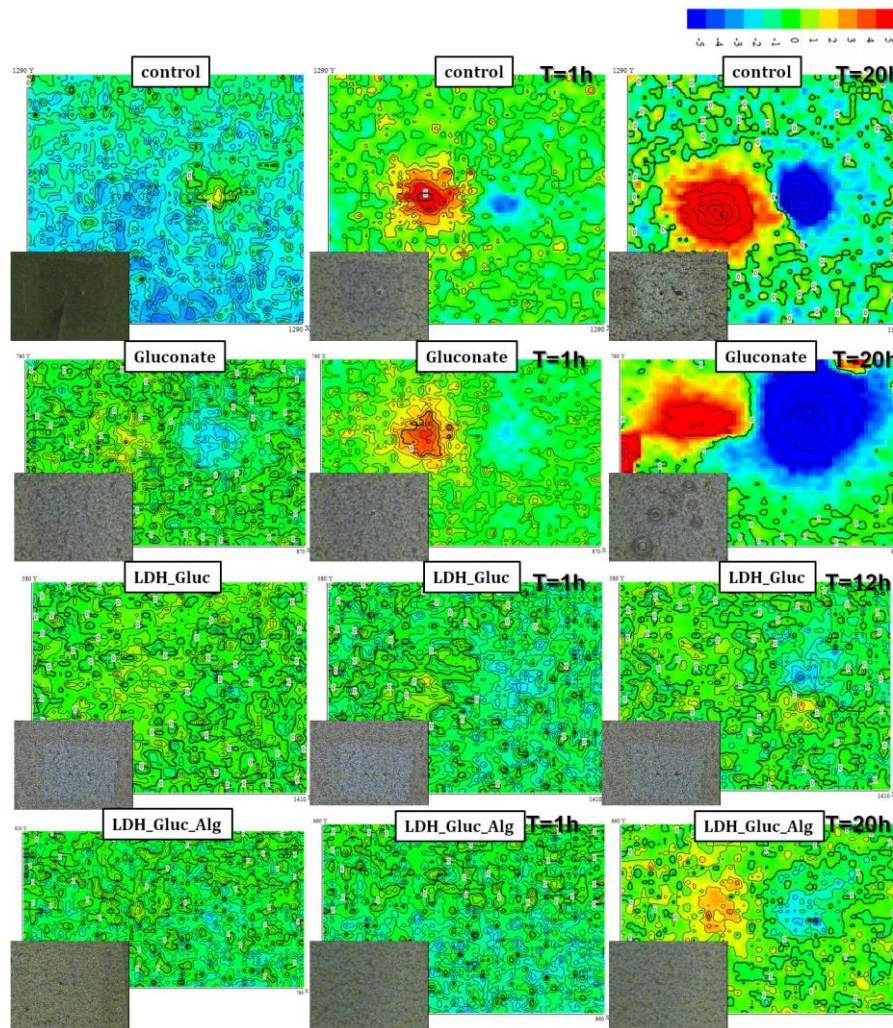
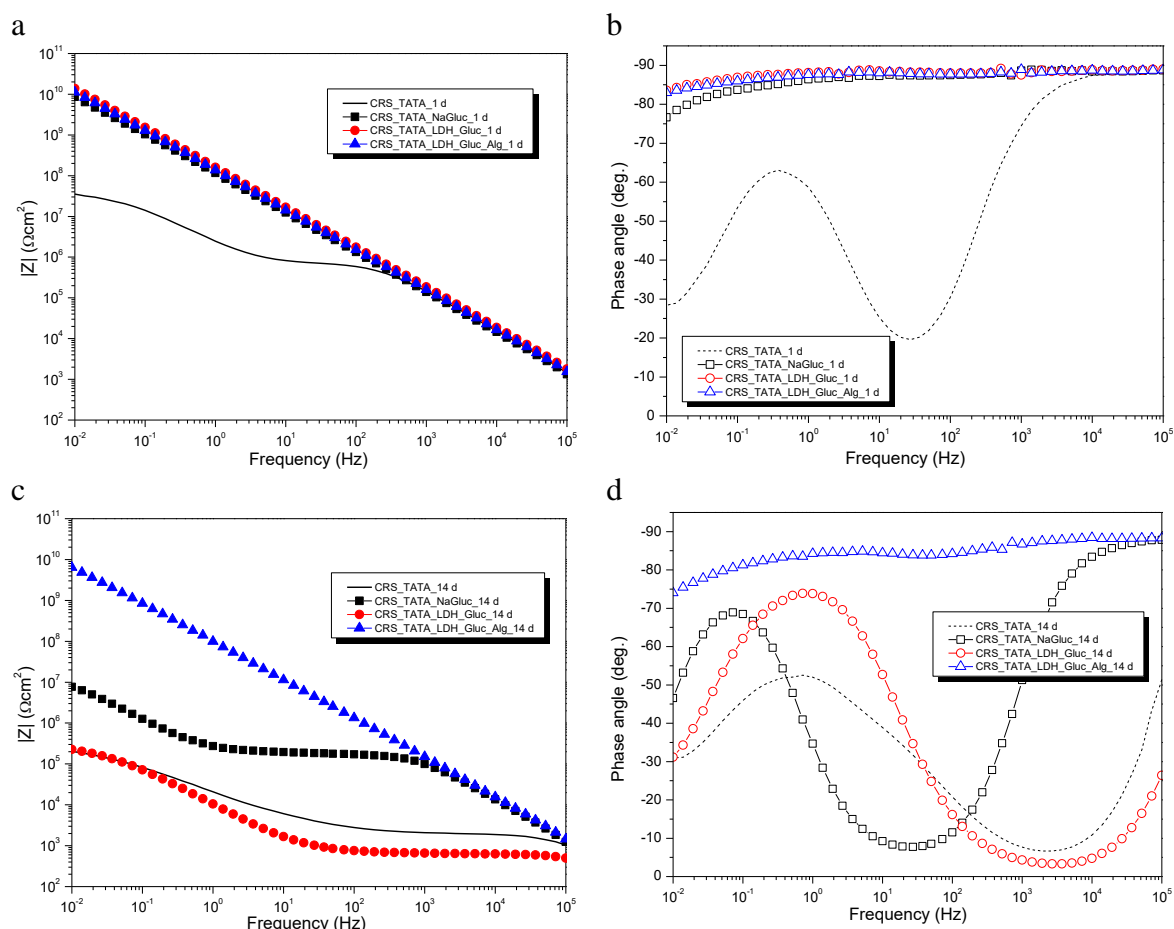


Figure 93: SVET analysis of coated GS, coating loaded with gluconate and LDH with and without modification immersed in a 50 mM NaCl solution. The current color scale bar indicates ionic current densities between  $-5$  to  $5 \mu\text{A cm}^{-2}$ .

## 6.6.2 Modified coatings on CRS substrates

The effect that surface modification of LDHs with alginate has on the properties of coatings applied in CRS substrates was evaluated by EIS. In Figure 94, EIS spectra after 1 day and 14 days of immersion are depicted for TATA's (blank), NaGluc-, LDH-Gluc- and LDH-Gluc-Alg-loaded coatings. The direct addition of NaGluc and LDH-Gluc show similar results, both coatings presenting good barrier properties after 1 day of immersion, which contrasts with the response of the blank coating. The reference at low frequencies presented impedance values 2.5 orders of magnitude lower than coatings loaded with NaGluc, LDH-Gluc, and LDH-Gluc\_Alg. The existence of two well defined time constants for the reference, with one associated with the coating barrier effect (high frequencies  $10^3$ - $10^5$  Hz) and a second associated with corrosion processes (intermediate

frequencies  $10^{-1}$ - $10^0$  Hz), contrasts with the existence of only the capacitive response of the coating visible for all the other samples, associated with the coating barrier properties.



**Figure 94:** EIS spectra for coatings loaded with LDH-Gluc and modified LDH-Gluc after 1 day (a and b) and 14 days (c and d) of immersion in 0.5 M NaCl.

After 14 days of immersion, the coatings loaded with NaGluc and LDH-Gluc show a remarkable decrease in impedance with two-time constants being already detected. On the other hand, LDH-Gluc\_Alg still remain stable throughout the test and only the time constant associated with the coating barrier properties is visible. The reference shows also a considerable decrease in terms of impedance values, which was already visible after only one day of immersion. Thus, the degradation of the reference, NaGluc- and LDH-Gluc-loaded indicate that the LDH additives are not imparting any additional effect on the coating degradation. On the other hand, LDH-Gluc modified with alginate presents excellent results, with no signs of coating degradation even after 14 days of immersion. These results support the need to modify LDHs with polyelectrolytes to improve coating performance in terms of barrier properties.

The results obtained for CRS, regarding the ranking of the samples by coating barrier properties, are similar to the ones observed for GS. The best and worst systems coincide, coatings with LDH-Gluc\_Algl as the best and coating without nanocontainers as the worst. Nevertheless, samples with LDH-Gluc and NaGluc do not display the same performance for both substrates. In the case of CRS, NaGluc improves slightly comparing with GS, contrasting with the poor coating barrier properties displayed by coatings loaded with LDH-Gluc. There is no obvious explanation for this variation. One possibility could be related with gluconate interference with the CRS substrates affecting the overall coating properties, since one is directly added to the coating (NaGluc) and the second releases higher amounts than the modified counterpart (LDH-Gluc\_Algl), which could be producing a detrimental effect on the coating chemistry. Regardless of the order in which the intermediate systems are, the relevant result is the improvement provided by the surface modification with alginate, producing always the coating with the best barrier properties.

The fitting of the EIS results allows for a quantitative analysis of the coating barrier properties through the values of pore resistance ( $R_{coat}$ ). The EIS data were fitted using the equivalent circuits shown in Figure 95b and c, one time constant ascribed to the coating ( $CPE_{coat}$  and  $R_{coat}$ ) and two-time constants associated with the coating ( $CPE_{coat}$  and  $R_{coat}$ ) and another with the corrosion processes occurring at the metal surface ( $CPE_{dl}$  and  $R_{ct}$ ). Table 27 presents the results of the fittings after 1 and 14 days. After 1 day of immersion, only the reference coating presents significant signs of coating degradation, Figure 96, with the presence of two-time constants associated with the coating response and corrosion process taking place at the metal surface. The value of  $R_{coat}$  is significantly lower than the remaining systems  $6.70 \times 10^5 \Omega cm^2$ , at least four orders of magnitude lower than the remaining systems. All coatings loaded with additives presented only one time constant ascribed to the coating resistivity, with values of  $R_{coat}$  of  $3.68 \times 10^9 \Omega cm^2$  (NaGluc),  $9.77 \times 10^{10} \Omega cm^2$  (LDH-Gluc\_Algl) and  $1.33 \times 10^{11} \Omega cm^2$  (LDH-Gluc). The difference between the direct addition of NaGluc compared with inhibitor intercalated into the LDHs structure is significant. After one day of immersion the samples can be ranked as TATA  $\ll$  NaGluc  $<$  LDH-Gluc\_Algl  $\approx$  LDH-Gluc.

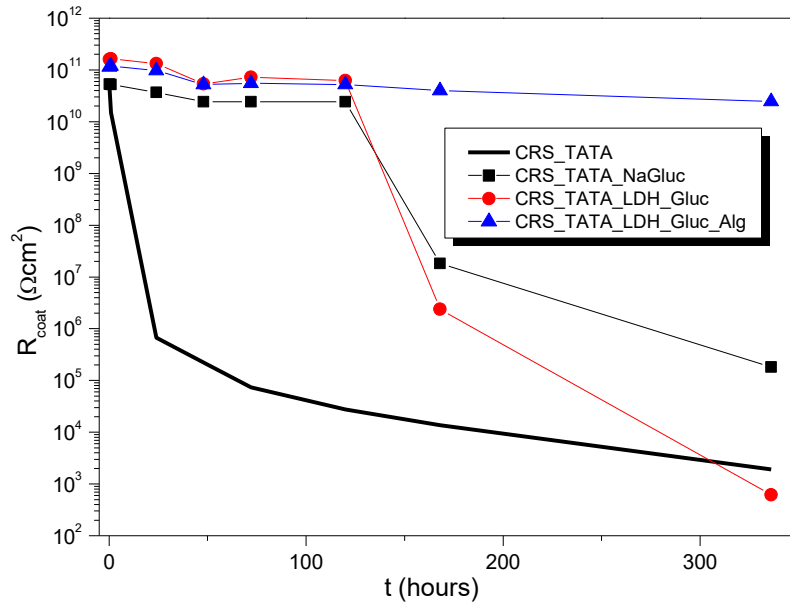
**Table 27: Results obtained from the fitting of EIS spectra depicted in Figure 94.**

System	Time	( $\chi^2$ )	Y(CPE <sub>coat</sub> ) Ss <sup>n</sup> cm <sup>-2</sup>	R <sub>coat</sub> Ωcm <sup>2</sup>	Y(CPE <sub>dl</sub> ) Ss <sup>n</sup> cm <sup>-2</sup>	R <sub>et</sub> Ωcm <sup>2</sup>
TATA	1 d	(1.86x10 <sup>-3</sup> )	1.25x10 <sup>-9</sup> (n=0.984)	6.70x10 <sup>5</sup>	9.61x10 <sup>-8</sup> (n=0.823)	4.13x10 <sup>7</sup>
	14 d	(1.10x10 <sup>-3</sup> )	4.14x10 <sup>-9</sup> (n=0.909)	1.91x10 <sup>3</sup>	1.50x10 <sup>-5</sup> (n=0.635)	3.57x10 <sup>5</sup>
NaGluc	1 d	(2.93x10 <sup>-3</sup> )	1.50x10 <sup>-9</sup> (n=0.971)	3.68x10 <sup>9</sup>		
	14 d	(2.37x10 <sup>-3</sup> )	1.55x10 <sup>-9</sup> (n=0.978)	1.81x10 <sup>5</sup>	1.20x10 <sup>-6</sup> (n=0.881)	1.50x10 <sup>7</sup>
LDH-Gluc	1 d	(7.01x10 <sup>-4</sup> )	1.03x10 <sup>-9</sup> (n=0.982)	1.33x10 <sup>11</sup>		
	14 d	(1.52x10 <sup>-3</sup> )	2.84x10 <sup>-8</sup> (n=0.790)	6.13x10 <sup>2</sup>	1.99x10 <sup>-5</sup> (n=0.859)	2.82x10 <sup>5</sup>
LDH-Gluc_Alg	1 d	(1.20x10 <sup>-3</sup> )	1.23x10 <sup>-9</sup> (n=0.978)	9.77x10 <sup>10</sup>		
	14 d	(5.92x10 <sup>-3</sup> )	1.79x10 <sup>-9</sup> (n=0.948)	2.47x10 <sup>10</sup>		

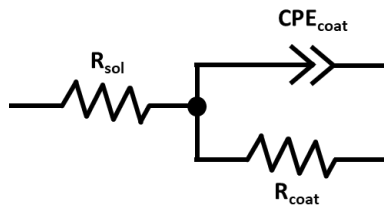
After 14 days significant changes occur, with coatings loaded with LDH-Gluc presenting a significant decrease in the coating barrier properties, falling from the best system to the worst in terms of coating barrier properties, as shown in Figure 95a. The same occurs with coating loaded with NaGluc, where a significant decrease in coating barrier properties starts to be visible after 7 days of immersion, around the same time as coating loaded with LDH-Gluc. The only system with the coating barrier properties intact is the one with LDH-Gluc\_Alg, with values of R<sub>coat</sub> of 2.47 x 10<sup>10</sup> Ωcm<sup>2</sup> after 14 days of immersion. The remaining systems present values of R<sub>coat</sub> considerably lower: 1.81 x 10<sup>5</sup> Ωcm<sup>2</sup> (NaGluc), 1.91 x 10<sup>3</sup> Ωcm<sup>2</sup> (TATA) and 6.13 x 10<sup>2</sup> Ωcm<sup>2</sup> (LDH-Gluc). Based on these values of R<sub>coat</sub> the systems can be ranked as follows: LDH-Gluc ≈ TATA < NaGluc << LDH-Gluc\_Alg.

The visual analysis of the samples under testing was carried out and results are presented in Figure 96. After one day of immersion only the reference coating show signs of corrosion (highlighted with the red circle), which is in agreement with the interpretation of EIS spectra. After 14 days of immersion the same level of corrosion is visible for the reference coating, as well as for coatings loaded with LDH-Gluc, while the direct addition of NaGluc yielded coatings with corrosion occurring but in less extent than the previous ones. After 28 days of immersion, these samples presented a severely damaged coating with widespread corrosion across the CRS surfaces. Coatings with modified LDHs (LDH-Gluc\_Alg) keep the appearance during all the monitored time.

a



b



c

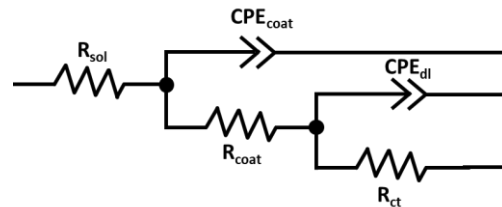


Figure 95: Evolution of  $R_{coat}$  (a) and  $R_{ct}$  (b) fitting parameters of CRS samples coated with TATA formulation, and TATA formulation loaded with NaGluc, LDH-Gluc and LDH-Gluc\_Alg. The samples were tested under immersion in a 5 mM NaCl; (c) and (d) equivalent circuits used for fitting of EIS data presented in Table 27.

The results indicate advantages when incorporating corrosion inhibitor NaGluc into LDH, in particular for shorter immersion times. For longer periods of testing the presence of LDH-Gluc seems to affect negatively the coating barrier properties leading to a sudden loss of coating efficiency. On the other hand, the results also indicate improvements in coating/nanocontainer interaction due to the presence of alginate on its surface, decreasing the level of matrix disruption, as a result of the presence of LDHs. The effect of the corrosion inhibition of gluconate is not clear, but some improvements were observed for coatings loaded with NaGluc, with  $R_{ct}$  values higher than the reference and LDH-Gluc. However, the results obtained for LDH-Gluc does not give any indication of corrosion inhibition processes taking place on the CRS surface. In the case of LDH-Gluc\_Alg coating degradation was not detected during at least 28 days, showing the absence of corrosion.

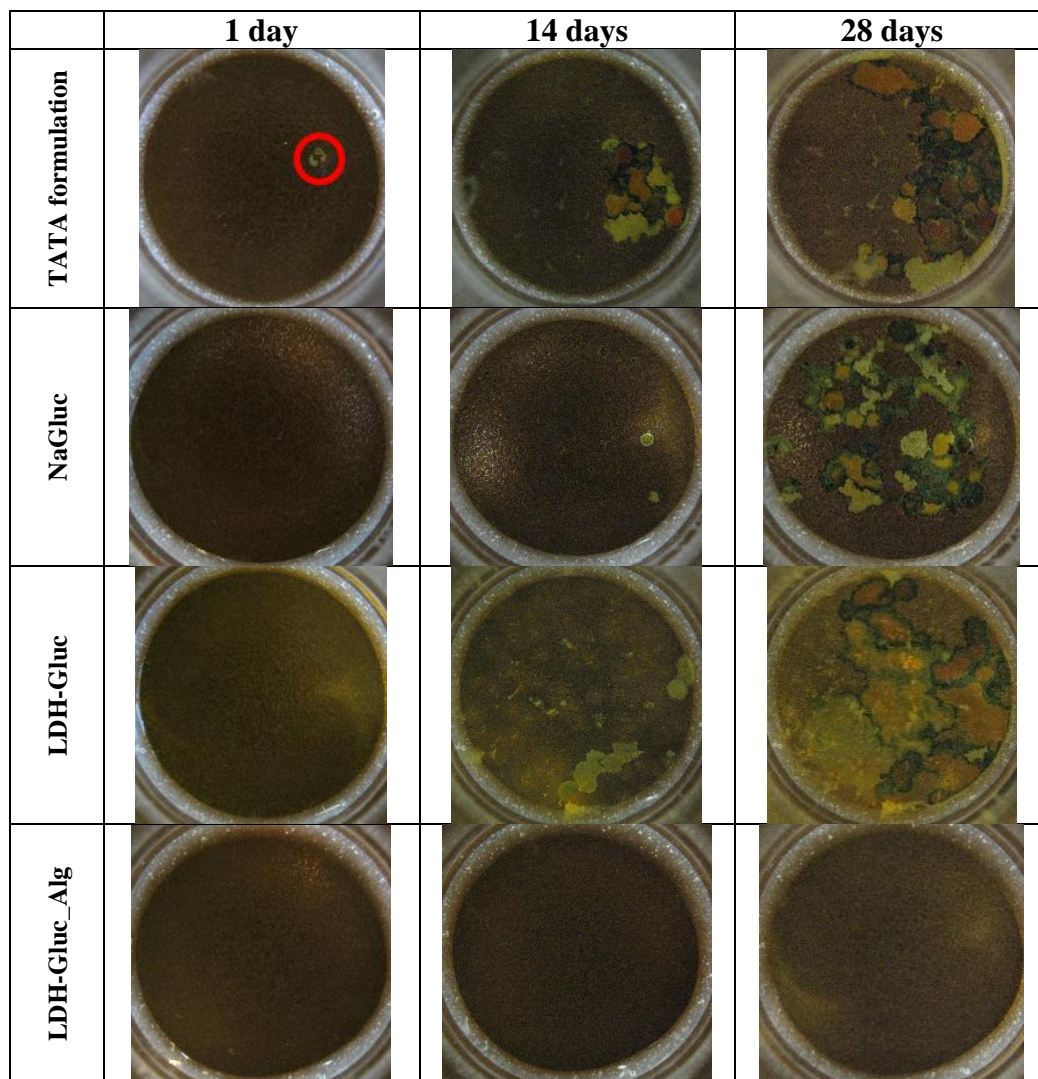


Figure 96: Photographs of coated samples with gluconate, LDH-Gluc with and without modification.

## 6.7 Partial conclusions

The deposition of polyelectrolyte shells onto LDH proved successful, even for LDH loaded with gluconate corrosion inhibitor, allowing the formation of a shell, which provides the double effect of preventing nanocontainer/formulation detrimental effects and changes in the release profile. Alginate was shown to enhance LDH dispersibility and the stability in water and water-based formulations. Moreover, the surface modification did not affect the anticorrosion ability of the LDH-Gluc.

The influence that the surface modification could have on the coating barrier properties was assessed only for LDH modified with alginate instead of PSS, due to options taken in the course of the industrial project in which this work was carried out. The option for alginate instead of PSS was based on environmental aspects and cost efficiency. The addition of modified LDH to the industrial coating, TATA's formulation, yielded good results compared to the reference and coating loaded with LDH-Gluc and direct addition of NaGluc. The modification with alginate delayed coating barrier properties degradation in the case of GS and maintained them for CRS, in the first case due to the inhibition effect of the gluconate on the GS substrate and in the second case due to the improvement in the coating barrier properties. The anticorrosion character of the LDH-Gluc was kept intact for GS since coatings loaded with gluconate-based systems yielded good corrosion inhibition results. In the case of CRS, such effect was not observed, probably due to a weaker inhibition effect on CRS by the gluconate. CRS tends to corrode faster than GS since the lack of the zinc protective layer in the case of GS could be impairing the gluconate inhibition mechanism, which is based on the adsorption of gluconate at the metal surface. When the nanocontainers or the coatings start to release gluconate the surface is already extensively corroded.



## 7

# Silica nanocapsules

## Prometheus

Titan! to whose immortal eyes  
 The sufferings of mortality,  
 Seen in their sad reality,  
 Were not as things that gods despise;  
 What was thy pity's recompense?  
 A silent suffering, and intense;  
 The rock, the vulture, and the chain,  
 All that the proud can feel of pain,  
 The agony they do not show,  
 The suffocating sense of woe,  
 Which speaks but in its loneliness,  
 And then is jealous lest the sky  
 Should have a listener, nor will sigh  
 Until its voice is echoless.

Titan! to thee the strife was given  
 Between the suffering and the will,  
 Which torture where they cannot kill;  
 And the inexorable Heaven,  
 And the deaf tyranny of Fate,  
 The ruling principle of Hate,  
 Which for its pleasure doth create  
 The things it may annihilate,  
 Refus'd thee even the boon to die:  
 The wretched gift Eternity  
 Was thine—and thou hast borne it well.  
 All that the Thunderer wrung from thee  
 Was but the menace which flung back  
 On him the torments of thy rack;  
 The fate thou didst so well foresee,  
 But would not to appease him tell;  
 And in thy Silence was his Sentence,  
 And in his Soul a vain repentance,  
 And evil dread so ill dissembled,  
 That in his hand the lightnings trembled.

Thy Godlike crime was to be kind,  
 To render with thy precepts less  
 The sum of human wretchedness,  
 And strengthen Man with his own mind;  
 But baffled as thou wert from high,  
 Still in thy patient energy,  
 In the endurance, and repulse  
 Of thine impenetrable Spirit,  
 Which Earth and Heaven could not convulse,  
 A mighty lesson we inherit:  
 Thou art a symbol and a sign  
 To Mortals of their fate and force;  
 Like thee, Man is in part divine,  
 A troubled stream from a pure source;  
 And Man in portions can foresee  
 His own funereal destiny;  
 His wretchedness, and his resistance,  
 And his sad unallied existence:  
 To which his Spirit may oppose  
 Itself—and equal to all woes,  
 And a firm will, and a deep sense,  
 Which even in torture can descry  
 Its own concentr'd recompense,  
 Triumphant where it dares defy,  
 And making Death a Victory.

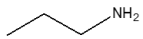
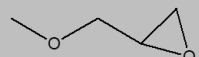
by Lord Byron



## 7.1 Synthesis and characterization of modified Si<sub>2</sub>NC

The selection of silica nanocapsules (Si<sub>2</sub>NC) as a model system for surface modification was based on two main reasons: (i) the possibility of using them as reservoirs for corrosion inhibitors, work which has been developed within our group,[160] and (ii) the versatility inherently associated to silane chemistry.[206, 335, 336] Si<sub>2</sub>NC are characterized by a core-shell structure with a gradual porosity, where it is possible to encapsulate active compounds, in a one-step synthesis, such as corrosion inhibitors[160] or pH indicators.[337] In contrast, mesoporous silica nanoparticles reported in the literature are usually characterized by a structure with uniform porosity on its surface, where active elements are encapsulated by adsorption, in a two-step process.[158]

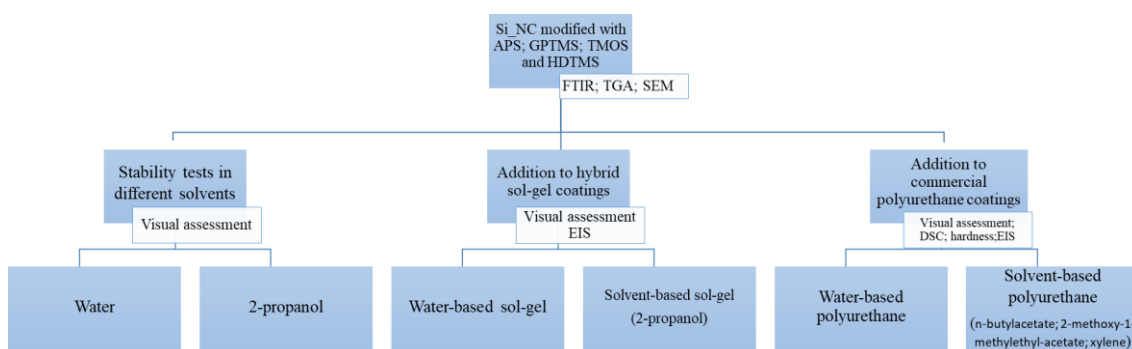
**Table 28: Samples' identification, modification agents, and main functional groups present at the nanocontainer surface after modification.**

Nanocontainer	Modification agent	Main functional group
Si <sub>2</sub> NC		Hydroxyl 
Si <sub>2</sub> NC_APS	(3-aminopropyl)triethoxysilane (APS)	Amine 
Si <sub>2</sub> NC_GPTMS	3-glycidoxypropyltrimethoxysilane (GPTMS)	Epoxy 
Si <sub>2</sub> NC_TMOS	trimethoxy(octadecyl)silane (TMOS)	Aliphatic chain 
Si <sub>2</sub> NC_HDTMS	hexadecyl trimethoxy silane (HDTMS)	Aliphatic chain 

The selection of functional groups, to be grafted into Si<sub>2</sub>NC, was made aiming at the improvement of the nanocontainer's stability in the coating formulations, compatibility with water- (APS and GPTMS) or solvent-based formulations (TMOS and HDTMS), chemical interactions with the coating formulation (APS and GPTMS) and overall improvement against aqueous electrolyte species due to the hydrophobic nature of the modifier agent (TMOS and HDTMS). A list with the selected siloxane derivatives is presented in Table 28.

The goal of the work carried out and presented in this chapter is to understand how the surface chemistry of modified Si<sub>3</sub>N<sub>4</sub> affects the coating performance (Scheme 6). The approach to this work was based upon a characterization of (un)modified particles in different steps, increasing the degree of complexity: stability in different solvents, testing in hybrid sol-gel systems developed in SECOP group and, finally, tests in organic coatings, commercially available.

The simple evaluation of stability in different solvents constitutes the first step to unveil whether good dispersion can be achieved later on in coating formulations based on those solvents. Then, the next step was to investigate how the addition of Si<sub>3</sub>N<sub>4</sub> can affect sol-gel coatings. The interesting aspect related to the selection of these coatings relies upon the similarity of chemistry between the Si<sub>3</sub>N<sub>4</sub> and the type of reactions occurring to obtain a 3D network -Si-O-Si- (hydrolysis/condensation reactions), [131, 132, 149] moving from solvent to a solvent/film-forming formulation. Finally, studies were carried out with conventional organic coating formulations in an attempt to extrapolate some of the lab-scale studies obtained to more complex formulations (composed of a solvent, film-forming agent, fillers, additives ...).



**Scheme 6:** Flow chart showing the experimental approach followed for testing Si<sub>3</sub>N<sub>4</sub> modification impact on coating formulations.

The present chapter is divided into two main sections: preparation and characterization of Si<sub>3</sub>N<sub>4</sub> with different functional groups, and compatibility tests. The latter is subdivided into the study of modified Si<sub>3</sub>N<sub>4</sub> in solvents, model sol-gel, and commercially available organic coating systems. At the end of this section, standard tests used by the industry are compared with electrochemical approaches, attempting the validation of EIS as a suitable technique to monitor the evolution with time of the barrier properties of nanocontainers-modified coatings.

### 7.1.1 Si\_NC modification with (3-aminopropyl)triethoxysilane

The first modification introduced in the Si\_NC was carried out using (3-aminopropyl)triethoxysilane (APS). Two procedures were selected to achieve this purpose: a two-step process (Si\_NC synthesis followed by modification); and a one-step process (Si\_NC synthesis and APS grafting combined in the same reaction). The one-step approach was found to cause problems since the uniformity and yields of nanocontainers synthesized were reduced. Thus, the two-step process was selected, with the modification being carried out in Si\_NC suspended in toluene under reflux, for different reaction times (2, 4 and 8 hours) and different Si\_NC:APS ratio (1:0.5, 1:1 and 1:2).[206]

The FTIR analysis is commonly used to verify qualitatively the successful grafting of APS moieties.[206, 338] In Figure 97 are presented the FTIR spectra for Si\_NC\_APS obtained for different reaction conditions. The characteristic absorption bands associated with Si\_NC can be found at  $1050\text{ cm}^{-1}$  and  $960\text{ cm}^{-1}$ , associated with the asymmetric stretching and bending of silanol groups (Si-OH) present at the surface.[336] At  $440\text{ cm}^{-1}$  the symmetric stretching vibration and bending vibration of siloxane groups (Si-O-Si) can be seen.[336, 338] The modification with APS produces some changes in the FTIR spectrum, with the appearance of a new band at  $1560\text{ cm}^{-1}$  attributed to the N-H bending vibration of primary amines (-NH<sub>2</sub>), which is usually detected in the region between  $1605$  and  $1560\text{ cm}^{-1}$ . [339] There is a decrease in intensity in the band at  $960\text{ cm}^{-1}$  as a result of the modification, with the Si-OH bond being replaced with Si-O-Si. Also, a new absorption band, ascribed to the APS structure, can be seen around  $1384\text{ cm}^{-1}$  and is associated with the Si-CH<sub>2</sub> bending mode.[336]

The degree of the modification in Si\_NC\_APS is difficult to determine by direct analysis of FTIR spectra. The strategy adopted in this work to investigate the extent of modification was via thermal characterization of the Si\_NC\_APS, namely by determining the weight loss by TGA within a wide temperature range ( $25\text{ }^{\circ}\text{C}$  to  $800\text{ }^{\circ}\text{C}$ ), which is a technique used for similar purposes in several works available in the literature.[160, 339]

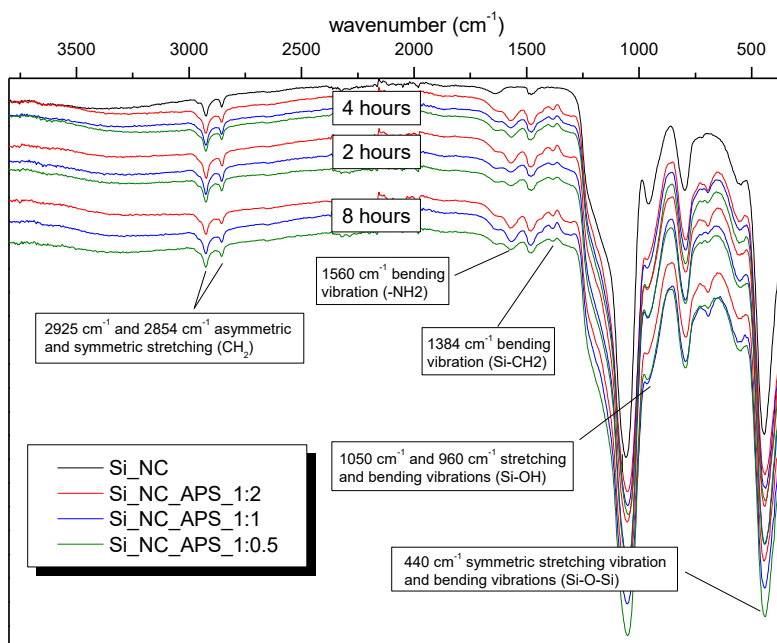


**Figure 97: FTIR spectra for Si\_NC and Si\_NC modified with APS.**

The TGA thermograms for Si\_NC and Si\_NC\_APS under different reaction conditions are presented in Figure 98. Typically, the first weight loss (50–160 °C) can be ascribed to the removal of the physically adsorbed water from the nanocontainers.[340] The second weight loss (160–800 °C) is due to the degradation of the non-hydrolyzed and non-condensed TEOS, some residual amount of surfactant and also with the APS grafted to Si\_NC.[160, 341] In the case of calcined Si\_NC, since all the groups capable of being decomposed had been eliminated previously, the second weight loss process could not be observed. The estimation of APS grafted was thus obtained by subtracting the content of adsorbed water together with unreacted hydroxyl groups in unmodified Si\_NC, which works as the reference material and accounts for roughly 20.3% of the weight loss, as shown in Figure 98. According to the results presented in Table 29, the largest degree of modification (inferred from weight loss) was found when longer reaction times and larger amounts of APS were combined. For cost- and time-effectiveness we selected, as reference conditions for surface modification with other functional groups, a ratio of Si\_NC:Silane 1:1 and 4 hours of reaction.

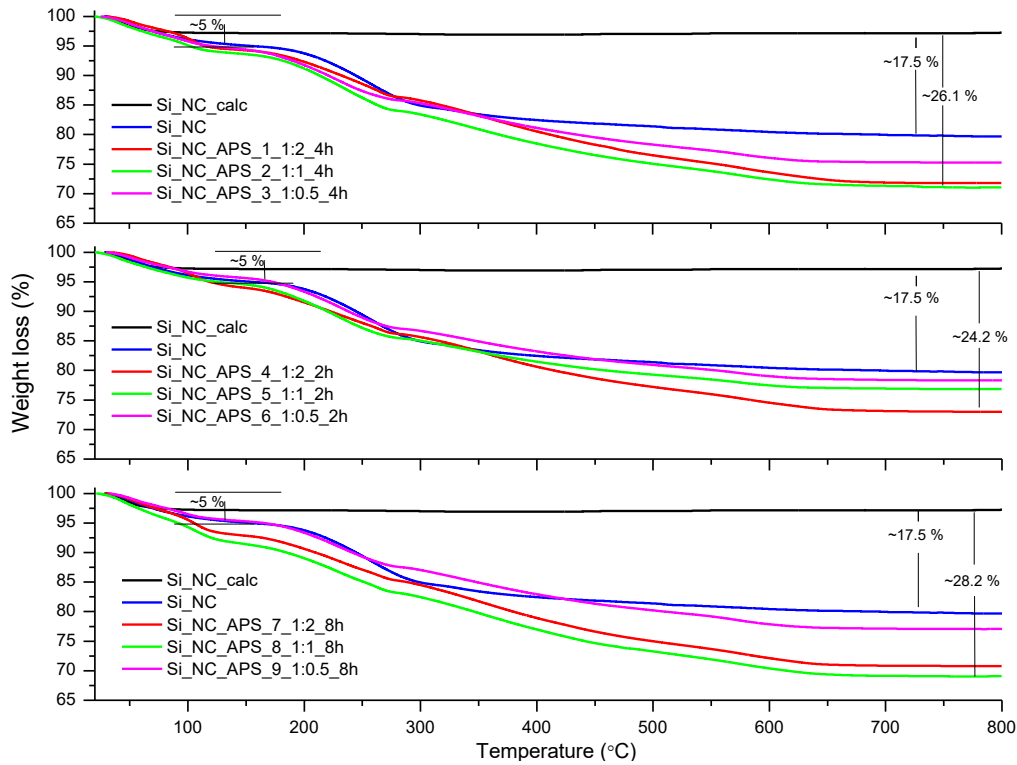


Figure 98: TG analysis of Si\_NC calcine, Si\_NC and Si\_NC modified with APS.

Table 29: Weight loss percentages obtained from TGA thermograms of Si\_NC and SI\_NC\_APS samples.

Sample	Weight loss (%)	Weight loss (%) after modification (APS)
Si_NC_calc	2.8	-
Si_NC	20.3	-
Si_NC_APS_1_1:2_4h	28.2	7.9
Si_NC_APS_2_1:1_4h	28.9	8.6
Si_NC_APS_3_1:0.5_4h	24.6	4.3
Si_NC_APS_1_1:2_2h	27.1	6.8
Si_NC_APS_2_1:1_2h	23.1	2.8
Si_NC_APS_3_1:0.5_2h	21.7	1.4
Si_NC_APS_1_1:2_8h	29.2	8.9
Si_NC_APS_2_1:1_8h	30.9	10.6
Si_NC_APS_3_1:0.5_8h	22.9	2.6

### 7.1.2 Si\_NC surface modification

In Figure 99 the FTIR spectra obtained for Si\_NC modified with APS, GPTMS, TMOS, and HDTMS, prepared under the experimental conditions indicated at the end of the previous section, are presented. The characteristic bands associated with Si\_NC can be found at  $1050\text{ cm}^{-1}$  and  $960\text{ cm}^{-1}$ , corresponding to the stretching and bending vibrations of silanol groups (Si-OH), and at  $440\text{ cm}^{-1}$  and  $800\text{ cm}^{-1}$ , ascribed to the symmetric stretching vibration and bending vibration of siloxane groups (Si-O-Si). Apart from these Si\_NC characteristic bands, a new one is observed at  $1560\text{ cm}^{-1}$  associated with the bending vibration of primary amines ( $-\text{NH}_2$ ) for Si\_NC\_APS. Also, an increase in intensity for the bands at  $2925\text{ cm}^{-1}$  and  $2854\text{ cm}^{-1}$  attributed to the asymmetric and symmetric  $\text{CH}_2$  stretching vibrational frequencies, respectively, for Si\_NC\_TMOS and Si\_NC\_HDTMS is observed.

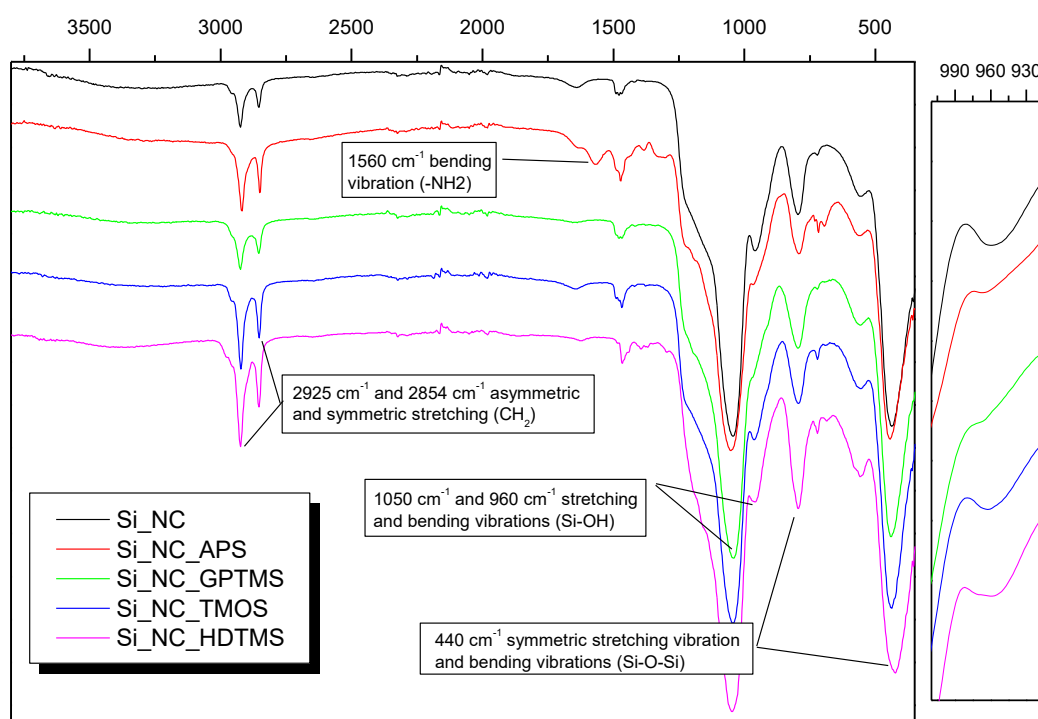
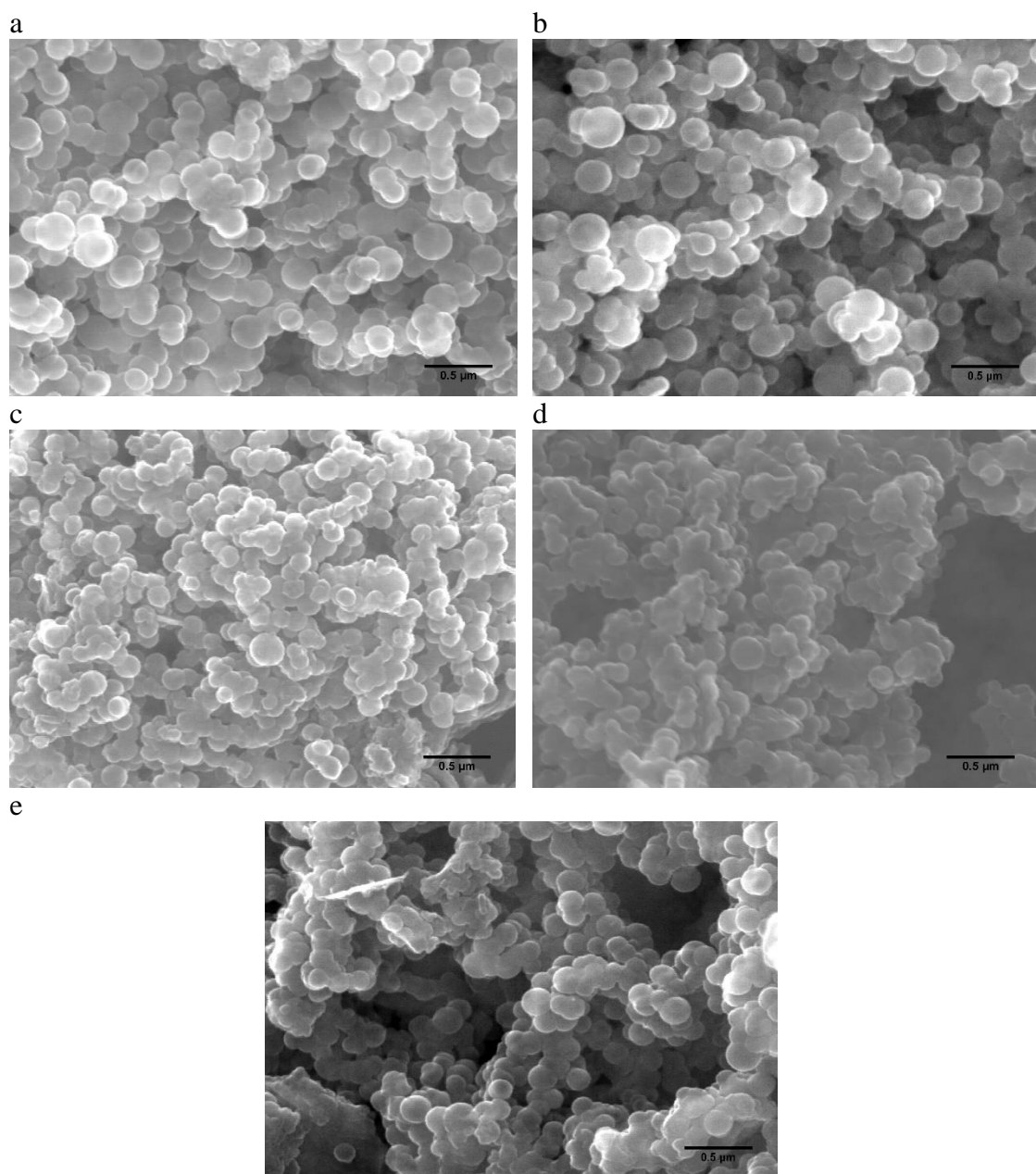


Figure 99: FTIR spectra for Si\_NC modified silane derivatives APS, GPTMS, TMOS, and HDTMS.

The FTIR spectrum obtained for Si\_NC\_GPTMS does not provide a clear evidence of the modification by the occurrence of new characteristic bands. Nevertheless, it presents a significant change, common to all the modified Si\_NC, which is the decrease in intensity of the band at  $960\text{ cm}^{-1}$  associated with the silanol groups, as observed in the inset shown in Figure 99. The decrease is in direct relation with the modification of Si\_NC

since Si-OH groups are replaced by Si-O-Si bonds, associated with the reaction between the nanocontainer and the modifying agent.[336, 338]



**Figure 100: SEM micrographs of Si\_NC (a), Si\_NC\_APS (b), Si\_NC\_GPTMS (c), Si\_NC\_TMOS (d) and Si\_NC\_HDTMS. The samples were dispersed in water and ethanol (Si\_NC\_TMOS and Si\_NC\_HDTMS) prior to deposition.**

The influence of surface modification on the morphology of Si\_NC was investigated by SEM (Figure 100). The images do not show significant changes in terms of shape or size after modification, with the Si\_NC exhibiting a perfectly spherical shape and a narrow size distribution. The nanocontainers presented size values around 200 nm in diameter.

## 7.2 Stability of silica nanocontainers in different media

One of the aims to change the surface chemistry of Si\_NC is the improvement of the nanocontainers dispersion and stability in different media. Having nanocontainers loaded with corrosion inhibitors able to disperse well and with good stability is an important aspect of coating development. The Si\_NC prepared and modified with different functional groups and presented in the previous section were tested in terms of dispersion and stability under suspension in two different solvents, water, and 2-propanol, the main components of the hybrid sol-gel based coatings presented in the next section. These results can be extrapolated with a certain degree of caution for water-based polyurethane coatings since they are composed roughly by more than 65 % water (recall section 4.3). In the case of the solvent-based polyurethane formulation, the extrapolation of the stability results observed for 2-propanol can be more speculative due to the more complex composition of the formulation: n-butyl acetate, 2-methoxy-1-methyl ethyl-acetate, and xylene. Besides, issues arising from the complexity of the solvent composition, there is also the significant percentage of solids present in the commercial formulations, 35 and 50 wt.% for water- and solvent-based, respectively. As a result, the solid content can be responsible for changing the viscosity and consequently affect several parameters rendering the direct comparison between the test performed on a based solvent, *e.g.* water, and a fully functional coating very difficult.

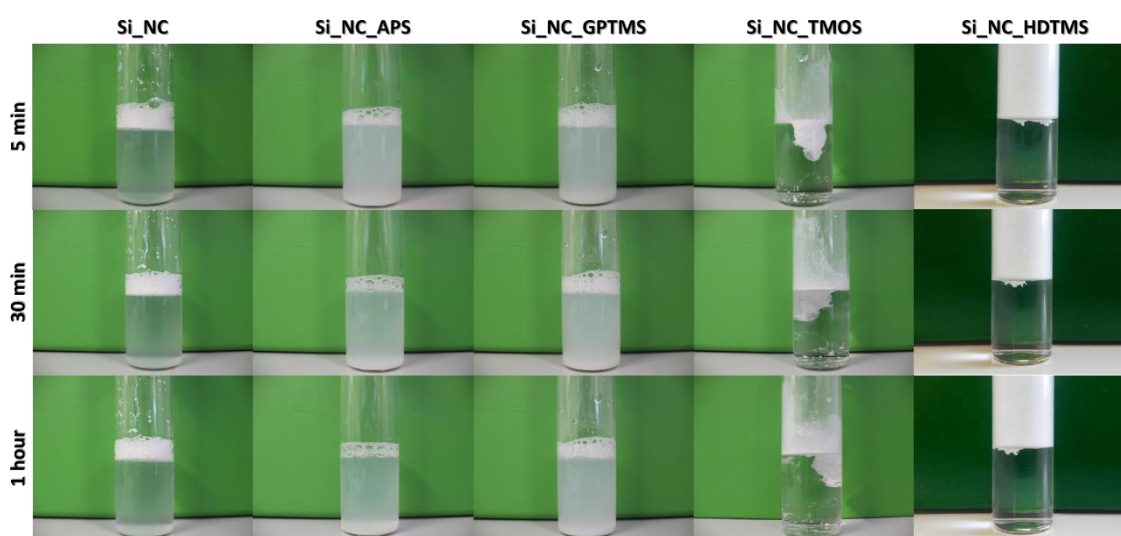


**Figure 101:** 0.5 wt.% (50 mg of nanocontainers in 10 ml of water) of Si\_NC and modified Si\_NC with APS, GPTMS, TMOS and HDTMS added to water to assess its stability as a function of time: 5, 10 and 60 minutes. The particles were added as dry powders, dispersed for 5 min in ultrasounds immediately before the test.

Figure 101 shows photographs of suspensions of Si<sub>3</sub>N<sub>4</sub> and modified Si<sub>3</sub>N<sub>4</sub> in water acquired as a function of time. As it can be seen, different functional groups affect differently the stability of the suspensions. The unmodified Si<sub>3</sub>N<sub>4</sub> tend to settle on the bottom of the vial after just a few minutes. On the other hand, clear improvements are observed in functionalization with APS and partially with GPTMS. In the case of GPTMS, the inclusion of epoxy groups seems to favor interactions with water molecules (*e.g.* dipole-dipole), whereas in the case of APS the presence of amine groups may allow the establishment of stronger secondary bonds (hydrogen bonding). Contrastingly, the modification with TMOS results in poor wetting, with the Si<sub>3</sub>N<sub>4</sub> remaining “dried” even after vigorous shaking. The strong hydrophobic character of Si<sub>3</sub>N<sub>4</sub>\_TMOS and Si<sub>3</sub>N<sub>4</sub>\_HDTMS results from the presence of aliphatic chains consisting of 18 and 16 carbons, respectively, and the stabilization of these groups in strong polar media is thus not favored.

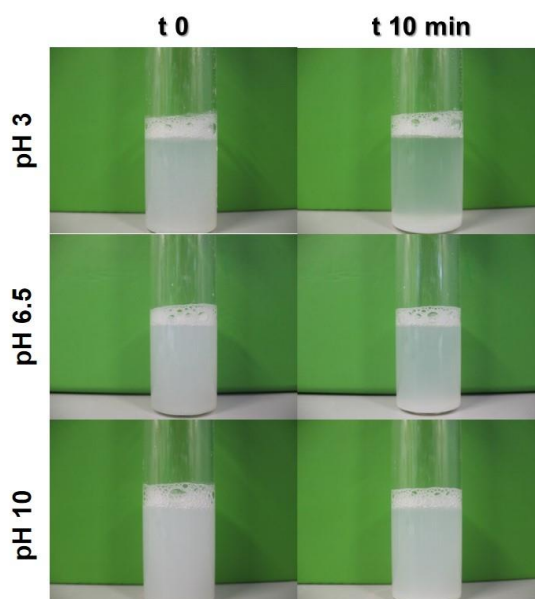


**Figure 102:** Photographs of different vials with water-based dispersions prepared with 0.5 wt.% (50 mg of nanocontainers in 10 ml of water) of Si<sub>3</sub>N<sub>4</sub>\_APS under different pH conditions (pH 3, 6.5 and 10), immediately after dispersion and after 10 minutes. The particles were added as dry powders, dispersed for 5 min in ultrasounds immediately before the test.

Based on the visual analysis a ranking of colloidal stability of the nanocontainers can be established: Si<sub>3</sub>N<sub>4</sub>\_APS > Si<sub>3</sub>N<sub>4</sub>\_GPTMS > Si<sub>3</sub>N<sub>4</sub> >> Si<sub>3</sub>N<sub>4</sub>\_TMOS ≈ Si<sub>3</sub>N<sub>4</sub>\_HDTMS. Due to the acid-base nature of the amine group, tests were also performed for Si<sub>3</sub>N<sub>4</sub>\_APS at different pHs. Figure 102 shows optical photographs of Si<sub>3</sub>N<sub>4</sub>\_APS dispersed in water with different pH values. After 10 minutes, the effect of

pH on the stability of Si\_NC\_APS is already clear, with dispersion being stable at pH 10 but not under acidic conditions. The tendency for sedimentation is less pronounced under neutral conditions. These results indicate that the extent of deprotonated amine groups impacts on the colloidal stability of APS-modified particles (pKa of APS is 10.37).[342]

Another solvent used for preliminary assessment of colloidal stability was 2-propanol. This solvent is less polar than water and is conventionally used in solvent-based hybrid sol-gel formulations (section 7.3.1.2). The stability of the nanocontainers as a function of time is shown in Figure 103. There are some differences when compared with the stability tests performed in water. Shortly after the preparation, dispersions of Si\_NC, Si\_NC\_TMOS and Si\_NC\_HDTMS are more stable than in water, though with time the nanocontainers tend to sediment. The polarity of this solvent still justifies why Si\_NC\_APS shows good stability, followed by Si\_NC\_GPTMS. However, the decrease in polarity and hydrogen bonding extent with respect to water may explain the improvement in wetting of Si\_NC\_TMOS. In 2-propanol the ranking of stability is as follows: Si\_NC\_APS > Si\_NC\_GPTMS > Si\_NC  $\approx$  Si\_NC\_TMOS  $\approx$  Si\_NC\_HDTMS.

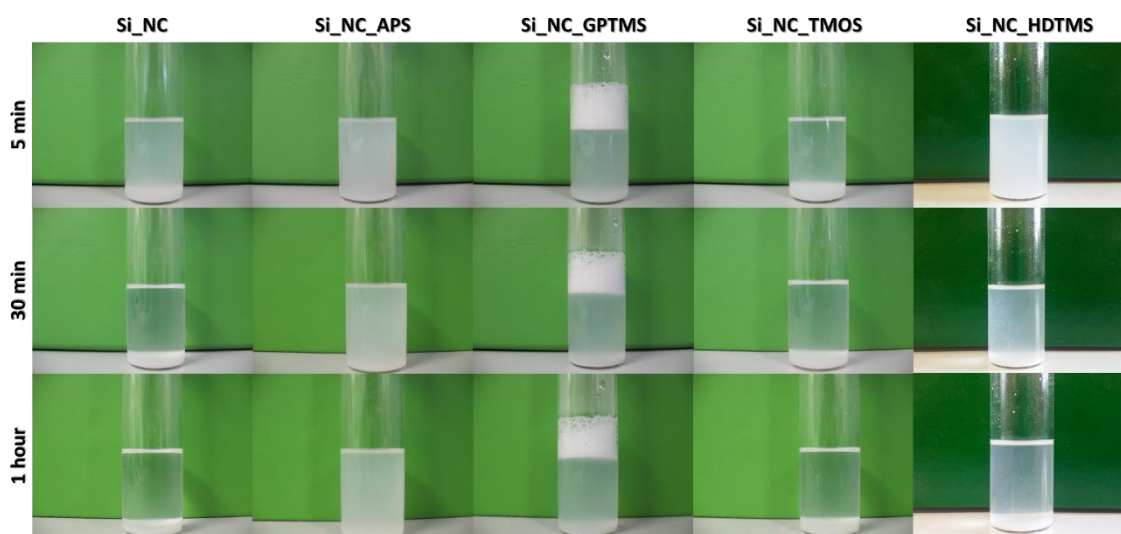


**Figure 103:** 0.5 wt.% (50 mg of nanocontainers in 10 ml of 2-propanol) of Si\_NC and modified Si\_NC with APS, GPTMS, TMOS and HDTMS added to 2-propanol to assess its stability over time: 5, 10 and 60 minutes. The particles were added as dry powders, dispersed during 5 min in ultrasounds and manually immediately before the test.

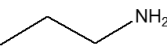
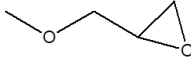
## 7.3 Coating performance

### 7.3.1 Addition of modified dried Si<sub>3</sub>N<sub>4</sub> to model sol-gel based coatings

The stability tests performed for different Si<sub>3</sub>N<sub>4</sub> in water and 2-propanol and presented in the previous section revealed the importance of surface chemistry in the colloidal stability of silica nanocapsules. In this section, the influence of surface modification of Si<sub>3</sub>N<sub>4</sub> on the barrier properties of sol-gel coatings obtained from water- and propanol-based formulations is presented and discussed.

The selection of hybrid sol-gel films as coating systems for Si<sub>3</sub>N<sub>4</sub> was not by chance. SECoP group holds extensive experience in the development of sol-gel coatings for anti-corrosion applications.[76, 92, 145, 156] At the same time, these systems have been finding important applications as pretreatment layers in different applications, namely on aluminum alloys for aeronautical applications.[86] Finally, and perhaps more relevant is the possibility of a high level of control in the formulation chemistry, something almost impossible when working with commercial coating formulations loaded with unknown additives.[160] Thus, in this thesis sol-gel coatings were used as an intermediate step between simple solvent and more complex commercially available coatings. Table 30 summarizes the functional group present in the nanocontainers and the type of formulation used.

**Table 30: Si<sub>3</sub>N<sub>4</sub> modified and hybrid sol-gel coatings used.**

Nanocontainer	Main functional group	Hybrid sol-gel
Si <sub>3</sub> N <sub>4</sub>	Hydroxyl 	• Solvent-based
		• Water-based
Si <sub>3</sub> N <sub>4</sub> _APS	Amine 	• Solvent-based
		• Water-based
Si <sub>3</sub> N <sub>4</sub> _GPTMS	Epoxy 	• Solvent-based
		• Water-based
Si <sub>3</sub> N <sub>4</sub> _TMOS	Aliphatic chain 	• Solvent-based
		• Water-based

To investigate the effect of Si\_NC on the protection performance of sol-gel coatings the technique used was electrochemical impedance spectroscopy (EIS). EIS is a powerful tool to monitor corrosion processes occurring on coated and uncoated active metal and metal alloys.[91, 92, 279] In particular, the separation of time constants of the applied coating and the interfacial process (corrosion-related reactions) allows one to focus on the coating response and how it can be influenced by a specific additive.[92] Therefore, the discussion below is based upon the qualitative description of EIS spectra acquired for coated AA2024 in NaCl solution at different times of immersion, followed by the data obtained from fitting using appropriate equivalent circuits.

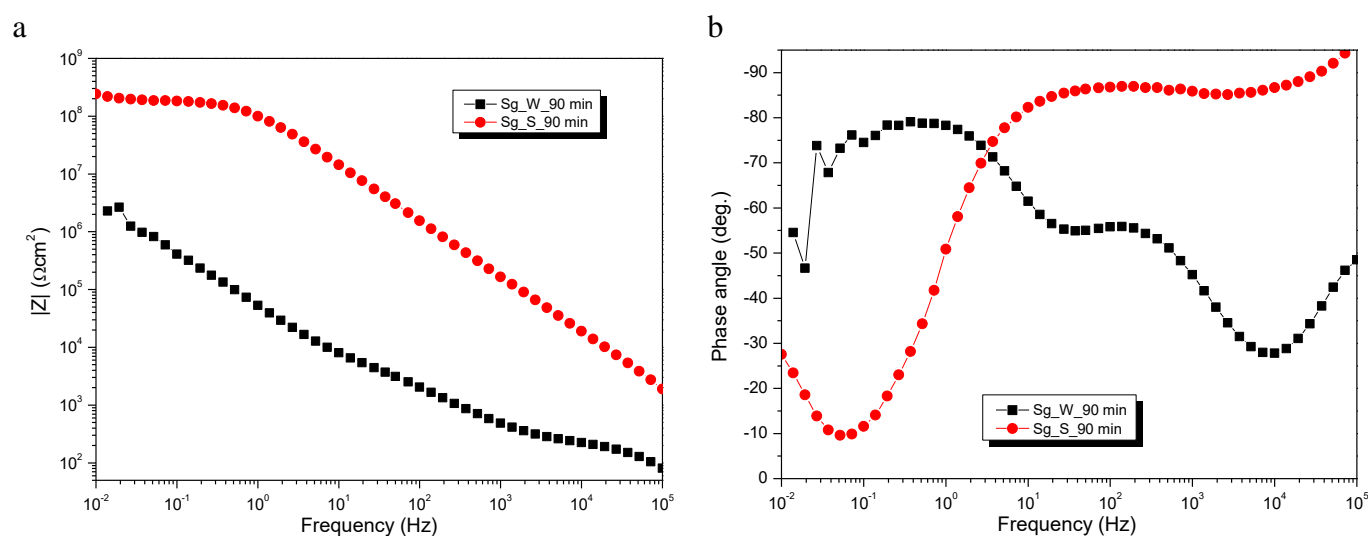


**Figure 104: Bode representation of EIS spectra for AA2024 panels coated with water-based sol-gel and solvent-based sol-gel after 90 min of immersion in a 0.5 M NaCl solution.**

Figure 104 presents the Bode representations of EIS spectra obtained for water- (Sg\_W) and solvent-based (Sg\_S) sol-gel coatings applied to AA2024, after 90 minutes of immersion in 0.5 M NaCl. The sol-gels provided different levels of corrosion protection, inferred from the number of time constants present and the values associated with them. For Sg\_S is visible one well defined time constant, associated with the coating response, and the start of a second one possibly associated with the AA2024 natural oxide layer. In contrast, Sg\_W already shows the presence of three-time constants, only after 90 minutes of immersion. The first time constant ( $10^5$ - $10^4$  Hz), barely visible, is associated with the coating response, while at intermediate frequencies ( $10^3$ - $10^1$  Hz) a time constant associated with the natural oxide layer of the AA2024 is detected. At low frequencies ( $10^1$ - $10^{-2}$  Hz) a third-time constant associated with corrosion processes occurring at the AA2024 interface is already visible. Furthermore, the impedance

magnitude values at  $10^{-2}$  Hz are two orders of magnitude lower for Sg\_W when compared to Sg\_S.

Based on the significant difference in terms of coating properties, the monitoring of coated substrates was adjusted. In the case of Sg\_W, the results presented only show the results for the first 4 hours of immersion, since for longer immersion times all the samples depicted extensive corrosion damage (results not shown). In contrast, for Sg\_S coating degradation was monitored up to 120 hours of immersion.

#### 7.3.1.1 Water-based hybrid sol-gel

The effect of the amount of nanocontainers on the coating barrier properties was studied by adding nanocontainers in two concentrations, 1 wt.% and 10 wt.%. The first concentration is closer to the concentration range usually used in industry for the additives,[77] while the second one can enhance the level of modifications introduced due to the presence of Si\_NC and impart properties typically associated to extenders.

Analyzing the EIS spectra for the sol-gel with 1 wt.% of nanocontainers (Figure 105) the effect produced by the presence of different functional groups on the nanocontainers surface becomes clear. A comparison with Sg\_W (without capsules) shows that the presence of nanocontainers leads to the maintenance or even an increase in the impedance magnitude values, except for Si\_NC\_APS (panels a, b). The impedance values at  $10^{-2}$  Hz after 15 minutes are one order of magnitude lower for Si\_NC\_APS ( $\sim 6 \times 10^5 \Omega \text{ cm}^2$ ) comparing with the best-performing coatings, Si\_NC and Si\_NC\_TMOS ( $\sim 9 \times 10^6 \Omega \text{ cm}^2$ ). After 4 hours of immersion, the gap increases up to two orders of magnitude ( $\sim 6 \times 10^4 \Omega \text{ cm}^2$  for Si\_NC\_APS and  $3 \times 10^6 \Omega \text{ cm}^2$  Si\_NC\_TMOS), reinforcing the perception that amine groups are negatively affecting Sg\_W coatings.

The low performance shown by the addition of Si\_NC\_APS is, in some extension, unexpected taking into account that it was the most stable system in water. Recalling the results of Figure 101, it is clear that pH conditions can play a role in the stability of APS-grafted Si\_NC, and the water-based sol-gel formulation used in this work was acid-catalyzed. But this should only affect the stability of the nanocontainers over time since the particles dispersed well with no significant formation of agglomerates visible to naked eye. Thus, the main reason for the underperformance of Si\_NC\_APS could have an origin in the sol-gel chemistry. The water-based sol-gel consists of two main components, GPTMS (silane derivative with an epoxy group) and TEOS. The epoxy groups present in the sol-gel could be reacting with the amine groups of the APS, in a reaction explored in

the literature to increase cross-linking in thermosetting polymers[343], but which in the case of sol-gel coatings may be hampering the optimal establishment of a Si-O-Si structure. On the other hand, in the particular case of water-based sol-gel, the addition of Si\_NC\_APS could deplete the coating barrier properties, leading to a significant decrease in the coating performance. The amine groups added to the sol-gel could also facilitate the ingress of water due to its hydrophilic character, decreasing significantly the coating barrier properties.

The improvement observed with some of the nanocontainers can be associated with some sort of “filler effect” due to the presence of nanocontainers, thereby working as extenders. The good dispersion of inorganic domains can enhance the coating integrity which reflects upon better barrier effect and delay in corrosion onset.[344-346]

In the beginning of immersion all the systems present three time constants, namely at high frequencies ( $f > 10^3$  Hz) ascribed to the sol-gel layer, at intermediate frequencies ( $f \approx 10^2$  Hz) ascribed to the native oxide film and at low frequencies ( $f \approx 10^{-1}$  Hz) associated with electrochemical processes at the metallic substrate.[92] Exceptions to this trend are the coatings with Si\_NC and Si\_NC\_APS. In the former case, two-time constants are detected, corresponding to the coating response ( $10^3 < f < 10^4$  Hz) and the native oxide film ( $f \approx 10^0$  Hz). In the latter case, Si\_NC\_APS, the coating response is not detected and only the native oxide (intermediate frequencies) and the onset of corrosion processes (low frequencies) are observed. A similar trend is observed after 4 hours of immersion for all the systems with a general reduction in impedance values. At this point, the sol-gel modified with Si\_NC exhibits one additional time constant at low frequencies, quite unstable as observed in the phase angle values, suggesting now the detection of electrochemical processes at the interface. The results are in agreement with the photographs taken during the immersion tests, shown in Figure 108, where Sg\_W loaded with Si\_NC\_APS is the worse system, with the remaining showing similar levels of coatings degradation. In particularly after 4 hours.

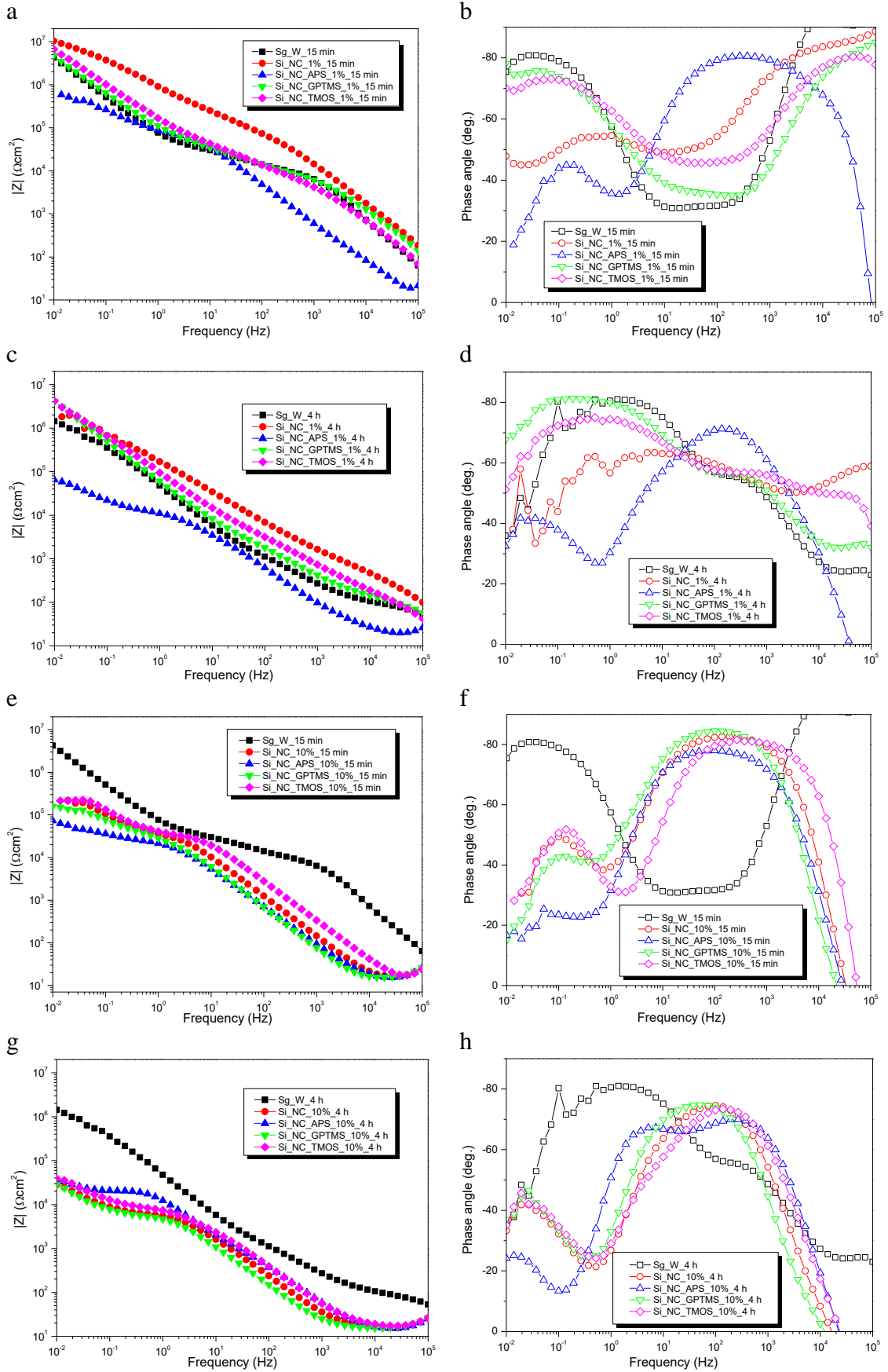
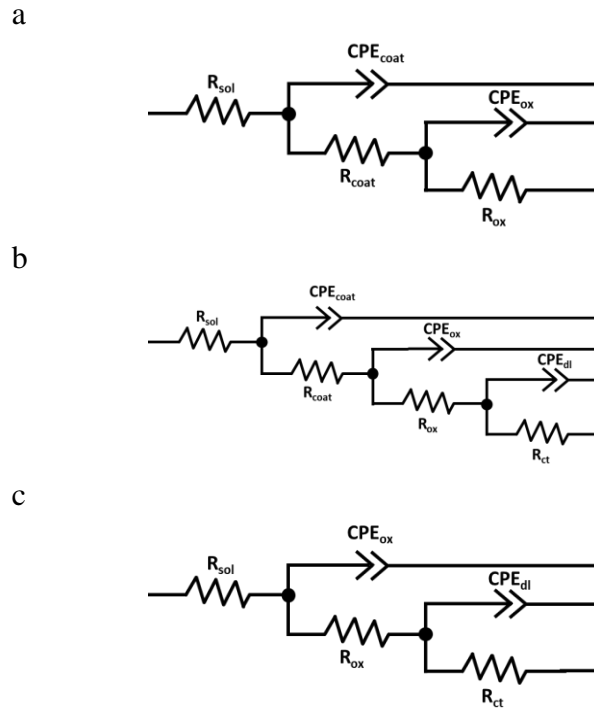


Figure 105: EIS spectra for AA2024 panels coated with water-based sol-gel loaded with Si\_NC, Si\_NC\_APS, Si\_NC\_GPTMS and Si\_NC\_TMOS after 15 min (a and b for 1 wt.%; e and f for 10 wt.%) and 4 hours (c and d for 1 wt.%; g and h for 10 wt.%) immersion in a 0.5 M NaCl solution.

The EIS spectra obtained in the presence of 10 wt.% of Si\_NC show remarkable differences when compared to coatings modified with 1 wt.%. In all the systems, the time constant assigned to the coating layer is no longer detected and the magnitude of impedance at intermediate and low frequencies is also smaller when compared to the unmodified sol-gel layer. For instance, the value of impedance at low frequencies ( $f \approx 10^{-2}$  Hz) for Sg\_W is around  $4 \times 10^6 \Omega \text{ cm}^2$ , comparing with values between  $8 \times 10^4 \Omega \text{ cm}^2$  for Si\_NC\_APS and  $2 \times 10^5 \Omega \text{ cm}^2$  for the remaining systems. With the increase of the immersion time, one can also observe a general decrease in the overall impedance magnitude. After 4 hours, Sg\_W remains as the best performing system, presenting impedance values 1.5 orders of magnitude higher than coating with capsules at  $10^{-2}$  Hz,  $1 \times 10^6 \Omega \text{ cm}^2$  for Sg\_W and  $\sim 3 \times 10^4 \Omega \text{ cm}^2$  for the remaining samples. The assignment of time constants is now different. After 15 minutes of immersion two time-constants are detected in the presence of Si\_NCs, associated with the native oxide (intermediate frequencies) and corrosion processes (low frequencies). For longer immersion times the response of the oxide layer is no longer detected and at this stage, the time constant detected at intermediate frequencies is associated with the electrochemical processes occurring at the metallic substrate and a low-frequency time constant is ascribed to mass transport controlled processes. The EIS results are verified by the visual assessment of the samples photographs, Figure 108, with Sg\_W as the best system, with less amount of corrosion products. Similarly to 1 wt.%, Si\_NC\_APS is the worse performing coating, displaying a significant higher coating degradation.

The EIS spectra were fitted using the equivalent circuits shown in Figure 106, and selected accordingly with the coating response throughout the test, following approaches described in the literature.[91, 145] The elements presented in the equivalent circuits have been presented in detailed previously (section 3.5.2.3):  $R_{\text{sol}}$  (solution resistance),  $\text{CPE}_{\text{coat}}$  (constant phase element associated with coating capacitance),  $R_{\text{coat}}$  (coating pore resistance),  $\text{CPE}_{\text{ox}}$  (constant phase element associated with natural oxide layer capacitance),  $R_{\text{ox}}$  (natural oxide layer resistance),  $\text{CPE}_{\text{dl}}$  (constant phase element associated with double layer capacitance) and  $R_{\text{ct}}$  (charge transference). The values obtained from the fitting are shown in Table 31, for immersion times up to 4 hours.



**Figure 106:** Equivalent circuits used to fit EIS data (Figure 105). The fitting parameters are summarized in Table 31.

As above mentioned, only the reference coating and some coatings loaded with 1 wt.% revealed the presence of a time constant ascribed to the sol-gel layer. To survey and rank the most suitable particles from a point of view of the barrier property, or coating integrity for corrosion protection the approach followed was to focus on the time constant associated with the coating layer and how this was affected by the presence of Si\_NC. The values of  $R_{coat}$  are presented, as a function of immersion time, in Figure 107. Several trends can be highlighted from the results obtained:

-as qualitatively discussed above, the introduction of Si\_NC\_APS results in a coating layer which performs worse than the reference system.

-the best system is Si\_NC with 1 wt.% particles, although Si\_NC\_TMOS and Si\_NC\_GPTMS demonstrate higher pore resistance when compared to the reference, unloaded coating, for longer immersion times. For Si\_NC, the fitted  $R_{coat}$  value corresponds to  $1.16 \times 10^3 \Omega \text{ cm}^2$  comparing with  $7.06 \times 10^1 \Omega \text{ cm}^2$  for Sg\_W after 4 hours. In the case of Si\_NC\_GPTMS and Si\_NC\_TMOS the same parameter has values of  $1.77 \times 10^2 \Omega \text{ cm}^2$  and  $4.05 \times 10^2 \Omega \text{ cm}^2$ , respectively.

-the increase in 10 times concentration of added Si\_NC results in the development of poor coating properties for all the systems.

**Table 31: Results obtained from the fitting of EIS spectra depicted in Figure 105. \*The value of  $R_{ct}$  is very high due to the few points available, at low frequencies, to properly fit the results.**

System	Wt. %	Time	Circuit ( $\chi^2$ )	$Y(CPE_{coat})$ $Ss^n cm^{-2}$	$R_{coat}$ $\Omega cm^2$	$Y(CPE_{ox})$ $Ss^n cm^{-2}$	$R_{ox}$ $\Omega cm^2$	$Y(CPE_{dl})$ $Ss^n cm^{-2}$	$R_{ct}$ $\Omega cm^2$
Sg_W		15 min	(3.74x10 <sup>-2</sup> )	2.47x10 <sup>-8</sup> (n=0.990)	1.21x10 <sup>4</sup>	6.37x10 <sup>-7</sup> (n=0.871)	3.00x10 <sup>4</sup>	2.26x10 <sup>-6</sup> (n=0.913)	*8.23x10 <sup>7</sup>
		4 h	(1.25x10 <sup>-3</sup> )	1.04x10 <sup>-7</sup> (n=0.990)	7.06 x10 <sup>1</sup>	2.81x10 <sup>-6</sup> (n=0.831)	2.34x10 <sup>3</sup>	1.32x10 <sup>-6</sup> (n=0.982)	*1.37x10 <sup>11</sup>
Sg_W_Si_NC	1	15 min	(2.78x10 <sup>-3</sup> )	1.44x10 <sup>-8</sup> (n=0.959)	5.92x10 <sup>4</sup>	3.54x10 <sup>-7</sup> (n=0.581)	4.64x10 <sup>7</sup>	-	-
		4 h	(2.07x10 <sup>-2</sup> )	3.16x10 <sup>-7</sup> (n=0.775)	1.16x10 <sup>3</sup>	1.26x10 <sup>-6</sup> (n=0.690)	1.83x10 <sup>6</sup>	-	-
	10	15 min	(2.22x10 <sup>-3</sup> )	-	-	1.73x10 <sup>-6</sup> (n=0.954)	3.78x10 <sup>4</sup>	1.41x10 <sup>-5</sup> (n=0.815)	2.99x10 <sup>5</sup>
		4 h	(2.64x10 <sup>-3</sup> )	-	-	1.38x10 <sup>-5</sup> (n=0.893)	6.39x10 <sup>3</sup>	3.01x10 <sup>-4</sup> (n=0.853)	3.98x10 <sup>4</sup>
Sg_W_Si_NC_APS	1	15 min	(2.69x10 <sup>-3</sup> )	-	-	5.61x10 <sup>-7</sup> (n=0.915)	8.23x10 <sup>4</sup>	5.39x10 <sup>-6</sup> (n=0.803)	6.03x10 <sup>5</sup>
		4 h	(1.31x10 <sup>-3</sup> )	-	-	8.31x10 <sup>-6</sup> (n=0.820)	1.32x10 <sup>4</sup>	9.08x10 <sup>-5</sup> (n=0.773)	1.05x10 <sup>5</sup>
	10	15 min	(1.27x10 <sup>-3</sup> )	-	-	4.12x10 <sup>-6</sup> (n=0.906)	2.63x10 <sup>4</sup>	8.30x10 <sup>-5</sup> (n=0.744)	5.42x10 <sup>4</sup>
		4 h	(5.83x10 <sup>-3</sup> )	-	-	1.46x10 <sup>-5</sup> (n=0.822)	2.39x10 <sup>4</sup>	6.95x10 <sup>-4</sup> (n=1)	3.09x10 <sup>4</sup>
Sg_W_Si_NC_GPTMS	1	15 min	(3.31x10 <sup>-3</sup> )	3.30x10 <sup>-8</sup> (n=0.914)	1.00x10 <sup>4</sup>	6.26x10 <sup>-7</sup> (n=0.813)	4.27x10 <sup>4</sup>	1.58x10 <sup>-6</sup> (n=0.842)	*9.60x10 <sup>9</sup>
		4 h	(2.74x10 <sup>-3</sup> )	4.95x10 <sup>-7</sup> (n=0.824)	1.77x10 <sup>2</sup>	1.15x10 <sup>-6</sup> (n=0.871)	4.01x10 <sup>3</sup>	1.39x10 <sup>-6</sup> (n=0.948)	*1.87x10 <sup>7</sup>
	10	15 min	(4.17x10 <sup>-3</sup> )	-	-	2.65x10 <sup>-6</sup> (n=0.980)	2.75x10 <sup>4</sup>	1.73x10 <sup>-5</sup> (n=0.726)	1.73x10 <sup>5</sup>
		4 h	(2.36x10 <sup>-2</sup> )	-	-	1.98x10 <sup>-5</sup> (n=0.912)	5.97x10 <sup>3</sup>	3.55x10 <sup>-4</sup> (n=0.893)	3.82x10 <sup>4</sup>
Sg_W_Si_NC_TMOS	1	15 min	(1.11x10 <sup>-2</sup> )	2.56x10 <sup>-8</sup> (n=0.990)	5.75x10 <sup>3</sup>	5.86x10 <sup>-7</sup> (n=0.747)	5.39x10 <sup>4</sup>	8.03x10 <sup>-7</sup> (n=0.831)	*9.49x10 <sup>10</sup>
		4 h	(1.30x10 <sup>-3</sup> )	3.29x10 <sup>-7</sup> (n=0.857)	4.05x10 <sup>2</sup>	8.18x10 <sup>-7</sup> (n=0.818)	6.49x10 <sup>3</sup>	1.06x10 <sup>-6</sup> (n=0.851)	9.50x10 <sup>6</sup>
	10	15 min	(8.57x10 <sup>-3</sup> )	-	-	7.92x10 <sup>-7</sup> (n=0.946)	3.50x10 <sup>4</sup>	1.17x10 <sup>-5</sup> (n=0.830)	2.93x10 <sup>5</sup>
		4 h	(5.02x10 <sup>-3</sup> )	-	-	1.01x10 <sup>-5</sup> (n=0.867)	7.90x10 <sup>3</sup>	1.67x10 <sup>-4</sup> (n=0.738)	8.92x10 <sup>4</sup>

From the results presented, it is clear that the simple colloidal stability of Si\_NCs in water cannot explain the differences, between the different modified coatings. We discussed before the particular case of APS reactivity within sol-gel formulations, possibly triggered by pH driven agglomeration and chemical interactions with epoxy groups present in the sol-gel formulation. The case of Si\_NC, Si\_NC\_GPTMS, and Si\_NC\_TMOS is an intricate one. We may rationalize the possible effects of different surface groups in the following manner:

- the presence of silanol groups in unmodified Si\_NC can establish cross-linking reactions with the sol-gel, through condensation reactions, thus being covalently fixed within the tridimensional Si-O network;

- the presence of less polar groups such as GPTMS or more remarkably TMOS contribute for the organic content of the hybrid matrix and may impart some additional level of interaction by establishment of secondary bonds which stabilize the particles in

the matrix (GPTMS is also a reactant in this sol-gel) or may difficult the ingress of water in the coating layer (large aliphatic chain);

-the reduction in coating barrier properties for high loadings of nanocontainers is an indication that disruption of barrier properties occur.

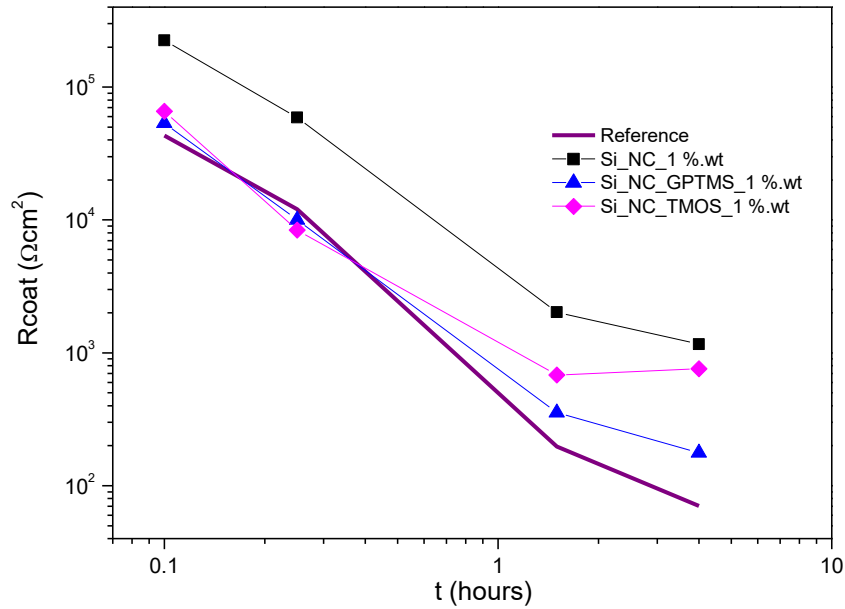
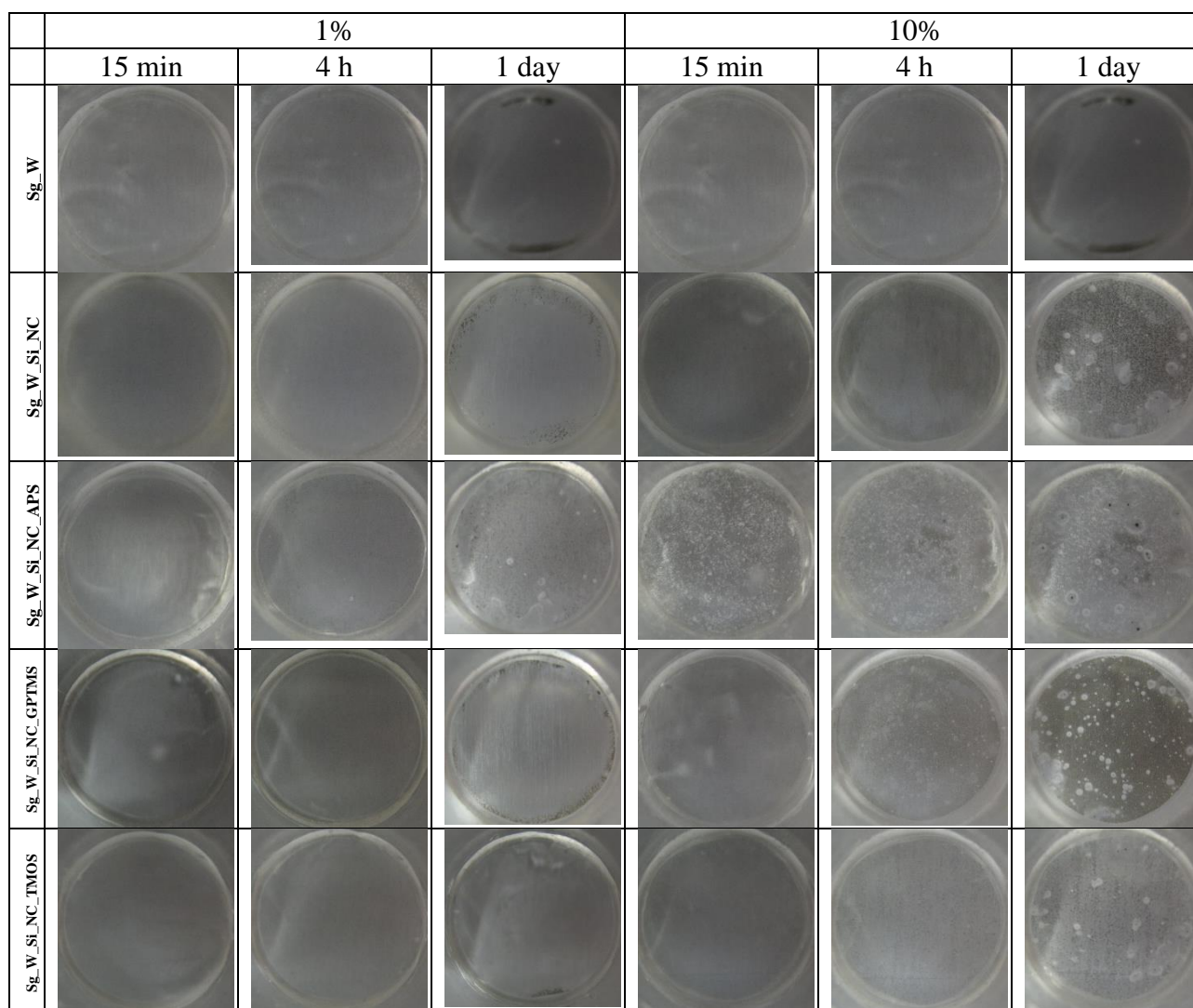


Figure 107: Evolution over time of the  $R_{coat}$  for AA2024 panels coated with a water-based sol-gel loaded with Si\_NC, Si\_NC\_GPTMS and Si\_NC\_TMOS immersed in 0.5 M NaCl solution.



**Figure 108:** Photographs of AA2024 coated with a water-based sol-gel and water-based sol-gel loaded with 1 wt.% and 10 wt.% of Si\_NC, Si\_NC\_APS, Si\_NC\_GPTMS and Si\_NC\_TMOS after 15 min and 4 hours, 1 day immersion in a 0.5 M NaCl solution.

### 7.3.1.2 Solvent-based hybrid sol-gel

In this section, the results associated with tests of Si\_NCs in a solvent-based sol-gel formulation are presented. Besides being a solvent-based system (2-propanol), the resulting sol-gel coating also displays higher barrier properties when compared with a water-based sol-gel, Sg\_W. The composition of the sol-gel formulation (Sg\_S) is presented in detail in section 4.3.1. As in the case of Sg\_W, two concentrations of nanocontainers were tested (1 wt.% and 10 wt.%).

Figure 109 depicts the EIS spectra of different sol-gel coatings with Si\_NCs 1 wt.%. After 90 minutes of immersion in 0.5 M NaCl (panels a and b), all the systems exhibit only one time constant and a resistive plateau at low frequencies. This can be ascribed to the sol-gel layer covering the metallic substrate. Moreover, the impedance

values are around two orders of magnitude higher than in the case of Sg\_W presented in the previous section, which denotes the comparatively better behavior of Sg\_S. The impedance values show some differentiation between the systems shown, at low frequencies ( $10^{-2}$  Hz). Sg\_S presents values around  $2 \times 10^8 \Omega \text{ cm}^2$ , which compares with values around  $2 \times 10^9 \Omega \text{ cm}^2$  for coatings loaded with nanocontainers.

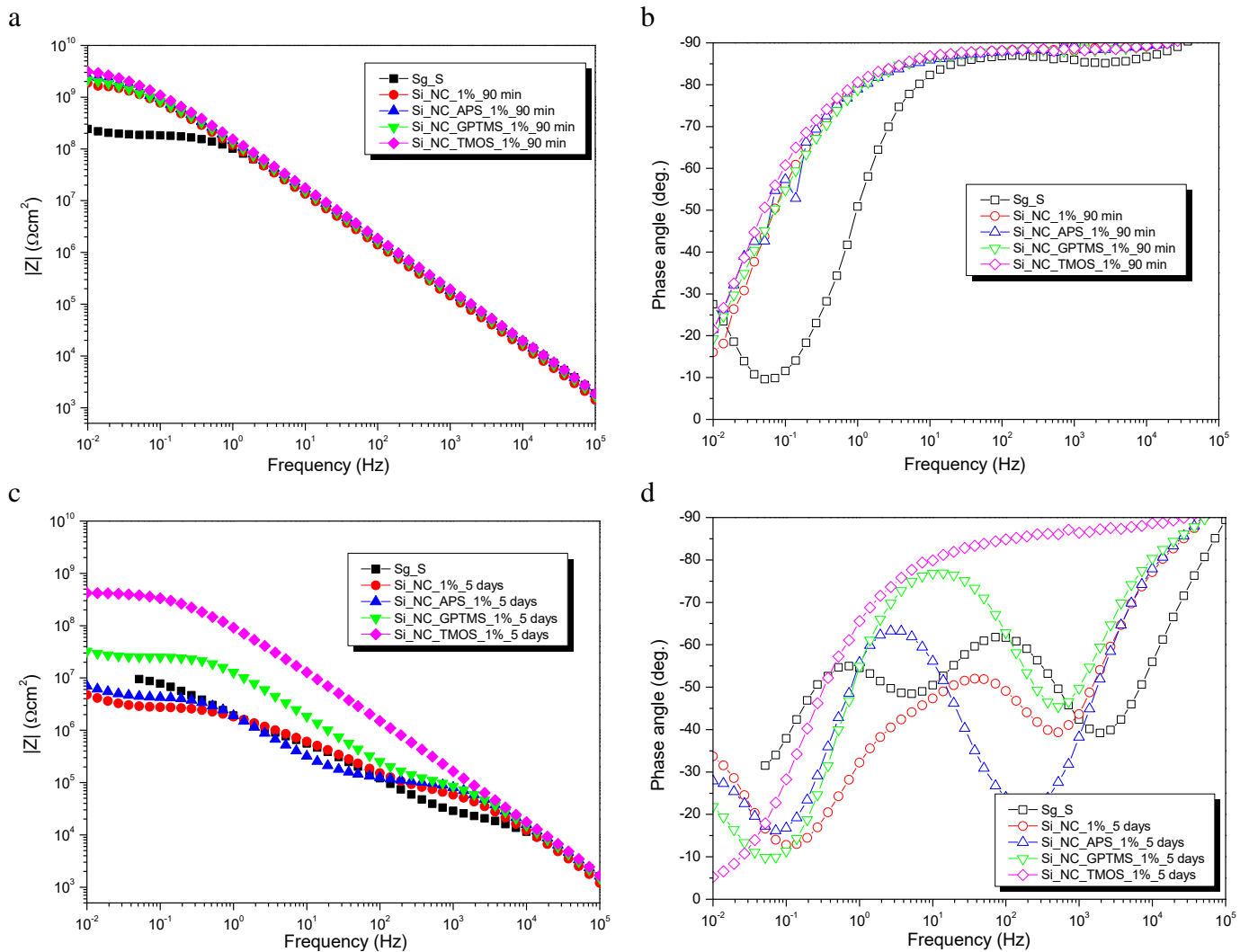


**Figure 109:** EIS spectra for AA2024 panels coated with hybrid solvent-based sol-gel loaded 1 wt.% of Si\_NC, Si\_NC\_APS, Si\_NC\_GPTMS and Si\_NC\_TMOS after 4 hours (a and b) and 5 days (c and d) immersion in a 0.5 M NaCl solution.

After 5 days of immersion (Figure 109c and d), there is now a clear difference in behavior for the different systems. The best performing system is the sol-gel layer loaded with Si\_NC\_TMOS, still presenting only one time-constant associated with the coating. All the other coatings reveal two or three-time constants. The two-time constant occurring at high ( $f \approx 10^4$  Hz) and intermediate frequencies ( $10^1 < f < 10^2$  Hz) may be associated with the sol-gel coating (following similar results reported in the literature [319-321]),

for Si\_NC\_GPTMS, Si\_NC, and Sg\_S. In addition, these systems show one additional time constant, at lower frequencies ( $f \approx 10^{-2}$  Hz), associated with the native oxide film. In the case of the addition of Si\_NC\_APS only two-time constants are observed, one at higher frequencies ( $f \approx 10^3$  Hz) ascribed to the coating response and the second one at lower frequencies ( $f \approx 10^{-1}$  Hz) ascribed to the AA2024 natural oxide response. In terms of barrier properties, the addition of any of the nanocontainers used, leads to improvement of the coating response with respect to the reference Sg\_S, although it seems that in the presence of unmodified Si\_NC the coating barrier properties tend to decrease. The best system is by far the one loaded with Si\_NC\_TMOS. At  $10^{-2}$  Hz Si\_NC\_TMOS\_1% presents impedance values around  $4 \times 10^8 \Omega \text{ cm}^2$  comparing with the second-best system, Si\_NC\_GPTMS\_1%, with  $\sim 4 \times 10^7 \Omega \text{ cm}^2$  and all the other systems under  $8 \times 10^6 \Omega \text{ cm}^2$ .

**Table 32: Results obtained from the fitting of EIS spectra depicted in Figure 109. For systems loaded with 1 wt.% of nanocontainers.**

System	Time	Circuit ( $\chi^2$ )	Y(CPE <sub>coat</sub> ) Ss <sup>n</sup> cm <sup>-2</sup>	R <sub>coat</sub> Ωcm <sup>2</sup>	Y(CPE <sub>coat</sub> ) Ss <sup>n</sup> cm <sup>-2</sup>	R <sub>coat</sub> Ωcm <sup>2</sup>	Y(CPE <sub>ox</sub> ) Ss <sup>n</sup> cm <sup>-2</sup>	R <sub>ox</sub> Ωcm <sup>2</sup>
Sg_S	90 min	(2.59x10 <sup>-3</sup> )	1.29x10 <sup>-9</sup> (n=0.964)	1.82x10 <sup>8</sup>	-	-	-	-
	5 d	(8.89x10 <sup>-3</sup> )	1.12x10 <sup>-9</sup> (n=0.990)	2.03x10 <sup>4</sup>	9.21x10 <sup>-8</sup> (n=0.719)	9.95x10 <sup>5</sup>	5.63x10 <sup>-7</sup> (n=0.990)	1.53x10 <sup>6</sup>
Si_NC	90 min	(9.93x10 <sup>-3</sup> )	1.47x10 <sup>-9</sup> (n=0.969)	1.66x10 <sup>9</sup>	-	-	-	-
	5 d	(2.29x10 <sup>-3</sup> )	1.42x10 <sup>-9</sup> (n=0.990)	6.04x10 <sup>4</sup>	8.97x10 <sup>-8</sup> (n=0.686)	3.02x10 <sup>6</sup>	4.68x10 <sup>-6</sup> (n=0.990)	7.55x10 <sup>6</sup>
Si_NC_APS	90 min	(1.64x10 <sup>-2</sup> )	1.23x10 <sup>-9</sup> (n=0.962)	2.27x10 <sup>9</sup>	-	-	-	-
	5 d	(1.69x10 <sup>-2</sup> )	1.25x10 <sup>-9</sup> (n=0.990)	1.05x10 <sup>5</sup>	-	-	1.05x10 <sup>-7</sup> (n=0.839)	5.12x10 <sup>6</sup>
Si_NC_GPTMS	90 min	(1.45x10 <sup>-2</sup> )	1.32x10 <sup>-9</sup> (n=0.964)	1.87x10 <sup>9</sup>	-	-	-	-
	5 d	(1.26x10 <sup>-3</sup> )	1.17x10 <sup>-9</sup> (n=0.990)	1.20x10 <sup>5</sup>	1.04x10 <sup>-8</sup> (n=0.919)	2.61x10 <sup>7</sup>	1.23x10 <sup>-6</sup> (n=0.990)	3.88x10 <sup>7</sup>
Si_NC_TMOS	90 min	(1.04x10 <sup>-2</sup> )	1.13x10 <sup>-9</sup> (n=0.967)	2.94x10 <sup>9</sup>	-	-	-	-
	5 d	(1.24x10 <sup>-2</sup> )	1.69x10 <sup>-9</sup> (n=0.944)	3.89x10 <sup>8</sup>	-	-	-	-

The EIS results were fitted using the equivalent circuits presented in Figure 111, following the qualitative assignment of time-constants as already described. Four fitting models were used to represent the stages observed for the samples throughout the immersion tests. The results of the fittings are presented in Table 32. The results of Sg\_S were fitted using equivalent circuits composed by the same elements used to fit Sg\_W results (see section 3.5.2.3 for a more detailed analysis): R<sub>sol</sub> (solution resistance), CPE<sub>coat</sub> (constant phase element associated with coating capacitance), R<sub>coat</sub> (coating resistance), CPE<sub>ox</sub> (constant phase element associated natural oxide layer capacitance), R<sub>ox</sub> (natural oxide layer resistance). At the initial stages, only one time-constant is visible, ascribed to the coating response (R<sub>coat</sub> and CPE<sub>coat</sub>). As the test progresses, new time constants start

to appear attributed to a second coating response ( $R_{\text{coat}}$  and  $\text{CPE}_{\text{coat}}$ ) and a third one associated with the natural oxide layer ( $R_{\text{ox}}$  and  $\text{CPE}_{\text{ox}}$ ) of the AA2024.

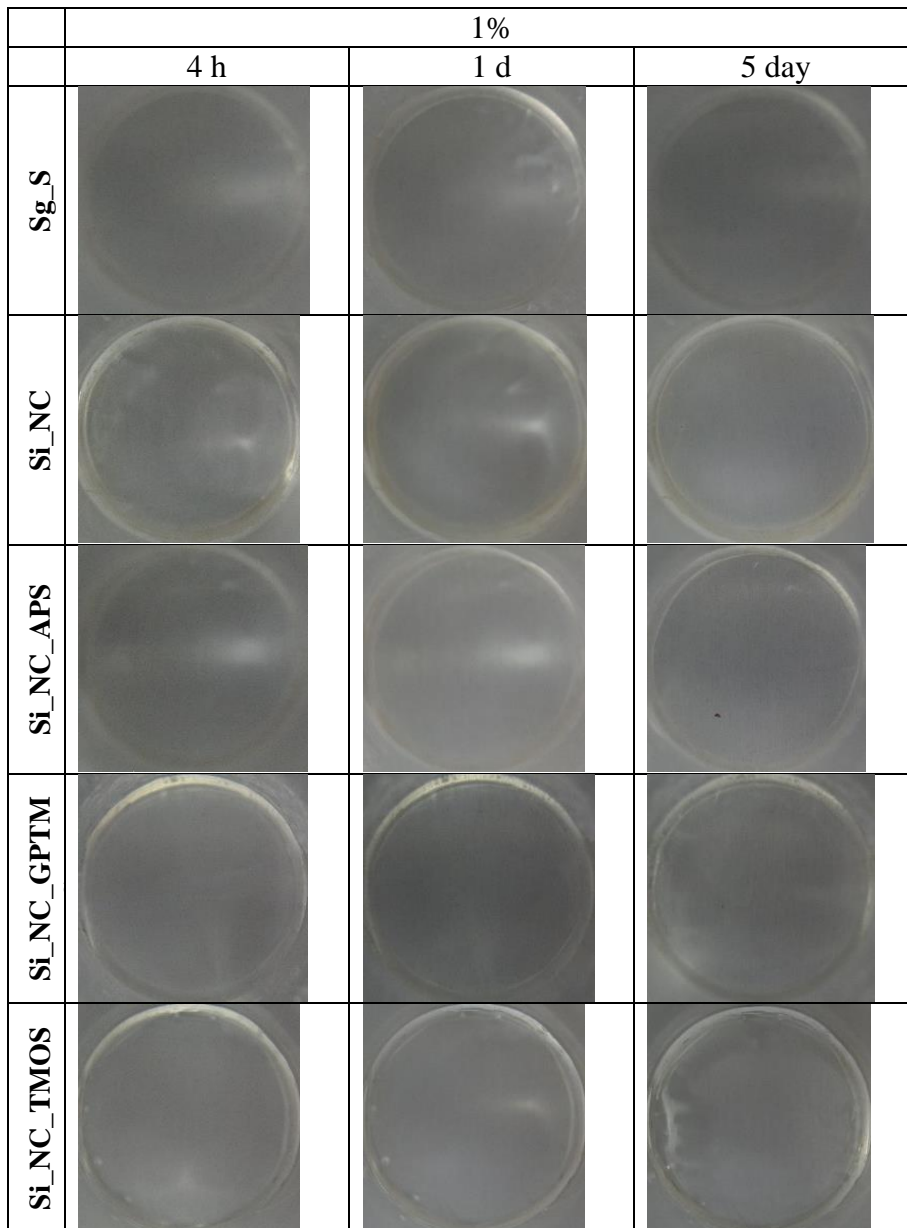


**Figure 110: Photographs of AA2024 coated with a 2-propanol-based sol-gel and 2-propanol-based sol-gel loaded with 1% of Si<sub>2</sub>NC, Si<sub>2</sub>NC\_APS, Si<sub>2</sub>NC\_GPTMS and Si<sub>2</sub>NC\_TMOS after 4 hours, 1 day and 5 days immersion in a 0.5 M NaCl solution.**

The visual assessment of the panels during the immersion test, shown in Figure 110, are in agreement with the EIS findings. The photographs were taken after 4 hours, 1 day and 5 days of immersion. The results show no significant changes between the systems, with no corrosion products visible on the metal surface, in agreement with the electrochemical analysis where the coating response is still detected after 5 days. In light of the results it is possible to establish a rank, based on the EIS qualitative results after 5

days of immersion, for the samples: Si\_NC\_TMOS\_1% > Si\_NC\_GPTMS\_1% > Si\_NC\_APS\_1% > Si\_NC\_1% > Sg\_S.

The EIS spectra obtained for coatings with Si\_NC 10 wt.% are presented in Figure 112. After 90 minutes of immersion one time-constant is detected for all the systems. Coatings loaded with Si\_NC, Si\_NC\_GPTMS and Si\_NC\_TMOS presented higher coating barrier properties, with impedance values around  $3 \times 10^9 \Omega \text{ cm}^2$  at low frequencies ( $10^{-2}$  Hz). In the case of Sg\_S and Si\_NC\_APS, the impedance values are  $3 \times 10^8 \Omega \text{ cm}^2$  and  $1 \times 10^9 \Omega \text{ cm}^2$ , respectively.

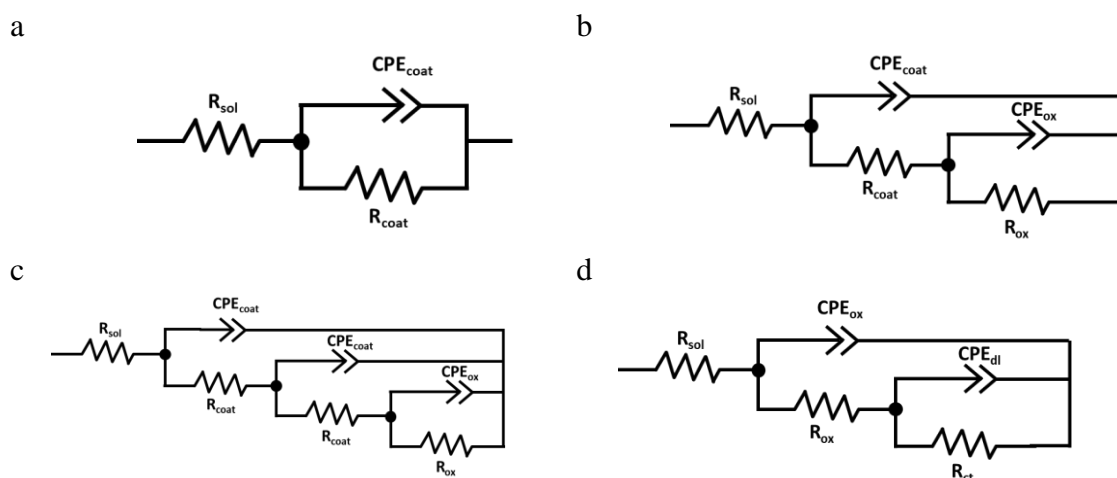


**Figure 111:** Equivalent circuits used to fit EIS data (Figure 109 (1 wt.%) and Figure 112 (10 wt.%)), summarized in Table 32 and Table 33 (see below).

After 5 days of immersion in 0.5 M NaCl, there is a general decrease in the impedance values, with Si\_NC\_TMOS and Si\_NC\_GPTMS showing the highest impedance values and one time-constant associated with the coating resistance. The next, best performing system is Si\_NC\_APS which shows two-time constants, one at high frequencies associated with the sol-gel coating and one at low frequencies ( $10^{-2}$  Hz) associated with the response of the native oxide layer. The coatings with Si\_NC and Sg\_S show two-time constants possibly associated with the coating degradation (high and intermediate frequencies) and another at low frequencies associated with the oxide layer.

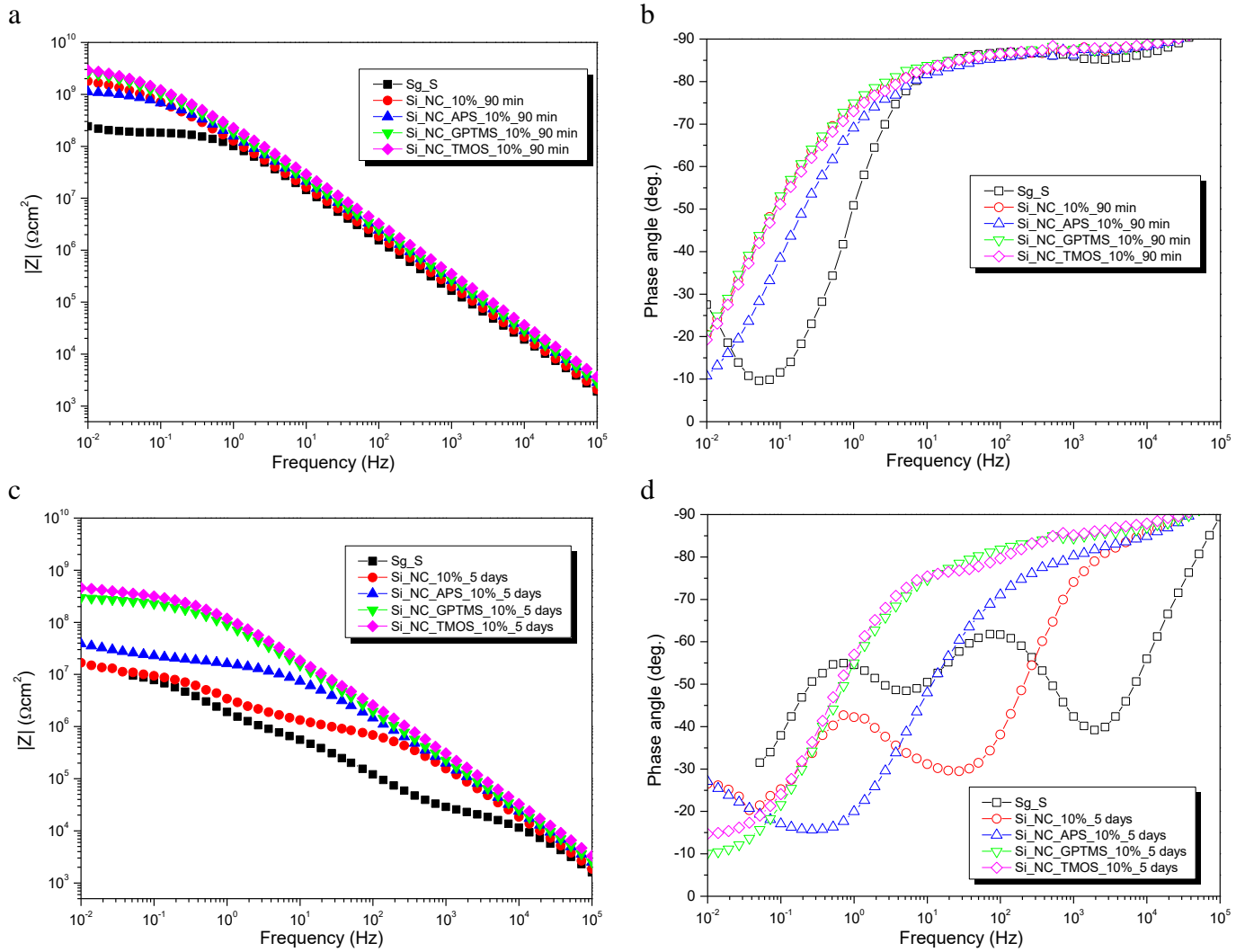


**Figure 112:** EIS spectra for AA2024 panels coated with a hybrid solvent-based sol-gel loaded 10 wt.% of Si\_NC, Si\_NC\_APS, Si\_NC\_GPTMS and Si\_NC\_TMOS after 90 minutes (a and b) and 5 days (c and d) immersion in a 0.5 M NaCl solution.

The EIS data were fitted using the equivalent circuit models shown in Figure 111, and the results are presented in Table 33.

The values of  $R_{coat}$ , after 90 minutes, can be separated into two groups: around  $1 \times 10^9 \Omega \text{ cm}^2$  for Si\_NC\_10%, Si\_NC\_GPTMS\_10%, Si\_NC\_TMOS\_10% and Si\_NC\_APS\_10% and around  $1 \times 10^8 \Omega \text{ cm}^2$  for Sg\_S without nanocontainers. Nevertheless, Si\_NC\_APS already show lower barrier properties than the remaining systems, a trend confirmed after 5 days of immersion. As in the case of 1 wt. % the addition of capsules modified with amine groups has a negative effect on the coating barrier properties, probably due to detrimental chemical interactions with the sol-gel formulation.

The best performing coatings, Si\_NC\_GPTMS\_10%, and Si\_NC\_TMOS\_10% only show one time constant with  $R_{coat} \sim 3 \times 10^8 \Omega \text{ cm}^2$ , though lower than the values

obtained after 90 minutes. In the case of Si\_NC\_APS\_10%, also only one-time constant is visible, but with lower values of  $R_{\text{coat}}$  ( $\sim 1 \times 10^7 \Omega \text{ cm}^2$ ). For the remaining systems, Sg\_S and Si\_NC\_10% three-time constants are visible. Besides the coating response and the AA2024 natural oxide layer a third time constant is visible, ascribed to the double layer and charge transfer processes.

**Table 33: Results obtained from the fitting of EIS spectra for AA2024 panels coated with a hybrid solvent-based sol-gel loaded 10 wt.% of Si\_NC, Si\_NC\_APS, Si\_NC\_GPTMS and Si\_NC\_TMOS after 90 minutes and 5 days immersion in a 0.5 M NaCl solution, depicted in Figure 112.**

System	Time	Circuit ( $\chi^2$ )	$Y(\text{CPE}_{\text{coat}})$ $\text{Ss}^n \text{cm}^{-2}$	$R_{\text{coat}}$ $\Omega \text{cm}^2$	$Y(\text{CPE}_{\text{coat}})$ $\text{Ss}^n \text{cm}^{-2}$	$R_{\text{coat}}$ $\Omega \text{cm}^2$	$Y(\text{CPE}_{\text{ox}})$ $\text{Ss}^n \text{cm}^{-2}$	$R_{\text{ox}}$ $\Omega \text{cm}^2$
Sg_S	90 min	(2.59x10 <sup>-3</sup> )	1.29x10 <sup>-9</sup> (n=0.964)	1.82x10 <sup>8</sup>	-	-	-	-
	5 d	(8.89x10 <sup>-3</sup> )	1.12x10 <sup>-9</sup> (n=0.990)	2.03x10 <sup>4</sup>	9.21x10 <sup>-8</sup> (n=0.719)	9.95x10 <sup>5</sup>	5.63x10 <sup>-7</sup> (n=0.990)	1.53x10 <sup>6</sup>
Si_NC	90 min	(2.06x10 <sup>-2</sup> )	1.42x10 <sup>-9</sup> (n=0.940)	1.52x10 <sup>9</sup>	-	-	-	-
	5 d	(4.15x10 <sup>-3</sup> )	1.26x10 <sup>-9</sup> (n=0.968)	7.63x10 <sup>5</sup>	8.32x10 <sup>-8</sup> (n=0.652)	1.45x10 <sup>7</sup>	1.28x10 <sup>-6</sup> (n=0.792)	1.01x10 <sup>11</sup>
Si_NC_APS	90 min	(1.63x10 <sup>-2</sup> )	1.06x10 <sup>-9</sup> (n=0.941)	9.71x10 <sup>8</sup>	-	-	-	-
	5 d	(1.24x10 <sup>-2</sup> )	2.09x10 <sup>-9</sup> (n=0.901)	1.44x10 <sup>7</sup>	-	-	-	-
Si_NC_GPTMS	90 min	(1.94x10 <sup>-2</sup> )	1.00x10 <sup>-9</sup> (n=0.945)	2.20x10 <sup>9</sup>	-	-	-	-
	5 d	(1.94x10 <sup>-2</sup> )	1.57x10 <sup>-9</sup> (n=0.918)	2.49x10 <sup>8</sup>	-	-	-	-
Si_NC_TMOS	90 min	(2.22x10 <sup>-2</sup> )	7.94x10 <sup>-10</sup> (n=0.943)	2.46x10 <sup>9</sup>	-	-	-	-
	5 d	(2.52x10 <sup>-2</sup> )	1.25x10 <sup>-9</sup> (n=0.914)	3.58x10 <sup>8</sup>	-	-	-	-

In Figure 113 the values of  $R_{\text{coat}}$  obtained from the fittings presented in Table 32 and Table 33 for systems loaded with 1 and 10 wt. % are presented. The results observed for a loading of Si\_NC 10 wt. % show similar trends, Si\_NC\_TMOS as the best coating and Si\_NC\_APS as the worse, to the systems with 1 wt. %, with two systems clearly showing higher coating barrier properties: Si\_NC\_GPTMS\_10% and Si\_NC\_TMOS\_10%. Moreover, if there is a gain in increasing 10 times the concentration of Si\_NC\_GPTMS, the  $R_{\text{coat}}$  for Si\_NC\_TMOS is already very high at 1 wt. % and the improvement in higher concentration are not significant.

The visual appearance of samples during the test is shown in Figure 114. No sign of corrosion on the AA2024 surface or degradation of Sg\_S are detected. The ranking of the samples accordingly with their barrier properties is similar to 1 wt. %: Si\_NC\_TMOS\_10% > Si\_NC\_GPTMS\_10% > Si\_NC\_APS\_10% > Si\_NC\_10% > Sg\_S.

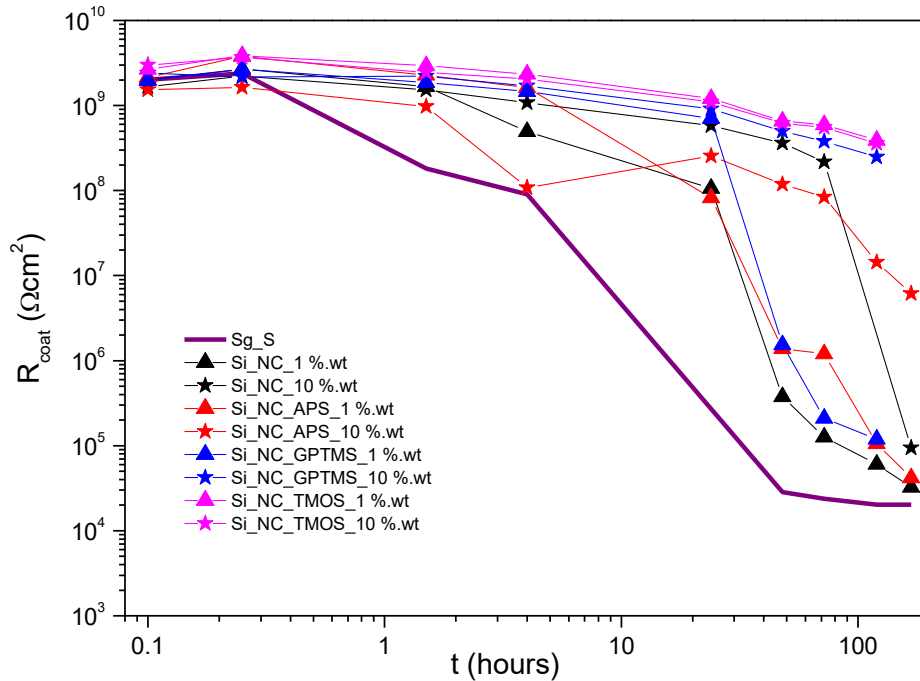


**Figure 113: Evolution overtime of the  $R_{\text{coat}}$  for AA2024 panels coated with a hybrid solvent-based sol-gel loaded with Si\_NC, Si\_NC\_APS, Si\_NC\_GPTMS and Si\_NC\_TMOS in different proportions (1 and 10%) immersed in 0.5 M NaCl solution.**

From the results obtained in this section several points can be established:

- the increase in the concentration of Si\_NCs added up to 10 wt.% leads to an improvement in the barrier properties of the resulting coatings;
- the best performing systems are those with Si\_NCs modified with TMOS and GPTMS;
- unmodified Si\_NCs display a lower performance when compared to modified nanocapsules.

Similarly to water-based sol-gel, different functional groups grafted to Si\_NC seem to play a role in the coating barrier properties of solvent-based sol-gel. Sg\_S (recall section 4.3.1) is composed of titanium (IV) propoxide (TPOT), 3-glycidoxypropyltrimethoxysilane (GPTMS), phenyl trimethoxysilane (PTMS) and hexadecyltrimethoxysilane (HDTMS), with hydrolysis and condensation reactions carried out under acidic conditions.[145] Comparing with Sg\_W the complexity of the formulation is higher, with new functional groups being present in the case of Sg\_S. In addition to epoxy and hydroxyl groups found in Sg\_W, there are also phenyl and aliphatic chains. Other two differences can be found: the solvent used (water vs 2-propanol) and the main component of the sol-gel matrix, which is not silica- but titanium-based (tetraethyl orthosilicate (TEOS) vs titanium (IV) propoxide (TPOT)).

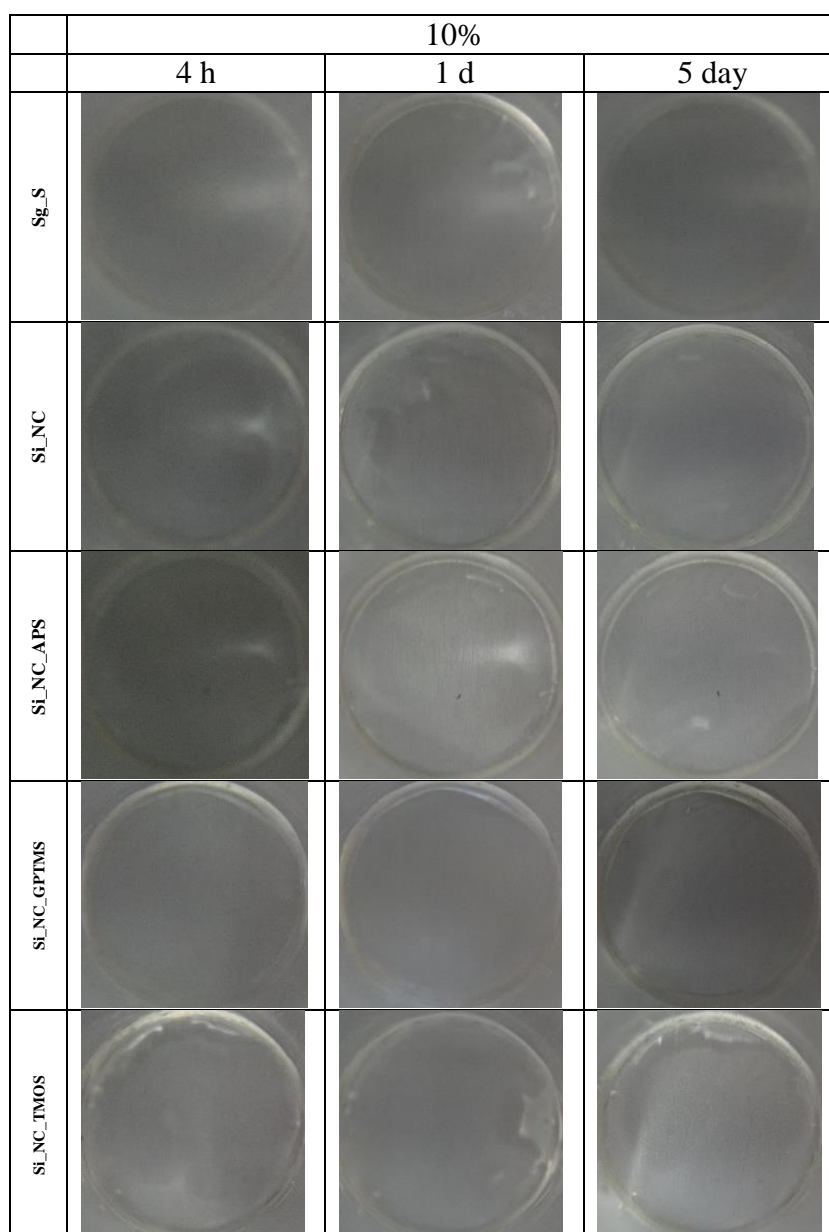


**Figure 114: Photographs of AA2024 coated with a 2-propanol-based sol-gel and 2-propanol-based sol-gel loaded with 10% of Si\_NC, Si\_NC\_APS, Si\_NC\_GPTMS and Si\_NC\_TMOS after 4 hours, 1 day and 5 days immersion in a 0.5 M NaCl solution.**

Based on this study some considerations can be drawn from the EIS results presented above:

- the addition of amine groups, as in the case of Sg\_W, could be affecting the coating performance, by reacting with epoxy moieties present in the Sg\_S, when compared with coatings loaded with other Si\_NC.

- the addition of Si\_NC with epoxy and aliphatic groups on its surface improves significantly the coating barrier properties over time, comparing with Sg\_S and Si\_NC.

The existence of the same functional groups in the Sg\_S formulation could be improving the nanocontainer stability.

There is a clear improvement of the coating barrier properties due to a filler effect produced by the addition of Si\_NC since all the samples presented higher coating barrier properties compared with the coating without nanocontainers. Nevertheless, the functional groups present on the Si\_NC surface play an important role, with different degrees of coating performance being observed for the different functional groups, pointing towards a different level of coating/nanocontainer compatibility, at a physical and chemical level. A general outcome is that any increase in the concentration of particles within the coating formulation must have as starting point proper compatibility in order to avoid coating barrier disruption.

### **7.3.2 Addition of modified Si\_NC to commercial coatings**

As seen in previous sections, the modification of silica nanocapsules with different functional groups affects the stability of the particles in solvents with different polarity.[225, 338] However when attempting their incorporation in sol-gel coating formulations, the performance of the resulting coating layers from a corrosion standpoint, against ingress of electrolyte the simple correlation with stability in the corresponding solvent cannot explain the responses obtained for the different surface chemistries. The reactivity of the different functional groups with the formulation (-OH, -NH<sub>2</sub>) and the favored interactions with the hybrid Si-O network (GPTMS, TMOS) seem to be important factors when adding a certain nanocontainer without causing disruption in the coating integrity.

At the same time testing these silica nanocapsules in real applications demands for a study using a wider range of coating formulations available commercially. This task is usually overlooked by scientists when designing novel nano additives and can jeopardize the use of new materials in the paint industry for commercial products.

In this section, one tries to go beyond the state-of-art from a product development perspective. Starting with commercially available coatings one tries to investigate the effect of the direct addition of the particles with different surface groups (variable investigated in the previous section) and in different physical states (dried powders, slurry) on the curing process, using DSC, and on the mechanical properties by measuring the microhardness. In the final part of this section, we try to infer the correlation between

these properties and coating performance using conventional characterization techniques and EIS. The study of the influence of the surface modification is now restricted to three different silica nanocapsule systems: unmodified Si\_NC<sub>s</sub>, Si\_NC\_APS and Si\_NC\_HDTMS. The reason to use HDTMS as “hydrophobic” alternative to TMOS relies on the fact that they show structurally related aliphatic chains (Table 28) and at the same time HDTMS is a significantly less expensive silane when compared to TMOS. Therefore, working in an industrially-driven approach we decided to use HDTMS.

### 7.3.2.1 Water-based polyurethane coatings

The coating selection was based on three criteria: commercially available (complex system to test the nanocontainers effect), water-based (with lower VOC's emissions) and transparent (to better assess the nanocontainers dispersibility). AQ CC 080 is a water-soluble acrylic urethane emulsion produced by SYNPO (4.3.2). The weight percentage of solids in the mixture was 35 wt. % and it was used in combination with the hardener AQ BU 16 (SYNPO), considering a mixing ratio of 2.5:1 AQ CC 080:AQ BU 16.

In this work, the Si\_NC<sub>s</sub> were dispersed using a high-speed dispersant equipment to ensure a more efficient dispersion, for 10 minutes at 10 000 rpm. The resulting suspensions had a high amount of foam and air bubbles, overcome by letting the suspension to rest for a few hours followed by a short period under vacuum until all the bubbles migrated to the surface. The AQ CC 080 coatings, loaded with Si\_NC, Si\_NC\_APS and Si\_NC\_HDTMS 1 wt.% added in both dried and as a slurry (with toluene) after application on AA2024 panels are displayed in Figure 115. Taking into account the nature of the formulation, water-based, polar thermosetting, one would expect some difficulties when dispersing Si\_NC\_HDTMS or when the silica nanocontainers were added as a toluene-based slurry. These empiric assumptions were not observed, with toluene-based slurry producing good dispersions. The same occurred for Si\_NC\_HDTMS both in dry as well as a toluene-based slurry. The exception in terms of film quality was observed in coatings loaded with Si\_NC\_APS, regardless of the physical state into which it was added, being worse when added as a toluene-based slurry.

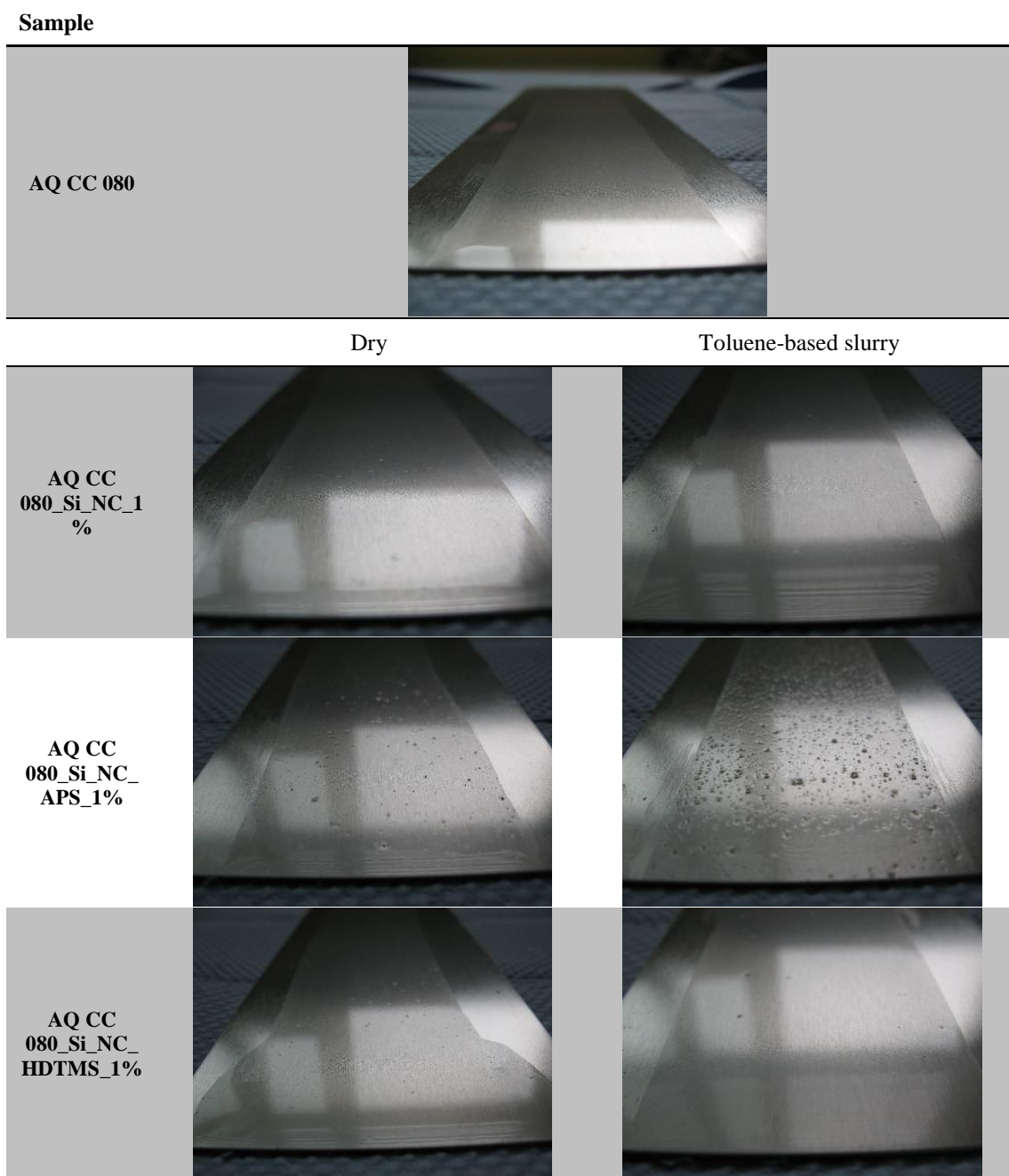


Figure 115: Photographs of AQ CC 080 coatings loaded with 1 wt.% of Si\_NC, Si\_NC\_APS and Si\_NC\_HD applied on carbon steel, added to the formulation as a dry powder and as a toluene-based slurry.

The glass transition temperature ( $T_g$ ) is a critical parameter for coatings performance and is quite sensitive to changes introduced in terms of the curing process. The coating glass transition reflects the thermal expansion when the coating goes from a hard, glassy state to a rubbery state. In this work, the  $T_g$  is reported as a single temperature, corresponding to the midpoint between the tangents of the heat flow curve corresponding to the glass state and the heat flow curve corresponding to the more rubbery state.

AQ CC 080 lacquer produces coatings with  $T_g$ 's around 58 °C (Table 34), which is high enough to obtain hard glassy state with favorable hardness and mechanical properties at room temperature, but low enough for the coating to cure without the need of higher temperatures that are inconvenient for large-scale industrial applications. With the addition of the nanocontainers, the  $T_g$  is kept at temperature values ideal for the same type of applications of the original lacquer. The addition of nanocontainers, regardless of the modification, yields  $T_g$  values lower than the original formulation, but not significant to change the coating properties. This is in agreement with other studies where the addition of silica nanoparticles left  $T_g$  nearly unaffected.[347]

**Table 34:**  $T_g$  of the cooling step for AQ CC 080 formulation with 1 wt.% of Si\_NC, Si\_NC\_APS, and Si\_NC\_HDTMS, added to the formulation as a dry powder and as a toluene-based slurry.

Sample	$T_g$ °C
AQ CC 080	58.01
AQ CC 080_Si_NC_1%_Dry	50.41
AQ CC 080_Si_NC_APS_1%_Dry	52.05
AQ CC 080_Si_NC_HDTMS_1%_Dry	54.46
AQ CC 080_Si_NC_1%_Tol	51.22
AQ CC 080_Si_NC_APS_1%_Tol	46.56
AQ CC 080_Si_NC_HDTMS_1%_Tol	51.34

An important parameter related to the coating mechanical properties is the coating micro-hardness. The coating micro-hardness was assessed using a pendulum hardness test. The results obtained from this methodology are not only dependent on the coating chemistry but also on the surface roughness. The poorly dispersibility of Si\_NC\_APS, which results in a considerable number of aggregates on the coating surface affected the ability to measure the coating micro-hardness appropriately, since it limits the correct operation of the equipment. For the remaining systems, the results are similar for AQ CC 080, regardless of the presence of nanocontainers, as shown in Table 35.

EIS was employed in a similar approach to the one used for sol-gel based-coatings, to assess the influence of the different functional groups on the coatings barrier properties, but also to compare the findings using EIS with the results obtained in conventional tests used by the industry (micro-hardness and DSC shown before). The EIS results for AQ CC 080 coatings are presented in Figure 116, for immersion times corresponding to 4 hours and 7 days in 0.05 M NaCl solution. After 4 hours of immersion, it is possible to

observe at high frequencies, a time-constant ascribed to the organic coating applied onto AA2024 substrate ( $f > 10^3$  Hz). This region of the EIS spectra is very similar for all the systems implying that the coatings prepared had similar properties in terms of thickness (assuming similar dielectric constant). A second time constant at ( $10^0$  Hz  $< f < 10^1$  Hz) can be ascribed to the oxide film and a third time-constant is observed, for longer immersion times, at low frequencies, possibly due to the corrosion processes initiating at the metal substrate. At this stage, the samples can be ranked into three groups: Si\_NC\_dry, Si\_NC\_APS\_dry, Si\_NC\_APS\_tol and Si\_NC\_HDTMS\_dry as the best systems ( $2 \times 10^7 \Omega \text{ cm}^2$ ); the undoped coating as an intermediate result ( $1 \times 10^7 \Omega \text{ cm}^2$ ); Si\_NC\_tol and Si\_NC\_HDTMS\_tol as the worst systems ( $8 \times 10^6 \Omega \text{ cm}^2$ ). Nevertheless, the differences are not considerable to conclude a definitive ranking.

**Table 35: Microhardness according to Martens for AQ CC 080 formulation with 1 wt.% of Si\_NC, Si\_NC\_APS, and Si\_NC\_HDTMS, added to the formulation as a dry powder and as a toluene-based slurry.**

Sample	Reverse Vickers / N/mm <sup>2</sup>
AQ CC 080	151.45
AQ CC 080_Si_NC_1%_Dry	150.58
AQ CC 080_Si_NC_APS_1%_Dry	166.32 Very rough - lots of aggregates - Difficult measurement
AQ CC 080_Si_NC_HDTMS_1%_Dry	153.09
AQ CC 080_Si_NC_1%_Tol	148.9
AQ CC 080_Si_NC_APS_1%_Tol	205.92 Very rough - lots of aggregates - Difficult measurement
AQ CC 080_Si_NC_HDTMS_1%_Tol	158.34

After 7 days of immersion (Figure 116c and d), the differences between the different coatings are more evident. The samples are now organized in a clear ranking performance, with Si\_NC\_HDTMS\_dry ( $1 \times 10^7 \Omega \text{ cm}^2$ ) as the best system, followed by Si\_NC\_HDTMS\_tol, Si\_NC\_dry and the reference coating (all with  $9 \times 10^6 \Omega \text{ cm}^2$ ). The least performing coatings are those containing Si\_NC\_APS,  $3 \times 10^6 \Omega \text{ cm}^2$  and  $2 \times 10^6 \Omega \text{ cm}^2$  for toluene based-slurry and dry, respectively, together with Si\_NC\_Tol ( $3 \times 10^6 \Omega \text{ cm}^2$ ).

As done in the previous chapters the idea was to fit the EIS results making use of equivalent circuits. However, the fitting of AQ CC 080 coatings proved to be difficult in particular to extract parameters associated with the coating response. In this system, the coating tended to give two time-constants ascribed to the coating, which made it difficult

to compare systems. The physicochemical explanation for this finding can be that the coating behaves as a two-layer system based upon segregation of the solid content particles, differentiated density and, as a result, dielectric constant. Different models were employed to try to fit the EIS spectra, but the resulting values had high fitting errors associated. An alternative to quantify the coating barrier properties is to obtain the impedance value at a given frequency, from a frequency region which can be ascribed to the coating response.

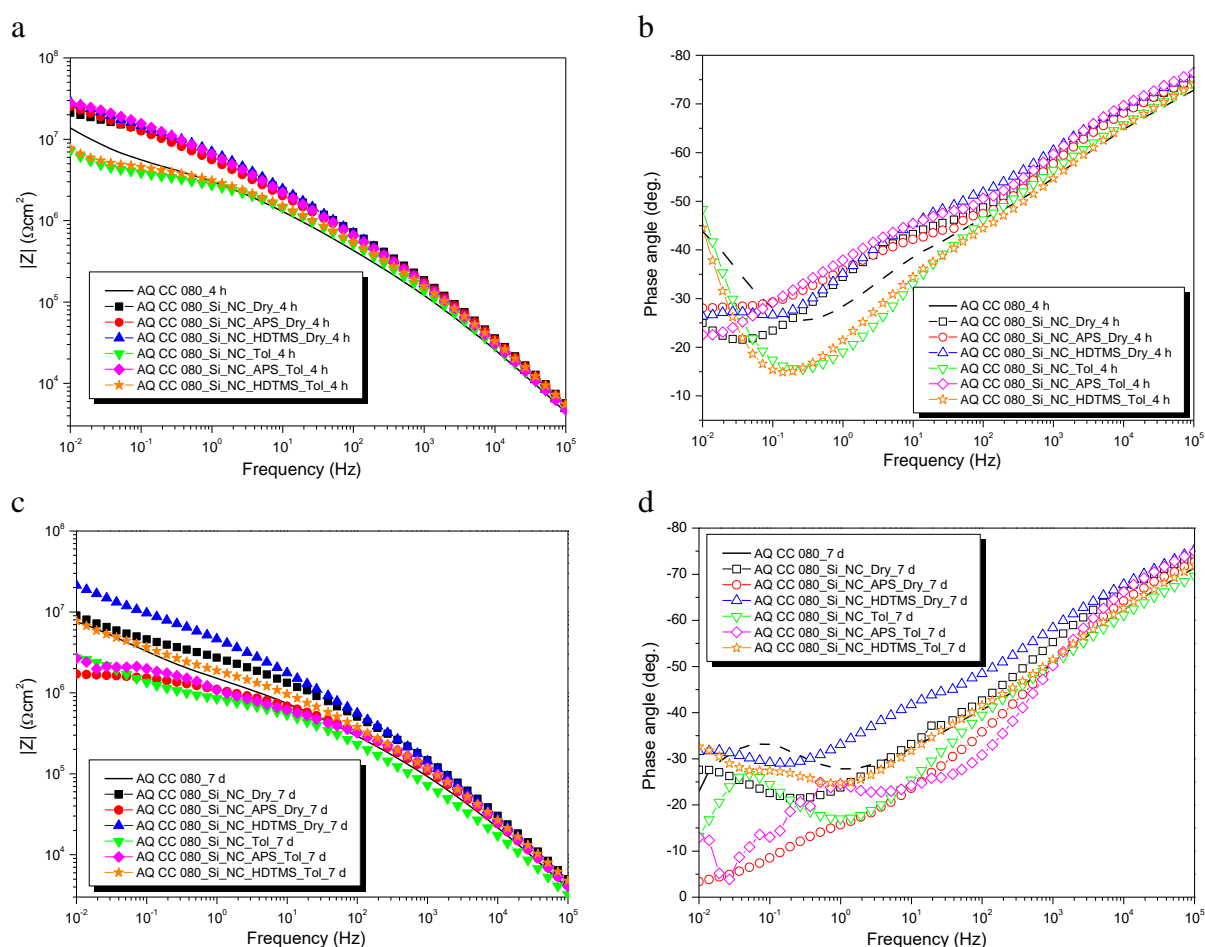
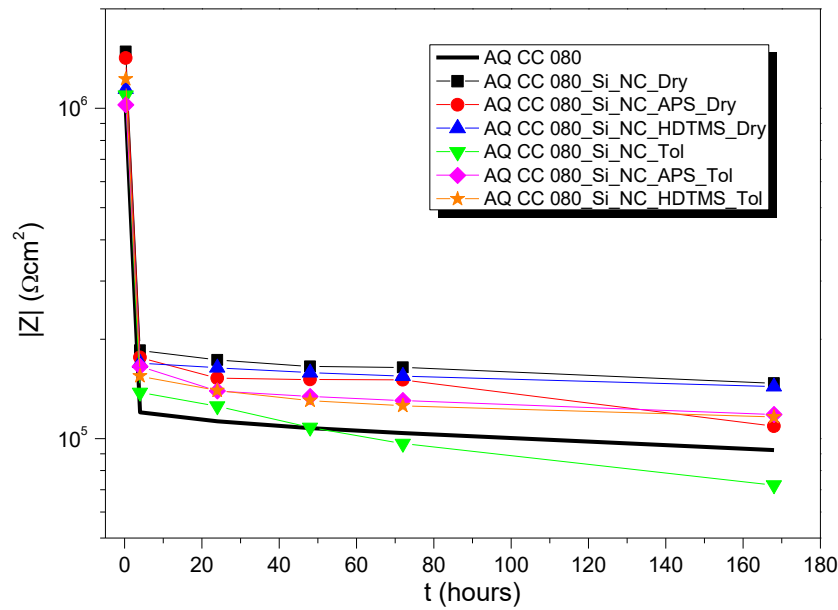


**Figure 116:** EIS spectra for AA2024 panels coated with a water borne polymeric formulation (AQ CC 080) loaded 1 wt.% of Si<sub>NC</sub>, Si<sub>NC</sub>\_APS and Si<sub>NC</sub>\_HDTMS, added to the formulation as a dry powder and as a toluene-based slurry, after 4 hours (a and b) and 7 days (c and d) immersion in a 0.05 M NaCl solution.

In Figure 117a the evolution of the impedance values at 1 kHz up to 7 days of immersion is presented. These are in any case compared against values of  $R_{coat}$  obtained from fittings (Figure 117b) using the highest frequency time constant, though a high fitting error is expected. An important aspect is that both approaches show a similar trend revealing the same system as the best performing coating - Si<sub>NC</sub>\_HDTMS<sub>dry</sub> – as well as the worst one - Si<sub>NC</sub><sub>dry</sub>. All samples show a similar behavior, with initial

impedance values around  $1 \times 10^6 \Omega \text{ cm}^2$ , decreasing one order of magnitude just after 4 hours of immersion, to values around  $1 \times 10^5 \Omega \text{ cm}^2$ . After 4 hours, the impedance values tended to decrease slightly over time. Using the values in Figure 117a is possible to rank the samples accordingly with their coating barrier properties after 7 days of immersion, as follows:  $\text{Si\_NC\_HDTMS\_dry} \approx \text{Si\_NC\_dry} > \text{Si\_NC\_HDTMS\_tol} \approx \text{Si\_NC\_APS\_tol} \approx \text{Si\_NC\_APS\_dry} > \text{reference coating} >> \text{Si\_NC\_tol}$ .

a



b

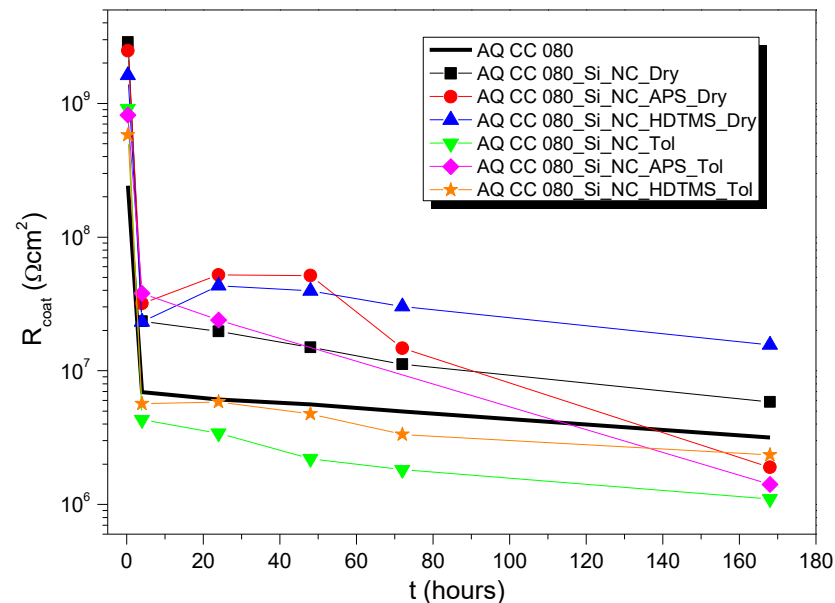


Figure 117: a) EIS values at 1 kHz for AA2024 panels coated with a waterborne polymeric formulation (AQ CC 080) loaded 1 wt.% of Si\_NC, Si\_NC\_APS and Si\_NC\_HDTMS, added to the formulation as a dry powder and as a toluene-based slurry, until 7 days immersion in a 0.05 M NaCl solution. In b) are presented the values of  $R_{\text{coat}}$  obtained from the same samples during the same time period.

From the qualitative analysis, presented in Figure 116 and the quantitative assessment based on the values shown in Figure 117a and b several points can be inferred:

- the presence of toluene is detrimental for the water-based formulation;
- APS functionalization of Si\_NC particles is detrimental to the formulation used, regardless of the physical state of the added material;
- Si\_NC modified with HDTMS dry give the best results in terms of coating performance.

The visual assessment of samples during the immersion tests are presented in Figure 118. In all samples clear signs of corrosion are visible after 7 days of immersion, becoming more extensive after 60 days. In addition, the changes in the barrier properties due to the presence of particles appear to have some contribution to the corrosion protection at the metal interface. Coatings loaded with Si\_NC\_HDTMS, as a dry powder, appear to be slightly less corroded than Si\_NC\_APS and significantly less corroded than coatings loaded with Si\_NC. Based only on the photographs, in particular after 7 and 60 days, it is possible to rank the samples as follows: Si\_NC\_HDTMS\_dry > reference coating > Si\_NC\_HDTMS\_tol > Si\_NC\_APS\_tol  $\approx$  Si\_NC\_APS\_dry > Si\_NC\_dry >> Si\_NC\_tol. This ranking is similar to the one based on the EIS analysis, with the best and worse systems coinciding, Si\_NC\_HDTMS\_dry as the best and Si\_NC\_tol as the worse.

The poor performance of Si\_NC\_APS can be associated with the issues related with the nanocontainer dispersion, as observed after coating application, and due to detrimental interactions between the amine groups and the chemistry of the coating formulation, polyurethane-based. The coating chemistry, in this case, is based on the formation of urethane bonds, isocyanate-polyol reaction. When in the presence of amine groups a competing reaction could occur between isocyanate and amine groups, leading to the formation of urea bonds (Figure 119). Thus, the presence of amine groups on the Si\_NC surface appears to be competing with the hydroxyl groups of the AQ CC 080 for the available isocyanate groups in the hardener. The result of these side reactions seems to be an impairment of the coating barrier properties.

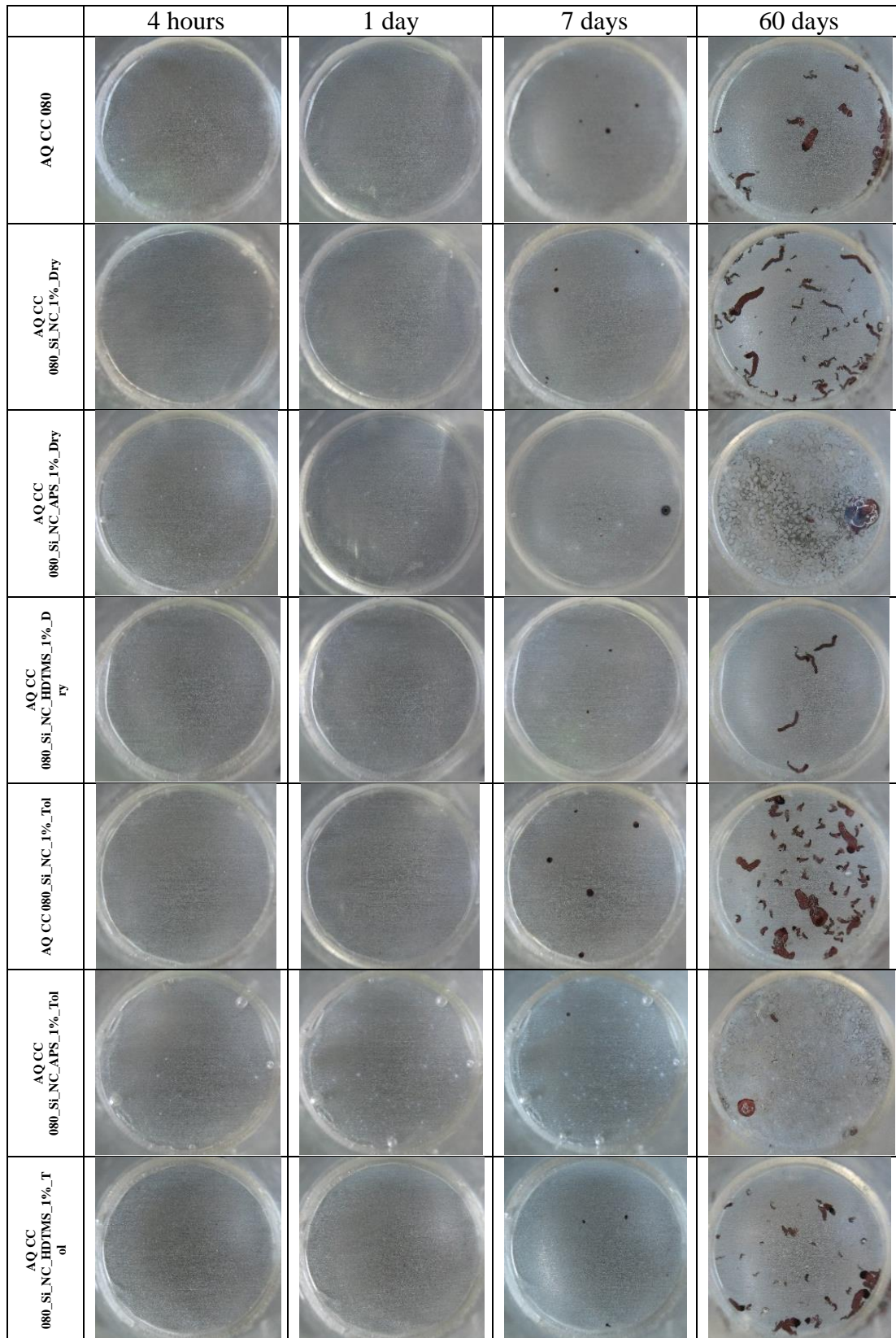


**Figure 118: Photographs of AA2024 coated with a water born polymeric formulation (AQ CC 080) loaded 1 wt.% of Si\_NC, Si\_NC\_APS, and Si\_NC\_HDTMS, added to the formulation as a dry powder and as a toluene-based slurry, after 4 hours, 1 days, 7 days and 60 days immersion in a 0.05 M NaCl solution.**

Assuming that the EIS shows the behavior of coatings under constant immersion and the extent of degradation via ingress of electrolyte through pores, cracks, creating conducting pathways to allow corrosion processes at the metal/coating interface, the ingress of electrolyte is dependent upon the coating properties. Assuming the immiscible nature of toluene with respect to water and different rates of evaporation, possibly the presence of toluene contributes to the presence of small voids that allows for a faster water penetration. On the other hand, the presence of inorganic particles can reflect on the strengthening of the coating matrix through the establishment of additional primary or secondary interactions.

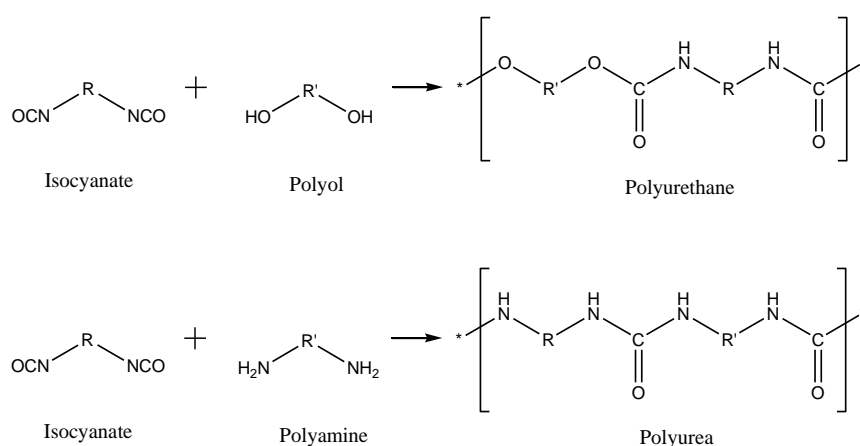


**Figure 119: Chemical reaction to form polyurethane and polyurea groups.**

Comparing the data obtained by DSC, micro-hardness, and EIS some aspects can be highlighted. It seems that, although the curing process of the coating is not affected by the presence of toluene, the presence of this solvent actually contributes for a faster degradation of the coating under constant immersion in NaCl solution as observed by EIS. The effect of the addition of amine-modified Si\_NC also does not appear to change the curing properties of the coating, as observed by DCS. Nevertheless, when analyzing the EIS results, the detrimental effect provided by the presence of Si\_NC\_APS is clear on the coating barrier properties. The results indicate EIS as a more sensitive technique considering the coating barrier properties under accelerated corrosion conditions.

### 7.3.2.2 Solvent-based polyurethane coatings

Coatings prepared from solvent-based formulations are still very common despite the great pressure exerted on the industry to find more environmentally friendly solutions, namely coatings with low volatile organic compounds (VOC's) emission.[348, 349]

Despite the debate, is advantageous to assess the effect of surface modification in solvent-based formulations and the effect of the physical state in which the nanocontainers were added, following the same approach used for AQ CC 080. The fact that part of the Si<sub>3</sub>N<sub>4</sub> particles added to the formulation are in a toluene-based slurry could, in principle, be advantageous by producing a higher affinity with the solvent-based coating. AQ CC 100 is a polyurethane-based coating provided by SYNPO (the detailed composition is shown in section 4.3.3).

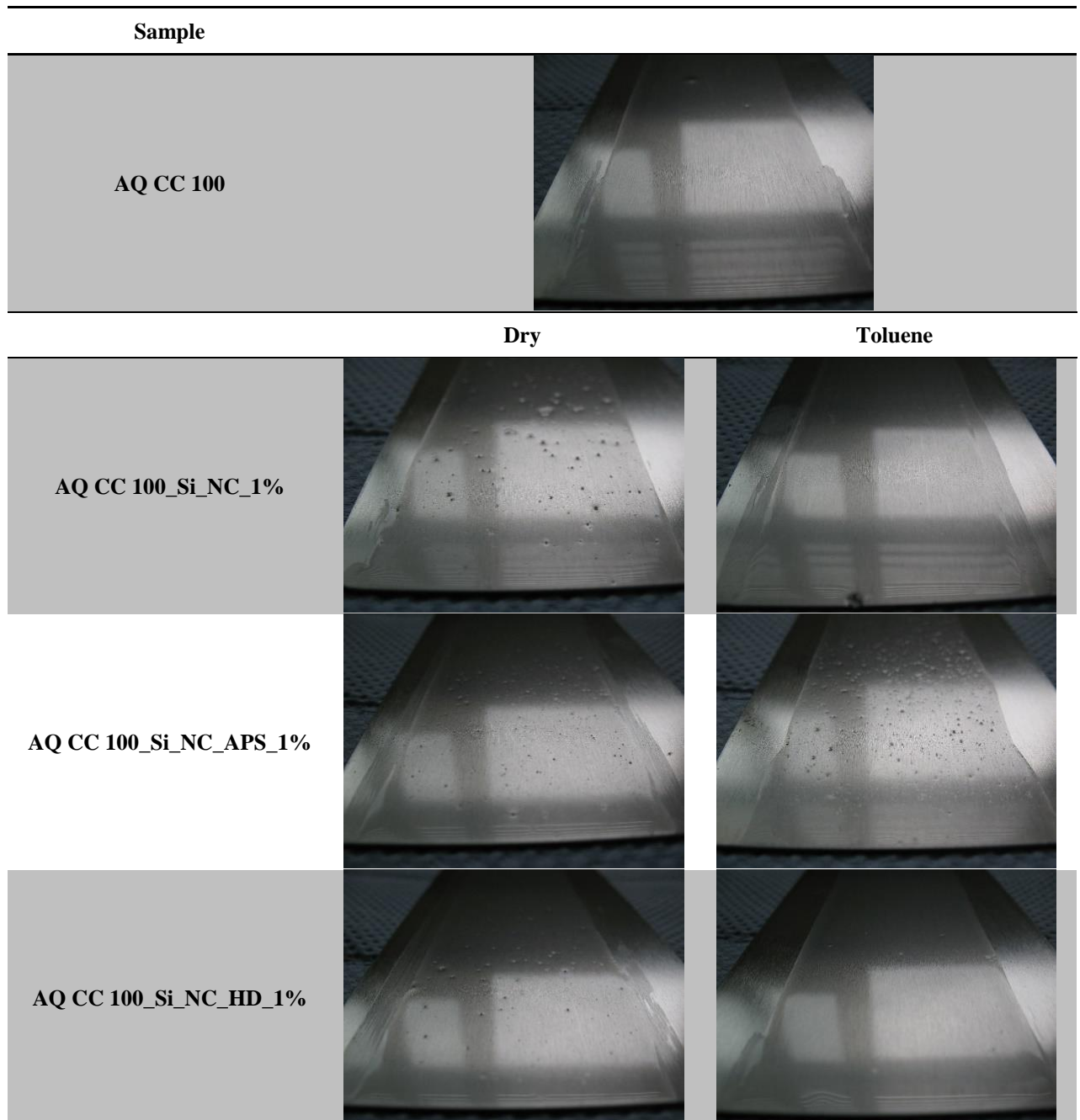


Figure 120: Photographs of AQ CC 100 coatings loaded with 1 wt.% of Si<sub>3</sub>N<sub>4</sub>, Si<sub>3</sub>N<sub>4</sub>\_APS and Si<sub>3</sub>N<sub>4</sub>\_HDTMS applied on carbon steel, added to the formulation as a dry powder and as a toluene-based slurry.

Figure 120 shows photographs of AQ CC 100 coatings without nanocontainers and loaded with 1 wt.% of Si\_NCs, with different surface modifications and in two physical states. The addition of nanocontainers as a slurry yields better results compared with the addition of Si\_NC in the dry form. Exception made for Si\_NC\_APS, with no significant changes compared with the addition in the dry form. More than the surface chemistry when adding Si\_NC to AQ CC 100 the most significant factor was the physical form in which the nanocontainers were added. These observations differ from what was observed for AQ CC 080, where APS was the main (worse) factor responsible for the significant number of aggregates present in the coating. A factor influencing the poor nanocontainer dispersibility could be the solids content of the coatings, leading to an increase in viscosity, which affects the mechanical dispersion of the nanocontainers.

The glass transition values for the coatings are presented in Table 36. AQ CC 100 has  $T_g$  values smaller than AQ CC 080, 51.08 °C for the former and 58.01 °C for the latter. Nevertheless, in both cases, the coatings display hard glassy state with favorable values of hardness and mechanical properties at room temperature. The presence of nanocontainers in AQ CC 100 coatings shows no significant change in the  $T_g$  values. The difference is considered small, meaning that coatings loaded with nanocontainers, regardless of their surface chemistry, render coatings with similar properties, from the curing process perspective.

**Table 36:**  $T_g$  of the cooling step for AQ CC 100 formulation with 1 wt.% of Si\_NC, Si\_NC\_APS, and Si\_NC\_HDTMS, added to the formulation as a dry powder and as a toluene-based slurry.

Sample	$T_g$ °C
AQ CC 100	51.08
AQ CC 100_Si_NC_1%_Dry	53.30
AQ CC 100_Si_NC_APS_1%_Dry	53.11
AQ CC 100_Si_NC_HDTMS_1%_Dry	54.41
AQ CC 100_Si_NC_1%_Tol	52.03
AQ CC 100_Si_NC_APS_1%_Tol	53.20
AQ CC 100_Si_NC_HDTMS_1%_Tol	54.89

The results from the microhardness tests give similar conclusions to the ones obtained from DSC, with the addition of nanocontainers not affecting significantly the coating properties. The results presented in Table 37 show microhardness values similar for all systems, exception made to Si\_NC\_APS\_tol due to the high amount of aggregates

on its surface, which have a significant influence on the test performance. In this case, the results obtained are not related only with the coating mechanical properties but also with high surface roughness, as mentioned in the previous section for AQ CC 080.

The curing process and mechanical properties appear to suffer no significant interference from the addition of nanocontainers. The negative influence of a poor dispersion is not so much evident in the overall coating curing properties but rather on the aesthetic appearance of the coating. Nevertheless, the analysis done so far does not give a full picture of the coating properties, namely the coating barrier properties under immersion in aggressive conditions.

The barrier properties were analyzed by EIS, and the results obtained are shown in Figure 121. The higher NaCl concentration used in AQ CC 100 (0.5 M NaCl) comparing with AQ CC 080 (0.05 M NaCl) was chosen based on the difference in terms of coating performance of the solvent-based coating with respect to the water-based system AQ CC 080, to accelerate the coating degradation in the former case and allow assessment of the system within a reasonable time.

**Table 37: Microhardness according to Martens test for AQ CC 100 formulation with 1 wt.% of Si\_NC, Si\_NC\_APS, and Si\_NC\_HDTMS, added to the formulation as a dry powder and as a toluene-based slurry.**

Sample	Reverse Vickers / N/mm <sup>2</sup>
AQ CC 100	153.05
AQ CC 100_Si_NC_1%_Dry	169.17
AQ CC 100_Si_NC_APS_1%_Dry	167.58
AQ CC 100_Si_NC_HDTMS_1%_Dry	149.55
AQ CC 100_Si_NC_1%_Tol	148.54
AQ CC 100_Si_NC_APS_1%_Tol	273.24 difficult to measure - very variable
AQ CC 100_Si_NC_HDTMS_1%_Tol	148.03

The results after 4 hours show all samples presenting only one time constant at high frequencies ( $f > 10^3$  Hz) ascribed to the coating applied to the AA2024. The Bode plot for Si\_NC\_APS\_dry show scattered values at low frequencies, indicative of some instability of the measurement that could be signaling the appearance of a second time constant. The impedance values at low frequencies (10 mHz) are around  $1 \times 10^{10} \Omega\text{cm}^2$  for Si\_NC\_APS\_dry and  $1 \times 10^{11} \Omega\text{cm}^2$  for the remaining samples.

After 60 days of immersion (Figure 121c and d), the presence of nanocontainers in the coating does not seem to improve the coating barrier properties. This is somehow

an expected outcome since the coating in itself displays already very high barrier properties. Noteworthy is the lack of negative effect that the presence of some nanocontainers has on the coating barrier properties over long periods of immersion in such an aggressive medium. The best systems only show one time constant at high frequencies ascribed to the coating: AQ CC 100, Si\_NC\_HDTMS\_dry, Si\_NC\_Tol and Si\_NC\_APS\_Tol (less defined). For Si\_NC\_dry and Si\_NC\_HDTMS\_Tol a second time constant at ( $10^0 \text{ Hz} < f < 10^1 \text{ Hz}$ ) can be ascribed to the oxide film. In the case of Si\_NC\_dry a third time constant at ( $10^{-2} \text{ Hz} < f < 10^{-1} \text{ Hz}$ ) can be observed associated with ongoing corrosion processes on the metal surface.

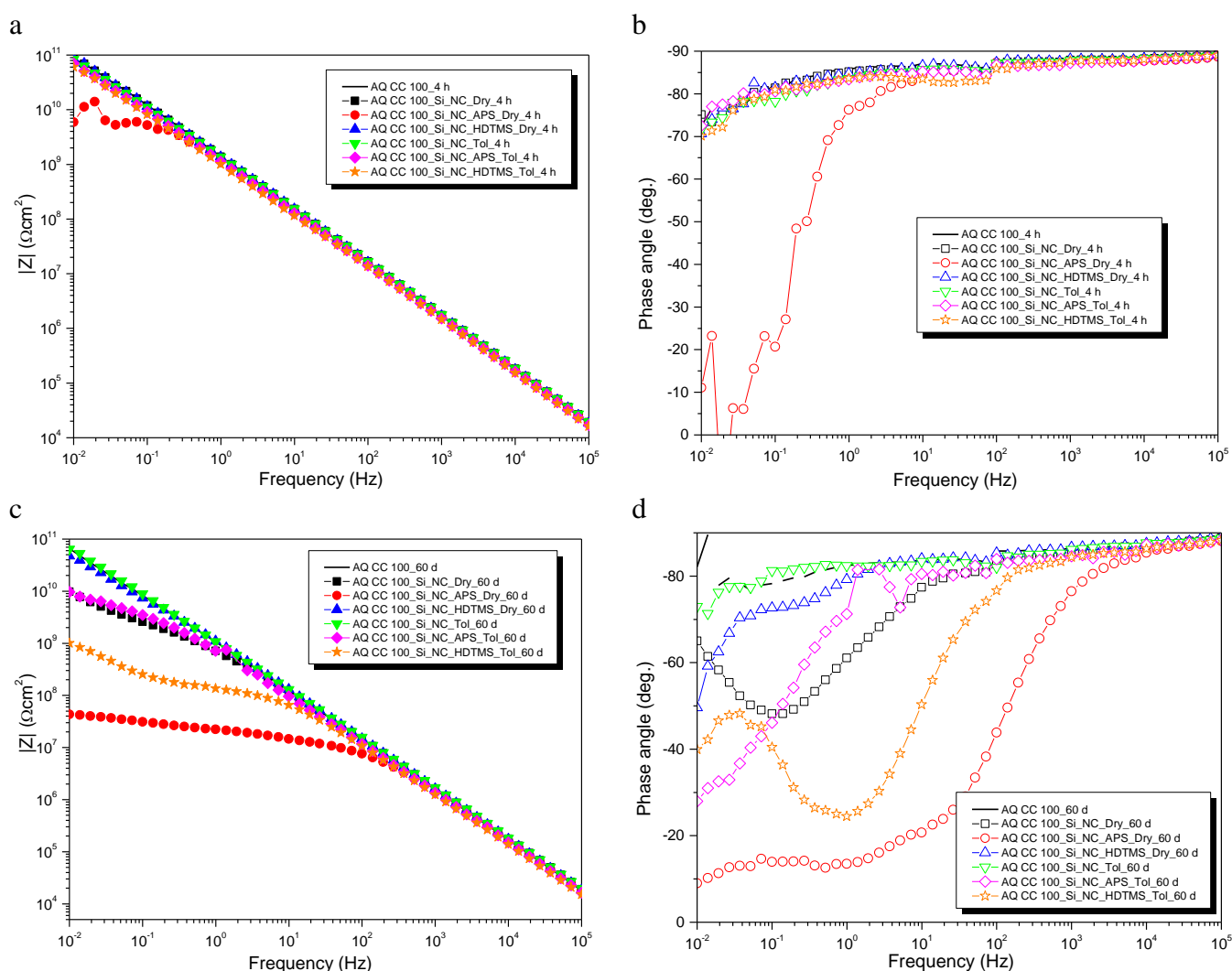


**Figure 121:** EIS spectra for AA2024 panels coated with a solvent based polymeric formulation (AQ CC 100) loaded with 1 wt.% of Si\_NC, Si\_NC\_APS and Si\_NC\_HDTMS, added to the formulation as a dry powder and as a toluene-based slurry, after 4 hours (a and b) and 60 days (c and d) immersion in a 0.5 M NaCl solution.

The EIS results were fitted to make a quantitative assessment of the coatings barrier properties. The fitting was done making use of the equivalent circuits presented in

Figure 122 with the results shown in detail in Table 38 for 4 hours and 60 days of immersion. The values of  $R_{\text{coat}}$  over time are presented in Figure 123. Three equivalent circuits were used accordingly with the sample response throughout the test. The first equivalent circuit consisted of only one-time constant (panel a), ascribed to the coating response. The second equivalent circuit (panel b) was used when the coating barrier properties started to decrease allowing the ingress of more water and electrolyte. It displays two-time constants ascribed to the coating layer and the AA2024 natural oxide layer. The third equivalent circuit (panel c) was used in cases where the water reached the metal surface and corrosion processes had started.

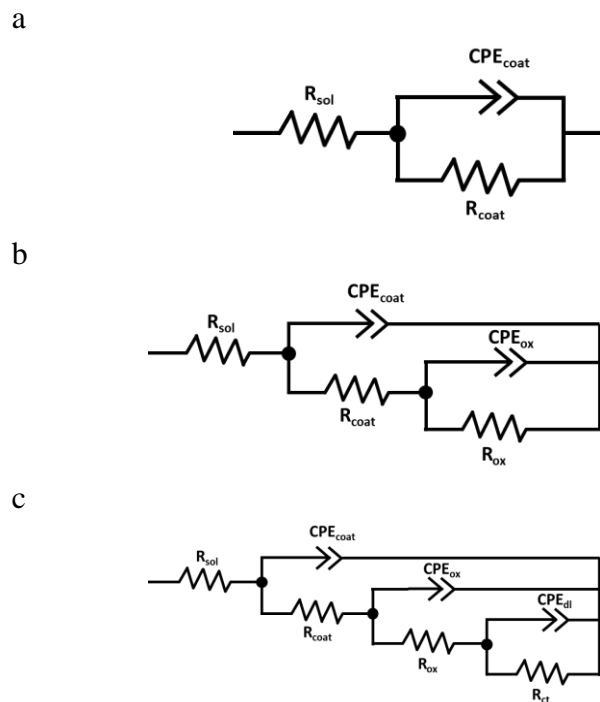


Figure 122: Equivalent circuits used to fit EIS data (Figure 121), summarized in Table 38.

The fitted parameters confirm that these coatings have high barrier properties after 4 hours of immersion. All samples presented values of  $R_{\text{coat}}$  around  $2 \times 10^{11} \Omega \text{ cm}^2$ , except for Si\_NC\_APS\_dry with a  $R_{\text{coat}}$  of  $5.90 \times 10^9$ . After 60 days of immersion, significant differences can be observed. The best systems are AQ CC 100 ( $6.59 \times 10^{11} \Omega \text{ cm}^2$ ), Si\_NC\_Tol ( $2.62 \times 10^{11} \Omega \text{ cm}^2$ ) and Si\_NC\_HDTMS\_dry ( $7.28 \times 10^{10} \Omega \text{ cm}^2$ ). In a second group are Si\_NC\_APS\_Tol ( $7.30 \times 10^9 \Omega \text{ cm}^2$ ) and Si\_NC\_dry ( $1.09 \times 10^9 \Omega \text{ cm}^2$ ). Si\_NC\_HDTMS\_Tol ( $1.17 \times 10^8 \Omega \text{ cm}^2$ ) and Si\_NC\_APS\_dry ( $4.50 \times 10^6 \Omega \text{ cm}^2$ ).

The EIS results are in agreement with the photographs shown in Figure 124. Only Si\_NC\_APS\_dry show signs of corrosion, already visible after 21 days of immersion. In

the remaining samples, there is no indication of corrosion processes taking place, indicating that all of them have similar barrier properties.

From both qualitative and quantitative analysis of the EIS several points can be inferred:

- Based on these results is possible to rank the samples accordingly with their coating barrier properties as AQ CC 100  $\approx$  Si\_NC\_HDTMS\_dry  $\approx$  Si\_NC\_Tol > Si\_NC\_APS\_Tol  $\approx$  For Si\_NC\_dry > Si\_NC\_HDTMS\_Tol > Si\_NC\_dry.

-the addition of nanocontainers, in most cases, have detrimental effects on a coating with high barrier properties.

-APS functionalization of Si\_NC particles is detrimental for the formulation.

-no definitive conclusion can be drawn regarding the effect of toluene based-slurries.

**Table 38: Results obtained from the fitting of EIS spectra for AA2024 panels coated with a solvent based polymeric formulation (AQ CC 100) loaded 1 wt.% of Si\_NC, Si\_NC\_APS, Si\_NC\_GPTMS and Si\_NC\_HDTMS after 4 hours and 60 days immersion in a 0.5 M NaCl solution, depicted in Figure 121. \*The value of R is very high due to the few points available, at low frequencies, to properly fit the results.**

System	Time	Circuit ( $\chi^2$ )	Y(CPE <sub>coat</sub> ) Ss <sup>n</sup> cm <sup>-2</sup>	R <sub>coat</sub> Ωcm <sup>2</sup>	Y(CPE <sub>ox</sub> ) Ss <sup>n</sup> cm <sup>-2</sup>	R <sub>ox</sub> Ωcm <sup>2</sup>	Y(CPE <sub>dl</sub> ) Ss <sup>n</sup> cm <sup>-2</sup>	R <sub>ct</sub> Ωcm <sup>2</sup>
AQ CC 100	4 h	(4.20x10 <sup>-3</sup> )	1.30x10 <sup>-9</sup> (n=0.965)	2.76x10 <sup>11</sup>	-	-	-	-
	60 d	(8.12x10 <sup>-3</sup> )	1.80x10 <sup>-10</sup> (n=0.938)	6.59x10 <sup>11</sup>				
AQ CC 100_Si_NC_Dry	4 h	(3.69x10 <sup>-3</sup> )	1.30x10 <sup>-10</sup> (n=0.961)	3.03x10 <sup>11</sup>				
	60 d	(4.16x10 <sup>-3</sup> )	1.62x10 <sup>-10</sup> (n=0.946)	1.09x10 <sup>9</sup>	5.60x10 <sup>-10</sup> (n=0.643)	1.67x10 <sup>11</sup>		
AQ CC 100_Si_NC_APS_Dry	4 h	(2.18x10 <sup>-3</sup> )	1.30x10 <sup>-10</sup> (n=0.966)	5.90x10 <sup>9</sup>				
	60 d	(1.81x10 <sup>-4</sup> )	1.37x10 <sup>-10</sup> (n=0.968)	*4.50x10 <sup>6</sup>	1.89x10 <sup>-8</sup> (n=0.307)	*4.11x10 <sup>7</sup>	1.55x10 <sup>-7</sup> (n=0.959)	*1.46x10 <sup>7</sup>
AQ CC 100_Si_NC_HDTMS_Dry	4 h	(4.07x10 <sup>-3</sup> )	1.31x10 <sup>-10</sup> (n=0.963)	2.66x10 <sup>11</sup>				
	60 d	(1.39x10 <sup>-2</sup> )	1.84x10 <sup>-10</sup> (n=0.933)	7.28x10 <sup>10</sup>				
AQ CC 100_Si_NC_Tol	4 h	(6.37x10 <sup>-3</sup> )	1.36x10 <sup>-10</sup> (n=0.955)	2.49x10 <sup>11</sup>				
	60 d	(4.74x10 <sup>-3</sup> )	1.69x10 <sup>-10</sup> (n=0.938)	2.38x10 <sup>11</sup>				
AQ CC 100_Si_NC_APS_Tol	4 h	(5.28x10 <sup>-3</sup> )	1.65x10 <sup>-10</sup> (n=0.950)	2.62x10 <sup>11</sup>				
	60 d	(4.53x10 <sup>-2</sup> )	2.95x10 <sup>-10</sup> (n=0.904)	7.30x10 <sup>9</sup>				
AQ CC 100_Si_NC_HDTMS_Tol	4 h	(5.65x10 <sup>-3</sup> )	1.80x10 <sup>-10</sup> (n=0.947)	1.81x10 <sup>11</sup>				
	60 d	(2.61x10 <sup>-3</sup> )	2.19x10 <sup>-10</sup> (n=0.942)	1.17x10 <sup>8</sup>	6.80x10 <sup>-9</sup> (n=0.724)	2.70x10 <sup>9</sup>		

The standard tests performed on the coatings, DSC and microhardness, did not show any negative effect produced by the addition of nanocontainers to the coating. Besides the obvious aesthetic appearance of the coatings associated with the nanocontainer dispersion, the results show no significant changes in the curing process or

in the coating hardness. EIS, on the other hand, allowed for an analysis, focusing on the coating barrier properties under aggressive conditions. The results indicate the negative effect of adding nanocontainers to the coating. Compared with AQ CC 080, a coating with lower barrier properties, AQ CC 100 does not indicate a clear trend regarding the use of toluene based-slurry and the effect of the different functional groups present on the Si\_NC on the coating.

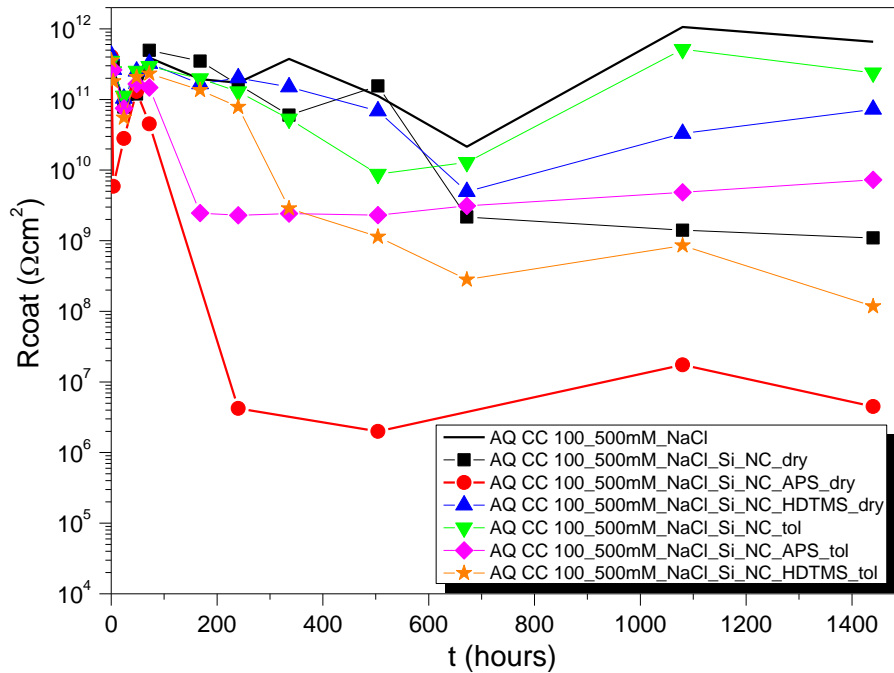


**Figure 123:** Evolution over time of the  $R_{coat}$  for AA2024 panels coated with a solvent-based polymeric formulation (AQ CC 100) loaded with 1 wt.% of Si\_NC, Si\_NC\_APS, Si\_NC\_GPTMS and Si\_NC\_HDTMS immersed in 0.5 M NaCl solution.

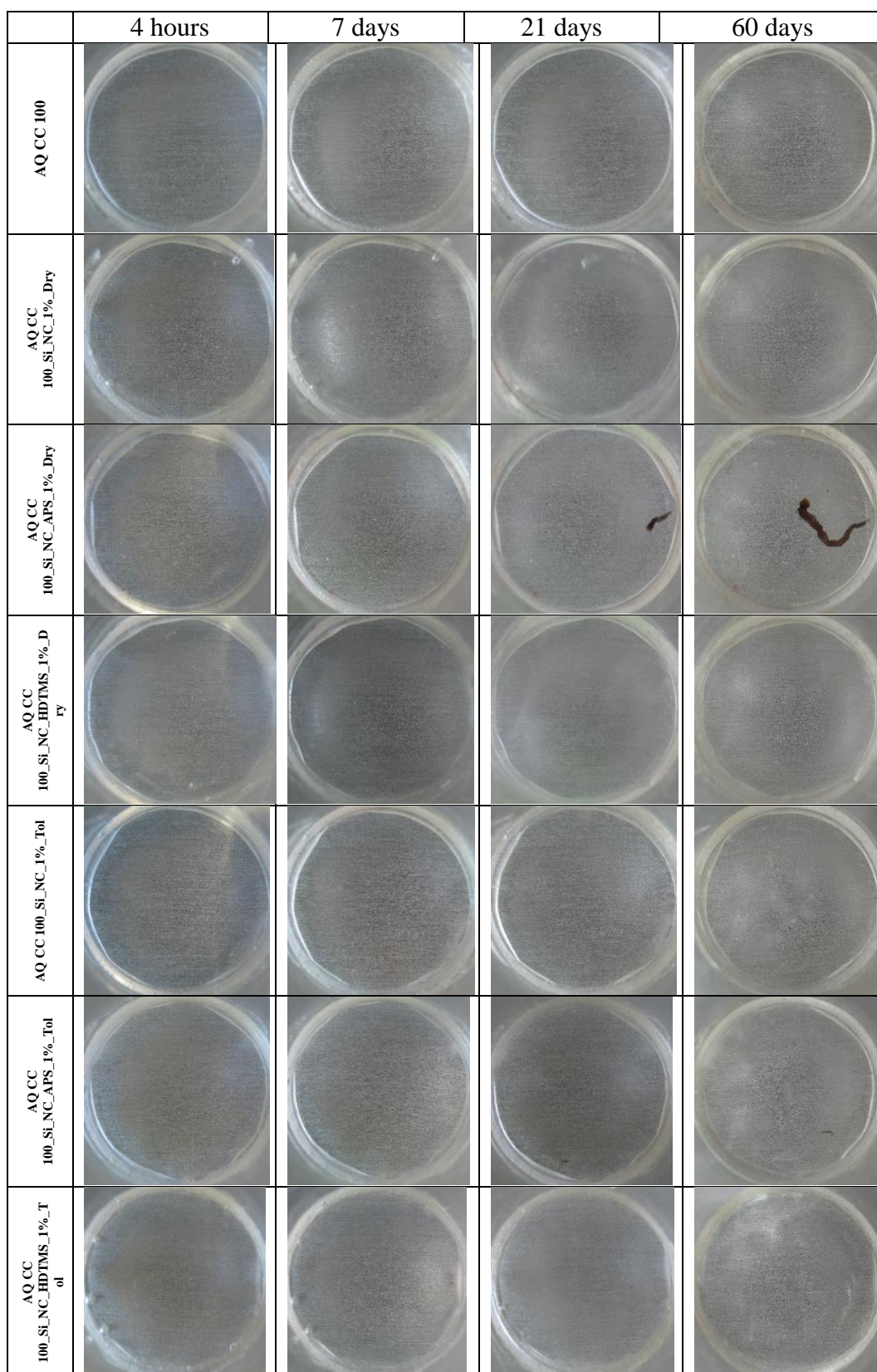


**Figure 124:** Photographs of AA2024 coated with a solvent based polymeric formulation (AQ CC 100) loaded 1 wt.% of Si<sub>3</sub>N<sub>4</sub>, Si<sub>3</sub>N<sub>4</sub>-APS and Si<sub>3</sub>N<sub>4</sub>-HDTMS, added to the formulation as a dry powder and as a toluene-based slurry, after 4 hours, 7 days, 21 days and 60 days immersion in a 0.5 M NaCl solution.

## 7.4 Partial conclusions

The surface modification of Si<sub>2</sub>NC nanocontainers with different functional groups, amine, epoxy and aliphatic, was achieved successfully. The aim was to study two factors: dispersibility and chemical compatibility between nanocontainers and coating formulations. The successful modification of Si<sub>2</sub>NC was achieved by chemical reactions, allowing the tailoring of the surface chemistry according to the needs. The changes in Si<sub>2</sub>NC physical interactions with the solvent, namely water, were clear, resulting in improvements for epoxy and amine-based modifications while hampering the wetting of nanocontainers with long aliphatic chains.

The dispersibility of modified nanoparticles revealed not to be the sole factor to achieve good barrier properties. Chemical interactions between the functional groups on the nanocontainers surface and functional groups from the coating matrix were found to be more relevant. The impact that modified Si<sub>2</sub>NC have on the coatings was studied for different types of coating: simple water-based hybrid sol-gel, solvent-based hybrid sol-gel, as well as for more complex industrial water-based polyurethane and solvent-based polyurethane formulations.

The use of a sol-gel-based coating constitutes an intermediate step between simple stability in solvents and addition to fully functional commercial coatings which allowed to draw some important conclusions. The results, as expected, have some level of variation depending on the nature of the coatings:

- Water-based sol-gel coatings showed improved results using smaller amounts of nanocontainers; amine functionalization was not adequate for this system due to detrimental reactions between the amines (nanocontainers) and epoxy groups (sol-gel coating). On the other hand, functionalization with epoxy (Si<sub>2</sub>NC\_GPTMS) and aliphatic (Si<sub>2</sub>NC\_TMOS) groups when added in reduced amounts (1 wt.%) lead to improved barrier properties.
- In solvent-based sol-gel coatings, the addition of nanocontainers seems to improve the coating barrier properties in some cases. Again, the presence of amine moieties affected negatively the coating barrier properties in contrast with epoxy (Si<sub>2</sub>NC\_GPTMS) and aliphatic (Si<sub>2</sub>NC\_TMOS), as in the case of water-based sol-gel.

The barrier properties herein analyzed by EIS can be explained by taking into account a combination of physical (nanocontainer dispersibility) parameters and the chemical reactivity associated with coating formulations. The addition of higher amounts of particles tend to affect negatively the sol-gel matrix; on the other hand, the addition of highly reactive groups such as amines affects the sol-gel curing process.

To solve some issues arising from the nanocontainer dispersibility into formulations the analysis was extended to Si\_NC in the form of a slurry. The effect was analyzed by adding the nanocontainers to commercial polyurethane-based coatings, solvent- and water-based. The comparison between modified nanocontainers in the dry- and slurry-based forms produced some interesting results.

The barrier properties were analyzed by EIS, with distinct results depending on the coating nature. For the waterborne coating, the addition of particles increase the coating barrier properties in particular for particles added as a dry powder. Moreover, the modification with HDTMS results in improvement of the system, with the conjugation of both factors reflected in the best system, Si\_NC\_HDTMS\_Dry. The dispersion of the nanocontainers, with the exception of Si\_NC\_APS, was achieved for all the nanocontainers regardless of their physical state, though decay of the barrier properties for samples prepared with toluene was found to be more evident.

The results obtained for the solvent-based coating systems show a different effect of the nanocontainers. Firstly, there is no improvement in the coating barrier properties after the addition of nanocontainers. On the other hand, there is no loss of those properties for most of the nanocontainers, exception made to Si\_NC\_APS, after 60 days of immersion. The physical state in which the nanocontainers were added seems to play a secondary role on the properties of the final coating systems obtained. Nonetheless, one must combine the effect of the nanocontainers on the coating barrier properties together with the quality of the dispersion to obtain uniform coatings. In this sense, the addition of nanocontainers in a toluene-based slurry improved their dispersion in the coatings. When combining the results from the EIS analysis together with the nanocontainers dispersion quality, Si\_NC\_tol and SI\_NC\_HDTMS\_dry were found to be the best systems.

The results show the versatility of Si\_NC in terms of addition of different functional groups to its surface and consequently tuning its properties. Nevertheless, surface chemistry alone does not dictate all the rules concerning particles dispersion or coating barrier properties. The form in which the nanocontainers are added proved to be relevant for some coatings. Another aspect is that the presence of amine groups on the

Si<sub>3</sub>N<sub>4</sub> impaired considerably the coating barrier properties in all the coatings tested. HDTMS appears to have a good effect on the coating properties, with the dispersion issues overcome by the use of slurry, which culminates in this being the best system for both coatings when combining the results from EIS (barrier properties) and visual analysis (quality of capsule dispersion in the coating).

EIS was found to be more sensitive to changes in the coating barrier properties imparted by the addition of nanoparticles than DSC and micro-hardness, indicating that EIS can be used as a useful tool to complement results obtained in the industry and contribute for efficient product development.



# 8

## Conclusions

### The optimistic frog

Two frogs fell into a deep cream bowl,  
One was an optimistic soul;  
But the other took the gloomy view,  
“We shall drown,” he cried, without more ado.  
So with a last despairing cry,  
He flung up his legs and he said, “Goodbye.”

Quoth the other frog with a merry grin,  
“I can’t get out, but I won’t give in.  
I’ll just swim ’round till my strength is spent,  
Then will I die the more content.”

Bravely he swam till it would seem  
His struggles began to churn the cream  
On the top of the butter at last he stopped,  
And out of the bowl he gaily hopped.  
What of the moral? ‘Tis easily found  
If you can’t hop out, keep swimming ’round.

Author unknown



## 8.1 Holistic overview of the work carried out

The overall idea behind this work was the improvement of the compatibility between nanocontainers and coatings, to be explored in the context of corrosion protection. In the first stage, an academically driven approach was followed making use of a well-known corrosion inhibitor (2-MBT) loaded in a well-known nanocontainer (LDH) to be modified (the novelty) and added to a well-known coating (hybrid sol-gel) applied to a well-known metallic substrate used in aeronautical applications (AA2024). This approach allowed to focus on the surface modification process, through the layer-by-layer self-assembly technique (PSS and PAH). To further exploit this modification, incorporation of a second corrosion inhibitor in the same nanocontainer was carried out (cerium nitrate). The results reveal improvements in corrosion protection, inhibitor release profile, and improvement in coating barrier properties.

With a positive experience regarding the use of polyelectrolytes to modify LDHs, the next step was to apply this approach to commercial coatings, inherently more complex in their chemistry. Since the work was focused on an industrial solution, some constraints had to be dealt with: the type of metal substrate, cost, simplicity and environmental friendliness. The nanocontainer was kept the same, LDH, but due to a change in the metal substrate (galvannealed and cold rolled steel), the corrosion inhibitor had to be changed. The selected species were gluconate, a molecule with known anticorrosion properties towards steel substrates. The cost and environmental efficiency of the methodology were addressed in the selection of the materials used: LDH, alginate, and gluconate. All considerably cheap, widely available and so-called “green” materials. The simplicity was addressed in the methodology as well, with all the preparation steps consisting of dispersion and stirring, to achieve intercalation of gluconate and surface modification.

Being an industrial approach it was important to prove first the need to incorporate the corrosion inhibitor into nanocontainers and secondly if there were any performance gains with the surface modification step which would justify the extra work. The incorporation of gluconate into LDHs proved to be a necessity, with the results showing a significant decrease in the overall protection when gluconate was added directly to the coating. On the other hand, surface modification was also demonstrated as a relevant step for the improvement of the coating barrier properties. The results obtained for LDH modified with polyelectrolytes proved to be an interesting route with significant potential

for industrial application. However, surface modification with polyelectrolytes is based mostly on electrostatic interactions and can somehow limit the range of interaction with coating matrices, as it is restricted to the functional groups available in the polyelectrolytes. The aim of extending this topic to the grafting of functional groups via covalent bonds cannot be easily done with LDHs. Thus, silica-based particles or nanocapsules appears as a versatile solution in this regard. For that reason, silica nanocapsules Si\_NC, also a well-established nanocontainer system in our group, were used. Using concepts based on sol-gel chemistry, grafting of different silane derivatives via hydrolysis and condensation reactions was carried out. Due to constraints regarding the incorporation of corrosion inhibitors during the synthesis and modification steps, the option was to focus mainly on the compatibility part of the research and, unlike LDH, not assess the active protection of the systems. This simplification in objectives allowed for more emphasis to be placed on the coating barrier properties. The choice of functional groups was based considering the subsequent incorporation in specific coating formulations, namely sol-gel and polymeric commercial coatings (solvent and coating chemistry). For this purpose, hydroxyl, amine and epoxy groups were grafted to assess the reactivity and the hydrophilic character, whereas aliphatic chains were selected for their hydrophobic character potential effect for a solvent-based system.

The studies performed before with LDH were focused more on nanocontainer/coating compatibility and the active protection. This was due to the already good dispersibility of the LDHs, usually added as a water-based slurry to the coatings. In this case, the addition process was simple and resulted in coatings with no aggregates and well-dispersed nanocontainers. Such was not the case for Si\_NC, usually added as dry powders. This created the necessity to study the dispersibility of the modified nanocontainers first in different solvents and then moving to increasingly more complex formulations. When tested in solvents, namely water, and 2-propanol, the modified nanocontainers produce the expected results. Amine functionalized Si\_NC improved the Si\_NC dispersibility and stability, while hydrophobic moieties were almost impossible to disperse, particularly in water. But the study in solvents only is very far from a functional coating, and even with good indications, the results cannot be taken as a direct indication of guaranteed compatibility.

The next step increased the complexity of the study, by adding the modified Si\_NC into sol-gel coatings. These two formulations were developed in the SECOP group differing in chemical composition, and solvent. If the logic observed for simple solvents

prevailed, amine modified Si<sub>3</sub>N<sub>4</sub> should be the best performing nanocontainers. That was not the case: the chemical reactivity of the amine groups surpassed any potential improvements in stability, thus producing the worst performing coatings. To fully invert the results with the solvents, the incorporation of hydrophobic moieties produced the best results, regardless of the nature of the sol-gel.

The results obtained for sol-gel coatings further increased the need to test the influence of functional groups in fully complex coating dispersions. The selection of the coatings was again done based on their nature, water- and solvent-based. What was observed for sol-gel coatings was confirmed in polyurethane-based coatings as well, with hydrophobically modified nanocontainers yielding the best results. At this stage, the form in which the nanocontainers were added to the coating formulation needed some clarification. The addition of the capsules as dry powders proved to be problematic with the formation of aggregates. The solution to overcoming this issue was to use the same approach followed for the addition of LDH. The application of Si<sub>3</sub>N<sub>4</sub> in a solvent-based slurry form enabled better dispersions in general although some loss in the coating barrier properties could be observed as well.

Overall, the main objective of this thesis was to use a surface modification of nanocontainers to improve compatibility and overall performance of protective coatings. The work followed a lab-to-industrial process, and for that reason, the approaches presented in different chapters, the selection of systems and characterization tests carried out are inevitably heterogeneous. However, the work carried out demonstrated the need to modify nanocontainers if protective coatings based on these smart additives are to become an industrial reality in the forthcoming years.

## 8.2 Final conclusions

The objective of this work was the improvement of anticorrosion systems by surface modifying nanocontainers used in the storage and release of corrosion inhibitors. During this process, not only the compatibility issue was addressed but also a variety of other possibilities were studied: the ability of nanocontainers to release two inhibitors at the same time, the tuning of the nanocontainer release profile of inhibitors.

The selection of LDH and Si<sub>3</sub>N<sub>4</sub> was made based on the know-how available in SECOP group, their demonstrated ability as hosting structures for corrosion inhibitors and their specific properties (structure, composition and corresponding release mechanisms).

LDH was selected due to its ability to release inhibitor “on demand” by ion exchange and its capacity to host anion inhibitors (e.g. 2-MBT, BTA). Si<sub>3</sub>N<sub>4</sub> was selected due to its versatility for surface modification, release profile and its surface chemistry, which opens considerable opportunities to graft different functional groups.

Two different approaches were considered for surface modification of nanocontainers, depending on the systems selected. LDH was modified by physical adsorption based on electrostatic interactions using polyelectrolytes; Si<sub>3</sub>N<sub>4</sub> were covalently modified with different functional groups using different silane derivatives. For studies of LDH at lab scale, the approach was to modify these clays to obtain a system with the dual release of inhibitors. This aim was achieved by modifying LDH loaded with 2-MBT by the LbL approach, using PSS and PAH, and incorporating a second corrosion inhibitor (cerium nitrate) during the modification process. The prepared nanocontainer was able to release two corrosion inhibitors, cerium cations and 2-MBT, plus the release mechanism started to be influenced by the medium ionic strength, due to the presence of the polyelectrolyte shell and also pH. The same type of surface modification with polyelectrolytes was also attempted using alginate in Gluc-loaded LDH for an industrial application using steel alloys. Si<sub>3</sub>N<sub>4</sub>s were chemically functionalized using different silane derivatives, and different functional groups were incorporated. The presence of these different functional groups allowed the assessment of the influence of the surface chemistry on the nanocontainers dispersibility and reactivity towards the coating components. To fulfill this objective chemical groups from more reactive and hydrophilic (amine and epoxy) to less reactive and hydrophobic (aliphatic chains) were selected. The

surface modification was successfully done in a two-step process for nanocontainers without corrosion inhibitors.

The influence that the surface chemistry has on the nanocontainers stability in solution was surveyed for water and 2-propanol. The results showed the importance of tuning the surface chemistry according to the coating solvent. The dispersibility of LDH modified with PSS and alginate was tested in water. The results indicate some improvement in the stability of modified nanocontainers over time. In the case of Si<sub>3</sub>N<sub>4</sub> NCs results show that amine and epoxy groups improve the dispersibility of dry Si<sub>3</sub>N<sub>4</sub> NCs into solution and stability of suspensions over time. The presence of long aliphatic chains affects considerably the dispersibility of Si<sub>3</sub>N<sub>4</sub> NC, preventing even the wetting of the nanocontainers in the case of water. For amine modified Si<sub>3</sub>N<sub>4</sub> NC the influence of the pH was also analyzed. The results indicate an improvement in stability for higher pH conditions (around 10).

Regarding the release tests, the modification of LDH-MBT with PSS/PAH lead to loss of inhibitor during the LbL process. Nevertheless, the active properties of the nanocontainers and coatings were not detrimentally affected. Moreover, the modification changed the main triggering conditions of release of inhibitors intercalated within layered double hydroxides, from ion exchange to a pH-dependent release. For LDH-Gluconate modified with alginate, the presence of an alginate layer around the LDHs appears to enhance the inhibitor release dependence on the ionic strength. For more concentrated NaCl solutions the release of inhibitors followed the expected trend, with higher gluconate concentration released under more concentrated NaCl solutions.

Unmodified and surface modified nanocontainers were tested in media of increasing complexity. First, only in solvents, followed by a coating with known chemical composition (hybrid sol-gel coatings) and finally in industrial-based coatings. The surface modification proved to be advantageous in most cases, owing their improved performance to improve dispersibility, nanocontainer/coating compatibility and improved active protection by the presence of corrosion inhibitors.

In the lab scale tests using sol-gel as coating system, the shell around the LDHs based on PSS and PAH improved the coating barrier properties over time, compared with undoped coating and with coatings loaded with unmodified nanocontainers. A similar trend was found for LDH modified with alginate only and tested in an industrial polymeric formulation provided by TATA STEEL.

Comparing Si\_NC-loaded with unloaded coatings, the presence of nanocontainers appeared to be beneficial, in particular for coatings with low barrier properties based on sol-gel. In the case of an industrial-based systems, nanocontainers can have some detrimental effect but the physical presence of nanocontainers is not the sole factor that affects the coatings barrier properties. The surface chemistry of Si\_NC proved to be the main factor when determining the best performing coatings. Si\_NC functionalized with amine groups were found to be incompatible with different coatings. On the other hand, the addition of Si\_NC modified with aliphatic chains provided coatings with improved barrier properties, compared with unloaded coatings and unmodified nanocontainers.

One final objective of this work was to use electrochemical impedance spectroscopy as a tool for monitoring the quality of coating barrier properties. Comparing the results obtained by EIS with those obtained from standard industrial tests it is possible to validate EIS as a suitable, greener and in some cases more advantageous technique to characterize coating quality, particularly on the effect of nanocontainers addition.

Overall, the results presented in this thesis show advantages, from a performance perspective, in modifying the surface of nanocontainers to be used as compatible, anti-corrosion additives. Some of the approaches herein presented may be used in the future to aid on the improvement of formulation activities by coating producers.

### 8.3 Future perspectives

Considering all the results obtained, some points remain to be explored. In particular, the use of modified Si<sub>3</sub>N<sub>4</sub> loaded with corrosion inhibitors needs to be addressed in order to combine active corrosion protection with enhanced coating barrier properties. Other activities include the grafting of silane derivatives in LDH which could bring new functional groups into surface of LDHs, improvement of inhibitor loading content in LDH modified with polyelectrolytes by changing the LbL modification process, investigate the possibility of synthesizing and surface modifying Si<sub>3</sub>N<sub>4</sub>s in one step and extend surface modification to novel additives (e.g. graphene).



# 9

# References



- [1] P.R. Roberge, Handbook of Corrosion Engineering, McGraw-Hill, 2000.
- [2] Official Journal of the European Union, Directive 2000/53/EC, 2000.
- [3] S. Kango, S. Kalia, A. Celli, J. Njuguna, Y. Habibi, R. Kumar, Surface modification of inorganic nanoparticles for development of organic–inorganic nanocomposites—A review, *Progress in Polymer Science*, 38 (2013) 1232-1261.
- [4] V. Cicek, B. Al-Numan, Corrosion Chemistry John Wiley & Sons, Inc., 2011.
- [5] P. Sudarsanam, P.R. Selvakannan, S.K. Soni, S.K. Bhargava, B.M. Reddy, Structural evaluation and catalytic performance of nano-Au supported on nanocrystalline Ce<sub>0.9</sub>Fe<sub>0.1</sub>O<sub>2</sub>-[small delta] solid solution for oxidation of carbon monoxide and benzylamine, *RSC Advances*, 4 (2014) 43460-43469.
- [6] E. Bardal, Corrosion and protection, 2004.
- [7] J.R. Davis, The Effects and Economic Impact of Corrosion., in: Corrosion: Understanding the Basics, ASM International, 2000, pp. 1-20.
- [8] V.S. Sastri, E. Ghali, M. Elboudjaini, Corrosion Prevention and Protection Practical Solutions, John Wiley & Sons Ltd, 2007.
- [9] D.L. Engelberg, 2.06 - Intergranular Corrosion A2 - Cottis, Bob, in: M. Graham, R. Lindsay, S. Lyon, T. Richardson, D. Scantlebury, H. Stott (Eds.) Shreir's Corrosion, Elsevier, Oxford, 2010, pp. 810-827.
- [10] C. Duret-Thual, 1 - Understanding corrosion: basic principles, in: Understanding Biocorrosion, Woodhead Publishing, Oxford, 2014, pp. 3-32.
- [11] A. Almubarak, W. Abuhaimed, A. Almazrouee, Corrosion Behavior of the Stressed Sensitized Austenitic Stainless Steels of High Nitrogen Content in Seawater, *International Journal of Electrochemistry*, 2013 (2013) 7.
- [12] J.R. Davis, Corrosion of Aluminum and Aluminum Alloys ASM International, 1999.
- [13] C. Luo, X. Zhou, G.E. Thompson, A.E. Hughes, Observations of intergranular corrosion in AA2024-T351: The influence of grain stored energy, *Corrosion Science*, 61 (2012) 35-44.
- [14] H.P. Hack, 2.07 - Galvanic Corrosion A2 - Cottis, Bob, in: M. Graham, R. Lindsay, S. Lyon, T. Richardson, D. Scantlebury, H. Stott (Eds.) Shreir's Corrosion, Elsevier, Oxford, 2010, pp. 828-856.
- [15] B.N. Popov, Chapter 6 - Galvanic Corrosion, in: Corrosion Engineering, Elsevier, Amsterdam, 2015, pp. 239-287.
- [16] M.J. Pryor, D.S. Keir, Galvanic Corrosion: II . Effect of pH and Dissolved Oxygen Concentration on the Aluminum-Steel Couple, *Journal of The Electrochemical Society*, 105 (1958) 629-635.
- [17] F. Bellucci, Galvanic Corrosion between Nonmetallic Composites and Metals: I Effect of Metal and of Temperature, *CORROSION*, 47 (1991) 808-819.
- [18] P.R. Roberge, Corrosion Engineering: principles and practice, The McGraw-Hill Companies, Inc, 2008.
- [19] Corrosion: Understanding the Basics, ASM International, 2000.
- [20] M.G. Alvarez, J.R. Galvele, 2.04 - Pitting Corrosion A2 - Cottis, Bob, in: M. Graham, R. Lindsay, S. Lyon, T. Richardson, D. Scantlebury, H. Stott (Eds.) Shreir's Corrosion, Elsevier, Oxford, 2010, pp. 772-800.
- [21] D.L. PIRON, E.P. KOUTSOUKOS, K. NOBE, Corrosion Behavior of Nickel and Inconel in Acidic Chloride Solutions, *CORROSION*, 25 (1969) 151-156.
- [22] M.B. Ives, Metallography of pitting corrosion, *Materials Characterization*, 28 (1992) 257-270.
- [23] N. Bensalah, Pitting Corrosion, InTech, Rijeka, 2012.

- [24] J. Bhandari, F. Khan, R. Abbassi, V. Garaniya, R. Ojeda, Modelling of pitting corrosion in marine and offshore steel structures – A technical review, *Journal of Loss Prevention in the Process Industries*, 37 (2015) 39-62.
- [25] E. Ghali, Corrosion resistance of aluminum and magnesium alloys : understanding, performance, and testing, John Wiley & Sons, Inc, New Jersey, 2010.
- [26] A.P. Boag, D.G. McCulloch, D.N. Jamieson, A.E. Hughes, L. Pedrina, C.G. Ryan, Analysis of Pitting Corrosion in Aerospace Aluminium Alloy AA2024-T3, *Microscopy and Microanalysis*, 11 (2005) 1984-1985.
- [27] K.A. Yasakau, M.L. Zheludkevich, S.V. Lamaka, M.G.S. Ferreira, Mechanism of Corrosion Inhibition of AA2024 by Rare-Earth Compounds, *The Journal of Physical Chemistry B*, 110 (2006) 5515-5528.
- [28] V. Guillaumin, G. Mankowski, Localized corrosion of 2024 T351 aluminium alloy in chloride media, *Corrosion Science*, 41 (1998) 421-438.
- [29] B.N. Popov, Chapter 7 - Pitting and Crevice Corrosion, in: *Corrosion Engineering*, Elsevier, Amsterdam, 2015, pp. 289-325.
- [30] R.G. Kelly, Crevice Corrosion, in: *Encyclopedia of Electrochemistry*, Wiley-VCH Verlag GmbH & Co. KGaA, 2007.
- [31] N. Corlett, L.E. Eiselstein, N. Budiansky, 2.03 - Crevice Corrosion A2 - Cottis, Bob, in: M. Graham, R. Lindsay, S. Lyon, T. Richardson, D. Scantlebury, H. Stott (Eds.) *Shreir's Corrosion*, Elsevier, Oxford, 2010, pp. 753-771.
- [32] Z. Szklarska-Smialowska, Pitting and Crevice Corrosion, NACE International Houston, Texas, 2005.
- [33] G.F. Hays, Now is the Time in, World Corrosion Organization World Corrosion Organization 2017.
- [34] H.H. U., The Cost of Corrosion to The United States, *Corrosion*, 6 (1950) 29-33.
- [35] C.o.C.o.C.i. Japan, Survey of Corrosion Cost in Japan, in, Japan Society of Corrosion Engineering; Japan Association of Corrosion Control
- [36] T.P. Hoar, Großbritannien, T. Department of, Industry, Report of the committee on corrosion and protection : a survey of corrosion and protection in the United Kingdom, HMSO, London, 1971.
- [37] U.S.N.B.o. Standards, L.H. Bennett, B.M.I.C. Laboratories, Economic effects of metallic corrosion in the United States: a report to the Congress, The Bureau : for sale by the Supt. of Docs., U.S. Govt. Print. Off., 1978.
- [38] G.H. Koch, M.P.H. Brongers, N.G. Thompson, Y.P. Virmani, J.H. Payer, Chapter 1 - Cost of corrosion in the United States A2 - Kutz, Myer, in: *Handbook of Environmental Degradation of Materials*, William Andrew Publishing, Norwich, NY, 2005, pp. 3-24.
- [39] J.V. G. Koch, N. Thompson, O. Moghissi, M. Gould, J. Payer, International measures of prevention, application, and economics of corrosion technologies study, in, NACE International, Houston, 2016, pp. 216.
- [40] S. Benavides, *Corrosion Control in the Aerospace Industry*, Woodhead Publishing, 2009.
- [41] R.N. Lumley, 1 - Introduction to aluminium metallurgy, in: *Fundamentals of Aluminium Metallurgy*, Woodhead Publishing, 2011, pp. 1-19.
- [42] I.J. Polmear, 1 - The light metals, in: *Light Alloys (Fourth Edition)*, Butterworth-Heinemann, Oxford, 2005, pp. 1-28.
- [43] T.I.A. Institute, world aluminium, in, 2016.
- [44] T.A. Association, Aluminum Statistical Review for 2014, in, The Aluminum Association, Arlington, VA, USA, 2015.
- [45] 8 - Aluminium alloys for aircraft structures A2 - Mouritz, Adrian P, in: *Introduction to Aerospace Materials*, Woodhead Publishing, 2012, pp. 173-201.

- [46] U. Chakkingal, 1 - Aluminium and its alloys A2 - Guo, Z. Xiao, in: *The Deformation and Processing of Structural Materials*, Woodhead Publishing, 2005, pp. 1-28.
- [47] T.A. Association, 2015 ANNUAL REPORT - The Aluminum Association, in, 2015.
- [48] J.P. Immarigeon, R.T. Holt, A.K. Koul, L. Zhao, W. Wallace, J.C. Beddoes, *Microstructural Characterization of Lightweight Structural Materials Transportation* Lightweight materials for aircraft applications, *Materials Characterization*, 35 (1995) 41-67.
- [49] E. Hughes Anthony, R. Parvizi, M. Forsyth, *Microstructure and corrosion of AA2024*, in: *Corrosion Reviews*, 2015, pp. 1.
- [50] R.G. Buchheit, R.P. Grant, P.F. Hlava, B. McKenzie, G.L. Zender, *Local Dissolution Phenomena Associated with S Phase (Al<sub>2</sub>CuMg) Particles in Aluminum Alloy 2024-T3*, *Journal of The Electrochemical Society*, 144 (1997) 2621-2628.
- [51] A. Boag, A.E. Hughes, N.C. Wilson, A. Torpy, C.M. MacRae, A.M. Glenn, T.H. Muster, *How complex is the microstructure of AA2024-T3?*, *Corrosion Science*, 51 (2009) 1565-1568.
- [52] A. Boag, A.E. Hughes, A.M. Glenn, T.H. Muster, D. McCulloch, *Corrosion of AA2024-T3 Part I: Localised corrosion of isolated IM particles*, *Corrosion Science*, 53 (2011) 17-26.
- [53] J.S. Spoerl, *A Brief History of Iron and Steel Production*, in, Saint Anselm College.
- [54] I.E. Britannica, *Britannica Student Encyclopedia-Encyclopædia Britannica*, Inc. Encyclopaedia Britannica, 2010.
- [55] w.s. association, *World steel in figures 2015*, in, 2015, pp. 30.
- [56] R.H. Harry Bhadeshia, *Steels: Microstructure and Properties*, 2006.
- [57] R. Singh, Chapter 6 - Classification of Steels, in: *Applied Welding Engineering (Second Edition)*, Butterworth-Heinemann, 2016, pp. 57-64.
- [58] A. Ltd, *SAE/AISI Carbon Steel Naming Conventions*, in, 2016.
- [59] F. Cardarelli, *Materials handbook a concise desktop reference*(BookZZ.org), 2nd ed., Springer-Verlag, London, 2008.
- [60] W.E. Bryson, 7 - Making Steel, in: *Heat Treatment*, Hanser, 2015, pp. 26-34.
- [61] S.B. Lyon, 3.01 - Corrosion of Carbon and Low Alloy Steels, in: *Shreir's Corrosion*, Elsevier, Oxford, 2010, pp. 1693-1736.
- [62] B.s.s. association, *The Discovery of Stainless Steel*, in, 2016.
- [63] R. Singh, Chapter 8 - Stainless Steels, in: *Applied Welding Engineering (Second Edition)*, Butterworth-Heinemann, 2016, pp. 83-90.
- [64] R.F. Wegman, J. Van Twisk, 4 - Steel and Stainless Steel, in: *Surface Preparation Techniques for Adhesive Bonding (Second Edition)*, William Andrew Publishing, 2013, pp. 67-82.
- [65] W.E. Bryson, 8 - Making Stainless Steel, in: *Heat Treatment*, Hanser, 2015, pp. 35-37.
- [66] A. Iversen, B. Leffler, 3.04 - Aqueous Corrosion of Stainless Steels A2 - Cottis, Bob, in: M. Graham, R. Lindsay, S. Lyon, T. Richardson, D. Scantlebury, H. Stott (Eds.) *Shreir's Corrosion*, Elsevier, Oxford, 2010, pp. 1802-1878.
- [67] H.S.K.B. Raj, *Corrosion of autenitic stainless steels: mechanism, mitigation and monitoring*, Woodhead Publishing limited, Cambridge England, 2002.
- [68] S.M.A. Shibli, B.N. Meena, R. Remya, *A review on recent approaches in the field of hot dip zinc galvanizing process*, *Surface and Coatings Technology*, 262 (2015) 210-215.
- [69] A.R. Marder, *The metallurgy of zinc-coated steel*, *Progress in Materials Science*, 45 (2000) 191-271.

- [70] V. Kuklík, J. Kudláček, 2 - Hot-dip galvanizing, in: *Hot-Dip Galvanizing of Steel Structures*, Butterworth-Heinemann, Boston, 2016, pp. 7-16.
- [71] C.E. JORDAN, A.R. MARDER, Fe-Zn phase formation in interstitial-free steels hot-dip galvanized at 450°C: Part II 0.20 wt% Al-Zn baths, *Journal of Materials Science*, 32 (1997) 5603-5610.
- [72] I.Z. Association, Galvanneal – Differences from Galvanize in.
- [73] C.E. Jordan, A.R. Marder, Morphology development in hot-dip galvanneal coatings, *Metallurgical Transactions, A (Physical Metallurgy and Materials Science)*; (United States), (1994) Medium: X; Size: Pages: 937-948.
- [74] Chapter 6 - Corrosion inhibitors, in: J. Fink (Ed.) *Petroleum Engineer's Guide to Oil Field Chemicals and Fluids (Second Edition)*, Gulf Professional Publishing, Boston, 2015, pp. 215-254.
- [75] R.J.K. Wood, 6.09 - Erosion/Corrosion, in: I.M.O.R. Karihaloo (Ed.) *Comprehensive Structural Integrity*, Pergamon, Oxford, 2007, pp. 395-427.
- [76] K.A. Yasakau, M.L. Zheludkevich, O.V. Karavai, M.G.S. Ferreira, Influence of inhibitor addition on the corrosion protection performance of sol-gel coatings on AA2024, *Progress in Organic Coatings*, 63 (2008) 352-361.
- [77] A.G.H.-J. Streitberger, *Basics of Coating Technology*, 2<sup>a</sup> ed., Vincentz Network, 2007.
- [78] N.B.D.T.S. Sudarshan, *Intermetallic and Ceramic Coatings*, Marcel Dekker, Inc., New York, 1999.
- [79] S. Ebnesajjad, Chapter 6 - Material Surface Preparation Techniques, in: *Surface Treatment of Materials for Adhesive Bonding (Second Edition)*, William Andrew Publishing, Oxford, 2014, pp. 95-138.
- [80] S. Ebnesajjad, Chapter 1 - Introduction to Surface Preparation, in: *Surface Treatment of Materials for Adhesive Bonding (Second Edition)*, William Andrew Publishing, Oxford, 2014, pp. 3-6.
- [81] S. Ebnesajjad, *Handbook of Adhesives and Surface Preparation: Technology, Applications and Manufacturing*, William Andrew, 2010.
- [82] S.S. Golru, M.M. Attar, B. Ramezanzadeh, Effects of different surface cleaning procedures on the superficial morphology and the adhesive strength of epoxy coating on aluminium alloy 1050, *Progress in Organic Coatings*, 87 (2015) 52-60.
- [83] W. Pinc, S. Geng, M. O'Keefe, W. Fahrenholtz, T. O'Keefe, Effects of acid and alkaline based surface preparations on spray deposited cerium based conversion coatings on Al 2024-T3, *Applied Surface Science*, 255 (2009) 4061-4065.
- [84] S.K. E. Matter, Correlation between preliminary pretreatments and the behaviour of AA2024 aluminium alloy in 3.5% NaCl model corrosive medium, *Annu Proc. "Angel Kanchev" Univ. Ruse*, 49 (2010) 14-19.
- [85] R.F. Wegman, J. Van Twisk, 2 - Aluminum and Aluminum Alloys, in: *Surface Preparation Techniques for Adhesive Bonding (Second Edition)*, William Andrew Publishing, 2013, pp. 9-37.
- [86] S. Ebnesajjad, Chapter 7 - Surface Preparation of Metals, in: *Surface Treatment of Materials for Adhesive Bonding (Second Edition)*, William Andrew Publishing, Oxford, 2014, pp. 139-183.
- [87] A. Ghicov, P. Schmuki, Self-ordering electrochemistry: a review on growth and functionality of TiO<sub>2</sub>nanotubes and other self-aligned MO<sub>x</sub> structures, *Chemical Communications*, (2009) 2791-2808.
- [88] B. Arkles, *Commercial Applications of Sol-Gel-Derived Hybrid Materials*, *MRS Bulletin*, 26 (2001) 402-408.

- [89] K. Yasakau, Active corrosion protection of AA2024 by sol-gel coatings with corrosion inhibitors, in: Departamento de Engenharia de Materiais e Cerâmica, University of Aveiro, Aveiro, 2011, pp. 332.
- [90] P. Judeinstein, C. Sanchez, Hybrid organic-inorganic materials: a land of multidisciplinary, *Journal of Materials Chemistry*, 6 (1996) 511-525.
- [91] M.L. Zheludkevich, K.A. Yasakau, S.K. Poznyak, M.G.S. Ferreira, Triazole and thiazole derivatives as corrosion inhibitors for AA2024 aluminium alloy, *Corrosion Science*, 47 (2005) 3368-3383.
- [92] M.L. Zheludkevich, R. Serra, M.F. Montemor, K.A. Yasakau, I.M.M. Salvado, M.G.S. Ferreira, Nanostructured sol-gel coatings doped with cerium nitrate as pre-treatments for AA2024-T3: Corrosion protection performance, *Electrochimica Acta*, 51 (2005) 208-217.
- [93] K.A. Yasakau, J. Carneiro, M.L. Zheludkevich, M.G.S. Ferreira, Influence of the Sol-Gel Processing on the Protection Properties of the Coatings using Electrochemical Impedance Spectroscopy, *Surface and Coatings Technology*, (2014).
- [94] J. Carneiro, A.F. Caetano, A. Kuznetsova, F. Maia, A.N. Salak, J. Tedim, N. Scharnagl, M.L. Zheludkevich, M.G.S. Ferreira, Polyelectrolyte-modified layered double hydroxide nanocontainers as vehicles for combined inhibitors, *RSC Advances*, 5 (2015) 39916-39929.
- [95] J. Carneiro, J. Tedim, S.C.M. Fernandes, C.S.R. Freire, A.J.D. Silvestre, A. Gandini, M.G.S. Ferreira, M.L. Zheludkevich, Chitosan-based self-healing protective coatings doped with cerium nitrate for corrosion protection of aluminum alloy 2024, *Progress in Organic Coatings*, 75 (2012) 8-13.
- [96] J. Tedim, S.K. Poznyak, A. Kuznetsova, D. Raps, T. Hack, M.L. Zheludkevich, M.G.S. Ferreira, Enhancement of Active Corrosion Protection via Combination of Inhibitor-Loaded Nanocontainers, *Acs Applied Materials & Interfaces*, 2 (2010) 1528-1535.
- [97] M.L. Zheludkevich, S.K. Poznyak, L.M. Rodrigues, D. Raps, T. Hack, L.F. Dick, T. Nunes, M.G.S. Ferreira, Active protection coatings with layered double hydroxide nanocontainers of corrosion inhibitor, *Corrosion Science*, 52 (2010) 602-611.
- [98] W. Zhang, G.S. Frankel, Transitions between pitting and intergranular corrosion in AA2024, *Electrochimica Acta*, 48 (2003) 1193-1210.
- [99] M.B. Bethencourt, F. J.; Calvino, J. J.; Marcos, M.; Rodriguez-Chacon, M. A., Lanthanide compounds as environmentally-friendly corrosion inhibitors of aluminium alloys: A review, *Corrosion Science*, 40 (1998) 1803-1819.
- [100] D. Snihirova, L. Liphardt, G. Grundmeier, F. Montemor, Electrochemical study of the corrosion inhibition ability of "smart" coatings applied on AA2024, *J. Solid State Electrochem.*, 17 (2013) 2183-2192.
- [101] O. Lopez-Garrity, G.S. Frankel, Synergistic Corrosion Inhibition of AA2024-T3 by Sodium Silicate and Sodium Molybdate, *Ecs Electrochemistry Letters*, 3 (2014) C33-C35.
- [102] M. Iannuzzi, G.S. Frankel, Mechanisms of corrosion inhibition of AA2024-T3 by vanadates, *Corrosion Science*, 49 (2007) 2371-2391.
- [103] S.A.S. Dias, A. Marques, S.V. Lamaka, A. Simões, T.C. Diamantino, M.G.S. Ferreira, The role of Ce(III)-enriched zeolites on the corrosion protection of AA2024-T3, *Electrochimica Acta*, 112 (2013) 549-556.
- [104] G.M. Liu, L. Yang, N. Du, Study of molybdate-phytic acid passivation on galvanised steel, *Corrosion Engineering Science and Technology*, 46 (2011) 542-546.
- [105] I.M. Zin, S.B. Lyon, V.I. Pokhmurskii, Corrosion control of galvanized steel using a phosphate/calcium ion inhibitor mixture, *Corrosion Science*, 45 (2003) 777-788.

- [106] T.K. Rout, N. Bandyopadhyay, Effect of molybdate coating for white rusting resistance on galvanized steel, *Anti-Corrosion Methods and Materials*, 54 (2007) 16-20.
- [107] I. Fayala, L. Dhouibi, X.R. Nóvoa, M. Ben Ouezdou, Effect of inhibitors on the corrosion of galvanized steel and on mortar properties, *Cement and Concrete Composites*, 35 (2013) 181-189.
- [108] G. Kong, J. Lu, H. Wu, Post treatment of silane and cerium salt as chromate replacers on galvanized steel, *Journal of Rare Earths*, 27 (2009) 164-168.
- [109] M.F. Montemor, A.M. Simões, M.G.S. Ferreira, Composition and corrosion behaviour of galvanised steel treated with rare-earth salts: the effect of the cation, *Progress in Organic Coatings*, 44 (2002) 111-120.
- [110] T. Peng, R. Man, Rare earth and silane as chromate replacers for corrosion protection on galvanized steel, *Journal of Rare Earths*, 27 (2009) 159-163.
- [111] S. Roselli, N. Bellotti, C. Deyá, M. Revuelta, B. del Amo, R. Romagnoli, Lanthanum-exchanged zeolite and clay as anticorrosive pigments for galvanized steel, *Journal of Rare Earths*, 32 (2014) 352-359.
- [112] F. Deflorian, M. Fedel, S. Rossi, P. Kamarchik, Evaluation of mechanically treated cerium (IV) oxides as corrosion inhibitors for galvanized steel, *Electrochimica Acta*, 56 (2011) 7833-7844.
- [113] M.N.M.I. Ebrahim Akbarzadeh, Afidah Abdul Rahim, Corrosion Inhibition of Mild Steel in Near Neutral Solution by Kraft and Soda Lignins Extracted from Oil Palm Empty Fruit Bunch, *Int. J. Electrochem. Sci.*, 6 (2011) 5396-5416.
- [114] A. Dutta, S.K. Saha, P. Banerjee, D. Sukul, Correlating electronic structure with corrosion inhibition potentiality of some bis-benzimidazole derivatives for mild steel in hydrochloric acid: Combined experimental and theoretical studies, *Corrosion Science*, 98 (2015) 541-550.
- [115] M. Chigondo, F. Chigondo, Recent Natural Corrosion Inhibitors for Mild Steel: An Overview, *Journal of Chemistry*, 2016 (2016) 7.
- [116] M. Finšgar, J. Jackson, Application of corrosion inhibitors for steels in acidic media for the oil and gas industry: A review, *Corrosion Science*, 86 (2014) 17-41.
- [117] F. Zucchi, I.H. Omar, Plant extracts as corrosion inhibitors of mild steel in HCl solutions, *Surface Technology*, 24 (1985) 391-399.
- [118] M.S. Al-Otaibi, A.M. Al-Mayouf, M. Khan, A.A. Mousa, S.A. Al-Mazroa, H.Z. Alkhatlan, Corrosion inhibitory action of some plant extracts on the corrosion of mild steel in acidic media, *Arabian Journal of Chemistry*, 7 (2014) 340-346.
- [119] L.R. Chauhan, G. Gunasekaran, Corrosion inhibition of mild steel by plant extract in dilute HCl medium, *Corrosion Science*, 49 (2007) 1143-1161.
- [120] N.P. Andreeva, L.P. Kazanskii, I.A. Selyaninov, Y.I. Kuznetsov, V.A. Ostrovskii, Adsorption of 5-phenyltetrazole on iron and its inhibition of the dissolution of low-carbon steel in a neutral solution, *Protection of Metals and Physical Chemistry of Surfaces*, 45 (2009) 806-811.
- [121] Y.L. Zhu, X.P. Guo, Y.B. Qiu, Inhibition mechanism of sodium laurate to underdeposit corrosion of carbon steels in NaCl solutions, *Corrosion Engineering, Science and Technology*, 45 (2010) 442-448.
- [122] S.A.M. Refaey, Inhibition of chloride pitting corrosion of mild steel by sodium gluconate, *Applied Surface Science*, 157 (2000) 199-206.
- [123] R. Touir, M. Cenoui, M. El Bakri, M. Ebn Touhami, Sodium gluconate as corrosion and scale inhibitor of ordinary steel in simulated cooling water, *Corrosion Science*, 50 (2008) 1530-1537.
- [124] B. Elsener, U. Angst, 14 - Corrosion inhibitors for reinforced concrete, in: *Science and Technology of Concrete Admixtures*, Woodhead Publishing, 2016, pp. 321-339.

- [125] T.A. Söylev, M.G. Richardson, Corrosion inhibitors for steel in concrete: State-of-the-art report, *Construction and Building Materials*, 22 (2008) 609-622.
- [126] B. Elsener, E.F.o. Corrosion, I.o. Materials, Corrosion Inhibitors for Steel in Concrete: State of the Art Report, European Federation of Corrosion, 2001.
- [127] C. Alonso, C. Andrade, C. Argiz, B. Malric, Na<sub>2</sub>PO<sub>3</sub>F as inhibitor of corroding reinforcement in carbonated concrete, *Cement and Concrete Research*, 26 (1996) 405-415.
- [128] S.E.R.H.J.J.B.R.B. Ping Gu, B. Baldock, A Study of Corrosion Inhibitor Performance in Chloride Contaminated Concrete by Electrochemical Impedance Spectroscopy, *Materials Journal*, 94.
- [129] F. Delaunois, F. Tosar, V. Vitry, Corrosion behaviour and biocorrosion of galvanized steel water distribution systems, *Bioelectrochemistry*, 97 (2014) 110-119.
- [130] C.A. Della Rovere, R. Silva, C. Moretti, S.E. Kuri, Corrosion failure analysis of galvanized steel pipes in a water irrigation system, *Engineering Failure Analysis*, 33 (2013) 381-386.
- [131] L.L. Hench, J.K. West, The sol-gel process, *Chemical Reviews*, 90 (1990) 33-72.
- [132] C.J.B.G.W. Scherer, Sol-gel science: The physics and chemistry of sol-gel processing, Academic Press, Inc., San Diego, 1990.
- [133] H. Schroeder, Oxide layers deposited from organic solutions, in: R.E.T. Georg Hass (Ed.) *Physics of Thin Films*, Academic Press, 1969, pp. 87-141.
- [134] R. Ciriminna, A. Fidalgo, V. Pandarus, F. Béland, L.M. Ilharco, M. Pagliaro, The Sol-Gel Route to Advanced Silica-Based Materials and Recent Applications, *Chemical Reviews*, 113 (2013) 6592-6620.
- [135] Aqueous and Nonaqueous Sol-Gel Chemistry, in: *Metal Oxide Nanoparticles in Organic Solvents: Synthesis, Formation, Assembly and Application*, Springer London, London, 2009, pp. 7-18.
- [136] J. Livage, M. Henry, C. Sanchez, Sol-gel chemistry of transition metal oxides, *Progress in Solid State Chemistry*, 18 (1988) 259-341.
- [137] J.-P. Jolivet, *Metal oxide chemistry and synthesis*, John Wiley & Sons Ltd., Chichester, England, 2000.
- [138] M. Guglielmi, Sol-gel coatings on metals, *Journal of Sol-Gel Science and Technology*, 8 (1997) 443-449.
- [139] E. Kiele, J. Senvaitiene, A. Griguceviene, R. Ramanauskas, R. Raudonis, A. Kareiva, Application of Sol-gel Method for the Conservation of Copper Alloys, *Microchemical Journal*.
- [140] A.F. Galio, S.V. Lamaka, M.L. Zheludkevich, L.F.P. Dick, I.L. Müller, M.G.S. Ferreira, Inhibitor-doped sol-gel coatings for corrosion protection of magnesium alloy AZ31, *Surface and Coatings Technology*, 204 (2010) 1479-1486.
- [141] R.-G. Hu, S. Zhang, J.-F. Bu, C.-J. Lin, G.-L. Song, Recent progress in corrosion protection of magnesium alloys by organic coatings, *Progress in Organic Coatings*, 73 (2012) 129-141.
- [142] M. Criado, I. Sobrados, J.M. Bastidas, J. Sanz, Steel corrosion in simulated carbonated concrete pore solution its protection using sol-gel coatings, *Progress in Organic Coatings*, 88 (2015) 228-236.
- [143] R.B. Figueira, C.J.R. Silva, E.V. Pereira, Hybrid sol-gel coatings for corrosion protection of hot-dip galvanized steel in alkaline medium, *Surface and Coatings Technology*, 265 (2015) 191-204.
- [144] S. Bera, T.K. Rout, G. Udayabhanu, R. Narayan, Comparative Study of Corrosion Protection of Sol-Gel Coatings with Different Organic Functionality on Al-2024 substrate, *Progress in Organic Coatings*, 88 (2015) 293-303.

- [145] K.A. Yasakau, J. Carneiro, M.L. Zheludkevich, M.G.S. Ferreira, Influence of sol-gel process parameters on the protection properties of sol-gel coatings applied on AA2024, *Surface and Coatings Technology*, 246 (2014) 6-16.
- [146] N.N. Voevodin, V.N. Balbyshev, M.S. Donley, Investigation of corrosion protection performance of sol-gel coatings on AA2024-T3, *Progress in Organic Coatings*, 52 (2005) 28-33.
- [147] Z. Feng, Y. Liu, G.E. Thompson, P. Skeldon, Sol-gel coatings for corrosion protection of 1050 aluminium alloy, *Electrochimica Acta*, 55 (2010) 3518-3527.
- [148] A.N. Khramov, N.N. Voevodin, V.N. Balbyshev, R.A. Mantz, Sol-gel-derived corrosion-protective coatings with controllable release of incorporated organic corrosion inhibitors, *Thin Solid Films*, 483 (2005) 191-196.
- [149] D. Wang, G.P. Bierwagen, Sol-gel coatings on metals for corrosion protection, *Progress in Organic Coatings*, 64 (2009) 327-338.
- [150] D.G. Shchukin, D.O. Grigoriev, 10 - The use of nanoreservoirs in corrosion protection coatings, in: *Corrosion Protection and Control Using Nanomaterials*, Woodhead Publishing, 2012, pp. 264-282.
- [151] M.F. Montemor, Functional and smart coatings for corrosion protection: A review of recent advances, *Surface and Coatings Technology*, 258 (2014) 17-37.
- [152] D. Li, F. Wang, X. Yu, J. Wang, Q. Liu, P. Yang, Y. He, Y. Wang, M. Zhang, Anticorrosion organic coating with layered double hydroxide loaded with corrosion inhibitor of tungstate, *Progress in Organic Coatings*, 71 (2011) 302-309.
- [153] T.T.X. Hang, T.A. Truc, N.T. Duong, N. Pébère, M.-G. Olivier, Layered double hydroxides as containers of inhibitors in organic coatings for corrosion protection of carbon steel, *Progress in Organic Coatings*, 74 (2012) 343-348.
- [154] J. Tedim, A. Kuznetsova, A.N. Salak, F. Montemor, D. Snihirova, M. Pilz, M.L. Zheludkevich, M.G.S. Ferreira, Zn-Al layered double hydroxides as chloride nanotraps in active protective coatings, *Corrosion Science*, 55 (2012) 1-4.
- [155] S.P.V. Mahajanarn, R.G. Buchheit, Characterization of inhibitor release from Zn-Al- V10O28 (6-) hydrotalcite pigments and corrosion protection from hydrotalcite-pigmented epoxy coatings, *Corrosion*, 64 (2008) 230-240.
- [156] M.L. Zheludkevich, D.G. Shchukin, K.A. Yasakau, H. Möhwald, M.G.S. Ferreira, Anticorrosion Coatings with Self-Healing Effect Based on Nanocontainers Impregnated with Corrosion Inhibitor, *Chemistry of Materials*, 19 (2007) 402-411.
- [157] D. Raps, T. Hack, M. Kolb, M.L. Zheludkevich, O. Nuyken, Development of Corrosion Protection Coatings for AA2024-T3 Using Micro-Encapsulated Inhibitors, in: J. Baghdachi, T. Provder (Eds.) *Smart Coatings Iii*, 2010, pp. 165-189.
- [158] D. Borisova, H. Moehwald, D.G. Shchukin, Mesoporous Silica Nanoparticles for Active Corrosion Protection, *Acs Nano*, 5 (2011) 1939-1946.
- [159] D. Borisova, H. Moehwald, D.G. Shchukin, Influence of Embedded Nanocontainers on the Efficiency of Active Anticorrosive Coatings for Aluminum Alloys Part I: Influence of Nanocontainer Concentration, *Acs Applied Materials & Interfaces*, 4 (2012) 2931-2939.
- [160] F. Maia, J. Tedim, A.D. Lisenkov, A.N. Salak, M.L. Zheludkevich, M.G.S. Ferreira, Silica nanocontainers for active corrosion protection, *Nanoscale*, 4 (2012) 1287-1298.
- [161] N. Wang, K. Cheng, H. Wu, C. Wang, Q. Wang, F. Wang, Effect of nano-sized mesoporous silica MCM-41 and MMT on corrosion properties of epoxy coating, *Progress in Organic Coatings*, 75 (2012) 386-391.

- [162] A. Joshi, E. Abdullayev, A. Vasiliev, O. Volkova, Y. Lvov, Interfacial Modification of Clay Nanotubes for the Sustained Release of Corrosion Inhibitors, *Langmuir*, 29 (2013) 7439-7448.
- [163] Y.M. Lvov, D.G. Shchukin, H. Möhwald, R.R. Price, Halloysite Clay Nanotubes for Controlled Release of Protective Agents, *ACS Nano*, 2 (2008) 814-820.
- [164] S.P. Newman, W. Jones, Synthesis, characterization and applications of layered double hydroxides containing organic guests, *New J. Chem.*, 22 (1998) 105-115.
- [165] C. Forano, U. Costantino, V. Prévot, C.T. Gueho, Chapter 14.1 - Layered Double Hydroxides (LDH), in: B. Faïza, L. Gerhard (Eds.) *Developments in Clay Science*, Elsevier, 2013, pp. 745-782.
- [166] A.M. Scheidegger, G.M. Lamble, D.L. Sparks, Spectroscopic Evidence for the Formation of Mixed-Cation Hydroxide Phases upon Metal Sorption on Clays and Aluminum Oxides, *Journal of Colloid and Interface Science*, 186 (1997) 118-128.
- [167] I.C. Regelink, E.J.M. Temminghoff, Ni adsorption and Ni-Al LDH precipitation in a sandy aquifer: An experimental and mechanistic modeling study, *Environmental Pollution*, 159 (2011) 716-721.
- [168] S.K. Poznyak, J. Tedim, L.M. Rodrigues, A.N. Salak, M.L. Zheludkevich, L.F.P. Dick, M.G.S. Ferreira, Novel Inorganic Host Layered Double Hydroxides Intercalated with Guest Organic Inhibitors for Anticorrosion Applications, *ACS Applied Materials & Interfaces*, 1 (2009) 2353-2362.
- [169] T. Lopez, P. Bosch, E. Ramos, R. Gomez, O. Novaro, D. Acosta, F. Figueras, Synthesis and characterization of sol-gel hydrotalcites. Structure and texture, *Langmuir*, 12 (1996) 189-192.
- [170] P. Benito, F.M. Labajos, J. Rocha, V. Rives, Influence of microwave radiation on the textural properties of layered double hydroxides, *Microporous and Mesoporous Materials*, 94 (2006) 148-158.
- [171] J.A. Rivera, G. Fetter, P. Bosch, Microwave power effect on hydrotalcite synthesis, *Microporous and Mesoporous Materials*, 89 (2006) 306-314.
- [172] T.T.X. Hang, T.A. Truc, N.T. Duong, P.G. Vu, T. Hoang, Preparation and characterization of nanocontainers of corrosion inhibitor based on layered double hydroxides, *Applied Clay Science*, 67-68 (2012) 18-25.
- [173] R.B. Leggat, W. Zhang, R.G. Buchheit, S.R. Taylor, Performance of hydrotalcite conversion treatments on AA2024-T3 when used in a coating system, *Corrosion*, 58 (2002) 322-328.
- [174] W. Zhang, R.G. Buchheit, Hydrotalcite coating formation on Al-Cu-Mg alloys from oxidizing bath chemistries, *Corrosion*, 58 (2002) 591-600.
- [175] R.G. Buchheit, S.B. Mamidipally, P. Schmutz, H. Guan, Active corrosion protection in Ce-modified hydrotalcite conversion coatings, *Corrosion*, 58 (2002) 3-14.
- [176] F. Zhang, L. Zhao, H. Chen, S. Xu, D.G. Evans, X. Duan, Corrosion Resistance of Superhydrophobic Layered Double Hydroxide Films on Aluminum, *Angew. Chem. Int. Ed.*, 47 (2008) 2466-2469.
- [177] J.-Y. Uan, J.-K. Lin, Y.-S. Tung, Direct growth of oriented Mg-Al layered double hydroxide film on Mg alloy in aqueous  $\text{HCO}_3^-/\text{CO}_3^{2-}$  solution, *J. Mater. Chem.*, 20 (2010) 761-766.
- [178] J. Tedim, M.L. Zheludkevich, A.N. Salak, A. Lisenkov, M.G.S. Ferreira, Nanostructured LDH-container layer with active protection functionality, *J. Mater. Chem.*, 21 (2011) 15464-15470.
- [179] J. Tedim, M.L. Zheludkevich, A.C. Bastos, A.N. Salak, A.D. Lisenkov, M.G.S. Ferreira, Influence of preparation conditions of Layered Double Hydroxide conversion films on corrosion protection, *Electrochim. Acta*, 117 (2014) 164-171.

- [180] W.F. Stober, A. Bohn, E., Controlled Growth of Monodisperse Silica Spheres in Micron Size Range, *Journal of Colloid and Interface Science*, 26 (1968) 62-&.
- [181] S. Schacht, Q. Huo, I.G. Voigt-Martin, G.D. Stucky, F. Schüth, Oil-Water Interface Templating of Mesoporous Macroscale Structures, *Science*, 273 (1996) 768-771.
- [182] I.I. Slowing, J.L. Vivero-Escoto, C.-W. Wu, V.S.Y. Lin, Mesoporous silica nanoparticles as controlled release drug delivery and gene transfection carriers, *Advanced Drug Delivery Reviews*, 60 (2008) 1278-1288.
- [183] F. Tang, L. Li, D. Chen, Mesoporous Silica Nanoparticles: Synthesis, Biocompatibility and Drug Delivery, *Advanced Materials*, 24 (2012) 1504-1534.
- [184] D. Borisova, H. Möhwald, D.G. Shchukin, Influence of Embedded Nanocontainers on the Efficiency of Active Anticorrosive Coatings for Aluminum Alloys Part II: Influence of Nanocontainer Position, *Acs Applied Materials & Interfaces*, 5 (2013) 80-87.
- [185] C.T. Kresge, M.E. Leonowicz, W.J. Roth, J.C. Vartuli, J.S. Beck, Ordered mesoporous molecular sieves synthesized by a liquid-crystal template mechanism, *Nature*, 359 (1992) 710-712.
- [186] J.S. Beck, J.C. Vartuli, W.J. Roth, M.E. Leonowicz, C.T. Kresge, K.D. Schmitt, C.T.W. Chu, D.H. Olson, E.W. Sheppard, S.B. McCullen, J.B. Higgins, J.L. Schlenker, A new family of mesoporous molecular sieves prepared with liquid crystal templates, *Journal of the American Chemical Society*, 114 (1992) 10834-10843.
- [187] R. Schiller, C.K. Weiss, J. Geserick, N. Hüsing, K. Landfester, Synthesis of Mesoporous Silica Particles and Capsules by Miniemulsion Technique, *Chemistry of Materials*, 21 (2009) 5088-5098.
- [188] T. Siva, S. Mayavan, S.S. Sreejakumari, S. Sathiyarayanan, Mesoporous silica based reservoir for the active protection of mild steel in an aggressive chloride ion environment, *RSC Advances*, 5 (2015) 39278-39284.
- [189] M. Saremi, M. Yeganeh, Application of mesoporous silica nanocontainers as smart host of corrosion inhibitor in polypyrrole coatings, *Corrosion Science*, 86 (2014) 159-170.
- [190] M. Yeganeh, M. Saremi, H. Rezaeyan, Corrosion inhibition of steel using mesoporous silica nanocontainers incorporated in the polypyrrole, *Progress in Organic Coatings*, 77 (2014) 1428-1435.
- [191] A. Chenan, S. Ramya, R.P. George, U.K. Mudali, 2-Mercaptobenzothiazole-Loaded Hollow Mesoporous Silica-Based Hybrid Coatings for Corrosion Protection of Modified 9Cr-1Mo Ferritic Steel, *Corrosion*, 70 (2014) 496-511.
- [192] D.G. Shchukin, S.V. Lamaka, K.A. Yasakau, M.L. Zheludkevich, M.G.S. Ferreira, H. Möhwald, Active Anticorrosion Coatings with Halloysite Nanocontainers, *The Journal of Physical Chemistry C*, 112 (2008) 958-964.
- [193] B. Singh, R.J. Gilkes, An electron-optical investigation of the alteration of kaolinite to halloysite, *Clays and Clay Minerals*, 40 (1992) 212-229.
- [194] S.R. Levis, P.B. Deasy, Characterisation of halloysite for use as a microtubular drug delivery system, *International Journal of Pharmaceutics*, 243 (2002) 125-134.
- [195] D.G. Shchukin, H. Möhwald, Surface-Engineered Nanocontainers for Entrapment of Corrosion Inhibitors, *Advanced Functional Materials*, 17 (2007) 1451-1458.
- [196] E. Abdullayev, R. Price, D. Shchukin, Y. Lvov, Halloysite Tubes as Nanocontainers for Anticorrosion Coating with Benzotriazole, *ACS Appl. Mater. Interfaces*, 1 (2009) 1437-1443.
- [197] A.P. Esser-Kahn, S.A. Odom, N.R. Sottos, S.R. White, J.S. Moore, Triggered Release from Polymer Capsules, *Macromolecules*, 44 (2011) 5539-5553.

- [198] S. Hyuk Im, U. Jeong, Y. Xia, Polymer hollow particles with controllable holes in their surfaces, *Nat Mater*, 4 (2005) 671-675.
- [199] F. Maia, K.A. Yasakau, J. Carneiro, S. Kallip, J. Tedim, T. Henriques, A. Cabral, J. Venâncio, M.L. Zheludkevich, M.G.S. Ferreira, Corrosion protection of AA2024 by sol-gel coatings modified with MBT-loaded polyurea microcapsules, *Chemical Engineering Journal*, 283 (2016) 1108-1117.
- [200] D. Snihirova, S.V. Lamaka, M.M. Cardoso, J.A.D. Condeço, H.E.C.S. Ferreira, M. de Fatima Montemor, pH-sensitive polymeric particles with increased inhibitor-loading capacity as smart additives for corrosion protective coatings for AA2024, *Electrochimica Acta*, 145 (2014) 123-131.
- [201] A.K. Gupta, M. Gupta, Synthesis and surface engineering of iron oxide nanoparticles for biomedical applications, *Biomaterials*, 26 (2005) 3995-4021.
- [202] J. Conde, G. Doria, P. Baptista, Noble Metal Nanoparticles Applications in Cancer, *Journal of Drug Delivery*, 2012 (2012) 12.
- [203] Z. Ma, H. Liu, Synthesis and surface modification of magnetic particles for application in biotechnology and biomedicine, *China Particuology*, 5 (2007) 1-10.
- [204] J. Shen, Z. Song, X. Qian, W. Liu, Modification of papermaking grade fillers: a brief review, *Bioresources*, 4 (2009) 1190-1209.
- [205] Z. Ma, J. Wang, X. Zhang, Effect of silane KH-550 to polypropylene/brucite composite, *Journal of Applied Polymer Science*, 107 (2008) 1000-1005.
- [206] P. Rostamzadeh, S.M. Mirabedini, M. Esfandeh, APS-silane modification of silica nanoparticles: effect of treatment's variables on the grafting content and colloidal stability of the nanoparticles, *Journal of Coatings Technology and Research*, 11 (2014) 651-660.
- [207] L. Wang, J. Sheng, Preparation and properties of polypropylene/org-attapulgitic nanocomposites, *Polymer*, 46 (2005) 6243-6249.
- [208] J.V. Koleske, *Paint and coating testing manual*, 15 ed., 2012.
- [209] J.C. Williams, T. Allen, *Handbook of Powder Technology*, *Handbook of Powder Technology*, 7 (1988) ii.
- [210] B.E. Rabinow, Nanosuspensions in drug delivery, *Nat Rev Drug Discov*, 3 (2004) 785-796.
- [211] G. Trefalt, M. Borkovec, Overview of DLVO theory, *Laboratory of Colloid and Surface Chemistry*, University of Geneva, (2014).
- [212] B. Derjaguin, L. Landau, Theory of the stability of strongly charged lyophobic sols and of the adhesion of strongly charged particles in solutions of electrolytes, *Progress in Surface Science*, 43 (1993) 30-59.
- [213] E.J.W. Verwey, Theory of the Stability of Lyophobic Colloids, *The Journal of Physical and Colloid Chemistry*, 51 (1947) 631-636.
- [214] M. Elimelech, J. Gregory, X. Jia, R.A. Williams, CHAPTER 3 - Surface interaction potentials, in: *Particle Deposition and Aggregation*, Butterworth-Heinemann, 1995, pp. 33-67.
- [215] Y. Chen, A. Lin, F. Gan, Improvement of polyacrylate coating by filling modified nano-TiO<sub>2</sub>, *Applied Surface Science*, 252 (2006) 8635-8640.
- [216] M. Ganjaee Sari, B. Ramezanzadeh, M. Shahbazi, A.S. Pakdel, Influence of nanoclay particles modification by polyester-amide hyperbranched polymer on the corrosion protective performance of the epoxy nanocomposite, *Corrosion Science*, 92 (2015) 162-172.
- [217] T.H. Yun, J.H. Park, J.-S. Kim, J.M. Park, Effect of the surface modification of zinc powders with organosilanes on the corrosion resistance of a zinc pigmented organic coating, *Progress in Organic Coatings*, 77 (2014) 1780-1788.

- [218] M. Plawecka, D. Snihirova, B. Martins, K.Szczepanowicz, P. Warszynski, M.F. Montemor, Self healing ability of inhibitor-containing nanocapsules loaded in epoxy coatings applied on aluminium 5083 and galvanized substrates, *Electrochimica Acta*, 140 (2014) 282-293.
- [219] C. Déjugnat, G.B. Sukhorukov, pH-Responsive Properties of Hollow Polyelectrolyte Microcapsules Templated on Various Cores, *Langmuir*, 20 (2004) 7265-7269.
- [220] K.B. Blodgett, Monomolecular films of fatty acids on glass, *Journal of the American Chemical Society*, 56 (1934) 495-495.
- [221] G. Decher, Fuzzy Nanoassemblies: Toward Layered Polymeric Multicomposites, *Science*, 277 (1997) 1232-1237.
- [222] D. Grigoriev, E. Shchukina, D.G. Shchukin, Nanocontainers for Self-Healing Coatings, *Advanced Materials Interfaces*, (2016) n/a-n/a.
- [223] K. Szczepanowicz, D. Dronka-Góra, G. Para, P. Warszyński, Encapsulation of liquid cores by layer-by-layer adsorption of polyelectrolytes, *Journal of Microencapsulation*, 27 (2010) 198-204.
- [224] M. Delcea, H. Möhwald, A.G. Skirtach, Stimuli-responsive LbL capsules and nanoshells for drug delivery, *Advanced Drug Delivery Reviews*, 63 (2011) 730-747.
- [225] H. Kamiya, M. Iijima, Surface modification and characterization for dispersion stability of inorganic nanometer-scaled particles in liquid media, *Science and Technology of Advanced Materials*, 11 (2010) 044304.
- [226] E.J.W.O. Verwey, J.Th.G. Theory of the Stability of Lyophobic Colloids Elsevier, New York, 1947.
- [227] L. Palmqvist, K. Holmberg, Dispersant Adsorption and Viscoelasticity of Alumina Suspensions Measured by Quartz Crystal Microbalance with Dissipation Monitoring and in Situ Dynamic Rheology, *Langmuir*, 24 (2008) 9989-9996.
- [228] K. Sato, S. Kondo, M. Tsukada, T. Ishigaki, H. Kamiya, Influence of Solid Fraction on the Optimum Molecular Weight of Polymer Dispersants in Aqueous TiO<sub>2</sub> Nanoparticle Suspensions, *Journal of the American Ceramic Society*, 90 (2007) 3401-3406.
- [229] S.-C. Liufu, H.-N. Xiao, Y.-P. Li, Adsorption of cationic polyelectrolyte at the solid/liquid interface and dispersion of nanosized silica in water, *Journal of Colloid and Interface Science*, 285 (2005) 33-40.
- [230] F. Tang, T. Uchikoshi, K. Ozawa, Y. Sakka, Effect of polyethylenimine on the dispersion and electrophoretic deposition of nano-sized titania aqueous suspensions, *Journal of the European Ceramic Society*, 26 (2006) 1555-1560.
- [231] J. Yoshikawa, J.A. Lewis, B.W. Chun, Comb Polymer Architecture, Ionic Strength, and Particle Size Effects on the BaTiO<sub>3</sub> Suspension Stability, *Journal of the American Ceramic Society*, 92 (2009) S42-S49.
- [232] K. Prabhakaran, C.S. Kumbhar, S. Raghunath, N.M. Gokhale, S.C. Sharma, Effect of Concentration of Ammonium Poly(acrylate) Dispersant and MgO on Coagulation Characteristics of Aqueous Alumina Direct Coagulation Casting Slurries, *Journal of the American Ceramic Society*, 91 (2008) 1933-1938.
- [233] F. Nsib, N. Ayed, Y. Chevalier, Dispersion of hematite suspensions with sodium polymethacrylate dispersants in alkaline medium, *Colloids and Surfaces A: Physicochemical and Engineering Aspects*, 286 (2006) 17-26.
- [234] I.A. Rahman, V. Padavettan, Synthesis of silica nanoparticles by sol-gel: size-dependent properties, surface modification, and applications in silica-polymer nanocomposites &#8212; a review, *J. Nanomaterials*, 2012 (2012) 8-8.

- [235] T. von Werne, T.E. Patten, Atom Transfer Radical Polymerization from Nanoparticles: A Tool for the Preparation of Well-Defined Hybrid Nanostructures and for Understanding the Chemistry of Controlled/"Living" Radical Polymerizations from Surfaces, *Journal of the American Chemical Society*, 123 (2001) 7497-7505.
- [236] G. Kikelbick, Concepts for the incorporation of inorganic building blocks into organic polymers on a nanoscale, *Progress in Polymer Science*, 28 (2003) 83-114.
- [237] S. Kang, S.I. Hong, C.R. Choe, M. Park, S. Rim, J. Kim, Preparation and characterization of epoxy composites filled with functionalized nanosilica particles obtained via sol-gel process, *Polymer*, 42 (2001) 879-887.
- [238] B. Wei, S. Song, H. Cao, Strengthening of basalt fibers with nano-SiO<sub>2</sub>-epoxy composite coating, *Materials & Design*, 32 (2011) 4180-4186.
- [239] Y. Sun, Z. Zhang, C.P. Wong, Study on mono-dispersed nano-size silica by surface modification for underfill applications, *Journal of Colloid and Interface Science*, 292 (2005) 436-444.
- [240] R.P. Bagwe, L.R. Hilliard, W. Tan, Surface modification of silica nanoparticles to reduce aggregation and non-specific binding, *Langmuir : the ACS journal of surfaces and colloids*, 22 (2006) 4357-4362.
- [241] Y.-Y. Yu, C.-Y. Chen, W.-C. Chen, Synthesis and characterization of organic-inorganic hybrid thin films from poly(acrylic) and monodispersed colloidal silica, *Polymer*, 44 (2003) 593-601.
- [242] A. Liberman, N. Mendez, W.C. Trogler, A.C. Kummel, Synthesis and surface functionalization of silica nanoparticles for nanomedicine, *Surface science reports*, 69 (2014) 132-158.
- [243] R.Y. Hong, J.H. Li, L.L. Chen, D.Q. Liu, H.Z. Li, Y. Zheng, J. Ding, Synthesis, surface modification and photocatalytic property of ZnO nanoparticles, *Powder Technology*, 189 (2009) 426-432.
- [244] A. Ulman, Formation and Structure of Self-Assembled Monolayers, *Chemical Reviews*, 96 (1996) 1533-1554.
- [245] C.-P. Tsai, C.-Y. Chen, Y. Hung, F.-H. Chang, C.-Y. Mou, Monoclonal antibody-functionalized mesoporous silica nanoparticles (MSN) for selective targeting breast cancer cells, *Journal of Materials Chemistry*, 19 (2009) 5737-5743.
- [246] J.T. Park, J.A. Seo, S.H. Ahn, J.H. Kim, S.W. Kang, Surface modification of silica nanoparticles with hydrophilic polymers, *Journal of Industrial and Engineering Chemistry*, 16 (2010) 517-522.
- [247] P. Larkin, *Infrared and Raman Spectroscopy: Principles and Spectral Interpretation*, Elsevier, 2011.
- [248] A. Subramanian, L. Rodriguez-Saona, Chapter 7 - Fourier Transform Infrared (FTIR) Spectroscopy A2 - Sun, Da-Wen, in: *Infrared Spectroscopy for Food Quality Analysis and Control*, Academic Press, San Diego, 2009, pp. 145-178.
- [249] B.H. Stuart, *Infrared Spectroscopy: Fundamentals and Application*, John Wiley & Sons, Ltd, 2004.
- [250] M. Tasumi, *Introduction to Experimental Infrared Spectroscopy: Fundamentals and Practical Methods*, Wiley, 2014.
- [251] B.C. Smith, *Fundamentals of Fourier Transform Infrared Spectroscopy*, Second Edition, CRC Press, 2011.
- [252] S.J.L.B. R.E. Dinnebier, A. Le Bail, Ian Madsen, L.M.D. Cranswick, *Powder Diffraction: Theory and Practice*, Royal Society of Chemistry, 2008.
- [253] J. Epp, 4 - X-ray diffraction (XRD) techniques for materials characterization, in: *Materials Characterization Using Nondestructive Evaluation (NDE) Methods*, Woodhead Publishing, 2016, pp. 81-124.

- [254] E.M. Yoshio Waseda, Kozo Shinoda, X-Ray Diffraction Crystallography\_ Introduction, Examples and Solved Problems, Springer, Verlag Berlin Heidelberg 2011.
- [255] H. Seyama, M. Soma, B.K.G. Theng, Chapter 12.4 X-ray Photoelectron Spectroscopy, in: B.K.G.T. Faïza Bergaya, L. Gerhard (Eds.) Developments in Clay Science, Elsevier, 2006, pp. 865-878.
- [256] H. Bluhm, 4 - X-ray photoelectron spectroscopy (XPS) for in situ characterization of thin film growth, in: In Situ Characterization of Thin Film Growth, Woodhead Publishing, 2011, pp. 75-98.
- [257] H. Seyama, M. Soma, B.K.G. Theng, Chapter 2.5 - X-Ray Photoelectron Spectroscopy, in: B. Faïza, L. Gerhard (Eds.) Developments in Clay Science, Elsevier, 2013, pp. 161-176.
- [258] B.J. Inkson, 2 - Scanning electron microscopy (SEM) and transmission electron microscopy (TEM) for materials characterization, in: Materials Characterization Using Nondestructive Evaluation (NDE) Methods, Woodhead Publishing, 2016, pp. 17-43.
- [259] C.W. Oatley, D. McMullan, K.C.A. Smith, The Development of the Scanning Electron Microscope A2 - Hawkes, Peter W, in: The Beginnings of Electron Microscopy, Academic Press, 1985, pp. 443-482.
- [260] A. Yoshida, Y. Kaburagi, Y. Hishiyama, Chapter 5 - Scanning Electron Microscopy A2 - Inagaki, Michio, in: F. Kang (Ed.) Materials Science and Engineering of Carbon, Butterworth-Heinemann, 2016, pp. 71-93.
- [261] L.C. Xu, C.A. Siedlecki, 3.302 - Atomic Force Microscopy A2 - Ducheyne, Paul, in: Comprehensive Biomaterials, Elsevier, Oxford, 2011, pp. 23-35.
- [262] G. Binnig, H. Rohrer, Surface imaging by scanning tunneling microscopy, Ultramicroscopy, 11 (1983) 157-160.
- [263] M.K. Khan, Q.Y. Wang, M.E. Fitzpatrick, 1 - Atomic force microscopy (AFM) for materials characterization, in: Materials Characterization Using Nondestructive Evaluation (NDE) Methods, Woodhead Publishing, 2016, pp. 1-16.
- [264] M. Duman, I. Neundlinger, R. Zhu, J. Preiner, C. Lamprecht, L.A. Chtcheglova, C. Rankl, T. Puntheeranurak, A. Ebner, P. Hinterdorfer, 2.7 Atomic Force Microscopy A2 - Egelman, Edward H, in: Comprehensive Biophysics, Elsevier, Amsterdam, 2012, pp. 111-143.
- [265] A.W. Coats, J.P. Redfern, Thermogravimetric analysis. A review, Analyst, 88 (1963) 906-924.
- [266] W. Nernst, E.H. Riesenfeld, Ueber quantitative Gewichtsanalyse mit sehr kleinen Substanzmengen, Berichte der deutschen chemischen Gesellschaft, 36 (1903) 2086-2093.
- [267] J. Czarnecki, J. Sestak, From recording balances to thermogravimetric instruments and back, Journal of Thermal Analysis and Calorimetry, 120 (2015) 157-166.
- [268] H.J. Moltzan, 22 - Thermogravimetric Analysis (TGA), in: Characterization of Integrated Circuit Packaging Materials, Newnes, Boston, 1993, pp. 250-251.
- [269] W.M. Groenewoud, Chapter 1 - Differential scanning calorimetry, in: Characterisation of Polymers by Thermal Analysis, Elsevier Science B.V., Amsterdam, 2001, pp. 10-60.
- [270] P. Zhou, T.P. Labuza, Analytical Methods | Differential Scanning Calorimetry A2 - Fuquay, John W, in: Encyclopedia of Dairy Sciences (Second Edition), Academic Press, San Diego, 2011, pp. 256-263.
- [271] M. Griepentrog, C. Ullner, A. Dück, Instrumented indentation test for hardness and materials parameter from millinewtons to kilonewtons, in: Proceedings of the International Conference on Force, Mass, Torque, Hardness and Civil Engineering Metrology in the Age Globalization, VDI-Verl., Düsseldorf, 2002, pp. 105-111.

- [272] L.L.S. D.G. Enos, The Potentiodynamic Polarization Scan, in, Solartron Instruments a division of Solartron Group Ltd, UK, 1997.
- [273] G. instruments, Quantitative Corrosion Theory, in, Gamry instruments, 2018.
- [274] T. Ohtsuka, A. Nishikata, M. Sakairi, K. Fushimi, Electrochemistry for Corrosion Fundamentals, Springer Singapore, 2017.
- [275] A. Lasia, Electrochemical Impedance Spectroscopy and its Applications, 1 ed., Springer-Verlag New York, 2014.
- [276] O. Heaviside, Electrical Papers, MacMillan, New York, 1894.
- [277] B.T. Mark E. Orazem, Electrochemical Impedance Spectroscopy, Wiley, 2008.
- [278] J.R. Macdonald, Impedance spectroscopy, Annals of Biomedical Engineering, 20 (1992) 289-305.
- [279] A. Amirudin, D. Thieny, Application of electrochemical impedance spectroscopy to study the degradation of polymer-coated metals, Progress in Organic Coatings, 26 (1995) 1-28.
- [280] G. instruments, Basics of Electrochemical Impedance Spectroscopy, in, 2010.
- [281] R. Serra, Weathering resistance of thin plasma polymer films on pre-coated steel in: Departamento de Engenharia de Materiais e Cerâmica, University of Aveiro, Aveiro, 2010, pp. 231.
- [282] D.D. Macdonald, M. Urquidi-Macdonald, Application of Kramers-Kronig Transforms in the Analysis of Electrochemical Systems: I . Polarization Resistance, Journal of The Electrochemical Society, 132 (1985) 2316-2319.
- [283] W.M. Bos, Prediction of coating durability - Early detection using electrochemical methods, Tom Bos, 2008.
- [284] G.W. Walter, The application of impedance spectroscopy to study the uptake of sodium chloride solution in painted metals, Corrosion Science, 32 (1991) 1041-1058.
- [285] P. Marcus, F.B. Mansfeld, Analytical Methods In Corrosion Science and Engineering, CRC Press, 2005.
- [286] H.S. Isaacs, The measurement of the galvanic corrosion of soldered copper using the scanning vibrating electrode technique, Corrosion Science, 28 (1988) 547-558.
- [287] A.C. Bastos, S.A.S. Dias, T.C. Diamantino, M.y.S. Ferreira, Uma introdução à técnica svet, Corrosão e Protecção de Materiais, 32 (2013) 50-57.
- [288] M.C. Capel-Sanchez, L. Barrio, J.M. Campos-Martin, J.L.G. Fierro, Silylation and surface properties of chemically grafted hydrophobic silica, Journal of Colloid and Interface Science, 277 (2004) 146-153.
- [289] S.K. Yun, T.J. Pinnavaia, Water Content and Particle Texture of Synthetic Hydrotalcite-like Layered Double Hydroxides, Chemistry of Materials, 7 (1995) 348-354.
- [290] C. Barriga, W. Jones, P. Malet, V. Rives, M.A. Ulibarri, Synthesis and characterization of polyoxovanadate-pillared Zn-Al layered double hydroxides: An x-ray absorption and diffraction study, Inorganic Chemistry, 37 (1998) 1812-1820.
- [291] J. Das, D. Das, K.M. Parida, Preparation and characterization of Mg-Al hydrotalcite-like compounds containing cerium, Journal of Colloid and Interface Science, 301 (2006) 569-574.
- [292] K. Verschuere, Handbook of Environmental Data on Organic Chemicals, Second Edition ed., Van Nostrand Reinhold Ltd, New York, 1977.
- [293] A.K.S. Rai, R.; Singh, K. N.; Singh, V. B., FTIR, Raman spectra and ab initio calculations of 2-mercaptobenzothiazole, Spectrochimica Acta Part a-Molecular and Biomolecular Spectroscopy, 63 (2006) 483-490.
- [294] M.R. Waterland, A.M. Kelley, Far-ultraviolet resonance Raman spectroscopy of nitrate ion in solution, The Journal of Chemical Physics, 113 (2000) 6760-6773.

- [295] A.N. Salak, J. Tedim, A.I. Kuznetsova, J.L. Ribeiro, L.G. Vieira, M.L. Zheludkevich, M.G.S. Ferreira, Comparative X-ray diffraction and infrared spectroscopy study of Zn–Al layered double hydroxides: Vanadate vs nitrate, *Chemical Physics*, 397 (2012) 102-108.
- [296] T. Tanaka, Y. Kameshima, S. Nishimoto, M. Miyake, Determination of carbonate ion contents in layered double hydroxides by FTIR spectrometry, *Analytical Methods*, 4 (2012) 3925-3927.
- [297] F.Z. Mahjoubi, A. Khalidi, M. Abdennouri, N. Barka, Zn–Al layered double hydroxides intercalated with carbonate, nitrate, chloride and sulphate ions: Synthesis, characterisation and dye removal properties, *Journal of Taibah University for Science*, 11 (2017) 90-100.
- [298] S.V. Lamaka, D.G. Shchukin, D.V. Andreeva, M.L. Zheludkevich, H. Möhwald, M.G.S. Ferreira, Sol-Gel/Polyelectrolyte Active Corrosion Protection System, *Adv. Funct. Mater.*, 18 (2008) 3137-3147.
- [299] S.-H. Lin, S.-M. Lai, C.-M. Lin, C.-W. Chou, C.-H. Lee, Preparation and characterization of polystyrene sulfonic acid-co-maleic acid copolymer modified silica nanoparticles, *Journal of Polymer Research*, 23 (2016) 44.
- [300] Q. Dai, X. Wang, G. Chen, Y. Zheng, G. Lu, Direct synthesis of Cerium(III)-incorporated SBA-15 mesoporous molecular sieves by two-step synthesis method, *Microporous and Mesoporous Materials*, 100 (2007) 268-275.
- [301] M. Chelliah, J.B.B. Rayappan, U.M. Krishnan, Synthesis and Characterization of Cerium Oxide Nanoparticles by Hydroxide Mediated Approach, *Journal of Applied Sciences*, 12 (2012) 1734-1737.
- [302] N. Nesakumar, S. Sethuraman, U.M. Krishnan, J.B.B. Rayappan, Fabrication of lactate biosensor based on lactate dehydrogenase immobilized on cerium oxide nanoparticles, *Journal of Colloid and Interface Science*, 410 (2013) 158-164.
- [303] A. Kotani, H. Ogasawara, Theory of core-level spectroscopy of rare-earth oxides, *Journal of Electron Spectroscopy and Related Phenomena*, 60 (1992) 257-299.
- [304] S. Sharma, M.S. Hegde, Pt metal-CeO<sub>2</sub> interaction: Direct observation of redox coupling between Pt<sup>0</sup>/Pt<sup>2+</sup>/Pt<sup>4+</sup> and Ce<sup>4+</sup>/Ce<sup>3+</sup> states in Ce<sub>0.98</sub>Pt<sub>0.02</sub>O<sub>2-δ</sub> catalyst by a combined electrochemical and x-ray photoelectron spectroscopy study, *The Journal of Chemical Physics*, 130 (2009) 114706.
- [305] L. Katta, P. Sudarsanam, G. Thrimurthulu, B.M. Reddy, Doped nanosized ceria solid solutions for low temperature soot oxidation: Zirconium versus lanthanum promoters, *Applied Catalysis B: Environmental*, 101 (2010) 101-108.
- [306] K. Glinel, C. Déjugnat, M. Prevot, B. Schöler, M. Schönhoff, R.v. Klitzing, Responsive polyelectrolyte multilayers, *Colloids and Surfaces A: Physicochemical and Engineering Aspects*, 303 (2007) 3-13.
- [307] Y. Zhou, X. Sun, K. Zhong, D.G. Evans, Y. Lin, X. Duan, Control of Surface Defects and Agglomeration Mechanism of Layered Double Hydroxide Nanoparticles, *Industrial & Engineering Chemistry Research*, 51 (2012) 4215-4221.
- [308] J.B. Swadling, J.L. Suter, H.C. Greenwell, P.V. Coveney, Influence of Surface Chemistry and Charge on Mineral-RNA Interactions, *Langmuir*, 29 (2013) 1573-1583.
- [309] S. Patil, A. Sandberg, E. Heckert, W. Self, S. Seal, Protein adsorption and cellular uptake of cerium oxide nanoparticles as a function of zeta potential, *Biomaterials*, 28 (2007) 4600-4607.
- [310] J.A. Hiller, M.F. Rubner, Reversible Molecular Memory and pH-Switchable Swelling Transitions in Polyelectrolyte Multilayers, *Macromolecules*, 36 (2003) 4078-4083.

- [311] J. A. J. Aldykiewicz, A.J. Davenport, H.S. Isaacs, Studies of the Formation of Cerium-Rich Protective Films Using X-Ray Absorption Near-Edge Spectroscopy and Rotating Disk Electrode Methods, *Journal of The Electrochemical Society*, 143 (1996) 147-154.
- [312] B. Davó, J.J. de Damborenea, Use of rare earth salts as electrochemical corrosion inhibitors for an Al–Li–Cu (8090) alloy in 3.56% NaCl, *Electrochimica Acta*, 49 (2004) 4957-4965.
- [313] A. Aballe, M. Bethencourt, F.J. Botana, M. Marcos, CeCl<sub>3</sub> and LaCl<sub>3</sub> binary solutions as environment-friendly corrosion inhibitors of AA5083 Al–Mg alloy in NaCl solutions, *Journal of Alloys and Compounds*, 323–324 (2001) 855-858.
- [314] M.A. Arenas, M. Bethencourt, F.J. Botana, J. de Damborenea, M. Marcos, Inhibition of 5083 aluminium alloy and galvanised steel by lanthanide salts, *Corrosion Science*, 43 (2001) 157-170.
- [315] B.A. Bilal, E.Z. Muller, Thermodynamic study of cerium(4+)/cerium(3+) redox reaction in aqueous solution at elevated temperatures. Reduction potential and hydrolysis equilibria of cerium(4+) in perchloric acid solutions *Naturforschung A: Physical Sciences*, 47 (1992) 974-984.
- [316] E. Barsoukov, J.R. Macdonal, *Impedance Spectroscopy*, 2<sup>nd</sup> ed., Wiley Interscience, New Jersey, 2005.
- [317] A.C. Bastos, M.L. Zheludkevich, M.G.S. Ferreira, Concerning the Efficiency of Corrosion Inhibitors as Given by SVET, *Port. Electrochim. Acta*, 26 (2008) 47-54.
- [318] I.A. Kartsonakis, A.C. Balaskas, G.C. Kordas, Influence of cerium molybdate containers on the corrosion performance of epoxy coated aluminium alloys 2024-T3, *Corrosion Science*, 53 (2011) 3771-3779.
- [319] B. Chico, J.C. Galván, D. de la Fuente, M. Morcillo, Electrochemical impedance spectroscopy study of the effect of curing time on the early barrier properties of silane systems applied on steel substrates, *Progress in Organic Coatings*, 60 (2007) 45-53.
- [320] L. Claire, G. Marie, G. Julien, S. Jean-Michel, R. Jean, M. Marie-Joëlle, R. Stefano, F. Michele, New architected hybrid sol-gel coatings for wear and corrosion protection of low-carbon steel, *Progress in Organic Coatings*, 99 (2016) 337-345.
- [321] A. Franquet, C. Le Pen, H. Terry, J. Vereecken, Effect of bath concentration and curing time on the structure of non-functional thin organosilane layers on aluminium, *Electrochimica Acta*, 48 (2003) 1245-1255.
- [322] M.Y. Ghotbi, M.Z.b. Hussein, A.H. Yahaya, M.Z.A. Rahman, LDH-intercalated d-gluconate: Generation of a new food additive-inorganic nanohybrid compound, *J. Phys. Chem. Solids*, 70 (2009) 948-954.
- [323] D.P.I. Nikolić V.D., L. B. Nikolić, L. P. Stanojević, M. D. Cakić, A. D. Tačić, S. S. Ilić-Stojanović, The synthesis and characterization of iron(II): Gluconate, *Savremene tehnologije*, 3 (2014) 16-24.
- [324] M. Ibrahim, A. Nada, D.E. Kamal, Density functional theory and FTIR spectroscopic study of carboxyl group, *Indian J. Pure Appl. Phys.* 43 (2005) 911-917.
- [325] E. Kanazaki, K. Kinugawa, Y. Ishikawa, Conformation of intercalated aromatic molecular anions between layers of Mg/Al- and Zn/Al-hydrotalcites, *Chemical Physics Letters*, 226 (1994) 325-330.
- [326] S. Velu, V. Ramkumar, A. Narayanan, C.S. Swamy, Effect of interlayer anions on the physicochemical properties of zinc–aluminium hydrotalcite-like compounds, *Journal of Materials Science*, 32 (1997) 957-964.
- [327] T.L.P. Galvão, C.S. Neves, A.P.F. Caetano, F. Maia, D. Mata, E. Malheiro, M.J. Ferreira, A.C. Bastos, A.N. Salak, J.R.B. Gomes, J. Tedim, M.G.S. Ferreira, Control of crystallite and particle size in the synthesis of layered double hydroxides:

- Macromolecular insights and a complementary modeling tool, *Journal of Colloid and Interface Science*, 468 (2016) 86-94.
- [328] H. Daemi, M. Barikani, Synthesis and characterization of calcium alginate nanoparticles, sodium homopolymannuronate salt and its calcium nanoparticles, *Scientia Iranica*, 19 (2012) 2023-2028.
- [329] M. Ibrahim, A. Nada, D.E. Kamal, Density functional theory and FTIR spectroscopic study of carboxyl group, *Indian Journal of Pure & Applied Physics*, 43 (2005) 911-917.
- [330] V. Wernert, R. Denoyel, Adsorption of styrene sulfonate from aqueous solutions onto carbon fibers and mesoporous carbon, *Microporous and Mesoporous Materials*, 222 (2016) 247-255.
- [331] U.A. Shinde, M.S. Nagarsenker, Characterization of Gelatin-Sodium Alginate Complex Coacervation System, *Indian Journal of Pharmaceutical Sciences*, 71 (2009) 313-317.
- [332] A.A. Antipov, G.B. Sukhorukov, H. Möhwald, Influence of the Ionic Strength on the Polyelectrolyte Multilayers' Permeability, *Langmuir*, 19 (2003) 2444-2448.
- [333] F.A.H. Franco, Upscaling challenges for LDH-containing active protection coatings, in: *Department of Materials Engineering and Ceramics*, University of Aveiro, Aveiro, Portugal, 2013, pp. 92.
- [334] M.L.Z. A. C. Bastos, M. G. S. Ferreira, Concerning the Efficiency of Corrosion Inhibitors as Given by SVET, *Portugaliae Electrochimica Acta*, 26 (2008) 47-54.
- [335] N.R.E.N. Impens, P. van der Voort, E.F. Vansant, Silylation of micro-, meso- and non-porous oxides: a review, *Microporous and Mesoporous Materials*, 28 (1999) 217-232.
- [336] I.A. Rahman, M. Jafarzadeh, C.S. Sipaut, Synthesis of organo-functionalized nanosilica via a co-condensation modification using  $\gamma$ -aminopropyltriethoxysilane (APTES), *Ceramics International*, 35 (2009) 1883-1888.
- [337] F. Maia, J. Tedim, A.C. Bastos, M.G.S. Ferreira, M.L. Zheludkevich, Active sensing coating for early detection of corrosion processes, *RSC Advances*, 4 (2014) 17780-17786.
- [338] X. Li, Z. Cao, Z. Zhang, H. Dang, Surface-modification in situ of nano-SiO<sub>2</sub> and its structure and tribological properties, *Applied Surface Science*, 252 (2006) 7856-7861.
- [339] J. Zhao, M. Milanova, M.M.C.G. Warmoeskerken, V. Dutschk, Surface modification of TiO<sub>2</sub> nanoparticles with silane coupling agents, *Colloids and Surfaces A: Physicochemical and Engineering Aspects*, 413 (2012) 273-279.
- [340] S. Pazokifard, S.M. Mirabedini, M. Esfandeh, M. Mohseni, Z. Ranjbar, Silane grafting of TiO<sub>2</sub> nanoparticles: dispersibility and photoactivity in aqueous solutions, *Surface and Interface Analysis*, 44 (2012) 41-47.
- [341] A. Mirabedini, S.M. Mirabedini, A.A. Babalou, S. Pazokifard, Synthesis, characterization and enhanced photocatalytic activity of TiO<sub>2</sub>/SiO<sub>2</sub> nanocomposite in an aqueous solution and acrylic-based coatings, *Progress in Organic Coatings*, 72 (2011) 453-460.
- [342] W. Luo, Q.-m. Feng, L.-m. Ou, K. Liu, Surface modification of magnesium hydroxide by  $\gamma$ -aminopropyltriethoxysilane, *Journal of Central South University of Technology*, 15 (2008) 318-323.
- [343] I.R. Fontinha, M.M. Salta, M.L. Zheludkevich, M.G.S. Ferreira, EIS Study of Amine Cured Epoxy-silica-zirconia Sol-gel Coatings for Corrosion Protection of the Aluminium Alloy EN AW 6063, *Portugaliae Electrochimica Acta*, 31 (2013) 307-319.
- [344] M. Iijima, H. Kamiya, Surface Modification for Improving the Stability of Nanoparticles in Liquid Media, *Kona Powder and Particle Journal*, (2009) 119-129.

- [345] Z. Luo, X. Cai, R.Y. Hong, L.S. Wang, W.G. Feng, Preparation of silica nanoparticles using silicon tetrachloride for reinforcement of PU, *Chemical Engineering Journal*, 187 (2012) 357-366.
- [346] M. Ba, Z. Zhang, Y. Qi, The Dispersion Tolerance of Micro/Nano Particle in Polydimethylsiloxane and Its Influence on the Properties of Fouling Release Coatings Based on Polydimethylsiloxane, *Coatings*, 7 (2017) 107.
- [347] S. Sprenger, Epoxy resins modified with elastomers and surface-modified silica nanoparticles, *Polymer*, 54 (2013) 4790-4797.
- [348] A. Schieweck, M.-C. Bock, Emissions from low-VOC and zero-VOC paints – Valuable alternatives to conventional formulations also for use in sensitive environments?, *Building and Environment*, 85 (2015) 243-252.
- [349] M.S. Kamal, S.A. Razzak, M.M. Hossain, Catalytic oxidation of volatile organic compounds (VOCs) – A review, *Atmospheric Environment*, 140 (2016) 117-134.